Dissertation
submitted to the
Combined Faculties for the Natural Sciences and for Mathematics
of the Ruperto-Carola University of Heidelberg, Germany
for the degree of
Doctor of Natural Sciences

put forward by
Dipl.-Phys. Johannes Lampel
born in Henstedt-Ulzburg

Date of oral examination: 24.07.2014

Measurements of reactive trace gases in the marine boundary layer using novel DOAS methods

Referees: Prof. Dr. Ulrich Platt
Prof. Dr. Bernd Jähne

Abstract Reactive Halogen Species (RHS) can have a large impact on tropospheric chemistry. Already small concentrations in the marine boundary layer (MBL) can have a significant impact on the global budget of ozone and other trace-gases.
Shipborne measurements of BrO and IO were conducted in the MBL from 70°S to 90°N to obtain a global picture of their distribution over several years. A focus were upwelling regions, which can provide large amounts of precursor substances for RHS in the MBL, of which some were measured simultaneously by project partners. Measurements in the tropical Atlantic showed BrO concentrations below 2 ppt in agreement with previous observations. IO was detected with concentrations of up to 1 ppt, its distribution was found to correlate with surface water iodide concentrations. In the Peruvian upwelling region MAX-DOAS and CE-DOAS measurements showed agreeing surface VMR of up to 1.4 ppt. The MAX-DOAS retrieval agreed with previous satellite observations of IO in this region. For polar measurements, background concentrations of IO of 0.2–0.4 ppt during the respective summer period were observed. An additional source of reactive bromine in the MBL was observed for the first time from the ground: Polar air-masses were observed south of the Azores yielding BrO concentrations of 4–6 ppt. Glyoxal was not found in the remote MBL of the tropical Atlantic and Pacific above a detection limit of 35 ppt. Relative water vapour absorption band strengths in the wavelength interval from 400-480 nm were analysed systematically and correction factors from 0.5–2 were found, leading to improvements of the spectral retrieval. Vibrational Raman scattering of N_2 and O_2 was quantified for the first time in MAX-DOAS measurements, yielding a reduction of up to 30% of IO measurement errors.

Zusammenfassung Reaktive Halogenverbindungen (RHV) können einen großen Einfluss auf die troposphärische Chemie haben. Schon kleine Konzentrationen in the marinen Grenzschicht (MBL) können das globale Budget von Ozon und anderen Spurengasen signifikant beeinflussen. Schiffsgestützte Messungen dieser Spurengase wurden über mehrere Jahre von 70°S bis 90°N in der MBL durchgeführt um ihre globale Verteilung zu bestimmen. Ein Fokus waren Auftriebsgebiete, da diese große Mengen Vorgängersubstanzen emittieren können, die von Projektpartnern gemessen wurden. Messungen in der tropischen MBL ergaben weniger als 2 ppt BrO wie schon vorherige Beobachtungen. IO Konzentrationen bis zu einem ppt wurden gemessen, die mit der Oberflächenwasseriodidkonzentration korrelierten. Im peruanischen Auftriebsgebiet zeigten MAX-DOAS and CE-DOAS übereinstimmende IO-Konzentrationen von bis 1.4 ppt. MAX-DOAS Messungen stimmten mit vorhergehenden Satellitenbeobachtungen überein. Polare Hintergrundkonzentrationen im Sommer von 0.2-0.4ppt IO wurden beobachtet. Eine zusätzliche Bromquelle für die MBL durch Transport von polarer Luft wurde südlich der Azoren beobachtet und führte dort zu BrO Konzentrationen von 4–6 ppt. Glyoxal wurde weder im tropischen Atlantik noch Pazifik oberhalb der Nachweisgrenze von 35 ppt gefunden. Um die Nachweisgrenzen von RHS zu minimieren, wurden relative Wasserdampfabsorptionsbandenstärken analysiert und Korrekturfaktoren von 0.5–2 gefunden. Die Größe des Einflusses von Vibrationsramanstreuung an N_2/O_2 auf MAX-DOAS Messungen wurde bestimmt und führte zu einer Reduktion des Messfehlers von IO von bis zu 30%.

Contents

0. Motivation

The atmosphere of the Earth protects the biosphere by absorbing harmful radiation and it is furthermore responsible for maintaining an average temperature on the surface above the freezing point of water by the natural greenhouse effect. This allows for a complex evolution of life.
Stable and long-lived systems are usually found in a type of equilibrium, allowing for small perturbations without significant consequences. To some extent, this is also the case for the atmosphere. Understanding the stabilizing feedback mechanisms requires knowledge of all relevant driving factors. Once the unperturbed system is understood, the influence of changing boundary conditions of the system can be evaluated, such as the influence of anthropogenic emissions and/or climate change.
For instance, ozone plays a central compound in atmospheric chemistry, both in the stratosphere, where it protects Earth from UV radiation in the ozone layer, as well as in the troposphere, where it has a major influence on the overall oxidation capacity. It acts as a tropospheric greenhouse gas and is a major source of OH radicals, which react with many pollutants and other trace gases. But the ozone concentration itself is also influenced by other trace gases. Among these, halogen containing compounds and halogens itself play an important role. They can take part in auto-catalytic destruction mechanisms, i.e. large amounts of ozone can be destroyed before the halogen species itself are deposited.
The release processes of halogen compounds and their respective strengths are not well understood, neither is their global distribution well known. Due to their high reactivity, already small background concentrations can have a significant influence on ozone chemistry.
Both, bromine and iodine can influence cloud-condensation nuclei production in the marine boundary layer and can therefore modify the radiative forcing of the MBL.
One of the sources of halogen compounds is the Ocean. Due to its vast surface area, small fluxes can have a significant influence on ozone chemistry. Halogen compounds can be directly emitted at the sea surface by sea spray particles, produced from precursor gases and reactions at the sea surface. Hotspots on a global map for emissions of halogens are upwelling regions, which can emit large amounts of halogenated hydrocarbons. Nutrient-rich deep water arrives here at the ocean's surface and induces a high bio-productivity. A product of the metabolism of certain phytoplankton and macro-algae can be halogenated hydrocarbons, which are eventually photolysed after their release to the atmosphere. Their photochemical degradation leads to the production of reactive halogen species (RHS), of which measurements in the troposphere are presented in this thesis. Due to their high reactivity it is necessary to measure them directly within the atmosphere by in-situ or remote-sensing techniques.
Previous measurements in the MBL were conducted at different locations, several on

Cape Verde in the tropical Atlantic. The location for measurements of BrO and IO on Cape Verde was chosen since it it was assumed that this location is representative for open ocean conditions. Diurnal cycles of several ppt[1] of BrO and 1-2 ppt IO were observed by Read et al. [2008b], who estimated the total ozone loss due to halogens during the day to contribute up to 50% of the total ozone loss in that region. Similar measurements performed by Tschritter [2013] confirmed the clear detection of BrO in the MBL with a distinct diurnal cycle agreeing with chemistry models [Mahajan et al., 2010a], but could not detect IO at the previously reported concentrations. Furthermore halocarbon measurements on Cape Verde showed a significant difference to open ocean conditions. The observation that the observed chemistry on Cape Verde islands might not be representative for the tropical MBL implied the need for further investigations concerning the global distribution of these trace-gases.
The following measurements were performed:

1. MAX-DOAS measurements on R/V Polarstern, covering all latitudes on the Atlantic. These were performed by an automated instrument, requiring only a minimal amount of supervision.

2. Dedicated research cruises within the SOPRAN project, to obtain a more complete picture of marine halogen emissions combining different measurement techniques for a series of different trace gas species, within the MBL and within the Ocean. These campaigns were conducted in cooperation with project partners from SOPRAN and SHIVA.

3. Combination of measurements with cavity-enhanced and MAX-DOAS techniques to reduce uncertainties: Comparison of simultaneous measurements by both techniques. This allows to obtain reliable information of the vertical distribution of RHS in the troposphere.

4. Measurements outside the MBL for the identification of systematic evaluation difficulties: During a campaign in Mainz no significant amounts of tropospheric reactive halogen species were expected due to NO_x-chemistry. This allowed to test the spectral retrieval of these trace gases and identify systematic problems. Understanding and solving these issues improved the overall detection limits of RHS.

Due to the low concentrations of the respective compounds in the MBL, it is necessary to identify and minimize error sources, during the measurements as well as during evaluation. Previous studies indicated a possible influence on the data analysis from insufficiently accurate literature cross-sections for water vapour and the O_2-O_2 collision complex O_4 and additional restrictions due to insufficiently modelled inelastic scattering in the atmosphere were observed. These influences were quantified to allow for a reliable spectral retrieval of several trace-gases.
The campaign on *R/V Maria S. Merian* (2011) and on *R/V Meteor* M91 (2012) [Bange, 2013] were organized within the Surface Ocean Processes in the Antropocene (SOPRAN)

[1] parts per trillion ($1 : 10^{12}$)

project[2], a joint project funded by the Bundesministerium für Bildung und Forschung (BMBF) and the German national branch of the internal Surface Ocean Lower Atmosphere Studies (SOLAS) programme. DOAS measurements on-board *R/V Polarstern* since 2009 complemented these measurement campaigns to obtain a better overview about the latitudinal distribution of reactive trace gases along the Atlantic from the Arctic to Antarctica. Data from TransBrom [Krüger and Quack, 2013] was also included in some plots, provided by Katja Großmann [Großmann et al., 2013]. It was partly funded by the national WGL project TransBrom. The ship campaign on *R/V Sonne* was supported by the BMBF (German Federal Ministry of Education and Research) through grant 03G0731A and supported by the SOPRAN and SHIVA projects.

0.1. Outline

The relevant and basic mechanisms of atmospheric chemistry and physics are discussed in chapter 1 with an emphasis on Reactive Halogen Specie (RHS) (here: iodine and bromine monoxide) as well as other reactive trace gases which can have an influence on the chemistry within the Marine Boundary Layer (MBL).
The chemistry within the MBL interacts strongly via heat and trace-gas fluxes with the Ocean, therefore chapter 2 treats some properties of the Oceans with a focus on upwelling regions. These can have a large influence on atmospheric chemistry due to their high bio-productivity and trace-gas fluxes.
In chapter 3 the Differential Optical Absorption Spectroscopy (DOAS) measurement technique is described, which was used for measurements presented in this thesis. Methods for measurement error analysis and estimation are presented.
In this thesis no new DOAS-instrument was built, therefore chapter 4 only briefly covers the instruments used during different measurement campaigns and the necessary technical modifications.
Because trace gases in the MBL are typically found at low concentrations and are therefore difficult to detect at all, chapter 5 discusses a series of influences on the results of analysing measurement spectra. Possible absorption cross-sections which are not accounted for by currently known absorption cross-sections are discussed and the accuracy of literature cross-sections estimated. In addition, the influence of Vibrational Raman Scattering (VRS) on MAX-DOAS measurements as a known effect from Raman spectroscopy is estimated and for the first time actually identified in measurement data.
During this thesis, a number of measurement campaigns not only in the MBL were conducted, using different DOAS instruments. Chapter 6 gives an overview over their respective locations, dates and employed instruments.
The measurement campaign SOPRAN M91 is presented in chapter 7. During this campaign different measurement techniques were combined to prove their consistency. Furthermore this campaign allows to characterize properties of the upwelling system and compare it to previous observations in other upwelling regions (MSM18, P399) and also Polarstern observations like ANT XXVIII:

[2]Förderkennzeichen *03F0662F*

The measurement campaign MSM18 took place in the subtropical and tropical Atlantic showing the most significant detection of bromine monoxide throughout all cruises within this thesis. The measurements presented in chapter 8 can be used furthermore to derive typical background concentrations in the tropical marine boundary layer for iodine and bromine oxide.
Chapter 9 shows MAX-DOAS data on the Polarstern transect ANT XXVIII along the Atlantic from Germany to South-Africa. These measurements allow for the estimation of the latitudinal variability of the measured trace-gases and aerosol optical densities. The Cape Verde Atmospheric Observatory is located close to the cruise track, allowing for the comparison with previous long-term observations.
Measurement data from the Arctic are shortly discussed in chapter 10 and measurements during the **M**ulti **A**xis **D**oas - **C**omparison campaign for **A**erosols and **T**race gases (MAD-CAT) campaign in Mainz are shown in chapter 11. The measurement data from this campaign was primarily used to compare it to measurements in the MBL to identify systematic limitations of the spectral retrieval of trace-gases from MAX-DOAS measurements.
The combined overall obtained measurements of the global distributions of certain gases are presented in chapter 12, compared to previous measurements. Their implications for tropospheric chemistry are discussed.
The results are summarized in chapter 13, together with an outlook on further developments, possibilities and measurement campaigns.
A short description of the SHIVA campaign was moved to the appendix as Chapter B, since the MAX-DOAS measurements failed due to technical problems and the CE-DOAS measurements did not achieve the necessary precision to gain information about the iodine monoxide concentration in the coastal MBL in South-East Asia.

1. Atmospheric Chemistry

Atmospheric chemistry is closely related to transport processes in the atmosphere. While the Planetary Boundary Layer (PBL) is well mixed in most cases, due to convection and turbulence, the stratosphere on the other hand side is more isolated, since its temperature profile inhibits mixing processes. This subdivision of the atmosphere separates layers, which then, due to their characteristic properties, also show characteristic behaviours regarding their dominant chemical reactions.

1.1. Structure of the Atmosphere

One way to subdivide the atmosphere into layers is according to the vertical temperature profile. Starting at the Earth's surface, it is divided into the troposphere, the stratosphere, the mesosphere and the thermosphere. Each of those is characterized by a gradient in temperature. Their boundaries are defined by extrema in the temperature profile.
In the troposphere the temperature decreases at a rate of $6 - 10°C/km$, depending on the air's humidity, mainly due to adiabatic expansion or compression. The dynamics of the troposphere are driven by the warming of the Earth's surface during the day and by radiative cooling of its upper part above $\approx 8km$. A temperature minimum is reached at about 16 km in the tropics at $\approx -80°C$ and at about 8 km in Polar Regions at $\approx -90°C$, the tropopause.
The stratosphere contains the ozone layer and is thus heated by solar UV radiation. The temperature rises with $2-5°C/km$ in heights starting at $8-18$ km to the stratopause in a height of ≈ 50 km. This temperature inversion strongly reduces air exchange of different heights and makes the stratosphere a stable layer with low convection and mixing. It is also dry, since water vapour already condenses at low temperatures at the lower end of the stratosphere / upper troposphere.
Above the stratopause, the mesosphere exhibits again a temperature decrease of $3°C/km$ in heights of ≈ 50 km to ≈ 85km, because despite high amounts of UV radiation ozone production is significantly lower than in the stratosphere due to lower pressure.

The pressure profile can be approximated by a simple Boltzmann distribution, neglecting temperature variations and assuming a constant gravitational constant over height.

$$p(z) = p_0 e^{(-z/z_0)} \text{ with } z_0 = \frac{k_B T}{m_{mol} g} \tag{1.1}$$

with p_0 being the surface pressure and z_0 the scale height of about 8.3 km at which the pressure dropped to 1/e of its surface value. g is here the gravitational acceleration, k_B the Boltzmann constant and m_{mol} the average molar mass.

Even though different molecules have different masses, the main part of the atmosphere is well-mixed (at least its long-lived constituents) and no separation can be observed. This shows that at large scale transport processes are dominant over kinetic processes of single molecules. Above $\approx 100km$, separation can be observed.
In tropical regions mixing can occur between the troposphere and the stratosphere via deep convection, a phenomenon which occurs when high clouds in tropical regions reach the tropopause. Due to this mechanism an exchange of lower stratospheric air with upper tropospheric air is possible. This allows for transport of various trace gases such as water vapour [Fueglistaler et al., 2005] into the stratosphere and also the transport of stratospheric ozone into the troposphere. E.g. about one percent of the total produced ozone from the stratosphere is transported to the troposphere, which is about $1.25 \cdot 10^9$ t/a [Roedel, 1992]. (Anthropogenic CO_2 emissions 2012 were about 10^{10} t C/a.)

1.1.1. Boundary Layer

The troposphere can then again be subdivided into the free troposphere and the Planetary Boundary Layer (PBL). The PBL characterized by being influenced by the Earth's surface, whereas the free troposphere is independent. Turbulence due to convection, wind and surface roughness leads to a mixing of the boundary layer. The height of the boundary layer varies depending on the solar energy input and the surface roughness between 50 m for Polar Regions and up to 2 km for tropical conditions.
Mainly two different types of boundary layer exist, the convective and the stable boundary layer. Whenever the underlying surface is colder than the air, the boundary layer becomes stratified and stable. For oceanic conditions typically to a stable, convective boundary layer during the day, limited in its height by an inversion layer, showing a positive gradient of potential temperature.
The limit of the boundary layer is object to various meteorological definitions and can be defined by an inversion layer on top of the boundary layer, a decrease in humidity or by a threshold of the bulk Richardson number, which describes the proportion of kinetic and potential energy. The measurement data for these calculations (Temperature, humidity, pressure) is usually provided by radiosondes as in Fuhlbrügge et al. [2013].
On the open ocean typical convective boundary layer heights in tropical regions are found around 1 km. In upwelling areas also stable boundary layers are observed with heights of less than 200m [Fuhlbrügge et al., 2013].

1.2. Composition and Distribution of Constituents

The atmosphere surrounding Earth consists mainly of nitrogen and oxygen, the other 1% is composed by gases listed in Table 1.1. Their overall mixing ratios are low, but their impact on atmospheric physics and chemistry can be important. Some of them, like carbon dioxide, methane and nitrous oxide, show absorption properties making them important factors in the overall radiative balance in the atmosphere. Others (e.g. nitrogen dioxide, OH-radical, chlorine radical) influence atmospheric chemistry already at low mixing ratios due to their high reactivity. These radical molecules or atoms are

responsible for effects like the polar ozone holes, smog, acid rain etc. and are less homogeneously distributed in the atmosphere as the main constituents of the atmosphere and the less reactive ones.

Name	Mixing ratio by volume
Nitrogen	78.1%
Oxygen	20.9%
Argon	0.93%
Carbon dioxide	400 ppm
Neon	18 ppm
Helium	5 ppm
Methane	1.7 ppm
Krypton	1.1 ppm
Hydrogen	0.55 ppm
Nitrous oxide	0.3 ppm
Xenon	0.09 ppm
Ozone	0 – 0.07 ppm
Nitrogen oxides	0.1 – 50 ppm
Sulphur compounds	0.1 – 100 ppb
Carbon monoxide	0.05 – 0.2 ppm
...	...

Table 1.1.: Some constituents of the lower atmosphere.

Table 1.2 shows a number of substances which are usually called Very Short-Lived Substance (VSLS) in the context of global change. These can contribute up to 25% of the total bromine input to the stratosphere via convection, but can also contribute to concentrations of reactive halogens the troposphere. In the 'Scientific Assessment of Ozone Depletion' by the World Meteorological Organisation [WMO, 2007] VSLS are defined as follows:

> Very short-lived substances (VSLS) are defined as trace gases whose local tropospheric lifetimes are comparable to, or shorter than, tropospheric transport time scales, such that their tropospheric distributions are non-uniform. In practice, VSLS are considered to have atmospheric lifetimes of less than 6 months. We consider only halogenated VSLS. [...]

These compounds can be precursors for reactive halogen species, once they are oxidized or photolysed in the atmosphere.
Especially interesting for atmospheric chemistry, but also for DOAS measurements are the compounds which absorb in the UV/VIS range (see also chapter 3). Due to their absorptions they can be excited or photolysed, enabling them to take an active part in atmospheric chemistry. Within the scope of this thesis the chemical reactions of the reactive halogen species BrO and IO and their influence on tropospheric ozone chemistry

Compound	tropospheric lifetime	source	typ. trop. conc. [ppt]
CH_3I	about 5 days	Rasmussen et al. [1982]	0.3-0.6
CH_3I	several days	V. Rattigan et al. [1997]	
CH_2I_2	several minutes	Yokouchi et al. [2014]	
CH_2ClI	several hours	V. Rattigan et al. [1997]	
C_2H_5I	several days	V. Rattigan et al. [1997]	
CF_3I	one day	V. Rattigan et al. [1997]	
$CHBr_2Cl$	50 days	Bilde et al. [1998]	40-50
$CHBr_3$	26 days	Organization [2003]	7-8
CH_2Br_2	120 days	Organization [2003]	1-3
CH_2Br_2	47 days	Mössinger et al. [1998]	
CH_3Br			0.5-1.5
$CHBrCl_2$	60 days	Bilde et al. [1998]	
$CHCl_3$	6 months	Khalil et al. [1983]	6
CH_2BrI	30 minutes	Mössinger et al. [1998]	2(?)
CH_2I_2	5 minutes	Mössinger et al. [1998]	

Table 1.2.: Some halogenated compounds and their approximate tropospheric lifetimes. Preliminary average atmospheric mixing ratios from SHIVA (Appendix B) are listed if available [Elliot-Atlas, SHIVA-data server] as examples for concentrations of the these compounds in a tropical coastal environment. (see also subsection 7.1.5).

are relevant for interpreting observations. They can interact with NO_2, HCHO and glyoxal. These can also be used as indicators during the observations of reactive halogen species for the influence of anthropogenic and biogenic emissions of various trace-gases.

1.2.1. Atmospheric Ozone

The main part of atmospheric ozone is found in the stratosphere, where its concentration is governed by the Chapman-cycle described in section 1.4, but also influenced by stratospheric trace gases, which modify this cycle, such as NO_2, halogens and water vapour. The stratospheric ozone layer protects Earth from UV radiation below 320 nm, which is harmful to most organisms. It is therefore important to observe and understand the evolution of the stratospheric ozone layer in a changing environment.
The maximum in stratospheric ozone partial pressure is found between 15–30 km height (see figure 1.1), depending on latitude and season. The typical total vertical ozone column is 3mm thick under standard conditions. This is defined as 300 DU, corresponding to $8 \cdot 10^{18}$ molec cm^{-2}.
Tropospheric ozone is important since it influences the oxidation capacity of the troposphere. Via the production of OH radicals the removal of a series of trace gases in the troposphere is affected. Tropospheric ozone acts also as a greenhouse gas and can have a negative impact on the biosphere when present at high concentrations. It can

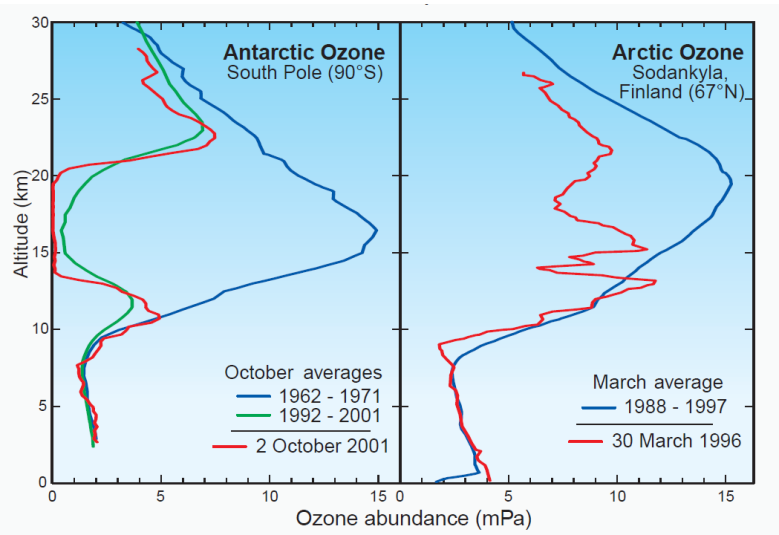

Figure 1.1.: Stratospheric ozone profiles from the WMO Ozone Assessment 2006 [WMO, 2007]: Normally the largest amount of ozone is found in a height of 20-30km, protecting the Earth from UV radiation. During polar spring-time stratospheric ozone depletion events (ozone holes) were observed, mainly caused by anthropogenic emissions of CFCs combined with extremely cold temperature at those heights.

e.g. cause irritation of the respiratory system of mammals [Miller et al., 1978]. Tropospheric ozone levels vary typically between typically 20-30 ppb in remote areas, but can reach higher values due to NO_x(NO_2+NO) and VOC chemistry in urban environments. Increasing NO_x emissions and concentrations contributed to an increase in tropospheric ozone concentrations [IPCC AR5, 2013](Figure 1.2). Due to the slightly higher NO_x concentrations in the northern hemisphere [Hilboll et al., 2013], also larger ozone concentrations are observed [Lelieveld et al., 2004]. The spatial distribution of tropospheric ozone is nevertheless not constant and can vary from year to year depending on a number of factors as observed for tropospheric ozone in the equatorial Atlantic by Winkler [1988], see also Figure 1.3. Halogen compounds can have a significant influence on ozone deposition [Read et al., 2008b, Ganzeveld et al., 2009]. For tropical marine air ozone loss due to halogen compounds can contribute up to 50% to the total diurnal ozone loss.

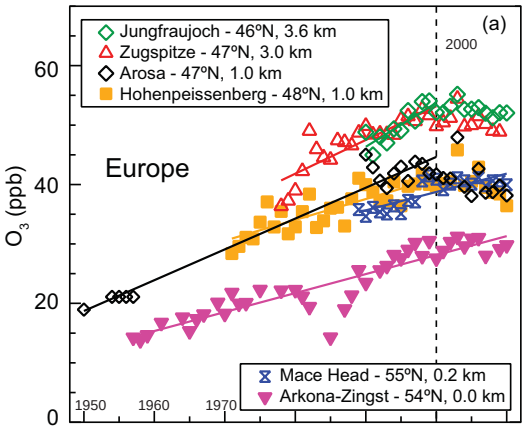

Figure 1.2.: Increasing tropospheric ozone concentrations were observed, partly due to an increasing NO_x background. [IPCC AR5, 2013] In the southern hemisphere typically lower values are observed, due to a lower NO_x background.

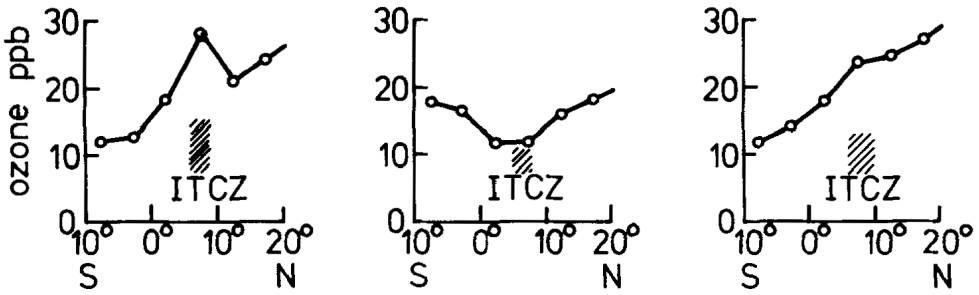

Figure 1.3.: Latitudinal ozone distribution do not need to show the same concentrations for each year and can vary significantly. [Winkler, 1988] This variation can also have an impact on release processes of RHS to the MBL, e.g. the release of iodide from seawater to the atmosphere. (see also subsection 1.4.3.1.

1.2.2. NO_2

NO_2 is a toxic trace gas, which can be produced at high temperatures, i.e. combustion processes, biomass burning and lightning, but can also be produced during nitrification or denitrification processes in soils. The largest emission sources are anthropogenic.NO_2 affects ozone chemistry throughout the atmosphere, a larger NO_x background can lead to enhanced ozone concentrations (see figure 1.2). It can react with halogens and act as a sink, but it can also enhance the release of reactive halogen species by acidification of salt particles due to nitric acid at NO_2 mixing ratios of more than 1 ppb [Bleicher et al., 2014]. The effective tropospheric lifetime of NO_2 during daylight is of the order of several hours [Beirle et al., 2011], concentrations on the open ocean are therefore expected to be low. [e.g. Lee et al., 2010, 15 ppt on average on Cape Verde during RHaMBLe]

1.2.3. Formaldehyde

Formaldehyde (HCHO) is the smallest aldehyde and belongs to the family of Oxygenated Volatile Organic Compounds (OVOCs). It is emitted to the atmosphere by incomplete fossil fuel combustion, but it also has natural sources, such as the oxidation of methane and Non-Methane Volatile Organic Compounds (NMVOCs). These can be of biogenic origin, such as isoprene. The oxidation of methane by OH is responsible for the main part of background formaldehyde, which has been measured at the surface between 0-500 ppt [Riedel et al., 1999, Mahajan et al., 2010b] and on the remote Pacific [Peters et al., 2012] at concentrations of 300 ppt. On Cape Verde typically 500 ppt HCHO were observed during the HaloCaVe campaign 2011, see figure 1.6.
Enhanced mixing ratios of HCHO have been found due to biomass burning [Anderson et al., 1996], due to biogenic emissions over forests [MacDonald et al., 2012], shipping emissions [Marbach et al., 2009] and other anthropogenic emission. Satellite data for HCHO and glyoxal as proxies for VOC oxidation has been used to model global emission strengths of NMVOC, e.g. isoprene [Stavrakou et al., 2009b].
The fate of atmospheric formaldehyde is governed by reaction with OH and wet deposition. These sinks lead to an atmospheric lifetime of only several hours, making it suitable as a tracer for emissions observed from satellite [Marbach et al., 2009].

1.2.4. Glyoxal

Glyoxal is the smallest α-dicarbonyl organic compound and a product of oxidative Non-Methane Volatile Organic Compound (NMVOC) chemistry [Grosjean et al., 1990] and was observed due to anthropogenic emissions in Mexico City by Volkamer et al. [2005b], but also in not as polluted environments at the MIT in Cambridge and in the Gulf of Maine on a ship by Sinreich et al. [2007]. Furthermore measurements of this compound were reported from open ocean MAX-DOAS measurements by Sinreich et al. [2010] in the tropical eastern Pacific with mixing ratios of up to 140 ppt clearly above detection limit. Different measurement campaigns with different DOAS instruments in the marine boundary layer compiled in Mahajan et al. [2014] show in general lower values of tropospheric glyoxal Differential Slant Column Densitys (dSCDs). No conclusions were

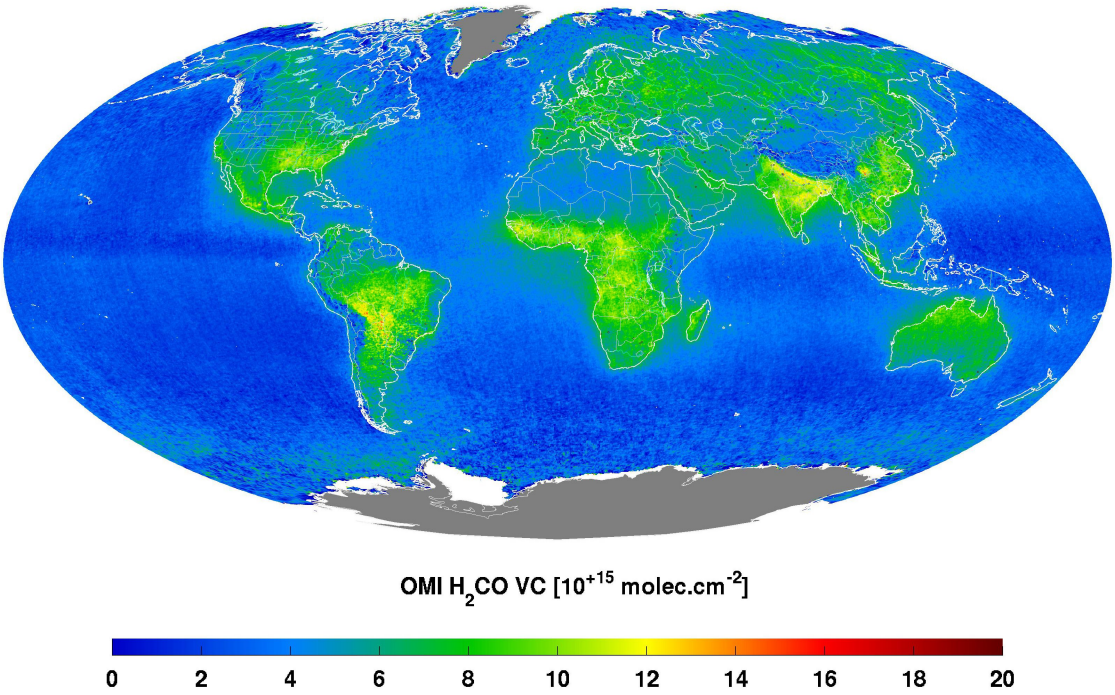

Figure 1.4.: Global vertical column densities from the OMI HCHO data product (BIRA-IASB v13), averaged for 2011. [De Smedt et al. [2012], http://h2co.aeronomie.be/]

drawn whether the reason for this discrepancy is seasonality, a special property of the Eastern Pacific Ocean or if evaluation uncertainties have introduced a large bias in the published data. Also in forested environments glyoxal was detected by Laser-Induced Phosphorescence (LIP) measurements [Huisman et al., 2011] (mostly <100 ppt) and by DOAS measurements [MacDonald et al., 2012] (close to detection limit, around several hundred ppt). An overview can be found in Table 5.14.

On the open ocean Sinreich et al. [2010] reported dSCDs in the range from $1.0{\cdot}10^{15}$ molec cm^{-2} to $2.5 \cdot 10^{15}$ molec cm^{-2} at elevation angles $\leq 3.8°$ corresponding to 140 ppt or an optical density of $1.4 \cdot 10^{-3}$, thus clearly significantly above the instrumental capabilities of the MAX-DOAS setup. Recent measurements during the Torero campaign in the equatorial Pacific showed glyoxal mixing ratios of 30-60 ppt [Sean Coburn, DOAS Workshop 2013, pers. comm.]. The lower values were observed during the day, when photolysis of glyoxal and the reaction with OH is limiting its lifetime.

Predominant precursors are terpenes, isoprene of biogenic origin and biomass burning in the tropics. These sources are continental and were sufficient to reproduce continental observations of glyoxal from space using chemical transport models [Stavrakou et al., 2009a]. The relatively short lifetime in the marine boundary layer due to photolysis, reaction with OH and HO_2, formation of secondary aerosol and deposition, imply that

observations of glyoxal on the open ocean require an additional source. The total average atmospheric lifetime for glyoxal for tropical noon conditions can be estimated to be about 2.5 hours. (see also Figure 1.5)
During Polarstern cruise ANT XXVII/4 from Cape Town to Bremerhaven van Pinxteren and Herrmann [2013] found 200ng/l glyoxal in the marine surface micro layer (SML). This converts into $c_{water} \approx 3.4\,\mathrm{nmol/l} = 3.4\,\mathrm{nM}$ in water. Given a Henry's law constant $H = 360000\,\mathrm{M^{-1}\,atm^{-1}}$ [Zhou and Mopper, 1990], this would result in equilibrium in a negligible atmospheric concentrations c_{water}/H. Observations of atmospheric glyoxal [Sinreich et al., 2010, Zhou and Mopper, 1990] are in the range of 100 ppt. Thus either the main production of glyoxal is within the Surface MicroLayer (SML) or the gas transfer into the water is limited e.g. by surfactants. The same discrepancy has been also observed for formaldehyde [Zhou and Mopper, 1990].
However, recent CE-DOAS measurements on the Pacific during the Torero campaign indicated lower mixing ratios of 30-40 ppt [S. Coburn, pers. comm.].
Global measurements from satellite by Wittrock et al. [2006] and Lerot et al. [2010] were retrieved from SCIAMACHY and GOME2 data, respectively. Over the oceans these measurements need to be evaluated with care, due to the overlaying effects of liquid water absorption and scattering, which is not known very precisely (see section 5.5), vibrational Raman scattering (see subsection 5.2.2.2 and Peters [2013], Dinter [2005]) as well as absorption by phytoplancton [Sadeghi et al., 2012].

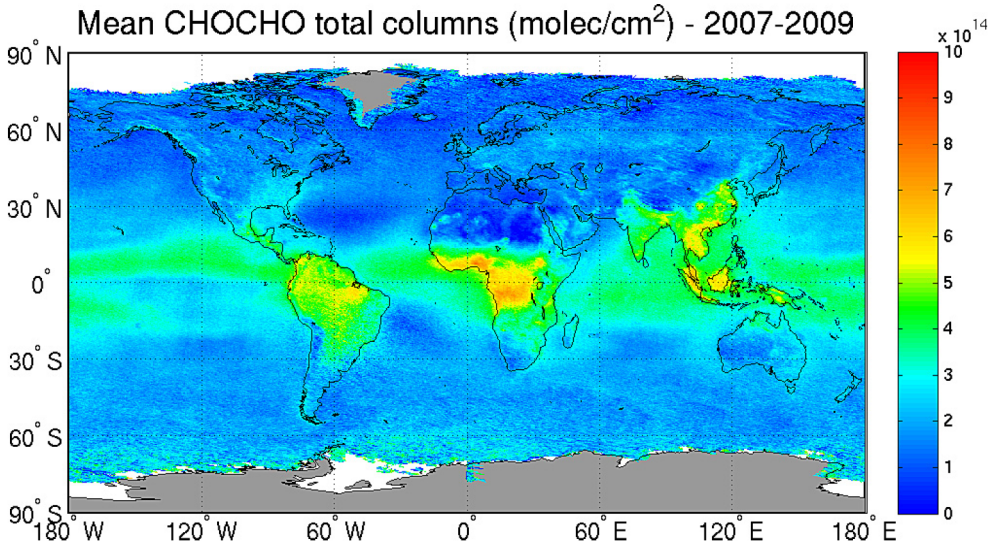

Figure 1.5.: Glyoxal SCD from GOME-2 by Lerot et al. [2010]. The distribution of retrieved glyoxal column densities looks similar to the distribution reported for water vapour by Noël et al. [2005].

1.2.5. Chlorine compounds

Compared to bromine and iodine, chlorine is even more reactive. Direct tropospheric measurements of reactive chlorine compounds are rare, since Cl can react fast with tropospheric methane and NMVOC forming HCl which is removed quickly. However, there are indirect Cl-measurement techniques such as 'hydrocarbon-clock' techniques, which make use of these reactions to determine the Cl-concentration. 15 ppt ClO were detected on a salt lake in Utah [Stutz et al., 2002]. Tropospheric OClO was detected in volcanic plumes [Gliß, 2014]. Stratospheric OClO was already observed in the stratosphere e.g. by Kühl et al. [2004]. Chlorine can be brought into the atmosphere by seasalt aerosol which has been acidified by sulfuric or nitric acids. Organic compounds containing chlorine are mostly of anthropogenic origin. Only CH_3Cl is produced biologically in large amounts and by biomass burning and represents 1/6 of the total tropospheric chlorine burden.
If any ClO or OClO is present, the cross-reaction of ClO and BrO (1.17) can contribute to the total ozone destruction [Buxmann, 2012].

1.2.6. Bromine compounds

Outside the marine boundary layer BrO can be observed in polar regions [Barrie et al., 1988, Frieß et al., 2011, Pöhler et al., 2010], above salt lakes [Hebestreit et al., 1999, Holla, 2013], volcanic plumes [Bobrowski and Giuffrida, 2012] and the stratosphere Dorf et al. [2006], WMO [2007]. Measurements in the free troposphere indicate also a BrO concentration of 0.3 ppt above the marine boundary layer in tropical regions [R. Volkamer, DOAS WS 2013 pers. comm].
In the marine boundary layer BrO was observed by Longpath Differential Optical Absorption Spectroscopy (LP-DOAS) measurements on the Cape Verde Atmospheric Observatory (CVAO) with concentrations of up to 3 ppt by Read et al. [2008b] and also Tschritter [2013], in the Mauritanian upwelling by Martin et al. [2009] and Tschritter [2013] locally restricted with concentrations up to 20 ppt. On the open Atlantic this compound was detected by Leser et al. [2003], who observed significant amounts of BrO (2.5 ppt) during a cruise from Bremerhaven to Cape Town only north of the Canary Islands and close to Cape Verde. Due to the vast surface area of the ocean already small BrO concentrations significantly influence ozone destruction [Read et al., 2008b], enhance the speed of oxidation of Dimethyl sulfide (DMS) [Boucher et al., 2003, Breider et al., 2010] and possibly mercury deposition [Ariya et al., 2004, Dibble et al., 2012].
Bromine compounds can also be found in the stratosphere [Dorf et al., 2006], where its main precursor substances are halons and brominated hydrocarbons.

1.2.7. Iodine compounds

The role of iodine compounds in the ocean and its processing by the marine ecosystem is not well understood, neither is their distribution. Databases for halogenated compounds have been recently established for a few species [Ziska et al., 2013] and the distribution of inorganic iodine in seawater is observed, but still far from covering the globe [Chance

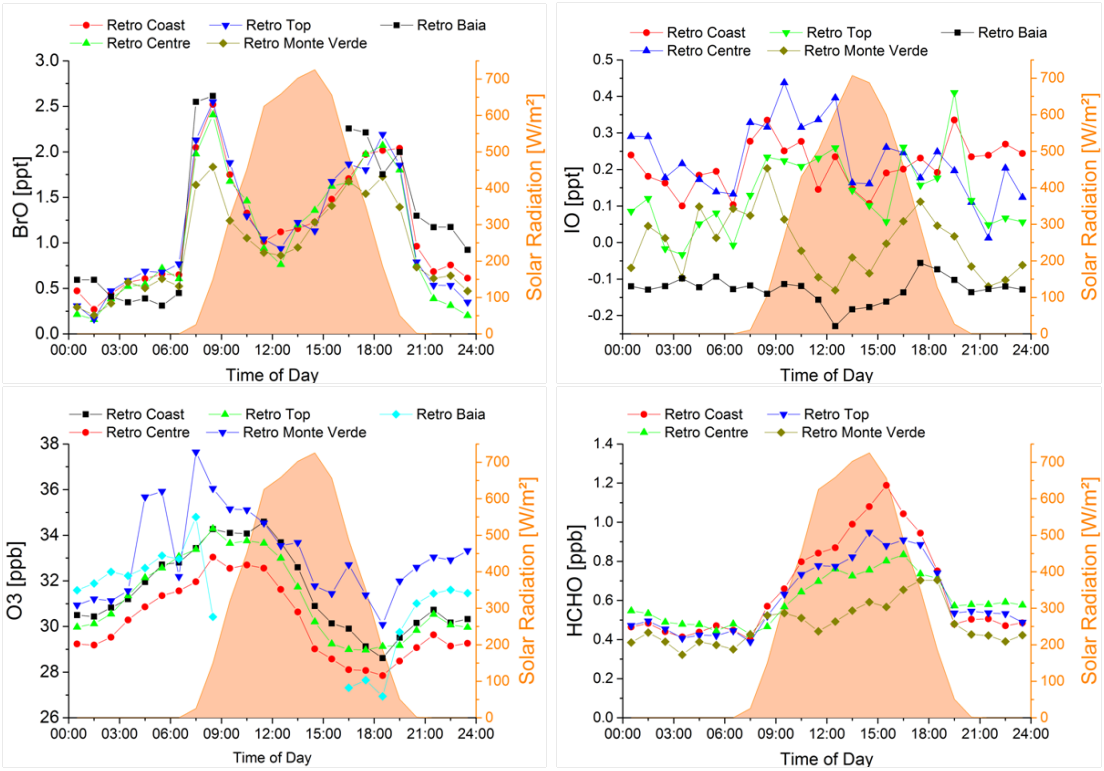

Figure 1.6.: Diurnal mixing ratios of BrO, O_3 and HCHO during the HaloCaVe campaign on Cape Verde 2011 [Tschritter, 2013] [D. Pöhler, pers. comm.]

et al., 2014]. Furthermore, the release processes to the atmosphere as well as the removal mechanisms from the atmosphere for iodine compounds remain uncertain, but of high importance, since iodine plays an important role for the diet of humans and other mammals. It is a constituent of hormones produced in the thyroid and in small amounts also needed by other organs. A typical daily ratio is around 150μg for an adult (WHO/FAO recommendation). Radioactive iodine which enters the human food-chain is of special importance, since it can be enriched in the thyroid and its radiation can cause thyroid cancer.

Together with bromine, atmospheric iodine can contribute to ozone destruction by increasing the ozone depletion rate of bromine already at low concentrations as shown in [Mahajan et al., 2010c] for Arctic spring-time BrO concentrations of several ppt BrO.

According to [O'Dowd et al., 2002a, and references therein], global emissions can be subdivided into emissions from macro-algae, phytoplankton and other sources yielding total iodine emissions which are estimated to be around $10^{11} - 10^{12}$g/yr^{-1}, with small contributions from macro-algae of $10^7 - 10^7$g/yr^{-1} and phytoplankton $10^9 - 10^{10}$g/yr^{-1}. The dominating source to explain global measurements of mixing ratios of IO in the boundary layer and the free troposphere is therefore still missing. This missing source could be the O_3-mediated release iodide in form of I_2 and HOI directly at the sea surface

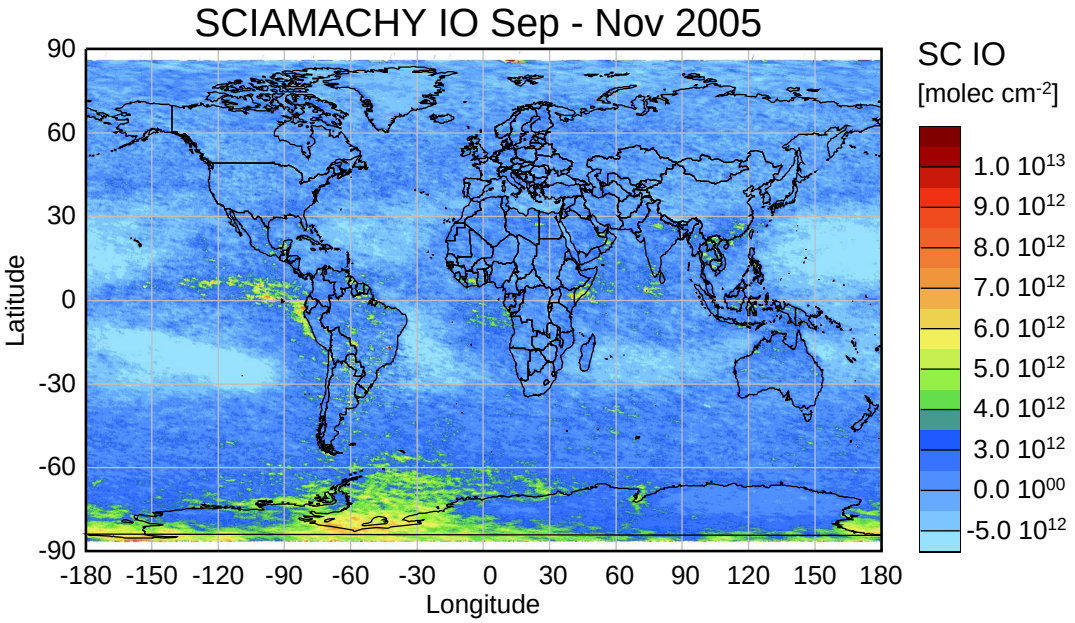

Figure 1.7.: Schönhardt et al. [2008], for a zoom-in plot showing the Peruvian upwelling region see figure 7.19.

explained below and in subsection 1.4.3.1.

First observations of atmospheric IO reported by Alicke et al. [1999] in Mace Head, Ireland, show significant IO mixing ratios, but seem to be dominated by locally restricted coastal iodine sources [Seitz et al., 2010]. For coastal measurements also the correlation with halocarbon concentrations was observed at the French coast in Brittany [Peters et al., 2005]. After having detected IO in Tasmania ($\approx$ 0.5 ppt) under measurement conditions which were dominated by air from the southern ocean, Allan et al. [2000] suggested a differentiation between high concentrations of IO caused by macro algae and background levels of about 1 ppt. The measurements on Tenerife also by Allan et al. [2000] agree roughly with volume mixing ratios of 1–2 ppt by Read et al. [2008b] for tropical environments. Furthermore it was detected above Spitsbergen by Wittrock et al. [2000], in Alert/Canada [Zielcke et al., 2014] and in Antarctica [Frieß et al., 2001, Frieß et al., 2006, Atkinson et al., 2012]. Saiz-Lopez et al. [2007b] observed IO throughout Antarctic summer, with a maximum daily average during summer of 7 ppt.

IO column densities were retrieved from data of the satellite instrument Scanning Imaging Absorption Spectrometer for Atmospheric CHartographY (SCIAMACHY) by [Saiz-Lopez et al., 2007a, Schönhardt, 2009, Schönhardt et al., 2012] and recent improvements by [Peters, 2013] concerning liquid water absorption. The main abundances were observed over Antarctica and the Peruvian upwelling, but also seasonal variations in IO column densities were observed close to Spitsbergen.

In the MBL widespread abundance of IO with levels around 1–2 ppt have been reported

for the western [Großmann et al., 2013] and eastern [Mahajan et al., 2012] Pacific Ocean, on the atmospheric measurement station on Cape Verde in the north-eastern Atlantic by [Read et al., 2008b] and further north on Tenerife by Puentedura et al. [2012]. IO also seems to be abundant in the free troposphere, as reported by Dix et al. [2013] and Puentedura et al. [2012].
Saiz-Lopez et al. [2006] reported night-time I_2 values for air-masses from the open ocean in Mace Head, interpreting these as the result of an open-ocean iodine source.
For coastal environments other release processes seem to dominate, forming so-called 'hot-spots' at coasts with specific algae, sometimes achieving concentrations of IO at which the self reaction is sufficient to create cloud condensation nuclei [Seitz et al., 2010, O'Dowd et al., 2002b].
Still, the halogenated volatile organic compounds were found to be not sufficient to explain the observed concentrations of IO in the MBL Mahajan et al. [2010a]. A possible inorganic pathway by the emission of I_2 and HOI has been described and underlined by measurements in Carpenter et al. [2013] and would explain the source of I_2 which has been postulated in modelling studies Großmann et al. [2013], Mahajan et al. [2010a]. Bluhm et al. [2010] reported values for iodide of 80-180 nM for the Mauritanian upwelling region, which agree with modelled iodide concentrations observed by Truesdale et al. [2000] and inferred from nutrient distributions by Ganzeveld et al. [2009]. Atkinson et al. [2012] reported iodide levels of >100 nM for the topmost 5 cm of an ice core from the Wedell sea while observing significant amounts of IO and surprisingly high values for I_2.
LP-DOAS measurements during the HALogens On Cape Verde (HaloCaVe) campaign at CVAO by Tschritter [2013] detected no significant amounts of IO in the marine boundary layer over a period of several weeks, which contradicts the measurements by Read et al. [2008b] and potentially MAX-DOAS measurements by Tschritter [2013] himself. The diagreement of MAX-DOAS and LP-DOAS measurements during HaloCaVe is not completely clear, since together with uncertainties of the radiative transfer modelling, the detection limit of the LP-DOAS and the values obtained from Multi AXis Differential Optical Absorption Spectroscopy (MAX-DOAS) might still agree.
A similar problem exists for data from Antarctica, where CE-DOAS and LP-DOAS measurements [Friess et al., 2013] could not confirm the observations by MAX-DOAS by Frieß et al. [2001], Frieß et al. [2010] and other LP-DOAS measurements by [Saiz-Lopez et al., 2007b].

OIO A product of the IO self reaction is OIO, which can then lead to the production of even larger molecules leading to the creation of Cloud Condensation Nuclei (CCN).
Observations are reported by Allan et al. [2001] in Tasmania close after sunset, up to 2 ppt and by Saiz-Lopez et al. [2006] for Mace Head/Ireland with several ppt OIO during the night. Hebestreit [2001] detected up to 7 ppt OIO in Mace Head, while Seitz et al. [2010] could not detect it in a similar field campaign. Stutz et al. [2007] detected daytime OIO with LP-DOAS and MAX-DOAS instruments in the Gulf of Maine with mixing ratios of 30 ppt close to fields of macro-algae.

Typical concentrations in the marine boundary layer are expected to be in the sub-ppt range during daytime [Mahajan et al., 2010a].

1.2.8. Sulphur compounds

The main source of reactive sulfur compounds found in the marine boundary layer are marine organisms, which can emit Dimethyl sulfide (DMS) [von Glasow et al., 2004, Zindler et al., 2013].
DMS can be oxidized by OH to SO_2 or methyl sulfonic acid (CH_3SO_3H). SO_2 has the potential to produce CCN and can thus influence the radiative budget. [Platt and Stutz, 2008] Oxidation of DMS to Dimethyl sulfoxide (DMSO) by halogen oxides can reduce the CCN production potential of DMS via H_2SO_4, since DMSO will be deposited on aerosol and thus increases the size of already existing CCN or can be converted into methyl sulfonic acid [Mahajan et al., 2010a]. A concentration of 1 ppt BrO contributes with about 25% of the dominating oxidation pathway of DMS by OH.
Capaldo et al. [1999] reports ambient SO_2 mixing ratios of 0.01-0.2 ppb on the open ocean, mostly due to shipping activity.

1.3. Origins of trace gases containing halogens

1.3.1. Gaseous emissions from the ocean

The average flux of RHS from the ocean is regarded to be small, but the surface size of the Oceans can compensate easily for 2-3 orders of magnitude of RHS flux compared to coastal areas or even more for salt-lakes.
Halogenated hydrocarbons can be metabolic products of phytoplancton and seaweeds and can have an effect on the troposphere as well as on the stratosphere, depending on their respective atmospheric lifetime (compare Table 1.2). The specific source strengths of these compounds is not well known, neither is their total global budget. [Ziska et al., 2013] Some compounds listed in Table 1.2 can already undergo photolysis within the surface water layer. Photolysis of CH_2I_2 can lead to production of CH_2ICl, which have an average lifetime in seawater of minutes and hours, respectively [Martino et al., 2005, Jones and Carpenter, 2005]. This photolytical destruction can reduce the flux into the atmosphere. On the other hand side, also production of iodinated halocarbons in the uppermost ocean is possible from DOM and iodide, leading to increased emission rates. The reaction of ozone with iodide leads to the production of HOI which can react with DOM to CH_3I, but also CH_2I_2 and $CHClI_2$ [Martino et al., 2008].
As pointed out in detail in subsection 1.4.3.1 iodine can be release directly from ocean water to the atmosphere, making the large reservoir of iodine in ocean water 'accessible' for atmospheric chemistry.
Surfactants can reduce exchange rates between ocean and atmosphere, but can also be a source of VOCs in the troposphere, which themselves can act as sinks for halogen species.

1.3.1.1. Release from marine Aerosol

The marine aerosol load is, if not dominated by import of large amounts of dust from deserts, dominated by sea salt aerosol [D O'Dowd and De Leeuw, 2007]. This can be created by bursting air bubbles reaching the surface or along coastlines. Sea salt aerosol dominates with respect to total mass, while sulphate aerosols, mostly from DMS oxidation, dominate in terms of number density.
Marine aerosol can be divided into primary and secondary aerosol: The primary aerosol is emitted directly and brought into the atmosphere, e.g. by sea salt ejected from seawater or dust storms in deserts. It's iron content can contribute significantly to the fertilization of ocean water, once deposited. It is estimated that within one year about 140Tg of dust from Africa are deposited in the Atlantic Ocean [Kaufman et al., 2005].
Secondary aerosol is formed within the atmosphere. The self-reaction of iodine can lead, for the case of high iodine concentrations, to bursts of aerosol particles (subsection 1.2.7), but also the photolysis of DMS (see figure 1.2.8) and oxidation of isoprene and other compounds can lead to the formation of aerosol particles.
For the chemistry of RHS, aerosols are important due to two reasons: They provide large amounts of chlorine and bromine to the MBL and furthermore provide surface area on which heterogeneous chemical reactions can take place, as e.g. needed for the recycling mechanisms of RHS (see also subsection 1.4.3) [Kerweg, 2005]. If the pH of the aerosol is low enough (< 6.5, see Fickert et al. [1999], Buxmann [2012], Bleicher [2012]), the bromine explosion mechanism can lead to emissions of Br_2. The typical pH of seawater is found between 7.5 and 8.4, therefore seasalt aerosol needs to be acidified first to contribute to the release of RHS via this pathway.

1.3.2. Continental sources

Continental sources of RHS can also be divided into abiotic and biotic source processes. Volcanoes can emit large amounts of chlorine and bromine [Kutterolf et al., 2013, Bobrowski and Giuffrida, 2012], while emissions of iodide have not been observed so far Gliß [2014]. Furthermore salt lakes can emit large amounts of bromine and iodine [Hebestreit et al., 1999] with concentrations of up to several 10 ppt of BrO Holla [2013].
As emissions of precursors of RHS have been observed in the marine biosphere, also plants on the continents have the potential to emit halogenated hydrocarbons. These emissions can be directly from a living plant Yokouchi et al. [2002], Weinberg et al. [2013] or e.g. due to biomass-burning Rudolph et al. [1995].
Anthropogenic emissions can also play a role for atmospheric chemistry, as did the emissions of long-lived CFCs followed by their transport to the stratosphere and the following observations of stratospheric ozone holes, which led to a larger interest in atmospheric halogen chemistry. For bromoform the anthropogenic emissions Quack and Wallace [2003] make up about 3% of total emissions, which are dominated by marine sources.
For polar regions the mechanisms are different and the direct emissions of bromine from aerosol and/or ice and frostflowers dominate. For iodine the role of polar sources and

their spatial extend is unclear, satellite retrievals indicate large amounts of IO over Antarctica, but less or none in Arctic regions.[Schönhardt et al., 2008] Large air masses with high BrO concentrations can be regularly observed in polar regions during spring [Frieß et al., 2011, Schönhardt et al., 2012, Sihler, 2012] and aerosol samples also show high concentrations of bromine during springtime and enhanced iodine concentrations during summer [Barrie and Barrie, 1990] (see also Figure 1.8). While the spring-time peak might be caused by the same mechanisms as those of bromine, the late-summer peak might be connected to iodide release of phytoplancton as described in subsection 1.4.3.1 due to the time of the year or direct biogenic production and/or transport of iodinated compounds. Yokouchi et al. [2014] detected larger CH_3I concentrations at Alert during winter, which was interpreted as long-range transport of this iodine containing compound in the absence of photolysis.

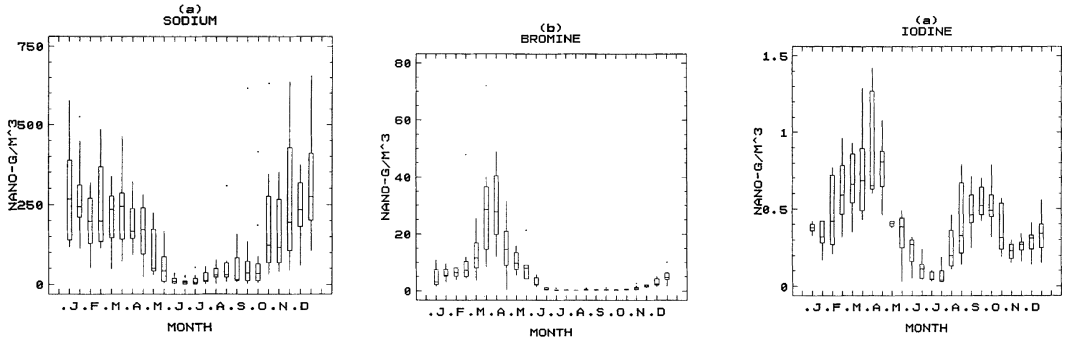

Figure 1.8.: Aerosol speciation data from Barrie and Barrie [1990]. The spring-time maximum in bromine coincides with with a maximum in iodine, which shows another maximum in late summer.

1.4. Ozone chemistry

Ozone is one of the central trace gases in the Earth's atmosphere: Due to its absorption cross-section it absorbs a large part of UV-A and UV-B radiation below 315 nm already in the stratosphere and therefore protects life on Earth from the influence of UV radiation. But it also plays an important role in the troposphere, were it influences the oxidative capacity of the troposphere by photolytically producing OH radicals.

1.4.1. Stratospheric Ozone chemistry

Stratospheric ozone is produced by photo dissociation of molecular oxygen, but it also is destroyed by photolysis. The net production depends on the available photons for photolysis of O_2 and O_3 as well as on the ambient pressure. This equilibrium has been first described by Chapman [1930], the so called Chapman-cycle:

$$O_2 + h\nu \longrightarrow 2\ O(^3P) \qquad \lambda < 242\,nm \tag{1.2}$$

$$O(^3P) + O_2 + M \longrightarrow O_3 + M \tag{1.3}$$

$$O_3 + h\nu \longrightarrow O_2 + O(^1D) \qquad \lambda < 320\,nm \tag{1.4}$$

$$O(^1D) + M \longrightarrow O(^3P) + M \tag{1.5}$$

$$O_3 + h\nu \longrightarrow O_2 + O(^3P) \qquad \lambda < 1180\,nm \tag{1.6}$$

$$2\ O(^3P) + M \longrightarrow O_2 + M \tag{1.7}$$

$$O(^3P) + O_3 \longrightarrow 2\ O_2 \tag{1.8}$$

Here 1.2 is the main ozone production mechanism, needing an additional collision partner M for momentum conservation. The other reactions contribute to loss of of ozone, balancing the total amount of stratospheric ozone. The total ozone loss is further increased by catalysts destroying ozone, such as H, OH, NO, Cl and Br, listed as e.g. in 1.13 and following.

1.4.2. Tropospheric Ozone chemistry

But ozone can also be found in the troposphere, even though practically no UV radiation below 242nm is available for photolysis of O_2. This is especially the case at high NO_x concentrations combined with high VOC mixing ratios: NO_2 is photolysed by photons at lower energies, producing NO and $O(^3P)$, which can form O_3 again after reaction with O_2. Since NO can also destroy O_3, an equilibrium is eventually established. The ratio between NO_2 and NO has been described by Leighton [1961] and their ratio is therefore called the Leighton ratio:

$$NO_2 \longrightarrow NO + O(^3P) \tag{1.9}$$

$$L = \frac{[NO_2]}{[NO]} = \frac{[O_3] \cdot k_{NO+O_3}}{J_{NO_2}} \tag{1.10}$$

Whenever a compound enters this equilibrium removing the NO, the equilibrium will be shifted towards higher ozone levels. This can be observed for higher concentrations of peroxy radicals, e.g. HO_2, CH_3O_2, which can be formed by OH radicals and methane, e.g.:

$$L_{HO_2} = \frac{[NO_2]}{[NO]} = \frac{[O_3] \cdot k_{NO+O_3} + [HO_2] \cdot k_{NO+HO_2}}{J_{NO_2}} \tag{1.11}$$

The photolysis frequency J_{NO_2} for reaction 1.9 can be calculated from the integral over the product of the actinic flux and the cross-section of the compound:

$$J(A) = \int \sigma(\lambda)\phi(\lambda)\zeta(\lambda)d\lambda \tag{1.12}$$

Here $\sigma(\lambda)$ is the cross-section of the compound, $\phi(\lambda)$ the quantum efficiency and $\zeta(\lambda)$ the actinic flux at the wavelength λ. Typical photolysis frequencies are 0.004-0.009s^{-1} for NO_2, 0.01-0.04 s^{-1} for BrO and 0.10-0.2s^{-1} for IO depending on the solar zenith angle (values from Bleicher [2012] and references therein).

1.4.3. Reactive Halogen Species

Reactive Halogen Species (RHS) affect the tropospheric as well as the stratospheric ozone chemistry by introducing another ozone destruction mechanism and having potentially a large impact on the HO_2/OH ratios. This can then also lead to changes in the Leighton ratio. In the stratosphere model calculations showed the need of further ozone destruction mechanisms when it was discovered that the ozone concentration is only half as high as expected. This difference led to calculations on the influence of NO_x on stratospheric ozone concentrations by Johnston [1971] and Crutzen [1970] and further to the discovery of the influence of chlorine by Molina and Rowland [1974], bromine, water vapour, and other compounds.

The term RHS denotes compounds containing chlorine, bromine and iodine. Astatine is virtually absent on Earth and Fluorine does not play a role in tropospheric chemistry, since it reacts very rapidly to HF. Chlorine is highly reactive towards hydrocarbons, bromine reacts with some hydrocarbons as e.g. HCHO, methanol and DMS and iodine can react with ozone but also shows a strong self-reaction leading to the production of larger molecules. In the following X and Y will represent Cl, Br and I, if not noted otherwise.

RHS can destroy ozone catalytically via the following reactions:

$$X_2 + h\nu \longrightarrow X + X \quad (1.13)$$
$$XO + h\nu \longrightarrow X + O \quad (1.14)$$
$$X + O_3 \longrightarrow XO + O_2 \quad (1.15)$$
$$Y + O_3 \longrightarrow YO + O_2 \quad (1.16)$$
$$XO + YO \longrightarrow X + Y + O_2 \quad (1.17)$$
$$\longrightarrow OXO + Y \quad (1.18)$$
$$\longrightarrow XY + O_2 \quad (1.19)$$
$$(+M) \longrightarrow XYO_2 \quad (1.20)$$

While reactions 1.15 and 1.16 depend linearly on the concentration of X and Y, reaction 1.17 depends on the product of their volume mixing ratios and thus becomes more important for high concentrations. For low concentrations also the reaction with HO_2 radicals is important to recycle the halogen radicals:

$$XO + HO_2 \longrightarrow HOX + O_2 \quad (1.21)$$
$$HOX + h\nu \longrightarrow X + OH \quad (1.22)$$
$$OH + CO + O_2 \longrightarrow HO_2 + CO_2 \quad (1.23)$$
$$X + O_3 \longrightarrow XO + O_2 \quad (1.24)$$
$$HO_2 + O_3 \longrightarrow OH + O2 \quad (1.25)$$

This is the dominant ozone destruction cycle in remote marine environments [Read et al., 2008b].
Photolysis of OXO produced in reaction 1.18 to XO and O(^{3}P) can reduce the efficiency of ozone destruction, because it produces an O(^{3}P) radical which can then form ozone again as in reaction 1.3. For the case of iodine an additional reaction from OIO to O_2 and I exists which increases the ozone destruction potential of reactive iodine [Gómez Martín et al., 2009]. The existence of the reaction and and its influence on the potential for ozone destruction has been a topic of active discussion.
HOX can also enter the liquid phase. For the case of HOBr, if there is bromine available in the liquid phase and the pH of the solution is low enough (< 6.5), this can trigger the so called 'bromine explosion' [Platt and Lehrer, 1997, Buxmann, 2012]. This describes an exponential growth of gas phase bromine and a method of very effective ozone destruction, which can be then the limiting factor for bromine emissions if virtually all ozone is destroyed e.g. in polar regions [Simpson et al., 2007, Sihler, 2012].
Due to its solubility HOBr can enter the liquid phase around an aerosol particle or on an ice surface. The reaction with Br^- and H^+ consumes H^+, which is the reason why an acidic environment is needed. In seawater this reaction is not possible, due to the buffering of the seawater acidity by the carbonate system. Typically the seawater pH is found around 7.5-8.4. Once Br_2 is formed, it can be emitted to the atmosphere. It is

eventually photolysed yielding 2 highly reactive bromine atoms which can participate in atmospheric chemistry, especially ozone destruction. BrO can react with HO_2, forming again HOBr, which can then continue in this reaction cycle. Because two bromine atoms are released for one molecule of HOBr, this can lead to an exponential growth of gas phase bromine, as long each of the necessary substances is available. In polar regions and volcanic plumes the available amount of ozone can be the limiting factor. The reaction cycle is shown as a diagram in figure 1.9.

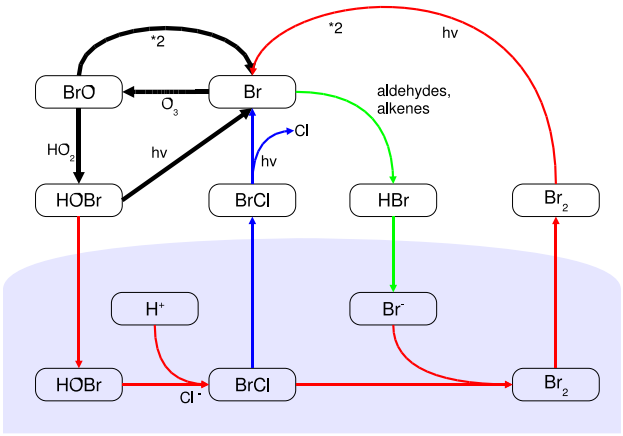

Figure 1.9.: A simplified diagram of the bromine explosion mechanism, adapted from Simpson et al. [2007]. The path marked in red can lead to an exponential increase of atmospheric reactive bromine.

Interhalogen reactions leading to the formation of BrI or BrCl can modify the speed of the release processes and ozone destruction. A chemistry-modeling study by [Mahajan et al., 2010c] reported a significant increase in ozone depletion rates in the presence of reactive iodine.

$$HOBr \longrightarrow HOBr_{aq} \tag{1.26}$$
$$HOBr_{aq} + Br^- + H^+ \longrightarrow Br_{2,aq} + H_2O \tag{1.27}$$
$$Br_{2,aq} \longrightarrow Br_2 \tag{1.28}$$
$$Br_2 + h\nu \longrightarrow 2Br \tag{1.29}$$
$$Br + O_3 \longrightarrow BrO + O_2 \tag{1.30}$$
$$BrO + HO_2 \longrightarrow HOBr + O_2 \tag{1.31}$$

1.4.3.1. Release of iodine from seawater

The total iodine content of seawater is relatively constant at $\approx 0.42 - 0.48\,\mathrm{nmol\,l^{-1}}$, this is ≈ 30 times less than bromine or even ≈ 20000 times less than chlorine (see also section 2.2). Therefore this huge reservoir of the RHS iodine can play a significant role, once it can be released to the marine boundary layer. Most of the iodine in seawater is present in the form of IO_3^-, which cannot be directly released. Iodine can be processed and released as a metabolic product from phytoplankton and macro algae. They can

release halogenated hydrocarbons which are eventually photolysed and RHS can be formed (see table 1.2 for lifetime of several compounds), or the iodine is emitted directly in the form of I_2 [McFiggans et al., 2004] or HOI or as iodide I^- into the water.

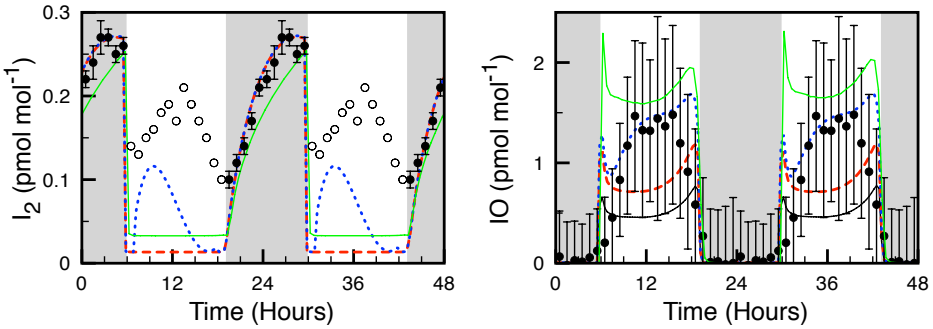

Figure 1.10.: THAMO box model results for four simulations (from Lawler et al. [2013]): BASE (halocarbons only): black solid line. FLAT (constant I_2 flux): red dashed line. PHOTO (enhanced daytime I_2 source): dotted blue line. HOI (added flux of HOI): green solid line. IO observations from Read et al. [2008b] are plotted as circles with one standard error bars. Dark shading represents nighttime hours.

Modelling studies (e.g. Mahajan et al. [2010a]) have found that only half of the iodine observed e.g. on the Pacific by Großmann et al. [2013] or on the Atlantic by Read et al. [2008b] can be explained by photolysis of halogenated hydrocarbons (compare Figure 1.10). Another pathway of iodine release in the context of ozone destruction was suggested already by Garland and Curtis [1981] who showed that ozone causes 'iodine vapour' to be released from the sea surface. Laboratory studies by Hayase et al. [2010] which showed the reaction of iodide (I^-) in solution with ozone and its release to the gas phase. Modelling studies to estimate the effect of iodine on dry ozone deposition in a global context by Ganzeveld et al. [2009] led together with the previous studies to further laboratory measurements by Carpenter et al. [2013], which showed the dependence of the emission flux on the ozone concentration and iodide content of the water. The reaction mechanism converts the I^- in the surface layer of the ocean with O_3 into HOI which might react further to I_2, both of which can be released into the gaseous phase. The reaction is not significantly temperature dependent as shown in MacDonald et al. [2013], but the iodide surface concentrations show a correlation with Sea Surface Temperature (SST) due to simultaneous difference in mixed-layer depths and/or bioproductivity [Chance et al., 2014].

$$H^+ + I^- + O_3 \longrightarrow HOI + O_2 \tag{1.32}$$

$$H^+ + HOI + I^- \rightleftharpoons I_2 + H_2O \tag{1.33}$$

This reaction mechanism is similar to the bromine explosion mechanism, but does not

need explicitly a heterogeneous reaction cycle. Furthermore it was observed to work at a pH of 8, increasingly fast at lower pH [Carpenter et al., 2013].
Since the iodine flux via this pathway is proportional to tropospheric ozone concentrations according to Carpenter et al. [2013], a increase of anthropogenic NO_x emissions and thus an increase in tropospheric background ozone levels could increase iodine emissions, which itself has the potential to destroy ozone.
In the liquid phase, a fraction of the HOI might react with Dissolved Organic Matter (DOM) and form Iodinated Volatile Organic Compound (IVOC) [Martino et al., 2008], which can later be photolysed in the gaseous phase and form RHS.

$$DOM + HOI + H^+ \quad \longrightarrow \quad H_2O + IVOC \tag{1.34}$$

Großmann et al. [2013] estimated an additional flux of I_2 to be around $1{\cdot}10^8$ molec cm^{-2} s^{-1} for the tropical Western Pacific. This would correspond, if extrapolated constantly to half of the total ocean surface on Earth, to $2.4 \cdot 10^{12}$ g yr^{-1}. This agrees with the upper limits given by [O'Dowd et al., 2002a, and references therein] on the total iodine flux to the atmosphere. The contribution of macro-algae is four, the contribution of phytoplankton emissions two orders of magnitude smaller.
Lawler et al. [2013] did first field measurements of I_2 in the marine boundary layer presumably in absence of large amounts of macro-algae at Cape Verde and measured I_2 concentrations in agreement with previous modelling studies. It was shown that night-time concentrations of I_2 are usually below 1 ppt for the tropical Atlantic, during daytime the concentrations of I_2 were close to the detection limit of 0.2 ppt. The night-time I_2 was three times higher in May 2007 compared to May 2009, which indicates the high variability of released iodine.

1.4.4. Sinks of reactive halogen species

Due to the background of methane in the troposphere the lifetime of ClO is about a few hours during daytime for low BrO concentrations and only several minutes at high BrO concentrations of e.g. 30 ppt in polar regions. BrO lifetimes on the other hand are often longer, since Br only reacts only with aldehydes, alkenes and HO_2 [Simpson et al., 2007]. HO_2 is produced to a large extend by oxidation of methane via Cl atoms, together with HCHO.

$$OH + CH_4 \longrightarrow \cdot CH_3 + H_2O \quad (1.35)$$
$$Cl + CH_4 \longrightarrow \cdot CH_3 + HCl \quad (1.36)$$

In semi-polluted environments a possible sink for reactive halogen species is the formation of halogen nitrates. This cycle does not contribute to ozone destruction, but via deposition of the halogen nitrates on aerosol this can represent a sink for RHS.

$$XO + NO \longrightarrow X + NO_2 \quad (1.37)$$
$$X + NO_2 + M \longrightarrow XONO_2 \quad (1.38)$$
$$XONO_2 + h\nu \longrightarrow X + NO_3 \quad (1.39)$$
$$XONO_2 + h\nu \longrightarrow XO + NO_2 \quad (1.40)$$
$$XONO_{2,liq} + H_2O \longrightarrow HOX + HNO_3 \quad (1.41)$$
$$NO_3 + O_2 + h\nu \longrightarrow NO_2 + O_3 \quad (1.42)$$
$$X + O_3 \longrightarrow XO + O_2 \quad (1.43)$$

These reactions with NO/NO_2 are also important for remote areas, because due to the relatively large reaction constant (see Table 1.3) of reaction 1.38, already a few ppt are sufficient to reduce the amount of reactive halogens compounds significantly. A hint that this is indeed the case are observations, that the strongest ozone destruction was observed e.g. during *RHaMBLe* [Lee et al., 2010] on the days with the lowest NO_2 mixing ratios of around 1 ppt.
On the other hand it was shown that NO_x can enhance the bromine and chlorine explosion mechanism (Bleicher et al.2014) by acidification of aerosol particle surfaces and the following reactions via HOX, but additionally by direct release of XNO_2 and $XONO_2$ also at night-time.

1.4.4.1. Sinks for reactive bromine

The dominating sink for bromine in the tropical MBL is reaction with VOCs to form HBr. HBr can contribute to particle growth [Simpson et al., 2007], but it can be also recycled in the aqueous phase on the particles in the presence of HOBr for a pH<6.5. HBr can also be converted by OH in the gas phase into H_2O and Br, but the lifetime of HBr with respect to OH is of the order of days, whereas the lifetime of BrO is of the order of minutes or hours. Therefore HBr effectively acts as a sink for Br.

Compound	k_{Br} $[\frac{cm^3}{molec \cdot s}]$	k_{BrO} $[\frac{cm^3}{molec \cdot s}]$	typ. conc. (CVAO)	loss rate ppt/h (via k_{Br}/k_{BrO})
Ozone	$1.1 \cdot 10^{-12}$		30 ppb	
NO_2	$1.8 \cdot 10^{-11}$		10-30 ppt	2.4-6.9
HCHO	$1.16 \cdot 10^{-12}$	$1.5 \cdot 10^{-14}$	300 pptv	4.5 / 1.2
CH_4	$3.6 \cdot 10^{-14}$	$< 1.6 \cdot 10^{-14}$	1.8 ppbv	0.9 / < 7.8
CH_3CHO	$3.49 \cdot 10^{-12}$		200–800 pptv	9–36
Ethane	$3 \cdot 10^{-19}$	$< 1.66 \cdot 10^{-14}$	500–1500 pptv	$< 10^{-5} / < 2-6$
Acetone			500–1500 pptv	
Methanol	$2.67 \cdot 10^{-12}$		500–2000 pptv	15-60
CH_3O_2	$1.6 - 6 \cdot 10^{-12}$		15 ppt	0.3-1.2
Isoprene	$7.4 \cdot 10^{-11}$		4-20 pptv	4-20
Propane	$4 \cdot 10^{-17}$		40 pptv*	$< 10^{-5}$
Butane	$0.2 - 4.8 \cdot 10^{-10}$			
DMS		$4 \cdot 10^{-13}$	10-400 pptv	
HO_2	$2 \cdot 10^{-12}$	$3.5 \cdot 10^{-11}$	$1 - 2 \cdot 10^8$	

Table 1.3.: Typical reaction rates and calculated loss rates for typical concentrations at CVAO for various compounds assuming a BrO concentrations of 1 ppt. Concentration values from Lucy Carpenter [Talk during CVAO/CVOO meeting, 2012, pers. comm.]. Reaction rates from kinetics.nist.gov. *(SHIVA, Elliot-Atlas)

BrO lowers the average tropospheric lifetime of DMS from typically one day to about 10h [Read et al., 2008a] for a BrO concentration of 3 ppt. But since the reaction does not lead to a net reduction of Br, it cannot be regarded as a sink mechanism for BrO, as long as there is enough ozone.

$$BrO + DMS \longrightarrow Br + DMSO \tag{1.44}$$

Br can react with HCHO at a reaction rate similar to the one of the reaction of ozone and bromine atoms. Additionally also BrO can directly react with HCHO forming HOBr and CHO [Hansen et al., 1999].

$$BrO + HCHO \longrightarrow HOBr + CHO \tag{1.45}$$
$$Br + HCHO \longrightarrow HBr + CHO \tag{1.46}$$

While at CVAO methanol mixing ratios of 500–2000 ppt were found [L. Carpenter, Talk in 2012 on CVAO/CVOO meeting, Mindelo], Yang et al. [2014] reported 500–600 ppt for the tropical Atlantic.

$$Br + CH_3OH \longrightarrow HBr + CH_3O \tag{1.47}$$

Example for HCHO: For a situation comparable to the atmospheric conditions on the CVAO/Cape Verde, we assume a BrO VMR or 3 ppt, 30 ppb O_3, 0.5 ppb of HCHO and a marine boundary layer height of 500m. With J(BrO)=$0.04s^{-1}$ and k_{Br+O_3} [O_3] = $0.8s^{-1}$ the ratio BrO/Br can be approximated by $\frac{0.84}{0.04} = 21$ and thus [Br] $\approx 3/21$ ppt. With $k_{Br+HCHO}$ from Table 1.3 and a well mixed marine boundary layer at least until 500m (compare LP-DOAS measurements by Tschritter [2013]), this then results in a flux of Br of $2.6 \cdot 10^9$ molec cm^{-2} s^{-1} = 156nmol m^{-2} h $^{-1}$. This does not include recycling of HBr on aerosol particles, which would require lower pH than standard seawater and would reduce the necessary flux to maintain atmospheric BrO concentrations of 3 ppt.
Maximum fluxes of Br have been reported to be around 18nmol m^{-2}h^{-1} for $CHBr_3$ and 3nmol m^{-2}h^{-1} for CH_2Br_2 in Hepach et al. [2013] which is together about 7.5 times smaller and was found in the Mauritanian coastal upwelling, where also higher BrO values were observed [Martin et al., 2009, Tschritter, 2013]. Together with the small spatial extend and the relatively long lifetime of $CHBr_3$ and CH_2Br_2 this indicates that source of BrO during those events are other halocarbons and/or direct emissions of bromine from aerosol.

1.4.4.2. Sinks for reactive iodine

High IO mixing ratios in the troposphere can lead via the self reaction of IO to the formation of new particles by polymerisation. Due to the nature of the self reaction, this process dominates for high IO mixing ratios and has been observed e.g. at the Irish coast [O'Dowd et al., 2002b, O'Dowd and Hoffmann, 2006] over fields of macro algae showing a high flux of organic iodine compounds and/or I_2. Burst of ultra fine particles of 3-10nm size have been observed simultaneously to high IO mixing ratios [Seitz et al., 2010].
For the case of $IONO_2$, Vogt et al. [1999] does not regard this as a sink process, since $IONO_2$ and INO_2 will eventually hydrolyse on aqueous aerosol to HOI, which can then again be released again via I_2, ICl or IBr. Vogt et al. [1999] assumed therefore that the largest iodine sink will be iodate.
The iodine content of aerosol in marine aerosol was found to be 60-600 fold of the seawater iodine content and is therefore a candidate of a major iodine sink [Baker et al., 2000, Baker, 2004]. Assuming a deposition velocity of aerosol of 1cm s^{-1} [Jickells and Spokes, 2001] and an aerosol iodine content of 10-60 pmol m^{-3} for the tropical Atlantic [Baker, 2004], this results in a iodine deposition rate of $0.6 - 3.6 \cdot 10^7$ molec cm^{-2}/s. Typical fluxes from methyl iodide are $8.3 \cdot 10^6$ molec cm^{-2} s^{-1} (tropical Atlantic, Hepach et al. [2013]), from CH_2ClI according to Varner et al. [2008] $7 - 42 \cdot 10^6$ molec cm^{-2} s^{-1}. A short overview of iodinated halocarbon fluxes can be found Großmann et al. [2013]. They estimated an additional flux of I_2 to be around $1 \cdot 10^8$ molec cm^{-2} s^{-1} to explain the observed IO mixing ratios. It is thus significantly higher than the estimate for the aerosol sink. HOI can also on aerosols react to IVOCs in the presence of DOM [Martino et al., 2008]. Iodine can then not be released any more by emission of I_2,IBr or ICl. This could also explain the high concentration of organoiodine compounds in rainwater samples.

Connected to aerosols, rainfall is consequently another possible sink for atmospheric iodine. In rainfall samples iodine was detected. Measurements by Gilfedder et al. [2007] show that its main iodine constituents are light organic iodine containing compounds (56%) and iodide (27%), while the fraction of iodate is below 10%. This contradicts the assumption by Vogt et al. [1999] that most of the iodine is removed from atmospheric recycling by conversion to iodate.
Like BrO, IO also reacts with DMS to I and DMSO, but at a rate which is 30-times slower. Since I is released again, this is not actual net sink.
First order loss rates for IO according to Sommariva et al. [2012] assuming a set of volume mixing ratios for the respective trace gases is shown in Figure 1.11. Here the dominant loss pathway is HO_2, which converts IO into HOI, which can either be transferred to the liquid phase or photolyse again. The reaction rate of CH_3O_2 with IO is unclear and varies as shown also in Figure 1.11.
An important pathway for removal of reactive iodine from the atmosphere is the self-reaction of IO and subsequent particle formation, at least for high atmospheric concentrations of reactive iodine. These can, at least in coastal environments which large locally restricted iodine sources, dominate CCN production [D O'Dowd and De Leeuw, 2007]. Seitz et al. [2010] showed simultaneous measurements of particle formation events with large IO concentrations over fields of macro-algae at the Irish coast. However, estimations for the total contribution of iodine to CCN production under open-ocean conditions with 0–1 ppt of IO are rare. Particle creation events were only observed for high iodine concentrations e.g. at the Irish coast and lab experiments were also conducted at significantly higher IO mixing ratios [D O'Dowd and De Leeuw, 2007, and references therein].

$$IO + IO \rightleftharpoons I + OIO \tag{1.48}$$
$$OIO + IO \rightleftharpoons I_2O_3 \tag{1.49}$$

To estimate the effect of the self-reaction of IO (Equation 1.48) on the formation of CCN, it can be compared to the oxidation of H_2SO_4 [Schönhardt, 2009]: Given the reaction constants $k_{IO+IO} = 8{\cdot}10^{-11}$ cm^3 molec^{-1} s^{-1} and $k_{SO_2+OH} = 2{\cdot}10^{-12}$ cm^3 molec^{-1} s^{-1} for an OH concentration of 0.04 ppt, a SO_2 concentration of 100 ppt [Capaldo et al., 1999] and a typical IO mixing ratio of 1 ppt (see e.g. subsection 7.2.4), the ratio of the formation rate of sulphate particles and larger iodine compounds yields the following estimate for an OH concentration of 0.04 ppt and 100ppt of SO_2:

$$\alpha = \frac{k_{IO+IO}(1\text{ ppt})^2}{k_{SO_2+OH}100\text{ ppt }0.04\text{ ppt}} = 10 \tag{1.50}$$

Even though I_2O_3 from 1.49 is an important step to iodine particle formation according to Kaltsoyannis and Plane [2008], this estimate in 1.50 overestimates the actual rate, since the intermediate OIO can be photolysed, before it reacts with another IO molecule to I_2O_3. Therefore the details of this mechanism need to be studied in a chemistry model to estimate the effect of the IO self-reaction on the total CCN production in the MBL.

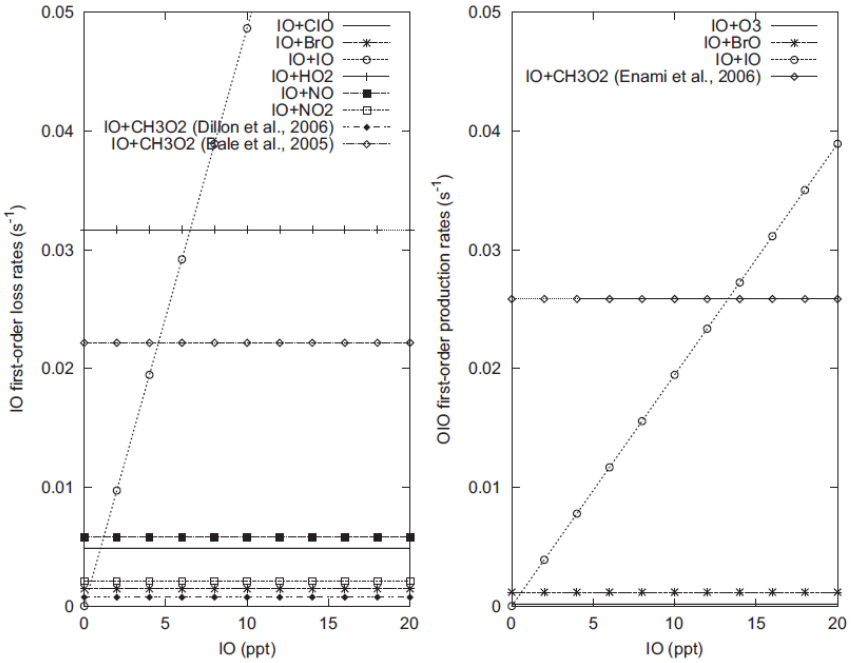

Figure 1.11.: First order IO loss rates and OIO production rates based on model calculations for typical MBL conditions (ClO = 2 ppt, BrO = 0.6 ppt, HO_2 = 15 ppt, NO = 12 ppt, NO_2 = 24 ppt, CH_3O_2 = 15 ppt, O_3 = 30 ppb). For open ocean concentrations of IO below 2 ppt the self reaction is not dominant. (from Sommariva et al. [2012])

2. Ocean

2.1. Global circulation system

2.1.1. Upwelling systems

Upwelling is an oceanographic phenomenon which leads to upward transport of cold and often nutrient rich, deep water to the surface. This transport is a motion of water masses which results from wind-driven currents, Coriolis forces and Ekman transport. Upwelling areas can often be identified by cold surface water temperatures and high amounts of Chlorophyll-a (Chla) at the surface due to the large input of nutrients. Upwelling areas can be found in the Atlantic at the coast of Mauritania as well as further south at the coast of Namibia. On the eastern border of the Pacific Ocean also upwelling areas exist, e.g. the upwelling system connected to the Humboldt current transporting cold and nutrient rich waters from the Southern Ocean into tropical regions [Bakun and Nelson, 1991]. Upwelling systems can be divided into three main categories: The coastal upwelling (Mauritania, Peru, ...), equatorial upwelling (Atlantic and Pacific) and upwelling in the Southern Ocean. While the coastal upwelling is wind-driven and the Coriolis force acting on the (usually) southward moving waters to the east (the other way around on the southern hemisphere) enables cold deep water to rise to the surface close to the coast. The equatorial upwelling is also wind-driven, but despite the absence of a coastline and the coriolis force, the currents resulting from the steadily blowing trade winds result in upwelling just along the equator. The third upwelling system in the southern ocean is a coastal upwelling, but driven by strong westerly winds effectively driving the water masses northwards. This leads to upwelling of nutrient rich water around Antarctica, feeding an extensive ecosystem. These water masses leading on average to the maximum surface water nitrate concentration values [Levitus et al., 2010] represent one significant difference between the Arctic and the Antarctic in the properties of the water masses surrounding polar regions. The only larger upwelling region on an eastern shoreline is the Somalian upwelling, the 'Great Whirl' [Beal and Donohue, 2013].
Due to varying wind and trade wind conditions, the upwelling system show seasonality effects in upwelling strength, but also in Chla concentrations, which are both not necessarily directly linked, but also affected by stratification, nutrient or light limitations [Echevin et al., 2008]. The Peruvian and the Mauritanian upwelling is strongest in the respective winter period. The maximum of Chla concentrations in the Peruvian upwelling is usually found in summer, when enough light is available.
Furthermore the strength of the upwelling is modulated on the scale of several years by effects of other oscillations. For the Peruvian Upwelling these are called 'El niño' and 'La niña': El niño is a weakening of the cold Humboldt current in the eastern Pacific, which has a strong impact on the continental weather systems of South America and

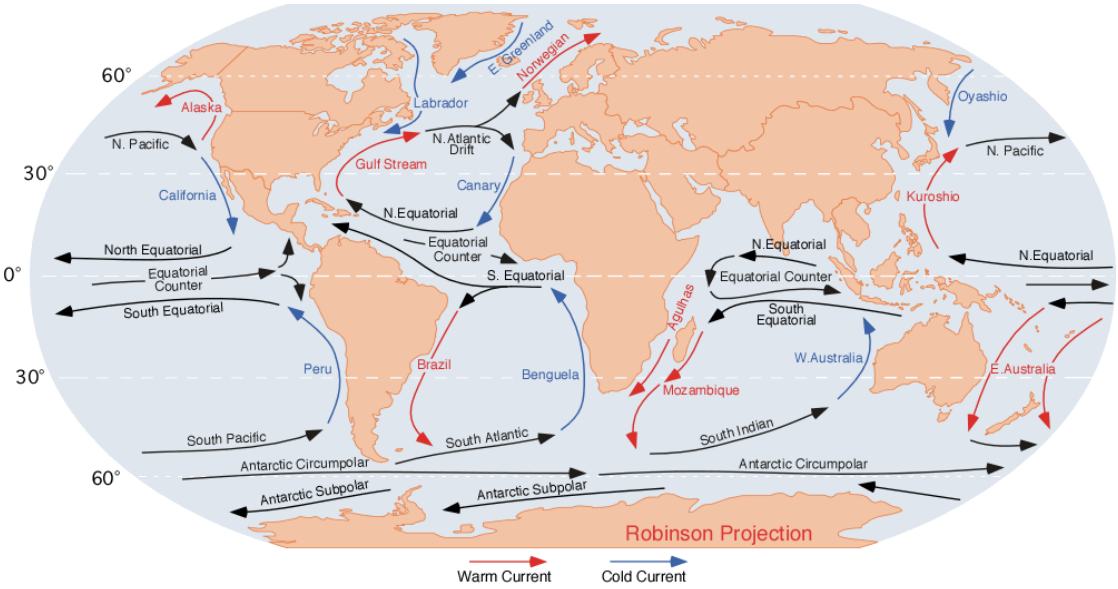

Figure 2.1.: The global oceanic circulation system. [Pidwirny, 2006] The largest upwelling regions can be found along the western coasts of Africa, North- and South-America, along the Antarctic coast and in the Arabian Sea.

leads via a weakening of the effective coastal upwelling due to a lower thermocline to a decrease in bioactivity. The opposite effect is observed for 'La niña'.

The upwelling does not only have an effect on available nutrients of surface waters: Sedimentation of the biomass produced in surface waters transports this biomass to into deeper waters, where it is processed, consuming oxygen. As the oxygen levels drop significantly, severe changes in the ecosystem can occur. It limits the habitat of certain species [Stramma et al., 2012], alters microbial processes and can lead to enhanced emissions of trace gases, such as the greenhouse gas N_2O [Bange et al., 2010], but also N_2 [Zehr, 2009]. Also chemical balances can be changed, as pointed out below for iodide and iodate.

2.2. Seawater

Seawater contains a large number of different compounds, of which the main part is salt, contributing ≈3.5% of the total weight [Millero et al., 2008](see Table 2.1). For seawater with a salinity of 35 (so called standard seawater), the ratio of Cl:Br:I is 650:1:0.032. Typically the seawater pH is found around 7.5–8.4. As an example, during SOPRAN M91 in the Peruvian upwelling (chapter 7) it varied between 7.7–7.8 for water in depths of more than 20–30m and 8.1-8.4 in surface water samples.

Substance	[mol/kg]	Reference
H_2O	53.6	
Cl^-	0.546	
Na^+	0.469	
${Mg_2}^+$	0.0528	
${SO_4}^{2-}$	0.0282	
TOC	0.0161	Sugimura and Suzuki [1988]
${Ca_2}^+$	0.0103	
K^+	0.0102	
TIC	0.00206	
Br^-	0.000844	
B_{Total}	0.000416	
${Sr_2}^+$	0.000091	
F^-	0.000068	
...	...	
(I^-+${IO_3}^+$)	$(0.42 - 0.44) \cdot 10^{-6}$	Truesdale et al. [2000]
$CHBr_3$	$0 - 50 \cdot 10^{-9}$	Ziska et al. [2013]
CH_3OH	$5.4 \cdot 10^{-6}$	Beale et al. [2011]

Table 2.1.: The main constitutents of seawater according to Dickson and Goyet [1994], if not stated otherwise.

2.2.1. Iodine in seawater

Dissolved iodine in seawater is predominantly present in the form of iodide I^- and iodate ${IO_3}^-$ [Winkler, 1916]. Iodinated compounds, which might play a role in atmospheric chemistry when photolysed in the troposphere or especially when transported to the stratosphere [WMO, 2010], but which are only responsible for a small part of the total dissolved iodine in seawater. Usual concentrations of methyl iodide in seawater are of the order of 0-15 pmol l^{-1} and atmospheric concentrations of 0–3 ppt [Ziska et al., 2013]. To compare it to atmospheric iodine concentrations, an atmospheric layer of 1 km thickness containing 1 ppt of IO corresponds to the total iodine content of about 1 mm of seawater. The total iodine content of seawater is relatively constant at $\approx 420 - 480$ nmol l^{-1} and does not show a distinct latitudinal dependence [Tsunogai and Henmi, 1971, Truesdale et al., 2000, Bluhm, 2010]. Still, the partitioning of iodide and iodate changes, in the tropical Atlantic the minimum of iodate and thus the maximum of iodide is found in the surface layer waters, from 0-30m [Tsunogai and Henmi, 1971, Truesdale et al., 2000]. This effect is emphasized when the water column is stratified as in tropical waters which prevents mixing of surface layer water with deeper waters [Jickells et al., 1988]. In anoxic conditions iodide can even dominate the amount of total dissolved iodine, as it is the case for the black sea and layers in the Arabic sea [Farrenkopf and Luther III, 2002]. These conditions can also be found in upwelling areas were biomass from the upper layers of the ocean sinks to the ground and consumes oxygen below the euphotic zone. This leads to a distinct Oxygen Minimum Zone (OMZ) e.g. in the Peruvian upwelling

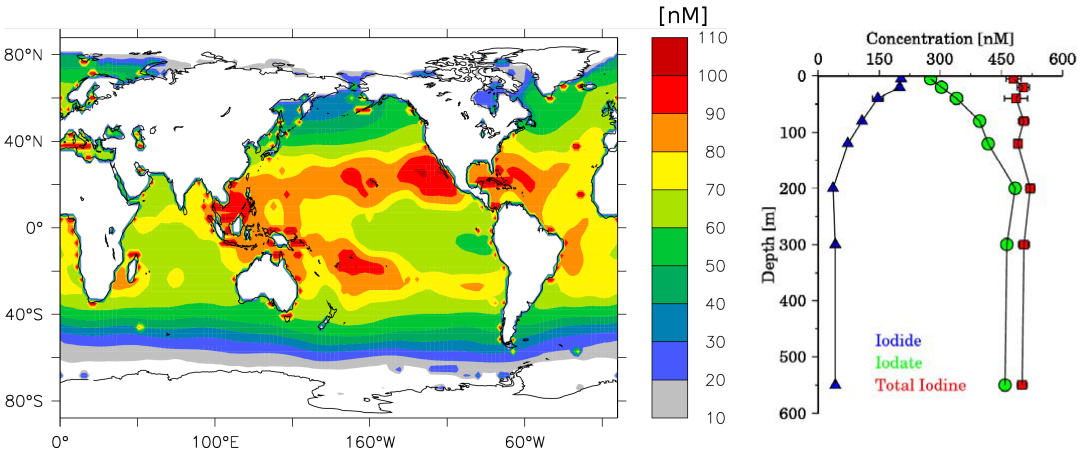

Figure 2.2.: Modelled surface water iodine concentrations from Ganzeveld et al. [2009] based on Truesdale et al. [2000] and nutrient distributions. The distribution is similar to Figure 2.5, but does usually not include coastal effects. The Iodide/Nitrate correlation was observed to be high in general, but lower for the region around the Cape Verdian islands due to upwelling. Nitrate data was used as a proxy to obtain a map of iodide. On the right a typical depth profile of iodide and iodate in the tropical Atlantic [Bluhm, 2010]. In the upper seawater layers a significant part of the total iodine content can be found as iodide.

region [Garcia et al., 2014].
Dissolved iodine in deep sea water is dominated by iodate with a small contribution of iodide, e.g. from 0-10nmol l^{-1} for Antarctic waters [Bluhm et al., 2011]. The same applies for tropical deep water, due to the transport processes of the thermohaline circulation. Iodate can be reduced to iodide e.g. in cold water diatoms as reported by Chance et al. [2007], Wong et al. [2002]. Different sort of algae have different capabilities in reducing iodate, ranging from 0.01-0.3 nmol $l^{-1}\mu g$ chl-a^{-1} day^{-1}. Bluhm [2010] made similar observations, but connected the iodide production to growing behaviour of the phytoplancton: No iodide was produced during the exponential growth phase, but started later during the stationary phase and peaked during senescent growth phase. The typical lifetime of diatoms is 2 months. A fast pathway for reduction of iodate to iodide is the reaction with bisulphide under anoxic conditions [Jia-Zhong and Whitfield, 1986], which has also been observed for profile measurements of iodide in the anoxic layers of the Black and Arabian Sea. It was observed that this reaction was faster whenever anoxic and oxic water masses were mixed. This might represent a contribution to enhanced surface water iodide concentrations in upwelling areas around Cape Verde and off the Peruvian coast, where Oxygen Minimum Zones (OMZs) are found below depths of 50-100m also exhibiting increased levels of iodide [pers. comm. P. Croot, data from Meteor expedition M77-1 in the Peruvian upwelling, [Croot et al., 2014, in prep.]] down to more than 300m and around 500 nmol l^{-1}. Normally the iodide concentration maximum is

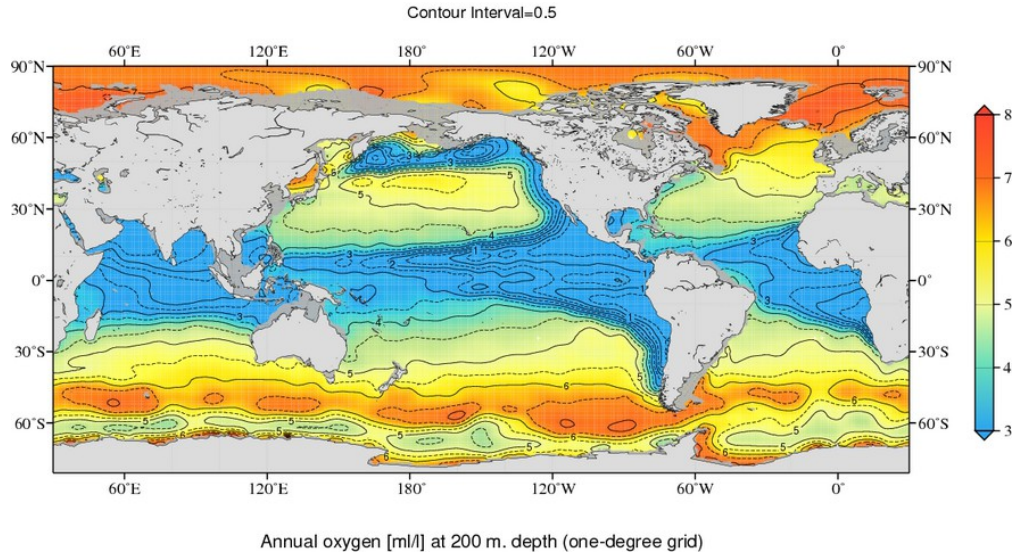

Figure 2.3.: Oxygen concentration in ml/l in a depth of 200m during December. From the World Ocean Atlas 2013 [Garcia et al., 2014].

found close to the surface. Deep iodide maxima in oxygen depleted waters have not been observed at the Mauritanian upwelling [Bluhm, 2010]: Maybe because the OMZ in the eastern tropical Pacific has a larger extend. Furthermore both areas are characterized by their upwelling characteristics, which is a pathway of iodide to surface waters. There it can be volatilized and released into the MBL. According to [Martino et al., 2008] this release has a pathway via enhanced emissions of halocarbons, which can be formed from iodide and DOM, apart from direct volatilization of iodide mentioned above.
Truesdale et al. [2000] observed a correlation of surface water iodide and nitrate concentration, which rises the question if there is a connection between the reduction processes for nitrate and for iodate. For the reduction of iodate via nitrate reductase the results are contradictory [Bluhm, 2010]: no direct connection was found by Waite and Truesdale [2003] at least for one type of phytoplancton (I. Galbana), while Tsunogai and Henmi [1971] suggested a pathway of iodate reduction via nitrate reductase based on the observed relation of nitrate and iodate/iodide concentrations (as used e.g. in Ganzeveld et al. [2009] and observed in [Truesdale et al., 2000, Chance et al., 2014]).
Reduction mechanisms via zooplancton activity, reaction with glutathione (an important antioxidant found in plants, animals, fungi and some bacteria and archaea) and reaction with Mn(II) in sediments were observed, but their rates are unknown. [Bluhm, 2010]
While the path from iodide to iodate has been studied, the reaction mechanism for the opposite direction from iodide to iodate is still unclear. Photochemical processes which can oxidize iodide to iodate are too slow to explain e.g. the low levels of iodide in deep waters. There are hints that this might be possible via enzymatic reactions in phytoplancton as well. A possible pathway of oxidation would be via atmospheric chemistry.

The dissolved iodine itself can act as a sink for tropospheric ozone [Garland and Curtis, 1981, Ganzeveld et al., 2009, Hayase et al., 2010] and can lead to emissions of I_2 and HOI which in turn are eventually photolysed to I and oxidized to IO. The above mentioned measurements have been partly repeated and published in Carpenter et al. [2013] (see subsection 1.4.3.1).

Using ambient ozone mixing ratios of 10-20 ppb for the remote western Pacific and a typical tropical iodide surface water concentration of 100 nmol l^{-1}. The plot (Figure 2.4) shown in Carpenter et al. [2013] yields similar estimations of the additional I_2 flux of $1 - 2 \cdot 10^8$ molecules $cm^{-2}s^{-1}$ postulated by Großmann et al. [2013] and Sommariva and von Glasow [2012], given ozone concentrations of 10-20 ppb and typical iodide concentrations for the Western Pacific during the TransBrom cruise. It is unclear from these measurements which role HOI plays at realistic ozone mixing ratios and iodide concentrations.

In contrast to Ganzeveld et al. [2009] who derived iodide concentrations based on nitrate as shown in Truesdale et al. [2000], MacDonald et al. [2013] inferred ocean surface iodide concentrations from sea surface temperature measurements. They showed that the release process itself seems not to be significantly temperature dependent and that in case of moderate winds the observed IO concentrations on the open ocean could be reproduced by this model. The model failed for low wind speeds and was based only on modelled ozone mixing ratios.

Chance et al. [2014] compiled a first overview of data for the world-wide surface water iodide distribution and found for their data set of iodide and iodate measurements a correlation of iodide with nitrate as well as with temperature.

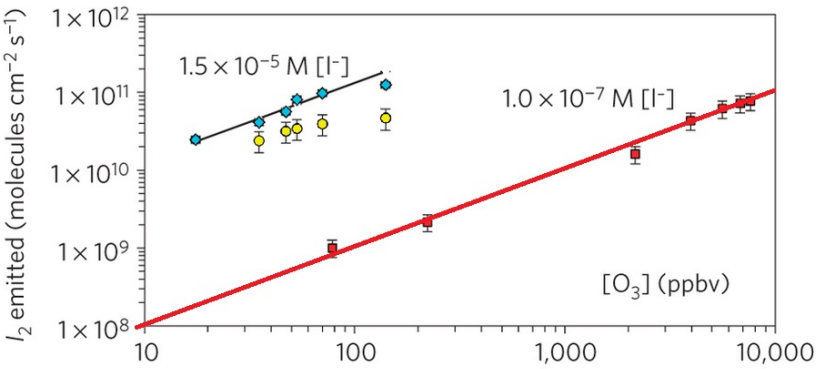

Figure 2.4.: I_2 flux and ozone concentrations, plot adapted from from Carpenter et al. [2013]. Extrapolating the linear fit of the measurements marked in red (100 nmol l^{-1} iodide) representative for tropical surface water iodide concentrations and using an ambient ozone concentration of 10-20 ppb results in an I_2 flux comparable to the one postulated in Großmann et al. [2013] ($1 - 1.8 \cdot 10^8$ molecules $cm^{-2}s^{-1}$). Note the double-logarithmic plot.

2.3. Coastal waters

For open ocean conditions the iodide content of seawater does not depend on salinity and of the Chla-concentrations [Chance et al., 2014], whereas in coastal water the freshwater input and other estuarine processes can be important for the iodine content in brackish water and are leading to strongly varying iodide concentrations. Low-oxygen zones are common in coastal areas and can increase the reduction of iodate and sedimentation can play a bigger role, leading to a larger influence of reactions within the sediment.

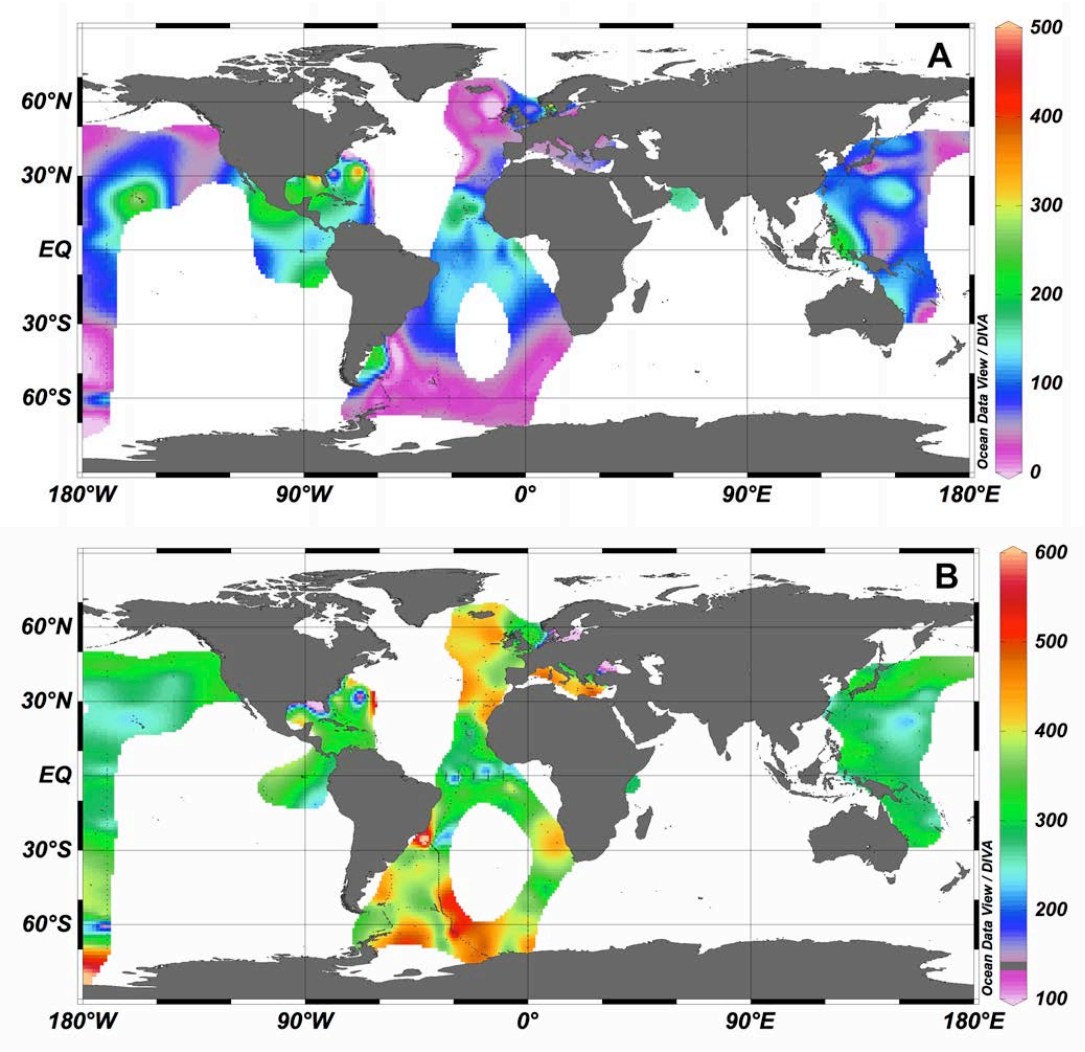

Figure 2.5.: Compilation of surface water iodide (A) and iodate (B) measurements. [personal communication T. Jickells and R. Chance, publication in prep. Chance et al. [2014]]. A plot of all data points over latitude is shown in figure 12.3. Surface water iodide concentrations during M77 in the Peruvian upwelling region indicated surface water iodide concentrations of around 500 nM [Croot et al., 2014, in prep.].

3. Differential Optical Absorption Spectroscopy

A well established measurement technique for atmospheric trace gases is the DOAS method [Platt and Stutz, 2008]. It can be used for a variety of trace-gases: aromatics, OH, SO_2, O_3, HCHO, BrO, HONO, O_4, NO_2, NO_3, OClO, IO, glyoxal, H_2O, OIO, I_2, O_2 and others in the ultra-violet/visible region, but also for CH_4 and CO_2 in the near infrared.

DOAS measurements can be divided into active and passive DOAS measurements: Active measurements use an artificial light-source and measure absorptions along a defined light-path (Long-Path-DOAS, e.g.) or within a resonator (Cavity-Enhanced-DOAS). Passive DOAS applications use direct or scattered sun- or moonlight for measurements on the ground, in the air or on satellites. Using different measurement geometries allows to retrieve height information of atmospheric absorbers (e.g. MAX-DOAS).

Within this thesis, mostly ground-based passive MAX-DOAS measurements were conducted in the marine boundary layer. During two campaigns, these were complemented by CE-DOAS measurements, allowing to

A detailed overview over different DOAS measurement techniques can be found in Platt and Stutz [2008].

3.1. The DOAS Method

The Differential Optical Absorption Spectroscopy (DOAS) method [Platt and Stutz, 2008] introduced by Perner and Platt [1979] is an application of the Beer-Lambert law. It is typically used to measure concentrations of trace-gas absorbtions along an absorption light-path. It relies on quantifying absorbers by their narrow-band, differential part of the absorption spectra and neglecting the broad-band part. This has the advantage that broadband absorption processes such as Mie and Rayleigh scattering with absorption cross-sections such as $\sigma(\lambda) \propto \lambda^{\kappa}$ can be left out. Technically, the broad-band part of the optical density is often represented by a polynomial or removed by binomial filters.

The Beer-Lambert law in its differential form describes the relation between incoming light and its attenuation due to a number of absorbers i of concentration c_i. This approximation holds as long as there is no emission of light by absorbers, due to black-body radiation, fluorescence or other effects.

$$dI(\lambda) = -\sum_i \sigma_i(\lambda) c_i dx \tag{3.1}$$

Integration gives then the well-known exponential relationship between a measured intensity I after a distance L and the original intensity I_0

$$I(\lambda) = I_0(\lambda) \exp\left(- \int_0^L \sum_i \sigma_i(\lambda) c_i(l) dl \right) \tag{3.2}$$

In experiments, L, I and I_0 are determined. From the two spectra the optical density τ averaged over L is calculated:

$$\tau(\lambda) = -\ln \frac{I}{I_0} = +L \sum_i \sigma_i(\lambda) c_i \tag{3.3}$$

The optical density is separated into a broad-band τ_b and a differential part τ'. The same applies to the absorption cross-sections $\sigma_i = \sigma_{b,i} + \sigma_i'$.
Having measured a sufficient number of wavelengths simultaneously and knowing the absorption cross-section from previous measurements or from literature allows then to determine all c_i simultaneously. Usually, the column densities $S_i := Lc_i$ are determined and later converted into concentrations. Typically the term 'Slant Column Density (SCD)' is used for evaluations using a fixed, often extraterrestrial Fraunhofer reference, as in the case of satellite measurements. 'Differential Slant Column Density (dSCD)' is used for the column densities obtained by a spectral retrieval using a ground-based reference spectrum. 'Vertical Column Density (VCD)' denotes the vertical integral over the respective concentration.

3.1.1. Saturation and I_0 effect

Both, the saturation and I_0 effect are caused by the fact that Beer-Lambert law does not commute with the convolution operation, which is needed to convert the cross-sections into the instrument's resolution [Wenig et al., 2005]. The **saturation effect** can be observed for absorbers of which parts have high optical densities and are not constant over the width of the instrument function $H(\lambda, \lambda_0)$. Then the linear operation of the convolution does not commute anymore with the exponential of the absorption law, since the high optical densities might effectively appear smaller after convolution. For weak absorbers $exp(-S * \sigma) \approx 1 - S * \sigma$ holds and therefore no saturation effect is expected. By using a column density or obtaining it from a previous fit, the convolution can be modified to account for the saturation effect:

$$\sigma^*_{Sat}(\lambda) = \frac{1}{S} \ln \left(\exp(-S \cdot \sigma(\lambda)) \otimes H \right) \tag{3.4}$$

Similarly to the saturation effect, the I_0 **effect** [Platt et al., 1997] is most prominent for highly structured cross-sections. This effect denotes the effective weighting of the absorption cross-section, if the light source is highly structured itself, such as the Sun. Therefore this needs to be corrected in MAX-DOAS measurements only, while the light sources of LP/CE-DOAS systems have usually broader structures than the absorbers itself. The zeroth order I_0 correction does therefore not rely on the optical densities of the absorber, but often it is corrected together with the saturation effect according to

[Aliwell et al., 2002] and Vogel et al. [2013] for a fixed dSCD. Here the corrections were calculated using the Kitt Peak solar flux atlas [Chance and Kurucz, 2010].

The I_0 effect can be estimated by calculating the absorption of an absorber $\sigma(\lambda)$ with a column density S at high spectral resolution. The resulting spectrum is then convoluted with the instrument function, as is the spectrum of the light source. From these convoluted spectra the effective optical density is calculated and the corrected cross-section is obtained by rescaling the optical density. For the case of $S \to 0$ the pure I_0 effect is corrected, for a realistic S this also corrects for the saturation effect.

$$\sigma^*_{I_0}(\lambda) = \frac{1}{S} \ln \left(\frac{I_0 \exp(-S \cdot \sigma(\lambda)) \otimes H}{I_0 \otimes H} \right) \tag{3.5}$$

From the side of the technical implementation the problem of limited numerical precision needs to be adressed when choosing S to be very small. In this case, $\ln(x)$ and $\exp(x)$ need to be replaced by separate implementations of $\ln(1 + x)$ and $\exp(x) - 1$, since the fixed number of digits of a floating point number might lead in this case to large numerical effects on the calculated cross-section[1].

If the column density is chosen iteratively for one DOAS fit, S will converge sufficiently after 1-2 iterations according to Lehmann [2014]. If strongly varying dSCD are expected, a possible approximation is the linearisation of the correction: Including additionally the difference of convoluted cross-section for different column densities S in Equation 3.5 can be used to avoid time-consuming re-convolutions for each DOAS fit. Furthermore, these linearised correction spectra can be used to determine if the correction itself is correct, relevant at all, or even introducing larger errors. The I_0 and the saturation effect correction depend on the accuracy and resolution of the trace gas cross-section, as well as on the actual high resolution solar reference spectrum. Therefore care needs to be taken for each of the corrected cross-sections, since a shift in the literature cross-section leads to an error in the I_0 correction, which cannot be compensated for by a shift in the DOAS fit.

3.1.2. Additive components of spectra

Corrections for effects taking place in intensity space, such as the influence of Raman scattering (see also section 5.2), are usually done by using a Taylor expansion of the optical density:

[1] Based on an article from http://www.codeproject.com/Articles/25294/Avoiding-Overflow-Underflow-and-Loss-of-Precision the functions *double SpecMath::ExpMinusOne(double x)* and *double SpecMath::LogOnePlusX(double x)* have been tested in MATLAB and were implemented in DOASIS. *SpecMath::ConvoluteI0SaturationCorrected_ext* makes use of these functions, but is not used by default.

$$\tau = -\ln\left(\frac{I+\sum_i I_{i,add}}{I_0}\right) \tag{3.6}$$

$$= -\ln\left(\frac{I}{I_0}\left(1+\sum_i \frac{I_{i,add}}{I}\right)\right) \tag{3.7}$$

$$\approx -\ln\left(\frac{I}{I_0}\right) + \sum_i \frac{I_{i,add}}{I_0} + \mathcal{O}(I_i) \tag{3.8}$$

This correction is typically also used to compensate for instrumental problems, such as the influence of a constant intensity offset due to stray-light within the spectrometer. This is often diffusely reflected on the walls of the spectrometer and therefore creates an intensity offset which is often approximated by a constant.
Whenever the $I_{i,add}(\lambda)$ are smooth and do not show strong structures, the effectively fitted spectra $\frac{I_{i,add}}{I_0}$ will look similar and thus they can compensate each another. This appears to be sometimes the case for the stray-light compensation and the liquid water Raman spectrum, since the liquid water Raman response is several nanometers broad and creates a smooth Raman spectrum. This is also the reason which makes the identification of structures caused by vibrational rotational Raman scattering (VRS) on N_2 and O_2 difficult, since often the straylight term included in several fits already compensates for at least half of the effect. It leaves differential structures, though.
Another source for potential residual structures is the $\mathcal{O}(I_i)$ term in equation 3.8: 10% constant additional offset to the intensity can be compensated by using the approximation given above of $1/I_0$ to the accuracy of a peak-to-peak optical density of $4 \cdot 10^{-5}$ in the BrO wavelength range, which is so far below typical instrumental capabilities. Using $1/S_0$, the reciprocal high resolution solar spectrum, and convolving it afterwards as it has been done e.g. in some cases for VRS in liquid water, this results in a peak-to-peak optical density of 10^{-4}, since division and convolution do not commute.
Another possibility is to calculate the Raman spectrum (RRS or VRS) from a solar atlas and divide it by the reference spectrum. Since this does not include quantum efficiency of the CCD and the grating efficiency, these effects do not cancel out and can create additional residual structures [Lübcke, 2014]. Using the same solar atlas to convolute the denominator[2], these effects will cancel out if they do not change significantly within the wavelength shift caused by the Raman scattering. Strong absorbers like ozone and water vapour might need to be considered separately when calculating Raman correction spectra from a solar atlas, since the ring signal can be as large as 2% of the original intensity.

3.1.3. Deconvolution of cross-sections recorded at low spectral resolution

If a cross-section to be used within a fit has been recorded at a resolution which is of the same order of magnitude as the spectral resolution of the DOAS instrument, either

[2]This was e.g. the recommended setting for Ring spectra during the CINDI and the MAD-CAT Campaign 2013 where a Raman spectrum and a solar spectrum were provided.

the cross-section can be deconvolved and then convoluted with the correct instrument function. Or the measured spectra and all but this cross-section need to be additionally convoluted with the instrument function, which was used to record the low-resolution cross-section. The latter approach reduces the spectral resolution as well as it makes the interpretation of the fit error more difficult, because adjacent pixels cannot be regarded as independent anymore. Therefore deconvolution of cross-sections is the favourable way to go, but it cannot be done, since the information for the high resolution spectrum is not available. In combination with the convolution to the instrument function with lower spectral resolution, it is possible. Unfortunately, the instrument function is usually not given in publications of literature cross-section, therefore often a Gaussian shape has to be assumed.
In the frequency domain a convolution with a constant point-spread function is transformed into a simple multiplication. Thus, a deconvolution with the instrument function of the literature cross-section $l(\lambda)$ and the convolution with the respective instrument function of the DOAS instrument $h(\lambda)$ can be implemented as multiplication with $\tilde{h}(\nu)/\tilde{l}(\nu)$, where $\tilde{}$ denotes the respective Fourier transformed spectra. Filtering is necessary because $|\tilde{l}(\nu)|$ can be close to zero.
The results of deconvolution were comparable for different tested methods:

1. Formulation of convolution as matrix operation C, singular value transformation, removal of degenerate eigenvalues and reconstruction of an inverse operation on the non-degenerate subspace S, having chosen the regularization value γ appropriately:

$$C = TDT^{-1}$$
$$D_{S,ii} = \begin{cases} 0 & \text{if } D_{ii} \leq \gamma \\ D_{ii} & \text{otherwise} \end{cases}$$
$$C_S^{-1} = T_S D_S^{-1} T_S^{-1}$$

2. Deconvolution using Lucy-Richardson method [Richardson, 1972] using the given resolution and a gaussian shape, implemented in MATLAB[3]

3. Blind deconvolution using a Gaussian instrument function as default value, implemented in MATLAB

4. QDOAS [4], which has an implementation of Fourier-based deconvolution/convolution

An example for the approaches 2. and 4. is shown in figure 3.1.

3.1.4. The relation of fit error and measurement error

The DOAS fit (e.g. in the software DOASIS[Kraus, 2006]) estimates a fit error based on the non-linear and the linear part of the problem $J = X\beta$ for each of the parameters

[3] Negative values will be zero after deconvolution using 'deconvlucy' in MATLAB, therefore adding an offset before deconvolution might be necessary.
[4] Homepage: http://uv-vis.aeronomie.be/software/QDOAS/

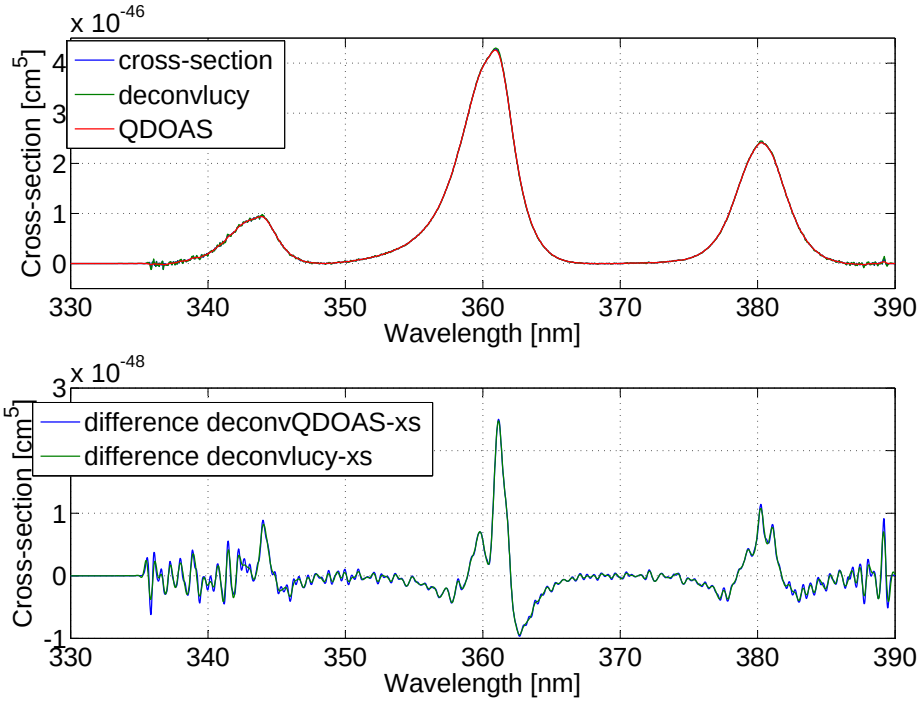

Figure 3.1.: The effect of deconvolution shown for the O_4 cross-section by Thalman and Volkamer [2013]. Here the deconvolved O_4 cross-sections were created using the *'deconvlucy'* function from MATLAB and the deconvolution routine from QDOAS. Above the total absorption cross-section is shown, below the difference between the convoluted cross-section and the convolution of the deconvolved cross-section. Typical dSCDs are $4 \cdot 10^{43}$ molec^2 cm^{-5}, therefore this effect is negligible.

in β based on the covariance matrix $\Theta = \hat{\sigma}^2[X^T X]^{-1}$. $\Delta\beta_i$ is then the square root of the diagonal entries $\sqrt{\Theta_{ii}}$, with σ as an estimate for the error for each pixel in the spectrum J. Thus, effectively the diagonal entries of the covariance matrix are used to indicate the error propagation from the residual to the fitted values. $X^T X$ contains the scalar products of each of the fitted spectra, therefore their squared lengths are found on the diagonal entries. Possible similar-shaped absorption cross-sections e.g. for different temperatures can introduce significant non-diagonal entries and should be avoided or orthogonalized, if their absolute value is of interest. For the error calculations these non-diagonal entries will result in larger diagonal entries in the inverse, thus increasing the fit error of the respective parameter. The fit error from the Levenberg-Marquardt algorithm is added quadratically.
This procedure can lead to an underestimation of the measurement error of the respective quantity, since this estimate for the error based on the residual might be misleading. The

fit error does not take into account any systematic structures in the residual, since the estimate for the error of the individual pixel J_i is derived from the overall residual spectrum. An absorption which is not included in the fit can be compensated by one of the fitted absorbers, thus the residual will underestimate the actual error.
The fit error underestimates the measurement error typically by a factor of two, depending on how structured the residual spectra are. In cases where the residual spectra are dominated by shot noise due to photon statistics, this factor can be even smaller than one [Vogel et al., 2013]. For a random residual spectrum the Monte-Carlo calculations presented in Stutz and Platt [1996] give an estimate on the size of the correction factor $C(\tau, W)$, given the absorption structure width τ of the absorber and the residual spectra W, respectively. For measurements where a constant concentration of an absorber is expected, comparing histograms of the distributions of measured quantities allows for an alternative estimate of this correction factor.

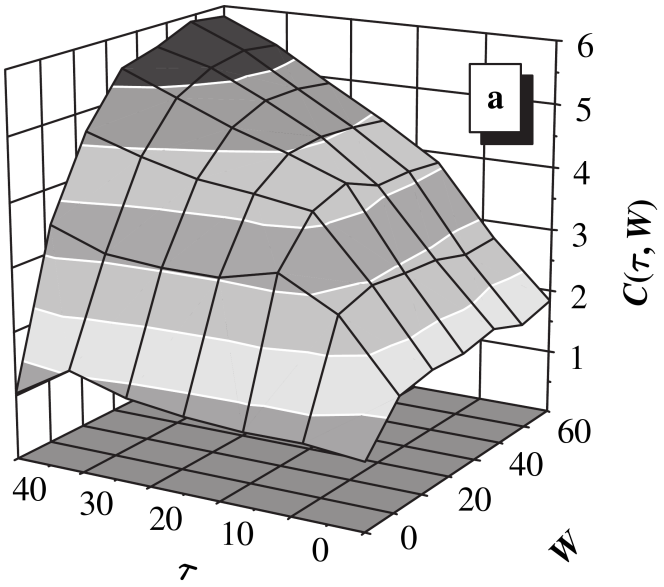

Figure 3.2.: Diagram to estimate the correction factor $C(\tau, W)$ to obtain the measurement error from the fit error. It depends on the width of the absorption structures τ and the width of the residual structures W. [Stutz and Platt, 1996]

In reality, however, the assumption that the structures in the residual spectra are random, is usually not true. The fact that neighbouring pixels are related and thus residual structures are created, points towards a systematic problem in the data evaluation. If several non-Gaussian error sources exist, the resulting distribution of the measured quantity might then indeed look Gaussian again. The above-mentioned estimation of the correction factor from histograms will give reasonable results, but the information of the dependency of the measured quantity on possibly recurring residual structures is lost and cannot be observed. An analysis of residual spectra allows to disentangle

residual structures, quantify them and compare them to any quantity of interest. Using this approach, hidden correlations and possible hints for improving the spectral analysis can be obtained. This analysis provides the possibility to quantify the impact on each of the retrieved trace gases. Three methods to analyse residual spectra are introduced in section 3.3
As an example the ubiquitous residual structure observed in the spectral evaluation range of BrO (subsection 5.1.1.2) might look at first as any other slightly structured residual spectrum. But correlating it to O_4 dSCDs reveals a strong correlation and furthermore also higher BrO dSCDs are observed whenever this structure is large. Since both, the residual structure and the retrieved absorption of BrO are of comparable size, this gives a new and better upper limit on the detection limit of tropospheric BrO. Due to overlaying shot noise and other factors deteriorating the residual, this connection would have not been possible to be seen without analysing residual spectra and could have led e.g. to the belief of observations of significant BrO during ARK27 (section 10.3), where actually the reason for the apparent BrO looks as it is an interference correlated with the O_4 dSCD and thus with some tropospheric absorber not correctly accounted for in the fit. In subsection 3.3.2.3 an approach to analyse residual spectra is described, which can allow for a better estimate of the fit error.

3.2. Experimental realisation

In experiments, a light-path needs to be realized, which is long enough to detect the trace gas of interest at given instrumental noise limitations and providing enough light to reduce noise due to photon statistics. For Long-path-DOAS measurements (subsection 3.2.2) the absorption light path is established between telescope and retro-reflector, typically placed in a distance of 1–10 km. Cavity-enhanced (CE-DOAS) measurements (subsection 3.2.5) the light-path is folded in between two highly reflective mirrors at a distance of typically 10–200 cm obtaining an effective light-path of 1–5 km. Passive DOAS applications use light from the Sun or the Moon instead of an artificial light-source. Zenith-sky measurements of scattered sunlight can be used to retrieve information about atmospheric absorbers using measurements at different Solar Zenith Angle (SZA). To obtain a higher sensitivity for tropospheric absorptions of trace gases, spectra of scattered light at different telescope elevation angles are obtained, so-called MAX-DOAS measurements (subsection 3.2.3). Passive measurements of scattered sunlight have a variable absorption light path, which needs to be estimated or modeled explicitly (subsection 3.2.4.1).
Furthermore, a number of issues need to be addressed:

- Instrument-specific corrections of the measured spectrum
- Detector pixels need to be mapped to wavelengths, see section 3.4
- Instrumental instabilities
- The response function of the spectrometer has a characteristic shape and is of finite width, i.e. it has a finite resolution

- The measured quantities, wavelengths as well as intensities, are quantized
- No I_0 spectrum might be available

For each measurement, the measured raw spectra need to be corrected for dark-current, offset and in some cases non-linearity of the detector. The dark current spectrum is a measurement of the leakage current of each element of the CCD due to random formation of electron/hole pairs in the detector. It is proportional to the exposure time. The offset spectrum is an electronic offset added to each readout operation before A/D-conversion to operate the A/D-converter in its linear range and is therefore proportional to the number of readouts, also called 'scans'. The non-linearity of the detector response relative to the incident intensity can be caused by readout process or during the measurement itself, since each measured photon also changes the potential within the CCD element.
The corresponding wavelength for each detector pixel needs to be determined, using calibration spectra or sunlight, see section 3.4.
Drifts in the pixel to wavelength mapping of the spectrometer can be compensated by allowing a shift of the cross-section when calculating the column densities S_i from the optical density. This step makes the fitting process non-linear, which implies the need for a different fit routine. This is normally done by alternatingly solving the linear and non-linear problem [Platt and Stutz, 2008] using the Levenberg-Marquardt [Levenberg, 1944, Marquardt, 1963] algorithm, which is a combination of gradient decent and Gauss-Newton algorithm. However, for small shifts the whole procedure can be linearised [Beirle et al., 2013] to save computing time.

3.2.1. Instrument function

The instrument function is defined as the response of the spectrometer to monochromatic light with a wavelength λ_0. In practice, this situation is approximated in most cases by observations of mercury, neon or krypton emission lines. An example of the high resolution structure of a mercury line is shown in figure 3.3. The instrument function $H(\lambda_0, \lambda)$ is used to calculate how a high-resolution literature absorption cross-section σ_{Lit} of a trace-gas looked like if they would have been measured with this instrument. This operation is in fact a convolution of the cross-section with the instrument function.

$$\sigma(\lambda) = H \otimes \sigma_{Lit} := \int H(\lambda_0, \lambda)\sigma_{Lit}(\lambda_0)d\lambda_0 \tag{3.9}$$

$H(\lambda_0, \lambda)$ is usually not constant over λ_0 due to optical properties of the spectrometer. Therefore, these changes over wavelength need to be simulated, fitted from measured spectra [Lehmann, 2014] or approximated from surrounding lines [Frieß, 2001, Yilmaz, 2012] or can in most cases be approximated to be constant over a certain wavelength interval.
For drifts of the wavelength calibration of the instrument, often shifts are allowed for in the fit. To clearly identify a position of an absorption line, a width of the instrument function of at least 5px is needed. Otherwise aliasing effects can occur, since the signal is not anymore well-defined by the points sampled according to the Nyquist theorem.

In Chance et al. [2005] a detailed mathematical analysis and a possibility to calculate correction spectra is presented. Usage of spectrometers with an instrument function of Gaussian shape with a width of 4.5-6.5px is therefore important. Furthermore, the shape of the lines itself is important, since an instrument with an instrument function of rectangular shape but a width of 6px will as well suffer from under-sampling effects.

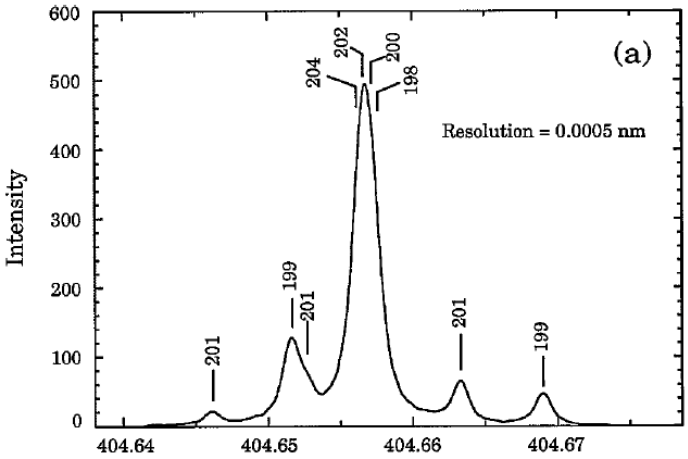

Figure 3.3.: High resolution spectrum of a mercury emission line. The single different lines are emissions by different mercury isotopes, which are separated due to their hyperfine structure. Above a spectral resolution of 20pm the emission can be treated as a single emission peak for most DOAS applications. (from Sansonetti and Reader [2001])

Convolution is a linear operation and the exponential of the Beer-Lambert law is not, therefore they do not commute. This effect can be observed for strong absorptions and is called *saturation effect*. Furthermore, structured I_0 spectra might effectively lead to a weighted sum of the literature cross-section over the width of the instrument function, an effect usually called I_0-*effect*. The correction for these effects is shown in subsection 3.1.1.

3.2.2. Long-Path-DOAS

The most simple DOAS system is the Long-Path-DOAS, which basically consists only of a light-source and a spectrometer, measuring absorbers along a defined absorption path. In practice, light-source and spectrometer are located at the same site, allowing for direct measurements of the light-source spectrum to obtain absolute concentrations and folding the light-path from a telescope back via a retro reflector. Typical LP-DOAS systems allow for recording of background spectra to avoid the influence of scattered/reflected sunlight.
LP-DOAS measurements have the advantage, that their light-path is well-defined, therefore concentrations can easily be calculated. During this work no LP-DOAS measure-

ments were performed, but measurements from the HaloCaVe campaign [Tschritter, 2013] were used together with MAX-DOAS observations to identify systematic deviations of water vapour absorption band strengths (see also section 5.3).

3.2.3. Multi-Axis-DOAS

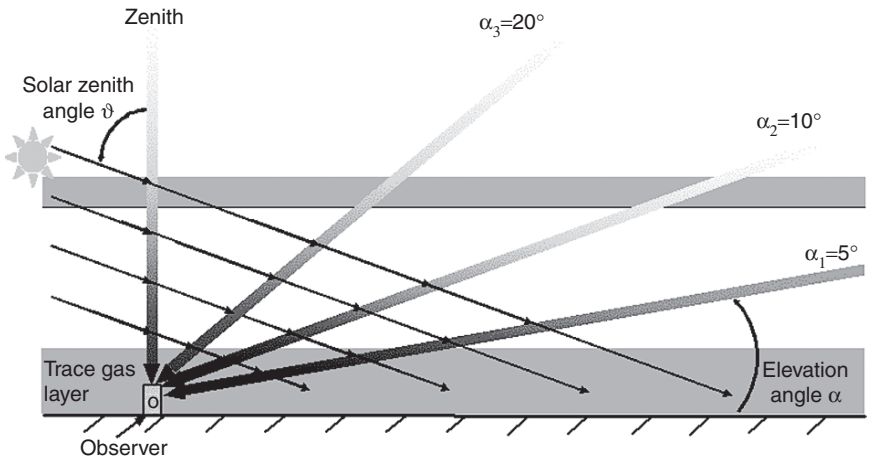

Figure 3.4.: Schematic of a MAX-DOAS measurement setup [Platt and Stutz, 2008]: Scattered sunlight is measured at different elevation angles α, yielding a higher sensitivity for tropospheric absorbers than zenith-sky measurements only. Typically spectra at elevation angles between 1-90° are recorded. Lower elevation angles provide more information about the height distribution of tropospheric absorbers, therefore typically more than half of the measured spectra are recorded at elevation angles below 10°. From zenith-sky measurements of scattered sunlight information of stratospheric absorbers can be obtained by observations at different SZA θ.

The method of Multi-Axis DOAS (MAX-DOAS) measurements was first described by Hönninger and Platt [2002] and uses scattered sunlight collected by a telescope pointing towards the sky at different elevation angles from 1° to 90° (relative to the horizon). Each elevation has a different sensitivity for absorptions in different heights of the atmosphere. Low elevation angles have a high sensitivity to absorbers close to the surface, because the difference in the corresponding light path compared to a zenith spectrum is mostly located within the lowermost layers of the atmosphere [Hönninger et al., 2004].
From the MAX-DOAS measurements differential slant column densities (dSCDs) can be calculated for each fitted trace gas: A Fraunhofer reference spectrum is chosen from one of the measurement spectra and the dSCD $\Delta S(\alpha) = S(\alpha) - S_{ref}$ is obtained from the DOAS fit for each elevation angle α relative to the Fraunhofer reference. The DOAS fit includes the convoluted cross-sections listed in section 5.6. By choosing references close to the measurement spectrum the influence of the instrumental instabilities on the result

can be minimized and the influence of stratospheric absorbers cancels out. The SCD is defined as the integral over the concentration along the light path and is hence given in units of *molec* cm^{-2}.
As Fraunhofer reference spectrum either a current, a noon or a fixed reference spectrum is used. For the current reference the two closest 90° spectra are averaged to minimize shot-noise and the effective time difference to the measurement spectrum recorded in between. This has the advantage that instrumental instabilities cancel out, since both spectra are recorded at a similar time. Furthermore, also stratospheric influence is mostly automatically removed from the measured Optical Density (OD), since the stratospheric Air Mass Factor (AMF) changes only slowly in time. Nevertheless it is important to estimate the stratospheric influence due to this change and eventually include stratospheric absorbers at their respective temperature in the fit scenario. A fixed or a noon Fraunhofer reference is used whenever stratospheric absorption is of interest. As shown by Lübcke [2014] for the case of SO_2, a high-resolution solar reference spectrum [e.g. Chance and Kurucz, 2010] can be used as a Fraunhofer reference spectrum. This requires to compensate large stratospheric absorptions of ozone, which can lead to larger residual structures due to variations in the instrument functions (especially for variable spectrometer temperatures) or imperfections of I_0/Saturation-correction and/or of the literature cross-sections for ozone. Furthermore the detector's quantum efficiency needs to be known.
To obtain actual concentration profiles from MAX-DOAS measurements it is necessary to convert the measured dSCDs into concentrations: This can either be done by simple geometric approximations or more sophisticatedly by using an inverse modelling approach based on a radiative transfer model.

3.2.4. Error estimation for non-linearity of the CCD-detector

For Avantes spectrometer a non-linear behaviour between incident intensity and measured intensity was observed, as for the CE-DOAS setup during M91 and SHIVA (subsection 4.4.1) and the MAX-DOAS during MAD-CAT. This can introduce apparent optical densities which will be structured according to the measured spectrum and can increase the residual of the fit and/or result in wrong column densities. CE-DOAS measurements are prone to larger effects of this non-linearity, since spectra were measured at a constant exposure time. MAX-DOAS measurements need to cover a larger range of intensities, therefore the exposure time is normally adapted automatically to record spectra at a fixed maximum saturation value to minimize instrumental noise.
But even for one telescope elevation, a spectrum consists typically of the sum of 600 individual spectra with an exposure time of 100 ms each, the mean relative intensity change within one minute is already 10% during a cloudy day and even more for a broken cloud-cover (Figure 3.5). Correcting the summed spectrum will only correct the average and can therefore create systematic structures. Applying the non-linearity $p(I)$ for a MAX-DOAS measurement spectrum I and calculating the apparent optical density for an intensity change of 5%, $\tau = \ln(p(I)/p(0.95 \cdot I)$ results in a residual spectrum with an amplitude of $3 - 6 \cdot 10^{-4}$ peak-to-peak when only fitting a polynomial, using the

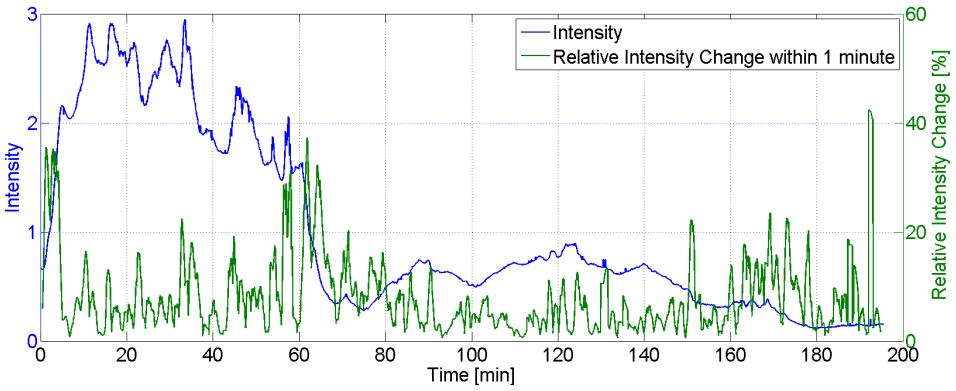

Figure 3.5.: Total intensity and relative intensity change within one minute for a series of spectra recorded at 90° elevation with 8Hz on a day with full cloud cover. After the first hour of measurements thicker clouds arrived.

measured non-linearity relation shown in figure 4.5. The size of the residual structure also depends the saturation of the measured spectrum in the fit range. Most of the residual is actually compensated in typical fit scenarios by the offset polynomial, leading to effective residuals which are one order of magnitude smaller. Nevertheless these residual structures might become relevant when summing several elevation sequences and/or interpreting the stray-light compensation term of the DOAS fit.

3.2.4.1. Radiative Transfer

Within this thesis SCIATRAN [Rozanov et al., 2005] has been used together with an IDL program written by Yilmaz [2012] to invert measurement data to obtain aerosol and/or tracegas profiles. Instead of SCIATRAN, the Monte-Carlo based Model McArtim [Deutschmann et al., 2011, Deutschmann, 2014] was used for case studies, e.g. for the wavelength dependency expected for water vapour dSCDs in subsection 5.3.1.1.

3.2.4.2. Profile Inversion

The aim of the profile inversion in remote sensing observations is to obtain profiles from a series of measurements which have probed the region of interest using each a different measurement geometry, thus containing information about the amount and the location of the quantity of interest. A model function $F(\vec{x})$, in this case a radiative transfer model, can then be employed to reproduce the measured quantities y_m (Intensities, O_4 dSCD, trace-gas dSCD or Ring signal) with an error $\sigma_{\epsilon,m}$ given the spatial information about the trace gas or aerosol distribution, represented by a state vector $\vec{x}$. Because the radiative transfer equation does not have an analytical solution, this problem is usually solved iteratively minimizing a cost function:

$$\chi^2(\vec{x}) = \sum_{m=0}^{M} \left(\frac{F_m(\vec{x}) - \vec{y_m}}{\sigma_{\epsilon,m}} \right)^2 \tag{3.10}$$

This problem can only be solved if the information content of the measurements is higher than the information content of the retrieved quantities. Since this is normally not the case for MAX-DOAS measurements, additional information is needed or the state vector needs to be parametrized in a suitable way. One way to constrain the model to reasonable results is to introduce an a-priori $\vec{x_a}$ with a certain error $\vec{\sigma_a}$. This information is often taken from climatologies.

$$\chi^2(\vec{x}) = \sum_{m=0}^{M} \left(\frac{F_m(\vec{x}) - \vec{y_m}}{\sigma_{\epsilon,m}} \right)^2 + \sum_{n=0}^{N} \left(\frac{x_n - x_{a,n}}{\sigma_{a,n}} \right)^2 \tag{3.11}$$

or rewritten with the matrices S_ϵ and S_a for the errors given for measurements and a-priori:

$$\chi^2(\vec{x}) = [F(\vec{x}) - \vec{y}]' \, S_\epsilon^{-1} \, [F_m(\vec{x}) - \vec{y_m}] + [\vec{x} - \vec{x_a}]' \, S_a^{-1} \, [\vec{x} - \vec{x_a}] \tag{3.12}$$

A solution $\hat{x}$ can be found for $\nabla_x \chi^2(\vec{\hat{x}}) = 0$. If $F(\vec{x})$ is linear in $\vec{x}$, $F(\vec{x}) = \mathbf{K}\vec{x}$, the solution can be found analytically. For the general situation where $F(\vec{x})$ is not linear in $\vec{x}$, $F(\vec{x})$ can be linearized $F(\vec{x}) = F(\vec{x}) + \mathbf{K}|_{x_0}(\vec{x} - \vec{x_0}) + \mathcal{O}(\vec{x} - \vec{x_0})^2$ and a solution can be found iteratively using a gradient descent, the Gauss-Newton method or more generally the Levenberg-Marquardt method [Levenberg, 1944, Marquardt, 1963]. Often the weighting function matrix $\mathbf{K}$ is then not calculated for each iteration step to save computation time. Details for these calculations can be found in Rodgers [2000] and for the case of MAX-DOAS in Yilmaz [2012].
Normally the atmosphere is modelled for MAX-DOAS applications in one dimension, assuming homogeneous layers. Therefore clouds can lead to misleading results in the interpretation of the outcome of radiative transfer modeling due to their limited size. When trace gas concentration profiles are retrieved, this influence needs to be considered and eventually data needs to be masked according to cloud cover. A possible cloud detection scheme for MAX-DOAS measurements has been suggested by Wagner et al. [2013a] based on relative intensities at two different wavelengths and O_4 dSCDs. Clouds can also lead to spectral interferences, since more light will reach the telescope at low elevation angles which has already been reflected at the ground when the sky is covered with clouds. This can lead to enhanced liquid water absorption, which can have an effect on the retrieval of trace-gases, see also section 5.5.

3.2.4.3. Characteristic Retrieval Properties

The properties of the retrieval can be characterized by the weighting function matrix K, the a-priori covariance matrix S_a and the measurements error S_ϵ. For a system which could be solved without having to introduce a-priori information, the so called retrieval

gain function matrix G would be just K'. It describes the sensitivity of the retrieval result, a state vector, with respect to the measured quantities. In the other direction, K describes the sensitivity of potential measurements on the state vector. Including the influence of the a-priori, the gain function can be written as

$$\mathbf{G} = \frac{\partial \hat{\vec{x}}}{\partial \vec{y}} = (\mathbf{S}_a^{-1} + \mathbf{K}'\mathbf{S}_\epsilon\mathbf{K})^{-1}\mathbf{K}'\mathbf{S}_\epsilon^{-1} \tag{3.13}$$

The dependence of the retrieved state vector $\hat{\vec{x}}$ on the real state vector $\vec{x_t}$ is expressed by the averaging kernel matrix A

$$\mathbf{A} = \frac{\partial \hat{\vec{x}}}{\partial \vec{x}_t} = \frac{\partial \hat{\vec{x}}}{\partial \vec{y}}\frac{\partial \vec{y}}{\partial \vec{x}_t} = \mathbf{GK} = (\mathbf{S}_a^{-1} + \mathbf{K}'\mathbf{S}_\epsilon\mathbf{K})^{-1}\mathbf{K}'\mathbf{S}_\epsilon^{-1}\mathbf{K} \tag{3.14}$$

This means that the retrieved state vector can be written as

$$\hat{\vec{x}} = \vec{x}_a + \mathbf{A}(\vec{x}_t - \vec{x}_a) \tag{3.15}$$

which signifies, that under ideal conditions the averaging kernel matrix is the identity matrix. Under real conditions, the averaging kernel matrix does not have full rank, since the problem is usually not overdetermined. This leads to the definition of the number of degrees of freedom of the retrieval $d_s := tr(\mathbf{A})$ [Rodgers, 1996]. Typical values for ground based measurements for d_s are 2-4.
An example for an averaging kernel matrix can be seen e.g. in figure 7.6. It cannot only be used to estimate the information content of the measurement, but also the height resolution of the retrieval.

3.2.4.4. Retrieval errors

Since the a-priori or regularization criteria introduce an effective smoothing of the final state vector, the total error of the final profile is not only the propagation of the measurement error, but a part is also introduced by the so-called smoothing error.
According to Rodgers [2000] the smoothing error is given by

$$\mathbf{S}_s = (\mathbf{A} - \mathbf{I})\mathbf{S}_a(\mathbf{A} - \mathbf{I})' \tag{3.16}$$

Since $\mathbf{A} \to \mathbf{I}$ for ideal conditions, in which the retrieved state vector is equal to the true state vector (see Equation 3.15), the smoothing error approaches zero for this situation. The retrieval noise part of the overall error and the connected covariance matrices is obtained by error propagation using the gain function matrix:

$$\mathbf{S}_m = \mathbf{G}\mathbf{S}_\epsilon\mathbf{G}' \tag{3.17}$$

and the total covariance matrix then yields

$$\hat{\mathbf{S}} = \mathbf{S}_s + \mathbf{S}_m \tag{3.18}$$

For a detailed error analysis see [Yilmaz, 2012].

3.2.5. Cavity-Enhanced-DOAS

For broadband Cavity-Enhanced Differential Absorption Spectroscopy (CE-DOAS) the setup also consists of a light source and a spectrometer. In between the light passes through two highly reflective mirrors, which act as a resonator and thus effectively provide a long light path which is necessary to archive low detection limits. A schematic setup is shown in figure 3.6.

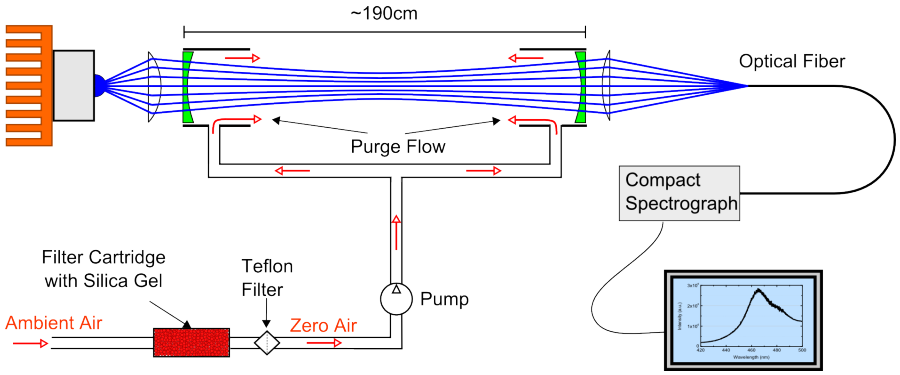

Figure 3.6.: Schematic of an open-path CE-DOAS setup as used during SHIVA and SOPRAN M91. [M. Horbanski, pers. comm.]

For the case of no absorption, the length of the lightpath L depends on the mirrors' reflectivity $R(\lambda)$. If absorbers are present, the effective length of the lightpath will decrease due to their absorption. This leads to an effective lightpath L_{eff}, which needs to be corrected for.
Given the incoming intensity from the light source I_0 there are losses on each of the mirrors and additionally within the cavity R, due to Rayleigh and Mie scattering and absorbers, named L. Thus the light coming out from the resonator will have contributions from each pair of reflections [Fiedler et al., 2005]:

$$I = I_0(1-R)(1-R)(1-L) + \tag{3.19}$$
$$I_0(1-R)(1-L)R(1-L)R(1-L)(1-R) \tag{3.20}$$
$$+... \tag{3.21}$$
$$= I_0(1-R)^2(1-L)\sum_{n=0}^{\infty} R^{2n}(1-L)^{2n} \tag{3.22}$$

Since $R(1-L) < 1$ this geometric series converges and can be written as

$$I = I_0 \frac{(1-R)^2(1-L)}{1-R^2(1-L)^2} \tag{3.23}$$

Since 3.23 is not straightforward to solve for L, another approach to evaluating measurement spectra from broadband CE-DOAS measurements is made in Platt et al. [2009]:

The change for each traverse of the cavity is

$$-\frac{dI_{in}(n)}{dn} = I_0((1-R)+(1-L)) \tag{3.24}$$

Even though n is the number of traverses of the light throught the cavity, the assumption can be made that this relation is true for any n, which allows to integrate Equation 3.24 over n. This then yields:

$$\frac{I_{in}(0)}{I_{in}(n)} = n((1-R)+(1-L)) \tag{3.25}$$

Combining the cavity losses R and the Rayleigh contribution to the losses $\epsilon_R d_0$ to $\rho_0 = (1-R)+\epsilon_R d_0$ (since the pathlength is usually determined for the air-filled cavity) and naming the remaining losses τ, Equation 3.25 will yield

$$\frac{I_{in}(0)}{I_{in}(n)} = n(\rho_0 + \tau) \tag{3.26}$$

The average number of traverses through the cavity is defined as $\bar{n} = \frac{1}{\rho_0+\tau}$, the length $\bar{L} = \bar{n}d_0$ after which the intensity is 1/e of the original intensity. The lightpath $L_0 = d_0/\rho_0$ can be determined by comparing overall intensities for gases with different Rayleigh cross-sections, such as helium and air, whose Rayleigh cross-sections differ by two orders of magnitude. Another possibility is to observe the development of the measured intensity behind the resonator for a pulsed light-source, the so called ring-down time, e.g. [O'Keefe and Deacon, 1988]. This measurement principle can be applied for different wavelengths of the incident light, allowing for the measurement of the wavelength-resolved reflectivity of the mirrors. This approach is less sensitive to disturbances and can be easily applied during measurement campaigns. Furthermore the shape of the measured path-length can be obtained from fitting a known absorber with several absorption features within the wavelength range of interest, such as NO_2. Then the absorption length needs only to be determined for one wavelength to obtain the total effective absorption length during measurements.
The optical absorption D_{CE} observed by the spectrometer is

$$D_{CE} = \ln\left(\frac{I_{tot,0}}{I_{tot}}\right) \tag{3.27}$$

with

$$I_{tot} = \int_0^\infty I_{in}(n)dn \tag{3.28}$$

and $I_{tot,0}$ for cavity filled with clean air and I_{tot} for the measurement. Since any absorption will contribute to the losses within on traverse as shown in 3.24, the effective lightpath $\bar{L}_{eff}$ will decrease. This decrease will be insignificant whenever $\rho_0 \gg \tau$, but needs to be corrected for otherwise. $\bar{L}_{eff}$ is determined in Platt et al. [2009] by comparing the optical density to a system in which the light-path is constant, which yields

$$\bar{L}_{eff} = \frac{D_{CE}}{(e^{D_{CE}}-1)\rho_0}\cdot d_0 = \frac{D_{CE}}{(e^{D_{CE}}-1)}\cdot \bar{L}_0 \tag{3.29}$$

Using the rescaled observed optical density $\alpha = \frac{D_{CE}}{\bar{L}_{eff}}$ yields together with 3.29 a corrected optical density

$$D_{eff} = e^{D_{CE}} - 1 = \left(\frac{I_{tot,0}}{I_{tot}}\right) - 1 \tag{3.30}$$

which can be decomposed into the different contributions from different absorbers by the DOAS fit in the common way as if the lightpath would be constant.

3.2.5.1. Strong absorbers

The main application of CE-DOAS within this thesis is to measure IO concentrations in the marine boundary layer in tropical regions. Here one of the main absorbers in the spectral region where IO is usually evaluated is water vapour. Water vapour with a mixing ratio of 0.02 in the marine boundary layer corresponds to a concentration of $c = 5.5 \cdot 10^{17}\text{cm}^{-3}$. With a maximum OD at 442.72 nm of $d_0 \cdot c \cdot \sigma_{max} = 1.1 \cdot 10^{-4}$ this corresponds to a loss from one mirror to the other for $d_0 = 200\text{cm}$ of $\tau = 1.1 \cdot 10^{-4}$. The mirror reflectivity itself is about $R_0 = 0.9998$ at 445 nm according to the manufacturer and calibration measurements comparing intensities of measurements in air and in helium. The lightpath within the absorption peaks of water vapour is therefore significantly smaller and the effective cross-section σ_{eff} will be distorted. The correction for the effective lightpath presented in Platt et al. [2009] does not compensate for those effects, since it is based on the measured spectra and therefore cannot account for effects caused by the finite resolution of the spectrometer.
In figure 3.7 an example of such a situation is shown. The optical density is calculated at a resolution of 1pm and then convoluted with the instrument function, whereas the cross-section in the fit is convoluted normally. A constant effective reflectivity $R = 0.9996$ has been assumed, including the losses due to Rayleigh scattering. The intensity was calculated using the geometric series in Equation 3.23. The resulting residual has a peak-to-peak size of $2 \cdot 10^{-4}$ for a water vapour optical density of $1.2 \cdot 10^{-2}$. Also the cases for $R = 0.9996, 0.9990, 0.9980$ are shown. Therefore this effect will be only noticable for situations with low aerosol load within the resonator and ideally clean mirrors. The shape of the correction does not change by more than 10% from R=0.9998 to R=0.9980 and might therefore be included in the fit scenario, if considering to include the water vapour absorption at 442 nm in the fit range. For M91 and SHIVA the effective path-length during measurements was mostly around 50-60% of the purge air measurements. Therefore this effect was not observed. Furthermore other effects apparently play a more important role (see subsection 5.7.1). Correcting for those by night-time measurement directly also compensates for this effect.
For closed path system the problem can be solved iteratively when there is no aerosol present within the lightpath, see Horbanski [2010].

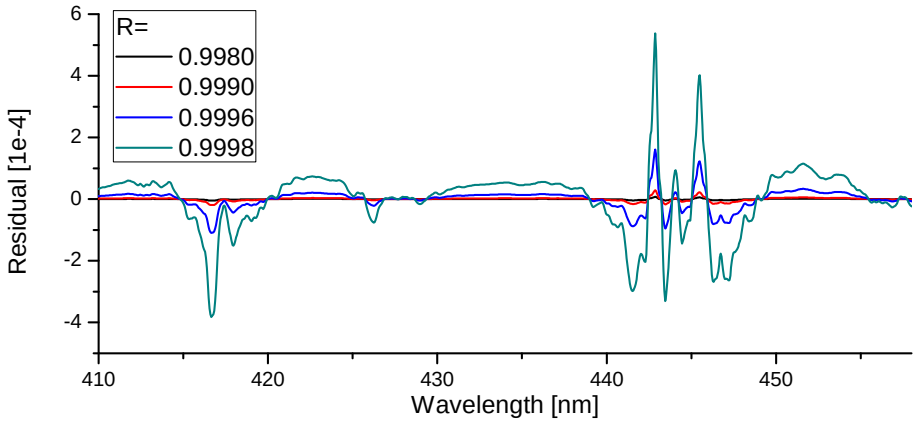

Figure 3.7.: Effect of pathlength reduction of highly resolved features of a cross-section on the shape of the apparent cross-section, shown is a fit to an artificial spectrum (using Equation 3.23) only containing water vapour when fitting a normally convoluted water vapour cross-section. These residual spectra have been calculated with a constant reflectivity, in reality however where the reflectivity is significantly smaller at 416 nm than at 445 nm, the left peak would have been suppressed. The shape of the correction does not change by more than 10% from R=0.9998 to R=0.9980. During M91 the lightpath during measurements was typically 3km, resulting in $R_{eff} \approx 0.9994$

3.3. Methods for analysing residual spectra

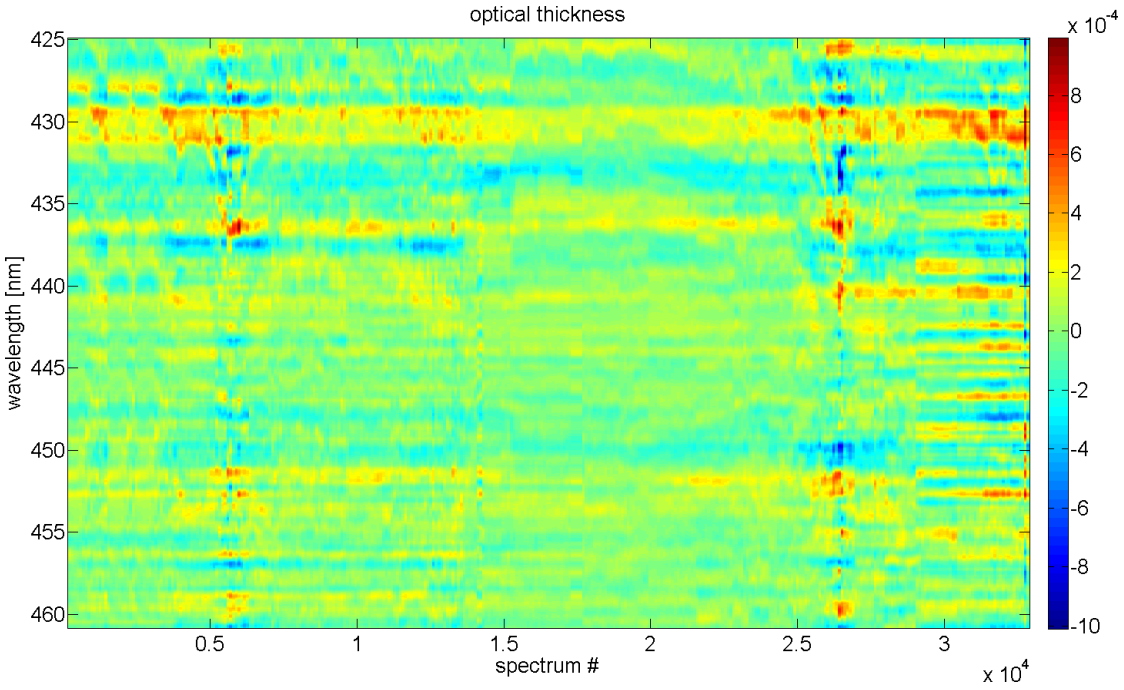

Figure 3.8.: Residual spectra for an evaluation of SOPRAN M91 CE-DOAS data. In this representation recurring features in the residual spectra are often already easy to identify.

The DOAS-fit does not only provide information on the abundance of certain absorbers within the light path of the measurement, but there is another source of information, and that is the absorptions that are not assigned to any absorber. These optical densities called residual spectra might be originating from instrumental issues [Lampel, 2010], by hot-pixels on the Charge-Coupled Device (CCD) sensor, by left-out absorbers, insufficiently saturation-corrected absorption cross-sections [General, 2013] or other factors.

Ideally the residual spectra consist only of noise, i.e. each pixel is independent of each other and their values show a Gaussian distribution around zero. In practice, this is not the case: optical absorption structures introduce correlations between neighbouring pixels and instrumental effects are usually also not independent for each pixel. Thus, the residual spectra from a normal DOAS evaluation contain some more information. Manually examining thousands of residual spectra of one measurement campaign alone is no viable solution, therefore the process of **evaluating residual spectra needs to be automatic, fast and easy to use**.

Quantifying the amount of information available from these spectra is a first step and useful to compare the quality of fits according to their residual structures. A simple approach would be to calculate the Shannon-Entropy of the dataset and compare it

to artificial noise spectra/randomized residual spectra[5]. For biometric information an approach has been suggested e.g. in Adler et al. [2006] to estimate the amount of information newly available by biometric features of a single person compared to a reference dataset. The dominant factor within the residual spectra is (hopefully) shot noise (which contains 'more information' than structured spectra), thus an approach to quantify information in the residual spectra could be entropy. This is tested in subsection 3.3.2.2.
The residual spectra themselves will be denoted by R_{ij}, where i denotes the row and j denotes the column. Plotting this matrix colour-coded sometimes intuitively shows correlated features as horizontal lines, see figure 3.8.
Correlation of residuals with already known possibly influencing factors is suggested in subsection 3.3.1 (Multiple linear Regression) and two methods for the analysis of residuals without prior knowledge are presented in subsection 3.3.2 (Principal Component Analysis (PCA)) and a possible alternative in subsection 3.3.3 (Independent Component Analysis (ICA)).

3.3.1. Multiple linear regression

Additionally to the residual spectra the respective column densities and other parameters obtained by the fit and during the measurement itself are available. An incorrect dark-current will produce residual features proportional to the exposure time, an incorrectly convoluted NO_2 cross-section creates residual structures correlated with the NO_2 column density.
To estimate their respective effects on the residual, a system of linear equations can be formulated, using the residuals as the desired outcome, the respective independent variables as factors and one vector assigned for each variable to represent its effect within the set of residual spectra.
This can be done by constructing a matrix V containing the coefficients of column densities and other measured parameters as vectors, the corresponding vectors $\vec{x}_1, \vec{x}_a, \vec{x}_b$, ... correspond to the coefficients and the residuals are known from the DOAS fit.

$$Ax + \epsilon = \begin{pmatrix} 1 & a_1 & b_1 & \cdots \\ 1 & a_2 & b_2 & \cdots \\ 1 & a_3 & b_3 & \cdots \\ \vdots & \vdots & \vdots & \ddots \\ 1 & a_n & b_n & \cdots \end{pmatrix} \cdot \begin{pmatrix} \vec{x}_1 \\ \vec{x}_a \\ \vec{x}_b \\ \cdots \end{pmatrix} + \epsilon = \begin{pmatrix} \vec{R}_1 \\ \vec{R}_2 \\ \cdots \vec{R}_n \end{pmatrix} \tag{3.31}$$

This usually overdetermined system of linear equations $Ax = R$ can be solved e.g. using a least square method. Possible effects of outliers are discussed in Chatterjee and Hadi [1986] and need therefore to be filtered out manually (e.g. by the RMS of the respective fit) before applying the linear regression or so called *'robust'* variants of linear regression algorithms have to be used. The correlation coefficient (*'Pearson's R'*) can be calculated

[5] Randomizing the actual residual spectra is an easy way to obtain residuals of the same size and intensity distribution as the original data.

and used for estimation of the significance of each of the spectra obtained corresponding to each parameter.

$$R(X,Y) := \frac{cov(X,Y)}{\sigma_X \sigma_Y} \tag{3.32}$$

Another possibility is to calculate errors of the correlation coefficients and test if they are within their error equal to zero. Special care needs to be taken for collinear or almost collinear regressors. For MAX-DOAS applications this might be trace gases with similar height profiles which are in some cases rather constant over time, as e.g. water vapour, O_4 and iodine monoxide.
An example of how such an approach can be used is shown in subsection 5.2.3.4 to identify the effect of VRS on spectral retrievals.

3.3.2. Principle Component Analysis

Principal Component Analysis (PCA) is a method which is applied in various fields for dimensionality reduction without previous knowledge. It can be used for processing images for automatic control of fabrication processes, it is used for pattern recognition such as face detection and motion detection in surveillance applications in varying environmental conditions [Hastie et al., 2001]. It is often used to characterize a subspace of background values for a series of measurements. Deviations from these background values can be easily detected and further investigated. For DOAS applications it can be used to retrieve atmospheric SO_2 [Li et al., 2013a] or to characterize the variability of the Ring spectrum [Vountas et al., 2003]. It is then useful whenever one is looking for residual structures of unknown origin, in situations were a relation to other fit parameters is not clear or not yet known. If a clear connection is suspected, the linear regression approach discussed in subsection 3.3.1 can provide information on the causes of residual spectra more specifically. The remaining residual structures which could not be attributed to certain fit parameters can then be used for a PCA anyway.
DOAS residual spectra have been analysed using the PCA method for the first time in the work of Ferlemann [1998] to analyse the residuals of ballon-borne DOAS measurements.
This approach has been first described in Pearson [1901] to find a set of planes describe an ensemble of points in the best way. In figure 3.9 an example can be seen: The task is to find a coordinate system which can best describe the position of each point. Best description means in this case to reduce the Root Mean Square (RMS) of the residual when reducing the data to a limited number of dimensions. This Ansatz leads to an alternative derivation which is also shown below.
Mathematically seen, there are correlations between each of the components i describing an n-dimensional element R_i. A matrix can be calculated describing these, the so called covariance matrix:

$$C_{ij} := \frac{1}{n+1} < R_i - \bar{R_i} | R_j - \bar{R_j} > \tag{3.33}$$

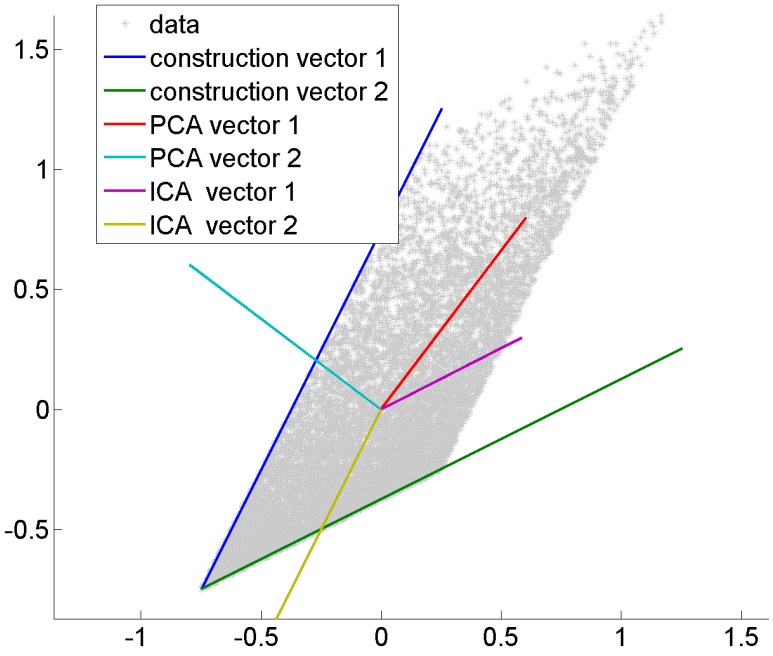

Figure 3.9.: PCA and ICA analysis of an artifically created 2D dataset based on two non-orthogonal vectors.

Its diagonal elements describe the respective variances of the respective components, the off-diagonal elements the covariances. Since this matrix is by definition real and symmetric, it can be diagonalized, yielding a transformation matrix T and a diagonal matrix D:

$$C = TDT^{-1} \tag{3.34}$$

In the new basis, all covariances are zero by definition. This way, a new basis is obtained in which the data can be described by only a few parameter. Additionally the variance of each component can be interpreted for normalized base vectors as a measure of information content for each component.
The diagonal matrix contains by definition on the diagonal the variances of the components, which correspond itself to the respective vectors in the new basis. This gives an idea about the importance of each vector. In plot 3.10 an example is shown of how these variances are distributed for a real dataset.
To compare these variances to a set of spectra of the same size consisting of noise, i.e. the ideal case, a set of noise spectra was created with the same RMS as the residual data. In the case of the real residual spectra the dominating structures can be clearly identified by their variances. For the noise spectra, as expected, the variances approach a constant for a high number of residual spectra. If the number of channels in a residual spectrum exceeds the number of residual spectra, the remaining diagonal entries will be

zero. These degenerate features can be removed without significant loss of information. The fact that these eigenvalues are not zero in typical calculations and a few orders of magnitude smaller than the other eigenvalues is caused by numerical rounding effects.
In figure 3.9 a problematic aspect of a PCA decomposition can be observed: Due the diagonalization process itself, the resulting set of vectors is a basis, i.e. the vectors are orthogonal (or even orthonormal). In this example the creating vectors of the two-dimensional dataset were not orthogonal and can therefore not be reproduced. This means that the PCA basis does not necessarily represent the nature of the problem and might limit the possibilities of how base vectors can be interpreted. A structure which is not dominating and for example the third principle component, might be difficult to identify, since the vector describing it is by construction orthogonal to the first two base vectors. An approach to overcome this limitation is described in subsection 3.3.3.
For DOAS applications there is a-priori knowledge that it is possible to distinguish between optical and non-optical properties of the residual spectra by using the instrument function: convolving the residuals each with a given Hg-line-spectrum, we obtain the 'optical' part[6]. The difference might have been introduced by problems with the electronics e.g., but also by incompletely modelled/measured instrument functions. (see figure 3.10)
An equivalent **alternative approach** to PCA is described in Hastie et al. [2001]: The overall aim of the process is dimensionality reduction, that means we are looking for a sequence of best linear approximations of our n-dimensional dataset. The rank $q < n$ linear model can be written as

$$f(\lambda) = \mu + V_q \lambda \tag{3.35}$$

where μ is a vector in R^n, V_q is a $n \times q$ matrix with q orthogonal unit vectors as columns and λ is a q-dimensional vector of parameters. This represents an affine q-dimensional hyperplane. Since we want to find the best linear approximation, we are looking for a minimum of the *reconstruction error*:

$$\min_{\mu,\lambda_i,V_q} \sum_{i=1}^{N} \|x_i - \mu - V_q \lambda_i\|^2 \tag{3.36}$$

This yields then for the solution $\widehat{\mu}, \widehat{\lambda_i}$

$$\widehat{\mu} = \bar{x} \tag{3.37}$$

$$\widehat{\lambda_i} = V_q^T (x_i - \bar{x}) \tag{3.38}$$

which means that the following minimum needs to be found:

$$\min_{V_q} \sum_{i=1}^{N} \left\| x_i - \bar{x} - V_q V_q^T (x_i - \bar{x}) \right\|^2 \tag{3.39}$$

This is again the eigenvector problem described above.

[6] approximately, at least. Since the convolution with the instrument function $\otimes H$ is not a projection, i.e. $\otimes H \neq \otimes H \otimes H$, the step of convolving residuals is only an approximation to the actual operation.

3.3.2.1. Application of PCA on a set of residual spectra

Applying PCA to residual spectra of Differential Optical Absorption Spectroscopy (DOAS) fits can be used as a tool to identify problems in the spectral retrieval. It creates usually a projection of the residual onto a small number of significant variables which can then be analysed manually.
Since the ideal residual spectra would be distributed as Gaussian noise around zero, it makes sense to calculate the covariance matrix assuming an average residual of zero, which is then just $C = RR'$. If no robust or error weighted version of PCA is used, it is usually necessary to filter the residuals by RMS. Filtering by RMS is usually sufficient to remove outlier.
The diagonal matrix $D = T^{-1}CT$ contains as eigenvalues the variances of each of the new base vectors (for a unitary T). Sorting them by size gives an overview over significant and insignificant contributions to the total size of the residuals (see figure 3.10).
The distribution of the eigenvalues approaches a constant value for noise-only residuals for a high number of residual spectra. If the number of residual spectra is finite, also the randomized dataset will give a slightly non-constant set of eigenvalues. If the number of residual spectra is even below the number of channels of the spectra, some eigenvalues would be theoretically zero, since each spectrum can be theoretically assigned to one of the new base vectors whereas a subspace is left undetermined. In practice these eigenvalues will be small, but not zero due to numerical accuracy. They are usually at least five orders of magnitude smaller than the smallest non-degenerate eigenvalue and can be clearly distinguished from the non-degenerate eigenvalues.
Using the matrix T, all residual spectra can be transformed to the new base:

$$S = T^{-1}R \tag{3.40}$$

S contains the residual spectra in the new basis. Looking at the coefficient corresponding to the largest eigenvalue gives a time series of this component of the residual spectra. Correlating these coefficients with other information available for the measurements allows to restrict the source of the structure observed in the residual. For MAX-DOAS applications the dependence on the elevation angle of a certain structure might hint towards a missing or incorrect cross-section, or a clear correlation with the Ring signal can identify the influence of inelastic scattering on the spectral retrieval. An example can be found also in subsection 5.3.5.

3.3.2.2. PCA, Entropy and Information

A question which arises from the analysed spectra is if this procedure also provides a measure for how 'good' a set of residual spectra is. A common way to test this is to sum residual spectra and observe if the size of the sum of spectra increases proportional to $\sqrt{N}$ due to the Poisson statistics of the photon shot noise and instrumental noise. Another way to test the compare the residuals in the context of PCA is to calculate their Kullback-Leibler distance relative to a noise dataset, in analogy to Shannon entropy or entropy in general [Adler et al., 2006]:

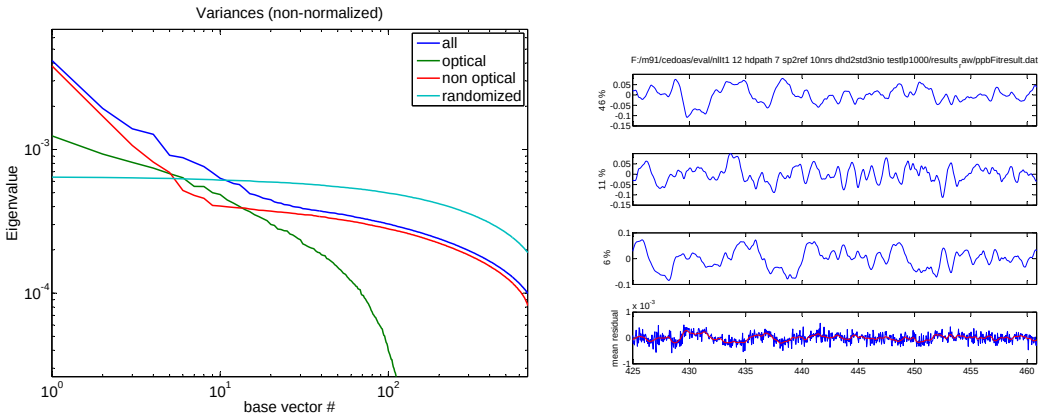

Figure 3.10.: Eigenvalues and eigenvectors (for the optical part of the residual spectra) for a set of 3190 residual spectra from CE-DOAS measurements during SOPRAN M91. To compare to a dataset which contains of noise only, the original data has been permuted channel-by-channel for each spectrum. Furthermore the residuals were divided into their 'optical' and their 'non-optical' part by convolution with the instrument function. For the mean residual both vectors are shown: the unfiltered average residual and the average of the filtered residuals. The amplitude of the principal components, the new base vectors, is arbitrary and depending on the decomposition, but typically $|v_i|_2 = 1$.

$$D(p||q) = p(x) \log \frac{p(x)}{q(x)} \tag{3.41}$$

$q(x)$ would be constant when comparing to noise, yielding the Shannon-entropy. shot noise has here the highest entropy, whereas a set of spectra which contains structures yields less. The entropy of noise should be close to the number of channel of the spectra minus the degrees of freedom of the fit. Depending on the number of residual spectra this behaviour can be seen in figure 3.12. The gap between the maximum entropy of noise spectra, the number of channels, and the actual value from measurements is actually a quality measure for our set of residual spectra.

Since the relation of fit error and measurement error is depending on the residual structures as described in subsection 3.1.4, the average size of the residual or the fit error itself together with the entropy of the residual spectra allows for a fast estimate of the quality of a spectral evaluation. Often only an example for a DOAS fit is given in typical publications, not allowing the reader to estimate the quality of the complete data set.

Summing spectra will reduce the noise of the residuals, but not systematic residual structures, relative entropy will decrease, but the overall RMS as well. Therefore information on both quantities is necessary when evaluating a set of residual spectra.

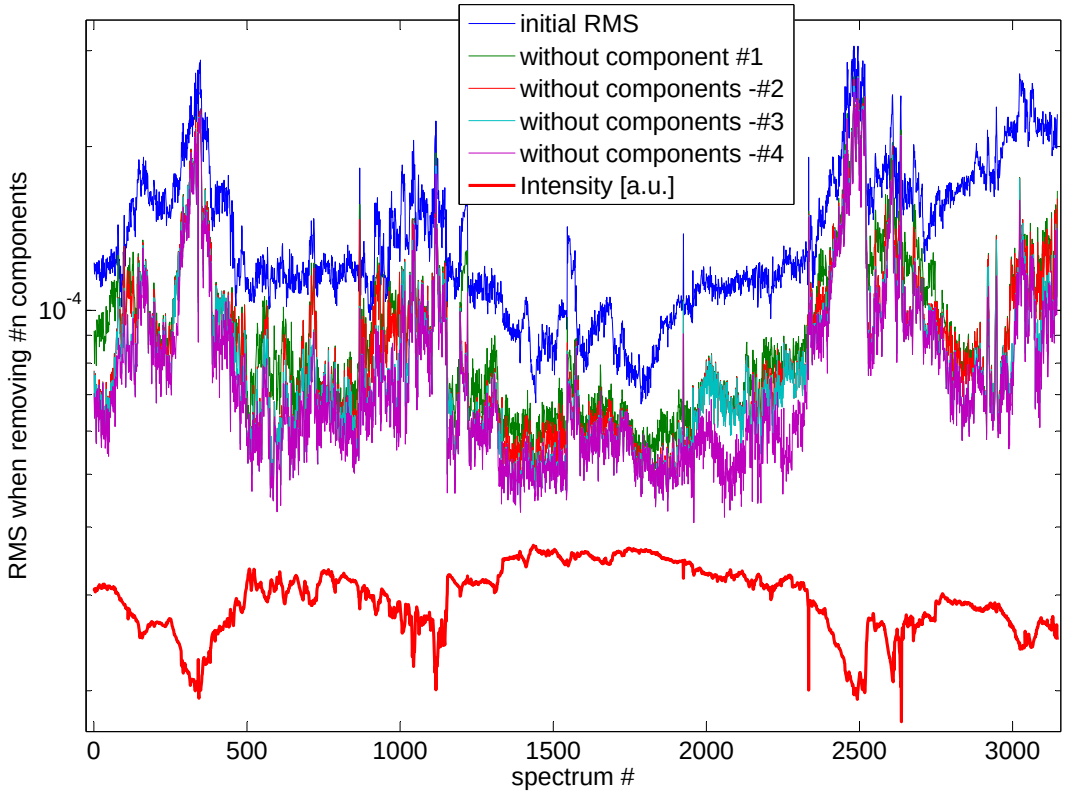

Figure 3.11.: Total RMS of the residual spectra from a standard fit containing only the convoluted cross-sections for NO_2, O_4, H_2O and IO. It shows also the calculated RMS after removing 1-4 eigenvectors. In this case it can be seen that in most cases the RMS can be minimized by the first PCA component while other components contribute insignificantly. The highest RMS values can be found in situations with a short lightpath due to fog, therefore the RMS is limited by instrumental noise and photon shot noise. (Same data as in figure 3.10, for fit errors see figure 5.43)

3.3.2.3. Fit error and residual structures

The fact that residual structures can lead to an underestimation of the measurement error by the fit error has been analysed in depth in Stutz and Platt [1996]. To estimate the factor with which the obtained fit error has to be multiplied to obtain the measurement error, the structure width of the respective absorber τ and of the residuals W has to be known (see also subsection 3.1.4). The latter is not easy to estimate and is not easy to quantify. Often these parameters are guessed and therefore the determination of the measurement error depends on the experience of the user.

Entropy can be used to estimate the width of the running mean which has been assumed in Stutz and Platt [1996] to create spectra from noise with similar structure width as

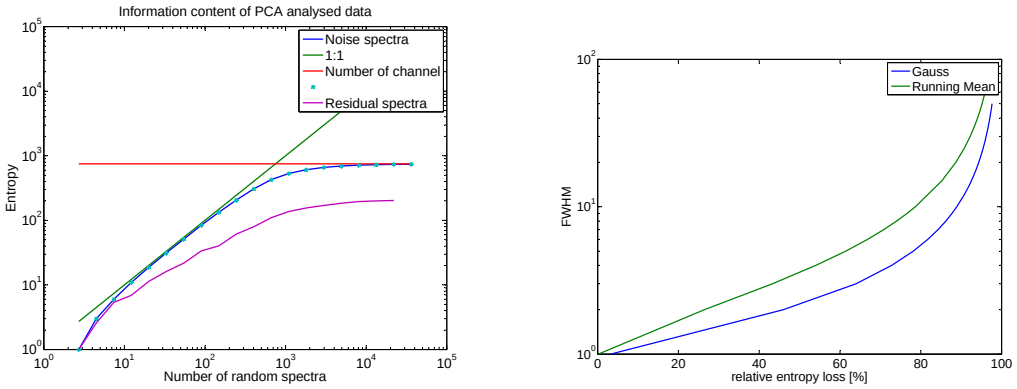

Figure 3.12.: **(left)** In analogy to Shannon-entropy the entropy of the PCA analysed data is plotted versus the number of samples. For a small number of samples the information content cannot be bigger than the number of spectra, for a higher number of samples the total information content is limited by the number of independent variables, which is here the number of channels of each spectrum. **(right)** To obtain the structure width of the residual as needed for the application of Stutz and Platt [1996] this plot can be used to estimate the structure width from the relative entropy loss derived from the difference in entropy of the residual data set and the theoretical maximum value, without the need to 'guess' residual structure widths.

observed in residual spectra. If the residuals are indeed pure noise, then their information content is, for a large number of residual spectra, close to the number of channels used for the fit (compare figure 3.12) reduced by the number of fit parameters. Model calculations can show the relationship between loss of information and the width of the running mean. This creates the possibility to calculate the width of the running mean which is needed to obtain the correction factor from the relationship of structure width of the residual, of the cross-section one looks for the correction factor for the fit error.
It has to be noted, that different smoothing algorithms create different relationships between smoothing width and entropy. Furthermore the most prominent correlated structures in residuals of real measurements are usually caused by errors in convoluted absorber cross-sections, air mass factor related effects and/or instrumental problems and cannot be reproduced by smoothing noise spectra (compare e.g. residual structures in the BrO evaluations in subsection 5.1.1.2 and imperfections of the water vapour cross-section in figure 5.36).
A typical BrO evaluation as discussed e.g. in subsection 5.1.1.2 shows an entropy of the residuals of 254 for a channel number of 357. This means that the entropy is 30% lower than for pure noise, which in turn is equivalent for a running mean applied to the residuals of two channels. This can then be used to estimate the correction factor to convert the fit error into a measurement error as given in Stutz and Platt [1996]. From the distribution of the measured BrO dSCD from days without significant amounts of

BrO a measurement error is estimated which is less than two times as large as the fit error (compare subsection 7.2.3). This is in agreement with the estimations from Stutz and Platt [1996]. The IO MAX-DOAS evaluation for the M91 data (subsection 7.2.4.2) shows even only a loss of 10% of the maximum possible information content of the residual spectra. Here no dominant systematic residual structure of the same size as in the case of the spectral evaluation of BrO is found.

Due to technical differences the residuals from ANT28 for BrO using the same cross-sections showed a loss of entropy relative to noise of 45%. This still translates to a running mean of three. As for M91 this means again that the measurement error is about two times the fit error. However, this estimate (Figure 3.2) applies only if the residual noise is purely random, which is usually not the case, as can be observed using the method of PCA. If an absorber of which the fit error has to be estimated is correlated with any residual structure, this can increase the measurement error significantly.

For the evaluation of MAX-DOAS data for IO during M91 (subsection 7.2.4.2), the entropy of all residuals was only 10% below the theoretical maximum.

3.3.3. Independent Component Analysis

The Independent Component Analysis (ICA) has been introduced in [Comon, 1994, Hyvärinen and Oja, 2000] to solve the *cocktail party problem*: The voices of two persons in a room are recorded by two microphones and the task is to distinguish both signals. That means we have two recordings $x_{1,2}(t)$ and two signal sources $s_{1,2}(t)$ which are related by a linear combination a_{ij}.

$$x_i(t) = \sum_j a_{ij} s_j(t) \tag{3.42}$$

The task is to obtain the factors a_{ij} to be able to reconstruct $s_{1,2}(t)$ given $x_{1,2}(t)$. The assumption made is that both signals are *statistically independent*. Technically two sets of variables y_1, y_2 are independent if their Probability Density Function (PDF) are factorizable, i.e. $p(y_1, y_2) = p(y_1)p(y_2)$. Having a number of PDF and regarding the overall PDF, the overall PDF will approach a Gaussian shape, analogously to the central limit theorem. This leads to the main principles of the ICA estimation, that non-gaussianity is interpreted as statistical independence. Non-gaussianity itself can then be measured in different ways, such as via kurtosis, negentropy, minimization of mutual information and maximum likelihood estimations. Iteratively $s_j(t)$ can be found which represent a maximum of being non-Gaussian.

For the two non-Gaussian signal sources shown in figure 3.9 ICA is able to reproduce the original construction vectors quite accurately. PCA is by definition not able to reconstruct these vectors, since they were not chosen to be orthogonal.

3.3.3.1. Technical Implementation

So far, this algorithm has been tested on data using the FastICA software package [7]. FastICA implements a fixed-point iteration scheme for finding a maximum of the non-gaussianity of a projection of the data onto a single vector w, $w \cdot x$ and its generalization for more than one vector. For details see Hyvärinen and Oja [2000].
High dimensional data needs to be preprocessed to allow for a convergence of the FastICA scheme in reasonable computing time. This can be done by transforming the dataset using a projection onto the first most important base vectors calculated from a PCA. Furthermore the components might need to be whitened, i.e. all components should have similar size, also to allow for a fast convergence of the iteration scheme. This can be done be using the inverse of the diagonal matrix $D = TCT^{-1}$ already calculated for the PCA, this will transform all variance for all components to unity.

3.3.3.2. Example

Despite already good results from PCA for a data set of CE-DOAS OD spectra from M91 shown in figure 5.43, the application of the FastICA package was not as successful as expected. Either the algorithm did no converge on the dimensionality reduced dataset (tested for 6, 10 and 20 dimensions), or the resulting vectors could not be unambiguously connected to the absorption cross-sections of water vapour and/or NO_2. Water vapour absorption was usually found, but the NO_2 cross-section was never recovered as good as already by the PCA. The results from the PCA were easier to interpret. The reason might be instrumental noise and/or artefacts from non-linearity correction, as shown in figure 5.43 as third component, or the large differences in absolute size of the independent absorptions, which is almost two orders of magnitude. The algorithm was run with and without the whitening operation.
Since the result of the pathological example shown in figure 3.9 looked promising, these expectation could not be transferred to real measurement data. If it would have worked, the residual spectra would have been easier to interpret, even though certain features would have been already compensated for by other absorbers during the DOAS fit, leading to wrong concentrations of those. This was e.g. the case when identifying the ODs caused by VRS(N_2) in subsection 5.2.3.4.

[7] http://research.ics.aalto.fi/ica/fastica/index.shtml

3.4. Pixel to Wavelength Mapping

After the actual measurement obtaining the intensities for each pixel of the detector, and after the spectrum has been corrected for dark-current and offset contribution, a wavelength needs to be assigned for each of the pixel at the beginning of the DOAS evaluation. Four methods to obtain a polynomial which maps the channel number to the according wavelength are presented here, two of which already need a pre-calibration with does not differ more than about one nanometer from the correct mapping.

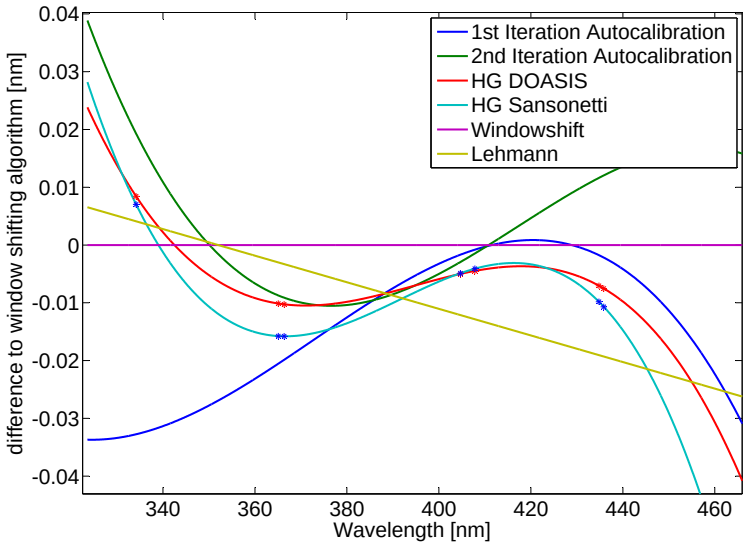

Figure 3.13.: Comparison of different wavelength calibration methods presented here. Lehmann is the method implemented in recent versions of DOASIS and is described and developed in Lehmann [2014] and was used here without including any absorbers, such as ozone. 'Lehmann' and 'Windowshift' need precalibrated spectra to work, which are less than 1 nm off the correct calibration.

3.4.1. Mercury Line Lamp Calibration

A simple way to determine the pixel-wavelength mapping of an unknown spectrometer are mercury discharge lamps, whose spectrum contains various single lines, which can easily be identified and which can be used to determine the wavelength at a certain channel. The assumption made here is that the actual line width is significantly smaller than the instrument's resolution and can therefore be neglected. The width of a single atomic line is about 2pm for mercury discharge lamps, which is broadened again by different Hg-Isotopes. A list of emission lines can e.g. be found in the PenRay Manual or within Sansonetti et al. [1996], Sansonetti and Reader [2001].

As shown in figure 3.13, the line positions listed in the PenRay Manual and from Sansonetti and Reader [2001] can differ by 6.5pm.

3.4.2. Solar Atlas fine tuning

The spectrum of a mercury discharge lamp contains only a very limited number of lines, some of which are not separated well enough to be used for calibration purposes at the spectral resolution of typical spectrometers used for DOAS applications. Compact spectrometer usually need a calibration polynomial of third degree to be able to reproduce their projection properties sufficiently. Thus, if the polynomial has 4 degrees of freedom, definitely more than four, unambiguously to be distinguished lines are needed to fit the polynomial.
A well structured and omnipresent light source is the Sun itself. Using the instrument function from a mercury lamp spectrum to convolute a high resolution solar spectrum such as by Chance and Kurucz [2010] allows for creation of a spectrum similar to the one measured.
An additional advantage is that this fine-tuning of the pixel-wavelength mapping can be easily done unsupervised within an evaluation script, in case the wavelength calibration changes often, e.g. due to temperature changes.

3.4.2.1. Algorithm

- Calibrate spectrum with polynomial $\lambda = p(c)$ calculated from mercury lamp spectrum
  - Convolute a high resolution solar spectrum with instrument function
  - Use fit windows of sizes around 5-10 nm to calculate the shift between convoluted solar spectrum and measured spectrum in this region, accounting for the Ring effect
  - fit a polynomial $q(c)$ to these shift values
  - add the correction polynomial $q(c)$ to the initial polynomial $p(c)$
- Iterate this procedure until $max|q(c)|$ is below some threshold

By changing the calibration polynomial, also the width of the instrument function in wavelength units changes, therefore there is the need for this iterative approach. In the fit routine it can be necessary to include strong absorbers such as water vapour, NO_2 or ozone in the respective wavelength ranges to obtain stable and good results. This depends on the used wavelength range. For the example spectrum used above in figure 3.13, the difference between including or not including ozone was ¡5pm.

3.4.3. 'Rough' precalibration using specific features in solar spectra

The purpose of the presented method for automatic wavelength calibration ('Autocalib') is to obtain preliminary wavelength pixel mapping of a sunlight spectrum without needing calibration spectra. This can be done with the help of the solar radiation atlas by

Chance and Kurucz [2010], which is a high-resolution sunlight spectrum from which atmospheric absorbers have been removed. The idea was to take the example of the human sight which is capable of distinguishing various features of sunlight spectra. By hand this can be relatively easily done by associating extrema of both spectra. Furthermore it can be shown that an estimate of the instrument function width can be obtained and used for a more accurate second iteration, which can then also be limited just to the measured wavelengths.
The goal was to implement an algorithm which is robust enough to locate the wavelength range of a sunlight spectrum within the range from 300-800 nm with only few assumptions concerning overall orientation of the spectrum and slit function width σ_k within 30-40%. Pairs of points from a measured sunlight spectrum with only channel information and a convoluted high-resolution sunlight spectrum with known pixel-wavelength mapping are found to create e.g. a polynomial to associate the pixel k with wavelength $\lambda = p(k)$. The challenge here is to rearrange possible pairs and exclude invalid pairs to have a good overall result.

This method can be combined with subsection 3.4.2.1 for fine-tuning. The results are shown in figure 3.13.

3.4.3.1. Background

Feature detection is a task which is frequently used e.g. in overlaying a series of images to stitch panorama images. The Scale-Invariant Feature Transform (SIFT) algorithm [Lowe, 2004] which is widely used has the ability to detect invariant features within several images, independent of scaling and rotation. The resulting properties of those obtained features can then be correlated using e.g. a robust fitting algorithm. RANdom SAmple Consensus (RANSAC) [Fischler and Bolles, 1981] is an approach which selects a subset of fitting points from a given set of feature descriptors and eventually choses a subset which contains as little as possible outliers, features which were not correctly associated with their respective counterpart.
The task to correlate features of a measured spectrum and the solar atlas is simpler because both vectors are one dimensional, yet with the addition that the width of the convolution kernel is also unknown. As an addition to RANSAC it might be desirable to look for second-best correlated features, which can overall increase the number of connected features and thus improve the stability and accuracy of the proposed algorithm.

3.4.3.2. Assumptions

To minimize the needed user input, only a few assumptions were made:

- the pixel wavelength mapping function $\lambda = p(k)$ is monotonically increasing
- σ_k is known within 30-40% and the slit function is a single peak of approximately Gaussian shape

If the a-priori knowledge is more accurate or can be extended e.g. by a limitation of the wavelength range possible, stability and speed of the algorithm can be drastically improved.

For each of the extrema a set of properties describing the extrema itself are calculated. Positions should be determined by interpolation to obtain sub-pixel accuracy. After extracting the properties of the extrema, for all combinations of extrema the correlation coefficient is calculated. Using the maximum of correlation coefficients to make the first connections between the artificial and the measured spectrum, results in a both wrong and right associations. To get a first pixel-to-wavelength mapping polynomial, one assumes that the majority of the obtained best correlations are correct and therefore also the polynomial obtained from fitting all correlating pairs (above a certain threshold in terms of correlation coefficient) is close enough the correct result. Applying the below described method selects (in most cases) the correct pairs of extrema and can eventually even find new and correct pairs and improve the end result. Re-iteration after estimation of the instrument function's width and limiting the algorithm to the actually covered wavelength range can then lead to further improvement of the accuracy of the polynomial $\lambda = p(k)$.

3.4.3.3. Algorithm

1. Prepare spectra
   - Low-pass filtering of measured spectrum to remove noise
   - convolute solar atlas spectrum with assumed slit function width
2. For both spectra:
   a) Search for valid extrema
   b) Calculate the following properties for each of the extrema
      - Position
      - Ratio of differences in intensity to neighbouring extrema on the left and right
      - Sum of differences in intensity to neighbouring extrema on the left and right
      - Ratio of difference in position to neighbouring extrema on the left and right
      - Second derivative (and thus if it's a minimum or maximum)
3. Calculate correlation coefficients for all possible combinations of groups of extrema (usually three extrema)
4. Find maxima in correlation coefficients to obtain a table linking channel numbers from the measured spectrum with wavelengths from the convoluted solar atlas spectrum

5. Remove all associations with a correlation coefficient below a certain threshold
6. Iterate the following until fit residual is smaller than some threshold:
   - Fit a straight line with positive slope using correlation coefficients as weights
   - replace the association with the highest absolute difference to the fitted slope with the second best choice. Remove old association.
7. Remove all associations with a correlation coefficient below a certain threshold
8. Iterate the following until fit residual is smaller than some threshold:
   - Fit a 2nd degree polynomial using correlation coefficients as weights
   - replace the association with the highest absolute difference to the fitted slope with the second best choice. Remove old association.
9. Remove all associations with a correlation coefficient below a certain threshold
10. Fit final polynomial to remaining associations to obtain result

The group size in which the extrema and their properties are compared to each other needs to be balanced: If the group only consists of one extremum, then the association via correlation coefficients might not be as unique as for a larger group. On the other side having a large group might introduce the problem of missing extrema in one of the spectra due to differences in instrument function width, which then in turn implies the need to handle this problem explicitly. Groups of three extrema turned out to be a good compromise.

3.4.3.4. Estimation of Instrument Function Width

Once the wavelength interval of the measured spectra has been determined, a simple method can be applied to estimate the instrument function width σ_k: for various slit function widths the number of valid extrema within this interval is determined. Comparing this to the number of extrema in the measured sunlight spectrum then gives a new estimate for the slit function width. (see figure 3.16)
Practically, the number of extrema $n(\sigma_k)$ was calculated for a series of σ_k within an interval also covering the actual width. A polynomial which was fitted to this data was used then to calculate a new approximation of σ_k. Simple divide-and-conquer approaches which might reduce the overall number of convolutions required do not necessarily succeed, since the function $n(\sigma_k)$ is not necessarily monotonous.

3.4.4. Wavelength pixel mapping with absorbers

Within the work of Lehmann [2014], a fitting routine based on the Levenberg-Marquardt algorithm for an unknown instrument function of the spectrometer was developed. Within this procedure, it is also possible to obtain a new pixel to wavelength mapping while accounting for strong absorbers such as ozone and water vapour in the fitting process.

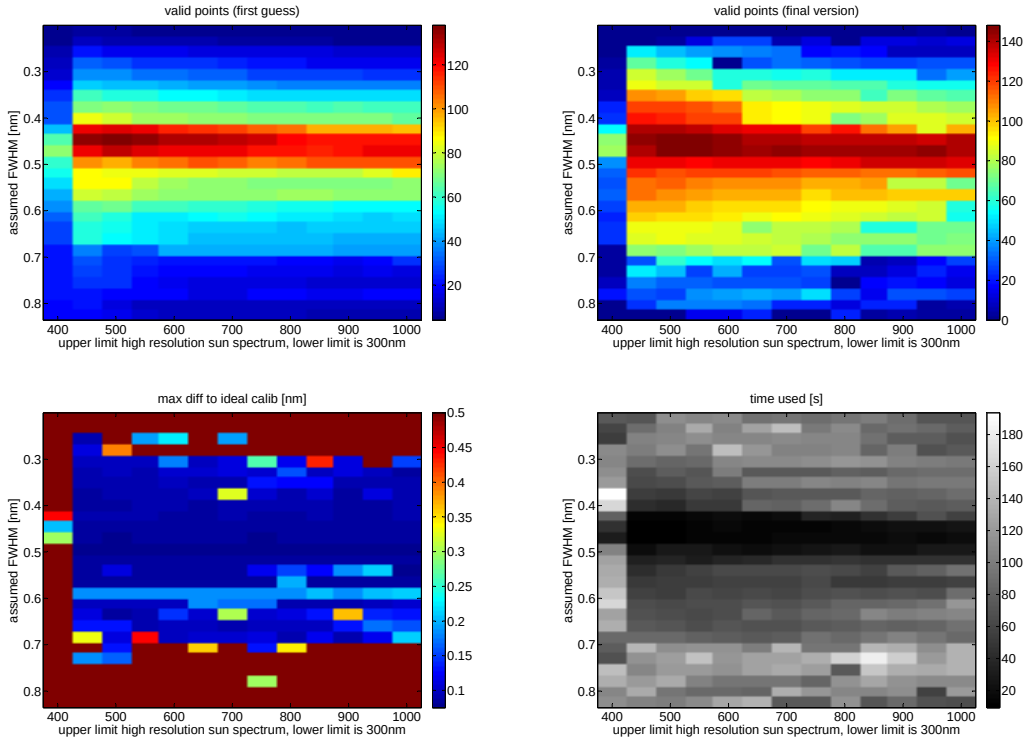

Figure 3.14.: Analysis of the performance of the presented auto-calibration routine using a MAX-DOAS spectrum from SOPRAN M91 (324-467 nm) and varying the end of the spectral range to be searched in (x-axis) and the assumed FWHM of the spectrometer (y-axis, correct value: 0.45nm). The correct calibration is found after two iterations whenever the wavelength range is fully included in the solar atlas spectrum and the assumed FWHM is found between 0.3-0.7nm.

3.4.5. Conclusions

To obtain an accuracy of the pixel-to-wavelength mapping of less than 20pm over the complete spectrum of the spectrometer (i.e. typically 20% of the width of one pixel), all calibration methods can be used, even the automatic calibration which needs only a minimum of a-priori information on the spectrum and furthermore yields an estimate of the width of the instrument function. The spectral stability of MAX-DOAS instruments is typically in the same range, compare figure 4.3.

Solar atlas fine tuning needs a preliminary calibration, but is easy to implement in DOASIS and has been used e.g. in Lübcke [2014], Vogel [2012] to evaluate data from spectrographs which were not temperature-stabilized. The same applies or the fit implemented in Lehmann [2014]. The accuracy of the fit for the complete spectrum can be deteriorated by not including the instrument's spectrally resolved quantum efficiency, as

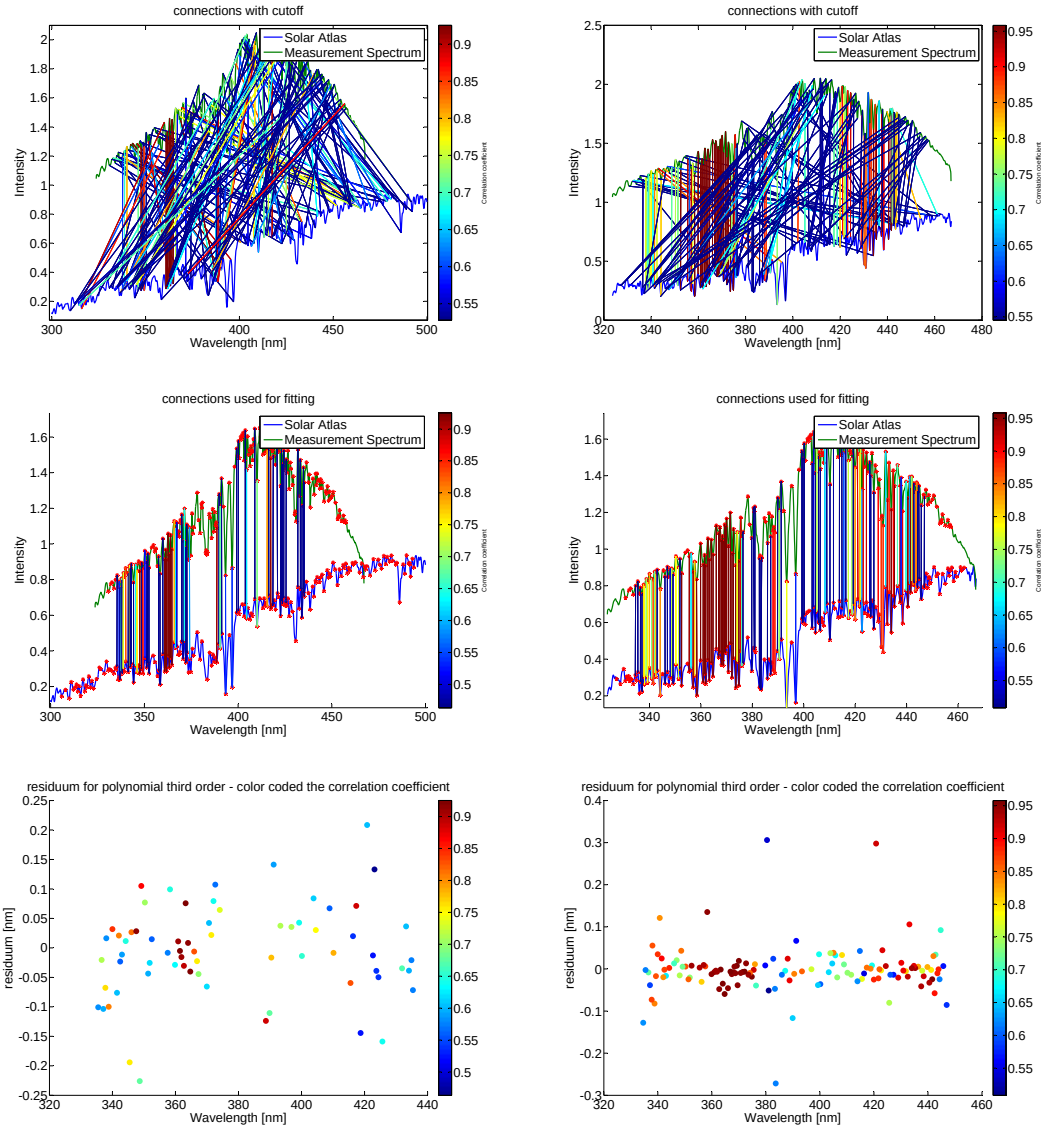

Figure 3.15.: Two iterations of the presented algorithm: On the left the first iteration with a slightly larger spectral range (300-500 nm) and an assumed FWHM of the spectrometer of 0.7 nm. On the right the second iteration with changed limits and the correct instrumental FWHM of 0.45 nm. In the first row the initial step is shown, the connections with the largest correlation coefficients. After the alorithm finished, the remaining connections between extrema are shown in the second row. Finally at the bottom the residuals of the final fit are shown. The colorcode is the correlation coefficient of the respective connection.

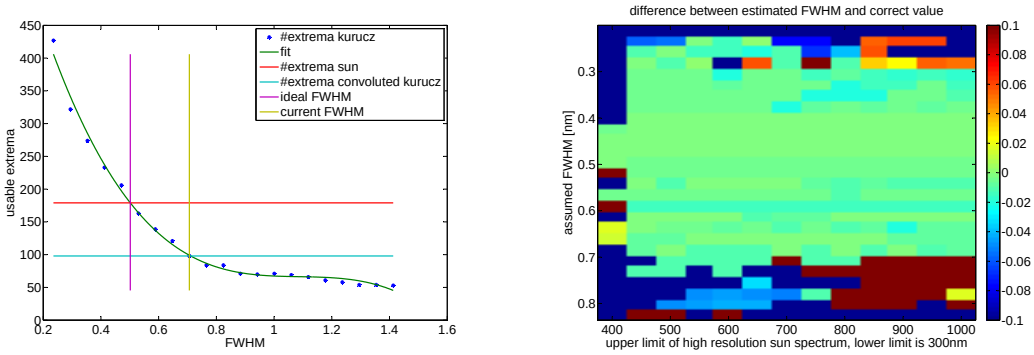

Figure 3.16.: Estimation of instrument function width. The correct FWHM is 0.45 nm.

it was observed in Lübcke [2014] for SO_2 retrievals using measurement spectra and the solar atlas. When fitting over only a small retrieval window as for the fine-tuning, these effects will be smaller than for a spectrum covering a larger wavelength range.
Emission line spectra of mercury, krypton or neon are still needed to obtain the instrument function with the needed precision, but fitting the positions of each emission line by hand is usually slower than using the automatic calibration on a sunlight spectrum.

4. Instrumentation

This chapter shortly describes the measurement instruments used within this thesis. All instruments existed already from previous projects. However, improvements and modifications as preparation for their deployment for measurements in the marine boundary layer were necessary and are described after short overview for each instrument.

4.1. Polarstern MAX-DOAS

Figure 4.1.: The permanent MAX-DOAS instrument on R/V Polarstern. The spectrometer is located inside, the inclination corrected telescope unit at the portside railing.

The Polarstern MAX-DOAS instrument was built during a diploma thesis Lampel [2010] and replaced at that time a setup using an *Ocean Optics USB2000* covering a spectral range from 285 - 425 nm using a 'Schwampel'-type telescope unit [Ibrahim, 2009]. Later on during Niebling [2010] an instrumental straylight problem was discovered and also fixed for the Polarstern MAX-DOAS in the course of modifying the setup from the Schneefernerhaus [Jurgschat, 2012] for the same reasons. Therefore the first cruises of the instrument installed in 2009 do not include UV data, which can be evaluated. More than 10% of instrumental stray light were observed. Additionally the readout electronics of both spectrometers were repaired in 2010 to fix stability issues as well as to minimize the odd-even structures reported by Lampel [2010].
The Polarstern MAX-DOAS instrument consists of three parts, a telescope unit mounted on the railing of the ship looking portside in a height of 28m above sea level, the spectrometers with a control computer located inside the ship and a fibre connecting them.

The fibre consists of 19 fibres of 100μm diameter, leading to four connectors with one and three times six linearly aligned fibres. The Newton telescope has a focal length of 76.2 mm and the light enters the telescope through a rotating prism within a quartz-glass cylinder, which also contains a mercury discharge and a halogen lamp for automatic calibration during the night. The field of view of the telescope has a FWHM of 0.5°.
The telescope unit has an inclinometer to correct the roll angle of the ship for elevation angles close to the horizon. Its output is directly fed into the motor controller and can correct the elevation angle at an accuracy of $\approx 0.5°$. Until the ship's roll is less than 8°, which is the case most of the time, since the ship itself is stabilized when sailing. The two Czerny Turner-type spectrometers with a focal length of 60mm cover the spectral region from 277-413 nm and 390-617 nm at a spectral resolution of 0.7 nm/9.5 px (UV) and 0.9 nm/6.9 px (VIS) in the configuration since ANT XXVIII. The detectors are peltier-cooled Hamamatsu S10141 back-thinned CCD-detectors at -6°C with 2048 channels, while the optical bench is stabilized at 22°C to avoid water condensation. The readout-electronics of both spectrometers including the A/D converter is temperature stabilized together with the optical bench, while the processing electronics is not temperature stabilized. To minimize instrumental stray light, the UV spectrometer contains a BG3 (blocking light between 470 and 700 nm) filter, the Vis spectrometer a BG40 filter, blocking most of the incoming intensity above 640nm.

4.1.1. Instrumental stray light

The original OMT spectrometers were built by the manufacturer without considering instrumental stray-light. Therefore the respective blinds and light-traps were constructed, tested and added later [Jurgschat, 2012]. The blinds built into the spectrometers were partly based on those used in Schmitt [2011] which can be adjusted from the outside, allowing for real-time observations of the signal of the spectrometer when adjusting them. Additional light traps were constructed from cardboard to cover the walls, e.g. to catch the light from the -1st order from the grating. The spectrometer's grating had to be adjusted in such a way that the zeroth order was placed between slit and grating, having only very limited space for a light trap (see figure 4.2). As it turned out the stray light above 380 nm could not be minimized sufficiently without losing too much light in total. Therefore it is not advised to use the UV spectrometer above 380 nm, a spectral region which is also covered by the VIS spectrometer.
All blinds shown in figure 4.2 were tested subsequently for their effect on the total stray light and eventually modified. Following the main blinds mounted in the cover of the spectrometer, the largest effect had the blinds on the sides of the grating, the cover of the mirror mount and the cover of the brass-like housing of the CCD. All other light-traps and blinds had only small effects: The light-trap for the -1st order lowered the total ambient stray-light by 20%, but had no influence on the stray light intensity distribution on the detector.
The total amount of stray light was measured with Schott GG filters, e.g. GG450 removing most intensity below 450 nm. When using the modified UV spectrometer without any filters, the amount of stray-light in the UV region was about 1-2% when

using a halogen lamp (normalized to the maximum intensity of the halogen lamp within the spectral range). Before the modifications, with a BG3 filter, the relative contribution to the total measured intensity was around 30%. After the modifications, the main part of the stray light originated from the red spectral region. For measurements under more realistic conditions with a halogen lamp and a BG3 filter the total stray light is about 0.5%. Still, sunlight is shifted towards shorter wavelength compared to the halogen lamp, which has a high intensity also for wavelengths above 700 nm, which are not blocked by the filter. This improves the overall stray light performance. Stray light measurements with sunlight have not been done using the final setup.

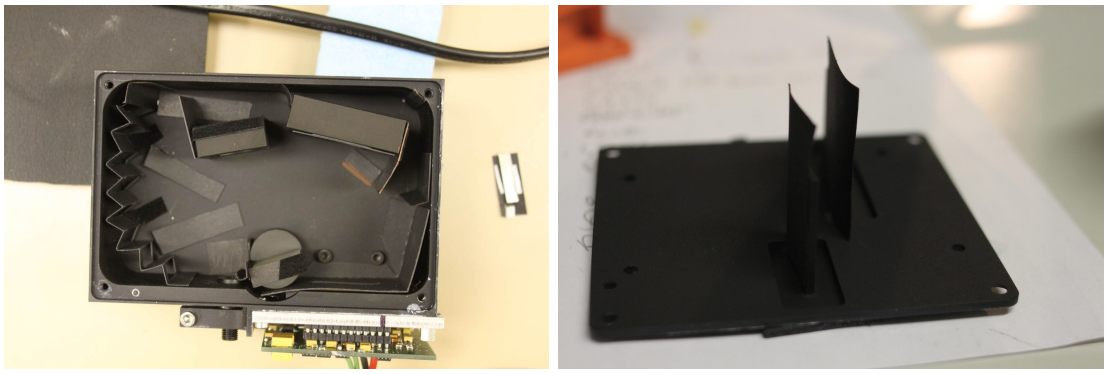

Figure 4.2.: Inside view of the UV spectrometer before ANTXXVIII. Apart from the blinds mounted in the cover of the spectrometer shown on the right, the most efficient blinds were covering the grating from the outside, hiding the metallic surface around the CCD detector and the light traps for -1st and zeroth order reflections on the grating.

In the same way the visible spectrometer was optimized, lowering the amount of instrumental stray light by a factor of 3-4 to 0.2% (measured with a halogen lamp), similar as for the UV spectrometer with BG3 filter.

4.1.2. Linearity

The linearity of the spectrometer was only investigated using a halogen lamp in Lampel [2010]. Recent non-linearity tests showed that the stability of a halogen lamp is often not sufficient to resolve the non-linearity of the spectrometer. Therefore this should be done whenever the instrument will be the next time in Heidelberg for maintenance.

4.2. Ship MAX-DOAS

The Ship MAX-DOAS used during the campaigns on Maria S. Merian in 2011 (chapter 8), during SHIVA along Malaysia in 2011 (Appendix B) and in the Peruvian upwelling region during M91 (chapter 7) had been used before by Großmann et al. [2013] and without elevation correction on land during the CINDI campaign [Piters et al., 2012] and in Barrow, Alaska [Frieß et al., 2011, Sihler, 2012].

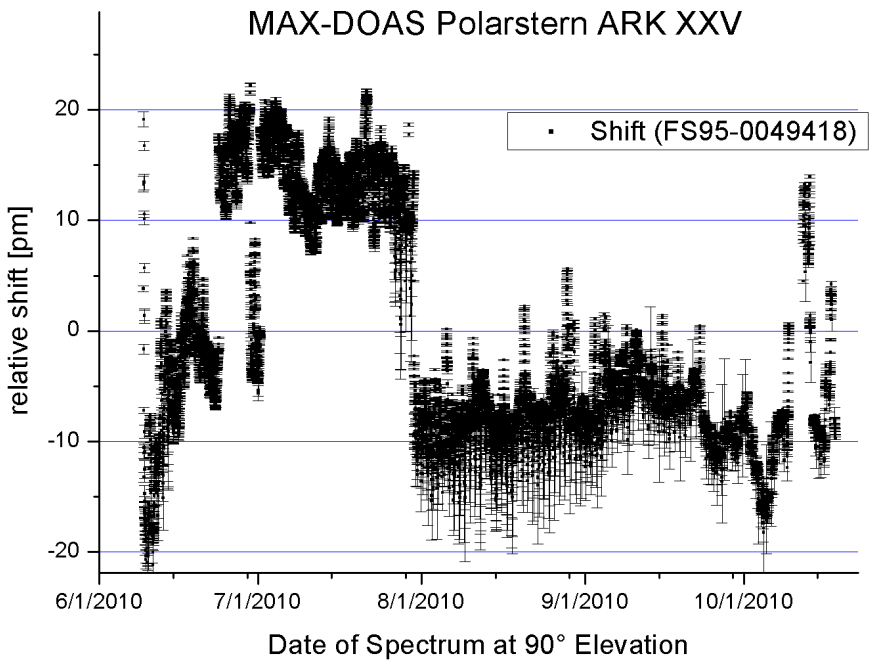

Figure 4.3.: Spectral stability of the Polarstern MAX-DOAS (vis) during ARK XXV for all recorded spectra measured at 90° elevation. The spectral shift has been determined by fitting a measurement spectrum with Ring spectrum, a DOAS polynomial of 3rd order and an additive polynomial of zeroth order in the range from 395-435 nm. The incontinuities were most probably caused by switching the instrument and thus the temperature control on and off in ports, e.g. at the end of July 2010 in Reyjkjavik.

The MAX-DOAS instrument consists of three main parts: A telescope unit mounted on top of the respective ship, a temperature stabilized Acton spectrometer located inside the lab and a PC to control the devices. The telescope unit has an inclinometer to correct the ships roll angle similar to the Polarstern MAX-DOAS. The light from the telescope is focussed via a lens onto 37 cylindrically situated fibres of 100μm diameter. These fibres are then again used as the entrance slit of the spectrometer. To avoid the influence of direct sunlight reflected in the entrance of the telescope, a 5cm long lens hood was attached to the telescope. The field of view of the instrument is 0.5° (FWHM). The spectrometer used was an Acton 300i which was temperature stabilized at 44°C with an Andor CCD Camera 'DU 440-BU'. The camera was used in imaging mode recording 256x2048 pixels. This setup covered a wavelength range from typically 324 nm to 467 nm. The full-width-half-maximum resolution was 0.45 nm or 6.5 pixels.

4.2.1. Calculating spectra from 2D-images

During the transport to MSM18/1 the original calibration from Heidelberg was lost and due to organisational limitations not sufficient time for readjusting the spectrometer was available. This resulted in an adjustment of the spectrometer which could have been better. But since the imaging spectrometer records a spectrally resolved image of the entrance slit/fibres, this problem was solved by rescaling the recorded image accordingly before adding the single rows to one spectrum, which is then used in the spectral retrieval. The total misalignment added up to four pixels over the whole illuminated height of the detector. To compensate, each line was remapped onto the correct position using spline interpolation. The correct position was determined by fitting gauss-functions to each of the mercury emission peaks in each row. The shifts of these peaks in units of pixel were then fitted with a polynomial of third order for each mercury emission peak. For each row then a polynomial of second degree was fitted to each of the interpolated HG emission peak positions. This procedure leads to smooth remapping polynomials for each of the rows, which were finally used for the spline interpolation of the measured intensities before summing all remapped rows.
This procedure led to an improvement of the spectral resolution of about 20% for MSM18/1. For MSM18/3 and M91 the alignment of the spectrometer was good and did not require this remapping.

4.3. Envimes MAX-DOAS

During the MAD-CAT campaign in Mainz a MAX-DOAS instrument based on a compact 'Avantes' ultra-low-straylight spectrometer ULS2048XL measured during June and July almost continuously on the roof of the Max Planck-Institute for Chemistry (MPIC) in Mainz. The spectrometer used was a UV spectrometer covering the spectral range between 294–459 nm at a spectral resolution of 0.59 nm (6.8 px) with a focal length of 75 mm. The back-thinned detector with 2048 pixels was a Hamamatsu S11155 detector, measuring in a temperature-stabilized housing at 20 ± 0.05°C. The spectral stability,

determined from fitting a fixed zenith sky spectrum with all other spectra in the wavelength range from 380-420nm allowing for a shift, was better than 10pm within one month.
The telescope head is controlled by measuring its orientation using a MEMS acceleration sensor. This data was then used to set the correct elevation, also considering the slackness of gearbox and motor. Due to an initial misalignment of the sensor an elevation offset of -0.35° was determined after the measurement campaign. The FOV of the instrument is 0.24° (FWHM).
As for all spectrometers with this CCD-chip, non-linearity of the spectrometer was observed. Since all MAX-DOAS spectra were recorded at a similar saturation, the effect was minimized, but the same argumentation for summing several individual spectra and correcting then for the non-linearity applies as for the CE-DOAS in subsection 4.4.1 also for MAX-DOAS. An estimate on the size of resulting residual structures in the DOAS evaluation is given in subsection 3.2.4.

4.4. The open-path CE-DOAS Instrument

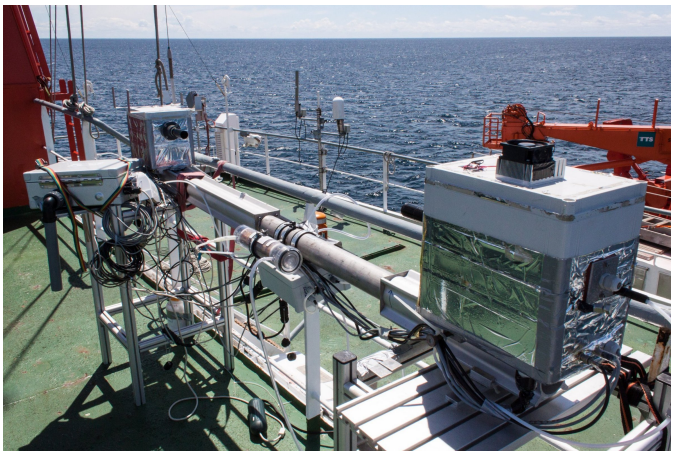

Figure 4.4.: The open-path CE-DOAS setup during SHIVA on R/V Sonne in November 2011.

The open-path CE-DOAS setup used during the SHIVA campaign and the SOPRAN M91 campaign has been largely modified for the use in field campaigns during the diploma thesis of [Anthofer, 2013]. It was then modified for the requirements onboard a ship.
The mirrors have a typical maximum reflectivity of 0.9996 at 446nm and are placed at a distance of $d_0 = 1.925$m, of which $d_{eff} = 1.592$m are outside the Teflon tubes flushed with dried and filtered air protecting the mirrors from dust. Typical effective path lengths within the resonator are 5-6km. For a RMS of the residual of the DOAS evaluation of $1 \cdot 10^{-4}$ this yields theoretical detection limits of ≈ 0.8ppt for IO, ≈ 64ppt for NO_2 and ≈ 46ppt for glyoxal for ideal conditions.
Modifications for the use on a ship:

- The pump for the air flow onto the mirrors and the purge air flow has been replace

by two separate pumps, to avoid the problem of strong wind in the direction of the cavity resonator, which could eventually lead to dust contamination of the mirrors.

- To reduce the consumption of desiccant, the purge air was cooled to about +1°C to remove humidity before drying the air again with silica gel during the SHIVA campaign. The air was heated to ambient temperatures within the tubing leading to the CE-DOAS setup.
- The spectrometer was replaced by an Avantes spectrometer to avoid instrumental straylight problem. This was done by Horbanski [2014].
- To minimize thermal and mechanical stress on the spectrometer, a 4 mm-thick aluminium plate covering the complete spectrometer on the side of the Peltier-element was added. The change of the overall measured intensity when heating the outside heatsink to more than 50°C was reduced to 1/10 compared to the original setup. Before the modifications, the change in intensity was 3% for thermal equilibrium and the maximum heating current of the peltier element ($\approx$ 40W electrically). Typical diurnal variations for the peltier cooling current during SHIVA were 1% of the maximum peltier current.
- The temperature control of the LED as well as of the spectrometer was replaced and optimized.
- After the SHIVA campaign, the 1W LED was replaced with a 3.5W LED.

4.4.1. Nonlinearity of Spectrometer

In the context of searching reasons for residual structures within the Drone-DOAS project of Martin Horbanski, it turned out that the Avantes spectrometers have a significant nonlinearity with respect to saturation, already at low saturation values.
The CE-DOAS setup included the same spectrometer in both campaigns, SHIVA and SOPRAN M91. The spectrometer was characterized with respect to nonlinearity after the M91 campaign. For M91, parts of intensity-correlated residual structures could be removed, even though not all of them. A significant temperature dependence of the linearity in the range of the used spectrometer temperatures (20-30°C) has not been observed.
To characterize the nonlinearity, spectra with different exposure times were recorded for the closed resonator (without purge flow) and a temperature stabilized LED-light source, as it is the case for the normal measurement setup during purge air reference measurements. The intensities were normalized to the exposure time. Then the intensities were normalized for each pixel of each spectrum of the measurement sequence to 30000 counts/scan. The contribution of the dark current to the non-linearity polynomial was found to be insignificant.
In typical spectral data evaluations the respective spectra were corrected after offset and background correction.

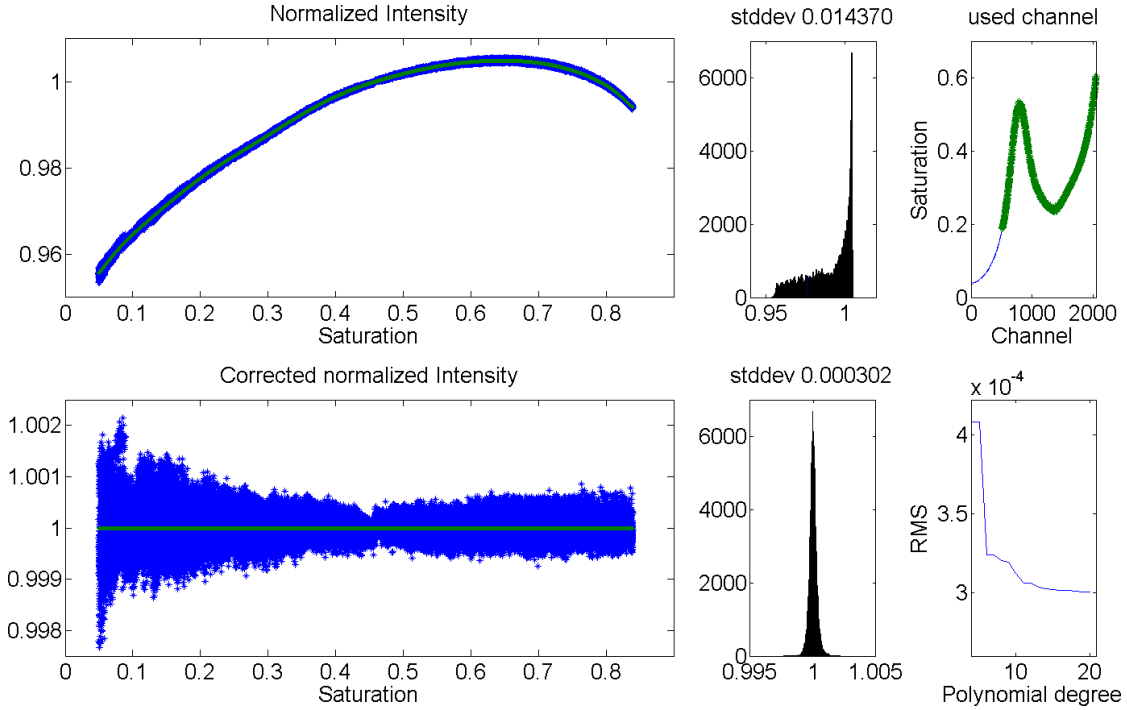

Figure 4.5.: Characterization of the open-path CE-DOAS spectrometer's non-linearity after SOPRAN M91. Before correction the non-linearity amounts to up to 4%. The normalized intensity curve looks similar to those listed in the data sheets of USB2000 spectrometers using a predecessor of the Sony ILX 554 chip used here.

5. Spectral retrieval

While retrieving the slant column density from two spectra according to equation 3.3 seems straight forward there are several parameters that leave space for interpretation. The results might vary, depending on the employed cross-sections, the applied corrections to them, the wavelength interval, cross-sensitivities and radiative transfer effects.
Which absorbers can be ignored and which effects need to be considered depends furthermore on the measurements geometry as well as on the expected absorbers. As an example, a MAX-DOAS evaluation using a noon reference as a Fraunhofer reference needs to take special care for the large influence of ozone absorption. For an evaluation of spectra that were recorded in close time proximity, this is less important.
In order to retrieve robust results from a DOAS evaluation, the following points need to be considered:

- All significant types of scattering need to be included
- All significant absorbers need to be included
- Wavelength dependence of absorptions and scattering effects
- Saturation/I_0 effect
- Changes in air mass factors due to absorption
- Errors in literature cross-sections
- Cross-sensitivities

All of these points depend additionally on the choice of retrieval wavelength interval and become increasingly important closer to the detection limit of the absorber to retrieve.
This chapter shortly introduces retrieval interval mapping as a useful visualisation technique in section 5.1. In subsection 5.1.1 the choice of retrieval interval for BrO and HCHO are discussed. Furthermore observations of residual structures in this spectral range, which are currently setting limits for the detection limit in the retrieval of BrO dSCDs in the MBL at concentrations of 1 ppt for MAX-DOAS observations, are presented and potential reasons are discussed. In subsection 5.1.2 the spectral retrieval of IO and its limitations are shown. The influence of water vapour and NO_2 absorption on the retrieval of IO is evaluated. Two effects have an influence on any spectral retrieval especially in the blue wavelength range: Vibrational Raman Scattering (VRS), which is described in section 5.2 and first observations of this effect in MAX-DOAS measurements are presented. Water vapour absorption uncertainties are evaluated in section 5.3, yielding correction factors for the strength of individual absorption band strengths. Water vapour absorptions can also alter the overall radiative transfer, leading to corrections for absorption cross-sections. This effect is discussed in section 5.4

for water vapour absorption at 442 nm. Liquid water absorption is shown in section 5.5 and the spectral retrieval settings for this thesis are listed in section 5.6. The retrieval of trace-gas concentrations from CE-DOAS measurements is shown in section 5.7.

5.1. Choice of spectral retrieval settings

The choice of the wavelength range used for the DOAS retrieval can have a large impact on the retrieved trace gas column densities. However, it can be difficult to determine the best retrieval range. A tool to simplify, visualize and understand the implications of choosing the wavelength interval for the retrieval of a specific absorber, the so called 'Retrieval Interval Mapping' has been suggested by Vogel et al. [2013]. First it is only the idea to plot column densities colour-coded on a plane whose axes represent the start and the end wavelength of the respective retrieval interval. This allows to estimate the overall variation, but also to identify problems, such as cross correlations between different absorbers. Synthetic spectra, as presented in Vogel et al. [2013], can be used to identify theoretical limitations and the influence of e.g. ozone and its accompanying corrections such as I_0 and saturation effect for different wavelengths. An example for the case of HCHO is shown in figure 5.3.
These plots can thus be used to find borders of reasonable fit ranges for actual measurement data due to chemistry or other a-priori knowledge: night-time data from LP-DOAS measurements might help to select fit ranges, since for example BrO concentrations are expected to vanish in darkness[1] or SO_2 dSCD should be small outside the plume of a volcano [Vogel, 2012]. Together with conditions imposed on RMS and other factors and conclusions obtained from synthetic spectra, this tool helps to chose a fit range. Using only synthetic measurements can be misleading, since the result might be affected by absorption of unknown absorbers or types of scattering which were not included in the model creating the synthetic spectra.
Furthermore Retrieval Interval Mapping can be used to identify problems with literature absorption cross-sections, as it has been the case for water vapour absorption described in section 5.3. An example for an evaluation of measurement spectra is shown in figure 5.12.

5.1.1. BrO / HCHO

The intercomparison campaign analysed in Aliwell et al. [2002] with respect to the spectral retrieval of BrO using a noon reference suggested a retrieval wavelength interval from 345–358 nm to minimize the effects of large absorptions of stratospheric ozone, especially during twilight. This wavelength interval yields reliable results for measurements of stratospheric ozone, but since it does not encompass any large absorption of HCHO and only includes relatively weak absorption lines of BrO, an extension of the wavelength range towards shorter wavelengths is needed to reliably retrieve tropospheric absorptions of BrO as well as HCHO.

[1] This has been applied for CVAO LP-DOAS data from the *HaloCaVe 2010* campaign by Tschritter [2013]

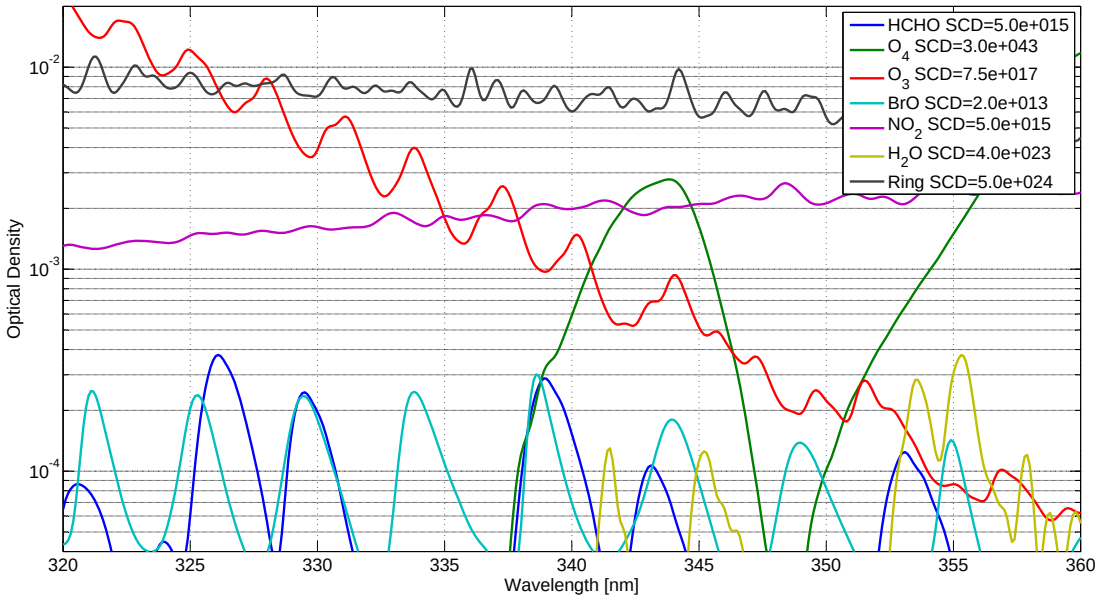

Figure 5.1.: Overview: Absorption cross-sections in the wavelength range used to retrieve BrO and HCHO absorption in the UV spectral range. SCDs are given in molec cm^{-2} and are representative for typical tropospheric column densities in the MBL when using the next zenith sky spectrum as Fraunhofer reference of the retrieval. The absorption of water vapour is highly uncertain.

Extensive sensitivity studies on the spectral retrieval of BrO and thus also HCHO in the same wavelength range were performed by [Vogel et al., 2013, Vogel, 2012] for ground-based measurements and Sihler [2012], Theys et al. [2011] for satellite retrievals and thus higher total ozone SCDs. Even though no influence of SO_2 is expected within the scope of this thesis, most limitations discussed in Vogel [2012] are ozone related and therefore the same retrieval interval was applied here when using a Fraunhofer reference selected from the same elevation angle sequence. When using a fixed Fraunhofer reference or a daily noon reference, ozone absorption will limit the retrieval window due to its large absorption on the side of shorter wavelengths. For MAX-DOAS measurements of HCHO and BrO throughout the day, the evaluation settings suggested by Pinardi et al. [2013] have proven to give reasonable results, e.g. in Peters et al. [2012]. Although for large SZA the settings from Aliwell et al. [2002] need to be applied to avoid the strong influence of large stratospheric ozone column densities on the retrieval of BrO.

A lower limit to the evaluation of MAX-DOAS measurements for BrO and HCHO might be already posed by the O_4 absorption measured by Salow and Steiner [1936] at 328.2 nm. No cross-section data for O_4 is available in this wavelength range, and therefore the wavelength range < 331 nm has to be observed carefully.

The size of this absorption is according to Salow and Steiner [1936] $\approx \frac{1}{25}$ of the O_4 absorption at 361 nm. Taking an absorption of 1.5% at 360 nm this results in an absorption

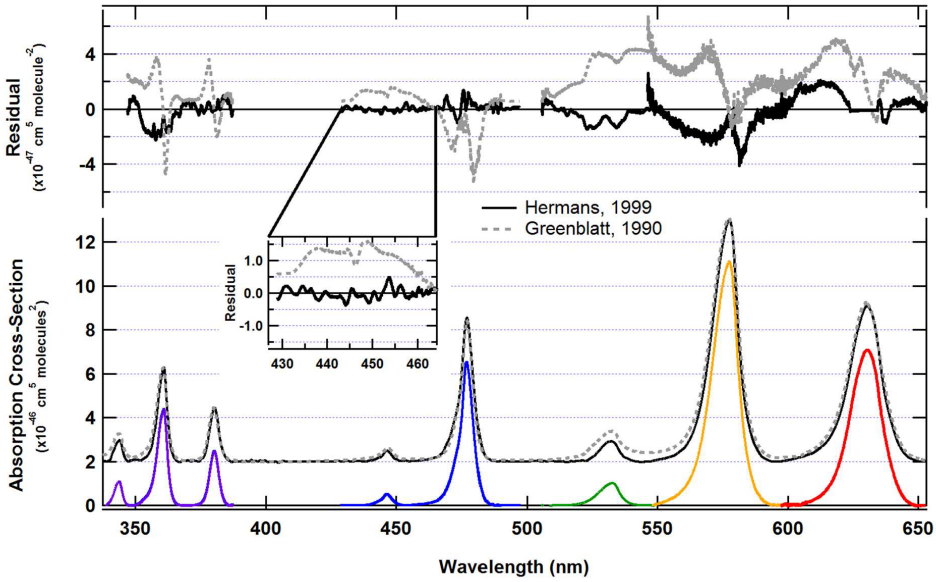

Figure 5.2.: Comparison of O_4 cross-sections by Hermans and Greenblatt to the O_4 cross-section published by Thalman. In the UV range the largest difference between Thalman and Greenblatt is a spectral shift, as can be seen from their difference. When this shift is removed, the difference between the cross-sections by Greenblatt and Thalman are actually smaller than the difference of Thalman und Hermans (in the BrO evaluation range from 332–358 nm). Figure from Thalman and Volkamer [2013].

of $6 \cdot 10^{-4}$ at 328 nm. (see figure 5.4 and 5.5) Another hint, that there might be indeed an absorption feature missing, is that typically higher formaldehyde dSCD are observed when extending the retrieval wavelength window below 330 nm. The possible absorption of O_4 at 328 nm coincides with formaldehyde absorption in this region.

This absorption is small, but can have a significant influence on the retrival: For one day (11/22/2011) of measurements during ANT XXVIII the difference in HCHO when evaluating spectra with a lower limit above and below 330 nm is 40% or $\approx 2 \cdot 10^{15}$ molec cm^{-2} which translates to an optical density in this region of $1.5 \cdot 10^{-4}$ (see also figure 5.3). In this case the average O_4 dSCD was $2.2 \cdot 10^{43}$ molec cm^{-2} corresponding to an optical density of $2.2 \cdot 10^{-3}$ at 343 nm. According to Salow and Steiner [1936], the absorption around 328 nm should be a factor of 6.7 smaller than the one at 343 nm, this would lead to an estimate of the optical density of O_4 at 328 nm of $3 \cdot 10^{-4}$, which is a factor of two larger compared to the estimate obtained from the observation of HCHO column densities. But since the HCHO absorption at 328 nm shows a double peak structure in the spectral region of the expected shape of an O_4 absorption and formaldehyde shows other absorption features in this spectral range (e.g. at 340 nm), this is still a valid hint that there are indeed problems in this spectral region. Another reason for this effect

could be water vapour absorption in the UV or any other absorber unaccounted for (see subsection 5.1.1.2). This could also lead to an underestimation of the HCHO dSCD when retrieved between 332–350 nm as compared to a fit wavelength interval starting <330 nm when another absorption feature of formaldehyde is included.
Dedicated MAX-DOAS measurements with a good spectrometer (e.g. the SMAX-DOAS) in clean air with a spectral range covering this spectral region at a high resolution might be useful. Since all retrieved absorptions in this spectral range are potentially influenced by O_3 absorption and also interferes with absorption of HCHO, it was not possible to retrieve this absorption band separately to the other O_4 absorptions when estimating its position and shape based on the shape of the other absorption. Therefore figure 5.4 should be regarded as a hint that there might be indeed some absorption, rather than a proof for this absorption. The correlation shown in figure 5.5 shows that it is not just an individual spectrum showing this absorption feature. Longpath-DOAS data from S. Schmitt was analysed, but it was not possible to disentangle the expected absorption from other systematic residual structures in the measured data. High-precision LP-DOAS measurements could provide more information about the actual shape and size of the O_4 absorption at 328 nm.
The most recent BrO cross-sections from different publications [Fleischmann, 2004, Wilmouth et al., 1999] were found to be accurate: Even for data from Polarstern ANT XXIX/6 with BrO dSCDs of more than 10^{15} molec cm^{-2} both cross-sections were almost equivalent, Wilmouth et al. [1999] showed slightly (1-2%) but not significantly lower RMS values. Also the corresponding dSCD in the wavelength range from 332 nm–358 nm varied within less than 1%. The older cross-section by Wahner et al. [1988] is recorded at a lower spectral resolution, leads to larger RMS and the wavelength calibration differs.

5.1.1.1. Choice of O_4 cross-section

The spectral retrieval of BrO is significantly influenced by the choice of cross-section for the absorption of O_4. Cross-section data is available in sufficient resolution for DOAS applications from Thalman and Volkamer [2013], Hermans et al. [1999] and Greenblatt et al. [1990] at spectral resolutions of 0.32 nm, 0.025 nm and 0.6 nm respectively: The choice which cross-section cannot be based on the overall fit RMS in the spectral region normally used for BrO retrievals, since their RMS values do not differ significantly, while the retrieved column densities may vary. Also the main residual structures are larger than the differences caused by different O_4 cross-sections, see subsection 5.1.1.2.
In the wavelength range from 332–358 nm the cross-sections by Thalman and Volkamer [2013](starting at 335.6 nm) and Greenblatt et al. [1990] (shifted by 0.2 nm) differ only by an optical density of $\Delta\tau = 3 \cdot 10^{-4}$ for a dSCD of $4 \cdot 10^{43}$ molec^2 cm^{-5} when also including a third degree polynomial, whereas Thalman and Volkamer [2013] and Hermans et al. [1999] differ by up to $\Delta\tau = 7 \cdot 10^{-4}$. For a direct comparison see figure 5.2. Extending the wavelength range to larger wavelengths (above 358 nm) Greenblatt et al. [1990] shows larger differences when compared to Thalman and Volkamer [2013] than Hermans et al. [1999] at the 360.8 nm O_4 absorption band.
Tschritter [2013] had found best agreement between LP-DOAS and MAX-DOAS mea-

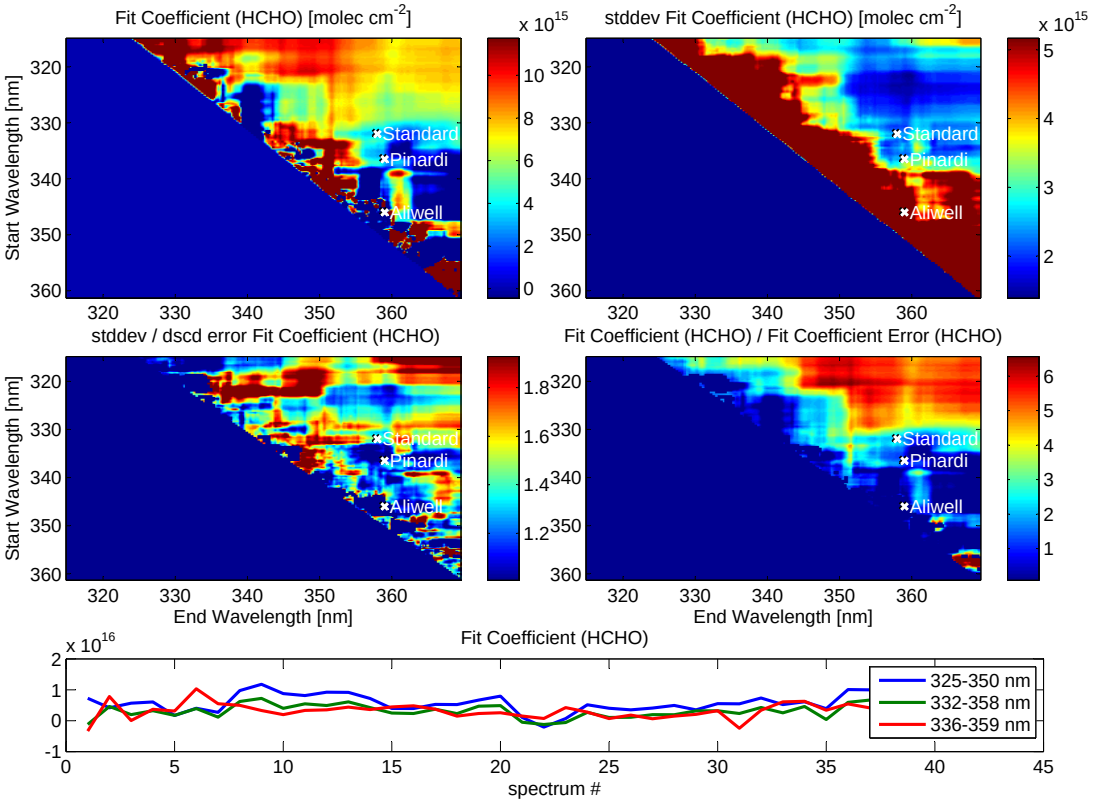

Figure 5.3.: Retrieval interval map for HCHO from UV MAX-DOAS data from ANT XXVIII (chapter 9) during November 22nd, 2011 in the southern tropical Atlantic, at 15°S, 0°W. 42 spectra were analysed separately. The dSCD for selected wavelengths intervals is plotted below. For retrieval intervals beginning below 330 nm, an stronger increase in HCHO dSCD is observed for higher O_4 dSCDs, which might give a hint for possible O_4 absorption at 328 nm. Additionally the standard fit range used in this thesis is marked (332–358 nm), the retrieval interval recommended by Pinardi et al. [2013] for HCHO(336.5–359 nm) and the Aliwell et al. [2002]-interval for zenith-sky BrO retrievals. The 'Aliwell'-interval is not suitable for the retrieval of tropospheric HCHO, since it includes only one absorption band of HCHO. This is also reflected in the larger variation throughout the day and the larger fit error. For the size of the respective cross-sections see figure 5.1.

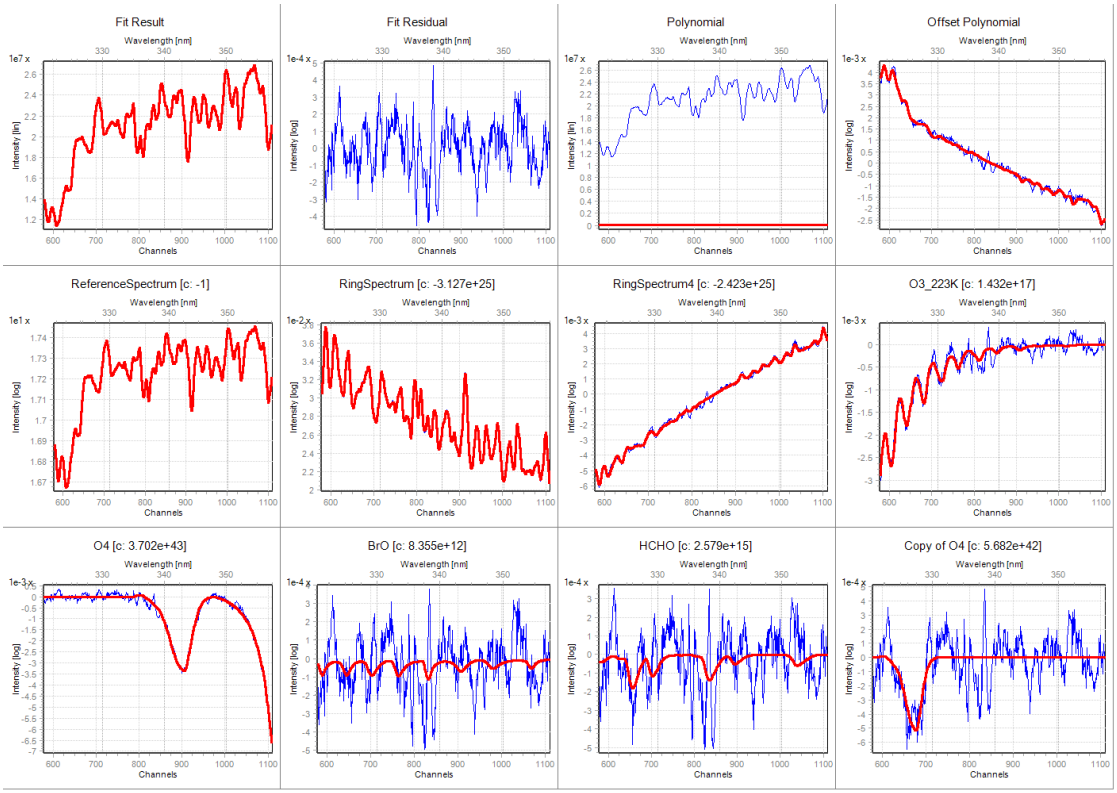

Figure 5.4.: Using the shape of the O4 absorption at 343 nm to estimate the absorption structure at 328 nm (*'Copy of O4'*) using data from Polarstern ANT XXVIII/1. The ratio of the optical densities at 328 nm and 343 nm is 6.5 ± 3 (6.7 according to Salow and Steiner [1936]) and the width is 10% smaller than the width of the peak at 343 nm, which in turn is also 20% smaller than the one of the absorption at 361 nm. A correlation plot is shown in figure 5.5.

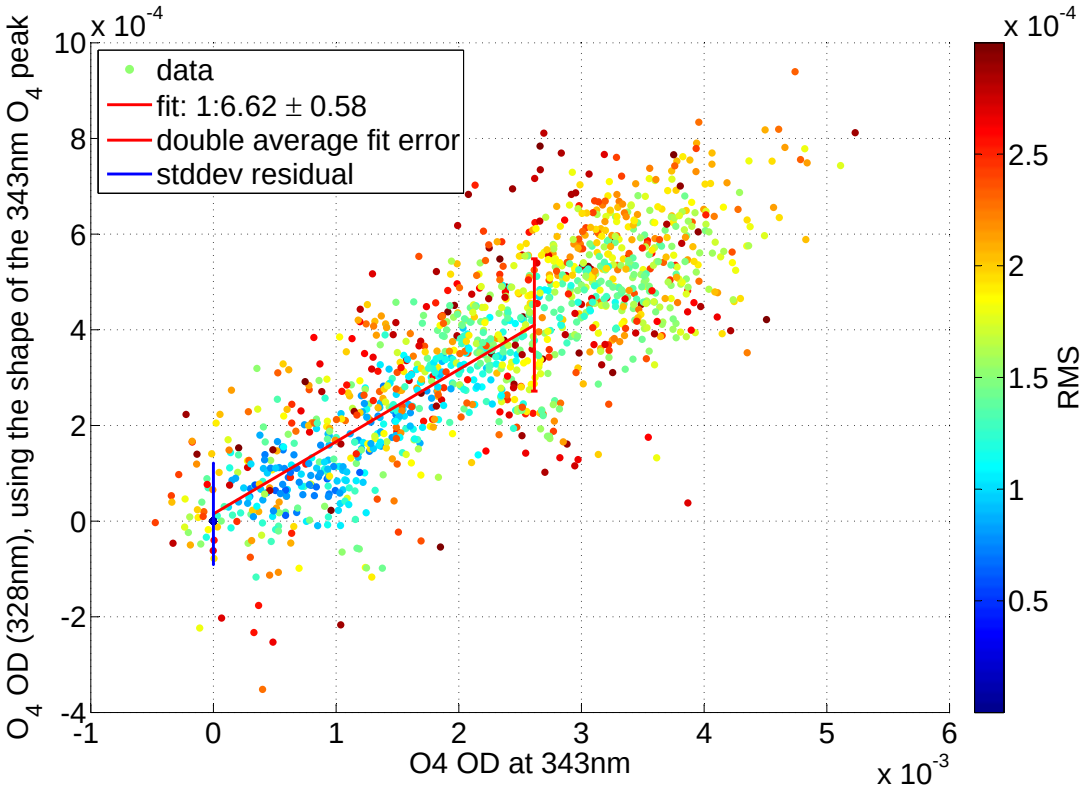

Figure 5.5.: Similarly as shown in figure 5.4, a correlation of the size of the absorption structure at 328 nm with the O_4 absorption at 343 nm with R=0.89 for a data set recorded with a the same type of instrument as during MADCAT (chapter 11). The obtained size of the absorption at 328 nm without considering possible variations due to different air mass factors at 328 and 343 nm is 6.6±0.6, thus agreeing with Salow and Steiner [1936] who reported a relative size of these absorptions of 6.7. The retrieval interval was 321–358 nm.

surements on the Cape Verde Atmospheric Observatory for spectral retrievals based on the wavelength corrected Greenblatt O_4 cross-section. However, during the time of Tschritter [2013] the cross-section by Thalman and Volkamer [2013] was not yet available.
In MAX-DOAS data from ANT XXVIII and Meteor M91 a correlation of the BrO dSCD and the O4 dSCD can be observed, depending on the choice literature cross-section for O_4. This has been also reported from HCHO retrievals by Pinardi et al. [2013]. Using the O_4 cross-section by Hermans et al. [1999] usually leads to negative BrO dSCD at low elevation angles (retrieval interval: 332–358 nm and also 336.5–359 nm). A correlation between BrO / O_4 has been found with $R = 0.8$ and a slope of $-3.7 \cdot 10^{13}$ molec cm^{-2} / $4 \cdot 10^{43}$ molec^2 cm^{-5} $\approx -9 \cdot 10^{-31}$molec cm^3 for MSM18/1 for open ocean conditions.
The O_4 cross-section by Greenblatt et al. [1990] on the other hand leads to a correlation with a positive sign for those measurement campaigns (MSM18/1: $1.5 \cdot 10^{13}$ molec cm^{-2} / $4 \cdot 10^{43}$ molec^2 cm^{-5}), either indicating a constant background of ≈ 0.5 ppt BrO in the MBL or again a problem with the cross-section.
The O_4 cross-section by Thalman and Volkamer [2013] does not show a correlation of O_4 and BrO for open ocean conditions within measurement errors (MSM18/1: $1 \cdot 10^{12}$ molec cm^{-2} / $4 \cdot 10^{43}$ molec^2 cm^{-5}).
It is difficult to distinguish from the ship measurements which O_4 cross-sections leads to the most trustworthy results, therefore MAX-DOAS measurement data from a place where no tropospheric BrO is expected might reveal further information. Already during the CINDI campaign in the Netherlands negative tropospheric BrO dSCDs were observed when using the Hermans cross-section, see Pinardi et al. [2013] (336.5–359 nm). Despite large NO_2 concentrations and usually significantly larger tropospheric HCHO concentrations, the MAD-CAT dataset measured in Mainz in 2013 was used as a reference dataset. Mainz is surrounded by large sources of anthropogenic NO_2, which makes it unlikely that large amounts of BrO arrive from coastal areas or polar regions.
Spectra from the MAD-CAT campaign were evaluated using the different O_4 cross-sections in the BrO retrieval interval from 332–358 nm, including the absorbers listed in table 5.12. The fit results from MAD-CAT were filtered to remove any measurements with a large residual or a strong influence of NO_2 absorption. The filter conditions were a RMS of $< 4 \cdot 10^{-4}$ and a maximum NO_2 dSCD of $< 4 \cdot 10^{16}$ molec cm^{-2} to avoid the influence of strong absorption by NO_2, which can led to strong residual structures. About 20% of the total measurement data was used for the analysis. Furthermore the HCHO dSCD during the MAD-CAT campaign were 10-20 times higher than on the open ocean, up to $10 \cdot 10^{16}$ molec cm^{-2} compared to values in the upper 10^{15} molec cm^{-2} range for measurements in the MBL. No correlation between HCHO dSCDs and BrO dSCDs was observed when using the Greenblatt cross-section ($< 1 \cdot 10^{13}$ molec cm^{-2} BrO / 10^{17} molec cm^{-2} HCHO). Table 5.1 shows the resulting slopes for the correlation plots with O_4. Again, the cross-section by Hermans is found to be unsuitable for the BrO in the retrieval interval from 332–358 nm. For MAD-CAT and MSM18/1 also the results for Thalman and Greenblatt agree reasonably, indicating a background BrO concentration of $\approx 3 \cdot 10^{-31}$ molec cm^{-3} BrO/O_4 for the subtropical open ocean measurements during MSM18/1.

Cross-section	MAD-CAT molec^{-1} cm^3	MSM18/1 molec^{-1} cm^3
Greenblatt et al. [1990]	$1 \cdot 10^{-31}$	$3.7 \cdot 10^{-31}$
Hermans et al. [1999]	$-9 \cdot 10^{-31}$	$-10 \cdot 10^{-31}$
Thalman and Volkamer [2013]	$-3 \cdot 10^{-31}$	$0.25 \cdot 10^{-31}$
typical error	$2 \cdot 10^{-31}$	$2 \cdot 10^{-31}$

Table 5.1.: BrO / O_4 dSCD ratios for different campaigns. The data had to comply with a RMS limit of $4 \cdot 10^{-4}$ and a maximum NO_2 dSCD of $< 4 \cdot 10^{16}$ molec cm^{-2}. The retrieval interval was 332–358 nm and the shift and squeeze parameters of all cross-sections were linked.

The average correlation between BrO and NO_2 for this fit range during MAD-CAT was $4.1 \cdot 10^{-5} \frac{\text{molec cm}^2}{\text{molec cm}^2}$, therefore the threshold used to filter data of $< 4 \cdot 10^{16}$ molec cm^{-2} would have introduced an additional systematic error of $< 0.1 \cdot 10^{-31}$ molec cm^{-3} to the MAD-CAT BrO/O_4 ratio and can be neglected.

The water vapour absorption line lists HITEMP and HITRAN2012 have shown hints that there might be indeed water vapour absorption below the current experimental validation measurements at 393 nm (see also subsection 5.3.3). The reported cross-sections would lead to water vapour absorption signatures in the 10^{-4} range, which could as well influence the spectral retrieval of small BrO dSCDs in tropical and mid-latitude regions. Looking at water vapour dSCDs at 440 nm, MAD-CAT and MSM18/1 are comparable.

Also vibrational Raman scattering could have an effect on the retrieval of BrO, but as for the water vapour absorption, it was not possible to detect it in this spectral range. Furthermore, the remaining residual structures primarily correlated with the O_4-dSCD, i.e. roughly the effective tropospheric lightpath. A dominant correlation with the Ring dSCD was not observed.

Temperature dependence of HCHO: Chance and Orphal [2011] performed an analysis of the temperature dependence of the formaldehyde cross-section based on the cross-section measurements by Meller and Moortgat [2000] and Cantrell et al. [1990]. The difference in cross-section for the absorption around 340 nm corresponds to $\Delta\sigma_{HCHO}/K = 6 \cdot 10^{-22}\text{cm}^2$. This means for a dSCD of $3 \cdot 10^{16}$ molec cm^{-2} the corresponding difference in optical density for a temperature difference of $20K$ is $\Delta\tau = 3.6 \cdot 10^{-4}$. The absolute differential absorption cross-section is larger for lower temperatures and the absorption bands are not as broad. This improves the situtation from the spectral point of view since most of the change is just a scaling effect and are 'just' resulting in a false dSCD and only a small part will be found in the residual if the cross-section has not been selected appropriately. Taking this scaling by 6% into account, this yields for the absorption bands around 340 nm $\delta\sigma_{HCHO} = 1 \cdot 10^{-22}\text{cm}^2 \approx \frac{1}{6}\Delta\sigma_{HCHO}$ for 20K temperature difference. To see this effect then with the current instruments, the temperature change must be especially high or concentrations must be higher than usual western european background values.

5.1.1.2. Persistent residual structures

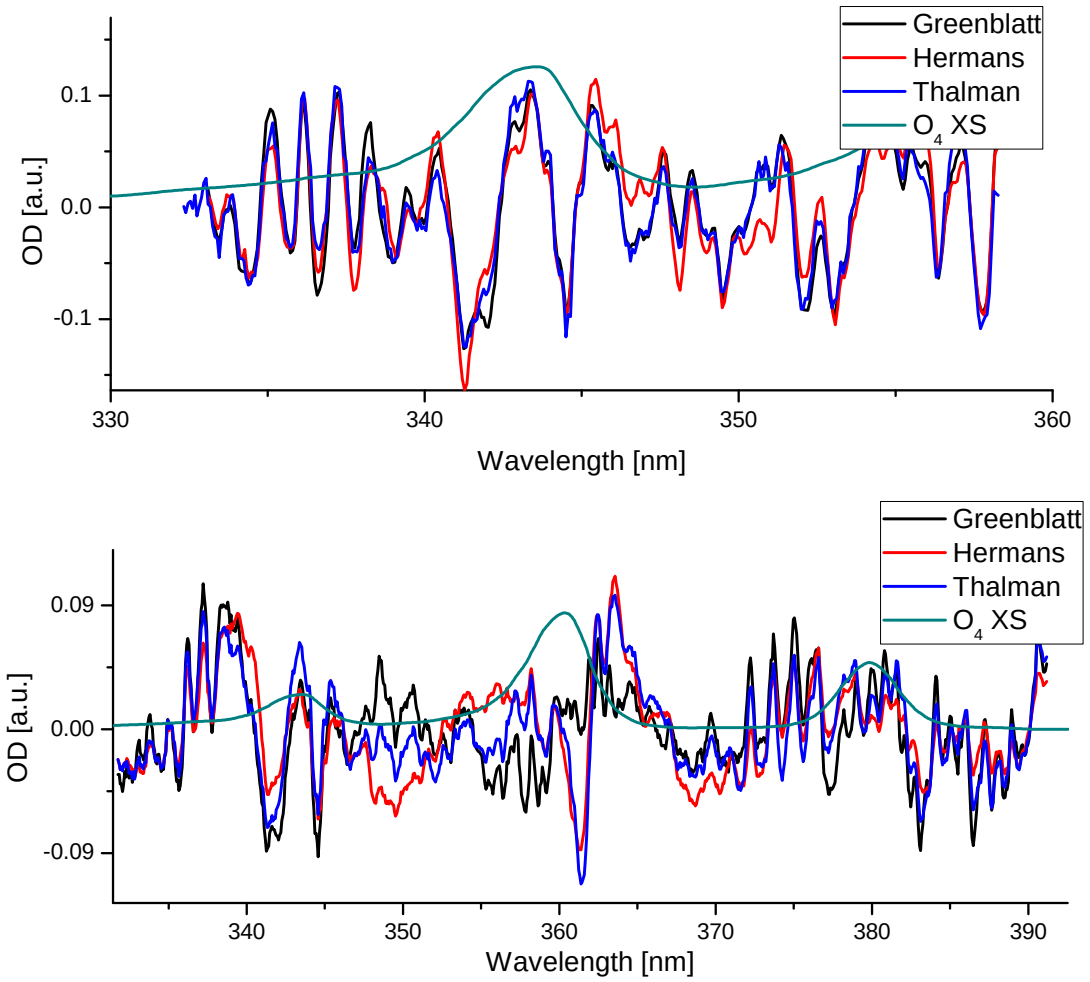

Figure 5.6.: First principal component of the residual spectra of BrO fits for M91 using different O_4 cross-sections. In the upper plot this has been done for the standard BrO wavelength range (332–358 nm) and below for an extended wavelength range (332–392 nm). The strength of these structures is clearly separated for different elevation angles, correlates with O_4 and was also observed during different campaigns, e.g. MAD-CAT and Polarstern data.

A Principal Component Analysis (PCA) (see subsection 3.3.2) was performed on BrO-fit residuals from an evaluation against a current Fraunhofer reference. The analysis revealed an elevation angle separated component accounting for optical depth of about $(3-4)\cdot 10^{-4}$ (peak-to-peak) for low elevation angles as shown in figure 5.7. This was observed for MAX-DOAS data from MAD-CAT (compact Avantes spectrometer, over land), Polarstern ANT XXVIII and ARK XXVII (compact OMT spectrometer, measure-

ments on the Atlantic and close to ice, 70°S-80°N), M77 (Ocean optics USB2000, eastern tropical Pacific) and SOPRAN M91 (300 mm Acton spectrometer, Eastern Pacific).
BrO fit errors of about $3 \cdot 10^{12}$ molec cm^{-2} corresponding to an optical density of $1 \cdot 10^{-4}$ (332–359 nm) for example during MSM18/1 demonstrate that the spectral retrieval could be significantly improved, if this residual structure can be explained. Since it furthermore shows a separation for elevation angles similar to any tropospheric absorber, the absorption causing these residual structures might as well have an influence on BrO dSCDs.
The structure correlates with the O_4 dSCD and is almost independent of the choice of O_4 cross-section. It is not dominantly related to the Ring dSCD, which excludes a possible dominant influence of vibration Raman scattering. The residual structure was detected during M91 on all days, thus suggesting absorption of a long-lived species which has not been included in the fit scenario. The shape of the observed residuals do not match the differences of saturation- or I_0- correction of the O_4 absorption.
The shape of the residual structure is similar for M91, MSM18 and MAD-CAT (compare figure 11.2). For ANT XXVIII and ARK XXVII a structure correlated with O_4 is found, too, but the spectral shape is a different one. The reason might be the relative low spectral resolution of 1 nm of the Polarstern UV spectrometer, thus different cross-sections will compensate each other and the unknown residual structure in a different way. The residual structure from M91 is also found in Polarstern data when it is convoluted to the lower spectral resolution of the Polarstern instrument (see figure A.5). At 360 nm it almost looks like the structure which is the difference of two slightly shifted Gaussian distributions. However, the DOAS fit was not able to compensate the residual structure when shift and squeeze of the O_4 cross-section were allowed to vary during the fitting process.
Potential reasons for the residual structure are briefly discussed here:

1. Since the structure is present for measurements over land and over the ocean, an effect of light passing ocean water can be excluded. Furthermore testing for structures possibly related to vibrational Raman scattering and Brillouin scattering in water [Xu and Kattawar, 1994, Peters, 2013] were not found and scattering on phonons in air leads to wavelength shifts below one picometer. Example calculations for Brillouin scattering show that the obtained structures are too small and their structure cannot explain the residuals. Chance and Spurr [1997] also reported that these effects should be negligible for typical DOAS applications.

2. A comparison of the Ring spectrum calculated by DOASIS and a Ring spectrum based on the work of Chance and Spurr [1997] showed a difference of about $5 \cdot 10^{-30}$, which would lead to similar sizes of residual structures for Ring dSCD of $\approx 5 \cdot 10^{25}$ molec cm^{-2}. On the other hand, the structure is not clearly related to the Ring signal in the measurement data.

3. One potential candidate is, beside imperfections of the O_4 cross-section, water vapour absorption below 400 nm. It has been calculated e.g. in the BT2 line list by Barber et al. [2006] and are partly included in HITEMP [Rothman et al., 2010]

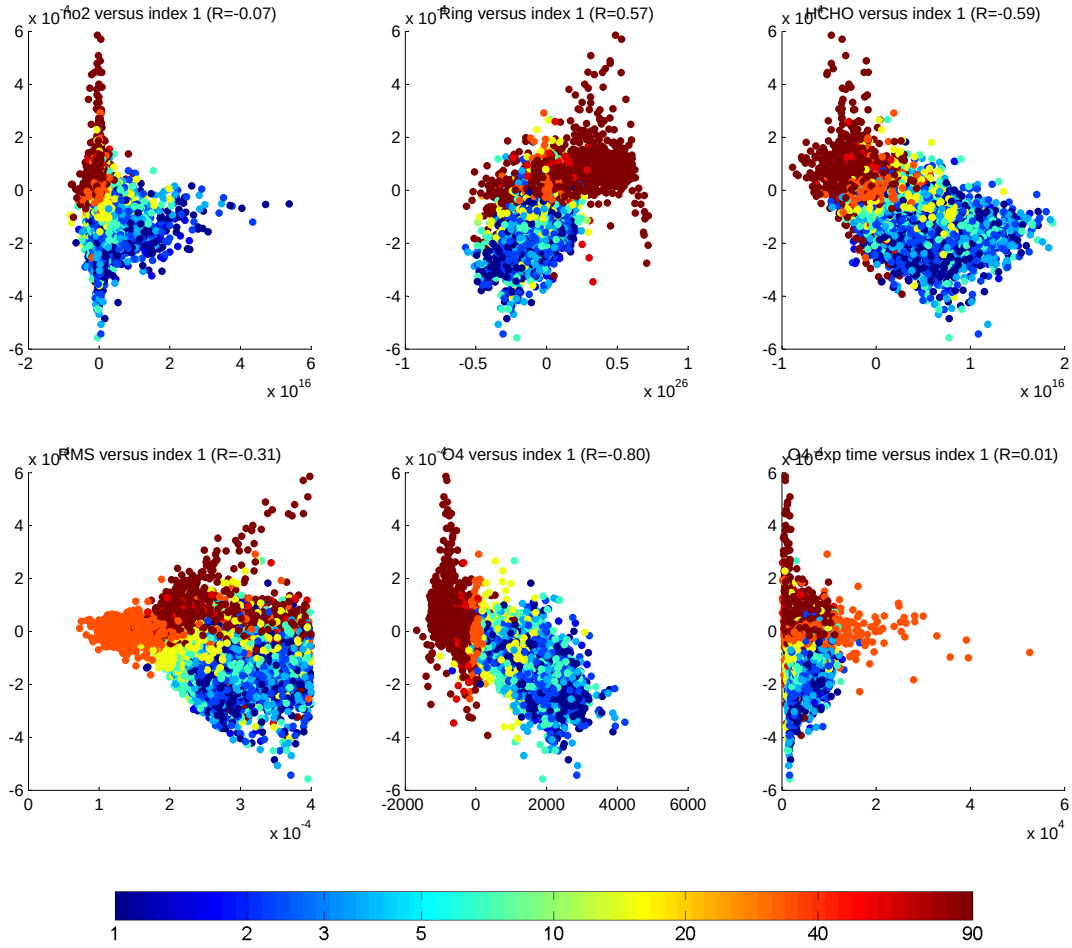

Figure 5.7.: Correlations of the dominant residual structure from MAX-DOAS BrO fits from M91 data using the Greenblatt O_4 cross-section. The first principal component is shown in figure 5.6. The telescope elevation angle is colour-coded, optical densities are given on the y-axis in 10^{-4}.

(compare figure 5.30). The residual absorption structures do not resemble the suggested shape of absorption, neither those from BT2 nor those from HITEMP. The cross-section data itself is highly uncertain [pers. comm. J. Tennyson, UCL]. Furthermore MAX-DOAS measurements from Antarctic and Arctic regions also show this absorption structure for high O_4 dSCD.

4. An influence of a varying instrument function, a different shape of the instrument function due to instrumental effects and/or an erroneous pixel-to-wavelength mapping can most probably be excluded, since the structure was found for different spectrometers with focal lengths from 60–300 mm.

5. The structure is not caused by shifting the O_4 cross-section, by AMF differences for

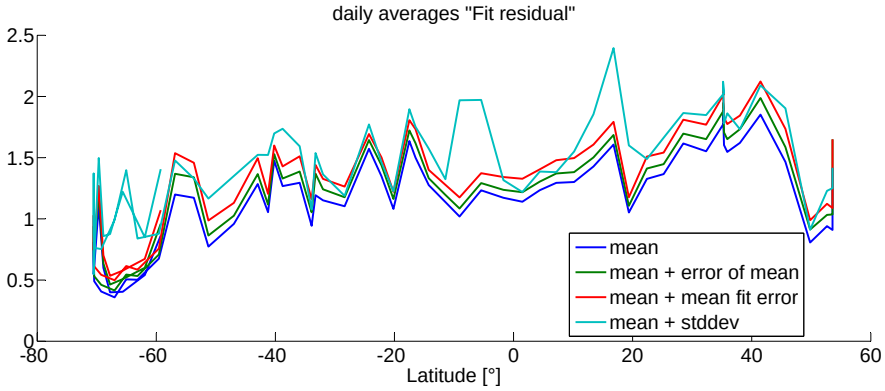

Figure 5.8.: A fit residual from a fit with a high O_4 dSCD from 20°N was included in the fit scenario to obtain a latitudinal distribution of this absorption for the *ANT XXVIII* dataset. '1' corresponds to an OD of $2.5 \cdot 10^{-4}$. The low values between Cape Town and Antarctica are due to small O_4 dSCD.

both O_4 absorption bands at 342 and 361 nm nor by the absorption cross-section of ozone at 293K. Absorption of HONO, OClO and SO_2 above detection limit were excluded. Criegee intermediates like CH_2OO or $(CH_3)_2COO$ have absorption structures in this spectral range, but their literature cross-sections are not well spectrally resolved and their concentrations are expected to be small. Maximum optical densities for 10km lightpath are expected to be $< 2.5 \cdot 10^{-4}$ for boreal areas (cross-section: $< 5 \cdot 10^{-17}$cm^2/molec [Beames et al., 2012, Liu et al., 2014], concentrations < 0.2 ppt [Taatjes et al., 2014]).

6. Impact of O_2 absorption: [Bogumil et al., 2003] reported some differential absorption features in this spectral range and also at 360 nm, but they do not match the observed structures. Furthermore the noise of the measurements is of the same size. While for the cross-section by Hermans et al. [1999] the exact extraction procedure of the cross-section is unclear, the cross-section by Thalman and Volkamer [2013] has been extracted from CE-DOAS measurements assuming no absorption of O_2 at atmospheric pressure. The Greenblatt et al. [1990] cross-section on the other hand has been extracted from the quadratic behaviour of the measured O_4 signal with respect to the pressure within the measurement cell, and therefore at higher total pressures. None of the publications of O_4 cross-section data mentioned significant absorptions of O_2 in the UV range, but their accuracy in terms of O_4 cross-section were of the same size as the residual structure observed. Modelled, hypothetical dSCDs of N_2 and O_4 are plotted in figure 5.9 for different Relative Solar Azimuth Angle (RZA) and SZA, calculated using McArtim [Deutschmann, 2014]. It shows that the deviation of the correlation of the residual structure from a linear fit cannot be detected since the signal-to-noise ratio of the fits of this persistent residual structure is about 10:1. Therefore any long-lived evenly distributed

trace gas could cause these residual structures.

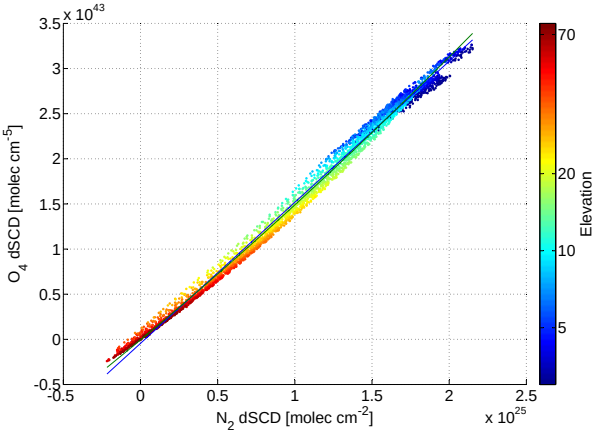

Figure 5.9.: N_2 and O_4 dSCD modelled for 340 nm using McArtim. A 90° spectrum was used as reference at an AOD of 0.11km^{-1}. Calculations were done for 0° <RZA< 180° and 0° <SZA< 90°.

7. CO_2 absorption above 300 nm can be present, at least at higher temperatures [Schulz et al., 2002]. Given the current ambient concentration of 400 ppm, a cross-section of about $4 \cdot 10^{-26}$cm^2 molec^{-1} would be sufficient to explain the residual structures. Differential cross-sections at 320 nm of $\sigma_{3050K} = 1 \cdot 10^{-19}$ cm^2 molec^{-1} were reported for temperatures of 3050 K. Assuming a Boltzmann distribution for the population of states, and using the measurements of the CO_2 cross-section at 3050 and 1160 K from [Schulz et al., 2002] which differ by two orders of magnitude, a cross-section at 298 K of $\sigma_{298K} = 1 \cdot 10^{-25}$ cm^2 molec^{-1} could be estimated. This is a size of the cross-section, which would be sufficient to explain the observed residual structures.

8. Another candidate is N_2O, which might have absorption structures in the region around 340 nm according to Orth and Dunbar [2008]. The given cross-section in this publication of about $5 \cdot 10^{-19}$ cm^2 on the other hand would be too large, given atmospheric mixing ratios of N_2O of $\approx$ 340ppb.

9. A problem concerning the absorption of HCHO can be excluded, since the HCHO dSCD varied by a factor of 10 from $1 \cdot 10^{16}$ molec cm^{-2} to $1 \cdot 10^{17}$ molec cm^{-2} at low elevation angles during MAD-CAT. This excludes HCHO absorption, since the dominant correlation of this residual structure is with the O_4 dSCD.

10. A part of the observed residual structures could be explained by temperature effects of O_4, measured also in Thalman and Volkamer [2013]. When using the two (currently available) cross-sections at 203K and 293K in the fit, the size of the primary principal component is reduced by 50%. The ratio of dSCDs (in

the BrO wavelength range) for both cross-sections is 0.30 ± 0.05, which yields an effective temperature of 266 ± 5K, corresponding to a height of 6.0 ± 1.5km (based on radiosonde data from GEOMAR). This is significantly higher than the expected main absorption of O_4. Leaving shift and squeeze of O_4 free also removes half of the residual structure, when limiting the fit range only to the four BrO absorption bands from 332–353 nm. Using the main absorption at 360 nm can be suitable to obtain temperature information from the fit, see figure 5.10. When the cross-section by [Thalman and Volkamer, 2013] is not deconvoluted before (see subsection 3.1.3 for deconvolution), this leads theoretically to a shift towards lower temperatures, since the convolution would be effectively done for a larger FWHM. From Thalman and Volkamer [2013] an increase in absorption band width for the absorption at 360 nm of 5pm/K can be derived. Convolution of the O_4 cross-section without deconvolution leads then theoretically to an overestimation of temperature of ≈ 14K, from figure 5.10 18 ± 2K were obtained. Although, the difference cannot be explained by the difference in the result from normal and deconvolved cross-sections, which is 1K, based on measurement data. This and the fact that the relation shown in figure 5.10 could also be quadratic might indicate that there is indeed another absorber causing residual structures.

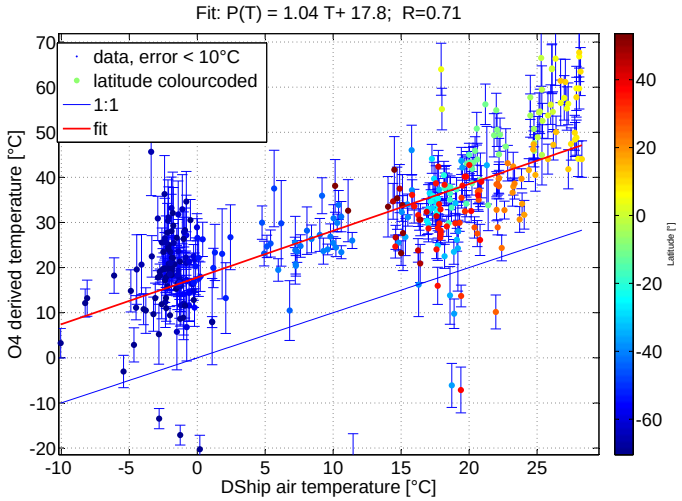

Figure 5.10.: Temperature derived from O_4 absorption at 360 nm and the air temperature from the weather station on R/V Polarstern during ANT XXVIII.

Temperature effect of O_4: When comparing the Thalman and Volkamer [2013] cross-sections for 293K and 203K, the resulting peak-to-peak residual structure is $1.6 \cdot 10^{-4}$/10K for the BrO evaluation range from 332–358 nm and $4.6 \cdot 10^{-4}$/10K for 345–375 nm for a typical dSCD of $3 \cdot 10^{43}$ molec^2 cm^{-5}. The residual structure observed in the BrO evaluation range are twice as large.

Tested for M91 MAX-DOAS data, including an additional O_4 cross-section from

Thalman and Volkamer [2013] in the fit scenario led to a reduction of BrO dSCD for low elevation angles of $(4.2 \pm 3.7) \cdot 10^{12}$ molec cm^{-2}, which is of the same size as the average fit error for BrO when summing four elevation sequences.

11. The structure can not be explained by a difference in literature cross-sections of ozone at 293K from Serdyuchenko et al. [2013], Voigt et al. [2001] or Burrows et al. [1999].

12. The structure is found in evaluations for single one-minute spectra as well as in evaluations summing over 16 elevation sequences. Therefore is cannot be an influence of larger ozone absorption due to a changing SZA among summed spectra.

13. The residual structures found looks also similar to the resulting difference when compensating the fact that the O_4 cross-sections have been measured at finite resolution. The spectral resolution at 360 nm is 0.32 nm for Thalman and Volkamer [2013] recorded at 293 K, 0.6 nm for Greenblatt et al. [1990] recorded at 298 K and $\approx$ 0.025 nm (2 cm^{-1}) for Hermans et al. [1999] recorded at 287 K. This means, that the cross-section should not be convoluted with the instrument function without compensating for the original resolution, since the effective instrument function will then overestimate the width of the correctly convoluted and/or observed cross-section. For a literature cross-section recorded at 0.32 nm and an instrument recording spectra at a spectral resolution of 0.45 nm, this means, that the result of the convolution will overestimate the correct instrument function by about 0.1 nm which leads to residual structures similar as those shown. If the cross-section is not convoluted at all or normally convoluted with the instrument function (FWHM=0.45 nm for M91, e.g.), the resulting residual at has a similar shape as observed from residual spectra.

    Figure 3.1 shows that the obtained structure for not deconvolving the literature cross-section of O_4 is similar to the structures obtained from a principal component analysis of the residual spectra (see figure 5.6). An interesting result is, that the cross-section by Hermans shows similar residual structures around 360 nm as the Thalman cross-section due to its limited spectral resolution, even though it was recorded at a spectral resolution (0.025 nm) which should be sufficient for any usual DOAS application. Thus either the Hermans cross-section has been filtered (this would also explain the 'wiggles' in the cross-section data between the main absorptions) and the effective resolution is therefore lower or the another absorber causes these residual structures.

    The structure shown in figure 3.1 looks similar to the residual structures, but the actual residual structure has a different sign and is about ten times larger. Therefore this does not seem to be the reason for the observed residuals.

The structure shown in figure 5.6 and within a DOAS fit in figure 11.2 might be divided into two parts, which would be the part on top of the O_4 absorption at 343 nm and the structures below 340 nm. The shape around 343 nm suggests that the O_4 absorption

band is actually narrower. This structure is observed for MAD-CAT and M91 with air temperatures above 20°C, and not as pronounced for colder temperatures as during ARK XXVII, where the structure below 340 nm is still present. The typical temperature dependence of the O_4 absorption cross-section is expected in the opposite direction.
In the end these residual structures might be eventually a combination of all effects: Temperature dependence of the O_4 cross-section, possible water vapour absorption, other absorbers and imperfections during convolution.
Since the structure obtained from evaluation of data from the Peruvian upwelling was found in data from MAD-CAT in Mainz (Figure 11.2), leads to the idea to generate the absorption structure from measurements in Mainz: Assuming that no tropospheric BrO absorption can be detected in Mainz (due to NO_x chemistry), residuals from fits without including BrO could deliver a spectrum of these systematic absorption structures. Unfortunately this would require ideally the same instrument at both locations, and the same evaluation procedure to avoid, that this structure is compensated in a different way by other literature cross-section. Furthermore it does not contribute to understand the origin of these absorptions.
The LP-DOAS measurements shown in Stutz et al. [2011] showed very small residuals, but a small gap around 341 nm was used in the fit retrieval window due to 'instrumental effects' and to exclude an influence of HCHO on the retrieval of BrO. It is unclear if this gap in the retrieval range and the structures observed for MAX-DOAS measurements are connected.

5.1.2. IO

The retrieval interval for IO is limited by water vapour absorption around 440 nm and either by a Fraunhofer line at 410 nm or the water vapour absorption at 416 nm. Additionally O_3 and NO_2 have to be included in the fit. The temperature dependence of the O_3 cross-section for the Chappuis band in the blue wavelength range is negligible and differences in the cross-sections for different temperatures might be due to offset problems [Serdyuchenko et al., 2013]. Therefore only one ozone cross-section needs to be included in the fit. For NO_2 two cross-sections for stratospheric and tropospheric NO_2 have to be included for a noon reference, while for a current reference only one cross-section to account for tropospheric NO_2 is sufficient.
The absorption of O_4 in this spectral region is not well-known, if present at all. The cross-sections by Hermans et al. [1999] and Greenblatt et al. [1990] do not agree on any characteristic absorption and Thalman and Volkamer [2013] does not include this region. The Hermans cross-section shows a wave-like structure which might be only caused by the fourier transformation of data close to the detection limit. The Greenblatt cross-section has a sharp bend around 432 nm, which leads often to negative and too large dSCDs (10^{45} molec^2 cm^{-5}) in ground-based MAX-DOAS data [e.g. Seitz, 2009]. Strong differential structures on the nm-scale contradict the short-lived nature of the O_2-O_2 complex, though.
At wavelengths of about 432 nm residual structures were observed using the standard fit scenario in data from the Polarstern instrument as well as from the Acton (SMAX-

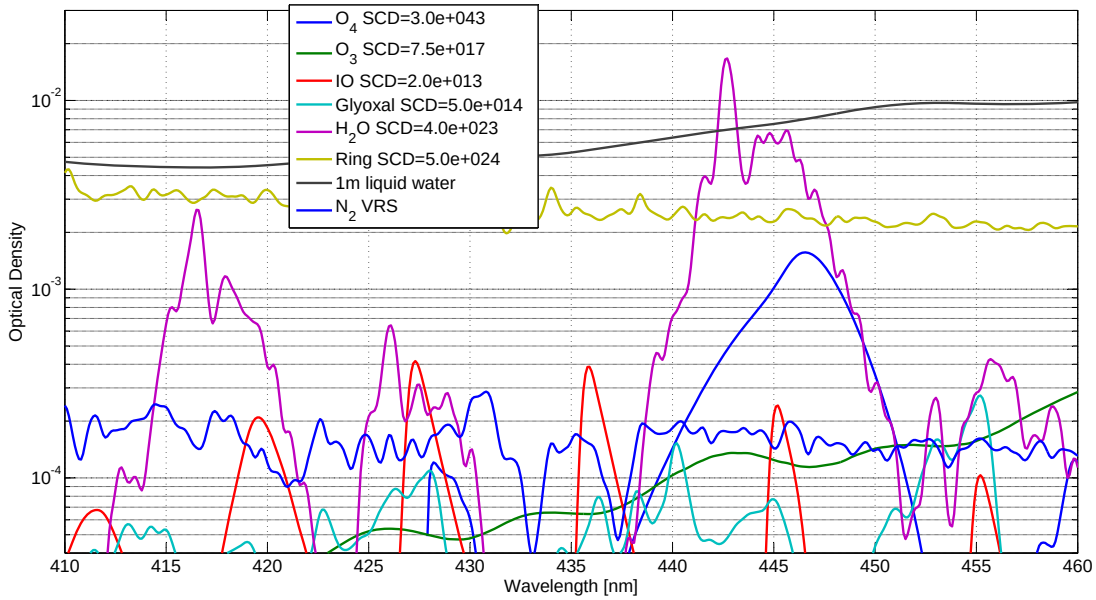

Figure 5.11.: Overview: Absorption cross-sections in the wavelength range used to retrieve IO and glyoxal absorption in the blue spectral range. SCDs are given in molec cm−2 and are representative for typical tropospheric column densities when using the next zenith sky spectrum as Fraunhofer reference of the retrieval. The differential part of the liquid water absorption has a maximum value of $3 \cdot 10^{-4}$ for 1m lightpath, but only available in low spectral resolution.

DOAS) measurements during M91 (Table 5.12, but without VRS). Negative dSCDs of O_4 based on the Greenblatt cross-section compensates for this effect, but this is unphysical and probably just a coincidence. There are several possible reasons for these negative dSCD:

- insufficient accurate cross-sections of O_3, O_4, IO or NO_2
- problems related to the Fraunhofer line at 430 nm, i.e. Ring-effect, spectrometer stray light or vibrational Raman scattering
- an unknown absorber

Schönhardt et al. [2008, 2012] used only a 2-absorption band fit (416–430 nm) and argued that the Fraunhofer line at 430–431 nm caused problems and recurring residual structures. An effect of this observation can be observed in the dSCD value in figure 5.12. Schönhardt et al. [2008] and Holla [2009] also noticed that these structures were the strongest whenever the Ring structure was strong. Given the position of the residual structures at 432 nm, this indicates that these structures are caused by vibrational Raman shifts caused by N_2. A detailed analysis can be found in subsection 5.2.2. The

VRS-shifted calcium K-line from 393.37 nm causes a structure at 433.08 nm, the VRS-shifted H-line at 396.85 nm causes a structure below the IO absorption at 437.30 nm (for N_2) (compare to figure 5.14). Tested for M91 data (16 co-added elevation sequences), a three-band IO fit (416–438 nm, typical fit error: $4.6 \cdot 10^{11}$ molec cm^{-2}) yields 40% lower fit errors than a two-band IO fit (416–430 nm, typical fit error: $7.5 \cdot 10^{11}$ molec cm^{-2}). Cross-correlations caused by other absorbers can be minimized when using a tree-band IO fit as well. Extending the fit range further did not reduce the IO fit error further, due to strong water vapour absorption (416–450 nm, typical fit error: $4.6 \cdot 10^{11}$ molec cm^{-2}).

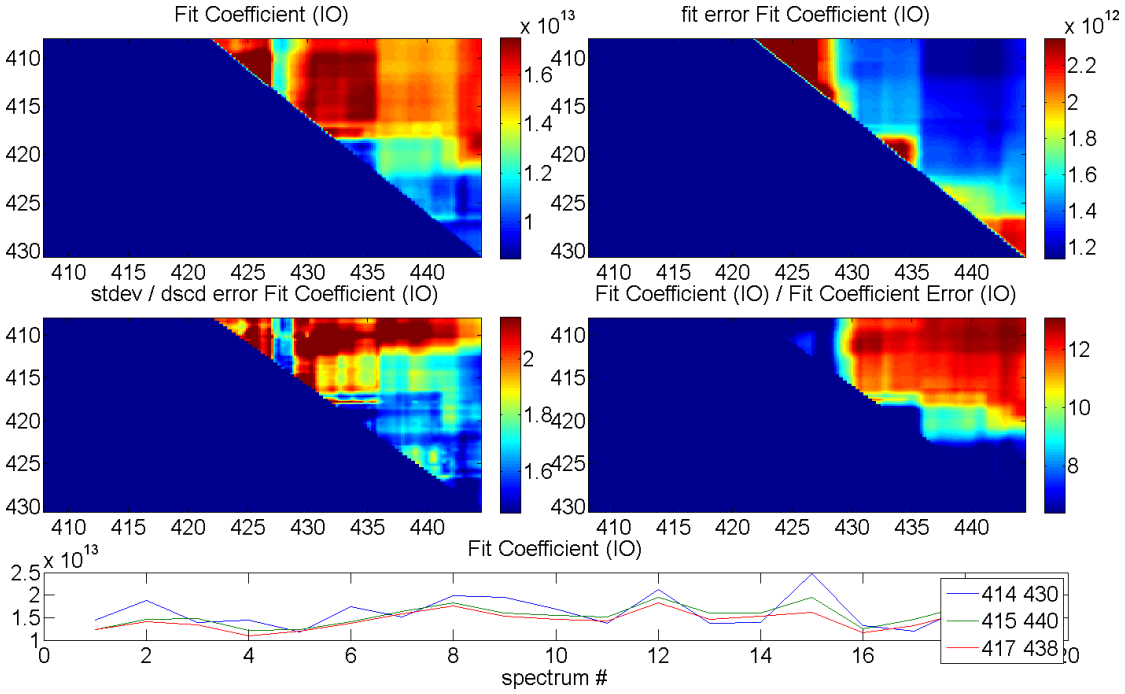

Figure 5.12.: Retrieval interval map for IO MAX-DOAS measurements at 3° elevation on the 12/10/2012 from 10:00 UTC - 22:00 UTC during SOPRAN M91. The effects of the IO absorption bands at 419.5, 427.5 and 436 nm are clearly visible in dSCD and fit error, but also the beginning of the strong water vapour absorption around 442 nm.

5.1.2.1. Water vapour and the influence on IO

During previous IO measurements, the influence of water vapour has been discussed in depth, e.g. during the preparation of Großmann et al. [2013]. The reasons were on the one side the large uncertainties of the water vapour cross-sections for older versions of HITRAN (compare figure 5.30) and other databases and the fact that the spectral retrieval of water vapour constantly yielded unrealistic results (e.g. about a factor of two too large dSCD with HITRAN 2009). Furthermore residual structures correlated with water vapour dSCDs were observed, as also shown in figure 5.36. Problems still

exist with recent water vapour cross-section such as HITRAN2012 and HITEMP, but the remaining residual structures are small (compare figure 5.36 and figure 5.35) in the blue wavelength range. The large dSCD can be explained by an underestimation of the water vapour cross-section due to using a relative large cut-off during the processing of the cross-section.
A candidate for testing the influence of water vapour on the spectral retrieval is again the MAD-CAT campaign, as for BrO. A drawback is the need to include the absorption of glyoxal, which has been detected in significant amounts during the campaign. From previous analysis glyoxal and IO are known to anti-correlate in the IO fit range from 414–438 nm. The fit scenario included a DOAS polynomial (3rd degree), additional offset polynomial of 1st degree and convoluted cross-sections for IO, O_3, glyoxal, Ring, VRS of O_2 and N_2, NO_2 223K, 296K and NO_2 at 296K scaled linearly to compensate the wavelength dependent airmass-factor. The apparent anti-correlation of glyoxal and IO was also observed for the MAD-CAT dataset, with a slope of about -10^{12} molec IO cm^{-2} / 10^{15}molec glyoxal cm^{-2} (R=-0.7). For water vapour a slope of $1.4 \cdot 10^{12}$ molec IO cm^{-2} / $5 \cdot 10^{23}$ molec H_2O cm^{-2} (R=0.21) was found. The contribution of tropospheric NO_2 is, despite large NO_2 dSCDs observed during the campaign, negligible: 10^{17} molec cm^{-2} NO_2 lead to a change of IO dSCD of -10^{11} molec cm^{-2} (R=-0.32). While the observation of IO and glyoxal would rather decrease the amount of IO observed, water vapour indeed leads to a small increase for these settings for the IO dSCDs. Given typical tropical IO dSCDs around $2 \cdot 10^{13}$ molec cm^{-2} the error is below 7% and the correlation is small, if significant at all.
The average IO dSCD observed during MAD-CAT with these settings was $3 \cdot 10^9 \pm 4.5 \cdot 10^{12}$ molec cm^{-2} with a fit error of $(2.0 \pm 0.8) \cdot 10^{12}$ molec cm^{-2}. Water vapour dSCD (from the larger glyoxal retrieval window encompassing also the main water vapour absorption at 442 nm) were in the range from $0 - 6.5 \cdot 10^{23}$ molec cm^{-2} with a mean value of $(3.5 \pm 1.2) \cdot 10^{23}$ molec cm^{-2}.
Therefore it can be concluded that the water vapour cross-section calculated from HITEMP or HITRAN2012 is accurate enough for the typical retrieval of IO. For stronger absorptions of water vapour outside the IO retrieval wavelength interval, the corrections necessary due to modification of the radiative transfer in MAX-DOAS measurements are larger than the uncertainties of the cross-section itself (compare section 5.4). Furthermore the relative size of each of the water vapour absorption bands can become important, see table 5.8.

5.1.3. OIO and I_2

OIO has its main absorption features between 500–600 nm, with the maximum around 550 nm of $\sigma_{max} = 1.3 \cdot 10^{-17}$cm^2 The retrieval interval which can be used for OIO is limited for non-polar measurements by water vapour absorptions on both sides and needs to be restricted to be retrieved in an interval between 514–538 nm or 548–568 nm. Additionally the available water vapour cross-sections might differ significantly compared to the optical density of the expected amounts of OIO, compare figure 5.13.
The photolysis of I_2 is fast during daytime with an average tropospheric lifetime of 5min

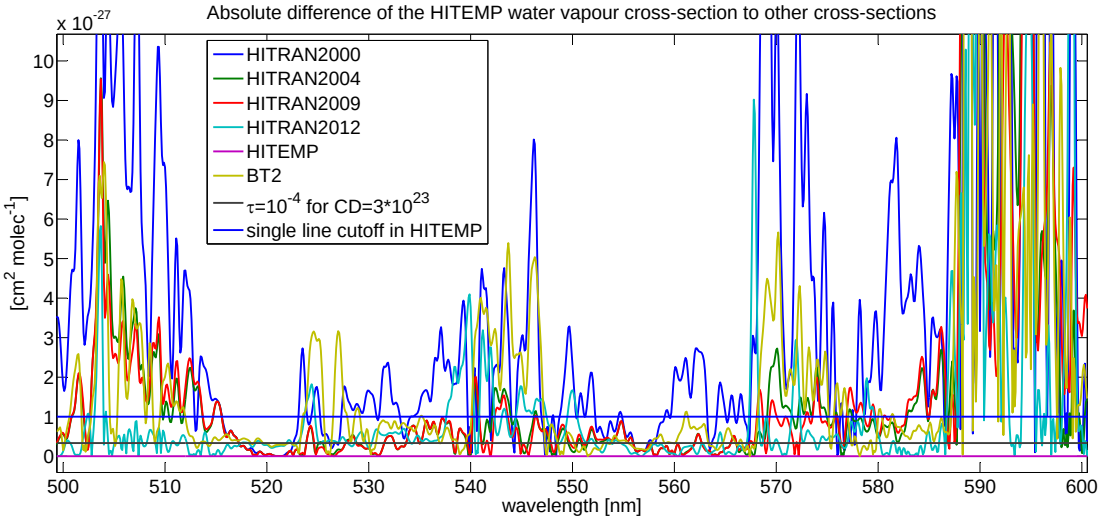

Figure 5.13.: Comparison of water vapour cross-sections in the spectral range from 500-600 nm. Here also absorptions of I_2 and OIO are found.

during the day. Therefore concentrations are expected to be low during daytime for MAX-DOAS measurements. An exception can be extraordinary strong sources of iodine e.g. above coastal algae. Even during night-time concentrations are expected to be below 1 ppt for open ocean conditions [Lawler et al., 2013]. This together with the relatively weak differential absorption cross-section also in the green wavelength range of $\approx 10^{-18}$ cm^2/molec will make the detection of I_2 and OIO using MAX-DOAS measurements difficult.

5.2. Raman scattering in MAX-DOAS measurements

MAX-DOAS measurements use the spectral structure of scattered sunlight to obtain information about trace gas concentrations. The scattering process itself modifies the intensities of the scattered light. The largest part of the light is scattered elastically of the so-called Cabannes line (Figure 5.14). About 2% of the scattered light has been inelastically scattered, leading to changes of angular momentum or even the vibrational quantum number of the involved molecule. The scattered photon can either gain or lose energy to the molecule. Due to historical reasons, elastic scattering processes and scattering processes involving changes in angular momentum are referred to as *Rayleigh* scattering [Chance and Spurr, 1997]. Even though for DOAS applications typically not of interest, the central Cabannes line is also broadened due to Doppler-broadening and Rayleigh-Brillouin scattering. Vibrational Raman scattering contributes with about 0.04% to the total intensity and is typically neglected in MAX-DOAS evaluations. Its size and further implications for the retrieval of trace-gases are discussed in this chapter. Furthermore vibrational Raman scattering associated with large wavelength shifts has been observed in liquid water and ice.
The strength of the Ring-signal is typically given in units of molec cm^{-2}, the same unit as column densities. What is typically measured here is not the light which is actually absorbed (as in the case of absorbers), but the light which is re-emitted at a different wavelength. The column density of the Ring is thus the number of Raman active O_2 and N_2 molecules along the lightpath contributing to the observed intensity of scattered light.

5.2.1. Rotational Raman Scattering

Anomalous Fraunhofer line shapes have been observed by Grainger and Ring [1962] in moonlight observations. The so-called 'filling-in' effect of Fraunhofer lines is also observed for scattered sunlight and has been explained by rotational Raman scattering by Chance and Spurr [1997]. This means, that observations of sunlight showed Fraunhofer lines, in which the overall intensity of scattered light was higher than for direct sunlight measurements. Its polarisation effect was measured e.g. by Bussemer [1993]. Here also a correction spectrum for this effect has been described, based on the energy shifts induced by Raman scattering on N_2 and O_2 molecules[2]. The total energy of a molecule can be subdivided into a vibrational and into a rotational part, E_{rot} and E_{vib}. Each of the eigenstates is described by the vibrational quantum numbers ν and the rotational quantum number J. When neglecting the coupling between vibrational and rotational eigenstates, the total energy E of the molecule is:

$$E(\nu, J) = E_{rot} + E_{vib} = hcBJ\,(J+1) + hc\tilde{\nu}\left(\nu + \frac{1}{2}\right) \tag{5.1}$$

[2]The contribution of CO_2 can be neglected. According to Penney et al. [1974] its rotational Raman cross-section is four times higher than the one of O_2, but its mixing ratio is three orders of magnitude smaller.

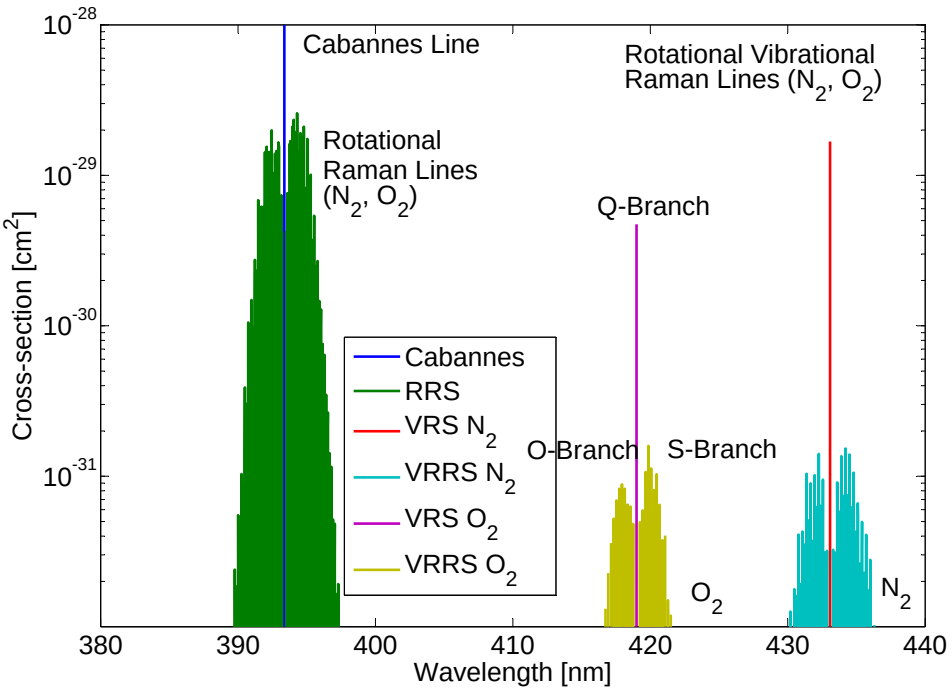

Figure 5.14.: Rotational Raman and vibrational Raman scattering calculated for monochromatic light with λ_0 =393.37 nm, the position of the calcium K-line. The vibrational Raman cross-section and the rotational vibrational Raman cross-section have been scaled according to She [2001], also listed in table 5.6.

Here h is the Planck-constant, c the speed of the light and B and $\tilde{\nu}$ the rotational and vibrational constant of the respective molecule.
Whenever a photon is absorbed by a molecule, the molecule might change to an excited electronic state. The photon can be emitted again and the molecule returns to its original electronic state. However, since the vibrational and/or rotational state can be different, the photon can have a different energy. This effect is most clearly visible around strong Fraunhofer lines, since more photons will be scattered onto the wavelength of a Fraunhofer line than will be scattered away from it. This results then in an effective 'filling-in' of Fraunhofer lines. Due to selection rules transitions with $\Delta J = 0, \pm 2$ and $\Delta\nu = 0, \pm 1$ are allowed. $\Delta\nu = 2$ transitions are possible, but more than three orders of magnitude weaker than the $\Delta\nu = 1$ transitions [Knippers et al., 1985] and therefore not relevant for DOAS measurements.
The scattered power density $I_{v,J\to v',J'}$ in $[W/m^2]$ scattered into the full solid angle 4π involving a transition $(v, J \to v', J')$ is given by Schrötter and Klöckner [1979]:

$$I_{\nu,J\to\nu',J'} = I_0 \cdot \sigma_{\nu,J\to\nu',J'} \cdot L \cdot N \cdot g_J(2J+1)\frac{1}{Z} \cdot e^{-E(\nu,J)/kT} \tag{5.2}$$

where I_0 is the incident power density, N the number of molecules in the scattering volume, L the length of latter and g_J is the statistical weight factor of the initial rotational state due to the nuclear spin. Z is the partition function and $\sigma_{\nu,J\to\nu',J'}$ the cross-section of the transition $\nu, J \to \nu', J'$.
Summing over all combinations of (ν, J, ν', J') for a given temperature weighted by the population density of the initial state yields $\sigma_R(\lambda_0, \lambda)$, the cross-section for an incident photon with the wavelength λ_0 to be scattered inelastically at a wavelength of λ.
To obtain the intensity spectrum of Raman scattered light, the cross-section $\sigma_R(\lambda_0, \lambda)$ for Raman scattering of a photon with λ_0 (see also figure 5.14) is convoluted with the measured sun light intensity I_0:

$$I_{Raman} = \int \sigma_R(\lambda_0, \lambda) I_0(\lambda_0) d\lambda_0 \tag{5.3}$$

From the calculation of the optical density (Equation 3.3) it follows that the additional intensity I_{Raman} included in the measured spectrum will change the measured optical density $\tau = -\ln\left(\frac{I+I_{Raman}}{I_0}\right)$. It follows that a pseudo absorber spectrum $\sigma_{Ring} = \frac{I_{Raman}}{I_0}$ (see also equation 3.8) can be used to compensate for this effect. Normally $\sigma_R(\lambda_0, \lambda)$ is calculated for a finite number of rotational eigenstates while neglecting vibrational and rotational-vibrational transitions. This is the way in which the Ring spectrum in DOASIS [Kraus, 2006] is calculated based on the work from Bussemer [1993]. By default it uses the first 25 rotational energy eigenvalues of the N_2 and O_2 molecules. The result from DOASIS calculations agrees with the data provided by Chance and Spurr [1997] ('Ring_NDSC2003') for a large Ring signal of $5 \cdot 10^{25}$ molec cm^{-2} within $4 - 5 \cdot 10^{-5}$ between 420–460 nm.
Wagner et al. [2009] additionally suggested an additional correction spectrum $\sigma'_{Ring4}(\lambda) = \sigma_{Ring}(\lambda) \cdot \lambda^4$ to compensate for radiative transfer effects. This often leads to optical densities of several 10^{-4} in the UV spectral range and the scaling factor be explained by a

different ratio of Mie and Rayleigh scattering in the measurement spectrum compared to the spectrum from which the Ring spectrum was calculated. This effect should be stronger for broken clouds and/or high aerosol load. Using a current zenith sky reference lowers its influence, since reference and measurement spectrum are more probably recorded for the same situation. Practically $\sigma_{Ring4}(\lambda) = \sigma_{Ring}(\lambda)((\frac{\lambda}{\lambda_0})^4 - 1)$ is used within the DOAS fit to preserve the information given by the standard Ring spectrum at a specific wavelength λ_0 [Sihler et al., 2012]. Otherwise both spectra might compensate for each other due to their similar differential structures.
The contribution to the total measured intensity by multiple rotational Raman scattering is expected to be at total optical densities of several 10^{-4}, but since the rotational Raman cross-section effectively blurs the Fraunhofer structures of sunlight (see also figure 5.16), twice the application of Equation 5.3 will lead to an intensity spectrum which is dominated by a constant intensity offset. Constant intensity offsets are compensated for an additional polynomial in typical DOAS evaluation settings.

5.2.2. Vibrational Raman Scattering

Raman scattering causing vibrational transitions of N_2 and O_2 have been studied within the scope of Raman spectroscopy, but the influence of these effects on radiative transfer in the atmosphere, and thus their influence on remote-sensing of atmospheric trace gases, were considered to be negligible, compared to the strong influence of the Ring-effect and when retrieving absorbers with large optical densities. Haug [1996] calculated the cross-sections and estimated the overall effect on the measurements, but was not able to identify the effect in zenith-sky DOAS measurements at that time due to high residuals caused by leaving out significant parts of water vapour absorption and/or instrumental problems.
Coburn et al. [2011] argued that vibrational Raman scattering on N_2 and O_2 might be the reason for a limit in RMS in the lower 10^{-4} range despite co-adding of spectra when characterizing their MAX-DOAS instrument in a typical IO retrieval wavelength interval from 415–438 nm. Schönhardt et al. [2008, 2012] observed problems of the IO fit in situations with large Ring signals when including the IO absorption band above 430 nm (see figure 5.15). Measurements of IO in Antarctica using the MAX-DOAS technique [Frieß et al., 2010], which could not be confirmed by ground-based CE-DOAS measurements (unpublished, pers. comm. Udo Frieß, Johannes Zielcke) give further motivation to study the VRS effect for N_2 and O_2 again to estimate its influence on the retrieval of trace gases, especially IO and glyoxal.

5.2.2.1. Theory

The term *Vibrational Raman Scattering* denotes inelastic scattering processes which involve transitions between different vibrational energy states of the molecules. In contrast to Rotational Raman Scattering described in the context of the *Ring Effect*, these scattering events involve usually higher energy differences.

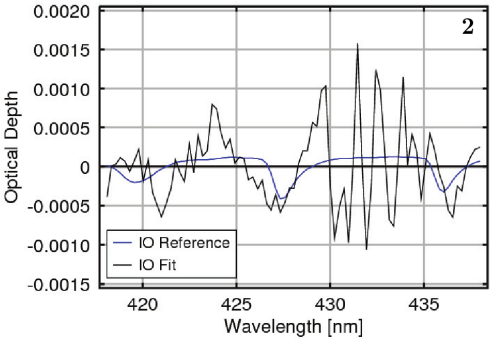

Figure 5.15.: Residual structures observed by Schönhardt [2009] indicate a problem with the Ring cross-section in the 430 nm region. She reported optical densities of the Ring effect of up to 10% for her measurements from SCIAMACHY. Therefore it was decided to limit the upper wavelength for the IO retrieval in Schönhardt et al. [2008] to 430 nm.

This leads effectively to a superposition of remapped sunlight spectra, e.g. shifted by 30-50 nm for scattering on O_2 and N_2 in the blue wavelength range as shown in figure 5.14. Light scattered on N_2 and O_2 molecules is eventually inelastically scattered shifted by 2330.7 and 1556.4 cm^{-1} respectively [Long and Curran, 2002] corresponding to a wavelength shift of the K-line at 393.37 nm of 39 and 25 nm and accordingly for the H-line at 396.85nm[3]. Additionally, changes in the rotational state of the molecule can occur, leading to similar Raman spectrum around the central vibrational Q-line as rotational Raman scattering. The ratio of these two effects was unclear in Haug [1996] and depends on molecular properties of N_2 and O_2, namely the isotropic a, a' and anisotropic γ, γ' components of their respective polarization tensor and their derivatives with respect to normalized nuclear coordinates. Inaba [1976] lists these values. The resulting 'differential optical density' caused by this inelastic scattering is estimated to be of the order of 5% (4%-14%) [Haug, 1996] of RRS, which would be around $\tau_{VRRS} = 1 \cdot 10^{-3}$.[4]
The cross-section for a scattering event $(\nu, J) \rightarrow (\nu', J')$ can be obtained by integrating over the full sphere [Schrötter and Klöckner, 1979]:

$$\sigma_{\nu,J\rightarrow\nu',J'} = \oint_{4\pi} \frac{d\sigma(\Theta)_{\nu,J\rightarrow\nu',J'}}{d\Omega} d\Omega \tag{5.4}$$

$$\frac{d\sigma(\Theta)_{\nu,J\rightarrow\nu',J'}}{d\Omega} = 8\pi^4 \frac{(\tilde{\nu}_{in} + \tilde{\nu}_{\nu,J\rightarrow\nu',J'})^4}{2J+1} \sum_{M,M'} \left\{ \sum_{ij} [\alpha_{ij}^2]_{(\nu,J,M\rightarrow\nu',J',M')} \cdot f_{ij}(\Theta)] \right\} \tag{5.5}$$

where $\tilde{\nu}_{in}$ and $\tilde{\nu}_{\nu,J\rightarrow\nu',J'}$ denote the wave number of the incident photons and the shift due to inelastic scattering (in wavenumbers). $f_{ij}(\Theta)$ the phase functions and the α_{ij}

[3] The rotational constant B is 2.01 cm^{-1} for N_2 and 1.45cm^{-1} for O_2 according to Hoskins [1975].
[4] The uncertainty from 4% to 14% comes from the fact that the partitioning of isotropic and anisotropic polarization tensor elements was unknown. Since the total cross-section of vibrational Raman scattering was known, this allowed to limit the values of a' and γ' for the two extreme cases in which one of the unknowns was zero.

Molecule	$g_j a^2$ cm^{-3}	$g_j \gamma^2$ cm^{-3}	$g_j a'^2$ cm^4/g	$g_j \gamma'^2$ cm^4/g
N_2	$3.20 \cdot 10^{-48}$	$0.90 \cdot 10^{-48}$	$0.45 \cdot 10^{-32} N_A$	$0.64 \cdot 10^{-32} N_A$
O_2	$2.66 \cdot 10^{-48}$	$1.40 \cdot 10^{-48}$	$0.27 \cdot 10^{-32} N_A$	$1.08 \cdot 10^{-32} N_A$

Table 5.2.: Averaged polarizability a, a' and anisotropy γ, γ' according to Inaba [1976]. The resulting differential cross-sections $d\sigma/d\Omega$ are listed in table 5.5.

	Transition	$\overline{[\alpha_{ii}^2]_{(\nu,J\to\nu',J')}}$	$\overline{[\alpha_{ij}^2]_{(\nu,J\to\nu',J')}}$
Cabannes	$\Delta\nu = 0, \Delta J = 0$	$a^2 + \frac{4}{45} b_{J\to J} \gamma^2$	$\frac{1}{15} b_{J\to J} \gamma^2$
RRS	$\Delta\nu = 0, \Delta J = \pm 2$	$\frac{4}{45} b_{J\to J\pm 2} \gamma^2$	$\frac{1}{15} b_{J\to J\pm 2} \gamma^2$
VRS	$\Delta\nu = 1, \Delta J = 0$	$(a'^2 + \frac{4}{45} b_{J\to J} \gamma'^2) \frac{h}{8c\pi^2\tilde{\nu}}$	$(\frac{1}{15} b_{J\to J} \gamma'^2) \frac{h}{8c\pi^2\tilde{\nu}}$
VRRS	$\Delta\nu = 1, \Delta J = \pm 2$	$(\frac{4}{45} b_{J\to J\pm 2} \gamma'^2) \frac{h}{8c\pi^2\tilde{\nu}}$	$(\frac{1}{15} b_{J\to J\pm 2} \gamma'^2) \frac{h}{8c\pi^2\tilde{\nu}}$

Table 5.3.: Spatial averaged polarisation tensor according to Long and Curran [2002]

the components of the polarisation tensor. Since the scattering molecules are oriented arbitrarily, these components can be averaged.

$$\overline{[\alpha_{ij}^2]_{(\nu,J\to\nu',J')}} = \frac{1}{2J+1} \sum_{M,M'} [\alpha_{ij}^2]_{(\nu,J,M\to\nu',J',M')} \tag{5.6}$$

The resulting averaged elements of the polarization tensor are listed in table 5.3. According to Haug [1996] the partitioning among a' and γ' is unknown. The partitioning of the vibrational Q and O,S-branches depends on them, whereas the Ring-effect is independent of them, see table 5.3.

$$b_{J\to J} = \frac{J(J+1)}{(2J-1)(2J+3)} \tag{5.7}$$

$$b_{J\to J+2} = \frac{3(J+1)(J+2)}{2(2J+1)(2J+3)} \tag{5.8}$$

$$b_{J\to J-2} = \frac{3J(J-1)}{2(2J+1)(2J-1)} \tag{5.9}$$

She [2001] reported that for LIDAR applications deviations in measured and modelled values for a and γ have been found to be of the order of 50%. This led them to take these parameters from measurements reported in Bridge and Buckingham [1966]. The resulting cross-sections are given in table 5.5. Inaba [1976] lists the values for a' and γ' for N_2 and O_2 respectively.
As shown in Haug [1996], the total cross section of the Q-branch of the vibrational transition can be calculated [Schrötter and Klöckner, 1979]:

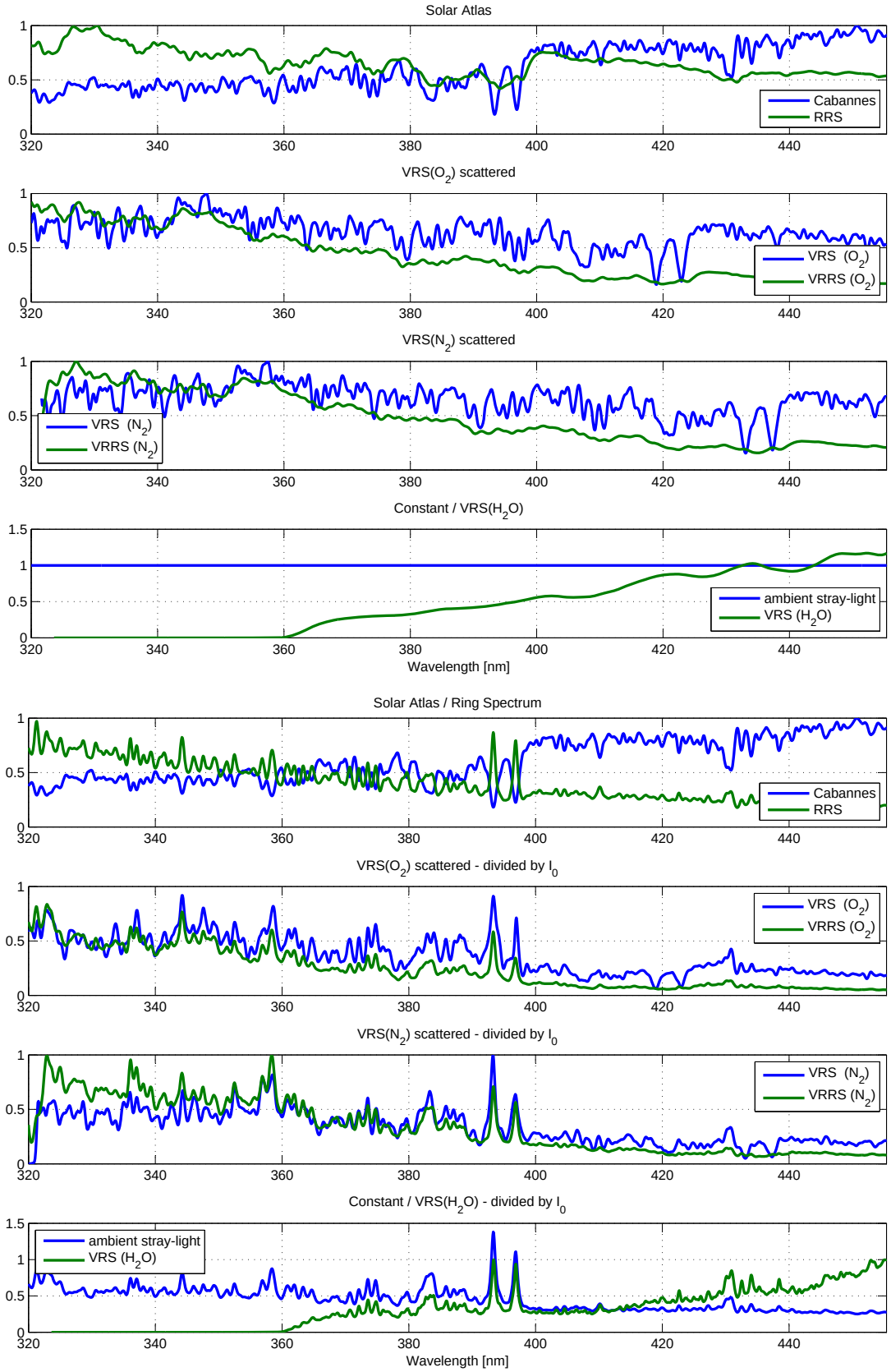

Figure 5.16.: Intensities (uppermost four plots) and apparent optical densities (below) for solar atlas, VRS(N_2), VRS(O_2) and the spectra corresponding to scattering involving rotational scattering processes, such as the rotational Raman scattering (Ring-effect) and vibrational-rotational transitions VRRS for N_2 and O_2. The fourth plot shows contribution of constant instrumental ambient stray-light and possible contribution from vibrational Raman scattering in liquid water. The spectra shown are convoluted to a resolution of 0.6 nm.

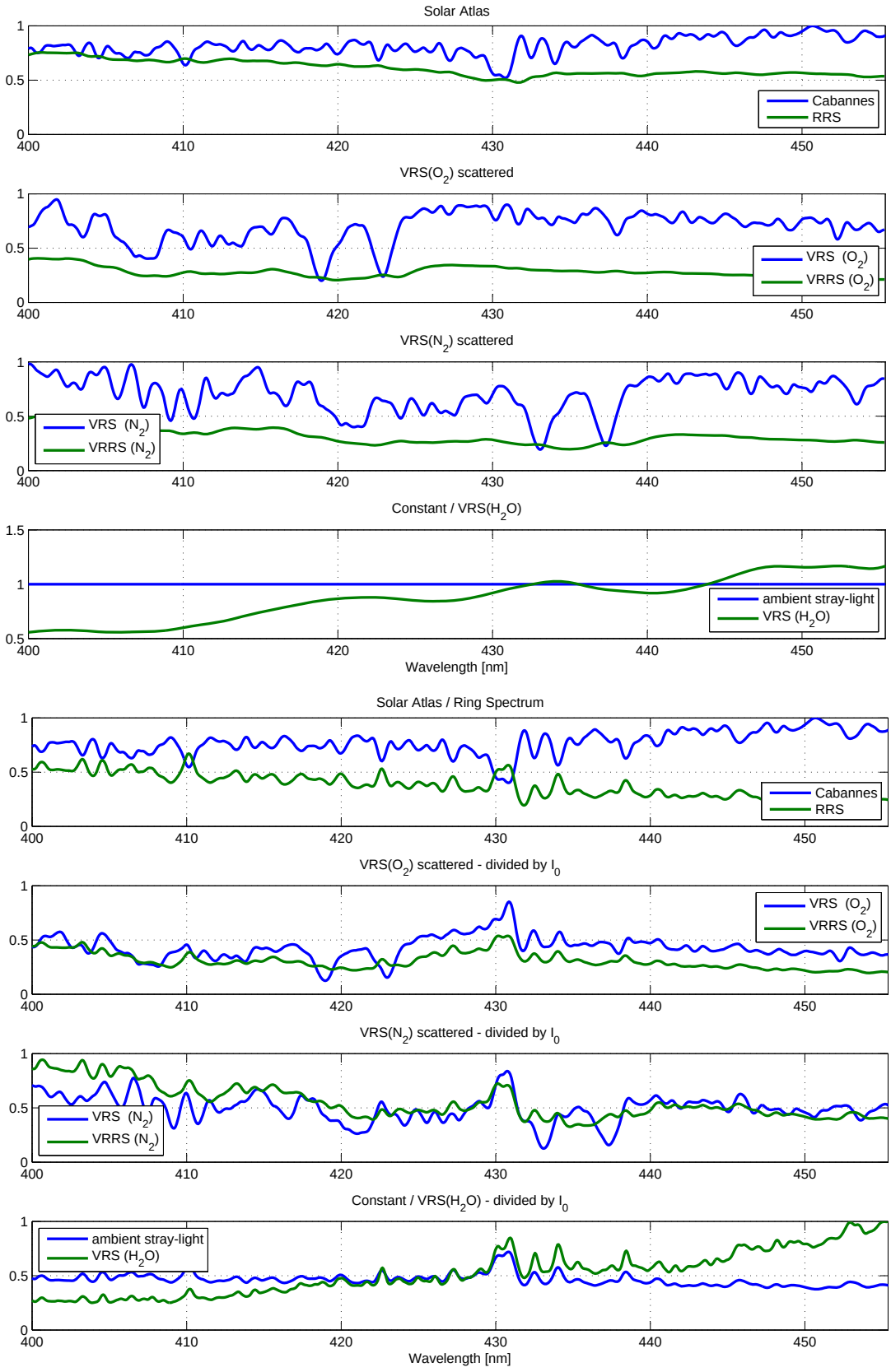

Figure 5.17.: The same plot as in figure 5.16, but limited to the spectral range from 400–455 nm. Here the main influence of VRS is expected, since the Ca-lines from 393.37 and 396.85 nm are shifted here.

$$\sigma^{Q,total} = \sum_{\nu,J} \sigma_{\nu,J\to\nu',J'} \cdot \frac{1}{Z} \cdot g_J \cdot (2J+1) \cdot e^{-E(\nu,J)/kT} \tag{5.10}$$

$$= \frac{128\pi^5(\tilde{\nu_{in}}+\tilde{\nu})^4}{9(1-e^{hc\tilde{\nu}/kT})} \left[3a'^2 + \frac{2}{3}\gamma'^2 \cdot S_{\Delta J=0}\right] \cdot \frac{h}{8c\pi^2\tilde{\nu}} \tag{5.11}$$

using

$$S_{\Delta J=0} = \sum_J \frac{1}{Z_{rot}} \cdot g_J \cdot (2J+1) \cdot b_{J,J+\Delta J} \cdot e^{-E_{rot}(J)/kT} \tag{5.12}$$

The important factor for DOAS applications in this calculation of the cross-section is the overall $\tilde{\nu}^4$ dependence. From averaging over all possible states and their population density for the given situation furthermore a factor $\frac{1}{1-\exp(-hc\tilde{\nu}/kT)}$ which originates from the Boltzmann distribution, is found in the final total cross-section. It can be neglected here, since it does not introduce differential structures as long as the retrieval wavelength interval is small (in terms of $h\Delta\tilde{\nu} \ll h\tilde{\nu}$ and temperatures $kT \ll h\Delta\tilde{\nu}$). Using the simple scaling by $\tilde{\nu}^4$ and shifting the spectra accordingly, vibrational Raman correction spectra can be calculated in first approximation without considering the respective phase functions.

Phase function The phase function is, similarly to the scattering of the Cabannes line and the rotational Raman scattering, different for scattering processes proportional to the polarizability a,a' and the anisotropy γ, γ'. This allows to separate the overall cross-section into two parts, one associated with $p(\Theta)^{VRS-iso}$ and one with $p(\Theta)^{VRS-aniso}$ based on table 5.3 and equation 5.5. For real measurements an effect of the different phase functions has not been observed, yet. Furthermore the anisotropic part causes about 15% of of the total VRS intensity, which is typically $4 \cdot 10^{-4}$ of the total intensity of scattered sunlight. The VRS-related intensity is therefore close to the RMS that can currently be achieved.

$$p(\Theta)^{VRS-iso} = \frac{3}{4}(1 + cos^2(\Theta)) \tag{5.13}$$

$$p(\Theta)^{RRS} = p(\Theta)^{VRS-aniso} = \frac{3}{40}(13 + cos^2(\Theta)) \tag{5.14}$$

Calculated N_2 VRS shifted spectra based on a solar atlas differed not more than 5% from those calculated based on measurement spectra. Given the overall optical density of $< 5 \cdot 10^{-4}$ shows that correction specta or Raman spectra can be calculated from a solar atlas without introducing too large errors. This might be also necessary due to the limited wavelength ranges of various instruments.
Vibrational Raman scattering processes with $\Delta\nu = -1$(Anti-Stokes) are very unlikely, because due to the Boltzmann distribution of states in air in equilibrium the energy states which could provide additional energy for the photon are only sparsely populated, (for 298 K, $E_{vib}/kT \approx 10$ for O_2 (and 11 for N_2)).

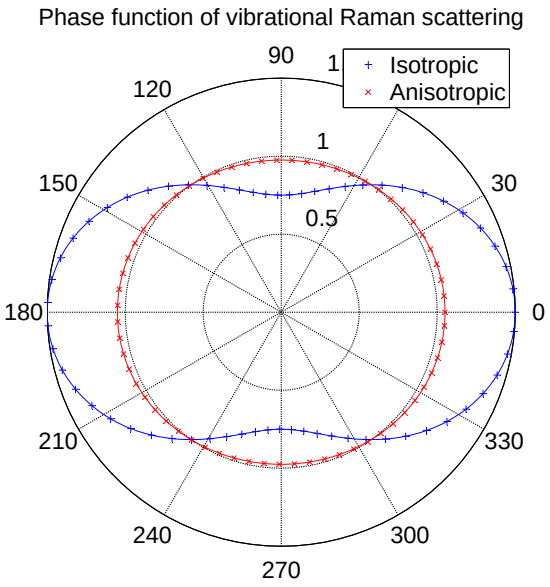

Figure 5.18.: Phase function $p(\Theta)$ of isotropic and anisotropic scattering events. This corresponds to the a,a' and γ, γ'-terms in table 5.3, respectively.

The resulting correction spectra for the spectral retrieval are shown in figure 5.16. The maximum (apparent) optical density attributed to VRS in air found during M91 was $5 \cdot 10^{-4}$.
The detection of VRS(N_2/O_2) for wavelength ranges including 430–440 nm, the interval where Fraunhofer ghosts of the Ca lines should be located at due to VRS(N_2/O_2), is discussed in subsection 5.2.3

Implications for other wavelength ranges The vibrational Raman scattering cross-section scales with $\nu^4 \propto 1/\lambda^4$, as the rotational Raman scattering cross-sections. But since the inelastic scattering processes shift photons towards longer wavelengths, the lower ≈ 23 nm of the solar spectrum will not be significantly affected. Furthermore, the variability in the spectral structure of the incident light is important, since otherwise an intensity similar to already compensated instrumental stray light will be created and might have been therefore already compensated. In spectral regions with strong and variable absorptions, such as O_3 from 300–340 nm, this absorption needs to be considered when calculating the VRS correction spectra. Therefore it can make sense to calculate the VRS correction spectrum from a measurement spectrum instead of using a solar atlas.
In the BrO wavelength range from 332–358 nm it was not possible to identify any structures related to the Ring effect, since other residual structures dominated. Nevertheless PCA allowed to identify a contribution in residual spectra from MAD-CAT possibly corresponding to VRS, leading to differential optical densities of up to $2-3 \cdot 10^{-4}$ (peak-to-peak) for large Ring signals of $5 \cdot 10^{25}$ molec cm^{-2}. The spectral structure could not be attributed to calculated VRS spectra, neither from a solar atlas nor from the measurement spectrum itself. The structure is correlated better with O_4 then with the Ring signal is discussed in subsection 5.1.1.2 and is twice as large for typical dSCDs as the

Transition	$d\sigma^{total}_{N_2}/d\Omega$ cm^2/sr	$d\sigma^{total}_{O_2}/d\Omega$ cm^2/sr	$d\sigma^{total}_{Air}/d\Omega$ cm^2/sr	Author
$\Delta\nu = 0, \Delta J = 0, \pm 2$ Rayleigh	-	-	$8.45 \cdot 10^{-28}$	BU
$\Delta\nu = 0, \Delta J = \pm 2$ O,S - branch	$1.64 \cdot 10^{-29}$ $\pm 8\%$	$4.26 \cdot 10^{-29}$ $\pm 5\%$	$2.16 \cdot 10^{-29}$ $\pm 10\%$	PE
$\Delta\nu = 1, \Delta J = 0$ Q - branch	$5.49 \cdot 10^{-31}$ $\pm 2\%$	$6.49 \cdot 10^{-31}$ $\pm 2\%$	$5.69 \cdot 10^{-31}$ $\pm 3\%$	SK
(aniso) $\Delta\nu = 1, \Delta J = 0, \pm 2$ $a'_{N_2} = a'_{O_2} = 0\text{cm}^4\text{g}^{-1}$	$2.20 \cdot 10^{-30}$ $\pm 3\%$	$2.60 \cdot 10^{-30}$ $\pm 3\%$	$2.28 \cdot 10^{-30}$ $\pm 4\%$	
(iso) $\Delta\nu = 1, \Delta J = 0, \pm 2$ $\gamma'_{N_2} = \gamma'_{O_2} = 0\text{cm}^4\text{g}^{-1}$	$5.49 \cdot 10^{-31}$ $\pm 2\%$	$6.49 \cdot 10^{-31}$ $\pm 2\%$	$5.69 \cdot 10^{-31}$ $\pm 3\%$	

Table 5.4.: Total differential cross-sections at 480 nm for forward scattering adapted from Haug [1996]. The last two lines show the two extreme cases in which either only isotropic scattering is observed and thus effectively only the Q-branch contributes or also rotational transitions contribute to the total cross-section. For 1013hPa and 20°C: $L = 1/\tau = 1/(N \cdot c \cdot 4\pi\sigma_{aniso}) \approx 15000km$) Abbreviations: BU:[Bussemer, 1993], PE [Penney et al., 1974], SK: [Schrötter and Klöckner, 1979]

optical density expected for VRS. Still, the correlation of the PCA transformed components of the residual with the Ring signal indicate that this effect is contributing with up to $2 - 3 \cdot 10^{-4}$ (peak-to-peak) in this spectral region to the observed residuals, but other contributions are still dominating. This size of the contribution of vibrational Raman scattering agrees with the theoretical values listed in table 5.5.
In general, the retrieval in the UV range shows higher RMS due to a limited amount of light. Evaluations are often already limited by photon statistics and more spectra need to be co-added to achieve sufficient RMS. This itself can create create residual structures due to varying absorption of stratospheric ozone.

5.2.2.2. Vibrational Raman Scattering in liquid water

Vibrational Raman Scattering also occurs within liquid water, but leads to other spectral structures, since liquid water has a different Raman spectrum. It has been measured and described in the context of DOAS measurements by Dinter [2005], Vountas et al. [2003, 2007]. Model calculations reported in Großmann et al. [2013] indicate that for measurements on the ocean at low elevation angles up to 10% of the simulated photons

Molecule $[10^{-31}(cm^2/sr)]$	Cabannes $d\sigma_C/d\Omega$	Rotational $d\sigma^{Rot}_{S+O}/d\Omega$	Vibrational $d\sigma^{Vib}_{Q}/d\Omega$	Rot.-Vib. $d\sigma^{Vib}_{S+O}/d\Omega$	Total Vib. $d\sigma^{Vib}_{sum}/d\Omega$
(393.37 nm)					
$\mathbf{N_2}$	20139	361	15.66	2.97	18.63
$\mathbf{O_2}$	16459	886	17.73	6.98	24.71
Air	19403	781	16.07	3.77	19.85
(532.0 nm)					
$\mathbf{N_2}$	6020	108	4.05	0.767	4.81
$\mathbf{O_2}$	4920	265	4.83	1.90	6.73
Air	5960	152	4.21	1.01	5.22
(relative)					
Air	100%	1.79 %	0.067 %	0.013 %	0.080 %
Air		100 %	2.77 %	0.66 %	3.43 %

Table 5.5.: Differential Raman backscattering cross-sections $d\sigma/d\Omega$ adapted from Inaba [1976] for the wavelengths of the incident light of 532 nm to be compared to table 5.4. It was scaled according to the $(\tilde{\nu} + \Delta\tilde{\nu})^4$ behaviour to 393.37 nm, the wavelength of the K Ca-Fraunhofer line.

have already been in contact with ocean water. This means, that the properties of liquid water have to be taken into account in such environments.
The theoretical basis for these scattering processes are calculations by Haltrin and Kattawar [1993] (Figure 5.20) resulting in an approximate Raman frequency distribution consisting of four Gaussian peaks around 3300cm^{-1} (In wavelengths: light from 400 nm is reemitted at 461 nm). Convoluting a high resolution solar spectrum with these peaks leads to a Raman spectrum which can be used as a correction in the spectral retrieval. Vountas et al. [2007] implemented this in the radiative transfer model SCIATRAN [Rozanov et al., 2005] to account for the according phase function correctly. The resulting correction spectrum still agrees reasonably well with simpler approximations such as simple convolution of a solar spectrum with the Raman shifts (see figure 5.19). Rizi et al. [2004] additionally reports a temperature dependence of the liquid water Raman spectrum.
The dominating structure in all four calculations shown in figure 5.19 is I/I_0, since the width of the Raman shift (figure 5.20) is almost 500cm^{-1} (10 nm at 440 nm), therefore resulting in a smooth additional intensity. Still, it follows the overall intensity of the incoming light and the increase of scattered sunlight intensity around 400 nm towards longer wavelengths will show up as an increasing additional intensity contribution around 460 nm.
For the VRS spectrum which was provided by T. Dinter and M. Vountas, the Raman spectrum obtained from SCIATRAN was calculated at a higher accuracy than usual DOAS spectrometers, and then divided by original intensity of the sun spectrum used. This procedure can introduce systematic deviations, since division and convolution do no commute. Using the Raman Frequency Distribution directly on a high resolution

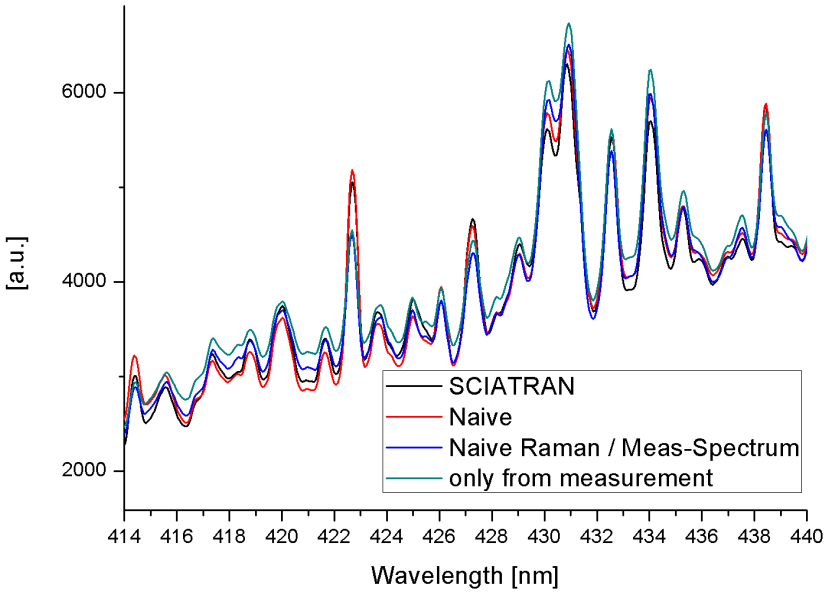

Figure 5.19.: Comparison of differently calculated liquid water VRS correction spectra. All spectra were scaled to the same size and broadband structures were removed by a polynomial. The SCIATRAN spectrum was provided in higher resolution by T. Dinter/IUP Bremen. The "'naive"' approach was based on the Chance and Kurucz [2010] solar atlas, for the second "'naive"' spectrum only the Raman spectrum was calculated based on the solar atlas and then divided by a measurement spectrum. The last version only based on the measured spectrum was possible, because the spectral range of the instrument reached to wavelengths lower than 50 nm of the spectral range shown here.

sun spectrum and dividing the calculated Raman spectrum by the Fraunhofer reference spectrum I_0 gives similar results. The deviations from each other are of the order of 10% and based on measurement data it was not possible to tell which spectrum compensates for this effect more accurately.

5.2.2.3. Vibrational Raman Scattering in water vapour

Also water vapour exhibits vibrational Raman transitions, located around 3654 cm^{-1} [Penney et al., 1974, Murphy, 1978] and with a cross-section of $8(\pm 20\%) \cdot 10^{-30}$ cm^2 sr^{-1} about 2.5 times as strong as the vibrational Raman scatter cross-section of the $\Delta\nu = 1$ transition of N_2 [Rizi et al., 2004]. This effectively leads to a wavelength shift of the Ca-Fraunhofer lines to about 460 nm, but shall usually not be observable in DOAS

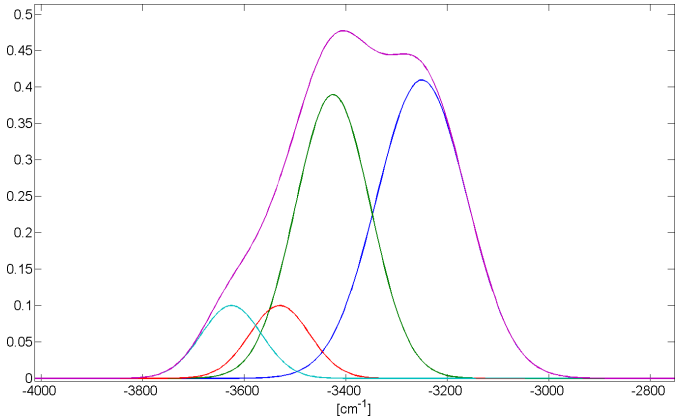

Figure 5.20.: Vibrational Raman shift of liquid water according to Haltrin and Kattawar [1993]. At a wavelength of 400 nm, this corresponds to a shift of 61 nm.

measurements since the expected optical density would be around $5 \cdot 10^{-6}$ due to the water vapour mixing ratio.

5.2.2.4. Raman Scattering in Ice

Raman scattering in ice leads to a shift of the incident wavelength of about 220, 900 and 3100–3400 cm^{-1} [Fukazawa and Mae, 2000], with a similarly broad distribution at 3100–3400 cm^{-1} as the Raman cross-section of liquid water [Shi et al., 2012]. At an incident wavelength of λ_0 =400 nm this leads to a shift of 3.5, 15 and 57–63 nm. Therefore differential spectral structures are not expected to be as strong as e.g. for N_2 and the intensities which are influenced are not within the usual retrieval interval range of IO at 445–455 nm. Most of the effect will be therefore compensated by the additional polynomial, since the light is scattered to a broad distribution of wavelengths. Apart from a possible contribution to Raman scattering of liquid water, the actual intensity and wavenumber shift of these scattering processes depends furthermore on the crystal lattice of the ice [Taylor and Whalley, 1964].

5.2.3. Detection of VRS of N_2 during M91

To test if the effect of vibrational Raman scattering can be actually detected in MAX-DOAS data, a N_2-Raman shifted sunlight spectrum has been calculated by shifting the intensities by 2330.7 cm^{-1}. The Raman spectrum calculated this way corresponds to a vibrational Raman transition $\Delta\nu = 1$ but $\Delta J = 0$, which might result in Fraunhofer ghost between 430–440 nm of the Calcium Fraunhofer lines (originally at 390–400 nm). Making the assumption that the rotational transitions are the same for vibrationally excited ($\nu = 1$) state, the usual Raman calculation of DOASIS based on Bussemer [1993] has been used to calculate the rotational Raman spectrum of the spectrum shifted according to $\Delta\nu = 1, \Delta J \neq 0$. Afterwards each of the Raman spectra was divided by the measurement spectrum according to Equation 3.8. The correction spectra for all transitions and N_2/O_2 were included in the fit.
The assumption that the rotational constant in independent of the vibrational quantum

number of the molecule is justified here, since the rotational constant B_ν of O_2 differs by 1.1% according to Krupenie [1972] for the two lowermost vibrational states.
The contribution to the measured optical density was estimated for each spectrum by multiplying the fitted optical density with I_0 to compare the overall intensities.
The M91 MAX-DOAS dataset covers a wavelength range from 330–460 nm and therefore allows for using a measured spectrum as basis for these calculations. This way also stratospheric absorbers which would not be accounted for if using a solar atlas only are accounted for, assuming a constant instrument function. The resulting optical density for correction spectra calculated from measured and modelled spectra were the same, though.
For the analysis spectra from 16 subsequent elevation sequences were co-added and a fit was performed subsequently. Co-adding of elevation sequences led to a significant reduction in RMS of the residual. Only fits with a RMS $< 1 \cdot 10^{-4}$ were selected for further analysis. The fit range was limited to 418–440 nm to keep the influence of water vapour absorption as small as possible but yet to include the most prominent features of the Raman spectra caused by O_2 at 419 and 423 nm and N_2 at 433 and 437 nm. Furthermore NO_2, IO, O_3, a Ring spectrum and a Ring spectrum scaled by $((\frac{\lambda}{\lambda_0})^4 - 1)$ were included in the fit, comparable to the usual IO fit settings. Pearson's R of the correlation of Ring spectrum and the optical density of the N_2-VRS correction was $R = 0.62$.
The phase function $p(\Theta)$ of vibrational scattering should broaden the correlation of the VRS signal and the Ring dSCD (see figure 5.18) since the phase function $p(\Theta)^{VRS-iso}$ is twice as large for the forward and backward direction than for $\Theta = 90°, 270°$. For vibrational-rotational scattering a linear relationship with the Ring signal is expected, but it is not observed within the noise of the measurements. Also strong aerosol absorption could modify the relation between VRS and Ring dSCD due to a change in colour-index (relative intensity) at the incident wavelength and the wavelength of the Fraunhofer ghost.
The spectrum obtained from calculating the rotational Raman scattering shifted by the vibrational energy difference ($\Delta\nu = 1, \Delta J \neq 0$) was not found in the spectral data.The problem with detecting these vibrational rotational Raman transitions is that their contribution are small and that their Raman spectrum itself is 'smooth' due to the rotational transitions around the ($\Delta\nu = 1, \Delta J = 0$) transition and therefore resembles other additive components of the spectra which are already compensated by the Ring spectrum ($\Delta\nu = 0, \Delta J \neq 0$), the stray light correction and sometimes VRS in liquid water. Still, including this correction spectrum also reduced the RMS, but since it could not be attributed to inelastic scattering, it might be as well compensating for other effects.
When comparing the observed optical densities with the theoretical derivation shown in Haug [1996], Haug lists two possible cases: The case that only an isotropic part can be observed in the scattered light, which means in turn that the rotational transitions vanish and only the pure vibrational transition can be observed. The other case is anisotropic scattering, which is in total a factor of four larger and combines both types. The signature of anisotropic vibrational Raman scattering was difficult to detect in the measured spectra, but the isotropic part was clearly detected. The ratio between the

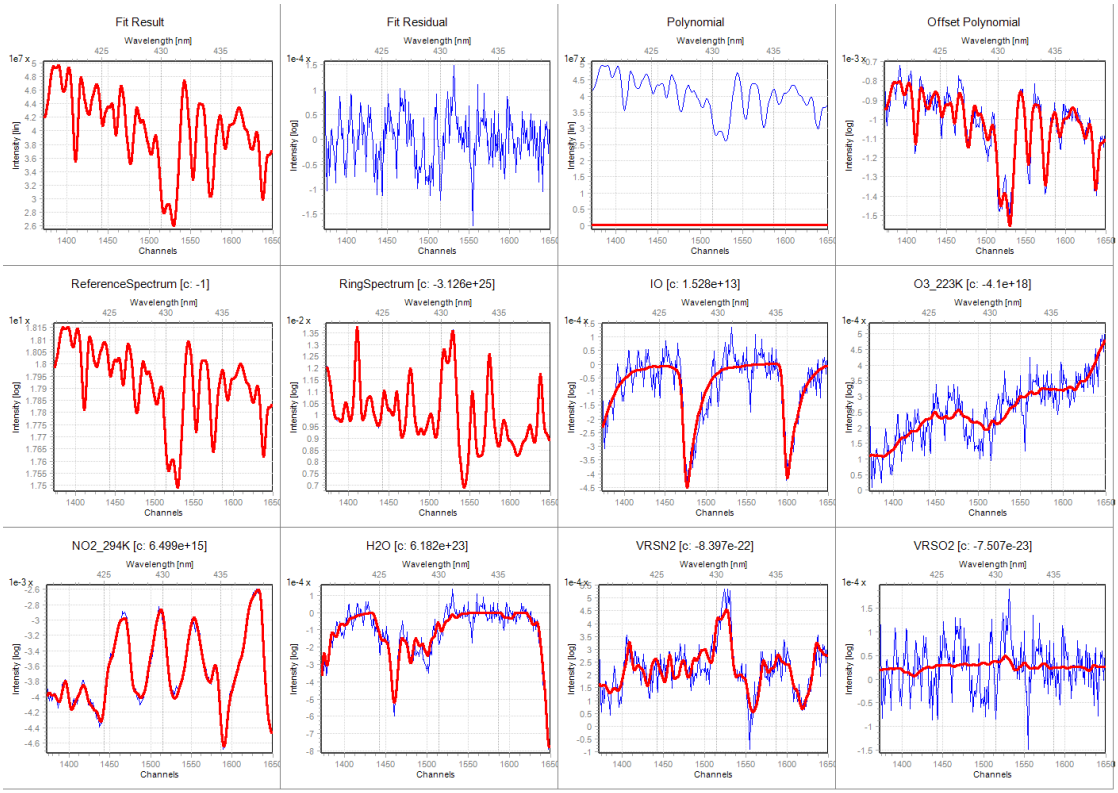

Figure 5.21.: A DOAS-fit showing the detection of structures from vibrational Raman scattering('VRSN2') on N_2 in MAX-DOAS data recorded during SOPRAN M91. The main peak at 430 nm originates from the reciprocal of a Fraunhofer structure at this wavelength from the Taylor expansion of the optical density. It vanishes when orthogonalizing the spectrum with the stray light compensation spectrum $1/I_0$, but can be also used to estimate the constant intensity added by vibrational Raman scattering. The two minima to at 432 and 436 nm are the red-shifted Calcium Fraunhofer lines. These structures appear with and without including the wavelength-scaled Ring spectrum and are correlated with the Ring spectrum dSCD shown in figure 5.22.

differential optical density of the VRS_{N2} ($\Delta J = 0$) versus RRS_{N2+O2} from figure 5.22 is $2 \pm 0.5\%$. Haug calculated a ratio of 3.6% for the case of isotropic scattering in N_2, therefore $0.6 \cdot 3.6\% = 2.2\%$ [5] in air, which agrees with She [2001]. Since we either cannot distinguish the anisotropic events from the Rotational Raman Scattering (RRS) or stray light compensation or isotropic scattering dominates, this agreement says, that the observed intensity of the VRS scattering ($\Delta\nu = 1, \Delta J = 0$) agrees with theoretical predictions made in Haug [1996].

[5] The cross-section for RRS for O_2 is 2.5 times larger than N_2

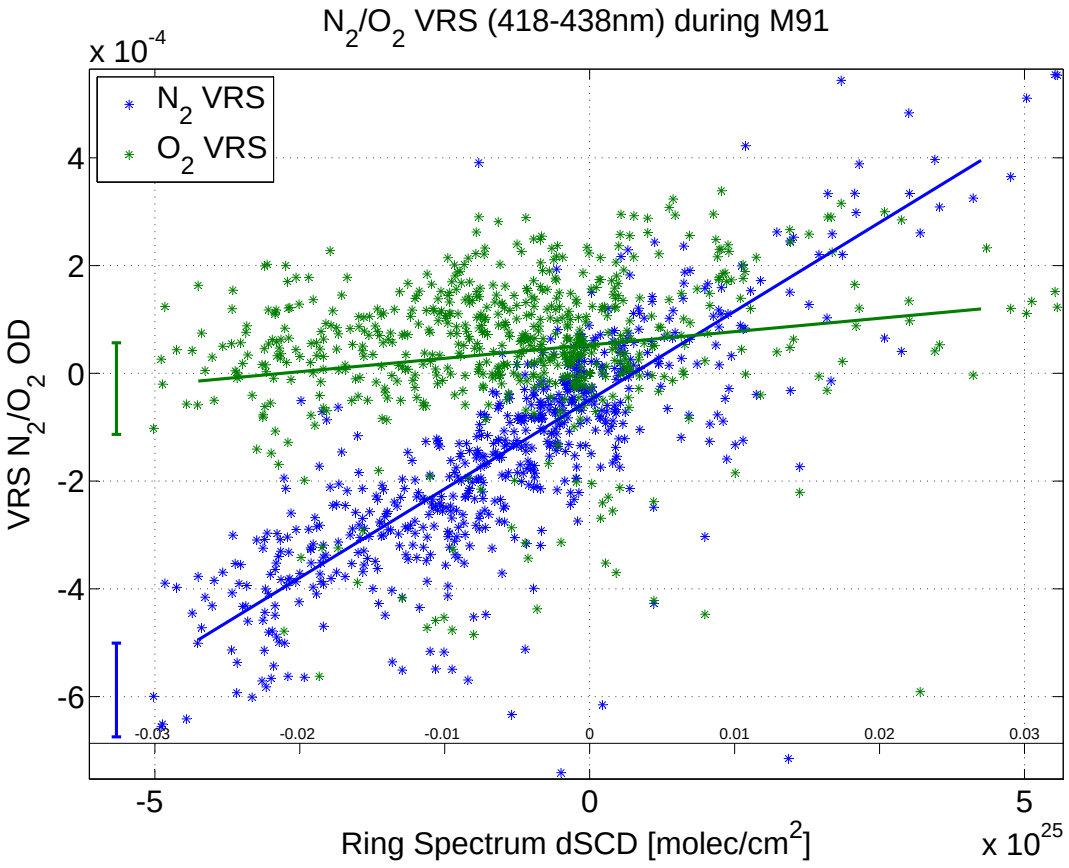

Figure 5.22.: Fit coefficients and optical density for Ring and optical density for the vibrational Raman correction spectrum for N_2 and O_2. Typically half of the contribution of vibrational Raman scattering on N_2 and O_2 can be compensated for by the additional offset polynomial, therefore here only the structures directly caused by the remapped Ca lines are shown. This compensation might also explain the offset for no inelastic scattering due to the Ring effect. Twice the mean DOAS fit errors is shown on the left as errorbars. The typical DOAS fit error of the Ring signal is $3 \cdot 10^{23}$ molec cm^{-2}. The small x-axis shows the total optical density of the Ring effect relative to the respective reference.

Since the $(\Delta\nu = 1, \Delta J \neq 0)$ transitions for $\Delta J < 4$ are within 0.45 nm of the $(\Delta\nu = 1, \Delta J = 0)$ transition they could also contribute to the optical density of the fitted $(\Delta\nu = 1, \Delta J = 0)$ transition, because they cannot be distinguished. The intensity caused by $(\Delta\nu = 1, \Delta J < 4)$ transitions is about 13% of the total rotational Raman scattered intensity for atmospheric conditions. Since the contribution of the total cross-section of the rotational vibrational transition is of the order of 20% of the purely vibrational transitions, it is beyond the precision of current measurements. Furthermore half of this

contribution is nevertheless compensated by the additional offset polynomial.
Correcting for the effect of VRS will reduce the total RMS of the fit residual for a large Ring signal and thus in most cases also the fit error (subsection 3.1.4). If the correction will have an impact on the retrieved column densities has to be tested for each trace gas and also for different spectral resolutions of the MAX-DOAS instruments, which can have an influence on the way in which the neglected apparent optical density was compensated for. The difference of the squares of the RMS χ of the evaluation with and without correcting for VRS is expected to have a linear relationship with the Ring column density, R:

$$\chi_1^2 - \chi_2^2 = a \cdot R^2 \tag{5.15}$$

This relation is found in MAX-DOAS data e.g. from M91, with $a = (0.25 \pm 0.05) \cdot 10^{-8}/(5 \cdot 10^{25}\text{molec cm}^{-2})^2$ for the IO fit interval, effectively reducing the RMS of a fit residual of $1 \cdot 10^{-4}$ by 15% for a Ring signal of $5 \cdot 10^{25}$ molec cm^{-2}.

5.2.3.1. Impact on IO dSCDs

To estimate the influence of having ignored the effect of VRS of N_2 before, the MAX-DOAS data from M91 was reanalysed for IO with and without VRS and Vibrational-rotational Raman Scattering (VRRS) (N_2) correction spectra and/or a spectrum compensating for the VRS in liquid water. Since this introduces another degree of freedom, the fit error can increase, even though structures in the residuum are compensated for. Using the spectra instead to correct the Ring spectrum is a possible alternative. Using an example spectrum with almost $2 \cdot 10^{-4}$ optical density caused by VRS, including the correction spectra decreased the fit error by 25%. Correcting the Ring spectrum directly according to the linear fit coefficient obtained from figure 5.22 results in a reduction of the fit error by 30%. Leaving the size of the correction independent of the Ring spectrum showed, that the IO dSCD in the wavelength range from 418–438 nm is independent of the amount of structures caused by VRS of N_2 up to $1 - 2 \cdot 10^{-4}$ as shown in figure 5.23. The same result was obtained from analysing data from ANT XXVIII (chapter 9) with an upper limit of IO dSCD change of $1 \cdot 10^{12}$ molec cm^{-2} / $1 \cdot 10^{-4}$ N_2 VRS. This data set was recorded at a spectral resolution of 0.9 nm instead of 0.45 nm.
The effect of the ($\Delta\nu = 1, \Delta J \neq 0$) transitions was not observed to be correlated to inelastic scattering, therefore its impact on IO dSCDs was not studied.

5.2.3.2. Impact on NO_2 dSCDs

When retrieving tropospheric NO_2 dSCD in the wavelength range also used for IO due to the relatively large absorption cross-section of NO_2 and the minimal influence of water vapour, often negative NO_2 dSCD are observed in clean and remote areas. Since this also frequently happens close to local noon, this excludes an effect of a changing AMF of stratospheric NO_2. Including the VRS correction spectra can lead to a reduction of the fit error by $\approx 15\%$ and furthermore the NO_2 dSCD changes by $4 \cdot 10^{14}$ molec cm^{-2} per 10^{-4} VRS(N_2) contribution This corresponds typically to 10-20 ppt NO_2. For background

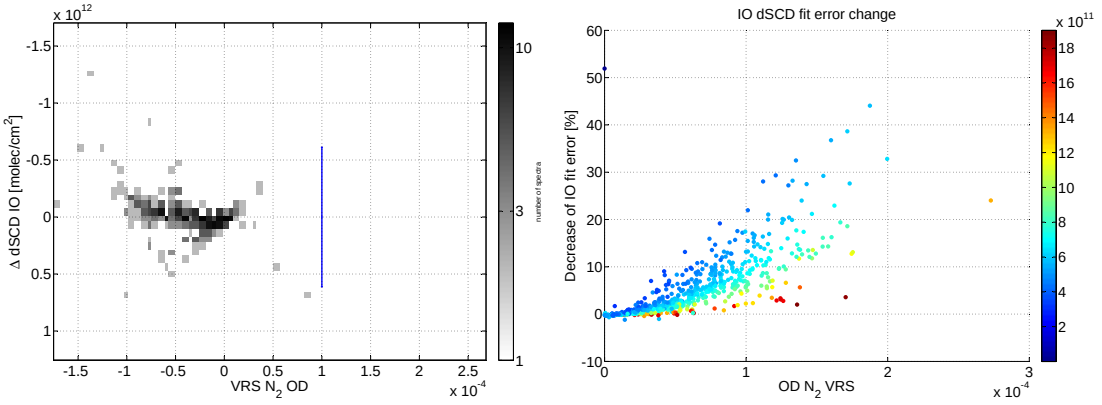

Figure 5.23.: Change of IO dSCD for M91 MAX-DOAS data when applying the correction spectrum for the N_2 VRS contribution. Compared to the typical fit error shown in blue no significant difference can be observed. The average decrease for all spectral retrievals shown here is $2 \cdot 10^{10}$ molec cm^{-2}. The fit error is reduced by up to 30% as shown on the right side. The absolute fit error is colour-coded. Typical absolute fit errors for IO (colour-coded) are $(6 \pm 3) \cdot 10^{11}$ molec cm^{-2} in this case.

measurements of NO_2 this difference can be significant, see figure 5.24 and measurement during M91: subsection 7.2.2.2. Usually a wider fit interval [e.g. Richter et al., 2011] or a fit interval above 450 nm [e.g. Peters et al., 2012] is used, which will then reduce the relative effect from VRS(N_2), but the instrument needs to cover this wavelength range and the stronger influence of water vapour absorption in this spectral range needs to be considered. The same analysis as figure 5.24 for a fit range from 432–460 nm leads only to a shift of the mean dSCD from $1.24 \cdot 10^{14}$ molec cm^{-2} without including VRS(N_2) correction spectra to a mean dSCD of $1.72 \cdot 10^{14}$ molec cm^{-2} when including the correction and is therefore within the typical fit error of $0.8 \cdot 10^{14}$ molec cm^{-2}. The IO fit range has the advantage of a large NO_2 absorption cross-section combined with only minimal absorptions of water vapour.

5.2.3.3. Impact on glyoxal dSCDs

To retrieve glyoxal, a fit window from 432 nm–460 nm was used, with and without including N_2-VRS. As described in section 5.4 also a correction spectrum for radiative transfer effects of water vapour absorption was included. Including a correction spectrum for N_2-VRS led to a reduction of fit RMS of 0-20%, the same amount as the glyoxal fit error was reduced. RRS Ring spectrum and N_2 VRS also correlated in this wavelength window, despite the large water vapour absorption. The glyoxal dSCD increased when including the N_2-VRS for strong Ring spectrum signals of around $-5 \cdot 10^{25}$ by up to $6 \cdot 10^{13}$ molec cm^{-2}.All other influences, such as water vapour and O_4 absorption, have a far stronger influence on the spectral retrieval of glyoxal (see subsection 5.6.4). In figure 5.40 an overview plot for glyoxal including VRS(N_2) correction is shown.

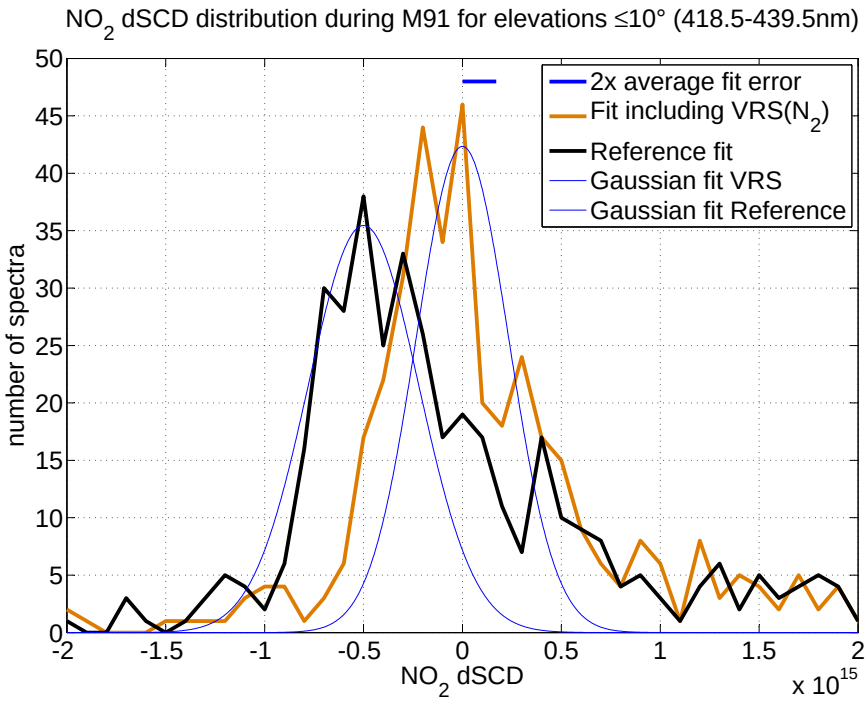

Figure 5.24.: Influence of including a VRS (N_2) correction spectrum in a fit from 418.5–439.5 nm using a current Fraunhofer reference.

5.2.3.4. Identification from residual spectra analysis

Figure 5.21 showing the correlation of the VRS correction spectrum for N_2 and O_2 also shows that their detection is close to the instrument's detection limit, despite co-adding already 16 elevation sequences. Adding more than 16 elevation sequences is typically not possible due to instabilities of the instrument and/or changing atmospheric conditions. Applying a linear fit averages the noise, but this only works if the scatter of the parameter is statistically distributed. The question remains, if e.g. the positive slope of the O_2-VRS signal is a coincidence or if it is real. To reduce the fit errors further, the detection of these effects from spectral data is favourable. The reduction of noise makes the identification of these spectra more reliable and trustworthy and might yield further possibilities to identify error sources.

Therefore the linear fit from figure 5.21 is not applied any more to a set of parameters from a fit of spectral data, but directly on a set of residual spectra. The resulting spectrum is used in a DOAS fit including all absorbers and the VRS correction spectra to obtain the final result.

As described in subsection 3.3.1, an overdetermined system of linear equations can be set up to identify spectral residual structures correlated to the dSCD of an absorber. If there is indeed an absorption structure which is not accounted for during fitting the optical density, this leads to errors in the fitted parameters. This means, that it will

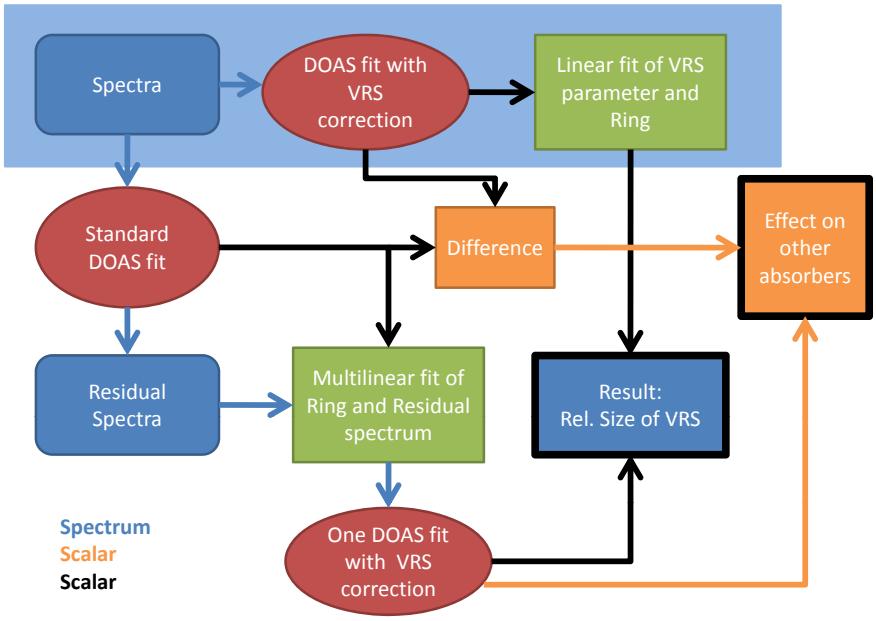

Figure 5.25.: The first line of this diagram shows the procedure which led to figure 5.21: The fit scenario is extended by the VRS correction, applied to all spectra and then the obtained fit coefficients are correlated with the Ring signal. The other possibility (subsection 5.2.3.4) uses a standard DOAS fit, correlates the residuals with the obtained coefficients from the fit and then uses this result to identify the the VRS correction spectrum and its coefficients in a final fit: Figure 5.26.

not only contribute to the residual spectrum. Therefore the solution of a linear system of equations will provide a correction spectrum $\vec{v}_i$ for each coefficient a_i, still with a potential influence of all other absorbers which have been included in the original fit scenario. On the other hand it is possible to distinguish between residual structures which have been introduced by different absorbers. Another advantage is that this approach allows to obtain an average over the residual structures associated with a certain absorber over the whole period of a campaign, e.g. a month or a year. This can reduce the influence of photon shot noise to a minimum. For a maximum Ring signal of $5 \cdot 10^{25}$ molec cm^{-2} the residual size from figure 5.26 is about $6 \cdot 10^{-5}$ peak-to-peak, which is significantly lower than the residual of usual, individual fits with current instruments. The complete M91 MAX-DOAS data set was fitted from 420–440 nm to avoid the main water vapour absorptions at 416 nm and 442 nm. The retrieval included a Ring Spectrum, NO_2, IO, O_3, a DOAS polynomial of 3rd degree and an additional offset polynomial of zeroth degree. All channels j from the residual spectra i were stored in a matrix R_{ij}. Only fits with a RMS of $< 4 \cdot 10^{-4}$ were used for the multilinear regression. Regressors were the dSCDs calculated by the first DOAS fit, the size of the intensity offset by the additional polynomial, exposure time and number of scans to test if dark current/offset

correction spectra might contribute to the residual.

$$\mathbf{C'} \cdot \mathbf{V} \quad = \quad (\overrightarrow{\mathrm{dSCD}_{Ring}}\ \overrightarrow{\mathrm{dSCD}_{H_2O}}...)' \cdot (\overrightarrow{v_{Ring}}\ \overrightarrow{v_{H_2O}}...) = \mathbf{R} \tag{5.16}$$

Here $\overrightarrow{\mathrm{dSCD}}$ and $\overrightarrow{v}$ are row vectors. Equation 5.16 was then solved for V using a least-squares approach. The resulting correction corresponding to the Ring dSCD was then fitted with the already included absorbers from the fit scenario and additionally the pseudo cross-section for vibrational and vibration-rotational Raman scattering of N_2 and O_2. This fit is shown in figure 5.26. Adding the other absorbers was necessary due to possible compensation of residual structures by other absorbers within the first fits to obtain the residuals. In other vectors corresponding to other absorbers or parameters the structure associated with N_2/O_2-VRS was not found.
The results from table 5.6 are in agreement with the predictions made in Haug [1996]. The isotropic case dominates, with a smaller contribution of rotation-vibrational transitions, if detectable at all in the DOAS measurements at current sizes of fit residuals.
The effective averaging over the whole phase function should lead to a value of the VRS cross-section which is below the value for backscattering by She [2001], if the observed scattering angles are equally distributed within a plane. Values from table 5.6 do not show this difference within their respective errors.
The example fit of the Ring-correlated residual structure shown in figure 5.26 yields more information than only the contribution of VRS to the observed OD: It also yields approximations for the changes of other involved trace gases in the respective spectral region, a factor with which the Ring signal can be multiplied to obtain the averaged effect on NO_2 e.g.: The fit yields a fit coefficient of $6.9 \cdot 10^{-12}$. For a maximum Ring signal of $5 \cdot 10^{25}$ molec cm^{-2} this results in a change of NO_2 dSCDs of $3.5 \cdot 10^{14}$ molec cm^{-2}, which agrees with the estimate from individual fits shown in figure 5.24.
The effective contribution to the measured intensity was estimated by using the Fraunhofer line at $\lambda = 430$nm: The intensity caused by each of the processes, RRS, VRS N_2 and VRS O_2 at this wavelength will create a maximum in the respective pseudo cross-section $I_{Raman_i}(\lambda)/I_0(\lambda)$, which then allows to estimate also constant intensity offsets due to these processes in the intensity space.

5.2.3.5. ARK XXVII

The complete dataset of ARK XXVII was also analysed to detect the signature of N_2 VRS scattering, using only the N_2 VRS cross-section. The correction spectrum for $(\Delta\nu = 1, \Delta J = 0)$ correlates with $R = 0.60$ with the Ring spectrum fit coefficient. On average the differential optical density is 2.5% of the differential Ring signal, shown in figure 5.27.
As for M91, the spectral structure associated with the spectrum obtained from calculating the rotational Raman scattering after having shifted the measured spectrum by the vibrational energy difference $(\Delta\nu = 1, \Delta J \neq 0)$ was not found in the spectral data, it did not correlate at all with the Ring spectrum or the N_2-VRS spectrum.

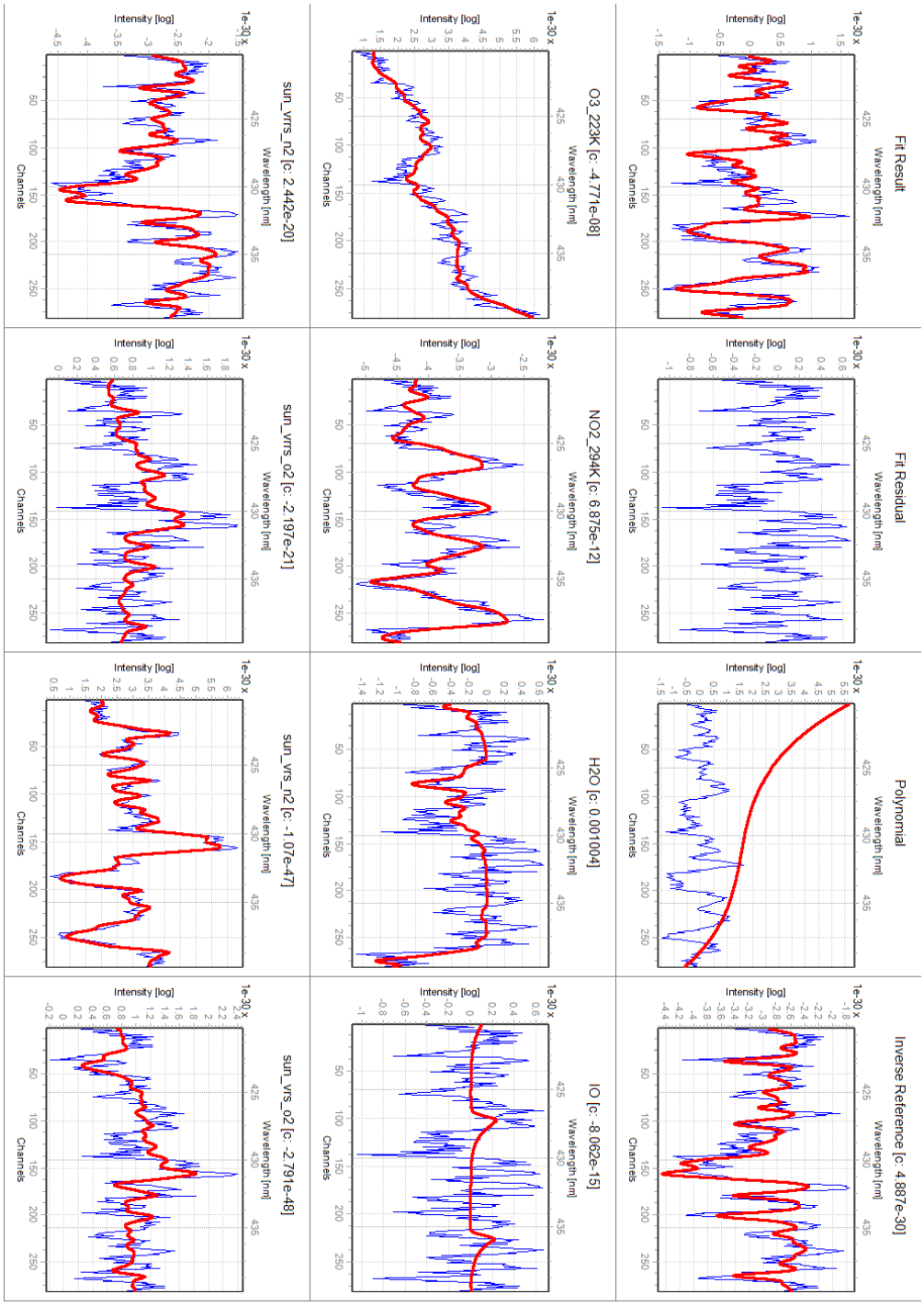

Figure 5.26.: Fit of Ring-signal-correlated residual structure. IO, H_2O, NO_2 and O_3 are from the original fits from which the residual spectra were used to solve the system of linear equations. The other spectra (sun_∗) are calculated from a solar atlas. The VRRS(N_2/O_2) components are not clearly significant here, since it is not distinguishable from the contribution of the inverse reference spectrum, which is usually necessary to compensate for instrumental straylight.

		Cross-section cm^2 (eff.)	%	direct corr. (Figure 5.22) %	Haug [1996] $\Theta = 0°$ %	She [2001] $\Theta = 180°$ %
(1)	RRS (393 nm)	$2.1 \cdot 10^{-28*}$	100	100	100	100
(2)	N_2 VRS	$4.5 \cdot 10^{-30}$	(2.2 ± 0.3)	(1.7 ± 0.5)	2.2(-3)	2.13
(3)	N_2 VRRS	-	-	-	0-6	0.40
(4)	O_2 VRS	$0.9 \cdot 10^{-30}$	(0.4 ± 0.3)	0.25 ± 0.6	0.6	0.63
(5)	O_2 VRRS	-	-	-	0-2	0.25

Table 5.6.: Values for different contributions to Raman scattered light at 430 nm measured during M91, derived from the solution of a system of linear equations and resulting in a fit shown in figure 5.26. The spectrum obtained from the linear system of equations had an 1σ-error of about 10%. The VRRS contributions were not significant. For comparison the relative size of the VRS derived from figure 5.22 is given. The data from She [2001] has been converted using an atmospheric mixing ratio of N_2:O_2 of 80:20. Note that this data was calculated for backscatter intensities, therefore not taking into account the complete phase function. *The cross-section for RRS scattering was calculated by DOASIS, based on Bussemer [1993].

Similar results for the ratio of Ring spectrum and VRS correction spectra were obtained for spectral data from ANT XXVIII and ANT XXIX (2012-2014).

5.2.3.6. MAD-CAT

Also during MAD-CAT the optical densities calculated for the VRS of N_2 have been observed. Due to high NO_2 concentrations and significant amounts of glyoxal absorption, the detection of VRS of N_2 was more difficult than for ARK XXVII and M91. To compensate the wavelength-dependency of the air mass factor of NO_2 it was necessary to include a wavelength-scaled NO_2 cross-section to compensate for radiative transfer effect (as e.g. for ozone absorption in Pukite et al. [2010]). After this modification, it was possible to detect the structures caused by VRS of N_2 molecules in the wavelength range from 416–440 nm as well as in the glyoxal evaluation range from 434–460 nm including the strong water vapour absorption at 442 nm. The correlation of Ring signal and VRS(N_2) signal was the same within error bounds for both evaluation wavelength ranges and agreed with the theoretical expectations and other campaigns.
An example for two fits with and without VRS correction is shown in figure 5.28 for data recorded in Mainz/Germany on 06/14/2013 at 14:46 UTC at a Solar Azimuth Angle (SAA) of 254° and a SZA of 47°. The telescope elevation was 3°. When it is not included (top), the residuum shows stronger structures. They can be partly removed by fitting the N_2 VRS pseudo cross-section (bottom). Remaining residual structures might be caused by strong NO_2 absorption. Here also a AMF-compensating cross-section for NO_2 had to be included in the fit scenario (NO2_294K_dL). Note that the size of the additional polynomial decreases as expected by almost 70%. The additional polynomial

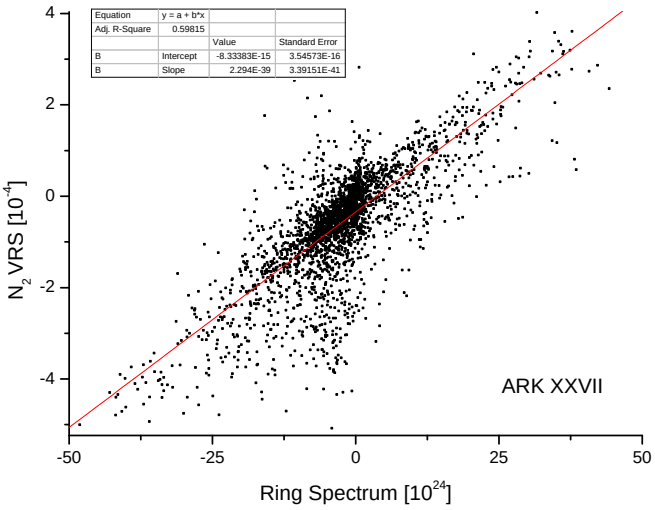

Figure 5.27.: Ring and N_2 VRS for ARK XXVII

had compensated the constant parts of the Raman correction spectrum of VRS(N_2/O_2). Including also separate spectra for VRRS(N_2/O_2) almost completely removes the contribution of the additive polynomial, but the fit becomes highly unstable and no clear relation between VRRS(N_2/O_2) and VRS(N_2/O_2) or the Ring is observed. Furthermore the change in the total residual size is below 10%. Therefore the combination of VRS and VRRS correction spectra for N_2/O_2 as suggested in subsection 5.2.4 seems reasonable.

5.2.4. Recommended retrieval settings to compensate for VRS in air

Correction spectra for VRS need to be included especially in the spectral retrievals of IO and glyoxal, but also water vapour in the blue spectral range, whenever wavelengths between 430–440 nm are included.

Since the atmospheric O_2/N_2 ratio is constant (at the precision relevant to correcting spectra for VRS contributions) and also their phase functions, it is advisable to include only one combined spectrum compensating for VRS contributions to measured intensities. The contribution by VRRS is mostly proportional to the VRS signal and can therefore be added to the VRS correction spectrum. On the other hand side the contribution of VRRS is relatively smooth due to the rotational shifts of the transitions and a large part is already compensated in fit settings by the additional polynomial.Given a Ring signal with an OD of 2% (maximally 10% for satellite measurement conditions and high albedo), this translates to an additionally measured intensity due to VRRS of $0.8 \cdot 10^{-4}$ ($4 \cdot 10^{-4}$). For the region between 414–440 nm where due to the Raman remapped Ca lines the largest variations are expected, the effect is already corrected by the additional polynomial except for a remaining part of 30-50%, which translates to total differential ODs of $< 0.4 \cdot 10^{-4}$ ($< 2 \cdot 10^{-4}$). This is currently negligible for most ground-based measurements, but this effect might need to be considered for geometries

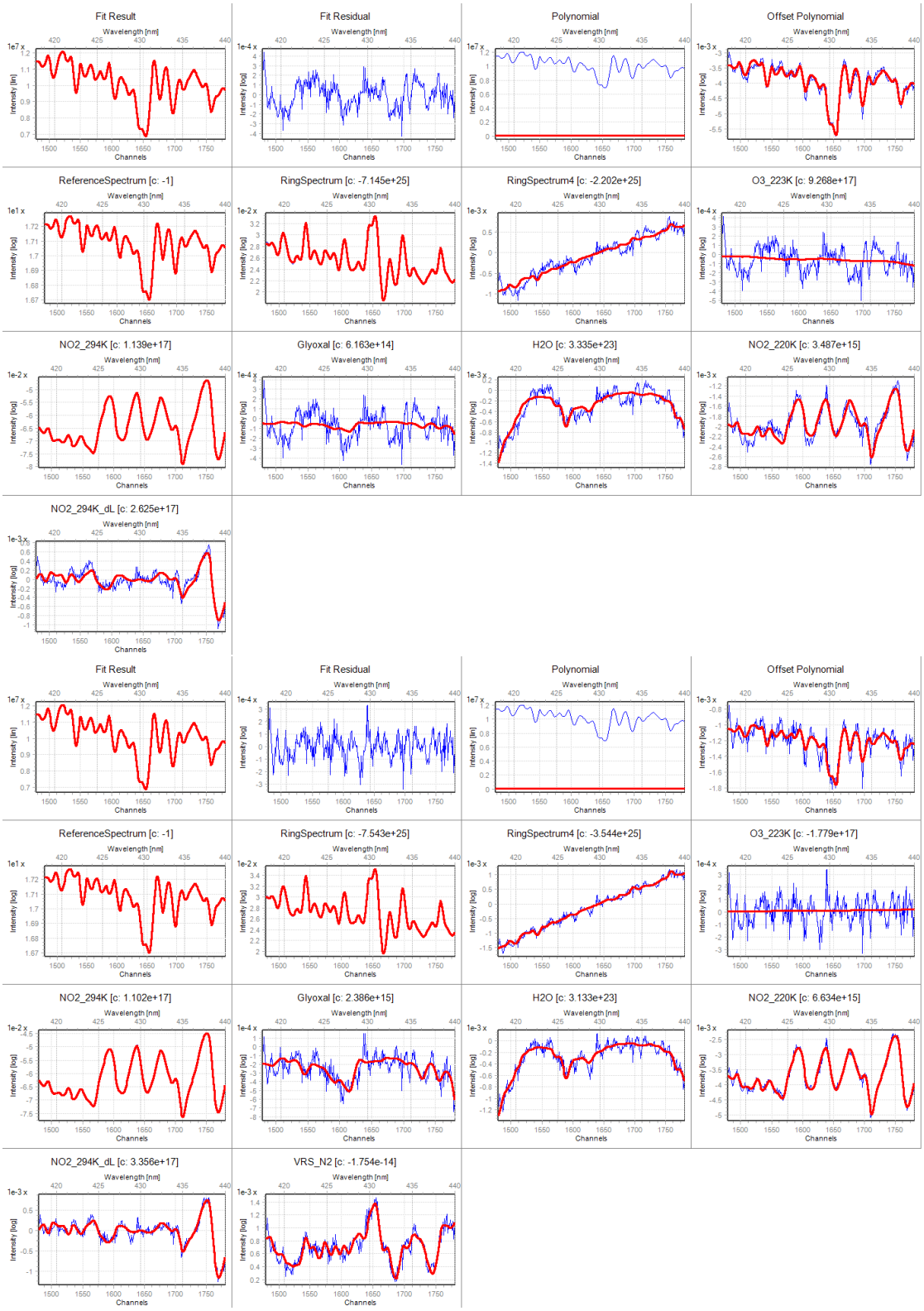

Figure 5.28.: Fit from MAD-CAT showing the detection of a N_2 VRS signature. A description is found in subsection 5.2.3.6.

where a strong filling in of Fraunhofer lines is observed[6].
Due to the observed correlation of the spectral signature of VRS scattering on N_2 and the Ring dSCD discussed in subsection 5.2.3, a direct correction of the Ring spectrum with the VRS signal seems reasonable, at least in the spectral ranges where an effect has been observed. The actual values of the cross-sections can be found in table 5.6. This allows furthermore to correct for VRRS scattering, which is also expected to behave in the same way as the Ring spectrum, but is often (by coincidence) corrected by the additional polynomial (see subsection 3.1.2), as estimated above. This correction of the Ring spectrum would therefore improve how the additional polynomial can be interpreted, which usually has been introduced in the first place to compensate for instrumental stray light. The contribution of the VRRS on O_2 and N_2 can then be removed from the additive polynomial, because the dominating factor for determining the Ring spectrum dSCD is the actual RRS contribution, which is about fifty times larger. A drawback is that the origin of the vibrational Raman scattering is shifted towards shorter wavelengths and thus can be influenced in a different way by aerosol extinction. For the case of rotational Raman scattering / the Ring effect, this is inherently compensated for, since the difference in wavelength due to the spectral dependence of the aerosol extinction is not significant. For the shift of 40 nm of N_2 VRS from the Ca Fraunhofer line at 393 nm, significant relative intensity differences at 393 nm/433 nm can be observed for different measurement geometries and/or aerosol loads. During MAD-CAT relative intensities at 390 nm and 432 nm, the so called colour-index $CI(390\,\text{nm}, 432\,\text{nm})$, were observed for zenith sky measurements between 0.3 and 0.8, even more if considering the complete elevation angle sequence. Therefore a direct correction of the Ring correction spectrum is not possible, if not considering these effects explicitly. The same argumentation can be applied for separating the influence of VRS(N_2) and VRS(O_2), since the wavelength shifts are different. However, the influence of VRS(O_2) is hardly detected in current measurement spectra. A potential dependence of VRS(N_2)-OD on the colour-index was not observed in measurement data, probably due to the scatter of the measured ODs.
A way to avoid this is to use a measured spectrum to include the effects due to changes in radiative transfer, such as aerosol and measurement geometry. When using measured spectra, this would require the same quantum efficiency of the instrument at both wavelengths or a radiometrically calibrated instrument, as well as a constant instrument function.
It is therefore recommended to include the correction spectrum for combined correction spectrum for VRS of N_2 and O_2 including the contribution from VRRS according to the values listed in table 5.6. If necessary, a scaling of the combined VRS/VRRS correction spectrum σ_{VRS} in analogy to the correction spectrum for the Ring effect $\sigma_{VRS4}(\lambda) = \sigma_{VRS}(\lambda)((\frac{\lambda}{\lambda_0})^4 - 1)$ is suggested to account for changes in colour-index, as mentioned above. This correction can be necessary for residual optical densities of significantly less than 10^{-4} peak-to-peak.
Another point which needs to be considered, but where no differences have been observed so far in measurement data, is that different contributions proportional to a,a' and γ, γ'

[6] All calculations for a spectral resolution of the instrument of 0.5 nm

in the cross-section correspond to different phase functions, thus Ring/VRS/VRRS do not need to be correlated exactly (for phase functions see section 5.2.2.1). This needs to be modelled in detail to estimate the error made when assuming the same phase function. Since this difference was not observed during one month of measurements shown in table 5.6, it is estimated to be below 20%. For a typical variation of the Ring dSCD of $3 \cdot 10^{25}$ molec cm^{-2} this error is found to be below $2 \cdot 10^{-5}$ peak-to-peak in the wavelength range between 430 - 440 nm, where the largest spectral structures were detected. This is five times smaller than the typical sizes of residual spectra of current MAX-DOAS instruments when summing spectra from several elevation sequences.

5.2.5. Significance of VRS in liquid water

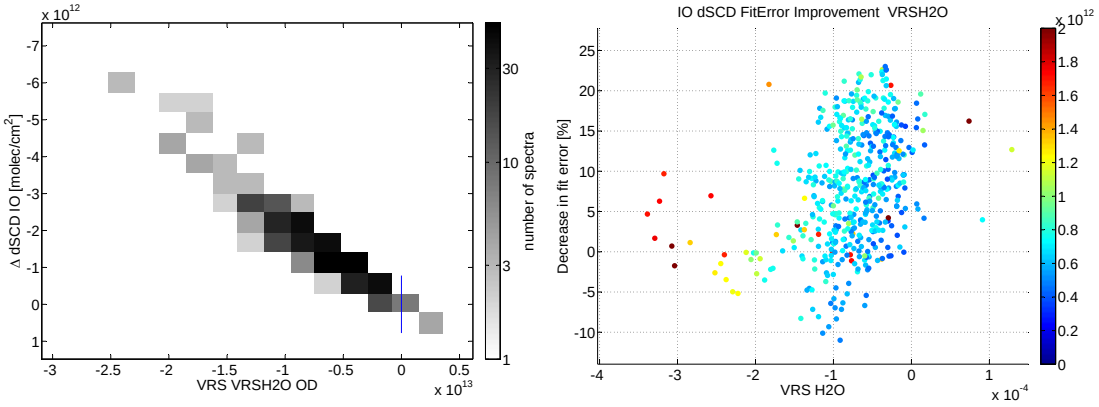

Figure 5.29.: Decrease of IO dSCD for M91 MAX-DOAS data when applying the correction spectrum for the liquid water VRS contribution. A clear increase with increasing VRS OD can be observed. The fit error is reduced by up to 20% as shown on the right side, even though no clear dependence on the fitted VRS OD can be observed. The absolute fit error is colour-coded there.

Großmann et al. [2013] argued that vibrational Raman scattering in liquid water reduces the RMS significantly while increasing IO dSCD, which led to the conclusion that this effects needs to be compensated and thus the liquid water VRS spectrum was included in the analysis (see also subsection 5.2.2.2). Furthermore radiative transfer modelling showed that about 10% of recorded photons for MAX-DOAS measurements on the ocean at low elevation angles had possibly been in contact with liquid water. For other geometries, i.e. looking downwards with a MAX-DOAS [Peters, 2013] or from a satellite [Vountas et al., 2007], VRS was also identified by correlation of liquid water column density and VRS signal.
For the M91 MAX-DOAS data set the impact on the additional VRS(H_2O) spectrum on the residuals' RMS, fit error and IO dSCD were analysed in he same way the impact of VRS(N_2/O_2) was analysed. The correction for N_2 VRS was included: Also a slight increase in IO dSCD was observed, together with a decrease in RMS and fit error. The

RMS of the residual spectra decreased by up to 15% and a clear dependence on the fitted VRS optical depth is observed. For the fit error, an overall decrease can be observed, but no correlation with the VRS optical depth is found (compare figure 5.29). The decision if this effect is real and significant cannot be decided based on this set of measurement data, but spectra recorded looking downwards into clear ocean water during Transbrom [Peters, 2013] and in a swimming pool [Vountas et al., 2003] show that this effect can have a significant influence on trace gas retrievals. Correlations of optical densities for VRS(H_2O) with those of liquid water in the wavelength range were not possible either due to too small differential absorptions by liquid water or instrumental limitations.
Thus there is no clear indication that the VRS(H_2O) spectrum needs to be included for spectra recorded at positive telescope elevations. The fact that it was improving the spectral retrieval in Großmann et al. [2013] might be due to the fact that the influence of VRS(N_2) was not included. A significant effect on the spectral retrieval of glyoxal was not observed for MAX-DOAS data from M91 (compare figure 5.40).

5.3. Water vapour absorption cross-sections

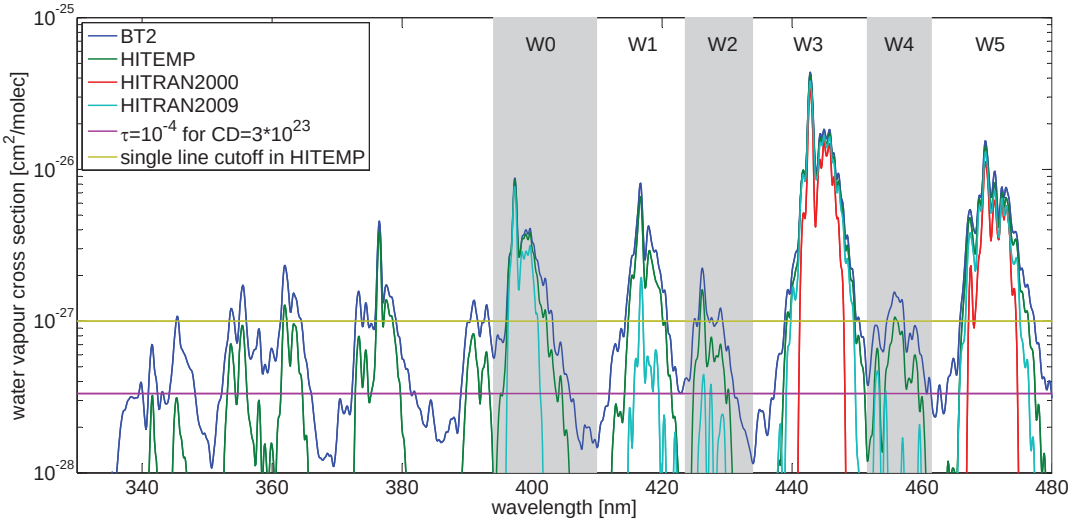

Figure 5.30.: Comparison of different water vapour cross-sections convoluted at 0.5 nm resolution.

For the water vapour cross-section a series of cross-sections exist, predominantly the HITRAN [Rothman et al., 2013] and HITEMP [Rothman et al., 2010] databases [7], but also databases by JPL [Pickett et al., 1998] (infrared and beyond), GEISA [Jacquinet-Husson et al., 2011] and EXOMOL [Hill et al., 2013]. Initially the HITRAN database only included absorption lines which are, as seen by the authors, of relevance for atmospheric measurements. That means only lines with optical densities of > 0.1 for standard atmospheric conditions with a tangent viewing geometry are considered. Still, theoretical calculations such as the BT2 line list [Barber et al., 2006] show, that there are more absorption lines for water vapour. These absorptions are important if the temperatures are higher, since the molecules' probability for higher excited states are significantly higher, but they can also play a role in atmospheric measurements as shown below. The database HITEMP combines the BT2 line list and the HITRAN database to assure that the experimentally proven absorption lines and line-mixing effects included within HITRAN also are considered in HITEMP. Details on the exact selection process for HITEMP can be found in Rothman et al. [2010]. Still, HITEMP and HITRAN2012 are processed with a single line cut-off of $1 \cdot 10^{-27}\mathrm{cm}^2$ molec^{-1}, which can be in some cases significantly above the accuracy archived by current DOAS setups. Tennyson et al. [2013] contains lists of experimentally observed lines and a comparison to current models. The H_2O cross-sections were calculated using modelled line width according to Kuntz [1997] from the respective HITRAN line list by Rothman et al. [2013] using an extraction program by Christian Frankenberg. For the BT2 line list, the BT2 database for

[7] http://www.cfa.harvard.edu/hitran/

Cross-section for initial OD	IO	Glyoxal
HITRAN 2000	$8.8 \cdot 10^{12}$ molec cm^{-2}	$4.8 \cdot 10^{14}$ molec cm^{-2}
HITRAN 2004	$6.6 \cdot 10^{12}$ molec cm^{-2}	$6.5 \cdot 10^{13}$ molec cm^{-2}
HITRAN 2009	$6.6 \cdot 10^{12}$ molec cm^{-2}	$3.0 \cdot 10^{13}$ molec cm^{-2}
HITRAN 2012	$2.2 \cdot 10^{12}$ molec cm^{-2}	$1.5 \cdot 10^{13}$ molec cm^{-2}
HITEMP	$2.2 \cdot 10^{12}$ molec cm^{-2}	$1.9 \cdot 10^{13}$ molec cm^{-2}
HITEMP with I_0	$0 \cdot 10^{12}$ molec cm^{-2}	$0 \cdot 10^{13}$ molec cm^{-2}
BT2	$3.3 \cdot 10^{12}$ molec cm^{-2}	$-1 \cdot 10^{14}$ molec cm^{-2}

Table 5.7.: Using the 418–439 nm for IO and 434–458 nm for glyoxal to compare the effect of the differences in water vapour cross-sections and their effect on retrievals. Here the HITEMP cross-section is assumed to be correct (without I_0 and saturation correction) , an optical density corresponding to $3 \cdot 10^{23}$molec cm^{-2} water vapour using the cross-section indicated on the left is fitted, including all absorbers from the standard fit scenarios, adding noise with a standard deviation of 10^{-4}. A detailed comparison of the different absorption bands of different water vapour cross-sections is shown in table 5.11. For a comparison of water vapour cross-section close to the main glyoxal absorption, see figure 5.35.

wavenumbers from 20000–30000 cm^{-1} has been converted into a line list in HITRAN2004 format using a python script provided by Christian Hill (christian.hill@ucl.ac.uk) [Hill et al., 2013], this data is also provided on exomol.com http://www.exomol.com. A major difference for MAX-DOAS measurements (or in general measurements with a structured light source) is that this conversion does not include line broadening parameters which would be needed for I_0 and saturation correction. A detailed description of how the broadening parameters have been included in HITEMP can be found in Rothman et al. [2010], but has not yet been performed for the complete BT2 line list.
For spectral retrievals in the blue wavelength range already different HITRAN versions show significant differences.

5.3.1. Relative line strength

A significant difference in the different water vapour cross-sections is the absorption line around 416 nm, which is almost of twice the size as it was until HITRAN 2009. This feature can be seen in HITEMP, HITRAN and BT2 as well, but the question is if one can show that this change is indeed physically correct, or not. Some parts of HITRAN / HITEMP are based on experimental observations, others on theoretical calculations. A summary of various experimental data on water vapour cross-section can be found in Tennyson et al. [2013], which shows that experimental data in the blue and upper UV range is seldom.
An approach to estimate the correctness of the strength of different absorbtion bands is to create retrieval interval maps according to Vogel et al. [2013] or only take a diagonal

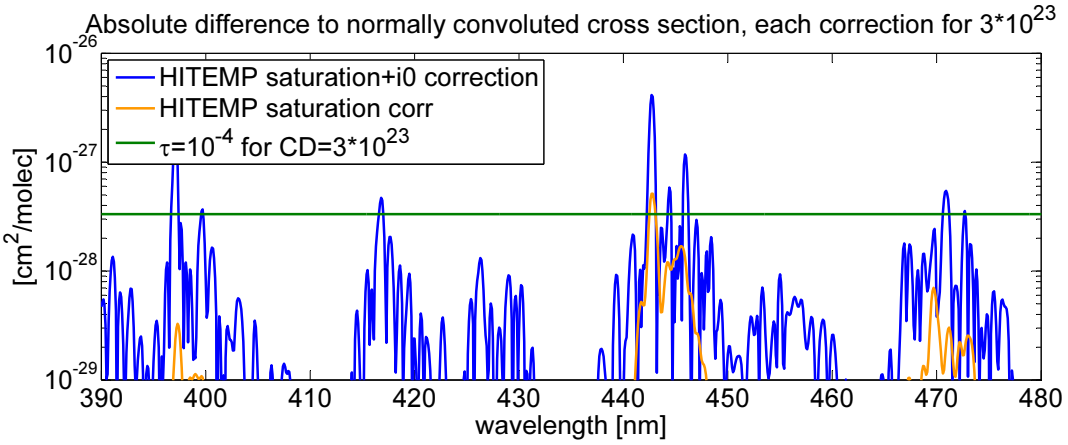

Figure 5.31.: Estimation of the effect of the saturation effect (due to convolution) and I_0-effect. Data is shown for a column density of $3 \cdot 10^{23} molec\, cm^{-2}$

of them, i.e. a fit window with fixed width, but changing starting wavelength. This approach might be prone to cross correlations of the different absorbers which need to be taken into account and might not be obtained in a sufficient precision, which might then in turn affect the calculated water vapour dSCD. An alternative, which allows for an overall bigger retrieval wavelength range, is to cut the water vapour absorption into intervals and compare the column densities obtained for the different absorption bands. Due to the bigger retrieval window this minimizes correlations with other absorber, since they are retrieved more accurately. For data measured during M91 and LP-DOAS data from Cape Verde this approach has been performed using the HITRAN2009, HITEMP and BT2 line lists, see figure 5.30 and Lampel et al. [2013][8].
From table 5.9 it can be seen that the shape of the absorption lines is reproduced better by HITEMP and BT2 than by HITRAN2009 which results in smaller fit errors, but their relative strength seem to differ up to a factor of 2 during the MAX-DOAS measurements of M91 as seen in table 5.8. The reason is so far unknown, but shows either the need to fit water vapour absorption bands separately or restrict retrieval wavelength ranges to single absorption bands. The latter might be a good option for the spectral retrieval of glyoxal.

5.3.1.1. Radiative transfer effects

The lightpath of the LP-DOAS measurement is well defined and constant, but might be often shorter than the effective lightpath of MAX-DOAS measurements. But the effective lightpath of MAX-DOAS measurements depends on several factors: aerosol and trace gas profiles, viewing direction, sun position etc. Furthermore it is wavelength-dependent

[8]Most of the data concerning water vapour absorption band strengths presented here is adapted from Lampel et al. [2013]

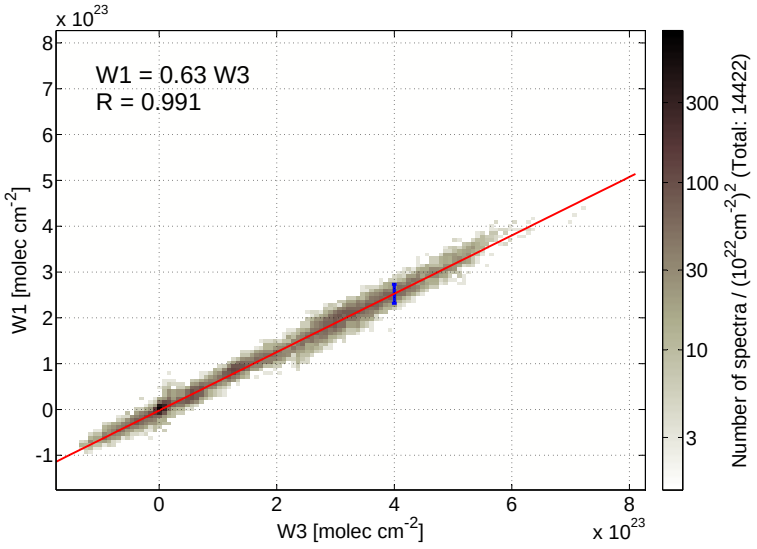

Figure 5.32.: Correlation of dSCDs for W1 (410–423.5 nm) and W3 (434–451.5 nm) using the HITEMP cross-section. A linear behaviour can be observed, as expected due to small optical densities, suggesting a constant correction factor of 0.63 for the W1 absorption relative to W3. The blue error bar indicates a typical measurement error.

Polyad		8ν	$7\nu + \delta$		7ν		$6\nu + \delta$
Name		W0	W1	W2	**W3**	W4	W5
Start of interval	[nm]	394.0	410.0	423.5	**434.0**	451.5	461.5
End of interval	[nm]	410.0	423.5	434.0	**451.5**	461.5	480.0
Cross-section	Campaign						
HITRAN 2009	M91	1.05 ± 0.03	2.04 ± 0.06	1.98 ± 0.27	**1**	0.71 ± 0.24	
	CVAO	1.01 ± 0.04	(1.13 ± 0.09)	(1.30 ± 0.23)	**1**	(0.28 ± 0.70)	1.00 ± 0.04
	ANT28				1		
HITEMP	M91	1.00 ± 0.03	0.63 ± 0.02	0.74 ± 0.10	**1**	0.66 ± 0.12	-
	CVAO	1.13 ± 0.04	0.50 ± 0.03	(0.93 ± 0.13)	**1**	(1.67 ± 0.33)	1.00 ± 0.04
	ANT28				1		
HITEMP (with glyoxal)	M91	1.00 ± 0.03	0.63 ± 0.02	0.69 ± 0.10	**1**	0.63 ± 0.11	-
	CVAO				**1**		
	ANT28				**1**		
BT2	M91	1.05 ± 0.04	0.53 ± 0.02	0.51 ± 0.09	**1**	0.85 ± 0.11	-
	CVAO	1.13 ± 0.04	0.46 ± 0.03	0.87 ± 0.11	**1**	(1.23 ± 0.24)	1.00 ± 0.04
	ANT28	0.85 ± 0.20	0.44 ± 0.05	0.48 ± 0.25	**1**	0.68 ± 0.20	1.20 ± 0.06

Table 5.8.: Relative line strengths for the different cross-sections with respect to the absorption at W3. Errors are RMS of the linear fit divided by maximum variation in dSCD(W3). Results with typical fit errors of more than 20% of the measured values were put in brackets. (adapted from Lampel et al. [2013])

due to the wavelength dependence of the scattering processes involved.

Using McArtim Deutschmann [2014] water vapour dSCD in the atmosphere were simu-

$[1 \cdot 10^{21}$ molec cm$^{-2}]$		W0	W1	W2	**W3**	W4	W5
Start of interval	[nm]	394.0	410.0	423.5	**434.0**	451.5	461.5
End of interval	[nm]	410.0	423.5	434.0	**451.5**	461.5	480.0
Cross-section	Campaign						
HITRAN 2009	M91	11	45	153	**2.7**	160	
	CVAO	19	79	235	**4**	348	14
	ANT28						
HITEMP	M91	10	11	45	**2.5**	65	-
	CVAO	20	27	107	**3.7**	192	13
	ANT28						
BT2	M91	10	9.5	32	**2.6**	51	-
	CVAO	12	14	54	**2.1**	90	7.4
	ANT28	15	10	30	**2**	30	8

Table 5.9.: Typical fit errors at a dSCD in W3 of $4 \cdot 10^{23}$ molec cm^{-2} for a single spectrum integrated over 60s(M91), 120s(ANT28) and 60s (CVAO). A dSCD of $2.3 \cdot 10^{21}$ molec cm^{-2} corresponds to an optical density of $1 \cdot 10^{-4}$. (adapted from Lampel et al. [2013])

lated at different wavelengths to estimate the effect of radiative transfer on the relative observed absorption band strengths for MAX-DOAS measurements. Since the data is taken from a measurement period of a whole month, a representative water vapour and aerosol profile with an AOD of 0.22 were used for the simulations. The resulting water vapour dSCD then agreed with the measurements and the wavelength dependence was calculated. The scatter in the correlations for the water absorption bands will then already include the scatter caused by different measuring conditions such as different aerosol profiles etc., which means that the observed differences in relative strengths of the absorptions especially for W1 and W2 are significant, despite the correction factors obtained from these calculations.

		W0	W1	W2	**W3**	W4	W5
Wavelength	[nm]	400	416	424	**442**	455	460
McArtim		0.80	0.90	0.91	**1.00**	1.05	1.12

Table 5.10.: Corrections according to radiative transfer modelling for the MAX-DOAS measurements.

The change of air mass factor within a water vapour absorption band in the region < 480 nm due to water vapour absorption is discussed in subsection 3.2.4.1.

5.3.2. Absolute absorption band strength

To test if the absorption cross-section is also correct with regard to its overall absorption strength, the main absorption W3 found in LP-DOAS data from the HaloCaVe cam-

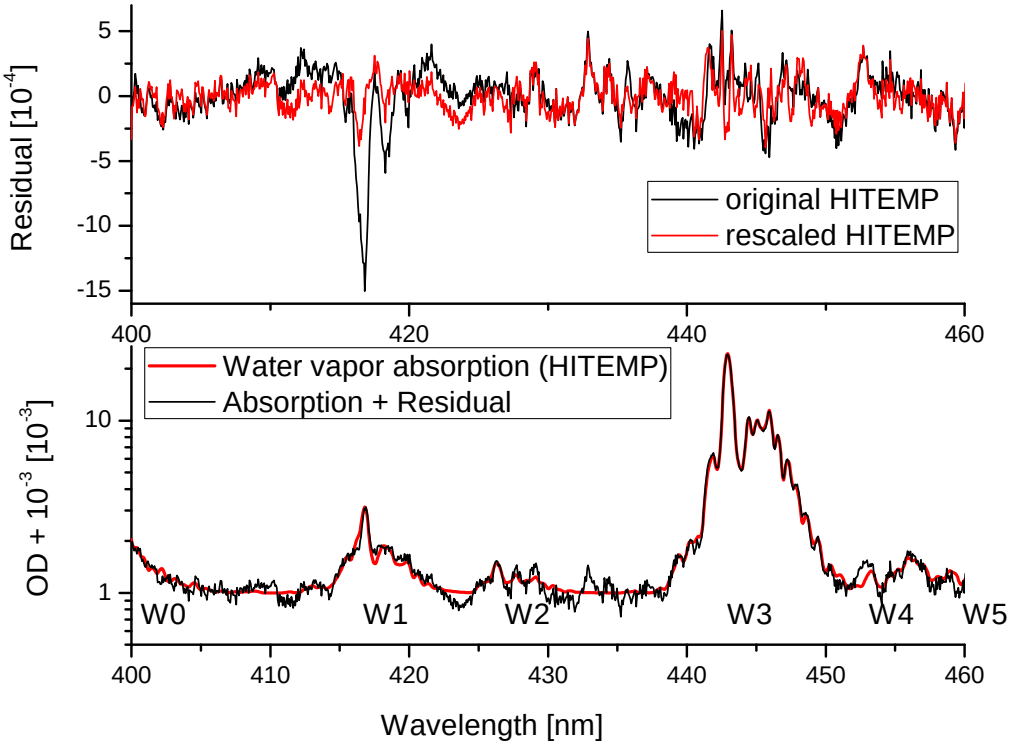

Figure 5.33.: Fit residuals (top panel) and water vapour OD for a MAX-DOAS measurement during M91 using the HITEMP cross-section. A residual from a single fit using the original HITEMP cross-section and a fit using separate column densities for each of the absorptions W0-W4 from HITEMP is shown. From a whole set of fits with separate absorption bands correlation plots with respect to W3 for each of the absorption bands were performed as shown exemplary in figure 5.32. The results are listed in table 5.8. The overall column density calculated from the data shown above is dSCD $= 5.31 \cdot 10^{23}$ molec cm^{-2}. For this analysis no correction spectrum for VRS(N_2) was included, leading to residual structures around 432 nm. These do not correlate with water vapour and therefore do not appear in figure 5.36. The absorption at 416 nm still produces residual structures, even after rescaling.

Polyad		8ν	$7\nu+\delta$		7ν		$6\nu+\delta$	
Name		W0	W1	W2	**W3**	W4	W5	W3 relative
Start of interval	[nm]	394.0	410.0	423.5	**434.0**	451.5	461.5	434.0
End of interval	[nm]	410.0	423.5	434.0	**451.5**	461.5	480.0	451.5
Cross-section								
HITRAN 2009		1.00	3.43	3.13	**1**	(49)	0.98	0.932
HITEMP		1	1	1	**1**	1	1	1
BT2		1.09	0.90	0.90	**1**	0.97	0.99	1.035
OD HITEMP for $CD = 4 \cdot 10^{23}$ molec cm^{-2}		36	27	6	**165**	4.5	62	[10^{-4}]

Table 5.11.: Expected ratios of dSCDs relative to the HITEMP cross-section and to the 7ν polyad (W3) for different spectral intervals and cross-sections based only on the cross-sections itself, convoluted to a resolution of 0.5nm. The difference of the cross-sections relative each other for the case of W3 is shown in the last column.

paign was compared water vapour mixing ratios calculated from parameters from the meteorological station at CVAO.
The meteorological station provides temperature, pressure and humidity data [Carpenter et al., 2010]. This data was used to calculate the water vapour mixing ratio using the Magnus formula and to compare the result with LP-DOAS data. Taking the measurement error given for the meteorological station, an error in the temperature measurements of 0.3°C results in 2% deviation, pressure uncertainties cancel out, since the same pressure measurements were used for the conversion of column densities from LP-DOAS to mixing ratios as well as in the Magnus formula. An error of 5% in relative humidity would directly translate in 5% error for the mixing ratio. This means, that the absolute differences of the cross-sections shown in table 5.11 cannot be absolutely validated, even though the water vapour mixing ratios ranged from $2.0 - -3.4\%$ and meteorological station data and LP-DOAS data correlated with a Pearson's $R = 0.95$. The LP-DOAS results based on the HITEMP cross-section were on average 10% lower than the values inferred from the meteorological station data. This means, that the HITRAN2009 cross-section fits the data from the meteorological station the best. Retrieving tropospheric water vapour profiles from the MAX-DOAS measurements even introduced larger errors due to uncertainties in retrieving the required aerosol profiles. Volume mixing ratios for water vapour during M91 from MAX-DOAS retrievals of $(2.3 \pm 0.5)\%$ agreed with meteorological station data from RV Meteor, but the observed width of the distribution of the retrieved water vapour mixing ratios is also too large to draw conclusions about the total size of the absorption cross-section.

5.3.3. UV Absorption cross-section

Experimental validations of water vapour absorptions are only available so far down to 395.7 nm (25337 cm^{-1}) [Dupré et al., 2005]. The absorption line lists below this wavelength are based only on calculations. Furthermore these calculations are unstable and no information on their accuracy can be given. [J. Tennyson, pers. communication] Given the above mentioned uncertainties in the sizes of the different absorption bands,

the procedure used in the 400–480 nm region above cannot be applied for this region, since the absorption bands are not as clearly separated (e.g. at $\approx$ 360 nm for HITEMP and BT2) and the expected optical densities are always close to the detection limit. Additionally uncertainties in available O_4 cross-sections make a spectral retrieval of water vapour difficult: While it seems to be clearly detected using the Hermans cross-section with reasonable dSCD of $\approx 4 \cdot 10^{23}$ molec cm^{-2} and a ten times smaller fit error, this is not the case for the Thalman or Greenblatt cross-section where no positive dSCD is found.
Du et al. [2013] reported measurements of the water vapour cross-section by ring-down spectroscopy of pure water vapour in the 290–350 nm region sampling the absorption cross-section in steps of 5 nm. Their measurements were in agreement with previous measurements for the absorption at 442.73 nm. The reported cross-section values of $\sigma_{max} = 2.94 \cdot 10^{-24}$cm^2 / molec at 330 nm are exceeding the maximum absorption of the BT2 line list in the spectral region from 330–350 nm by two orders of magnitude. This would lead to an OD of $\tau = S \cdot \sigma_{max} = 0.88$ for MAX-DOAS measurements with S_{H_2O}=$3 \cdot 10^{23}$ molec cm^{-2} (mid-latitude summer conditions) under a telescope elevation angle of 3°. During M91 in the Peruvian upwelling the residual size in the region from 332–370 nm was below $6 \cdot 10^{-4}$ peak-to-peak for a water vapour dSCD retrieved in the blue wavelength range of $4{\cdot}10^{23}$ molec cm^{-2}, resulting in an upper limit on the differential OD of water vapour of $3 \cdot 10^{-27}$cm^2 / molec at a resolution of 0.45 nm.
We therefore conclude that the cross-section values reported in Du et al. [2013] are significantly too high judging from UV MAX-DOAS measurements under atmospheric conditions or represent only individual absorption lines at each of the positions of the reported size, while in between no cross-section data is available and thus no conclusions can be made. At a spectral resolution of 0.45 nm the given upper limit applies.
The OD attributed to water vapour between 350 and 370 nm is according to HITEMP/BT2 $9.5 \cdot 10^{-4}$ and $5.5 \cdot 10^{-4}$ peak-to-peak for a typical dSCD of $4 \cdot 10^{23}$ molec cm^{-2}. O_4 has under similar measurement conditions with a dSCD of $4 \cdot 10^{43}$ molec^2 cm^{-5} an OD of $2 \cdot 10^{-2}$, a factor of 20–40 larger.
To estimate the overall influence of water vapour on the retrieval of O_4 further dedicated laboratory measurements of water vapour in this spectral region are needed.

5.3.4. Discussion of relative line strengths

From table 5.9 it can be seen that the development of water vapour absorption compilations from HITRAN 2009 to HITEMP/HITRAN2012 results in a better fit of the measurement data. The fit errors for intervals of the cross section are reduced. Nevertheless, the relative absorption strengths are inconsistent, they are listed relative to W3 in table 5.8. In the BT2 line list and in HITEMP the absorptions from 410–434 nm overestimate the observed absorptions approximately by a factor of two.

- For W0 the results from MAX-DOAS and LP-DOAS agree. The size of the absorption at W0 is found to be about $10 \pm 4\%$ smaller in measurements than what is reported in HITEMP.

- For W1 the agreement of MAX-DOAS and LP-DOAS measurements is not as good as for W0, but this absorption is also slightly smaller. Judging from MAX-DOAS measurements the absorption strength of W1 is $47 \pm 11\%$ too high, LP-DOAS measurements indicate even $100 \pm 6\%$ overestimation in HITEMP. For W1 in BT2 a better agreement is found, together with smaller fit errors. This leads to the assumption that the difference in the results of LP and MAX-DOAS for W1(HITEMP) are caused by interference with corrections needed in the MAX-DOAS retrieval (Ring Spectrum, Intensity offset) which compensate for some of the water vapour absorption not included in HITEMP.

- The absorption W2 was not regularly identified in LP-DOAS measurements, but is also close to the size of the residuals for MAX-DOAS data. Therefore the results for W2 need to be used with caution. Furthermore the residual structure which is visible at 429 nm in figure 5.33 is correlated with the overall water vapour dSCD, which gives a hint to a systematic problem of the shape of the absorption there. These correlations show that the water cross-section is reproduced correctly within $1 \cdot 10^{-27}$ cm^2 at 0.45 nm resolution.

- The absorption W3 is relatively strong and therefore requires correct application of saturation and I_0 corrections. Furthermore, neglecting the changes in radiative transfer for MAX-DOAS measurements for individual absorption lines leads to significant structures in the residual spectra, while the overall dSCD is only affected by $< 3\%$ for a dSCD $S < 5 \cdot 10^{23}$ molec cm^{-2}.

- The absorption W4 is small, but is regarding its optical density comparable to previous observations of glyoxal on the open ocean which also absorbs in this spectral region. A water vapour dSCD correlated structure in the residuals is found at the absorption at 453.0 nm (HITEMP) which can be also seen in figure 5.33. This absorption seems to be better reproduced in BT2, the absorption is rather at 452.5 nm. This is also seen in table 5.9 as a decrease in fit error from HITEMP to BT2. The same error estimate for the convoluted cross-section as for W2 applies for W4.

- For W5 good agreement in relative absorption strength for HITEMP, HITRAN2009 and BT2 and observed spectra was found within an error of 4%.

Due to the observed discrepancies in relative absorption band strength, it is advisable only to include wavelength intervals in a DOAS analysis where the relative absorption band strengths are sufficiently in agreement with each other. This means e.g. for IO that the water absorption band at 442 nm (W3) should be avoided, if the absorption at 426 nm (W2) or even also at 416 nm (W1) is included. For the retrieval of glyoxal with its main spectral absorption features above 440 nm, a wavelength window which does not include water vapour absorption at 426 and 416 nm should be preferred when using these water vapour cross-sections. The same argumentation applies for choosing a retrieval interval for NO_2.

The relative size of the absorption band W5 around 470 nm and the small fit errors indicate that the water vapour cross section is unlikely to cause interferences when retrieving O_4 dSCDs for radiative transfer modelling in this spectral region.

5.3.5. Reproduction of observed water vapour absorption

Since the most of the individual absorption lines of water vapour included in HITEMP/HITRAN are based on ab-initio calculations in the blue wavelength range, the question arises if these modelled absorptions reproduce observations sufficiently. Certainly the main water vapour absorption around 442 nm in this spectral region is found quite well in measurement data and the cross-section is that good that even radiative transfer corrections in the lower 10^{-3} / upper 10^{-4} range need to be applied at total absorptions of several percent, see subsection 3.2.4.1. Furthermore, the obtained mixing ratios for water vapour are realistic, see [Wagner et al., 2013b] and subsection 5.3.2.
Small absorption features are still questionable, as e.g. the absorption shape of the water vapour absorption from 450–460 nm, where the main absorption of glyoxal is found. Here an ubiquitous residual structure in situations with high water vapour dSCD can be found at 453 nm. The structure correlates well with the water dSCD as well as the O_4 dSCD, thus it might be also an absorption feature of a missing but yet well mixed constituent of the atmosphere. When comparing the size of the corresponding OD, it corresponds to $\approx 10^{15}$ molec cm^{-2} glyoxal at 456 nm. Therefore this structure can significantly influence the retrieval of glyoxal. Fortunately for the glyoxal retrieval, the correlation of this structure and glyoxal is small with $R = 0.25$, since the absorptions do not significantly overlap. For water vapour this correlation yields $R = 0.90$, for O_4 still $R = 0.85$ (see Figure 5.34). Since the O_4 absorption cross-section is not expected to have narrow-band absorption structures, the most probable candidate is water vapour. Additionally an absorbers with a similar profile as water vapour could cause these structures. The correlating residual structures were extracted by using PCA (subsection 3.3.2) as well as by an overdetermined system of linear equations. The resulting spectra for the main contributions to residual structures e.g. from water vapour were similar and the differences not relevant for the plots shown here.
As can be seen from figure 5.35, the real water vapour absorption cross-section in the wavelength range from 448 nm–459 nm seems to be within the range of currently available water vapour cross-sections. But since other absorbers might have compensated within the fitting process for absorptions of water vapour absolute corrections to the literature cross-section values cannot be given.
Figure 5.36 shows the same approach for a wavelength range in which the wavelength interval used for the retrieval of IO is found.
The maximum difference to the observed water vapour cross-section is then about $\pm 5 \cdot 10^{-28}$, which translates into residual structures of about $\pm 2 \cdot 10^{-4}$ for typical tropical water vapour dSCDs.

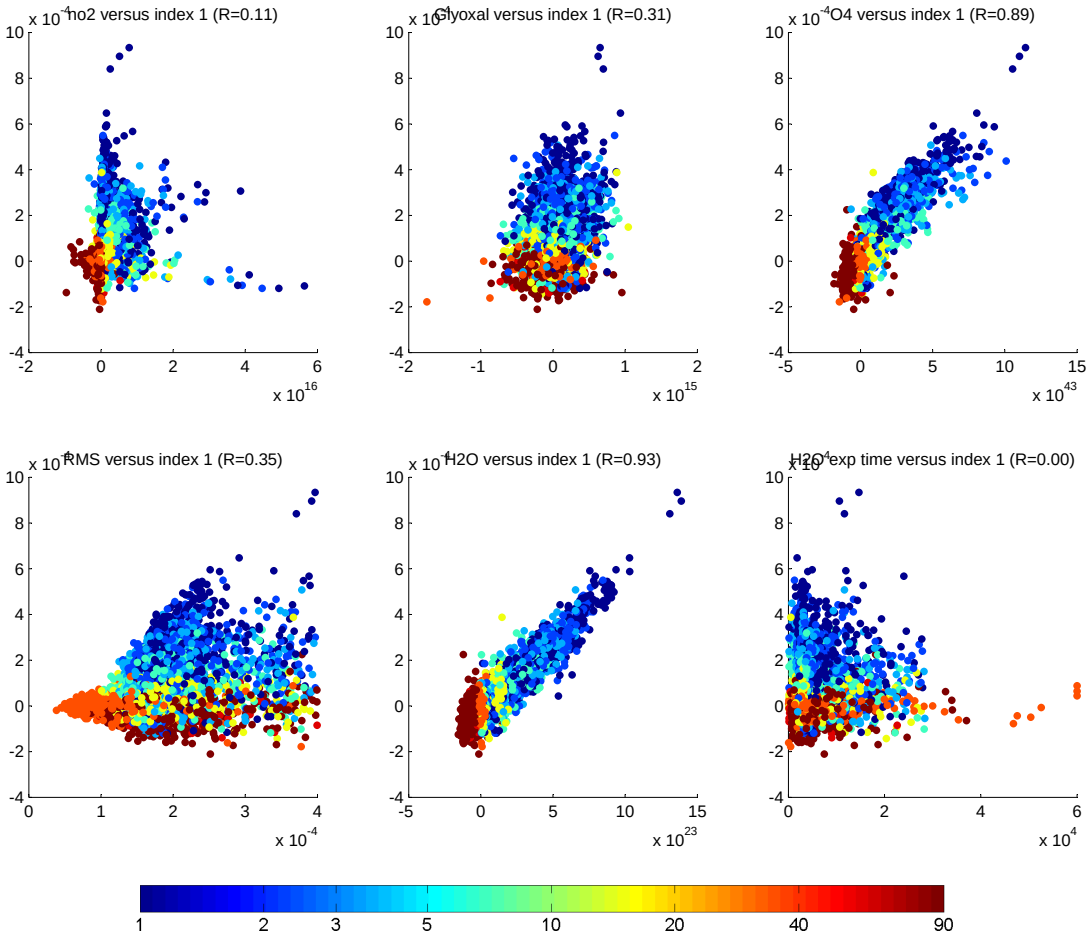

Figure 5.34.: Coefficients of a PCA from 448 nm–459 nm for MAX-DOAS data from M91. The total fit range was from 434–460 nm, covering the main water vapour absorption. Clearly the correlation of the residual absorption structure with water vapour and/or O_4 dSCD is seen.

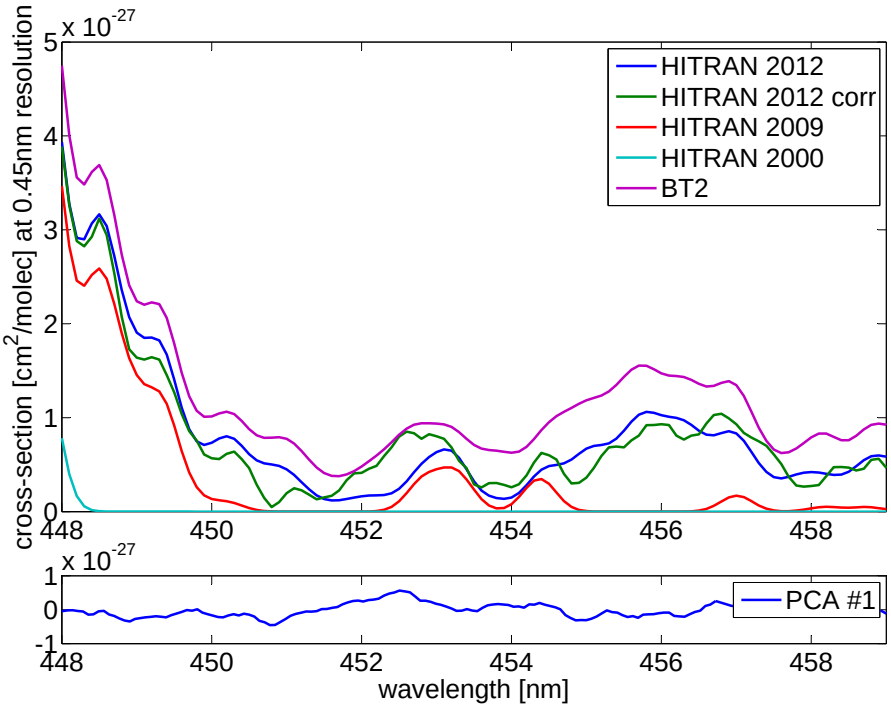

Figure 5.35.: Comparing the resulting first component from figure 5.34 with currently available water vapour cross-sections. The water vapour absorption at 442 nm was used to determine the water vapour dSCD of the respective measurement and correlated with the H_2O dSCD with R=0.93 as shown in figure 5.34. Note that this a differential correction, not yielding an absolute correction of the absolute literature cross-section.

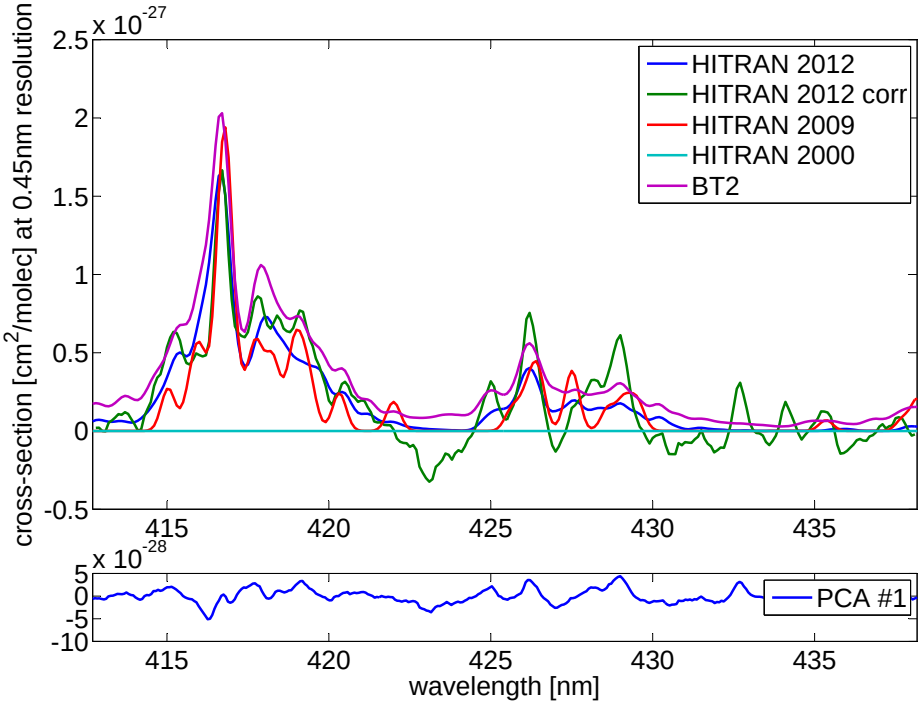

Figure 5.36.: As for glyoxal in figure 5.35, comparing the resulting first principal component from residual spectra from data from M91 with currently available water vapour cross-sections in the IO wavelength range. The first principal component correlated with water vapour dSCD. The difference introduced by applying the saturation and I_0 correction to the cross-section data during convolution is about 20% of the difference derived from the first principal component. HITRAN2012 and BT2 are divided by 2 in this spectral region according to table 5.8. Note that this a differential correction, not yielding an absolute correction of the absolute literature cross-section.

5.4. Strong absorbers and their influence on radiative transfer

The apparent absorption of strong absorbers is not only changed by the saturation effect (see subsection 3.1.1) but also its effective light path is altered in the atmosphere due to its absorption. This also influences the shape of the observed absorption, especially for highly structured cross-sections. Strong absorptions are typically causing shorter light-paths and therefore their optical density is reduced. The saturation effect works in a similar way, here strong absorptions are also decreased due to the exponential in the Lambert-Beer law. Therefore the overall effect of the radiative transfer on the shape of the absorption can sometimes look similar to not having corrected for the saturation effect.

Water vapour dSCD were modelled at 440 nm using McArtim [Deutschmann et al., 2011] for a SZA and RZA of 30°, using a water vapour profile until 15km from a radiosonde launched during M91 on 12/24/2012 [S. Fuhlbrügge, pers. comm.]. Analogous to the spectral retrieval during the cruise dSCDs were calculated for 3° relative to 40°, with and without using a exponentially decreasing aerosol profile with a total AOD of 0.22 km^{-1}. The cross-section was varied to obtain different ODs. The result for the part which is relevant for water vapour absorption in the blue wavelength range can be seen in figure 5.37. High water vapour dSCDs during this cruise of about $5 \cdot 10^{23}$ molec cm^{-2} translate into optical densities of 0.2 for individual absorption lines. This means, that these individual strong lines appear 10% smaller for MAX-DOAS measurements. Convoluted to the instrument's resolution this results in OD of about $7 \cdot 10^{-4}$. If this effect is ignored, most of the structure is compensated by the water vapour absorption itself, which is then 3% too small and the residual spectrum shows structures with up to $2 \cdot 10^{-4}$. This effect does strongly depend on the SZA, the slope of the line shown in figure 5.37 on the left varies by a factor of three for SZAs between 20–80°. The dependence on the RZA on the other hand is less than 10%.

When this structure is included in the DOAS fit for measurement data (tested here for data from M91 and a spectral window from 432 nm-460 nm, for an example see figure 5.38), the correction spectrum accounts for larger ODs as expected with OD of up to $3 \cdot 10^{-3}$, which is four times more than expected. The slopes shown in figure 5.37 with increasing AOD, but this cannot explain this difference. Since the residual structures in this spectral range are of the order of $4 - 5 \cdot 10^{-4}$, it might be as well an error in the water vapour cross-section and/or the instrument slit function. It reduces the overall RMS by about 40% and the water vapour dSCD increases by about 16%.

glyoxal dSCD decreased by about $-8.4 \cdot 10^{-10}$ molec glyoxal / molec H_2O, thus resulting for a dSCD(H_2O) of $5 \cdot 10^{23}$ molec cm^{-2} for a reduction of the glyoxal dSCD of $4 \cdot 10^{14}$ molec cm^{-2}, which is significant when comparing to observations in the Peruvian upwelling (see subsection 7.2.6). An overview of the different effects and their influence on the glyoxal dSCD can be found in figure 5.40.

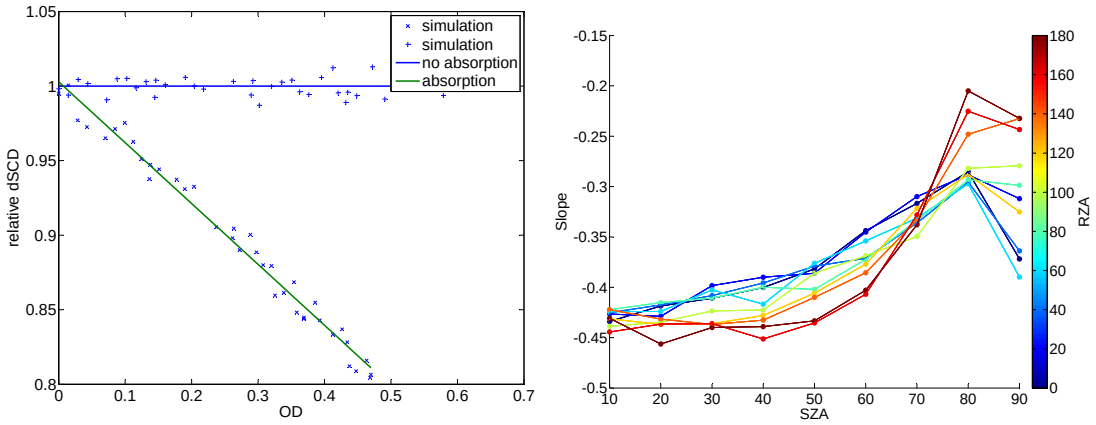

Figure 5.37.: Left: Relative water vapour dSCDs at different apparent optical densities for a SZA and RZA of 30° and a water vapour profile until 15km from a radiosonde launched during M91 on 12/24/2012, without including aerosols. Water vapour dSCDs during this cruise of about $5 \cdot 10^{23}$ molec cm^{-2} translate into optical densities of 0.2 for individual absorption lines. Right: The slope of the fit shown on the left is plotted for different SZA and RZA. The slope increases e.g. to 0.6 for small RZA and SZA with when increasing the aerosol optical depth to 0.2.

5.5. Liquid water absorption

Liquid water also absorbs light in the visible and UV region, its cross-section was measured e.g. by Pope and Fry [1997]. Unfortunately the cross-section provided there is measured at a resolution of about 2 nm and was decreased to 7 nm due to smoothing during data processing. Additionally there are differing other measurements [Dickey et al., 2011], but absorption structures similar to the Pope et al. cross-section have been identified in satellite measurements by Richter et al. [2011] and in MAX-DOAS measurements looking downwards [Peters et al., 2014]. According to radiative transfer modelling done by Großmann et al. [2013], about 10% of the light reaching the telescope at low elevation angles came thought the ocean water, for clear sky conditions. From MAX-DOAS measurements during ANT28/2 south of Cape Town, a problematic situation seems to be overcast conditions, when more light which once passed the ocean is reflected back down to earth by clouds. In this case, presumably liquid water absorption was causing significant negative glyoxal dSCDs. Still, retrieving reliable liquid water column densities requires a broad wavelength interval from around 400–500 nm. This wavelength range is often not fully covered. Apart from absorption by liquid water also absorption by phytoplancton and other particulates are expected, which can have differential absorption structures as well [Gordon et al., 2009].

One meter of liquid water absorption results in an absorption which can be interpreted as the absorption of about $-1.6 \cdot 10^{15}$ molec cm^{-2} glyoxal.

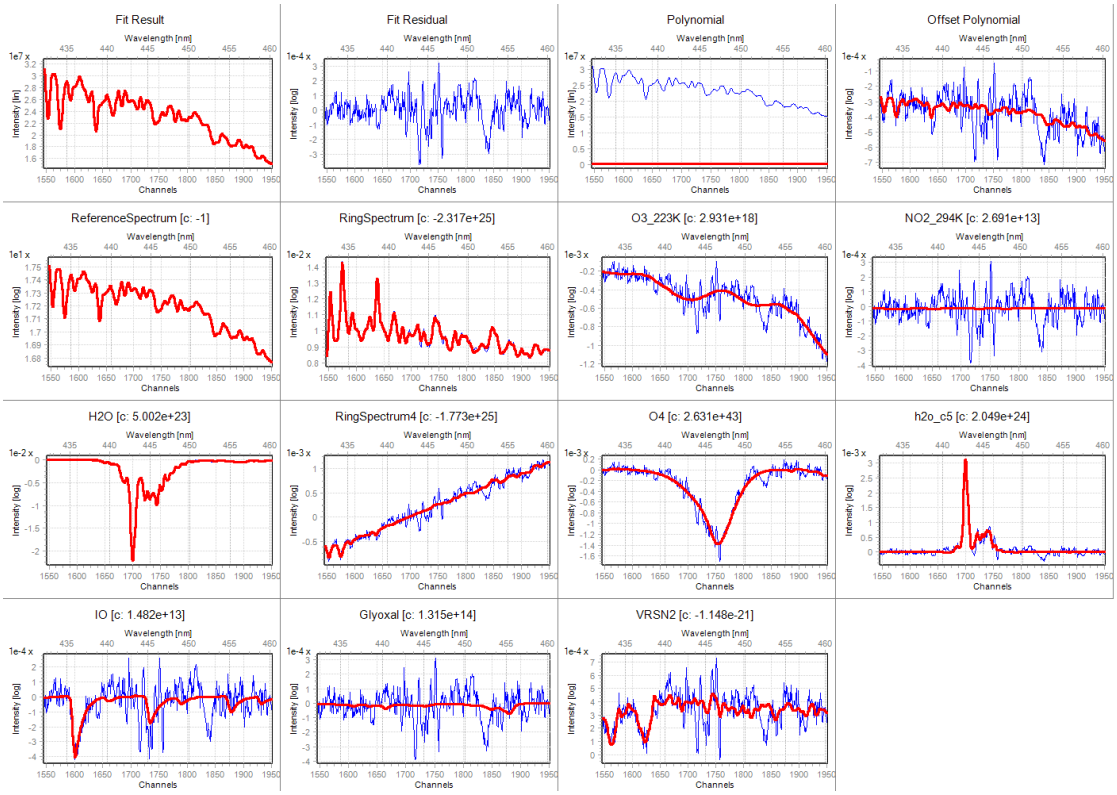

Figure 5.38.: Fit of a MAX-DOAS spectrum recorded at 2° elevation during M91 on 12/19/2012, 13:30 UTC (SZA=65°) in the Peruvian upwelling including a correction spectrum for radiative transfer effects on water vapour absorption (H2O_c5) and a N_2 VRS correction spectrum. The HITEMP water vapour cross-section was used. Note the structure at 453 nm which seems to be correlated to water vapour absorption, see figure 5.36.

During ANT XXIX liquid water columns were found to be below 1m at -4° elevation, slightly correlated with VRS by water with $R = 0.3$.
The approach chosen in Peters [2013], Peters et al. [2014] allows to compensate for liquid water absorption and inelastic scattering of sunlight in liquid water at the same time without the need for radiative transfer modelling: By separating downward looking spectra into white-cap data spectra and spectra with long light paths below the waterline, an effective correction spectrum for both effects and possible also other seawater constituents can be determined and used to correct atmospheric measurement data for possible seawater absorption influence.

5.6. Settings for different trace gases (MAX-DOAS)

For all campaign data the goal was a consistent setting for evaluating spectra for specific trace gases. In some cases different settings were used, still, due to instrumental

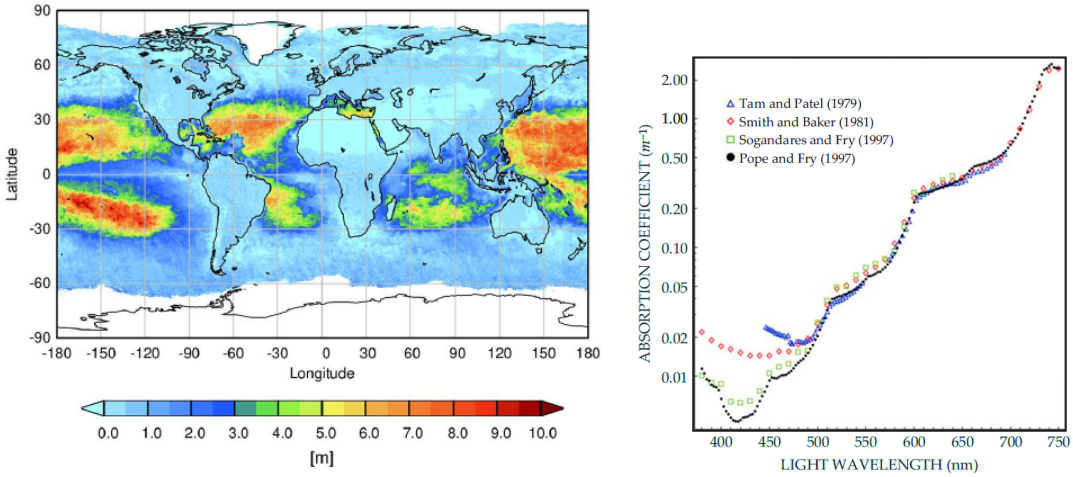

Figure 5.39.: Liquid water in backscattered light of SCIAMACHY measurements, from Peters [2013]. Regions with long lightpaths within the water column are clearly identified. On the right available liquid water absorption cross-sections adapted from Dickey et al. [2011].

limitations.

	SO_2	BrO	HCHO	O_4	IO	H_2O	Glyoxal	Glyoxal	S_{I0}
	315 327	332 358	332 358	350 373	415 440	432 450	415+447 440+460	432 458	molec/cm^2
Polynomial Add. Polynomial	3 1	3 1	3 1	3 1	3 1	3 1	4 1	3 1	
Ring	X	X	X	X	X	X	X	X	
Ring·λ^4	X	X	X	X	X	X	X	X	
SO_2	X								
O_3 223K	X	X	X	X	X	X	X	X	$1 \cdot 10^{18}$
O_3 243K	X	X	X						$1 \cdot 10^{18}$
BrO	X	X	X	X					$3 \cdot 10^{13}$
HCHO	X	X	X	X					$5 \cdot 10^{15}$
O_4		X	X	X		X	X	X	$3 \cdot 10^{43}$*
NO_2 224K		X	X	X	X				$5 \cdot 10^{15}$
NO_2 294K	X	X	X	X	X	X	X	X	$5 \cdot 10^{15}$
H_2O					X	X	X	X	$3 \cdot 10^{23}$
IO					X	X	X	X	$3 \cdot 10^{23}$
Glyoxal					(X)	(X)	X	X	$5 \cdot 10^{14}$
liq. H_2O							X	X	-
VRS(H_2O) VRS(N_2 / O_2)					X	X	X	X	

Table 5.12.: Retrieval wavelength intervals for MAX-DOAS measurements in this thesis. (*) in molec^2 cm^{-5}.

Typically shift and squeeze of all cross-section are linked for data evaluations in this thesis, unless otherwise noted. Sometimes shift and squeeze were determined from a fit

Ring	Bussemer [1993], DOASIS [Kraus, 2006]
Ring·λ^4	Wagner et al. [2009]
SO_2	Bogumil et al. [2003]
O_3	Serdyuchenko et al. [2013]
O_3	Serdyuchenko et al. [2013]
BrO	Fleischmann [2004]
HCHO	Chance and Orphal [2011]
O_4	Hermans et al. [1999] (Aerosol retrieval) Greenblatt et al. [1990] (BrO/HCHO) Thalman and Volkamer [2013] (Tests/Comparisons)
NO_2	Vandaele et al. [1998]
NO_2	Vandaele et al. [1998]
H_2O	Rothman et al. [2013] (HITEMP)
IO	Spietz et al. [2005]
Glyoxal	Volkamer et al. [2005a]
liq. H_2O	Fry et al. [1992]
VRS(H_2O)	Vountas et al. [2003]
VRS(N_2 / O_2)	Haug [1996], this work

Table 5.13.: Literature references for table 5.12.

of a convoluted solar atlas with the measured spectrum, if no strong absorptions are found within the retrieval wavelength interval.
Technical comment: The fits shown in this thesis are typically slightly modified output from DOASIS, as shown in figure 5.21. In these plots the measured spectra are plotted in blue, the modelled contributions are plotted as a thick, red line. In the top-left plot the raw data and the modelled data is shown. Then the residual spectrum, the difference between measured and modelled spectrum. Then for each absorber a box is shown with the modelled optical absorption according to the fit result (in red) and the sum of modelled absorption and residual spectrum (in blue). This allows to easily compare the size of the retrieved absorption with the size of the remaining residual. For MAX-DOAS fits the logarithm of the Fraunhofer reference spectrum is typically included in the fit, with a coefficient of -1 and shift and squeeze linked with the Ring Spectrum (corresponding to a division by I_0). Fixing them to 0 and 1, respectively, is typically leading to unstable fit results, despite that the fit results always in negligible shifts < 1 pm.

5.6.1. I_0 and Saturation effect

I_0 and Saturation effect were corrected according to the last column in table 5.12. Residual spectra have not shown the necessity to implement a iterative fitting procedure for any of the retrieved trace gases to account for the correct dSCD in the saturation correction, at least not when using a Fraunhofer reference spectrum from the same elevation sequence.

5.6.2. BrO and HCHO

The retrieval interval for BrO has been adapted from Vogel [2012], since the main limitations of the fit interval were ozone related and not influenced by SO_2 absorption.

5.6.3. O_4

The spectral retrieval for the purpose of aerosol retrievals has been discussed in Yilmaz [2012] also using the method presented in Vogel et al. [2013].
While saturation correction does not play a significant role at optical densities of about 1% at 360 nm, the I_0-correction also needs to be applied to the O_4 absorption cross-section. The resulting residual structure for neglecting this effect has been also found in MAX-DOAS data from cruise M91. The impact on the obtained column density is small, the relative change is of the order of $cdot10^{-3}$.
360 nm: The choice of fit wavelength range from Yilmaz [2012] can be confirmed, own sensitivity studies resulted in choosing 350–373 nm (Yilmaz: 350–375 nm). In most cases it was furthermore necessary to include cross-sections for formaldehyde and bromine monoxide, but this depends on the actual situation and the way the data is evaluated. For evaluations with a fixed or noon Fraunhofer reference spectrum BrO should be included to account for the stratospheric BrO absorptions.
470 nm: The absorption of O_4 around 477 nm is accompanied by water vapour absorption, but at least the wavelength range from 460–490 nm as in Yilmaz [2012] needs to be included for the spectral retrieval, since otherwise parts of the O_4 absorption might be compensated for by the DOAS polynomial. The relative strength of the water vapour absorption bands around this absorption peak of O_4 were found to be correct, compare table 5.8.

5.6.4. Glyoxal

The retrieval of glyoxal with its major absorption features in the 455 nm range [Volkamer et al., 2005a] is affected in its spectral retrieval by several other absorbers in the same spectral range, namely water vapour (section 5.3) and the oxygen dimer O_4. The fit range in which glyoxal is retrieved leaves not many possibilities to chose from, since the main absorption at 455 nm needs to be encompassed as well as the fit range should not be too small to correctly correct for the absorption of O_4. The second largest absorption feature of glyoxal is located below the maximum water vapour absorption in this range. There might be an influence of the vibrational Raman scattering in liquid water, liquid water absorption and absorption by phytoplancton [Sadeghi et al., 2012]. To estimate their effect the data from SOPRAN M91 recorded with the SMAX-instrument has been evaluated using different settings and cross-sections. Since water vapour is the main absorption feature in the spectral range of glyoxal absorption, this needs to be handled with care or the main absorption features of water vapour need to be excluded from the fit. The main absorption features of glyoxal can be found below 442 nm and above 450 nm, which favours an exclusion of this range. Nevertheless, reliable fits for the O_4 absorption at 447 nm are then often not possible any more. Additionally the instrument

function needs to be constant and/or precisely known to reproduce the water vapour absorption sufficiently. This is not the case for Polarstern data, thus there the main water absorption needs to be left out from the fit.
Correction for changes in radiative transfer due to strong water vapour absorption discussed in section 5.4 reduce the RMS of the residuals significantly and also reduce the amount of glyoxal observed.
Still, the measurement error is not dominated by photon shot noise, but residual structures are present, with or without including the main water vapour absorption in the fit range. This can be seen from the fit error summing over a number of 1, 4 and 16 elevation sequences. This behaviour is also reflected in the scatter of glyoxal dSCD observed during M91, which is a factor of 2.5, 3 and 4 bigger than the averaged fit errors for 1,4 and 16 summed sequences respectively. For noise dominated residual spectra roughly a factor of 1–2 would be expected according to Stutz and Platt [1996].
Systematic residual structures caused by water vapour absorption in the wavelength range of the maximum glyoxal absorption can be excluded, compare figure 5.35, when the most recent water vapour absorption cross-section HITRAN2012 or HITEMP is used.
In figure 5.40 an overview over different glyoxal fit settings for a fixed wavelength range from 432–460 nm during M91 is shown. The largest glyoxal dSCD are calculated when ignoring radiative transfer effects on the water vapour absorption and the influence of VRS of N_2. If these two effects are included, further spectra e.g. for liquid water absorption or vibrational Raman scattering in liquid water do not improve the RMS significantly, neither do they change the mean glyoxal dSCD.

Publication	Interval [nm]	Type -DOAS	H_2O XS HITRAN	Typical values (for MAX-DOAS at 3◦ elevation)	Location
Volkamer et al. [2005b]	420–465	LP		0-1ppb	urban
Sinreich et al. [2007]	420–460	MAX	2004*	140/350 ppt	urban / coastal
Sinreich et al. [2010]	433–458	MAX	2004*	$1.5 \cdot 10^{15}$ molec cm^{-2}	tropical MBL
Irie et al. [2008]	436–457	MAX	2004	81 ppt	urban
MacDonald et al. [2012]	422–442	LP	2000	1ppb	rural
Wittrock et al. [2006]	436–457	SCIAMACHY	1992?	VCD $5 \cdot 10^{14}$ molec cm^{-2} (trop.)	global
Li et al. [2013b]	415–442	MAX	2004	400 ppt	rural
Lerot et al. [2010]	435–460	GOME-2	2004	VCD $6 \cdot 10^{14}$ molec cm^{-2} (trop.)	global
Baidar et al. [2013]	433–460	AMAX	2004	max. 274±28 ppt	urban
Vrekoussis et al. [2009]	435–457	SCIAMACHY	200X	VCD $5 \cdot 10^{14}$ molec cm^{-2} (trop.)	global
Vrekoussis et al. [2010]	424–457	GOME-2	200X	VCD $5 \cdot 10^{14}$ molec cm^{-2} (trop.)	global
Mahajan et al. [2014]	433–460	LP (HaloCaVe)	2012	< 48 ppt	tropical MBL
	433–460	LP (Charlex)		< 50 ppt	tropical MBL
	433–460	MAX (Charlex)		< 50 ppt	tropical MBL
	420–460	MAX (TransBrom)	2012	$< 1 \cdot 10^{15}$ molec cm^{-2}	tropical MBL
	420–460	MAX (ANT26)	2012	$< 1 \cdot 10^{15}$ molec cm^{-2}	tropical MBL
	420–460	MAX (ANT28)	2012	$1.5 \cdot 10^{15}$ molec cm^{-2}	tropical MBL
	424–458	MAX (SHIVA)		$1 - 2 \cdot 10^{15}$ molec cm^{-2}	coastal

Table 5.14.: Fit ranges used for spectral retrievals of glyoxal. *The publications Sinreich et al. [2007, 2010] used HITRAN2004, which was then corrected manually.

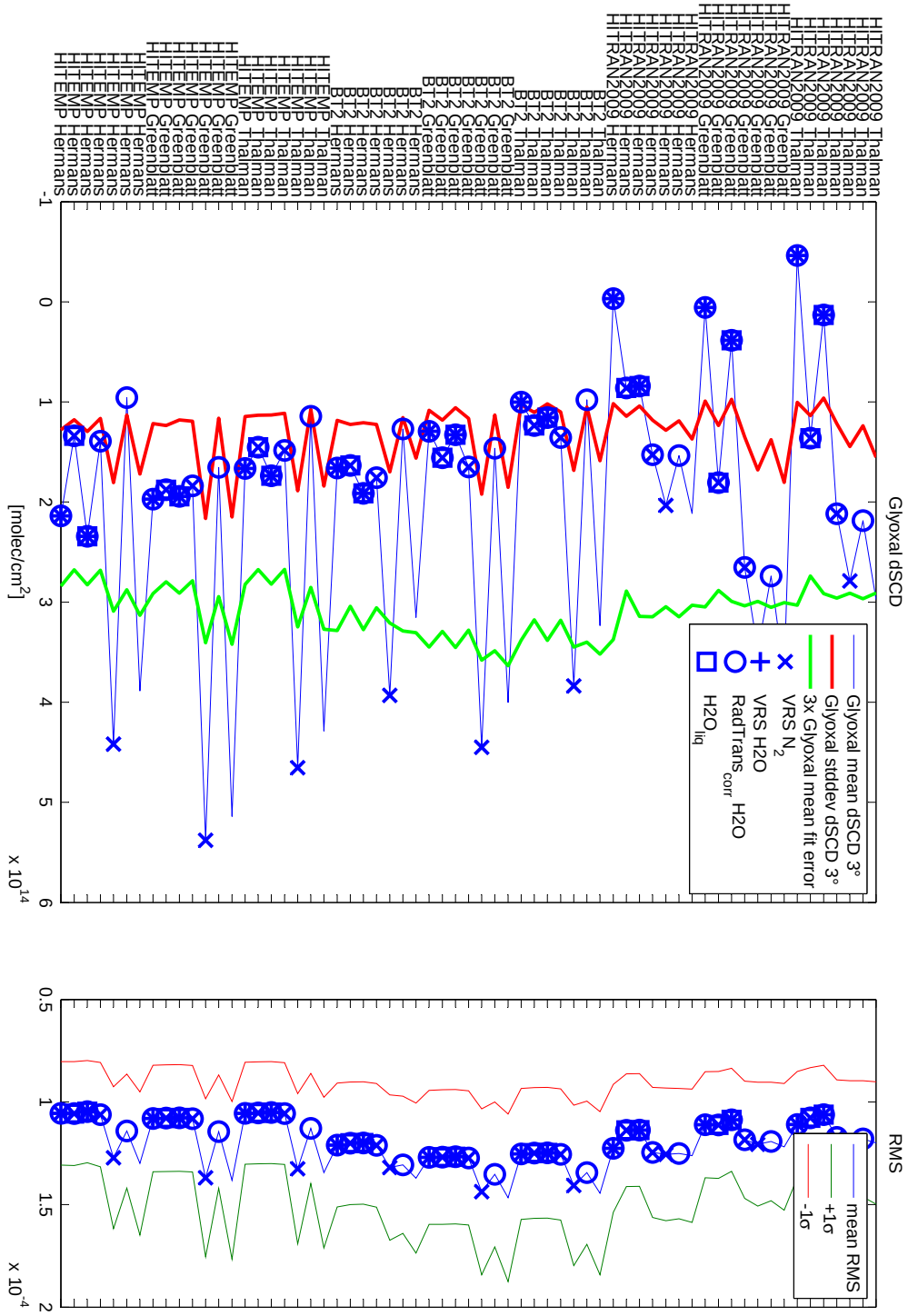

Figure 5.40.: M91 glyoxal data, evaluated with a current reference and 16 co-added elevation sequences for different water vapour and O_4 cross-sections and varying settings for the corrections included, from 432 nm–460 nm. While the choice of water vapour and O_4 cross-section does not result in large differences, neglecting the effects of the change in lightpath caused by water vapour absorption (see section 5.4) significantly influences the result of the fit. The smallest RMS were observed when using the HITEMP cross-section and correcting for this effect and VRS of N_2. Other corrections were then not improving the RMS any more for this dataset.

5.7. CE-DOAS Retrieval

The spectral retrieval of CE-DOAS data seems at first really straightforward. According to Platt et al. [2009] the optical density is calculated by using one of the approximations, namely here $\tau = \frac{I_0}{I} - 1$. The cross-sections are multiplied by the absorption light path length obtained from helium measurements and then fitted after having been filtered to remove the broadband part of the spectra. For details see also Anthofer [2013].
This procedure relies on a number of assumptions which need to be tested during evaluation:

1. The path-length is constant within the measurement period
2. The shape of the path length is constant within the measurement period
3. The path-length scales linearly and does not depend on the aerosol load
4. The path-length is zero after highpass filtering, i.e. the product of path-length and polynomial absorptions such as Rayleigh and Mie scattering do not leave a spectral signature in the measured optical density
5. The purge air reference spectrum I_0 is constant over the measurement period

Checks during measurements have therefore to be made in between the measurements:

1. By observing the overall intensity and by additional Ring down measurements the reflectivity of the mirrors and the correct alignment need to be monitored
2. This can be tested e.g. by fitting an additional multiplicative polynomial to the absorption spectra which would account for changes in the overall path-length.
3. This is not the case, since the relative decrease in light path length caused by aerosol will be stronger for wavelengths with higher mirror reflectivity. If strong absorption is not taking place for situations with high aerosol load, this might be neglected. If a higher aerosol optical density coincides with NO_2 absorption, this can lead to residual structures, since the shape of the path-length is changed.
4. This problem was addressed later on during the retrieval process, see subsection 5.7.1 for details.
5. This is assured by regulating the temperature of the LED and monitoring the overall intensity. Additionally I_0 spectra were also evaluated against a fixed reference to see variations in water vapour and/or NO_2.

To account for degradation effects, changes in alignment and/or optical properties, I_0 measurements of dried air were done at least at a daily basis during the SHIVA and M91 campaigns. Helium measurements were only successfully accomplished before and/or after those campaigns in the laboratory.

5.7.1. Residual structures

Structures in residual spectra appear, when absorbers are not appropriately accounted for. This is often the case for high concentrations of trace gases and/or an erroneous path length.
During M91 residual structures were observed which correlated with the measured intensity of the CE-DOAS setup. This led to the assumption that these structures were directly related to aerosol load. Similar structures (see also figure 5.41) where already observed during SHIVA, but since the aerosol load was relatively constant during that campaign, the correlation to the measured intensity was not seen. Also during measurements at Scott Base by Johannes Zielcke, Denis Pöhler and Udo Frieß similar residual structures were observed, with a similar pair of cavity mirrors, LEDs and the same type of spectrometer.

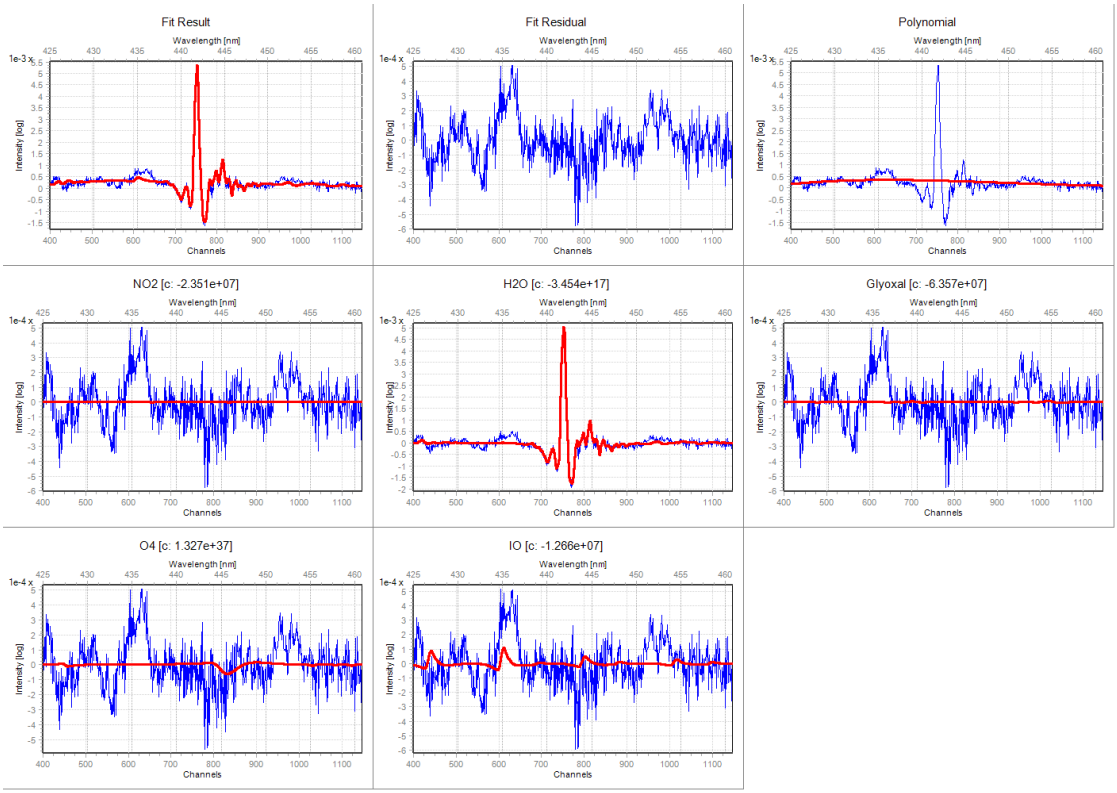

Figure 5.41.: Typical residual structure during M91 before linearity correction of the spectral data. This spectrum #19100 was recorded 12/6/2012 at 03:20 UTC for 1000s. $-2 \cdot 10^7$ molec cm^{-2} correspond to 1 ppt IO.

Possible explanations for these structures are:

- The idea of aerosol fluorescence [Pan et al., 1999, Immler et al., 2005] as the cause for these structures was abandoned since those emissions would not be directed,

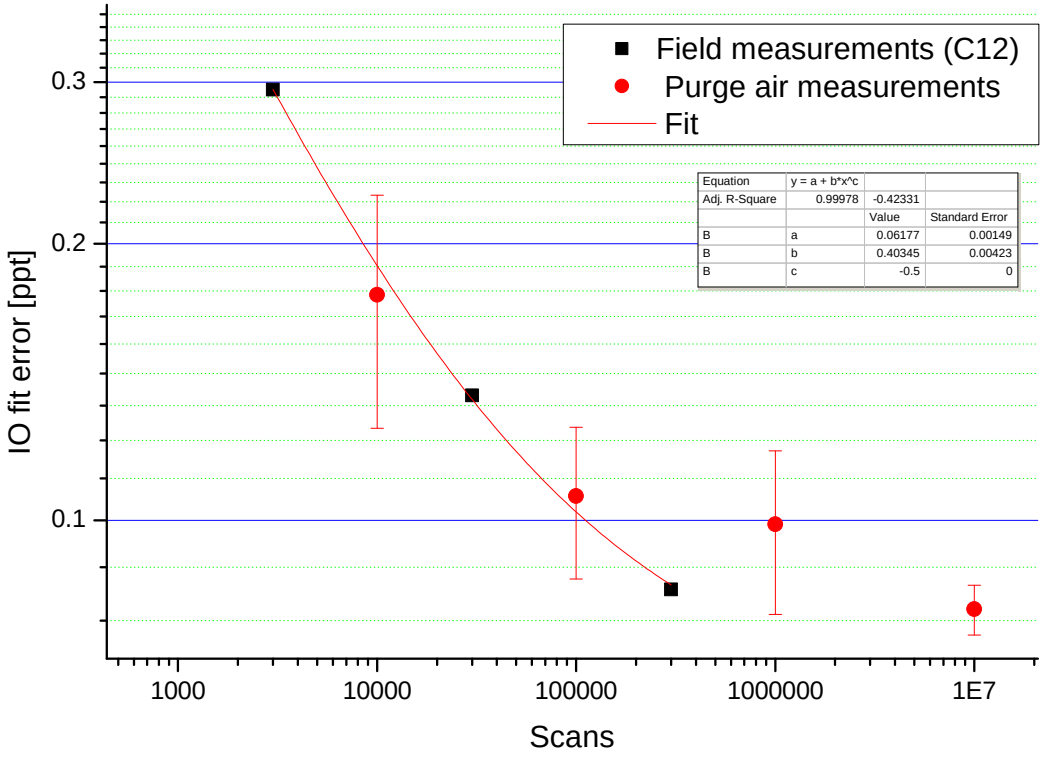

Figure 5.42.: CE-DOAS fit error as a function of scan number, at an exposure time of 10ms at a absorption light path length of 5.5km. Purge air measurements were evaluated against a reference with the same number of scans, measurement data was evaluated against a reference with 10^5 scans, therefore an offset to the $\sqrt{N}$ behaviour was expected. The measurement data was evaluated using six PCA components instead of convoluted cross-sections and the values represent the minimal values within the measurement period. Averaging more than $3 \cdot 10^5$ scans under measurement conditions was not possible due to an increase of aerosol and NO_2 concentration. Purge air reference measurements were evaluated using a fit scenario including H_2O, NO_2, IO, O_4 and a polynomial of 3rd degree. Variations and no further decrease for more than 10^5 scans are probably caused by instrumental instabilities.

thus lost for the measurement, and the emission shape should be rather broad Pan et al. [1999]. Ambient stray light from outside the resonator can be excluded by evaluating the background spectra of the measurements during M91. [9]

- Another explanation is that the reflectance curve of the mirrors used does not

[9] SHIVA CE-DOAS measurements were done with manually recorded background spectra, since the servo for the shutter broke at the beginning of the campaign.

vanish when applying a high-pass filter to it. Aerosol absorption is accounted for by a polynomial in Equation 3.30 and a binomial high-pass filter has been appplied beforehand to the optical density calculated in Equation 3.30. During M91 only low-resolution wavelength resolved ringdown measurements were performed, but afterwards He-calibrations were done in the laboratory with the same cavity setup, but with mirrors which had been cleaned in between and a setup that had been newly adjusted.

- a missing absorber
- Non-linearity of the detector
- Differently illuminated mirrors at high aerosol loads, which, due to inhomogenities of the mirrors' surfaces, might then in turn result effectively in different reflectance curves of the mirrors.

The following method was applied to measurement data to correct for the systematic residual structures, which would have prevented detection limits of IO < 2 ppt.

5.7.2. Extraction of characteristic spectral structures

The following conditions had to be met when selecting residual spectra to be analyzed using PCA (see subsection 3.3.2):

1. Measured intensity within reasonable bounds
2. RMS of the residual $< 4 \cdot 10^{-4}$
3. NO_2 concentration < 300 ppt
4. only night-time measurements

The first two conditions guarantee that the spectrum is valid and can be used for further analysis. The third condition excludes spectra which might be affected by strong NO_2 absorption. The last condition was applied for the IO retrieval under the assumption that there is no IO during night-time due to missing photolysis of I_2, HOI, methyl iodide and other possible precursors. In this case the fit corresponding to the analysed residuals did no include IO in the first place to avoid compensation effects of residual structures, IO and other cross-sections. Due to this assumption it is not possible to correct this residual structure for measurements of glyoxal, which might exhibit even higher mixing ratios during the night due to missing photolysis.
As it turned out the non-linearity of the detector of the Avantes spectrometer (see subsection 4.4.1) was the main reason the observed structures around 436 nm. Also the correlation to overall light intensity obtained from the PCA of the spectra pointed to this direction, yet it was not understood at that time. CE-DOAS measurements were performed at a fixed exposure time as opposed to MAX-DOAS measurements. Therefore the saturation changed with changes in aerosol load and subsequently the slope of the

linearity changed, leading to residual structures. Still, some structures remained in the residual spectra and the PCA analysis was also performed on the residual spectra from the non-linearity-corrected spectra. Typical apparent optical densities caused by not correcting the non-linearity of the detector where $\approx 4 \cdot 10^{-4}$ peak-to-peak.
An explanation for the remaining residual structures can be variation in intensity which are not resolved by individual spectra. Usually 1000 scans were added before saving. The non-linearity correction p(I) is by definition non-linear, which means that $P(I)+P(K) \neq P(I+K) = 2P(I)+\frac{\partial}{\partial x}|_{x=I}P(x)\cdot(K-I)+\mathcal{O}^2$. According to the non-linearity correction shown in figure 4.5 $\frac{\partial}{\partial x}|_{x=I}P(x)$ is typically 0.1 and assuming variations on small time-scales of about 10% yields a total error for the non-linearity correction of 0.01, after applying a high-pass filter 10^{-4}. The optical densities of the trace gases of interest (glyoxal and IO) are expected to be around several 10^{-4}. Since this effect cannot be corrected afterwards, the procedure to retrieve correction spectra from night-time data is still necessary.
Calculated correction spectra from non-linearity polynomial and measured intensities did not match the residual spectra from night-time measurements.

A brute force approach: In analogy to Li et al. [2013a] also an alternative approach was tested, leading to comparable results (see figure 5.44): instead of convolving known cross-sections, all optical density spectra were fitted with a polynomial only. The obtained residuals were then used for a PCA. A selection had to be made to ensure that spectra from situations with fog or instrumental problems do not dominate the resulting spectra obtained from PCA. This could be done via intensity or by selecting only residuals for the final PCA which comply with a threshold for the RMS after removing the first, e.g. 4 principal components calculated from all residual spectra. From this procedure several principal component spectra were obtained, the first two of them representing a linear superposition of water vapour and NO_2 absorption cross-sections (Figure 5.43). Spectra compensating for absorption $> 1 \cdot 10^{-4}$ were found until the sixth principal component. Selecting only residuals from measurements during night-time allows as described above to include the IO absorption cross-section in a second evaluation to obtain IO mixing ratios.
The resulting fit errors compared to a 'traditional' evaluation of purge air measurements are shown in figure 5.42. It shows that all methods of spectral retrieval of the CE-DOAS data deliver similar IO mixing ratios at similar measurement errors, but that extraction of typical residual structures from night-time measurements can improve the measurement error by 20–50%. Furthermore using a larger fit retrieval interval which allows also for the determination of glyoxal mixing ratios does not reduce the accuracy of the spectral retrieval of IO, despite large water vapour absorption of several 10^{-3} optical density.
A comparison between the standard evaluation, the evaluation including correction spectra obtained from night-time residuals and the brute force approach is shown in figure 5.44.
This approach needs several days of continuous measurement data under varying condi-

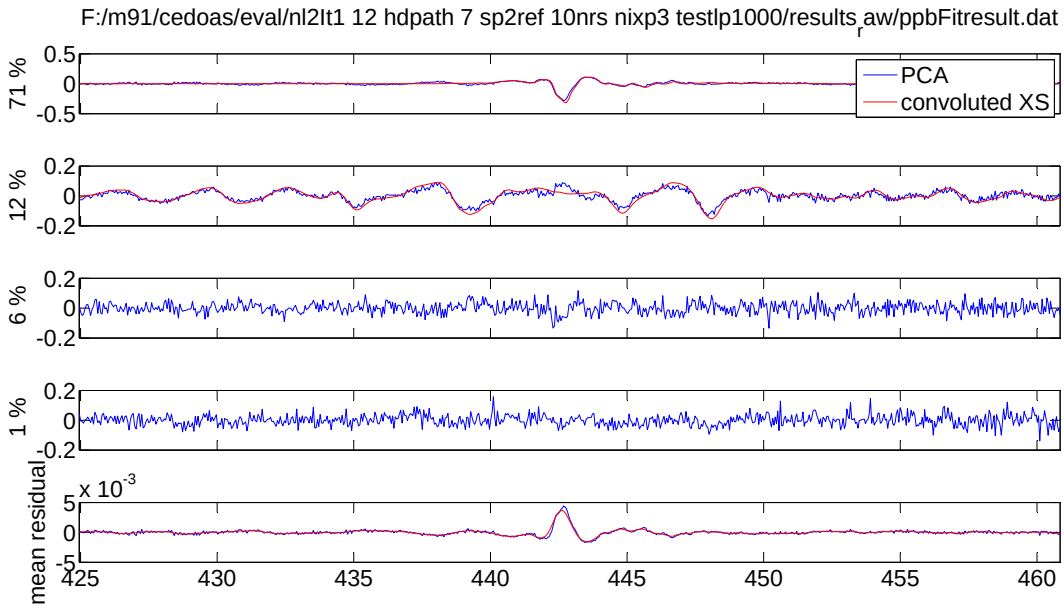

Figure 5.43.: The first four vectors from a PCA of the filtered optical densities measured during M91: The first one is similar to water vapour absorption in this region (red line), the second one similar to NO_2 absorption. Both vectors are a linear combination of the original water vapour and NO_2 absorption cross-sections. The third and fourth vector compensate for structures are systematic structures introduced by the spectrometer electronic, since their typical structures width is significantly smaller than the width of the instrument function. The first six vectors from the PCA were used in figure 5.44, see also figure 3.11.

tions without instrumental modifications to be able to extract the different absorbers. Therefore night-time data might be as important for the overall outcome of a CE-DOAS measurement campaign aiming for mixing ratios close to the detection limit as the data collected during daylight.

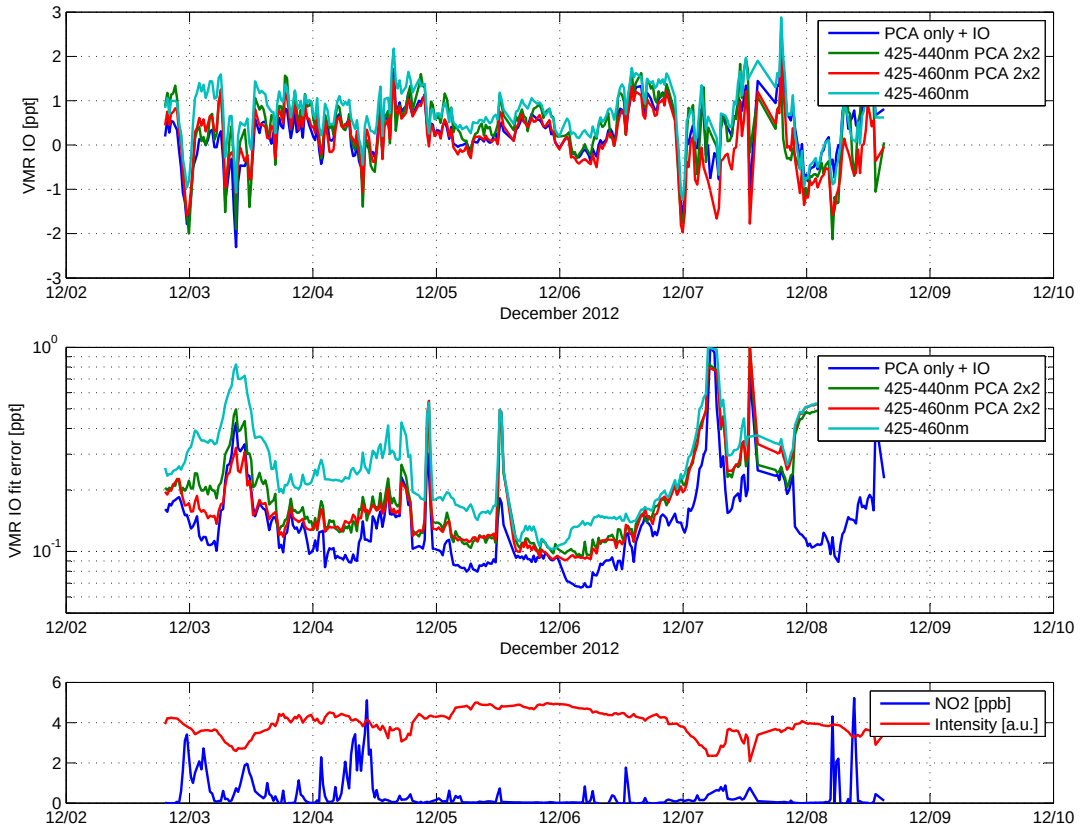

Figure 5.44.: IO mixing ratios and IO fit errors during SOPRAN M91 (chapter 7). The PCA evaluation is done similarly as Li et al. [2013a] described in section 5.7.2 using the first six PCA components and the convoluted and absorption light path length corrected IO cross-section. The evaluation from 425–460 nm was done without any corrections. The other two have two spectra for optical and non-optical residual structures from a PCA included. The only measurements above detection limit are found from 12/04/2012 to 12/07/2012 during a period with low NO_2 concentrations and low aerosol load (high intensity).

6. Overview Campaign data

Several years of MAX-DOAS measurement and 6 weeks of CE-DOAS observations in the marine boundary layer were obtained on different cruises on different ships at latitudes from 70°S to 90°N.

Year	**Duration**	**Name**	**Place** (Bhv = Bremerhaven)	**Spectrometer**	Species
2007	15.05 –	ANT/ARK	Bhv – Arctic – Antarctic	USB2000	1
2008	– 16.11	ANT/ARK	Antarctic – Bhv – Arctic	USB2000	1
2009	27.01. – 14.02.	M77	Lima – Panama	MiniDOAS	1,2
	10.05 – 13.05	ANT 25/5b	Las Palmas (Hotel)	VIS	2,3
	14.05 – 24.05	ANT 25/5b	Las Palmas – Bhv	VIS	2,3
	19.06 – 29.09	ARK 24	Bhv – Bhv (Arctic)	VIS	2,3
	16.10 – 25.11	ANT 26/1	Bhv – Pt. Arenas	VIS	2,3
	27.11 – 27.01	ANT 26/2	Pt. Arenas – Wellington NZ	VIS	2,3
2010	10.06 – 29.06	ARK 25/1	Bhv – Longyearbyen	VIS	2,3
	30.06 – 30.07	ARK 25/2	Longyearbyen – Reykjavik	VIS	2,3
	31.07 – 10.10	ARK 25/3	Reykjavik – Bhv	VIS	2,3
	25.10 – 20.05	ANT 27	Bhv – Cape Town – Wedell Sea	VIS	2,3
2011	16.04 – 08.05	MSM 18/1	Las Palmas – Mindelo	SMAX	1,2
	11.05 – 24.06	MSM 18/2	Mindelo – Mindelo	SMAX	1,2
	21.06 – 21.07	MSM 18/3	Mindelo – Libreville	SMAX	1,2
	28.10 – 01.12	ANT 28/1	Bhv – Cape Town	UV+VIS	1,2,3
	03.12 – 05.01	ANT 28/2	Cape Town – Cape Town	UV+VIS	1,2,3
	14.11 – 28.11	SO218	Singapore – Manila	SMAX + CE	4
2012	14.06 – 15.07	ARK 27/1	Bhv – Longyearbyen	UV+VIS	1,2,3
	15.07 – 30.07	ARK 27/2	Longyearbyen – Tromsoe	UV+VIS	1,2,3
	02.08 – 07.10	ARK 27/3	Tromsoe – Bhv	UV+VIS	1,2,3
	27.10 – 27.11	ANT 29/1	Bhv – Cape Town	UV+VIS	1,2,3
	30.11 – 09.01	ANT 29/2	Cape Town – Cape Town	UV+VIS, 12h/d	1,2,3
	28.11 – 27.12	M91	Lima – Lima	SMAX + CE + O_3-Mon.	1,2
2013	11.01 – 19.03	ANT 29/3	Cape Town – Pt. Arenas	UV+VIS, some gaps	1,2,3
	22.03 – 16.04	ANT 29/4	Pt. Arenas – Pt. Arenas	UV+VIS, some gaps	1,2,3
	18.04 – 29.05	ANT 29/5	Pt. Arenas – Cape Town	UV+VIS, some gaps	1,2,3
	June + July	MAD-CAT	Mainz	UV MAX-DOAS (Avantes)	1,2
	08.06 – 12.08	ANT 29/6	Cape Town – Pt. Arenas	UV+VIS	1,2,3
	14.08 – 16.10	ANT 29/7	Pt. Arenas – Cape Town	UV+VIS	1,2,3
	10.11 – 16.12	ANT 29/8	Cape Town – Cape Town	UV	1
2014	20.12 – 05.03	ANT 29/9	Cape Town – Cape Town	UV	1
	09.03 – 16.04	ANT 29/10	Cape Town – Bhv	UV	1

The last column shows the trace-gas species, which can be retrieved:

1. SO_2, O_3, BrO, HCHO, O_4(360 nm), OClO, HONO, NO_2
2. IO, Glyoxal, H_2O, NO_2
3. I_2, OIO, H_2O, O_4(470 nm), O_4(570 nm)
4. NO_2, IO, Glyoxal, H_2O

6.1. Polarstern

Since 2009 all Polarstern cruises were done with the same instrument, described in section 4.1. In the beginning, the measured data showed high amounts of stray light,

which have then been reduced in the middle of the year 2011 (see subsection 4.1.1) in parallel to the MAX-DOAS from Schneefernerhaus Schneefernerhaus [2013], Jurgschat [2012]. Before this modifications, UV spectra from 300-400nm cannot be used for the retrieval of HCHO and BrO. During *ANT XXVII/1* CE-DOAS measurements were done in parallel by M. Horbanski.
During the cruises from 2009–2014 the Polarstern MAX-DOAS instrument recorded more than 1050000 spectra in the marine boundary layer, which corresponds to a total, continuous measurement time of two years. Most of the time the instrument worked unsupervised.
The MAX-DOAS data from 2007–2008 was analysed for tropospheric O_4, NO_2, BrO and HCHO, but only the first two species were found above their respective detection limits due to instrumental limitations. Nevertheless this data might be useful for observations of stratospheric trace gas absorptions covering a wide range of latitudes.

6.1.1. ANT XXV/5b

The MAX-DOAS was performing measurements for the first time in the marine boundary layer from the balcony of a Hotel in Las Palmas in May 2009. On May 14th it was set up on RV Polarstern and measured until the harbour of Bremerhaven, from where it was brought back Heidelberg for maintenance.

6.1.2. ARK XXIV

The first unsupervised measurements campaign took place during *ARK24* starting from Bremerhaven. Low O_4 dSCD for the majority of the measurements indicate low visibility.

6.1.3. ANT XXVI

It was fully functioning during cruise legs 1+2, then failed due to problems with the readout electronics board.
For cruise leg 1 AERONET data for aerosol optical densities is available Smirnov et al. [2009], as well as LIDAR data from Kanitz et al. [2013].

6.1.4. ARK XXV

The MAX-DOAS instrument functioned well during the whole cruise.

6.1.5. ANT 27

It failed in tropics due to heat problems, but continued measuring south of Cape Town.

6.1.6. ANT XXVIII

The first two legs of *ANT XXVIII* it provided the first data in the UV range after the stray-light problems have been minimized (see subsection 4.1.1).

For cruise leg 1 AERONET data for aerosol optical densities is available Smirnov et al. [2009]. Details can be found in chapter 9.

6.1.7. ARK XXVII

During this expedition the MAX-DOAS system measured continuously without any problems during three months in total. Additionally to the usual elevation angle sequence also measurements at an elevation of -4° were recorded. This was the first cruise to the Arctic with the straylight-optimized UV spectrometer.

6.1.8. ANT XXIX

During leg ANT XXIX/1 the USB hub failed and thus measurements were restarted south of Cape Verde after the hub has been replaced. Due to technical problems on leg ANT XXIX/2 the position was not updated and measurements took place as if the instrument would have been in Cape Town. This resulted in only measuring during approximately one half of the total possible measurement time.

6.1.8.1. ANT XXIX/6+7

During cruise leg 29/6 the MAX-DOAS was supervised by Joëlle Buxmann, who additionally performed CE-DOAS measurements on board and on ice stations and the first MAX-DOAS measurements from a helicopter in the Antarctic. During cruise leg 29/7 CE-DOAS measurements, LP-DOAS measurements and Helicopter MAX-DOAS measurements were done by Johannes Zielcke and Jan-Marcus Nasse. The results of these measurements will be found in the Master's thesis of J.-M. Nasse [Nasse, 2014] and the dissertation of J. Zielcke.

6.2. SOPRAN MSM18

Year	Duration	Name	Place	Spectrometer
2011	16.04 – 08.05	MSM 18/1	Las Palmas – Mindelo	SMAX-DOAS
	11.05 – 24.06	MSM 18/2	Mindelo – Mindelo	SMAX-DOAS
	21.06 – 21.07	MSM 18/3	Mindelo – Libreville	SMAX-DOAS

The MAX-DOAS setup measured unsupervised after having been set up in the harbour of Las Palmas/Gran Canaria during cruise legs 1+2. Since the air chemistry lab's was not able to handle tropic temperatures during these unsupervised measurements, the temperature of the spectrometer had not been around 38°C as supposed and how it worked fine during TransBrom [Krüger and Quack, 2013], but increased significantly in between, leading to spectral shifts of the measured spectra of up to 1nm. (see figure 8.3) The MAX-DOAS measurement were supervised during MSM18/3.

6.3. SHIVA/Sonne SO218

Year	Duration	Name	Place	Spectrometer
2011	14.11 – 28.11	SO218	Singapore – Manila	SMAX-DOAS + CE-DOAS

Additionally to the SMAX-DOAS Instrument, a MAX-DOAS with two Acton spectrometers looking to starboard was operated, while the Heidelberg instrument was mounted on the portside of *RV Sonne*. Unfortunately the Heidelberg MAX-DOAS data cannot be evaluated at a sufficient detection limit due to variations in offset spectra, which were not regular and therefore could not be corrected for. The Bremen instrument measured correctly and was able to detect IO, HCHO and various other trace gases, first data will be published in Schreier et al. [2014].

6.4. SOPRAN Meteor M91

Year	Duration	Name	Place	Spectrometer
2012	28.11. – 27.12.	M91	Lima – Lima	SMAX-DOAS + CE-DOAS + O_3-Mon.

M91 was the last cruise with SOPRAN and investigated the upwelling region off the Peruvian coast. A MAX-DOAS, a CE-DOAS and an ozone monitor were operated during the almost full four weeks of the cruise. The CE-DOAS measurements were only interrupted for calibration measurements and cleaning.

6.4.1. Meteor M77

During Meteor cruise M77 in the Peruvian upwelling region leading from Lima straight out to the open ocean at 86°W, back to land north of Chiclayo and north to Panama along 86°W, a elevation corrected MiniDOAS equipped with a USB 2000 spectrometer were operated by Anette Kock and Evgenia Ryabenko from GEOMAR. Unfortunately it was not adjusted correctly and therefore the minimal elevation angle was 11°.

Year	Duration	Name	Place	Spectrometer
2009	27.01. – 14.02.	M77	Lima – Panama	HMT MiniDOAS

6.5. MAD-CAT Mainz

From June 6th to July 8th, the **M**ulti **A**xis **D**oas - **C**omparison campaign for **A**erosols and **T**race gases (MAD-CAT) campaign took place at the Max Planck-Institute for Chemistry (MPIC) in Mainz. Measurements were done with the Acton SMAX-DOAS instrument, a newly developed MAX-DOAS using acceleration sensors to measure the elevation angle and correct it dynamically. It is based on Avantes compact spectrometers. A third instrument from Heidelberg was the MAX-DOAS built within the EUSAAR project by Yilmaz [2012].

The measured data can be used to identify effects which might have been caused by liquid water below the ship and with the certainty that small elevation angles never look onto the ground/ocean. This sometimes simplifies argumentation for different measurement scenarios. For example an elevation angle separated principal component has been found in Polarstern data as well as in Mainz, giving a hint on an effect or an absorber in the lower troposphere rather than being caused by spectrometer stray light effects or vibrational raman scattering within the water column. Furthermore one might argue that in Mainz should be no detectable IO/BrO concentrations due to a lack of (known) sources and effective sinks (NO_2). Therefore these measurements can be used as a reference for other data.
Due to the high amounts of NO_2 observed, special care needs to be taken to avoid effects caused by large absorptions of NO_2. Additionally, later the non-linearity of the Avantes spectrometers was discovered and was determined for this instrument.

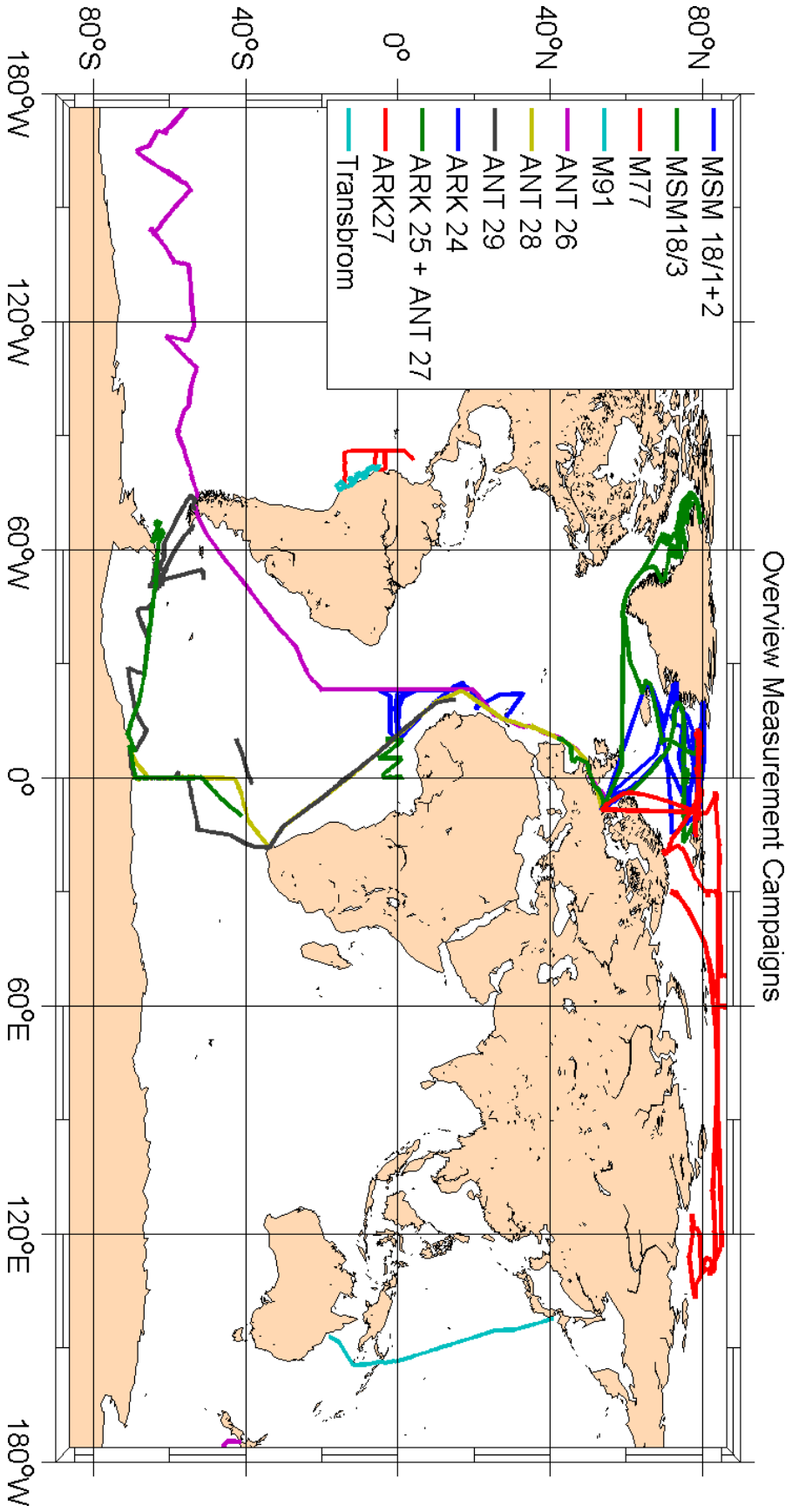

Figure 6.1.: Overview Measurement Campaigns: M77 in the eastern Pacific was an already existing data set, the data for TransBrom in the western Pacific was provided by K. Großmann [Großmann et al., 2013].

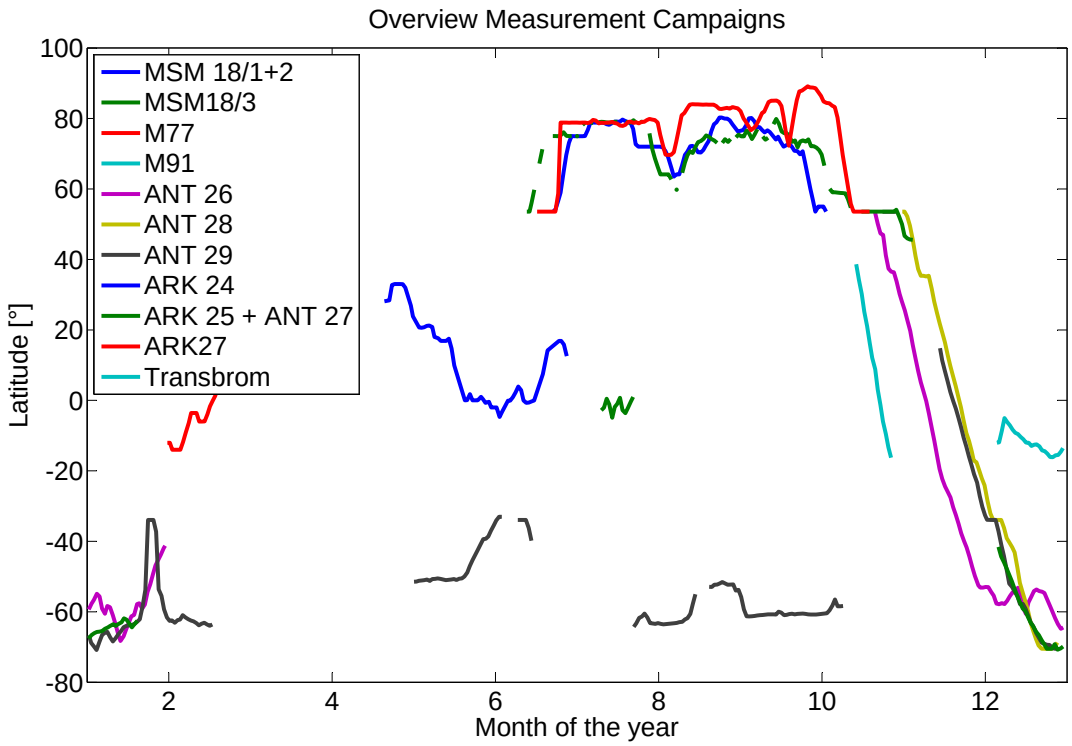

Figure 6.2.: Overview Campaigns, Latitude over Month of the year. Gaps during or in between cruises are caused by malfunction or also filtering by RMS which led to gaps in early Antarctic spring.

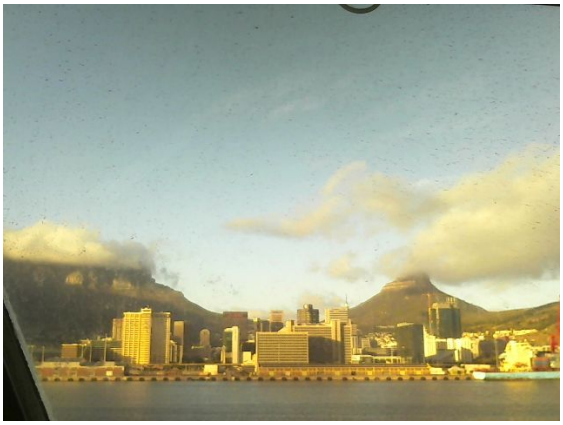

Figure 6.3.: MAX-DOAS data within ports needs to be handled with care, since either the lowest elevation angles are blocked by mountains or harbour buildings and/or permission for measurements in the respective terretory might not be given. The picture shows the view from Polarstern into the direction of the instrument in the harbour of Cape Town during ANT29/8 on 11/09/2013 at 04:43 UTC.

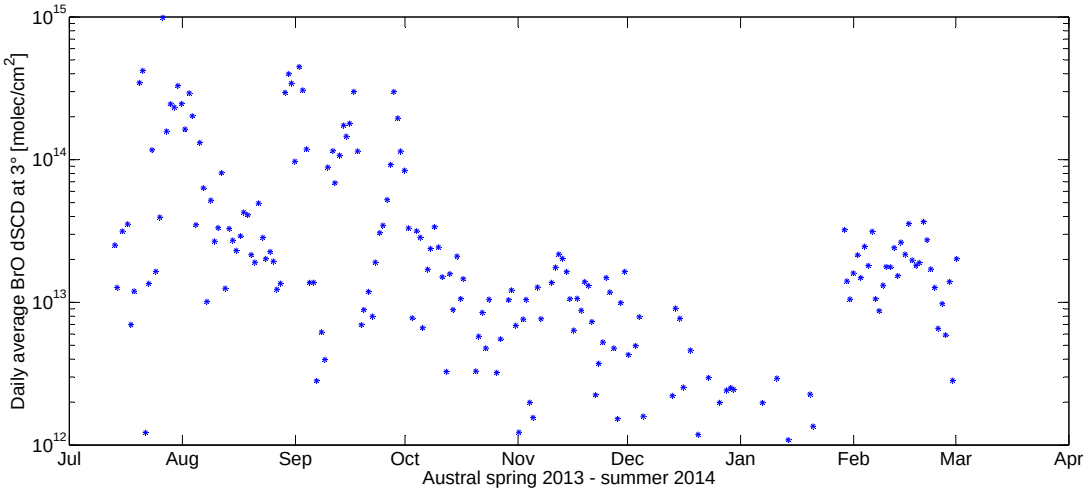

Figure 6.4.: Daily BrO concentrations during austral spring on ANT XXIX/6-9. The results of these measurements will be found in the Master's thesis of J.-M. Nasse [Nasse, 2014] and the dissertation of J. Zielcke. For a comparison: the maximum BrO value observed in the MBL outside polar regions was $6 \cdot 10^{13}$ molec cm^{-2} during MSM18/1 (subsection 8.1.1).

7. M91: The Peruvian Upwelling Region

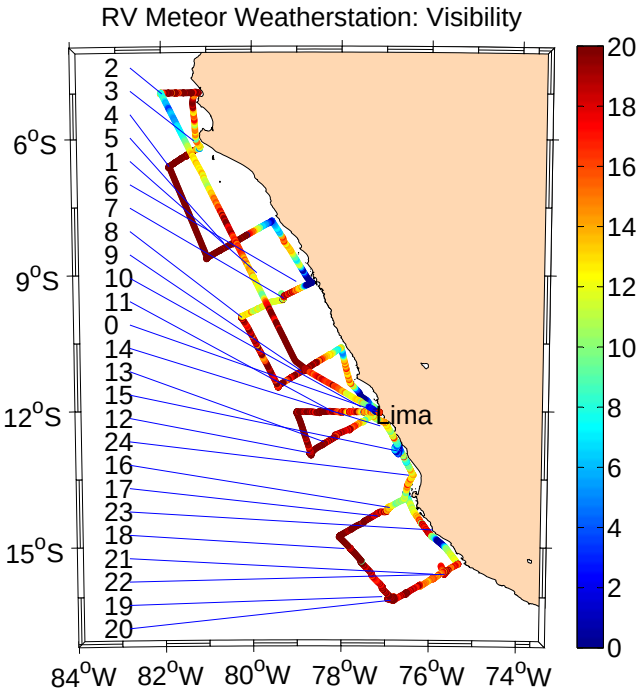

Figure 7.1.: The numbers and lines indicate the position of the ship on the respective day in December 2012 at 12:00 UTC, 07:00 local time during the campaign SOPRAN M91. The colour-coded dots represent the visibility in kilometres measured by the weather-station on RV Meteor. Reliable CE-DOAS measurements were possible when the visibility was larger than 10km and the cavity mirrors were clean.

The last cruise within the cooperation project SOPRAN took place on R/V Meteor as cruise leg M91 from December, 1st, 2012 until December 27th, 2012 in the Peruvian upwelling region. The cruise track of M91 was divided into several transects perpendicular to the coastline. During four days these transects were interrupted for diurnal stations, during which the diurnal variability at one location could be investigated. One MAX-DOAS, one CE-DOAS setup and an ozone monitor were installed together with a large number of other measurements for atmospheric and oceanic measurements.
The Peruvian upwelling region is interesting in many aspects: As already during previ-

ous studies within the SOPRAN project in the Mauritanian upwelling and the equatorial upwelling, the focus was on the detection of trace gases and gas-exchange processes at the ocean surface. Due to the high productivity of the upwelling regions, high fluxes of halocarbons, CO_2 and N_2O were found, which can eventually affect atmospheric chemistry and the atmosphere's radiative balance. But also the details of the upwelling processes and the upwelling velocities need to be studied to get a full picture of all factors governing the gas exchange at the surface. This includes quantifying the Surface Micro-Layer (SML) which can suppress exchange processes or might contribute to emissions to the atmosphere itself.
Therefore one of the objectives of M91 was to compare this region to long-term measurements on CVAO on Cape Verde as well as to previous cruises within SOPRAN, especially P399 in the Mauritanian upwelling [Tschritter, 2013] and the cruise MSM18/1 (section 8.2).
Concerning reactive trace gases, the total number of research cruises within this region is small. Measurements of IO from satellite by Schönhardt et al. [2008] indicated that strong oceanic sources for iodine compounds are present. Since the individual data points of these datasets are close or below the detection limit of the instrument and the maps were calculated by averaging over several years, dedicated ground-based measurements to prove these observations are of interest. Furthermore the vertical concentration profiles cannot be retrieved from satellite observations and the free troposphere can also contribute to the overall signal [Dix et al., 2013]. MAX-DOAS measurements of IO from the Atlantic already indicated larger IO concentrations in tropical latitudes, but if this is also the case on top of the cold Humboldt Current was not clear. Ship measurements of IO on the open Pacific by Mahajan et al. [2012] and calculated backward trajectories indicated that this region can be indeed a large source for atmospheric iodine. Ship-based MAX-DOAS measurements up to 150 ppt of glyoxal in the MBL by Sinreich et al. [2010] were surprising, since these observations, which are in agreement with observations from satellites, cannot be explained by continental precursor source fluxes (see subsection 1.2.4). Due to its tropospheric lifetime of several hours during daytime, this implies an unknown oceanic source. Previous measurements on the Atlantic never indicated concentrations of this amount (e.g. during MSM18/3, see section 8.2), and if, they were caused by the proximity to Africa and potential effects of biomass burning.
Additionally to anthropogenic emissions of NO_x and HCHO from the land, a potential influence on air chemistry is coming from copper smelters in southern Peru/northern Chile. SO_2 emissions at these locations have been observed from space [Carn et al., 2007] and have been detected in aerosol samples taken during the cruise [A. Baker, pers. communication].
For further details the cruise report by Bange [2013] contains the complete list of scientists, measurements and sampling stations.

7.1. Overview and other measurements

The visibility measured by the weather station was often low in coastal waters and larger on the open ocean, see figure 7.1. Warm continental air flowing onto the cold water of

the upwelling region frequently led to fog. This was the case on December 11th, 2012 close to Lima, resulting in fog and high NO_2 concentrations around the ship. Except for these situations, air and seawater temperature were mostly the same. Wind speeds were moderate and mostly below $10\frac{m}{s}$.
The prevailing wind direction was from south-south-east. Backward trajectories using HYSPLIT [Draxler and Hess, 1997] indicated that most of the air was not in contact with South America within the previous five days. A comparison with the ship-based weather station showed that for coastal measurements modelled and measured wind directions did not agree, probably due to the coarse grid of the GDAS data. The global GDAS dataset is provided by NOAA at a resolution of 1° and is therefore not suitable for trajectory calculations along the coast itself, but gives an estimate on the dominating large-scale transport processes. NO_2 and HCHO as well as increased O_3 concentrations are therefore used as indicators for continental air masses.
Radiosonde launches will provide temperature and humidity profiles during the cruise, apart from transects along the coastline, where no launches were allowed. Here the MBL height was found at one km for all launches [per. comm. Steffen Fuhlbrügge, GEOMAR]. The locations with freshly upwelled and cold water are typically found close to the coast, compare figure 7.2. Here a stable inversion might be found, but no profile data is available. Furthermore MAX-DOAS measurements cannot deliver any profile information for water vapour in most of these cases due to fog.

7.1.1. List of measurements

Details for each work package can be found in the cruise report Bange [2013].

1. Conductivity Temperature Density (CTD) and Oxygen Measurements in seawater
2. Current Observation
3. Shipborne Microstructure Measurements
4. Oceanic upwelling Velocity
5. Dissolved Oxygen and Hydrogen Sulphide Measurements
6. Dissolved Nutrients
7. Phytoplankton, Coccolithophorid Diversity, Dissolved inorganic carbon (DIC), TA, pH, Chlorophyll-a (Chla)
8. Dimethyl sulfide (DMS), Dimethylsulfoniopropionate (DMSP), Dimethyl sulfoxide (DMSO)
9. Dissolved and Atmospheric Halocarbons, Halogens, Radio Sounding, Disdrometer, Phytoplankton Pigments, Flow Cytometry, DNA
10. Isotope Composition of Halocarbons and Molecular Biological Analyses
11. Measurements of oceanic N_2O, CO, CO_2, CH_4 and short-lived N-compounds
12. Microbial Processes of the N Cycle
13. Nitrogen Isotopes and N_2/Ar
14. Sea-Surface MicroLayer (SML)
15. Air-Sea Gas Exchange, Wind Waves, CO_2 Eddy Covariance

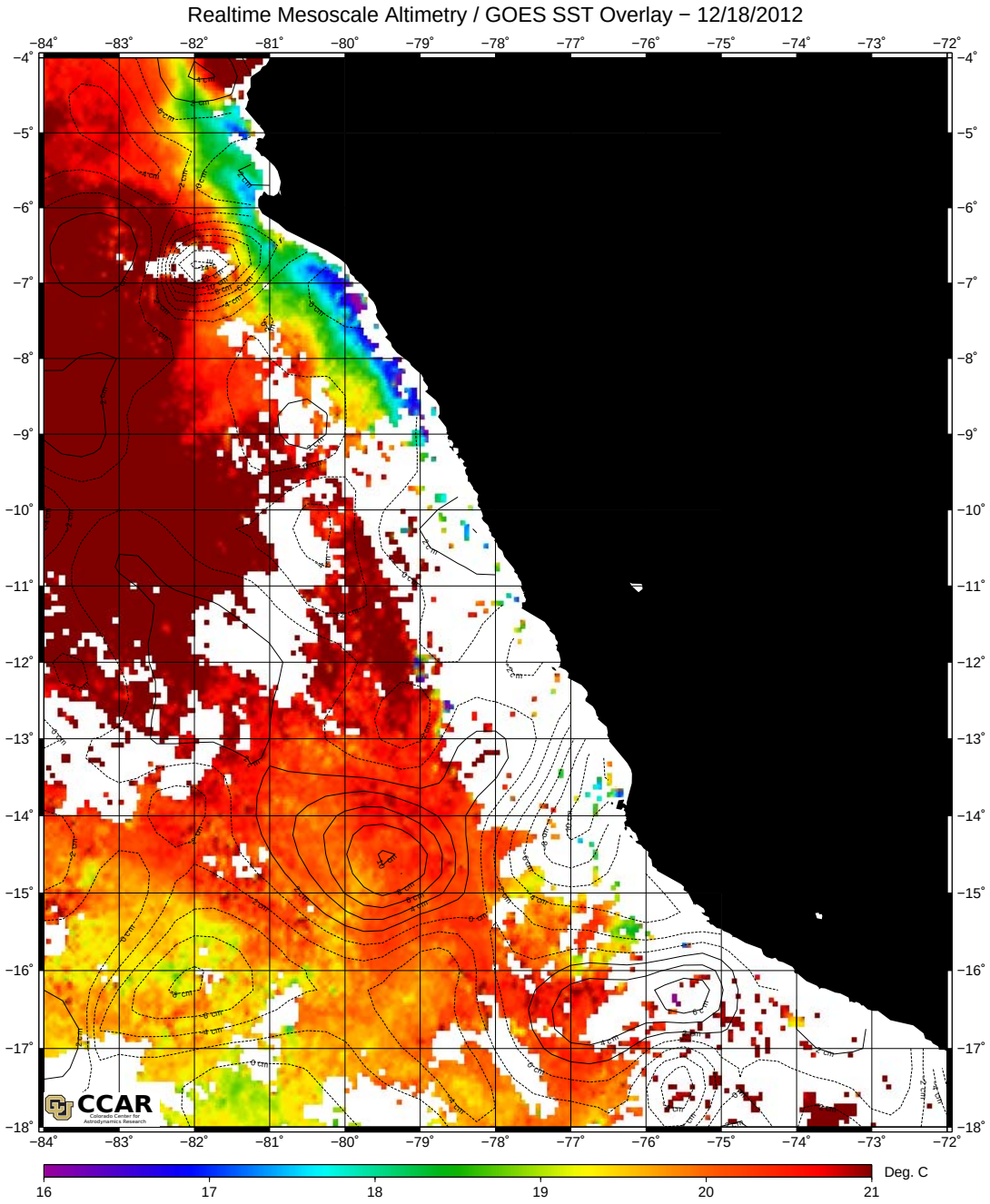

Figure 7.2.: SST and altimetry maps from December 18th, filtered for clouds, provided by CCAR. The upwelling cold water can be found in close vicinity of the coastline. The altimetry data indicates the presence of mesoscale eddy structures (around $14°30'S, 79°30'W$,), which have been probed within the cruise.

16. Volatile Organic Compound (VOC) and Oxygenated Volatile Organic Compound (OVOC) - MPIC Mainz
17. Differential Optical Absorption Spectroscopy (DOAS) Measurements of Reactive Trace Gases
18. Aerosol Sampling

The aerosol samples analysis with respect to bromine content might be biased due to the method of extraction of the filters with HCl, an analysis for iodine content is not planned [A. Baker, pers. comm.].

7.1.2. Ozone Monitor

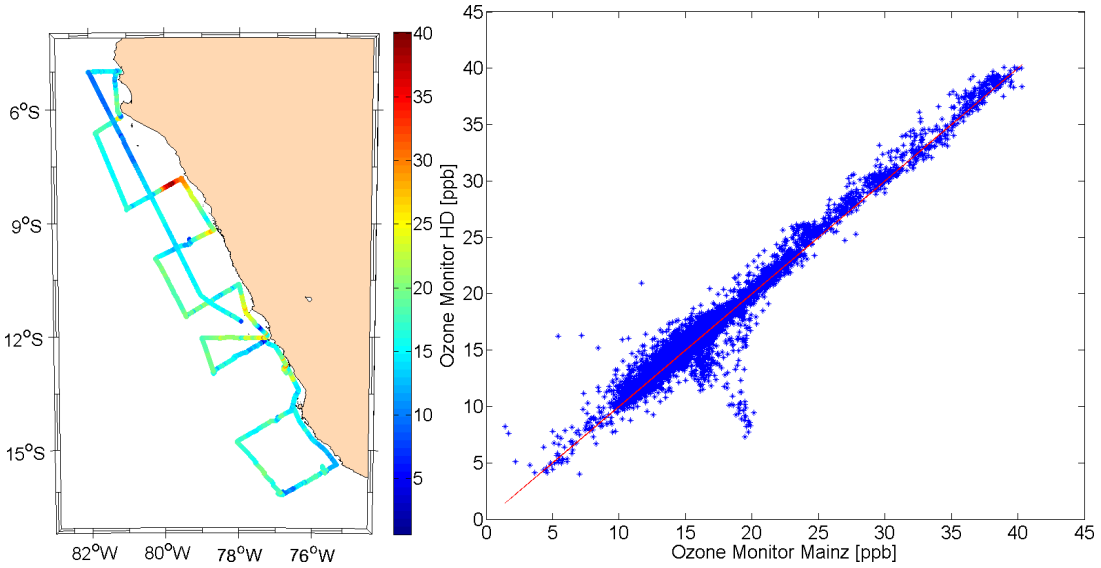

Figure 7.3.: Ozone mixing ratio along the cruise track during M91. The maximum at 8°S coincides with low visibility, indicating warm continental air transporting larger amounts of ozone. Both ozone monitors, from IUP HD and MPIC Mainz, showed good agreement. Individual data points did not agree, which often coincided with exhaust air from the ship reaching only one of the inlets, which were placed 3 m apart from each other.

A *Horiba* Ozone Monitor APOA350E (SN: 563179044) was operated from December 1st from the harbour of Lima until December 25th. As halogen oxide concentrations and especially BrO concentrations were low (typically <3 ppt), no ODE were expected and also not observed. The calibration of the ozone monitor was done using the second Horiba Monitor at the IUP as reference, which has been calibrated before within the work of Buxmann [2012] in Bayreuth. As seen in figure 7.3, this calibration also agreed with the calibration of the ozone monitor operated by MPIC Mainz.
Short ODE were still observed, caused by turbulent mixing of ambient air with air from the exhaust of the ship and following NO_x-mediated ozone destruction. This effect shows

small-scale turbulence, smaller than the distance between the inlets of the ozone monitors (about 3 m apart from each other) and the CE-DOAS (2 m), which would explain that some ODE were only observed by one of the ozone monitors and additionally the short peaks within the NO_2 concentrations of the CE-DOAS measurements do not appear simultaneously. The effect of ship emissions needs to be considered when evaluating the NO_2 mixing ratios measured by the CE-DOAS instrument.

7.1.3. MAX-DOAS

Measurements started on December 1st, stopped December 25th 2012, and were performed almost continuously, except for horizon scans and individual software problems. The MAX-DOAS instrument was the Ship-MAX-DOAS instrument with an Acton 350i spectrometer described in section 4.2. The elevation sequence throughout the cruise was 90°, 40°, 20°, 10°, 6°, 4°, 2°, 1°. The alignment of the telescope was tested twice during the cruise using horizon scans to check if it was still correct, after it has been adjusted initially in the lab before shipping the instruments. During twilight ($85° \leq \text{SZA} \leq 105°$) spectra were recorded alternating at 90° and 2° elevation. At night ($\text{SZA} \geq 110°$) dark current and offset spectra were recorded automatically. On Dec. 24th additional elevation angles (60°, 30°, 15°, 3°) were added to the regular sequence. A time series of dSCDs is shown in figure A.6.

7.1.4. CE-DOAS

The CE-DOAS instrument was the same as during the SHIVA campaign, except for some improvements. For details see section 4.4.
Every time the mirrors had to be cleaned or adjusted, the measurement sequence was divided into separate periods, called configurations. An overview of the obtained measurement data can be seen in figure 7.4. The overall loss in intensity during measurements was due to dirt and sea spray on the mirrors which were not easy to remove; additionally the adjustment of the LED might not have been optimal at the end of the campaign. The drops in intensity with short duration were caused by fog. The difference in intensity of purge air and normal measurements is caused by water vapour absorption and aerosol. During measurement periods usual intensities were about 60% of the purge air reference intensities. The measured path lengths during purge air measurements were controlled using wavelength resolved cavity ringdown measurements. To estimate the stability of the instrument and to check if the purge air measurements were contaminated in any way, it turned out to be useful to evaluate all purge air measurements in the same way the measurement data was evaluated.

7.1.5. Halocarbons

The group of Birgit Quack from GEOMAR measured some halocarbon species using a GC-ECD and a GC-MS (as during MSM18/3, SHIVA and described in Hepach et al. [2013]). Data is available for the seawater concentration of CH_3I, CH_2Cl_2, $CHCl_3$, CCl_4, CH_2Br_2, CH_2ClI, $CHBr_2Cl$, CH_2BrI, $CHBr_3$ and CH_2I_2 for different depths. The

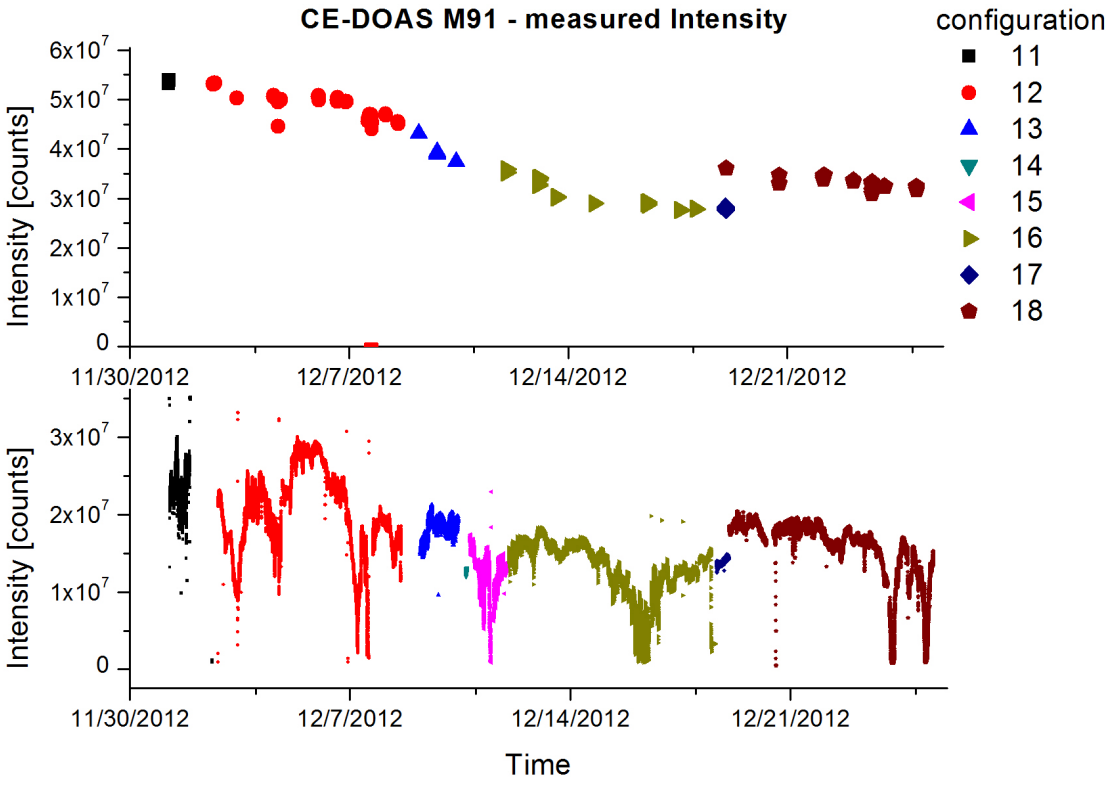

Figure 7.4.: Overview of CE-DOAS measurement data during SOPRAN M91. The first plot shows the intensity of the purge air measurements, the second plot shows the intensities of the actual measurement spectra. *c12* and *c16* could be used for relatively reliable retrievals of IO using correction spectra calculated from night-time fit residuals. *c18* showed high NO_2 concentrations (> 0.5 ppb) along the coast.

measurements were started around December 12th, i.e. when RV Meteor passed Lima at $\approx 12°$S going south. For CH_3I, CH_2I_2 and CH_2ClI preliminary data agreed for both instruments, all other compounds showed differences. $CHBr_3$ from the GC showed a similar behaviour as CH_3I. The largest concentrations in seawater were found for all species on the transect *I* leading from the coast southwest to the open Pacific at around 14.5°S on December 16th-20th.

3-hourly taken air canister samples were analysed for atmospheric VSLS after after the cruise, but so far only preliminary data is available for $CHBr_3$, CH_2Br_2, CH_3I, CH_2I_2 and CH_2ClI. Of these, no large variations were found for the 'long-lived' species $CHBr_3$ and CH_3I. For CH_2I_2 and CH_2ClI variations were found of the order of 8-10 times larger atmospheric concentrations during the time when larger surface seawater concentrations were found. In preliminary data typically both compounds showed mixing ratios of

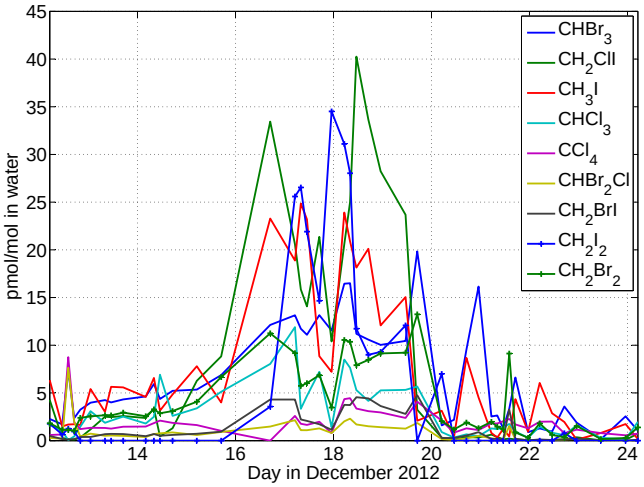

Figure 7.5.: Preliminary data for measurements of halocarbons in surface seawater [pers. comm. H. Hepach, GEOMAR]. The largest concentrations were found for all species on the transect *I* leading from the coast southwest to the open Pacific at around 14.5°S on December 16th-20th.

0.4 ± 0.1, up to 2–3 ppt during December 16th-20th at night [per. comm. Steffen Fuhlbrügge, GEOMAR].

7.1.6. VOCs

The PTR-TOF-MS instrument of the MPIC Mainz, which was also employed at other locations before [Veres et al., 2013], measured a large number of volatile compounds throughout the campaign. Until now the datasets for methanol, acetone and DMS are available. Measurements of glyoxal were not possible due to technical reasons.
During the days of the maximum halocarbon concentrations in seawater, December 16th-20th, the DMS concentration in air increased, while acetone decreased.

7.2. Results

For the retrieval of vertical profiles of trace gases from MAX-DOAS measurements and thus also surface volume mixing ratios which can be compared to the results from CE-DOAS measurements, it is necessary to retrieve aerosol profiles first. These profiles are then used in the profile retrieval of the respective trace gas.
The first trace gas which is compared for the simultaneous CE-DOAS and MAX-DOAS measurements is NO_2: During M91 it was clearly detected by both instruments, often at column densities of more than 10 or up to 100 times above the measurement error. CE-DOAS and MAX-DOAS surface mixing ratios are compared to validate the retrieval of the MAX-DOAS data and the path length calibration for CE-DOAS measurements. The result of the comparison motivates then the comparison of mixing ratios for IO and Glyoxal for both instruments and the absolute mixing ratios for other trace gases such as BrO and HCHO from MAX-DOAS measurements. These trace gases are typically

not as clearly detected as NO_2, if at all.
Trace gas profiles for a day without large continental influence is shown in figure 7.23. During some days the measurements at the ship's location were significantly influenced by continental, polluted air, as shown in figure 7.8 and 7.12.

7.2.1. Aerosol retrieval

For the aerosol retrieval the inversion algorithm implemented in Yilmaz [2012] was used on a 100m grid up to 4km height. The surface albedo was set to 0.05, the O_4 cross-section was scaled with 1.25 as reported before in Großmann et al. [2013] and Clémer et al. [2010]. This led to a minimum in the χ^2-value of the retrieval procedure (see also subsection 3.2.4.2 for details) when comparing the retrieval results on a relatively clear day (12/24/2012, no clouds, but limited visibility, see figure 7.6. Additional elevation angles are available.) for scaling factors of 0.9, 1.0, 1.1, 1.25 and 1.4. The minimum of χ^2 was found for a dSCD-scaling factor of 1.25.
An exponentially decreasing a-priori with an AOD of 0.05 with a scale height of 2km was used. For aerosol scattering, an aerosol single scattering albedo of 0.95 and a Henyey-Greenstein phase function with an asymmetry parameter of 0.72 was assumed. The O_4 data was retrieved using the cross-section by Hermans et al. [1999]. Intensities were not reproduced on cloudy days, therefore they were not used to retrieve aerosol profile information. This had also been observed before by Yilmaz [2012].
The time resolution of the profile data is 15 minutes.
No elevation offset was necessary to be introduced, which was confirmed by horizon scans during the cruise.

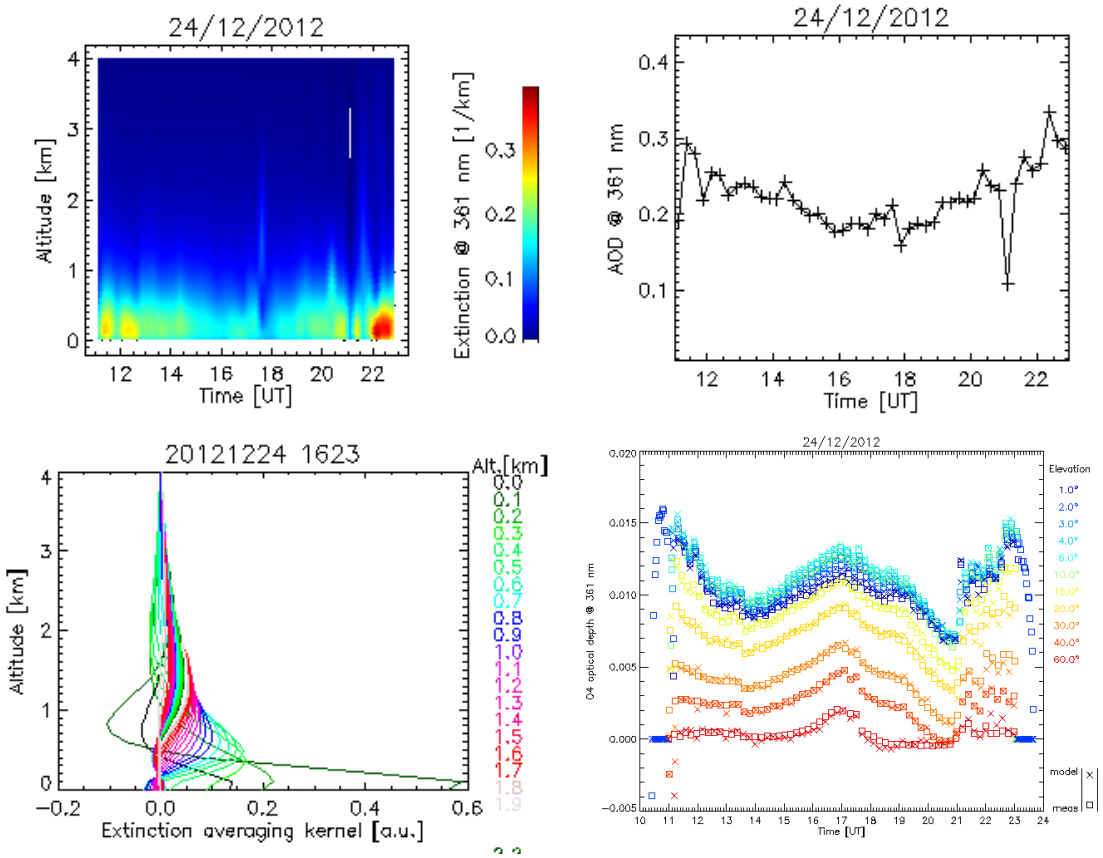

Figure 7.6.: December 24th, 2012: A clear day during which also an extended elevation angle sequence was recorded. The retrieval was performed using an O_4 dSCD scaling factor of 1.25. **Top left:** Aerosol extinction profile **Top right:** total tropospheric AOD **Bottom left:** Averaging kernel matrix **Bottom right:** Measured and modelled O_4 absorption at 360.8 nm.

7.2.2. NO_2

NO_2 concentrations were low throughout the cruise, only close to Lima due to influences of urban emissions as well as more ship traffic and emissions from local fishing boats higher NO_2 concentrations were measured.
Close to Lima on 12/11/2012, NO_2 concentrations of up to 4 ppb were observed. During the morning it was foggy and the ship's weather station indicated wind from Lima, from the East. HYSPLIT trajectories based on GDAS data cannot reproduce this situation, most probably due to its limited spatial resolution. High HCHO VMR of 4 ppb were observed simultaneously with lower IO mixing ratios and dSCDs than on the open ocean. (see figure 7.7 and figure 7.8 for the corresponding profiles)
With increasing visibility indicated by the weather-station, the aerosol and IO profile retrieval also indicates an increasing information content of the profiles of 3 and 2, respectively. (compare 3.2.4.2)

7.2.2.1. CE-DOAS

Most of the observed NO_2 probably originated from the ship's exhaust or other ships, since the NO_2 VMR changes rapidly over time, compare figure 7.9. A polar plot shown in figure 7.10 shows the distribution of two indicators for local pollution of the measured air within the CE-DOAS resonator with respect to the relative wind direction: fast changes in NO_2 VMR and high NO_2 VMR indicate both local emission sources in most cases. Furthermore the normalized frequency distribution of the relative wind direction is shown. The highest NO_2 values and changes are observed for wind from portside (the instrument was on starbord side), while the prevailing direction of the relative wind was almost straight ahead. This means that most NO_2 reached the CE-DOAS instrument indirectly via turbulence next to the ship downwind and a small part was transported directly from the exhaust to the CE-DOAS instrument (220°).
The typical NO_2 fit error was 14 ± 5 ppt at 1000s exposure time (typically 39 ± 17 ppt at 10s). Taking into account residual structures, the detection limit was 100 ppt NO_2.
Correcting the effects described in subsection 5.7.1 could lower the fit error by a factor of two at a time resolution of 1000s and consequently the detection limit even by a larger factor. If the structures, which have been observed, can be obtained from another source, or complete absence of NO_2 for a certain measurement period could have been guaranteed, these detection limits would apply.

7.2.2.2. MAX-DOAS

The comparison of the MAX-DOAS and CE-DOAS data showed in general good agreement, even though most data was close to the detection limit and if there were any elevated NO_2 mixing ratios, they were often caused by our ship's emissions and turbulence around the ship as can be seen from figure 7.10. There was also one case in which the MAX-DOAS looked along the plume of the ship, while the CE-DOAS also was affected by the plume. The MAX-DOAS showed lower NO_2 VMRs due to dilution effects.

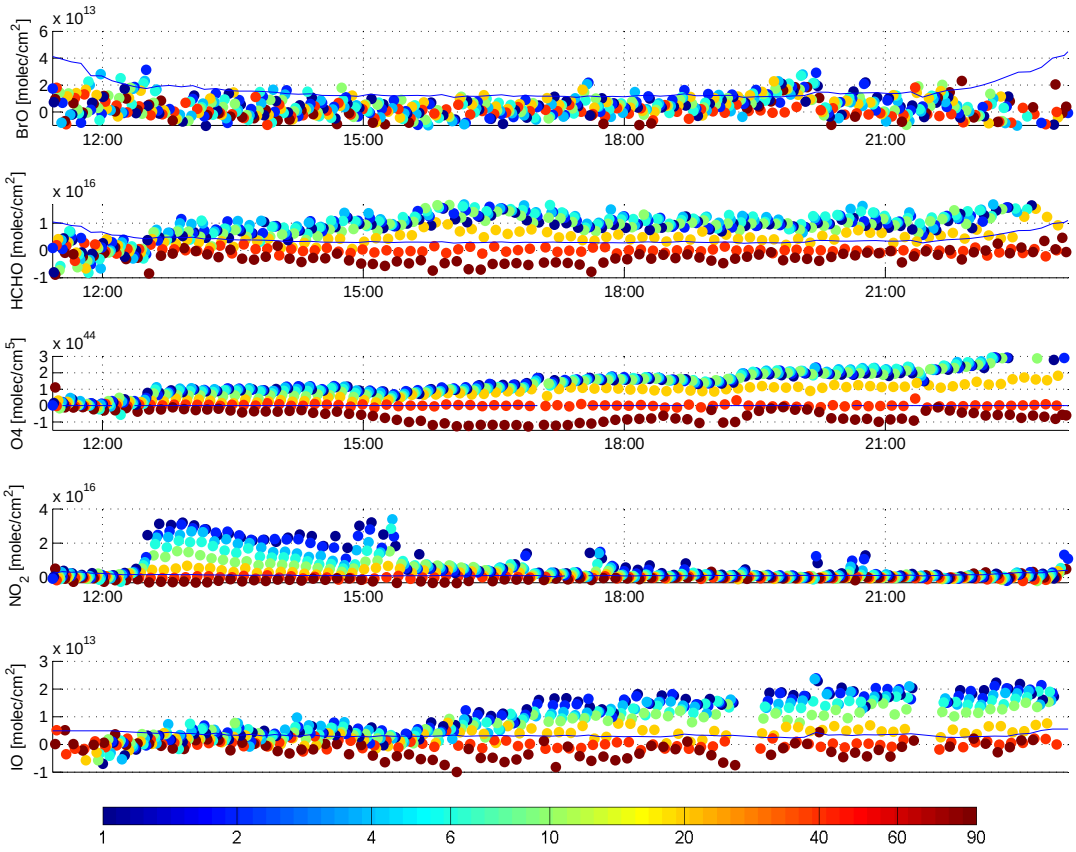

Figure 7.7.: MAX-DOAS measurements during 12/11/2012 approaching Lima/Peru (12° 2' S, 77° 1' W) from the north and leaving towards west. Easterly winds brought polluted air from the city which led to an increase of NO_2, HCHO and a decrease in IO. A part of the decrease in IO VMR is caused by lower visibility than in clean air (lower O_4 dSCD). The blue line indicates the measurement error, estimated by the double fit error.

The lowest NO_2 mixing ratios of several 10 ppt were observed on 9th and 10th of December as shown in figure 7.11, coinciding with the highest BrO mixing ratios during the cruise, shown in figure 7.14.

The agreement of NO_2 surface volume mixing ratios plotted in figure 7.13 shows that the inverse profile modeling as well as path length measurements of the CE-DOAS setup are correct (or wrong by the same factor). This is important for the interpretation of the IO profile inversion, since these are closer to their respective detection limits.

For the whole duration of the cruise, a correlation of MAX-DOAS and CE-DOAS data is not explicitly found. The reason is the high number of local NO_2 emissions by fishing vessels or from R/V Meteor itself, which is usually not detected by the MAX-DOAS due to the geometry of its measurements and the time resolution needed for the retrieval of

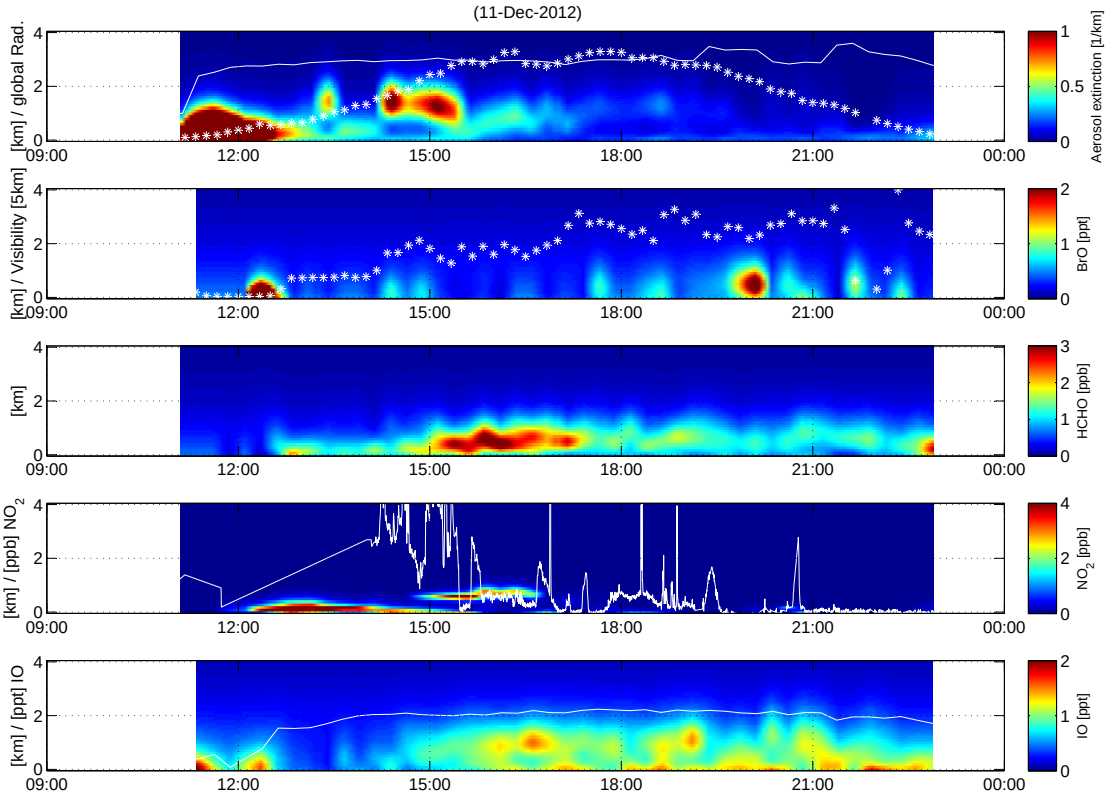

Figure 7.8.: Vertical profiles of Aerosol optical density, BrO, HCHO, NO_2 and IO corresponding to dSCDs shown in figure 7.7 from 12/11/2012. Any retrieved concentrations before 13:00 UTC can be discarded. As shown by the visibility data from the weather-station, the light-paths were short due to fog which resulted in small values for O_4-dSCDs. IO VMR increased to typical values on the open ocean after the NO_2 concentration dropped to values below 2 ppb. HCHO VMR were still high, indicating continental influence. Maximum HCHO concentrations at 16:00 UTC were 4 ppb. The CE-DOAS NO_2 mixing ratios are plotted in white on top of the MAX-DOAS NO_2 profile. For aerosol and IO profile retrieval the white line represents the number of degrees of freedom.

a complete vertical concentration profile.

The plume shown in figure 7.12 was found 150km south of Lima on December 15th, close to *La Oroya*, a mining area which can also be seen on SO_2 maps from satellite observations [Carn et al., 2007]. Closer to the coast some larger towns and industrial areas can be found. HYSPLIT [Draxler and Hess, 1997] trajectories based on GDAS data show for this situation (18:00 UTC) that the air in the MBL arrived from south-south-east (in agreement with the ship's weather-station), while air-masses in a height of 1000 m and above arrived from the east, possibly explaining the enhanced HCHO

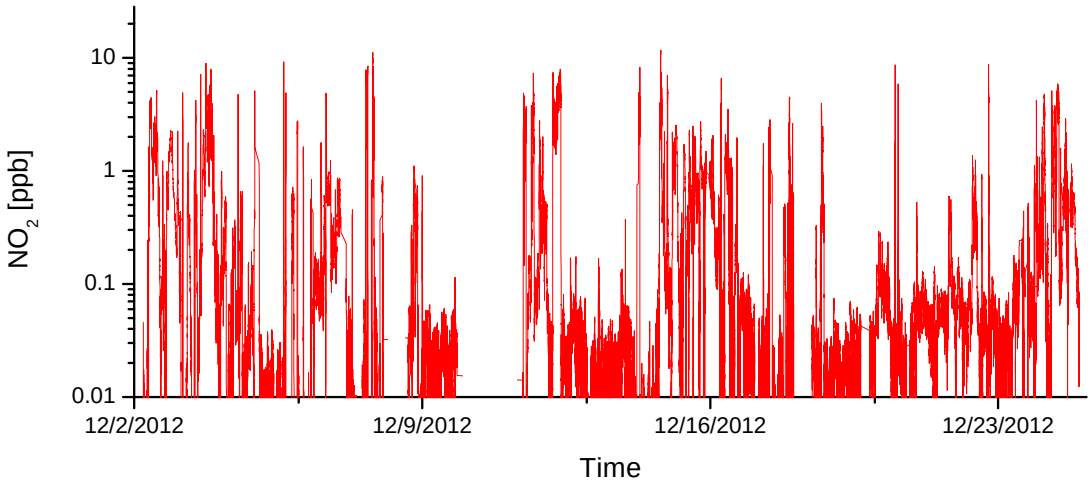

Figure 7.9.: NO_2 VMR from CE-DOAS measurements during SOPRAN M91 at two minute time resolution. The maximum NO_2 VMR observed was 25.9 ppb at 10s time resolution and the mean VMR was (0.34 ± 1.00) ppb.

values, but actually not allowing to identify the source of NO_2, which must be large due to its stability. The enhanced HCHO mixing ratios above heights of 1000 m might be due to biogenic and anthropogenic emissions on the land. The retrieval of SO_2 is not possible due to the limited spectral range of the spectrometer. Still, these air masses more than 1000 m above the ship originate from heights of 4000m above the Pacific according to the trajectories: They arrived from the west over Peru close to Lima, then changing their direction towards south-east due to the Andes. Here this air-mass is in contact with anthropogenic and biogenic emissions.
The height profile of IO shown in figure 7.12 for this day is surprising, since also for the continental air-masses with larger HCHO concentrations, significant amounts of IO are retrieved. This either indicates local emissions of iodine, which would require a higher MBL than the usual 1 km, or transport through a semi-polluted environment such as the Peruvian coast.

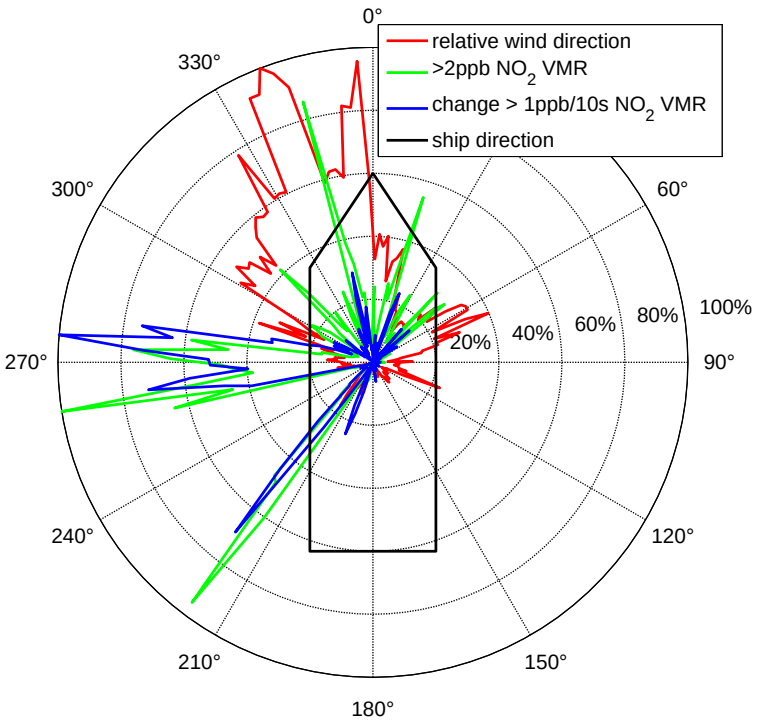

Figure 7.10.: Histograms showing the dependence of NO_2 mixing ratios on the relative wind direction on the ship. Only data points with wind speeds over 2m/s were included. (Maximum normalized to 100% for each plot, selected data points due to NO_2 criteria summarize each to about 5% of the total number of data points.)

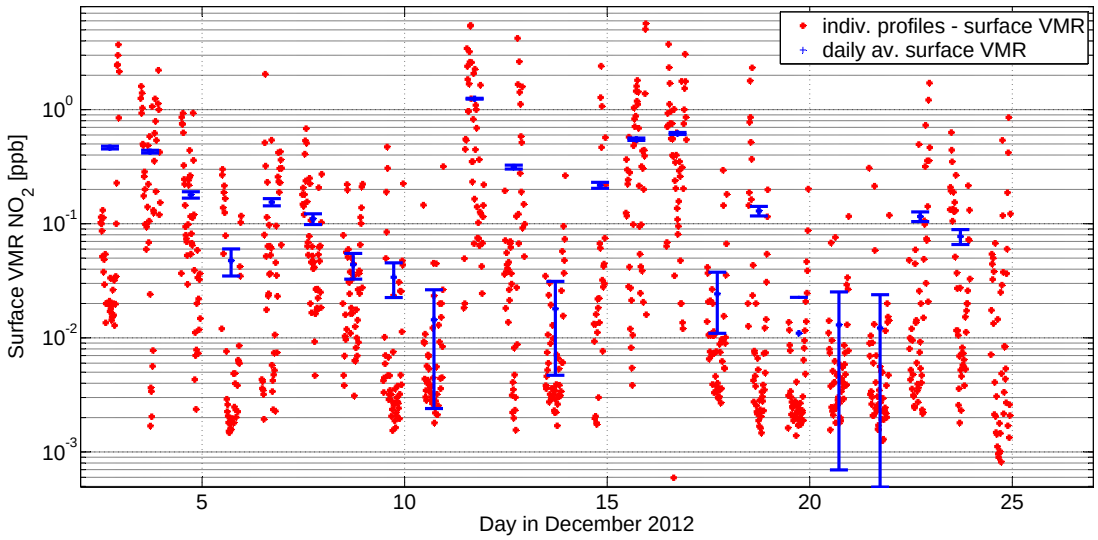

Figure 7.11.: NO_2 VMR from MAX-DOAS measurement during M91 and their daily averages, the error-bar indicating the typical retrieval error.

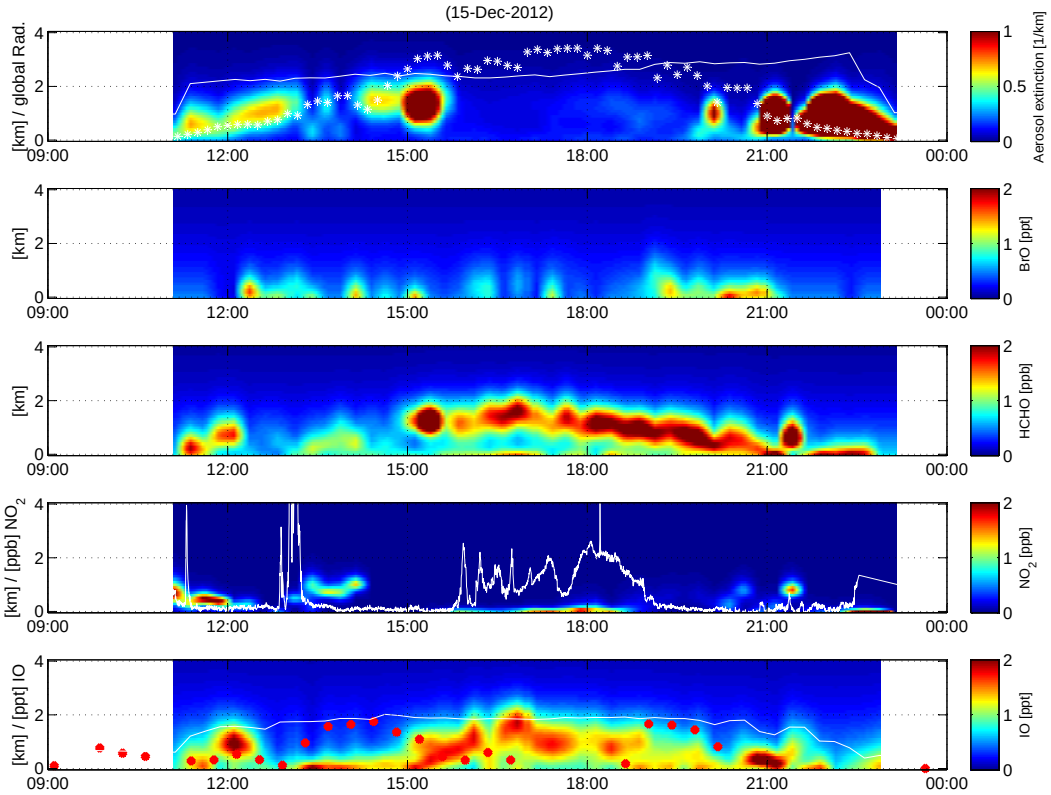

Figure 7.12.: For December 15th, a comparison of MAX-DOAS and CE-DOAS NO_2 data from M91: All retrieved vertical profiles are shown, the CE-DOAS IO mixing ratios are plotted in red on top of the MAX-DOAS IO profiles, for NO_2 in white, respectively. For the aerosol and IO profile retrieval the white line represents the number of degrees of freedom of the retrieval. The CE-DOAS IO VMR shown as red dots overlaying the vertical profile of IO during this time are not reliable due to high NO_2 absorption, but still show a behaviour which is also represented in the vertical profile data. A more detailed comparison of NO_2 surface VMR is shown in figure 7.13.

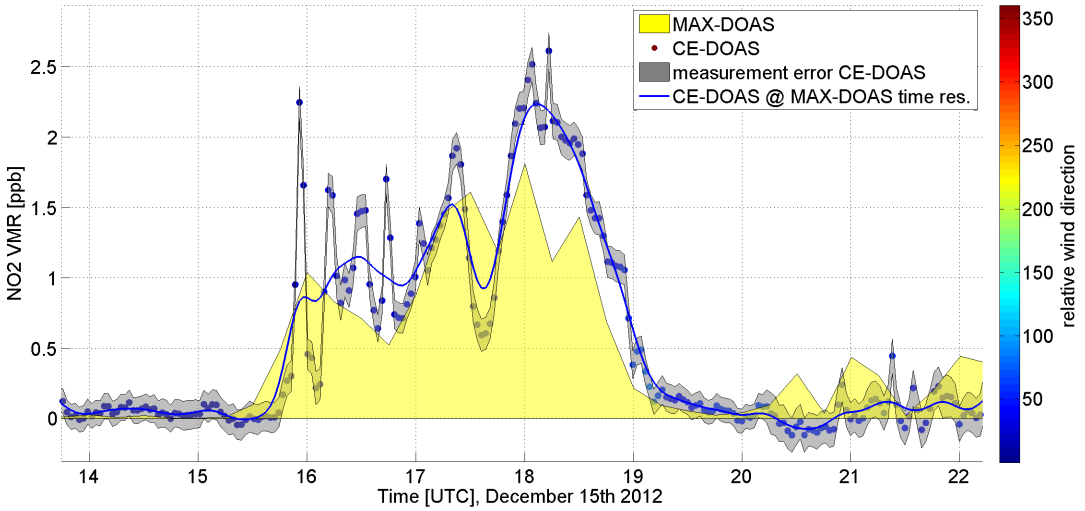

Figure 7.13.: For December 15th, a comparison of MAX-DOAS and CE-DOAS NO_2 data from M91: Surface mixing ratio of NO_2 from CE-DOAS and MAX-DOAS. This situation shows enhanced NO_2 concentrations for a duration of three hours, 150km south of Lima on December 15th, 12°33'S 76°52'W. The time lag between CE-DOAS and MAX-DOAS measurements of several minutes can be explained by transport effects and their different footprints of 2m and 10km, respectively. The wind came from starboard with a relative wind speed of 4-6$\frac{m}{s}$, i.e. it is not the ship's exhaust plume. The vertical concentration profiles are shown in figure 7.12.

7.2.3. BrO

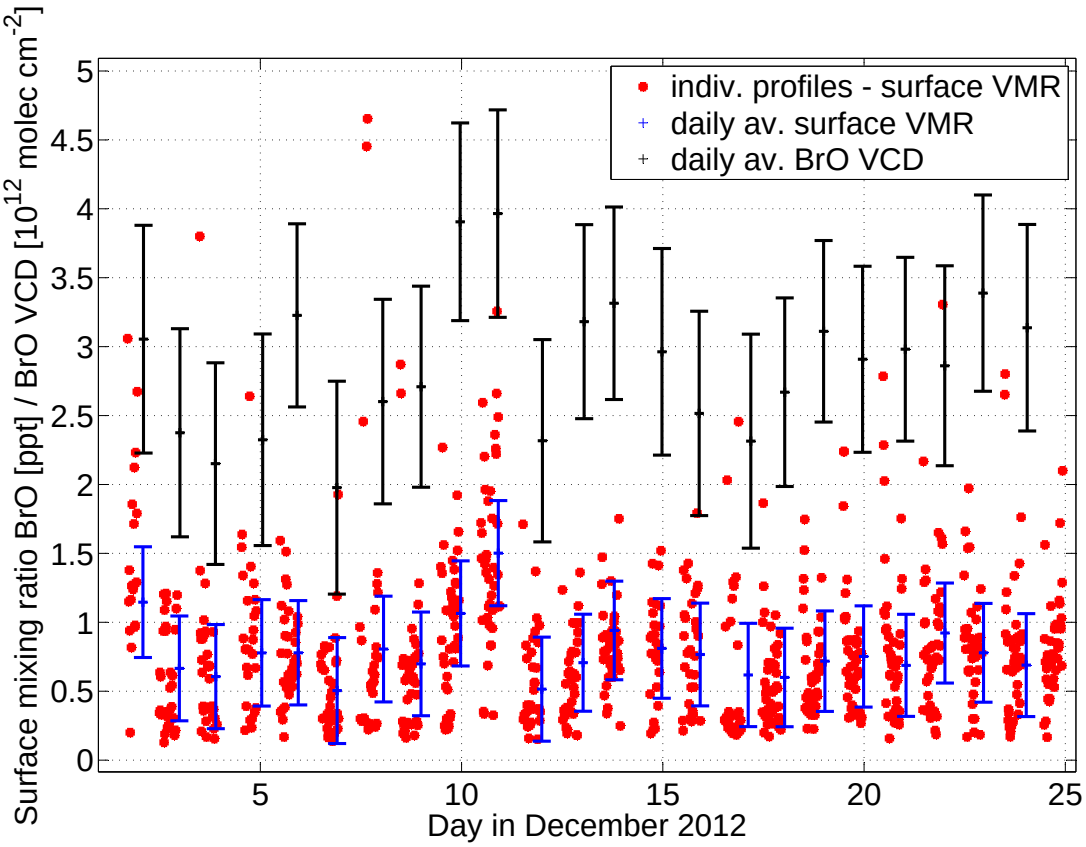

Figure 7.14.: Retrieval error weighted daily averages of BrO surface mixing ratios and tropospheric vertical column densities, and individual values for BrO surface VMR. Note that the profile retrieval does not allow for negative concentrations and therefore creates a positive bias when averaging mixing ratios. Still, averaged dSCDs for BrO are typically larger at small elevation angles indicating indeed to background of BrO below 1 ppt for the MBL.

The average fit error for BrO using the Greenblatt et al. [1990] literature cross-section for O_4 was $(7 \pm 2) \cdot 10^{12}$ molec cm^{-2} for a 1-minute spectrum, using a current Fraunhofer reference spectrum and an elevation angle of 3°. The distribution of BrO dSCDs during this time was $(8.5 \pm 12) \cdot 10^{12}$ molec cm^{-2} which would agree with a correction factor of 1-2 according to Stutz and Platt [1996]. These results are comparable to MSM18/1 (subsection 8.1.1) regarding the overall measurement error.
The only days on which BrO was elevated at 3° elevation with up to $3.6 \cdot 10^{13}$ molec cm^{-2} ($2.5 \cdot 10^{13}$ molec cm^{-2} when using the Thalman O_4 cross-section, see also subsection 5.1.1.1) were December 5th, 9th and 10th (see figure 7.15), which translates to 3–4 ppt BrO

within the lowermost 500m when performing radiative transfer modelling. The air masses at the ship during periods of higher BrO dSCD have all been within the lowermost 300m of the MBL during the last three days according to HYSPLIT trajectories. They are found outside the main upwelling close to Lima and mostly downwind from where the highest halocarbon concentrations in water were found after December 10th at 15°S (subsection 7.1.5). Additionally the surface VMR of NO_2 during these days is especially low. Due to technical problems the halocarbon measurements were not started before December 12th. On the 10th also high methanol concentrations were observed (subsection 7.1.6).
Vertical tropospheric BrO columns from the retrieved profiles yields $2-3{\cdot}10^{12}$ molec cm^{-2} BrO, with the exception of December 10th and 11th, yielding $3.5 \cdot 10^{12}$ molec cm^{-2} BrO. The retrieved error of the VCD is typically $7 - 8 \cdot 10^{11}$ molec cm^{-2}. On December 10th and 11th up to $9 \cdot 10^{12}$ molec cm^{-2} BrO were observed during 1-2 hours in the afternoon.

7.2.4. IO

Iodine monoxide was unambiguously identified during M91 in MAX-DOAS data and showed a diurnal cycle for CE-DOAS data as well. The CE-DOAS IO VMR values were only trustworthy in periods with low aerosol load and low NO_2 concentrations, but then it agreed well with the retrieved IO concentrations from MAX-DOAS observations (see figure 7.21).

7.2.4.1. CE-DOAS

Marine IO concentrations are still close to the current instrument's detection limits. For M91 the IO detection limit was 0.5 ppt for optimal conditions at a time resolution of 1000s, compare e.g. figure 5.44. The evaluation could then be still slightly improved by 20% for optimal conditions and even more otherwise, if correction spectra for various influences were extracted from night-time data, assuming that IO concentrations at night vanish. The length of a continuous data set of IO VMR during M91 was limited to the maximum time the mirrors stayed clean. Cleaning was time consuming and required readjustment of the instrument, therefore new references and eventually new correction spectra needed to be calculated.
None of the structures compensated for by the correction spectra correlated with the retrieved IO absorption.

7.2.4.2. MAX-DOAS

The average fit error for 60s spectra with an RMS of less than $3 \cdot 10^{-4}$ is $(1.4 \pm 0.4) \cdot 10^{12}$ molec cm^{-2}. This translates to a detection limit of ≈ 0.25 ppt. As shown in subsection 5.2.3.1, including a vibrational Raman spectrum for N_2 improved the typical fit error for low elevation angles by about 20%-30%. IO dSCDs are not affects, as shown in subsection 5.2.3.1. For single spectra the number of degrees of freedom in the residuals calculated from the entropy of the residual dataset is 90% of the maximum

possible value, corresponding to a structure width smaller than 2 pixels in typical residuals (compare subsection 3.3.2.3). This means that the fit error will not overestimate the measurement error and the detection limit is typically $2.8 \cdot 10^{12}$ molec cm^{-2}, corresponding roughly to ≈ 0.1 ppt. The first two principal components corresponding to 4% and 2% of the residual structures were not correlated with any tropospheric absorbers, only slightly to the Ring signal. The third component (1%) correlates with water vapour ($|\Delta\sigma|_{max} < 2 \cdot 10^{-28}$cm^2 molec^{-1}, compare figure 5.36) and due to their similar height profile also IO ($|\Delta\sigma|_{max} \approx 6 \cdot 10^{-18}$cm^2 molec^{-1}, corresponding to 1/4 of the maximum value of the IO cross-section). Co-adding of elevation sequences further reduced the fit error and the residual RMS.
Anja Schönhardt from Bremen provided averaged satellite VCDs from SCIAMACHY for the Peruvian upwelling region averaged from 2004-2011 for the month December and January. Also here the strongest signal was found closer to the coast, within the maximum upwelling. The vertical columns from these satellite agree with MAX-DOAS observations, but the different time scale of averaging needs to be considered. The overall distribution was also found in MAX-DOAS data from M77, see section 7.4.
The qualitative agreement of VCDs from M91 and SCIAMACHY does not provide information on the free tropospheric abundance of IO, since the satellite data was retrieved using a reference sector in the Pacific (at 40°S, 160°W and 10° into each direction). If there was a constant amount of background IO in the free troposphere, it would have cancelled out during the spectral retrieval.

7.2.4.3. Comparison

For config12 (December 2nd-6th, 2012) of the CE-DOAS measurements, a time series for MAX-DOAS surface volume mixing ratios and CE-DOAS results is shown in figure 7.21. When compensating a drift of apparent IO night-time concentration from CE-DOAS measurements (about 0.1 ppt/day), the correlation with MAX-DOAS observations yields $R = 0.53$ and is shown in figure 7.24. This correlation does not include night-time measurements. Assuming a concentration of IO measured by MAX-DOAS of 0 ppt at night, leads to $R = 0.80$, and calculating the correlation coefficient setting all night-time measurements to 0 ppt even $R = 0.91$.

7.2.5. HCHO

Formaldehyde was evaluated in the same wavelength range as BrO from 332–358 nm using a current Fraunhofer reference. Fit errors were $(1.8 \pm 0.5) \cdot 10^{15}$ molec cm^{-2} and dSCD were found up to $17 \cdot 10^{15}$ molec cm^{-2} at low elevation angles. As expected, the largest column densities were observed close to the coast and larger cities, such as Lima. A tropospheric VCD of $2 - -4 \cdot 10^{15}$ molec cm^{-2} or about 500–1000 ppt without large continental influence and close to Peru with tropospheric VCDs of $6 - 8 \cdot 10^{15}$ molec cm^{-2} and mixing ratios of up to 4 ppb were observed.
The slightly elevated layer of HCHO under marine background conditions as seen in figure 7.23 has also been reported by Peters et al. [2012].

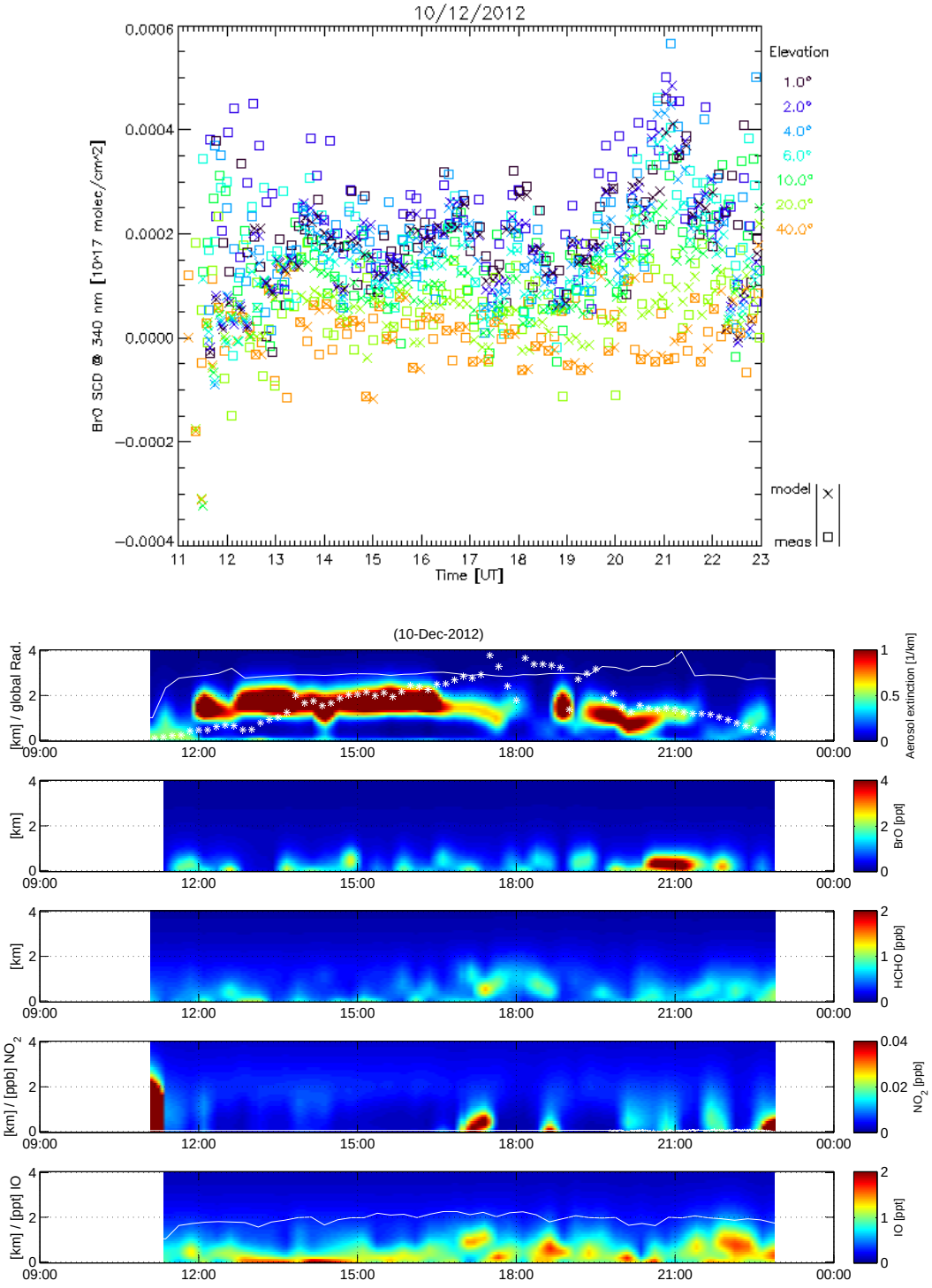

Figure 7.15.: VMR profiles for 12/10/2012 when the maximum BrO dSCD of $3.6 \cdot 10^{13}$ molec cm^{-2} was observed. The spectral retrieval was performed using the Greenblatt O_4 cross-section. The error of the profile retrieval of BrO at ground-level is 0.4–0.5 ppt. The CE-DOAS NO_2 VMR is overlayed in white and is found below 100 ppt. For the aerosol and IO profile retrieval the white line represents the number of degrees of freedom.

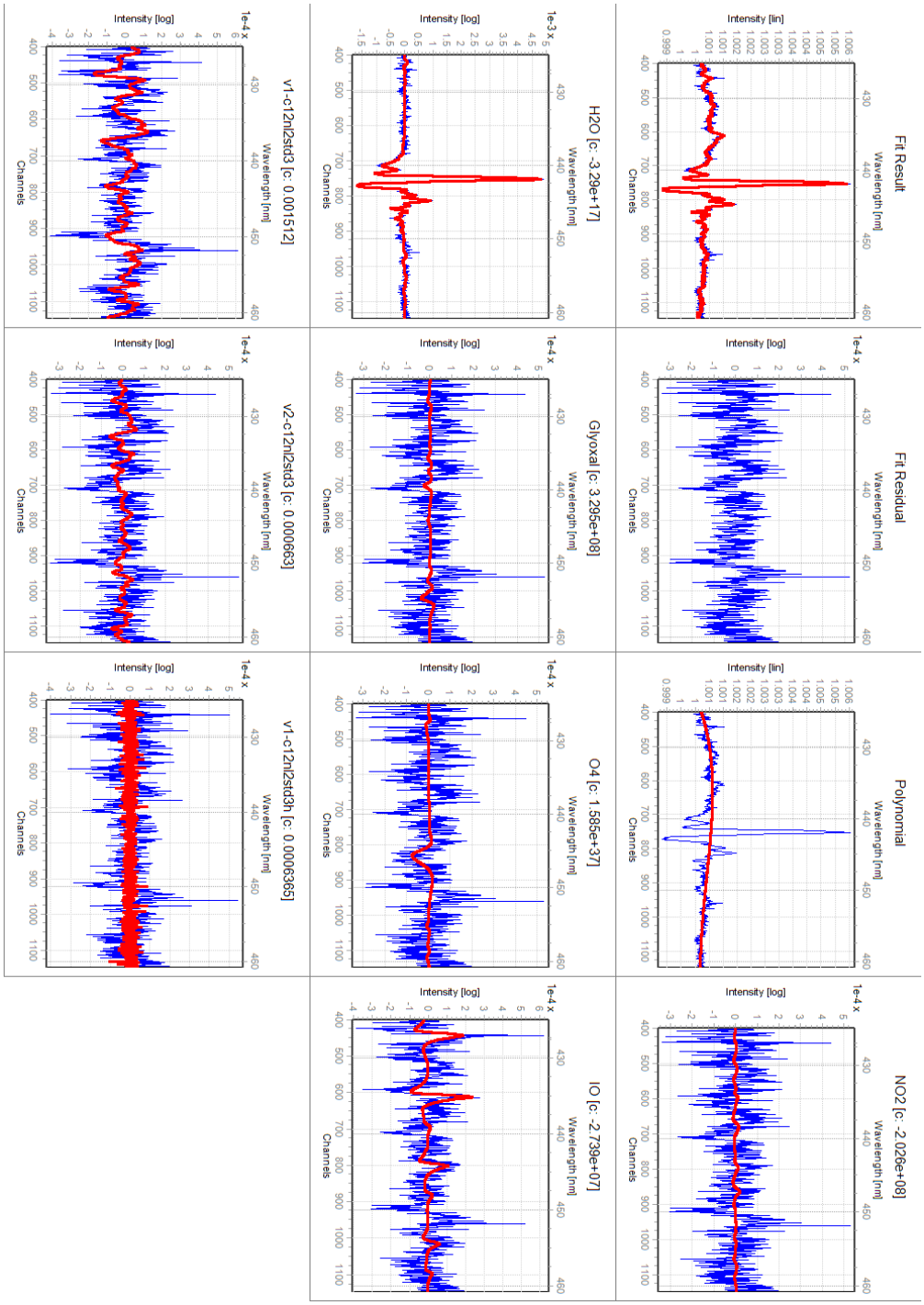

Figure 7.16.: Summed CE-DOAS spectrum #21900-21999 (1000s) with the maximal ratio of IO VMR and fit error of 8 from December 6th, 2012, 14:00 UTC at 8°20′S 80°26′W. The IO mixing ratio was 1.3 ppt, the RMS $1.8 \cdot 10{-}4$. The same residual structure at 453 nm as observed for MAX-DOAS measurements along longer light-paths is also observed here, presumably caused by water vapour absorption (compare figure 5.35).

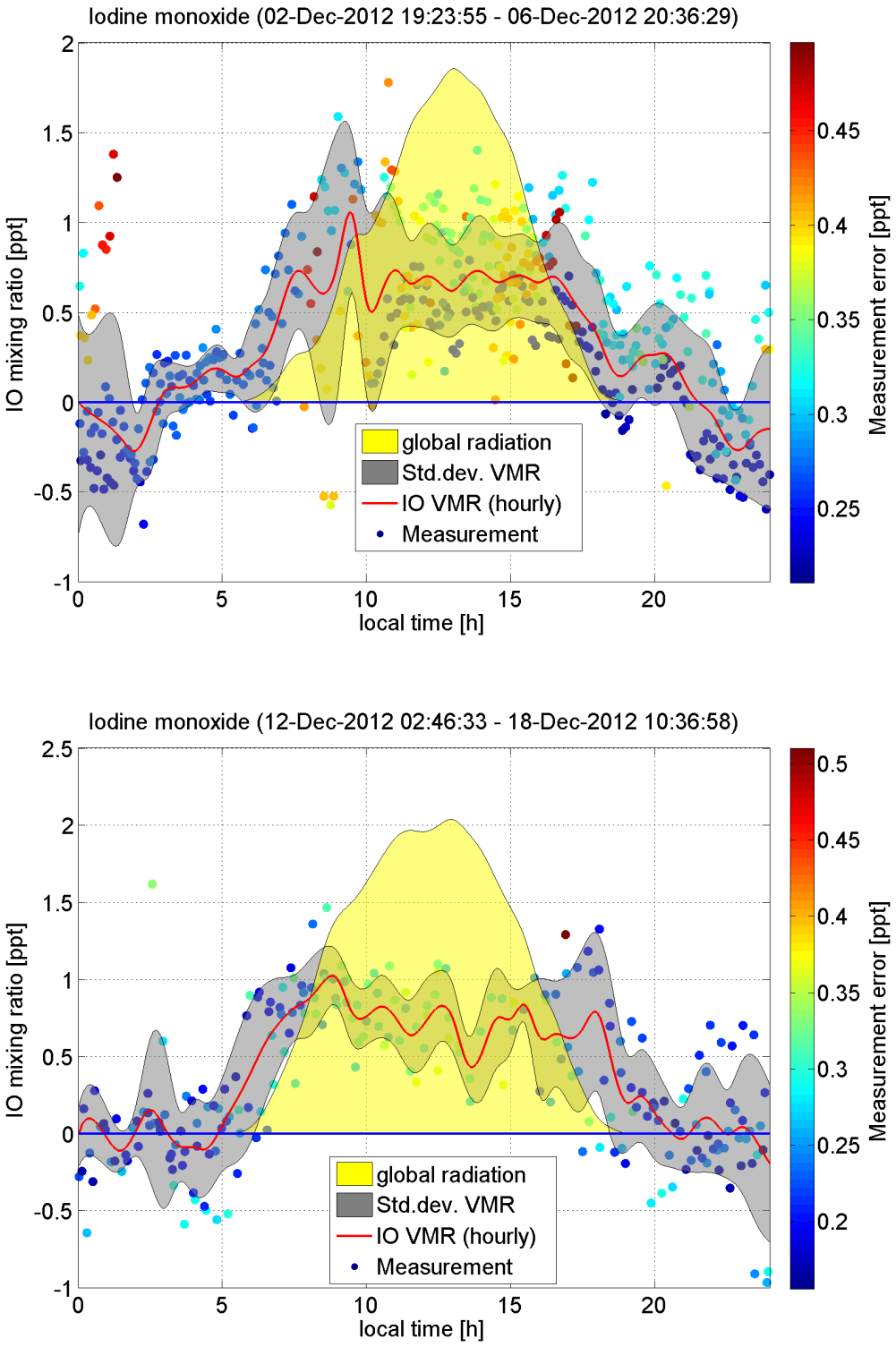

Figure 7.17.: Diurnal IO mixing ratios for the first measurement period outside (c12), the time series is shown in figure 7.21 together with MAX-DOAS data. The second plot shows the same for period (c16). The other periods did not allow for the generation of night-time correction spectra because of their duration, or they might have been affected by larger NO_2 concentrations (>0.5 ppb) as in the case for c18 during the last week of M91.

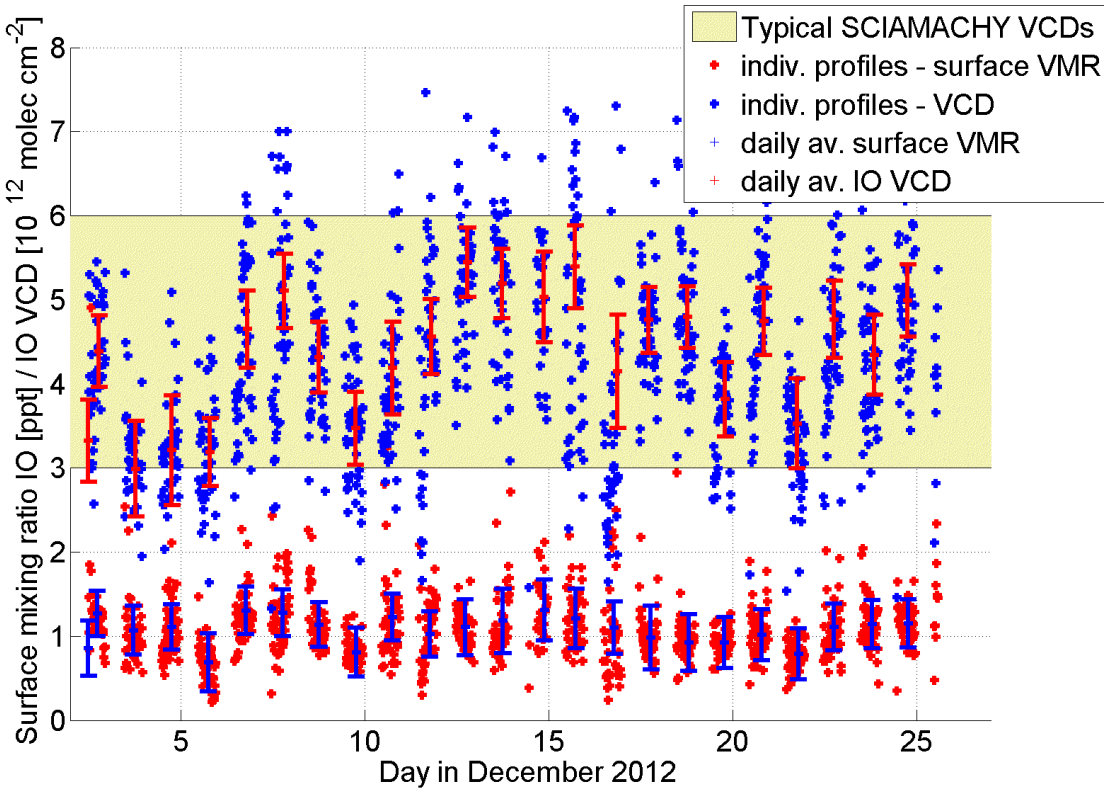

Figure 7.18.: IO surface volume mixing ratios and vertical column densities (VCDs) from MAX-DOAS measurements. The shaded area represents typical VCD values retrieved from SCIAMACHY shown in figure 7.19.

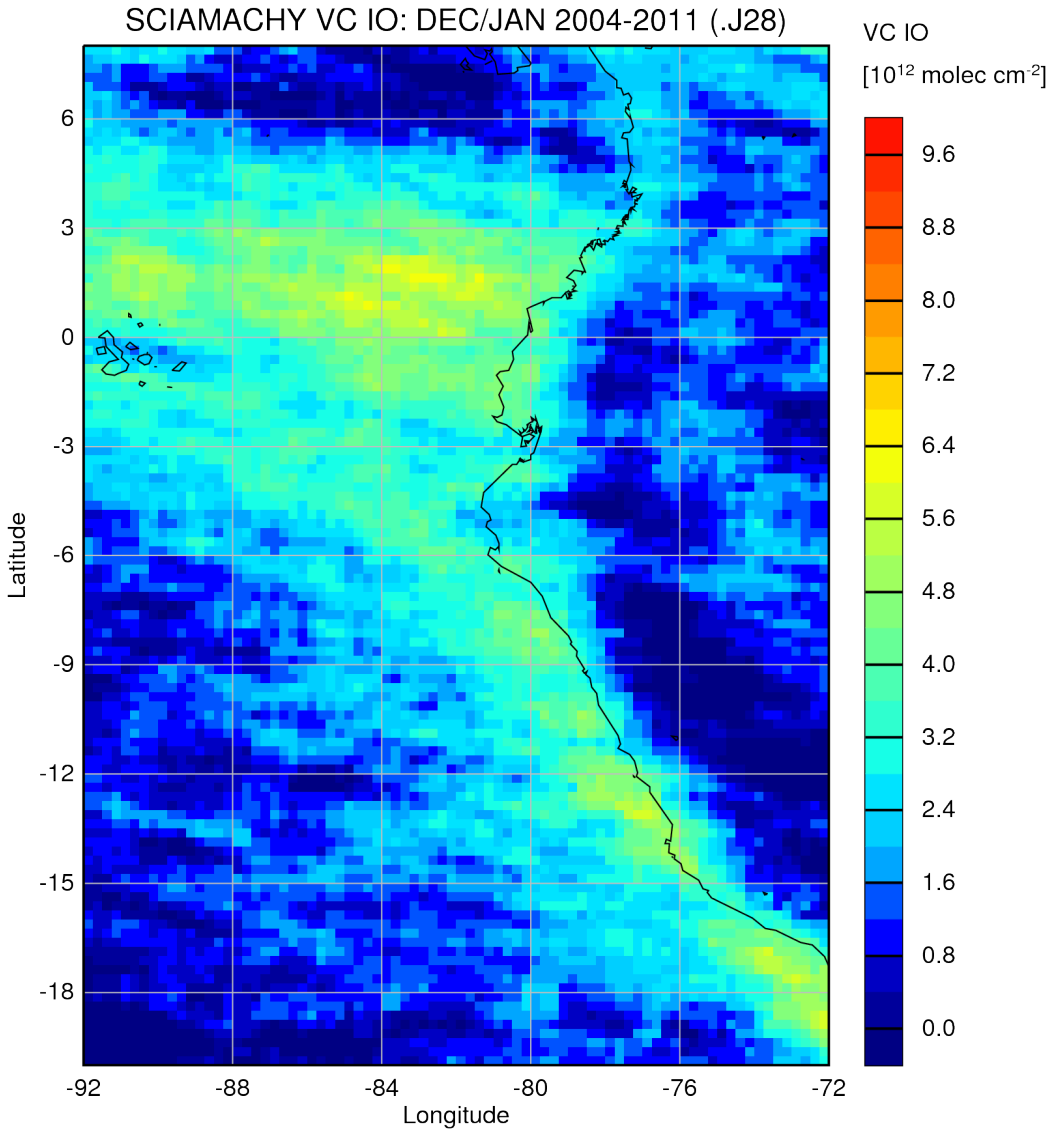

Figure 7.19.: IO VCD from SCIAMACHY from December and January 2004-2011, Courtesy of A. Schönhardt [Schönhardt et al., 2008, 2012]. These observations were not filtered for cloud-cover. Enhanced VCDs are still observed when applying a cloud-cover filter criterion [pers. comm. A. Schönhardt] . MAX-DOAS VCDs during M91 are shown in figure 7.18.

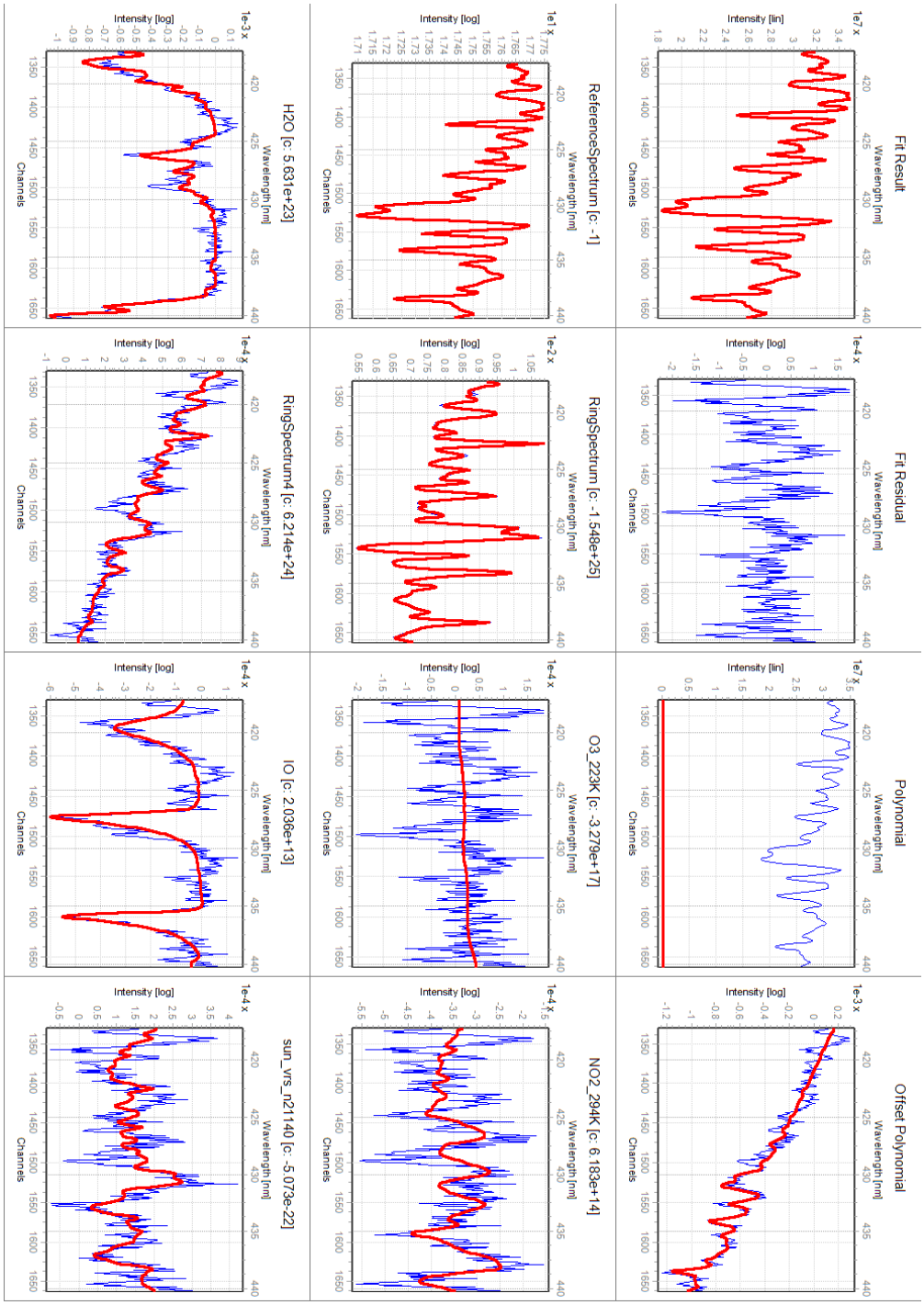

Figure 7.20.: MAX-DOAS IO fit for 16 co-added elevation sequences (#15147) on December 6th, 2012, around 14:00 UTC at 8°20′S 80°26′W, parallel to the CE-DOAS spectrum shown in figure 7.16 showing a concentration of 1.3 ppt. The IO dSCD of $2.04 \cdot 10^{13}$ molec cm^{-2} is 30 times larger than the fit error. The water vapour absorption bands were corrected according to table 5.8, but are still causing some residual structures. Both fits are based on spectra with a total exposure time of 16 minutes.

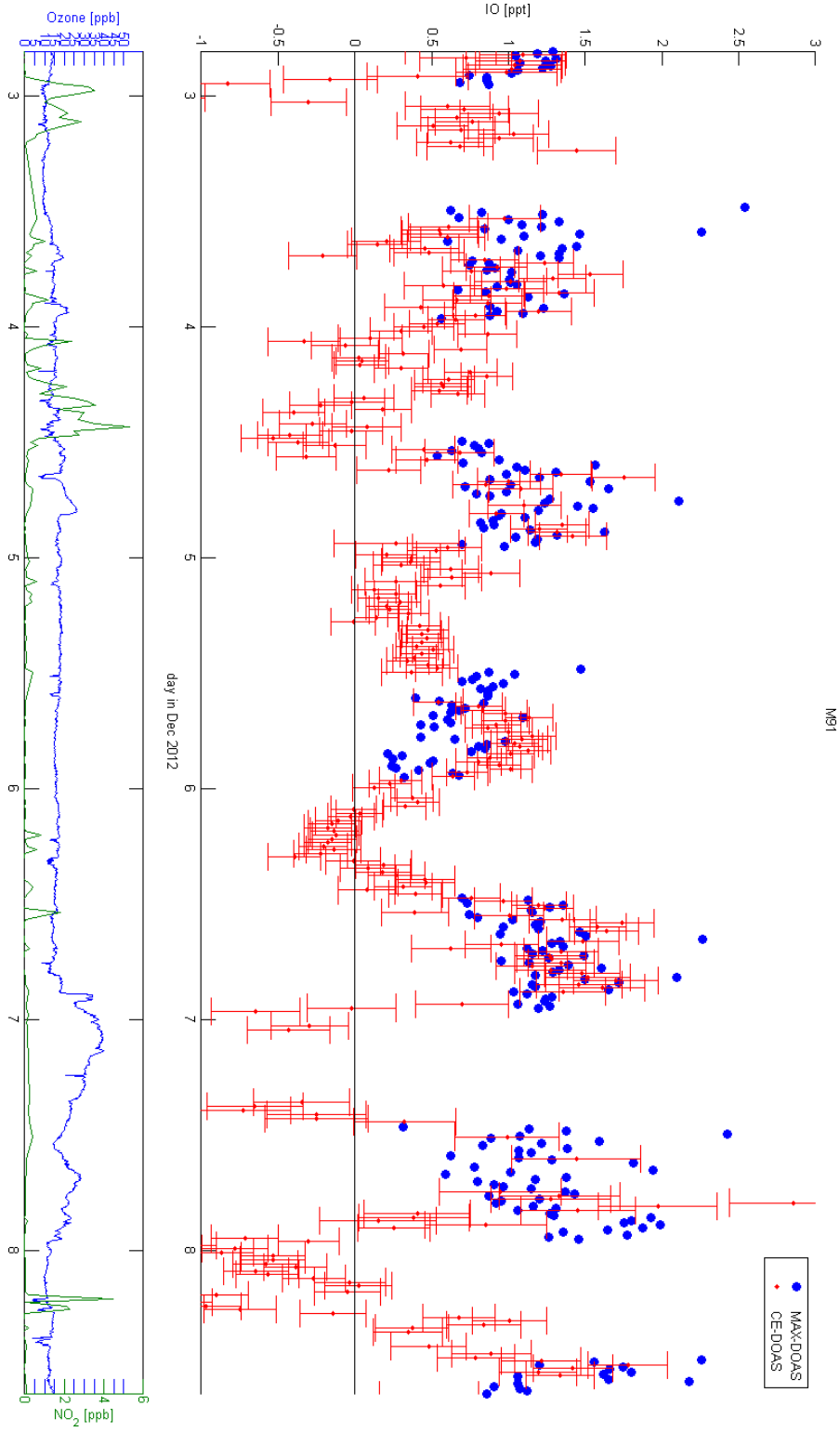

Figure 7.21.: Comparison of IO VMR obtained from CE-DOAS measurements and MAX-DOAS measurements during the first week of M91 (c12). Related aerosol and IO profiles for the December 6th are shown in figure 7.22. Errorbars indicate the double fit error of the CE-DOAS data. MAX-DOAS retrieval errors for surface concentrations are typically 0.4 ppt. Averaged diurnal concentrations are shown in figure 7.17 for this period.

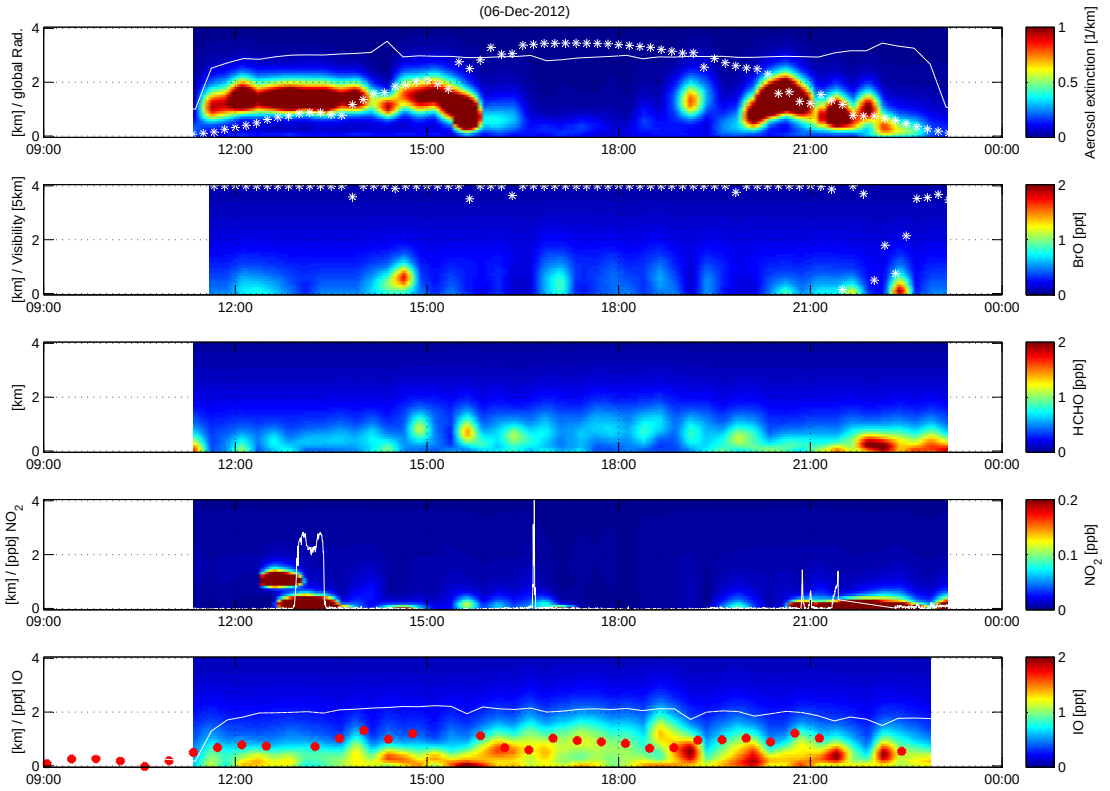

Figure 7.22.: MAX-DOAS profiles for 12/06/2012 shown also for IO surface mixing ratios in figure 7.21, recorded at 10°S, sailing from the coast towards the Pacific. The CE-DOAS IO mixing ratios are plotted in red on top of the MAX-DOAS IO profiles, for NO_2 in white, respectively. For the aerosol and IO profile retrieval the white line represents the number of degrees of freedom.

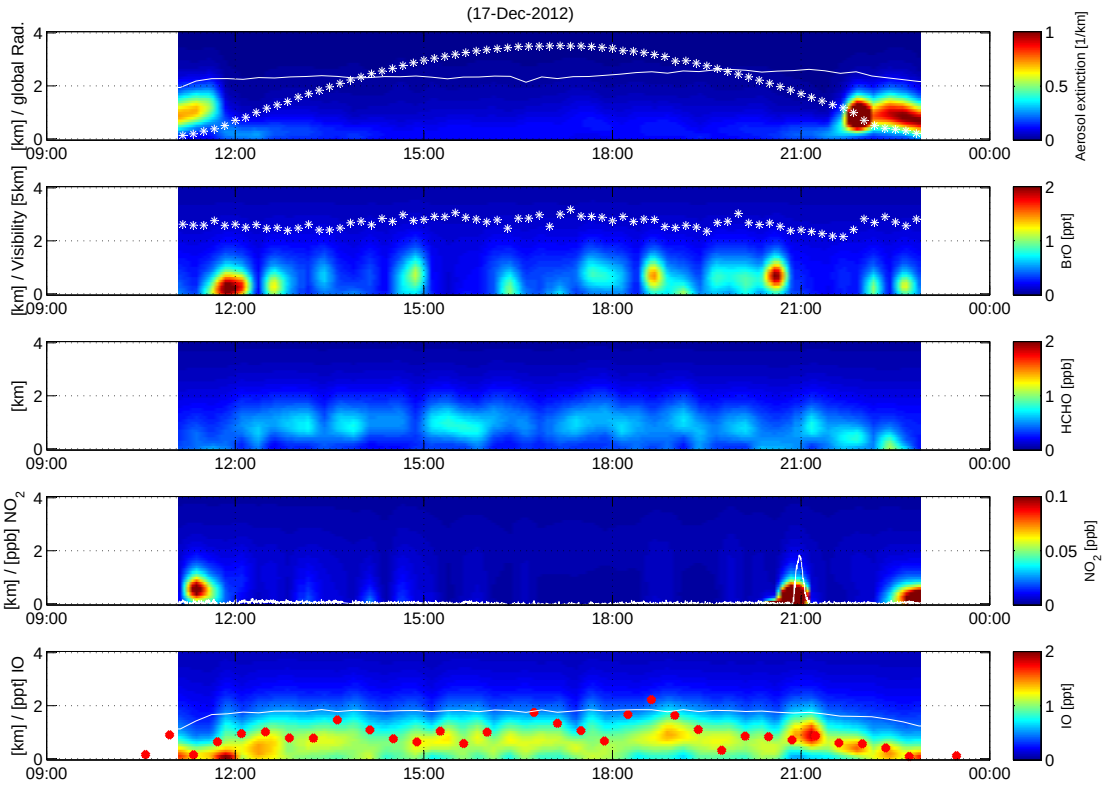

Figure 7.23.: Clear day and Open Ocean conditions without large continental influence on December 17th, 2012 at 14°S, 77°W. The CE-DOAS IO mixing ratios are plotted in red on top of the MAX-DOAS IO profiles, for NO_2 in white, respectively. For the aerosol and IO profile retrieval the white line represents the number of degrees of freedom. The MAX-DOAS profile shows non-zero values above 1km height due to the a-priori and the averaging kernels. The height resolution is slightly worse than for the aerosol retrieval shown in figure 7.6 due to the smaller signal-to-noise-ratio of the IO retrieval. BrO is practically below the detection limit and the HCHO concentration is around 500 ppt, a typical tropical background HCHO concentration in the MBL.

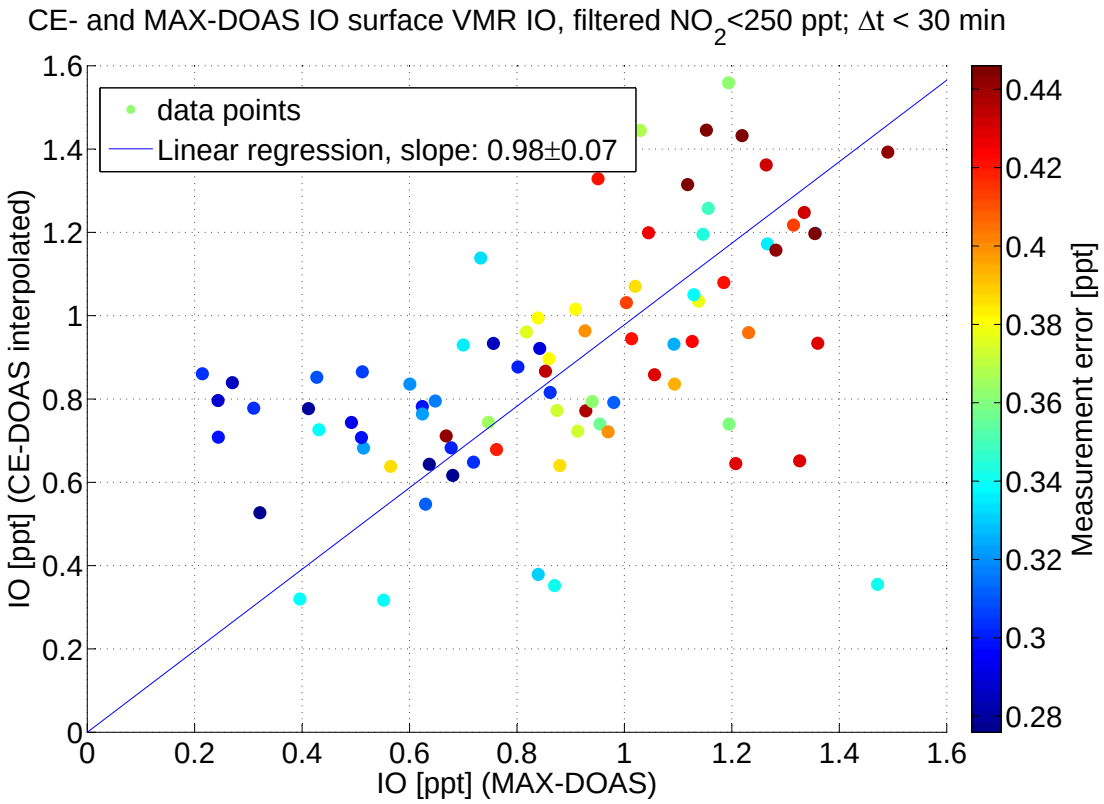

Figure 7.24.: Correlation of IO surface VMR from MAX-DOAS and CE-DOAS measurements (1000s time resolution) during *c12* (December 2nd-6th, 2012). The correlation coefficient is $R = 0.53$ for day-time measurements and $R = 0.8$ when assuming that night-time MAX-DOAS measurements yield an IO concentration of 0 ppt. The time series of the compared values is shown in figure 7.21. As measurement error three times the fit error was assumed.

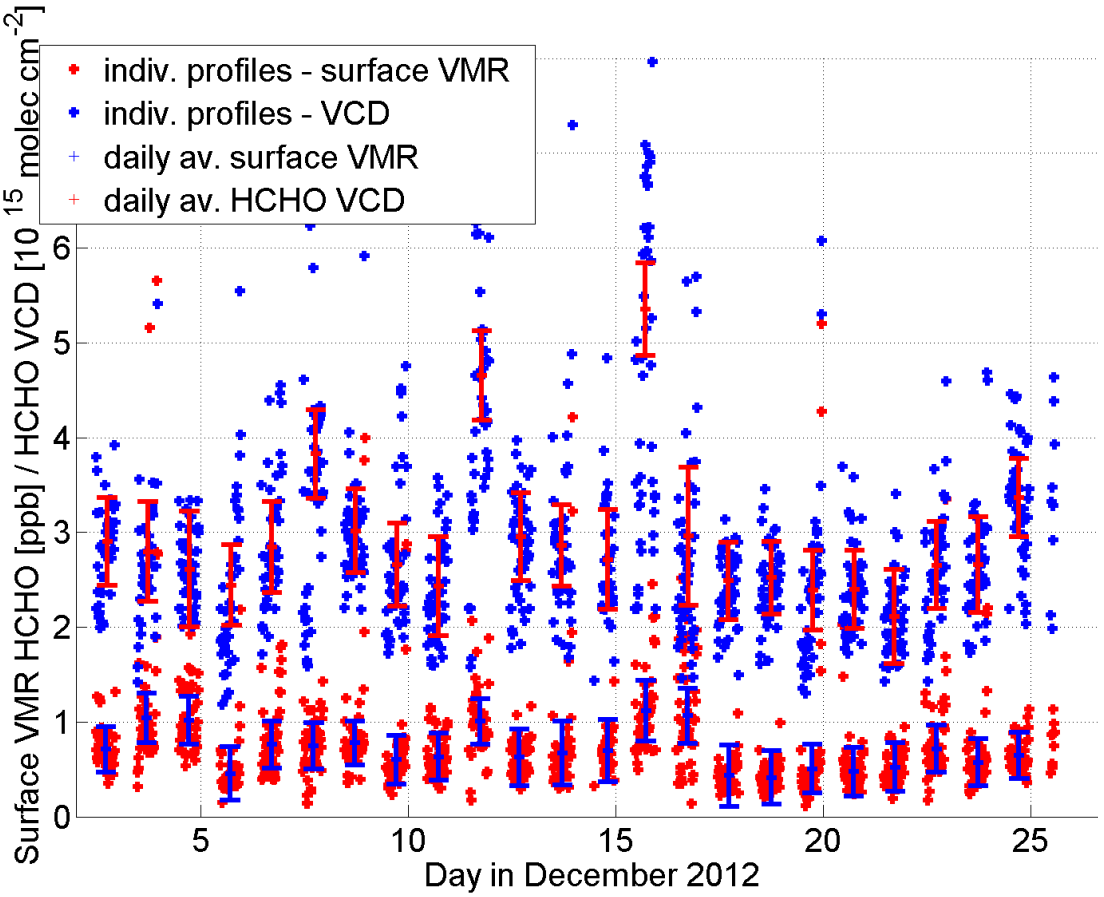

Figure 7.25.: Surface volume mixing ratios and vertical column densities for tropospheric Formaldehyde during M91: On 12/11/2012 and 12/15-16/2012 higher HCHO mixing ratios were measured due to continental air-masses.

7.2.6. Glyoxal

7.2.6.1. CE-DOAS

The detection limit of glyoxal for the CE-DOAS setup was 70 ppt and was not found to be above the detection limit at any time. Usual fit errors for 1000s exposure time were 17 ± 7 ppt, but the residuals were strongly structured as described in subsection 5.7.1. Furthermore it is not clear how the silica gel used in a filter cartridge during purge air reference measurements reacts with glyoxal. Since glyoxal is, if present, also expected to be found during night-time, the correction procedure described for IO could not be applied here. Correcting for these effects could reduce the measurement error by 50%. Even below detection limit, no day-night dependence was observed, also no correlation between glyoxal and NO_2 or water vapour.
An example fit is shown in figure 7.16, showing a glyoxal mixing ratio of -15 ppt.

7.2.6.2. MAX-DOAS

For the retrieval of glyoxal using MAX-DOAS data a number of tests have been performed on the M91 data, see subsection 5.6.4. The fit error was $2.2 \cdot 10^{14}$ molec cm^{-2}, $1.2 \cdot 10^{14}$ molec cm^{-2} and $0.95 \cdot 10^{14}$ molec cm^{-2} for one elevation sequence and 4, 16 elevation sequences respectively (when using the HITEMP, O_4-Greenblatt and VRS(N_2) cross-sections). The standard deviation of measured dSCD was $5.6 \cdot 10^{14}$ molec cm^{-2}, $3.5 \cdot 10^{14}$ molec cm^{-2} and $3.5 \cdot 10^{14}$ molec cm^{-2} respectively. Therefore a conversion factor of 3 according to Stutz and Platt [1996] from fit error to measurement error can be applied for four summed sequences. Since the residuals are structured due to the strong water vapour absorption, this value is reasonable, since the structured residual spectrum leads to an underestimation of the measurement error by the fit error, see subsection 3.1.4. Defining the detection limit as 2σ, this results in a detection limit of $7 \cdot 10^{14}$ molec cm^{-2}. Previously reported values of $15 \cdot 10^{14}$ molec cm^{-2} by Sinreich et al. [2010] should have been detectable, but values stayed below the detection limit.
Converting the 2σ detection limit of $7 \cdot 10^{14}$ molec cm^{-2} using the same radiative transfer settings and aerosol profiles as for IO, this corresponds to 35 ppt.
An overview over glyoxal dSCDs obtained from the spectral retrieval using different settings is found in figure 5.40.

7.2.7. H_2O

Since it was not allowed to launch radiosondes during the parts of the cruise close to Peru, vertical profiles of water vapour concentrations would be an alternative way to obtain the height of the MBL from MAX-DOAS measurements during daytime. The height resolution of the MAX-DOAS retrieval is limited to 200–400 m in an altitude up to 1 km, but here the question would be rather to try to identify situations in which a convective (heights around 1 km) or a stable boundary layer (heights typically < 300 m) is present, similarly as done by radiosonde-measurements during P399 [Fuhlbrügge et al., 2013].

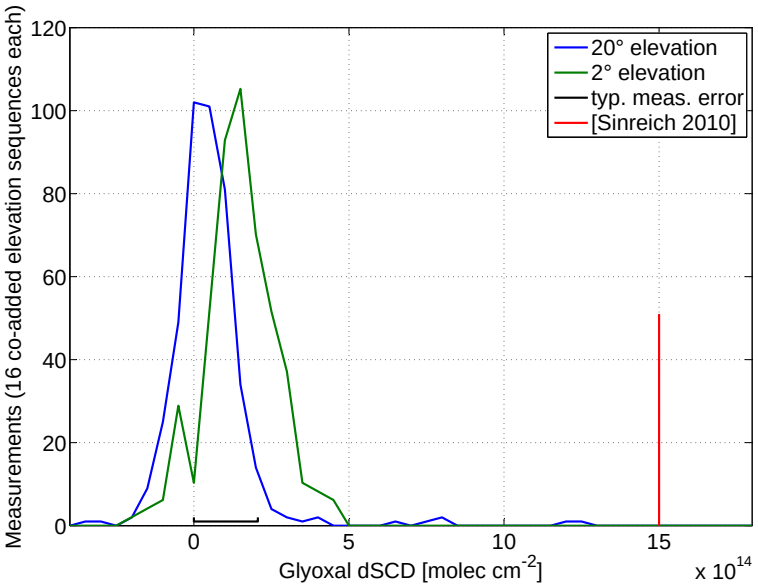

Figure 7.26.: Histogram for glyoxal dSCDs at 2°(green) and 20°(blue) elevation during M91 using HITEMP and O_4 [Thalman and Volkamer, 2013] cross-sections, including the correction for water vapour absorption induced changes in AMF (section 5.4). 16 elevation sequences were co-added before evaluation (using a 40° Fraunhofer reference). The difference in Glyoxal dSCDs for 2° and 20° elevation is comparable to the measurement error of typical $2 \cdot 10^{14}$ molec cm^{-2}. (20°: $(0.0 \pm 1.2) \cdot 10^{13}$ molec cm^{-2}, 2°: $(1.50 \pm 0.05) \cdot 10^{14}$ molec cm^{-2}) It is based on the same data as figure 5.40. Sinreich et al. [2010] reported glyoxal dSCD at low elevation angles of $1.5 \cdot 10^{15}$ molec cm^{-2} for the Peruvian upwelling and the open Pacific.

The MAX-DOAS data from this campaign has been analysed with respect to water vapour, but the retrieval of concentration profiles does not yield stable results. On average it agrees with calculated mixing ratios from temperature, pressure and humidity values from the weather station, but single profiles often show elevated layers of water vapour which do not agree with radiosonde measurements.

When analysing the CE-DOAS measurements for water vapour, negative volume mixing ratios are found, whenever the light-path is significantly shorter due to aerosol absorption. This can be explained if the air of the reference measurements was not completely dry, but about 10% of the ambient water vapour mixing ratio was able to pass the silica gel filter cartridge. At 10% of the original lightpath this will also yield an apparent mixing ratio of zero, for shorter light-paths even negative values are observed. During SHIVA this problem was not observed, probably because the filtered air had been cooled to 1°C before to remove the largest fraction of the atmospheric water vapour content.

7.3. Discussion

For the first time MAX-DOAS measurements of tropospheric IO have been validated by CE-DOAS measurements and showed good agreement. Also NO_2 VMR obtained from the retrieval of concentration profiles from MAX-DOAS measurements agreed with the results of the CE-DOAS measurements, confirming the reliability of the MAX-DOAS measurements and the retrieval algorithm.
For IO neither a correlation with ozone (R=0.01, for 5–30 ppb O_3) nor with sea surface temperature (R=-0.03, for T=16–23°C) was observed, but day-time variations in ozone were small and transport effects might be more important than the local sea surface temperature. Also the variations of IO surface volume mixing ratios are typically of the same size as the measurement errors and can be almost regarded as being constant throughout the cruise.
When comparing BrO dSCD or IO VMR from MAX-DOAS with the halocarbon surface water concentrations from the group of Birgit Quack/GEOMAR, no direct correlation is found (see figure 7.5). This is also not expected, since the compounds measured have mostly lifetimes of several days, therefore transport mechanisms will play a significant role when interpreting connections between measurements of IO and BrO and their possible halocarbon precursors. An air parcel travelling at a typical wind speed for this campaign of 10m s^{-1} will have passed the investigated region within less than two days. For compounds with tropospheric lifetimes of several days, the sources of possible precursors of reactive halogen species will most probably be found outside the probed region.
The fast increase in IO concentrations at the ground, which has been observed by CE-DOAS measurements at sunrise, shows that the dominant direct source in the MBL are short-lived species such as I_2, CH_2I_2, OIO and HOI. Since any instrumental instability induced by sunlight would take a certain time to heat up any component e.g., an instrumental effect can be excluded. If, as seen for BrO in figure 1.6 for measurement on Cape Verde, also a morning and evening maximum can be found for IO concentrations would require measurements at a better detection limit. Furthermore atmospheric IO can react with NO_2 after sunset, forming $IONO_2$. Sufficient NO_x is available, as shown by NO_2 mixing ratios, and the reaction constant $k_{IONO_2} = (9-15)\cdot 10^{-12}$ $molec^{-1}$ cm^3 s allows for a fast conversion. $IONO_2$ can be either photolysed after sunrise in the next morning ($J(IONO_2) = 4 \cdot 10^{-2} s^{-1}$ at noon in mid-latitudes [Mössinger et al., 2002]) or deposited on aerosol, where it can contribute to acidification. Possibly the iodine can be released again as I_2, IBr or ICl from the aqueous layer on the aerosol particle, which could enhance atmospheric iodine, bromine and chlorine concentrations already during the night [Mössinger et al., 2002]. However, higher BrO values in the Peruvian upwelling region compared to other measurement campaigns e.g. during MSM18 on the Atlantic have not been observed.
Iodinated halocarbons might still play a role to fill this atmospheric iodine reservoir by release of iodine during their photolysis. Still, the largest IO concentrations are located close to the upwelling itself, therefore the main source of atmospheric iodine in this region can only be the direct release of I_2 and HOI from seawater or relatively short-

lived iodinated species such as CH_2I_2, CH_2ClI and CH_2BrI, which are rapidly photolysed. Due to its long lifetime CH_3I will play only a minor role for the local tropospheric iodine chemistry.
However, no significant change in atmospheric IO concentrations was observed when passing the location with the highest halocarbon concentrations in surface water, often six times larger than during measurements before and afterwards. Also surface mixing ratios of CH_2I_2 and CH_2ClI showed variations from 0.4–3 ppt at night, but no impact on IO concentrations during the day were observed. No sea-to-air fluxes are available yet for these compounds, but if any change is observed at all for atmospheric iodinated halocarbons, a change in IO concentrations is expected in this region. This has not been observed, which points towards another source, providing a constant flux of iodine to maintain atmospheric IO concentrations of 1–1.5 ppt. This might be the direct release mechanism of I_2 and HOI from sea surface iodide [Carpenter et al., 2013].
The largest BrO dSCD were observed downwind from the area with the highest concentrations of halocarbons in water on December 9th and 10th. A possible correlation of BrO VCD and/or surface VMR with wind-speed cannot be confirmed, but BrO dSCDs were always close to their respective detection limits. Furthermore no stable inversion was observed as during the BrO event during P399 (Tschritter [2013] and Fuhlbrügge et al. [2013]). As shown in figure 7.11, these two days coincide with the minimum NO_2 concentrations. However, also on December 14th, 20th and 21st low NO_2 surface VMR in the range of 10 ppt were observed and no enhanced BrO VMRs.
Compared to the Mauritanian upwelling, the coastal vegetation is also different: While in Peru coastal vegetation is sparse, mangroves can be found along the coast of Mauritania, which can emit precursor substances for BrO [Manley et al., 2007].
For the observation of transport of continental air-masses from Peru onto the marine boundary layer, surprisingly high IO mixing ratios combined with enhanced HCHO mixing ratios were found in heights of more than 1000m, thus above the MBL. (see figure 7.12 for vertical profiles)
In comparison with the Mauritanian upwelling, the obtained mixing ratios and vertical column densities were 25-50% higher than in the highest measurements reported by Tschritter [2013] and shown in figure 12.2. Since during Polarstern cruises a high variability of IO dSCDs around Cape Verde was observed, the daily averaged IO dSCD values observed during M91 are sometimes even twice as large. If the IO dSCDs measured during M91 are representative itself for a longer time-series cannot be determined from one campaign. However, since the averaged satellite measurements of IO fit the ship-based observations quite well, this indicates that this ship-based data-set of IO is indeed representative for December/January in the Peruvian upwelling.

7.4. Meteor M77

During Meteor cruise M77 a HMT Mini-MAX-DOAS with a compact USB2000 spectrometer was operated by Annette Kock and Evgenia Ryabenko from GEOMAR, Kiel, Germany[1]. The cruise took place from 01/27 - 02/14/2009 in the Peruvian upwelling region leading from Lima to the open ocean until 86°W, and then heading north to Panama. The elevation sequence of the MAX-DOAS measurements was 5°, 10°, 15°, 20°, 90°. The instrument was looking to port side.
Low overall O_4 dSCDs indicated an elevation angle offset. An elevation angle offset of +6° was determined from varying the elevation angle offset parameter in the aerosol retrieval and minimizing the χ^2 value of the retrieval. The minimal elevation angle is then 11°, which does not allow for retrievals of IO or BrO at reasonable detection limits in the marine boundary layer. Furthermore the spectral evaluation showed large dSCDs when using 90° elevation spectra as a reference, especially during local noon. This indicates an influence of direct sunlight reaching the spectrometer. To avoid its influence, 20° (26° after applying the elevation angle offset) elevation spectra were used instead chosen as Fraunhofer reference spectra. This lowers again the detection limits. The retrieval of aerosol profiles was possible and showed reasonable results, but the trace gas retrieval for IO did not yield satisfying results, since all dSCDs were close or below detection limit when evaluating single spectra (compare figure 7.29 for a sum of 16 elevation sequences).
Nevertheless comparing it directly to the 10° and 20° measurements from M91 allows to estimate the overall distribution of IO also in more remote regions of the eastern Pacific. For IO, using the data from M91 shown in figure 7.27 for cases where the IO dSCD at 3° was above $1.5 \cdot 10^{13}$ molec cm^{-2} (to remove situations with low visibility, such as on 11/12/2012 close to Lima), dSCDs for M77 between 26° and 11° are expected to be found around $0.7 - 0.8 \cdot 10^{13}$ molec cm^{-2}.
No significant absorptions from glyoxal were found during M91 with a significantly better spectrometer and no significant glyoxal dSCD was found for M77.
The IO fit error for 16 co-added elevation sequences was $(1.4 \pm 0.4) \cdot 10^{12}$ molec cm^{-2}, RMS: $(1.5 \pm 0.4) \cdot 10^{-4}$ ($(1.8 \pm 0.4) \cdot 10^{12}$ molec cm^{-2} for 4 co-added elevation sequences, RMS: $(2.0 \pm 0.4) \cdot 10^{-4}$). Therefore the expected IO dSCDs of $0.7 - 0.8 \cdot 10^{13}$ molec cm^{-2} based on estimations from M91 should be slightly above detection limit.
At a typical RMS of the BrO evaluation of $4 \cdot 10^{-4}$ and a fit error of $(1 \pm 0.3) \cdot 10^{13}$ molec cm^{-2}, no significant amounts of BrO above $5 \cdot 10^{13}$ molec cm^{-2} were detected. The contribution of the residual structure discussed in subsection 5.1.1.2 was similar to the values obtained during MAD-CAT, but due to large residuals not as clearly to be seen as e.g. in figure 11.2.

7.4.1. Conclusion

Satellite measurements of IO (Figure 7.19) for the same region averaged for January and December from 2004-2011 show a similar pattern as seen in figure 7.28: Low IO VCD

[1]The instrument was prepared for the cruise by Tschritter [2013]

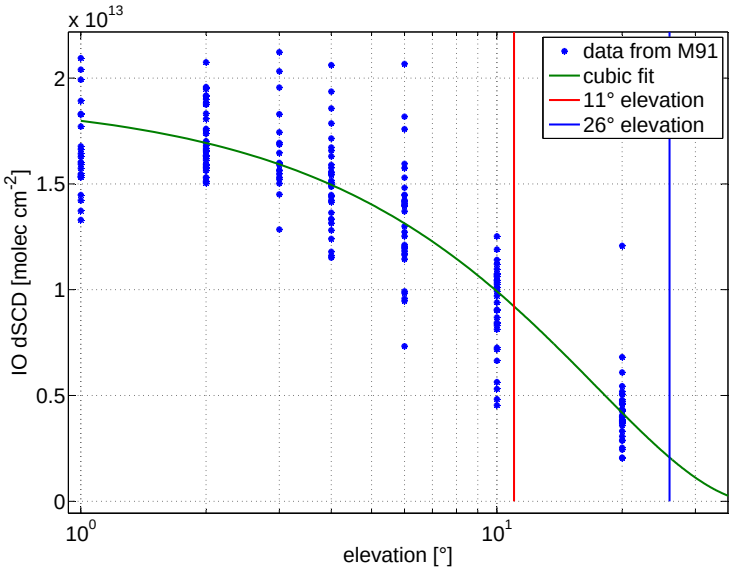

Figure 7.27.: IO dSCD for M91 for cases where the IO dSCDs at 3° were above $1.5 \cdot 10^{13}$ molec cm^{-2}. During M77 spectral data from elevations of 11° and 26° was analysed, therefore dSCD of about $0.7 - 0.8 \cdot 10^{13}$ molec cm^{-2} are expected to be seen for the M77 dataset. Spectra recorded at 40° elevation were used as reference spectra for the M91 data, therefore the dSCD at 40° is zero.

in the south-west and a continuation of the coastal maximum of IO VCDs towards the Galapagos islands. Since the VCDs obtained during cruise M91 for vertical IO profiles agree with satellite observations, this additional data from M77 also shows that the distribution of IO outside the coastal upwelling area probed during M91 decreases. This is useful when comparing the IO distribution in this area with the surface water iodide samples taken during M77/1-4 once they are published [Croot et al., 2014, in prep.]. The iodide measurements during M91 failed, but remaining water samples might be analysed again.
It shows furthermore that the observed IO dSCD is not directly related to tropospheric water vapour content and/or SST, but actually a property connected to the upwelling region. It furthermore agrees here with the satellite observations of IO, which proves that the enhanced IO VCDs observed in the Eastern Pacific are not an artefact of the spectral retrieval.

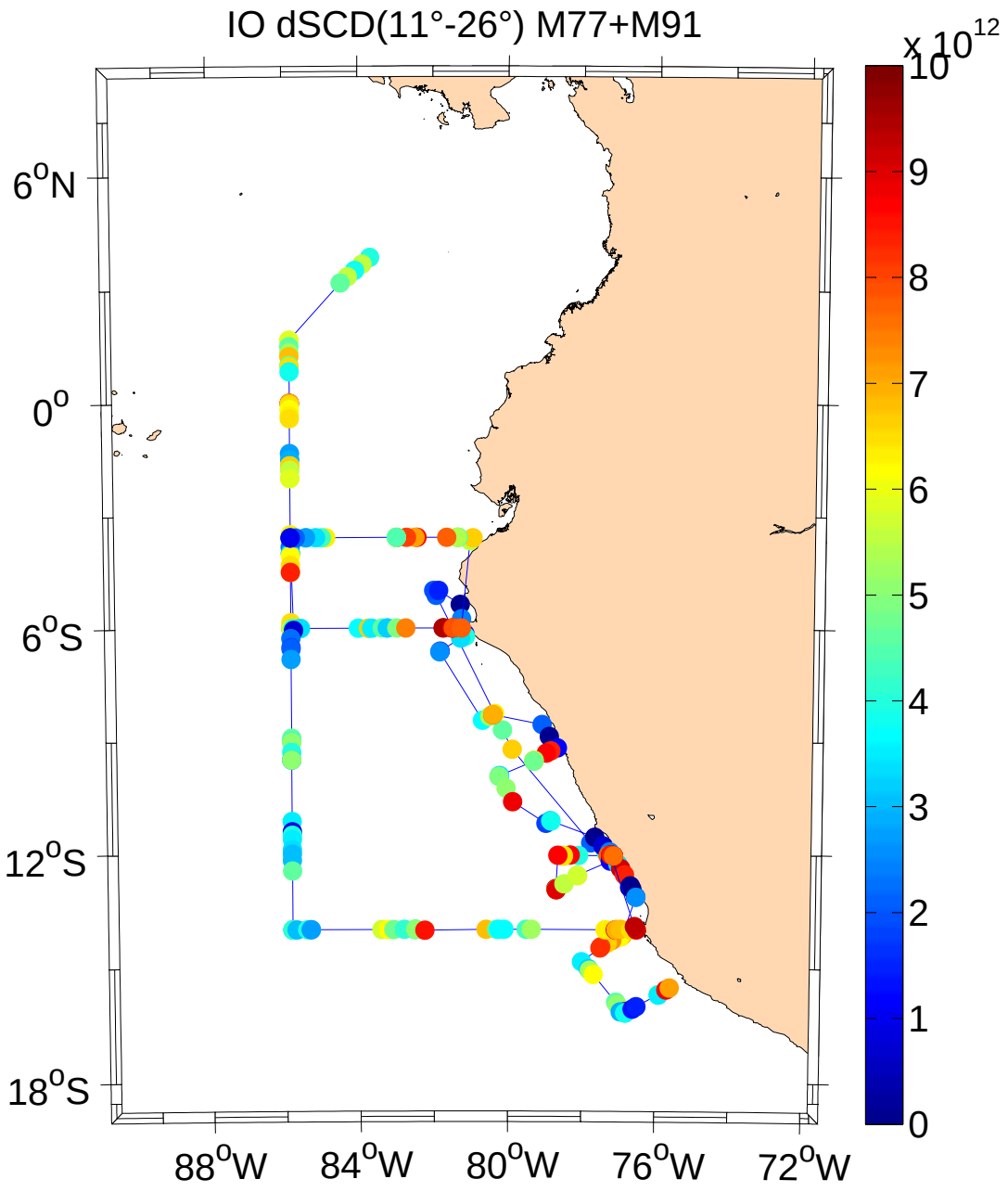

Figure 7.28.: M91 and M77 dSCDs, colour-coded in molec cm^{-2}. For M91 data from 10° spectra evaluated against a 40° Fraunhofer reference is shown. This value was then corrected by $2 \cdot 10^{12}$ molec cm^{-2} according to figure 7.27. Low columns during M91 close to the Peruvian coast are caused by low visibility due to fog. In general the higher values were observed closer to the coast. Satellite measurements of IO (Figure 7.19) for the same region show a similar pattern of low IO VCD in the south-west and a continuation of the coastal maximum of IO VCDs towards the Galapagos islands.

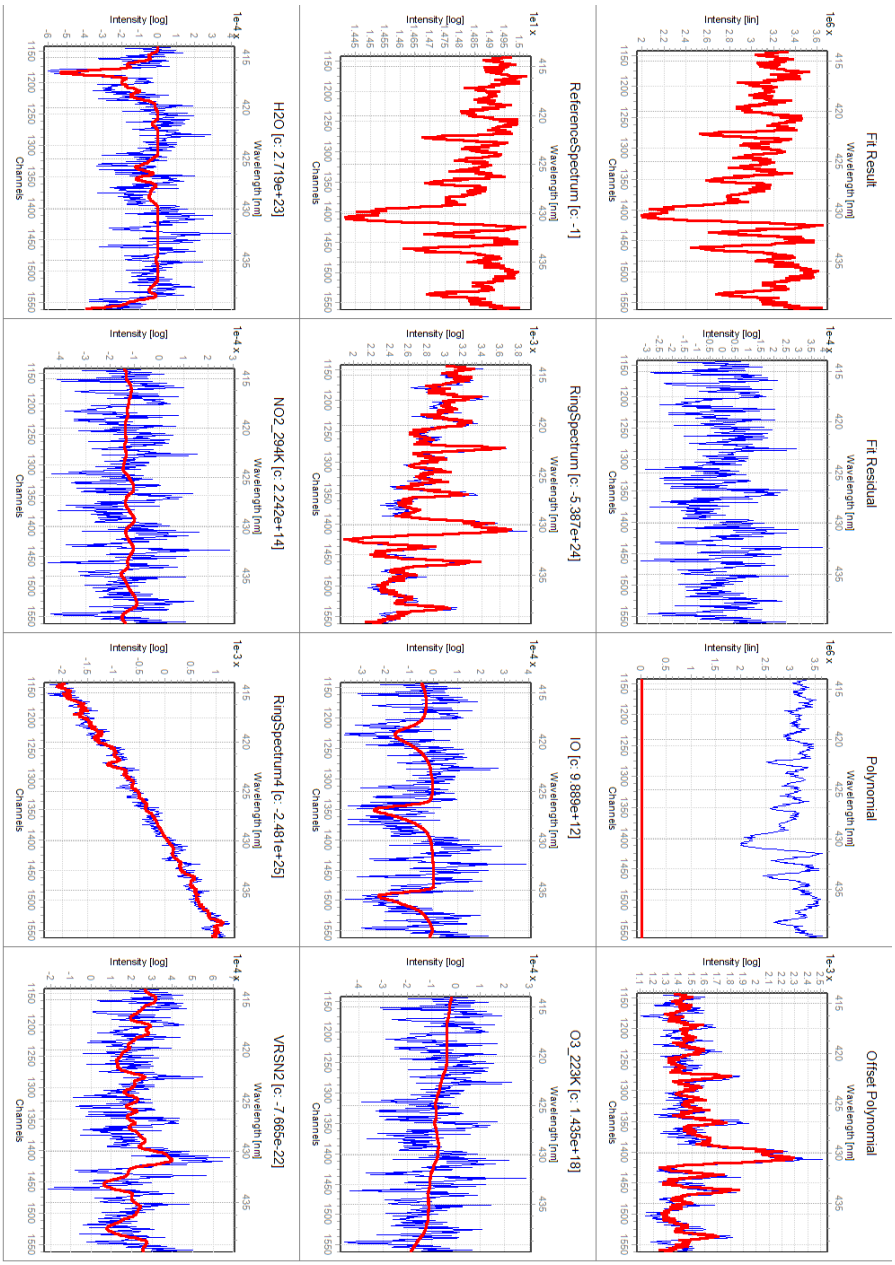

Figure 7.29.: IO fit from M77, 01/28/2009, 13:32 UTC, at 14°0'S 76°30'W at 11° elevation, evaluated against a reference spectrum recorded at 26° elevation. The observed IO dSCD is 10 times larger than the fit error. Figure 7.28 shows the complete dataset, together with data of 10° elevation from SOPRAN M91. The spectrum consists of 35832 scans for a total integration time of 13 minutes, the Fraunhofer reference spectrum also 13 minutes. It was recorded using a HMT mini-DOAS based on an Ocean Optics USB2000 spectrometer.

8. MSM 18: The Equatorial Upwelling Region

8.1. MSM 18/1+2

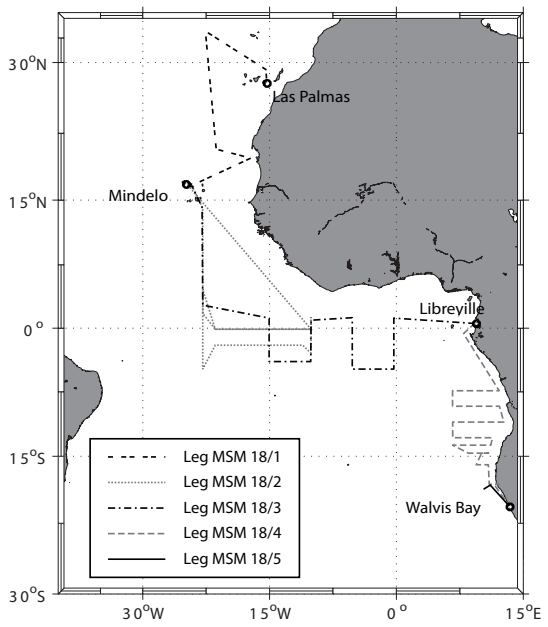

Figure 8.1.: Planned cruise tracks for MSM18/1-4. [MSM18 Expeditionsheft]

During cruise legs MSM 18/1+2 on R/V Maria S. Merian the SMAX-DOAS setup (section 4.2) measured unsupervised from 04/16/2011 to 06/24/2011. North of Cape Verde this worked well, except for some gaps, probably due to software problems. South of Cape Verde (beginning of May 2011) the air conditioning in the air chemistry lab on RV Maria S. Merian was not able to keep the room temperature at a level at which the spectrometer could be stabilized at 38°C by heating. This led to spectral shifts of up to 1 nm, see figure 8.3. The data from the first leg can be used, whereas the second leg from Mindelo to Mindelo needs to be interpreted with caution. During MSM18/3 the spectrometer temperature was raised to 44°C to avoid these problems.
Additionally the shutter failed sometimes, which then resulted in either completely dark spectra or, if the shutter stayed open, in high RMS of the fit. The reason was, that if the CCD is illuminated also during the readout procedure, that the effective instrument function changes, since it is not constant over the height of the CCD. The shifting of the readout process then leads to a different weighting of all possible instrument functions on the CCD chip and finally results in unusual large RMS ($> 10^{-3}$) in the spectral retrieval, which were filtered out. This is the reason for some of the gaps in the time series of cruise leg MSM18/1 (compare figure A.7).
Furthermore the GPS mouse was removed during the cruise, additionally the ship-internal data recording system DSHIP failed. Therefore the positions had to be interpolated from partly existing GPS data, the station list and ADCP data courtesy of Tim Fischer/GEOMAR. Even the German office for maritime shipping and hydrography *BSH*[1] could only provide stationlists, but their data set of position and speed of

[1] *BSH* - Bundesamt für Seeschifffahrt und Hydrographie

RV Maria S. Merian was also faulty. For periods were all data set only contained sparse data, hourly position data from http://sailwx.info was used.
The position for the plots was calculated based on all data available from MAX-DOAS, BSH, ADCP and ship-internal dship and data points resulting in unrealistic ship speeds were removed. The DSHIP data contains reasonable data for heading(most of the time) and meteorological parameters.
Due to the lack of continuous position and heading data for the first two cruise legs, radiative transfer modelling has not been done in depth. Heading information during periods without explicit data were deducted from the difference of relative and absolute wind direction from the meteorological data, if needed, as e.g. for the profile retrieval of the BrO event (see below).
The MAX-DOAS elevation angle sequence was 1, 2, 4, 6, 10, 20, 40, 60°, each elevation was recorded for one minute. A telescope elevation of 90° was not possible on this ship.
Large spectral shifts occur mainly during the second leg, the data from the first cruise leg is almost not affected. BrO has been detected with a dSCDs of up to 15 times the fit error or $6 \cdot 10^{13}$ molec cm^{-2} on 04/22/2011 during the afternoon. IO dSCDs are similar to previous observations e.g. during Polarstern cruises.

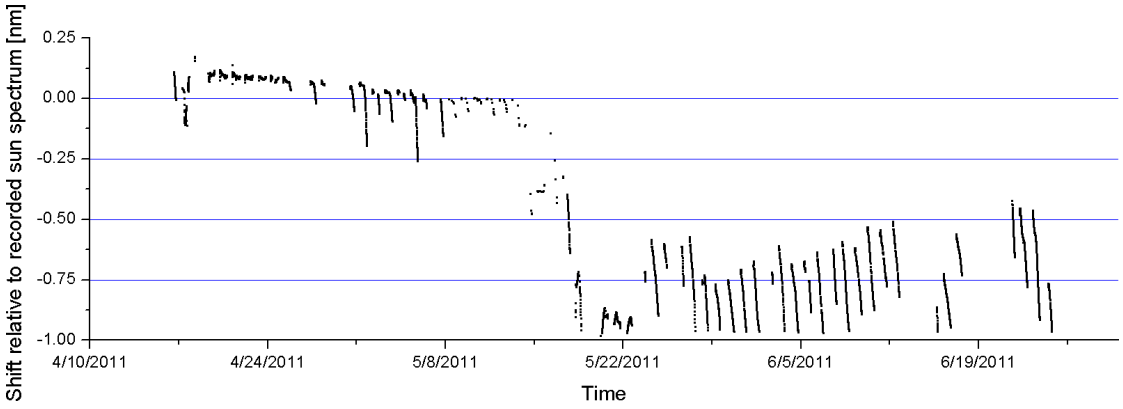

Figure 8.3.: Spectral shift relative to a spectrum recorded in the harbour of Las Palmas. Generally south of Cape Verde the air conditioning was not able to keep the temperatures in the lab at a reasonable level, which led then to too high spectrometer temperatures and spectral shifts.

8.1.1. BrO

The average fit error for BrO using the Greenblatt et al. [1990] cross-section for O_4 was $3.2 \cdot 10^{12}$ molec cm^{-2} during cruise leg 1. The distribution of BrO dSCDs during this time (without the BrO event on 04/22/2011) was $(1.7 \pm 0.9) \cdot 10^{13}$ molec cm^{-2}. This also means that assuming a lightpath of 10km in the marine boundary layer that the average BrO VMR is around $1.7 \cdot 10^{13}$ molec cm^{-2} $\approx$ 0.75 ppt. At 1° (3°) elevation this would correspond geometrically to the lowest 175m (500m).

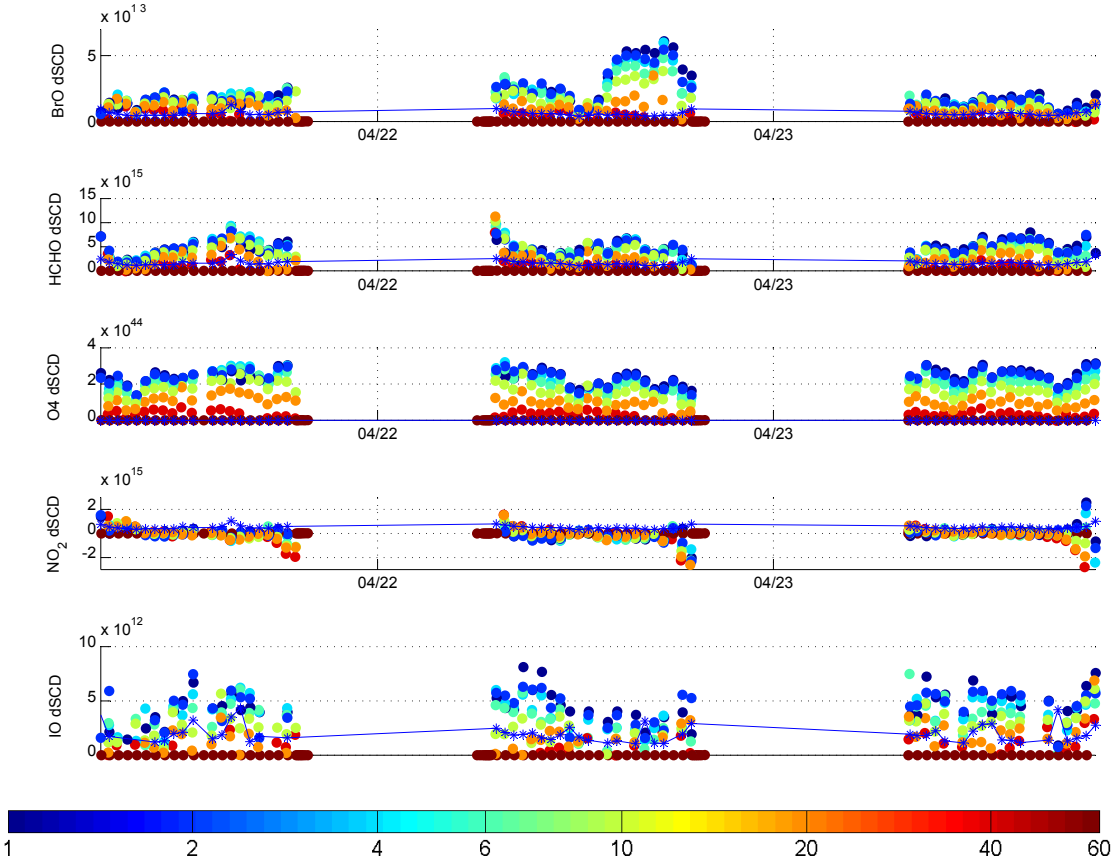

Figure 8.4.: BrO event during MSM 18/1. The blue line shows twice the fit error, the colours indicate the telescope elevation angle. Four consecutive elevation sequences are summed, the telescope elevation angle is colour-coded. Based on the BrO dSCD values at 3°, backward trajectories were calculated shown in figure 8.6.

Some values tend to be a bit higher around $(2 - -3) \cdot 10^{13}$ molec cm^{-2}, especially close the Cape Blanc/Mauritania as seen before with larger BrO mixing ratios during P399 [Tschritter, 2013] and closer to Cape Verde. Surprisingly a strong BrO signal of $6 \cdot 10^{13}$ molec cm^{-2} was measured north the Canary Islands, between Madeira and the Azores, at 33°N, 22°W. These dSCD translate when calculating profiles to $\approx 4 - -6$ppt BrO within the lowermost 500m (Figure 8.7). HYSPLIT backward trajectories indicate that during this time the probed air had passed the Azores a day before. Trajectories on the same day in the morning did not, neither on the following day. A fit is shown in figure 8.9, trajectories can be seen in figure 8.6.
Aqua MODIS Chlorophyll a maps show elevated Chl-a surface water concentrations for April 2011 around the Azores, see figure 8.13, but it does not vary as significantly as the BrO varies associated to the trajectories calculated each BrO measurement, also when

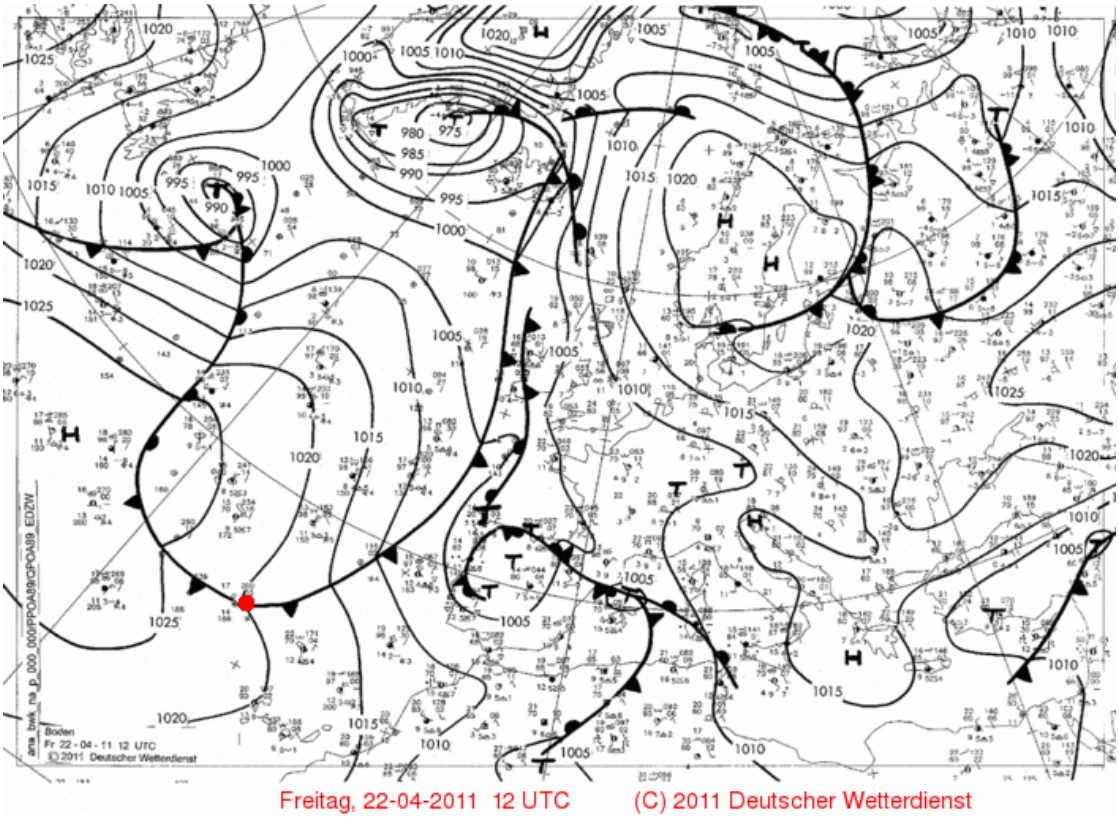

Figure 8.5.: DWD analysis for 22/04/2011 12:00 UTC, when the BrO values increased significantly in figure 8.4. At this time the front just passed the ship's position.

the trajectories remained within the lowermost 500m within the region of interest. Additionally trajectories can be observed, which pass the Azores and do not show elevated levels of BrO, while others do. Therefore bioproductivity as indicated by Chlorophyll-a and an influence of the islands of the Azores on the BrO release are not likely to have caused this BrO event. The trajectory calculations vary only slightly when using different end-point heights for the trajectories in the boundary layer.
The wind speeds during this day were with 8–12 ms^{-1} comparable to the days before and after.
Another option is the transport of Arctic BrO to mid-latitudes and has already been suggested by trajectory calculations by [Hollwedel, 2005]. Satellite BrO data shows slightly enhanced BrO concentrations in the Newfoundland/Labrador region northeast of Quebec [pers. comm. Holger Sihler, Figure 8.8]. At the same time when the BrO increased on 04/22/2011 a cold front passed the ship's position shown in figure 8.5. On that day the tropospheric BrO values are already higher than usual before noon (compare figure 8.4), but increase significantly in the afternoon. Trajectories show that the air masses came from northwest, while the day before and after the air masses arrived

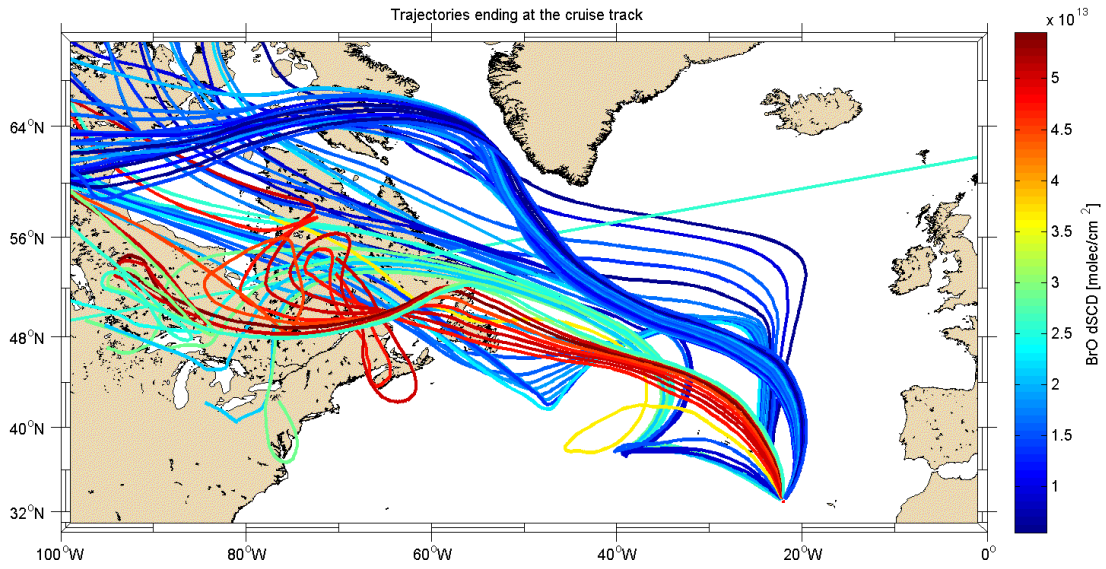

Figure 8.6.: Backward trajectories for five days during BrO event during MSM18/1, ending in a height of 100m at the ship's location at the time of the respective MAX-DOAS observation. All trajectories can be found in the lowermost 500m until 45°W and are thus expected to be within the MBL. The trajectories associated with low BrO dSCD leading along the coast of Greenland came down from heights of more than 2km but passed than a region with higher Chla concentrations as the other trajectories, compare figure 8.13. Therefore the influence of Chla as the main process for bromine emissions such as in the Mauritanian upwelling can be excluded here. The colour-code refers to the BrO dSCD of spectra recorded at 3° elevation.

from the north and also from outside the boundary layer.

Flux estimation: Assuming the BrO arrived at a front with about 1000km length, well mixed within the lower 500m with a BrO mixing ratio of 3ppt at an average wind speed of 13m/s, this results in a total flux of ≈ 1mol BrO/s. Further assuming that most of the total anorganic Br is present as BrO (Mahajan et al. [2010a] and subsection 1.4.4.1) and a total event duration of one day, this results in an input of 100kmol Br during this spillout event to the subtropical Atlantic. Hepach et al. [2013] reported for the Cape Verde/Mauritania upwelling region during Poseidon P399 a flux of 781 pmol m^{-2} h^{-2} $CHBr_3$, the assumed BrO transport would corresponds to a similar flux. Values on the open ocean for $CHBr_3$ fluxes are up to 50 times smaller, therefore this observed transport is a significant source of bromine on the open ocean even in subtropical regions. The frequency of events is unknown and will be also limited to several months, since only during spring-time large amounts of BrO are observed in polar regions.
Most of the air of the BrO event on 04/22/2011 was transported towards Brasil with

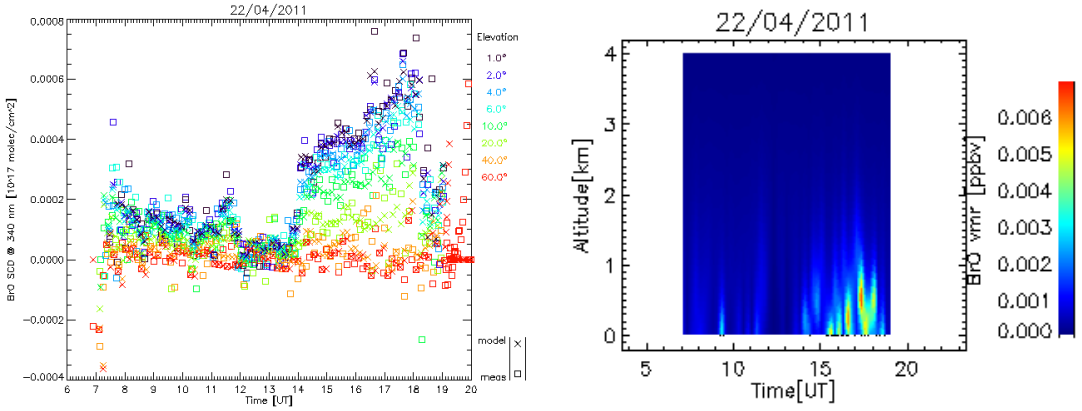

Figure 8.7.: BrO dSCDs and concentration profile during the BrO event on 04/22/2011. 4–6ppt BrO are found within the lowermost kilometre during the afternoon. The high variability of O_4 dSCD during the day indicate that it was a cloudy day. This observation is supported by the overall weather situation and satellite cloud cover images.

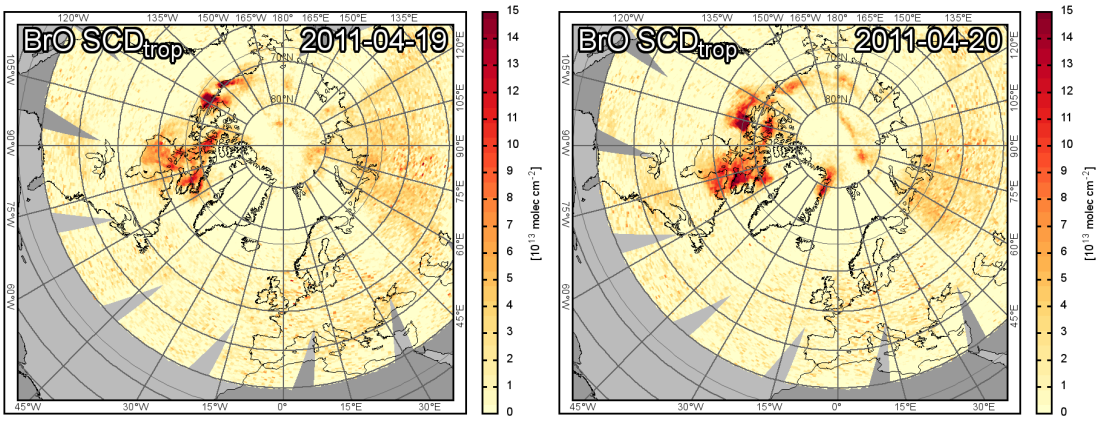

Figure 8.8.: Tropospheric BrO SCD from GOME-2, courtesy of Holger Sihler, Sihler et al. [2012].

the trade winds, some of it passed the Canary islands.
No surface ozone data was available for April 2011 from measurements stations on the Azores [pers. comm. Diamantino Henriques]. Also for the Canary islands only atmospheric ozone measurements were conducted during this time in the free troposphere, not within the MBL.
On the way towards Cape Verde about 100km north-east of Mindelo, also higher BrO column densities were observed, reaching values of up to $3.5{\cdot}10^{13}$ molec cm^{-2}. Air masses had passed the Mauritanian coastal upwelling area before. Tschritter [2013] observed during SOPRAN P399 dSCDs of more than $12 \cdot 10^{13}$ molec cm^{-2} corresponding to 10ppt BrO close to the Mauritanian coastline during an inversion [Fuhlbrügge et al., 2013].

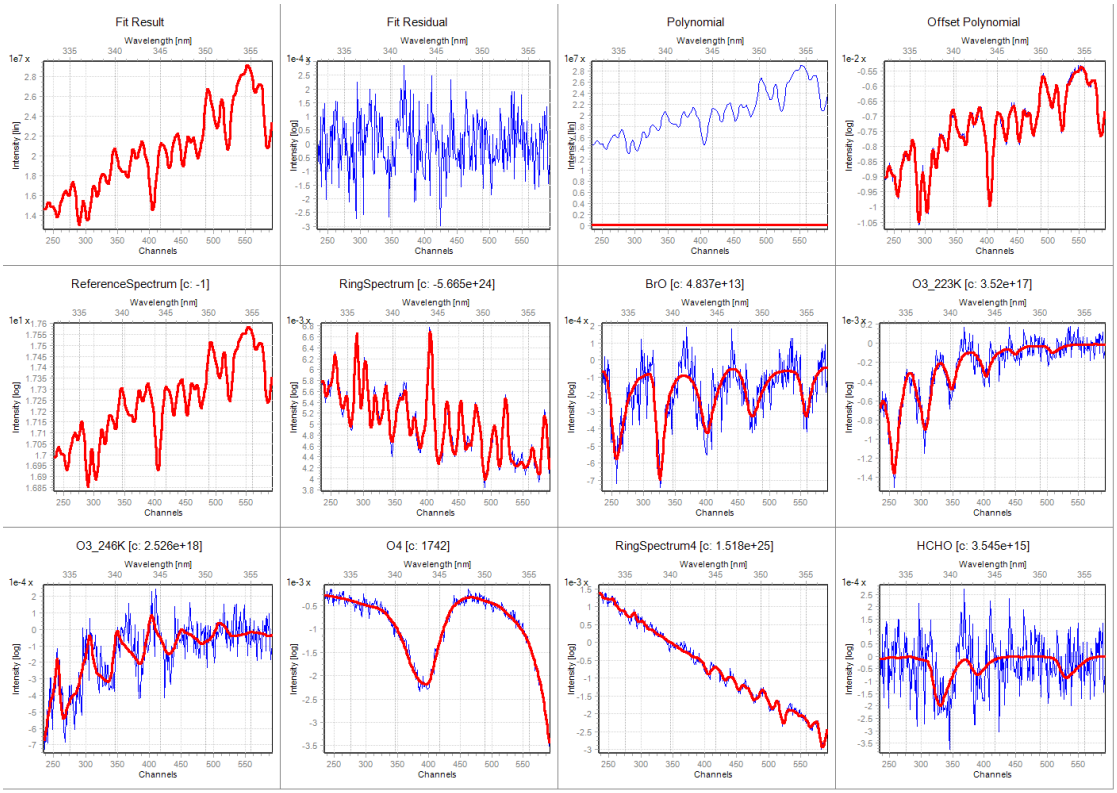

Figure 8.9.: BrO event during MSM18/1 at 16:00 UTC as shown in figure 8.7. The fit uses the Greenblatt et al. [1990] O_4 cross-section. NO_2 was omitted to simplify the plot, but was included in the analysis.

8.1.2. IO

When summing four consecutive elevation angle sequences with spectra of each one minute exposure time, typical fit errors are at $(10 \pm 4) \cdot 10^{11}$ molec cm^{-2} with RMS mostly between 5 and $10 \cdot 10^{-5}$.
The largest dSCDs were observed close to the Canary islands, close to Cape Blanche and during the last day before arriving in Mindelo, see figure 8.10. In general the daily averages of IO in this region were relatively small, compared to ANT XXVIII(chapter 9).

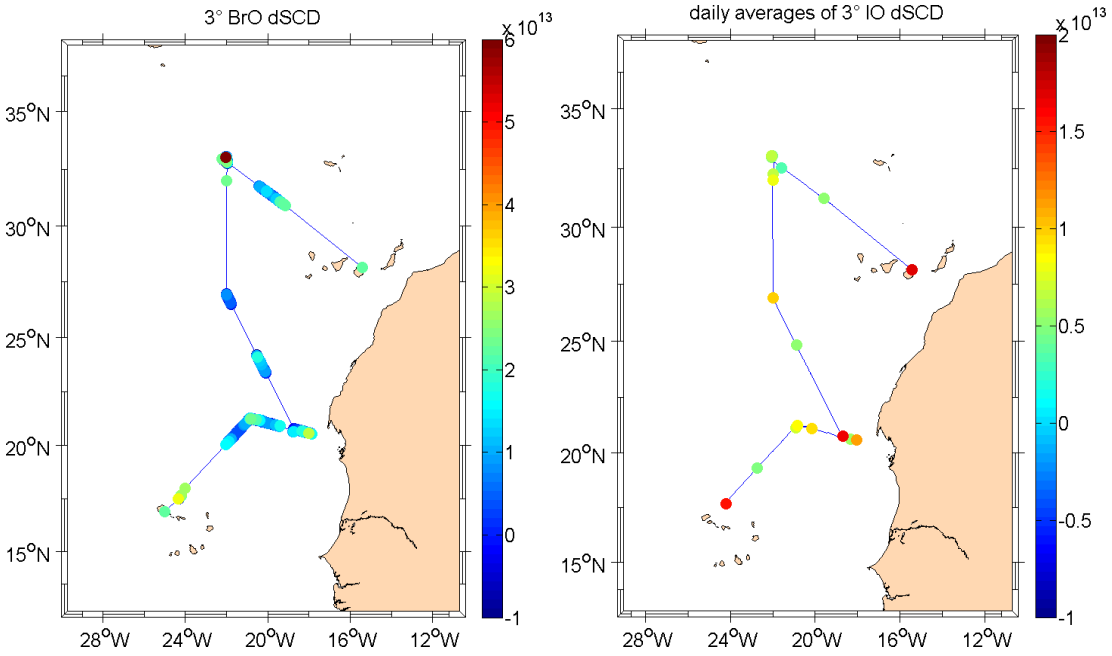

Figure 8.10.: BrO and IO dSCD for MSM18/1. The variations of daily averages of IO are mostly due to variations in O_4

8.1.3. Glyoxal

During MSM18/1 the spectrometer measured in a spectral region which was a bit shifted towards the UV compared to MSM18/3. Therefore the evaluation of glyoxal was not as stable as during MSM18/3. The retrieval interval window was set at 434–456 nm (432–460 nm for M91 and MSM18/3). Typical fit errors were of the order of $(1.5 \pm 0.6) \cdot 10^{14}$ molec cm^{-2} and the distribution of measured dSCDs was $(-0.4 \pm 3.9) \cdot 10^{14}$ molec cm^{-2}.

8.2. MSM 18/3

The cruise MSM 18/3 was a cruise planned within the SOPRAN project, with the overall goal to compare different upwelling areas. P399 focussed on the Mauritanian upwelling, MSM18/3 on the equatorial upwelling and M91 took place in the Peruvian upwelling.

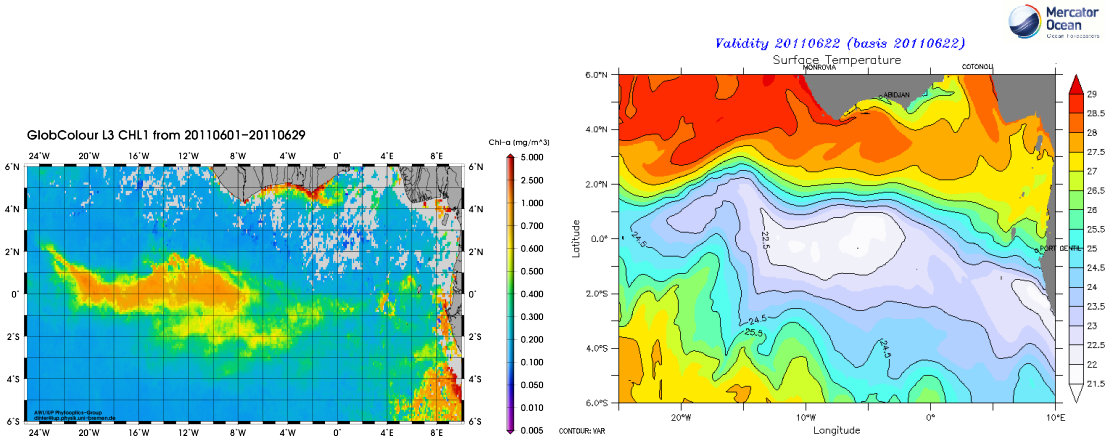

Figure 8.11.: Chl-a surface water concentrations averaged for the time of MSM18/3 (source!) and Mercator sea surface temperature from June 22th, 2011.

8.2.1. BrO

The average fit error for BrO using the Greenblatt et al. [1990] cross-section for O_4 was $6 \cdot 10^{12}$ molec cm^{-2} for an evaluation summing four consecutive elevation sequences. The standard deviation of BrO dSCDs during this time was $1.1 \cdot 10^{13}$ molec cm^{-2} which agrees with a correction factor of 2 according to Stutz and Platt [1996]. No measurements were found to be above the detection limit of $2.2 \cdot 10^{13}$ molec cm^{-2}.

Compared to MSM18/1 (subsection 8.1.1) this is almost twice the measurement error. The reason is, that the wavelength range covered does not allow for a 4-band retrieval of BrO from 332–358 nm, but just a 3-band retrieval from 338–358 nm.

8.2.2. IO

Overall the IO slant columns observed during the campaign were relatively low compared to observations on CVAO [Tschritter, 2013] or during ANT XXVIII (chapter 9), mostly around $1 \cdot 10^{13}$ molec cm^{-2} and only a few times up to $2 \cdot 10^{13}$ molec cm^{-2}.

As during MSM18/1 the fit error was typically around 1 molec cm^{-2} for single spectra with an exposure time of one minute.

Radiative transfer modelling using the same parameters as for the MAX-DOAS data of M91 (subsection 7.1.3) resulted in IO surface volume mixing ratios of about 0.5-1pptv.

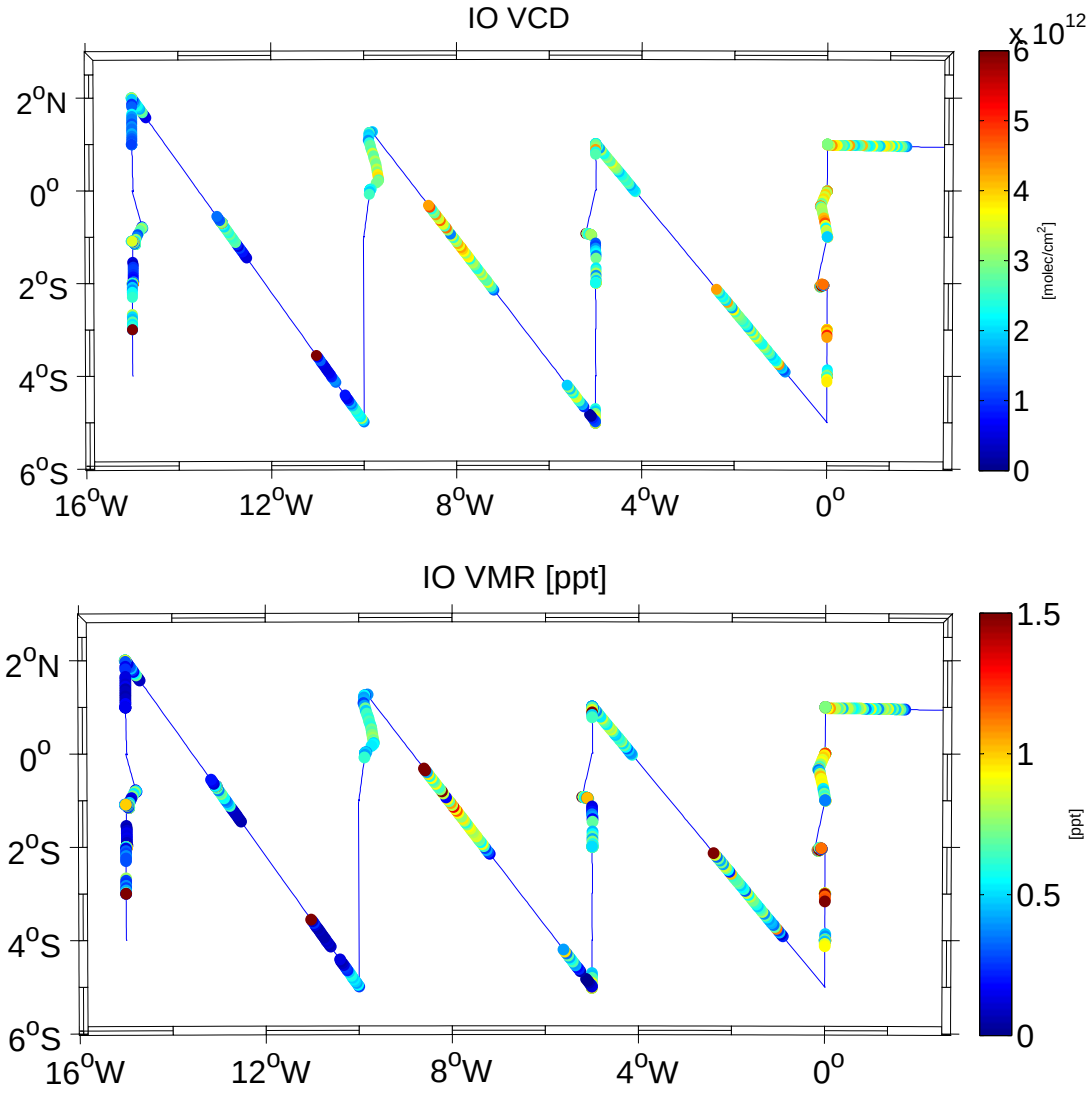

Figure 8.12.: IO surface VCD/VMR retrieved from MAX-DOAS data during MSM18/3. An overall increase towards the east can be observed, independent of chlorophyll concentration values (Figure 8.11).

8.2.3. NO_2

Typical MAX-DOAS fit errors for the evaluation of NO_2 in the IO retrieval window were $1 - 2 \cdot 10^{14}$ molec cm^{-2}, dSCDs were typically below $1 \cdot 10^{15}$ molec cm^{-2}. Ship traffic in this area was very low, only from Cape Verde to the Equator some ships were encountered, i.e. most high NO_2 values must have been caused by R/V Maria S. Merian itself.

8.2.4. Glyoxal

As for M91 (subsection 7.2.6), no glyoxal dSCD above detection limit was found. An average dSCD at 3° elevation was $(-0.3 \pm 2.1) \cdot 10^{14}$ molec cm^{-2} for single one minute spectra was observed when using cross-sections by Rothman et al. [2010], Greenblatt et al. [1990] for water vapour (HITEMP) and O_4 absorptions. (M91: see figure 5.40 for overview)

8.3. Discussion

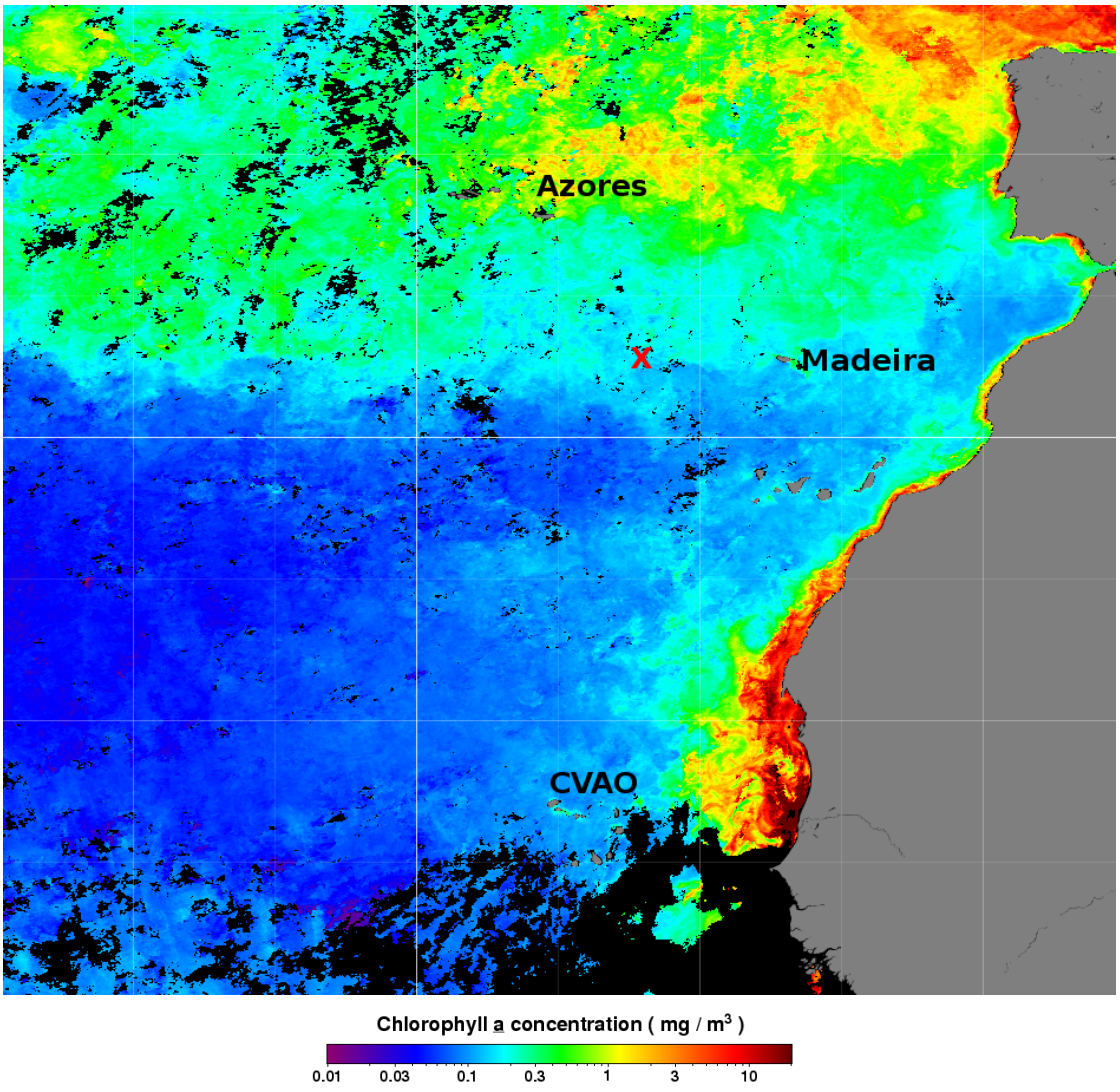

Figure 8.13.: Chla surface concentration by Aqua Modis averaged for April 2011. 33°N, 22°W, the position of the BrO event during MSM18/1 is marked.

For the IO observations during the third cruise leg, daily averaged dSCD, but also VMR and VCD (see figure 8.12) increased towards east, at the same time when Chl-a values decreased (compare figure 8.11), but the sea surface temperature stayed around 21°C, indicating freshly upwelled and nutrient rich water. Another influence could be transport of iodine from the coastal upwelling off the coasts of Namibia, Congo and Angola. Here higher concentrations of Chl-a as a marker of biological activity are found(Figure 8.11) and HYSPLIT trajectory calculations show that air masses from there arrive within a few days at the cruise track. This could explain the IO VMR east of 0°W, where water temperature was around 26°C again and the Chl-a values at 20% of the maximum found for in-situ sea surface water measurements found between 5-10°W. For sea surface concentration of CH_3I and CH_2I_2 no direct connection to IO VMR were observed [pers. comm. Helmke Hepach, GEOMAR, Figure 8.14]. The only common feature of the spatial distribution of CH_3I and IO VMR is, that west of 10°W the respective values are lower than east of 10°W. For atmospheric concentrations of various halocarbons measured during the cruise (CH_3I, CH_2Cl_2, $CHCl_3$, CCl_4, CH_2Br_2, CH_2ClI, $CHBr_2Cl$, CH_2BrI, $CHBr_3$, CH_2I_2, CH_3CCl_3, CH_2Br_2, pers. comm. H. Hepach, GEOMAR, preliminary data), no increase towards east was observed, either. This agrees from observations from other cruises (M91, P399, TransBrom) that the main source of reactive halogen compounds in the MBL is not directly related to the emissions of these halocarbons.
During MSM18/1 basically the same spatial pattern as for IO was also observed for BrO, mainly caused by the change in lightpath length, as inferred from O_4 dSCD. An exception is the BrO event at 33°N, where large amounts of BrO (4-6 ppt) were detected while the IO dSCD did not change on the respective days. This BrO event seems to be connected to a transport event of bromine-rich airmasses from the Arctic.
Radiative transfer modelling of concentration profiles was not possible for most days due to missing position and/or heading information during the first cruise leg.

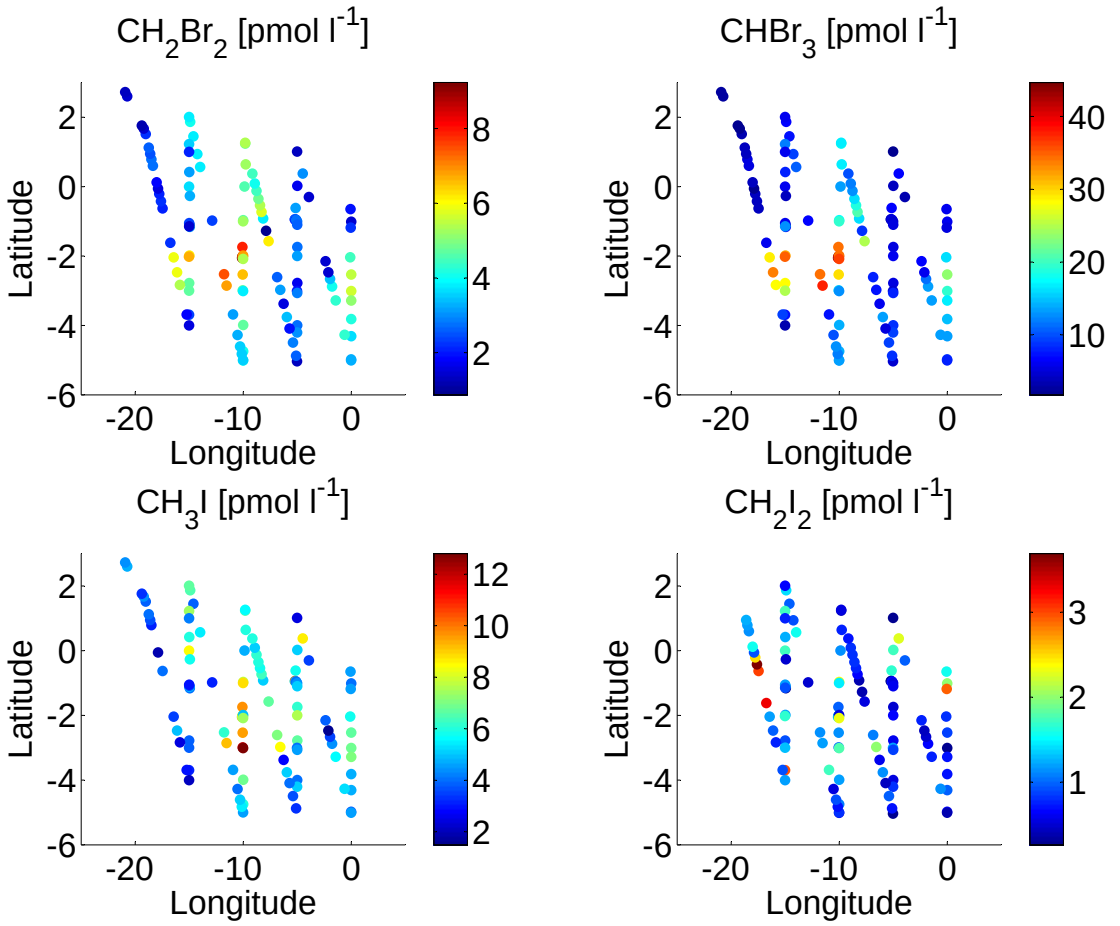

Figure 8.14.: Halocarbon measurements in surface sea water during MSM18/3 [pers. comm. H. Hepach/GEOMAR]. During M91 (Figure 7.5) maximum concentrations of CH_2Br_2, $CHBr_3$ and CH_3I differed not more than by a factor of two, but CH_2I_2 was found to be 10 times higher.

9. Polarstern ANT XXVIII: From Bremerhaven to Antarctica

Polarstern ANT XXVIII was the first cruise during which the whole distance between Bremerhaven and Antarctica was covered with data from both spectrometers, UV and VIS, after the UV and also the VIS spectrometer had been modified to lower the overall amount of instrumental stray light, see subsection 4.1.1 and Lampel [2010]. Therefore this cruise is given special attention, whereas the other Polarstern cruises are described less detailed. Additionally AERONET data is available for the first leg of this cruise, allowing for comparison of AOD from a Microtops instrument and the retrieved AOD from the MAX-DOAS.
The data from the ship's internal data system, the DShip system, contains errors for the first cruise leg for the geographic position data at the beginning of the second half of November 2012, but the spectra contain the correct position data. The DShip data the heading information and global radiation values seems to be incorrect during this time, too.
The second cruise leg from Cape Town to Cape Town via Neumayer station, allowing for MAX-DOAS measurements close to the permanent MAX-DOAS instrument on Neumayer station [Frieß et al., 2010].

9.1. Overview and additional measurements

Both spectrometers of the MAX-DOAS setup worked well during the first two cruise legs, until the mirror of the MAX-DOAS telescope fell off due to vibrations and/or ageing of the glue. The instrument was switched off in Cape Town for the following cruise legs.
Cruise leg ANT XXVIII/1 provides two more datasets which are of interest to be compared to the MAX-DOAS data:

1 2 3	IfT Leipzig	Aerosol sampling	physical properties optical properties chemical properties
4	MPIM Hamburg	Microtops	AOD
5 6 7 8	GEOMAR, GKSS, IfT	Oceannet container	H_2O vapour content HATPRO LIDAR [Kanitz et al., 2013] Meteorology Full sky imager

For comparisons of AOD, the AERONET data [Smirnov et al., 2009] will be used, see figure 9.2.1.
Cruise leg ANT XXVIII/2 did not include measurements which seem to be of relevance to be compared to MAX-DOAS measurements. During the second cruise leg R/V Polarstern left Cape Town and sailed south towards Neumayer station. On 12/20/2011

Polarstern reached the *Atka* bay to supply the Neumayer station.

9.2. MAX-DOAS results

9.2.1. Aerosol

9.2.1.1. Settings

For the aerosol retrieval the inversion algorithm implemented in Yilmaz [2012] was used on a 100m grid up to 4km height. The surface albedo was set to 0.05, the O_4 cross-section was scaled with 0.8 and an exponentially decreasing a-priori with an AOD of 0.05 with a scale height of 2km was used. For aerosol scattering, an aerosol single scattering albedo of 0.95 and a Henyey-Greenstein phase function with an asymmetry parameter of 0.72 were assumed. The O_4 data was retrieved using the cross-section by Hermans et al. [1999], because it appeared to produce more consistent results than the O_4 cross-section by Greenblatt et al. [1990], despite the problems which have been observed for the spectral retrieval of BrO (see subsection 5.1.1.2). As also reported by Yilmaz [2012] including intensities only improved the retrieval on clear-sky days slightly, but led in general to inconsistent results and stronger variations relatively to the AERONET AOD. Including the O_4 absorption at 477 nm did not lead to any improvement and a retrieval of the Ångstrom parameter was also not possible.
The averaging kernel matrix for the aerosol profile retrievals and the trace gas retrievals yields an information content of typically two degrees of freedom. Furthermore the available height information for any absorption above a height of 1km is small. This can be also seen when comparing the cloud ceiling height from the weather-station onboard Polarstern: Whenever the ceilometer yields values above 1km, the aerosol retrieval underestimates the height of the aerosols. This is particularly the case for the retrieval of the HCHO which has been transported on top of the MBL, see subsection 9.2.4.
The telescope elevation angles had an offset of about 1°, which was determined by varying the telescope elevation angle offset on a clear day while looking for minimum in the χ^2 of the retrieval. This was confirmed by the fact that the 1° elevation spectra were unusually dark compared to the ones recorded at 3° elevation. All elevations were corrected by -1°. The telescope was readjusted in Bremerhaven after the cruise. Elevation angles in the text of this chapter refer to the original elevation, not corrected for this offset.

9.2.1.2. Comparison with AERONET data

Reasonable agreement was found with AERONET data, as can be seen from figure 9.3. During two days at approximately 10°S the heading information from the ship's database was incorrect and caused these problems. These data points are marked with a circle in figure 9.3. Other problematic days which led also to deviating AODs were aerosol profile retrievals during cloudy days between Bremerhaven and the Bay of Biscay at the beginning of the cruise, which led to an overestimation of the AOD by MAX-DOAS measurements.
The other data points show a correlation with R=0.85 with the AERONET data.

The best agreement for AERONET data and the lowest χ^2 values were found for the retrievals using a correction factor for the O_4 cross-section of 0.8 as reported in Clémer et al. [2010] and Großmann et al. [2013].
A clear dependence of the difference of AOD from AERONET and MAX-DOAS on the colour index of the Fraunhofer reference spectra was not found. The sun photometer measurements were only possible when the direct lightpath from the sun to the instrument was not blocked, but this does not exclude broken cloud cover for the remaining part of the sky. Since the MAX-DOAS does not have the same viewing geometry as the sun photometer, an ideal correllation especially for cloudy or partly-cloudy sky is not expected.

9.2.2. IO

The average fit error for two-minute spectra with an RMS of less than $4 \cdot 10^{-4}$ is $(2.4 \pm 1.4) \cdot 10^{12}$ molec cm^{-2} during cruise legs 1 and 2. IO dSCD of up to $2.5 \cdot 10^{13}$ molec cm^{-2} were found, a measurement with one of the highest signal-to-noise ratios is shown in figure 9.4.
These column densities were used together with the aerosol data retrieved in subsection 9.2.1 to retrieve tropospheric concentration profiles of IO using the same settings as for the aerosol retrieval and an a-priori profile with a scale height of 2km and a ground concentration of 0.7 ppt. The surface volume mixing ratios obtained from these inversions are shown in figure 9.5. In tropical latitudes VCDs of $(2 - -4) \cdot 10^{12}$ molec cm^{-2} are obtained, which is slightly less than for M91 in the Peruvian upwelling($(3 - -6) \cdot 10^{12}$ molec cm^{-2}). It has to be noted that the information content for the IO retrieval was only 1–2 degrees of freedom and for the aerosol retrieval usually 2 degrees of freedom (typically 2 and 2–4 respectively for the M91 data). Consequently the averaging kernels only covered the lower part of the profile. Still, the IO is, as known from M91, within the lowermost 1000m, within the MBL, which is shown by the retrieval.
For both campaigns, M91 and ANT XXVIII, the height of the IO profile is higher than the height of the BrO profile. Final conclusions might require further improvements of the spectral retrieval of BrO.

9.2.2.1. IO in Antarctica

DOAS measurements by Frieß et al. [2010] showed IO dSCDs of up to $4 \cdot 10^{13}$ molec cm^{-2} measured at Neumayer station, Antarctica. Normally Polarstern brings supplies to the station in early austral summer, as in 2011, when Polarstern arrived around Dec. 19th in the Atka Bay to unload goods for Neumayer station.
A large part of the transect from Cape Town towards Antarctica shows low O_4 dSCD and low intensities, indicating a thick cloud cover. Approaching the coastline of Antarctica, higher O_4 dSCD were observed and the ceiling height measurements of the weather-station also showed larger values or no clouds at all. This also led to an increase in IO dSCD, up to $1.5 \cdot 10^{13}$ molec cm^{-2} at 5° elevation. Values recorded for 3° elevation showed lower values as did the O_4 dSCD. Unfortunately no webcam images are available,

maybe something was blocking the lowermost elevations while the ship was in Atka Bay. These problems were not observed for ANT XXIX, for which a general correlation of IO values with the O_4 dSCD was observed, see figure 9.6.
The correlation of IO and O_4 is similar to the values measured during ARK XXVII around Greenland, indicating a troposheric concentration of 0.2–0.4 ppt IO.

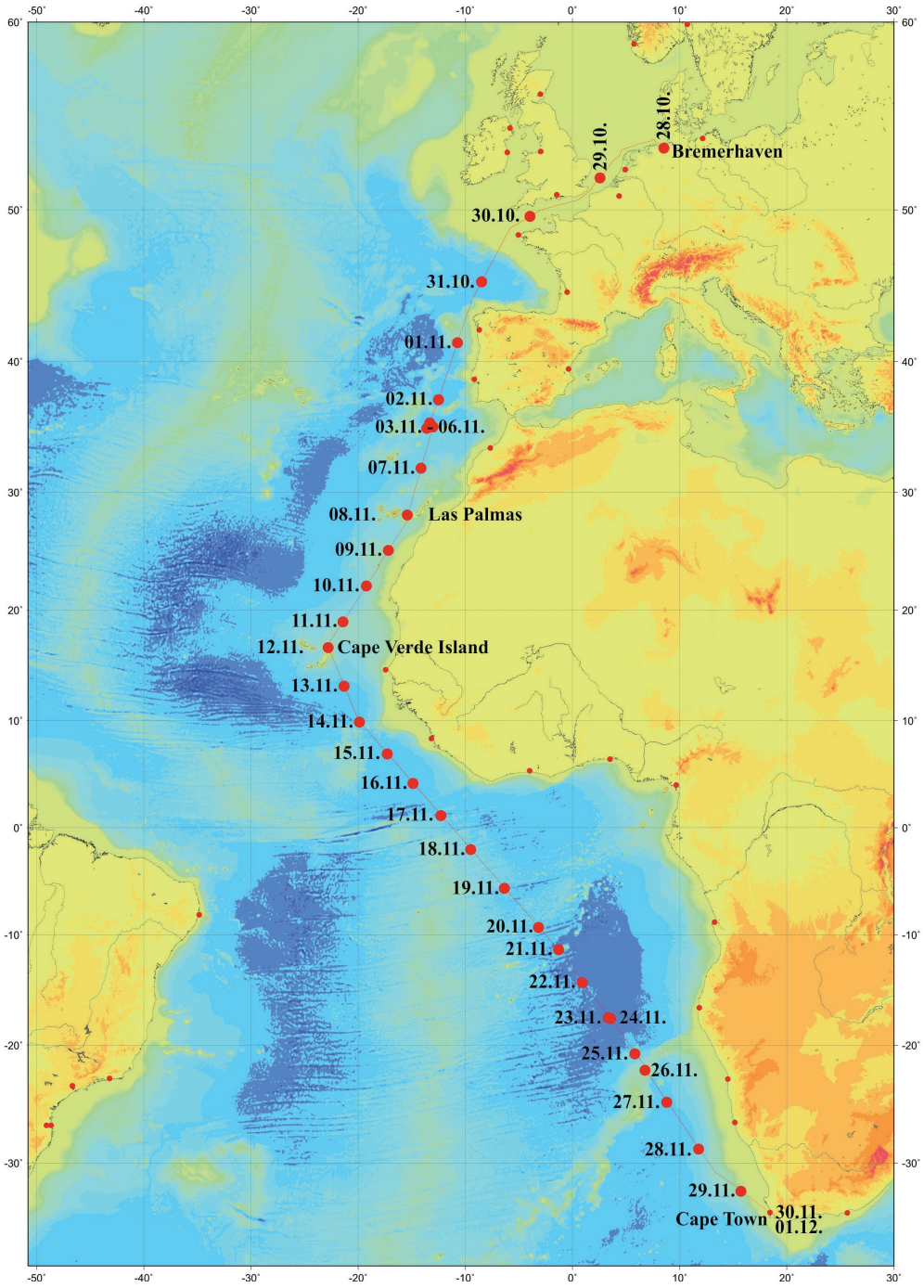

Figure 9.1.: Cruise track ANT XXVIII/1, from cruise report

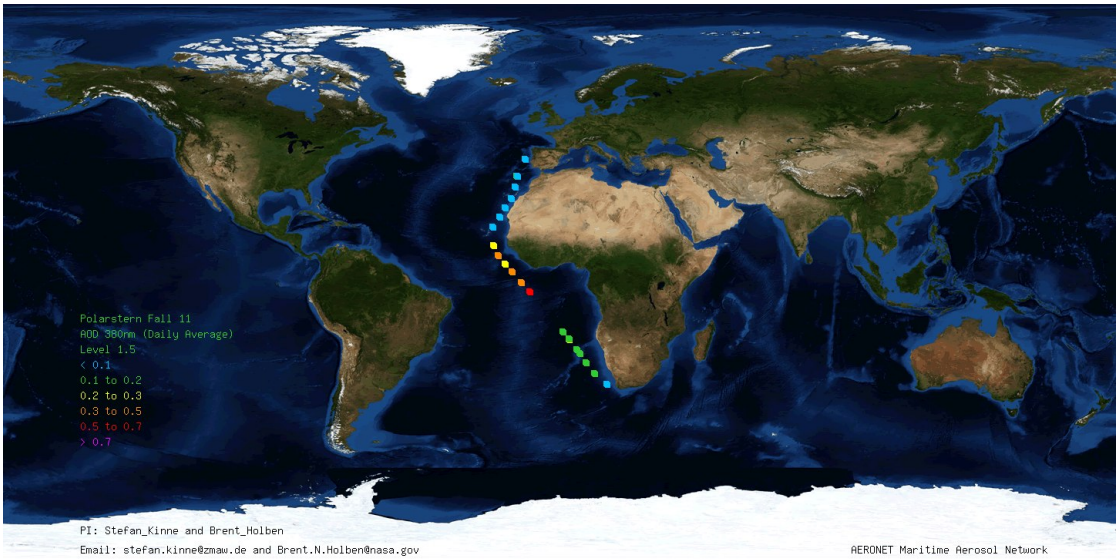

Figure 9.2.: AERONET aerosol optical densities data ANT XXVIII/1, Smirnov et al. [2009]

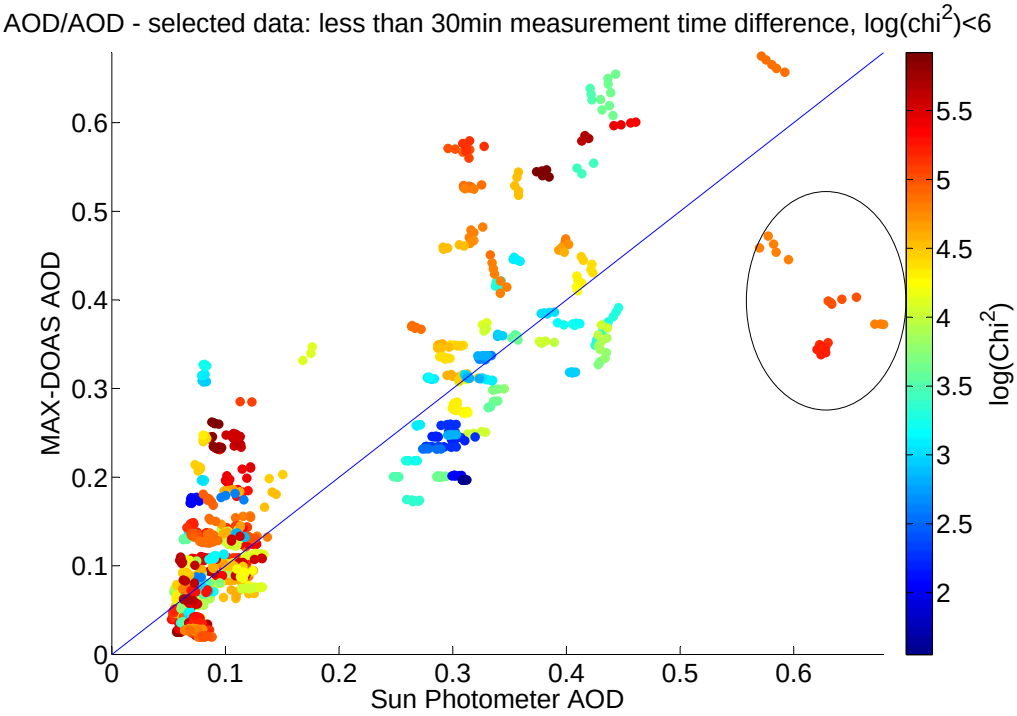

Figure 9.3.: Comparison of tropospheric AOD inferred from MAX-DOAS data and AERONET data. The data within the circle was recorded during two days during which the heading information for the ship was not stored correctly in the DSHIP system. Also at the beginning of the cruise the MAX-DOAS overestimated the AOD due to a broken cloud cover. Excluding the data points within the circle, a correlation coefficient of R=0.85 is obtained. Individual data points had to be measured at a time less than 30 minutes apart from each other.

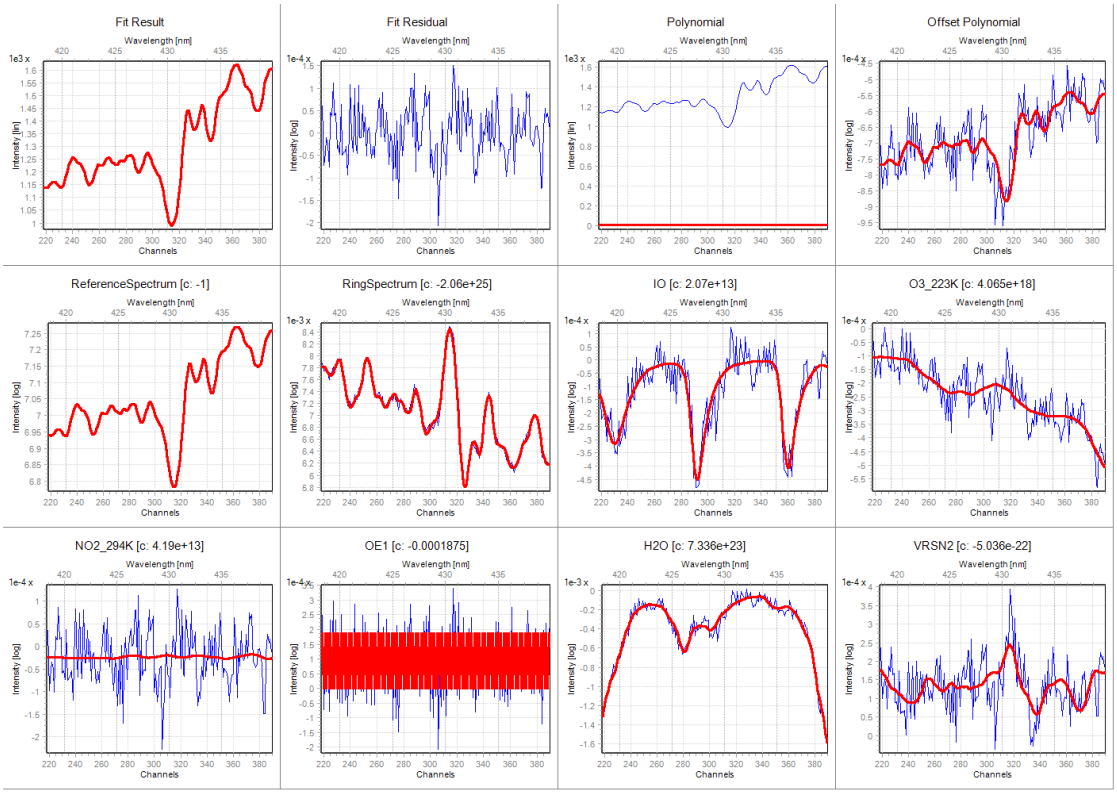

Figure 9.4.: IO fit from ANT XXVIII, 11/14/2011, 14:05 UTC at 10°N, 20°W of a single two-minute spectrum recorded at 3° elevation. The IO dSCD is 19 times above the fit error of $1.1 \cdot 10^{12}$ molec cm^{-2}. The fit used the modified HITEMP cross-section, scaled according to Table 5.8. The *OE1* spectrum is used to compensate for a residual structure caused by the readout-electronics.

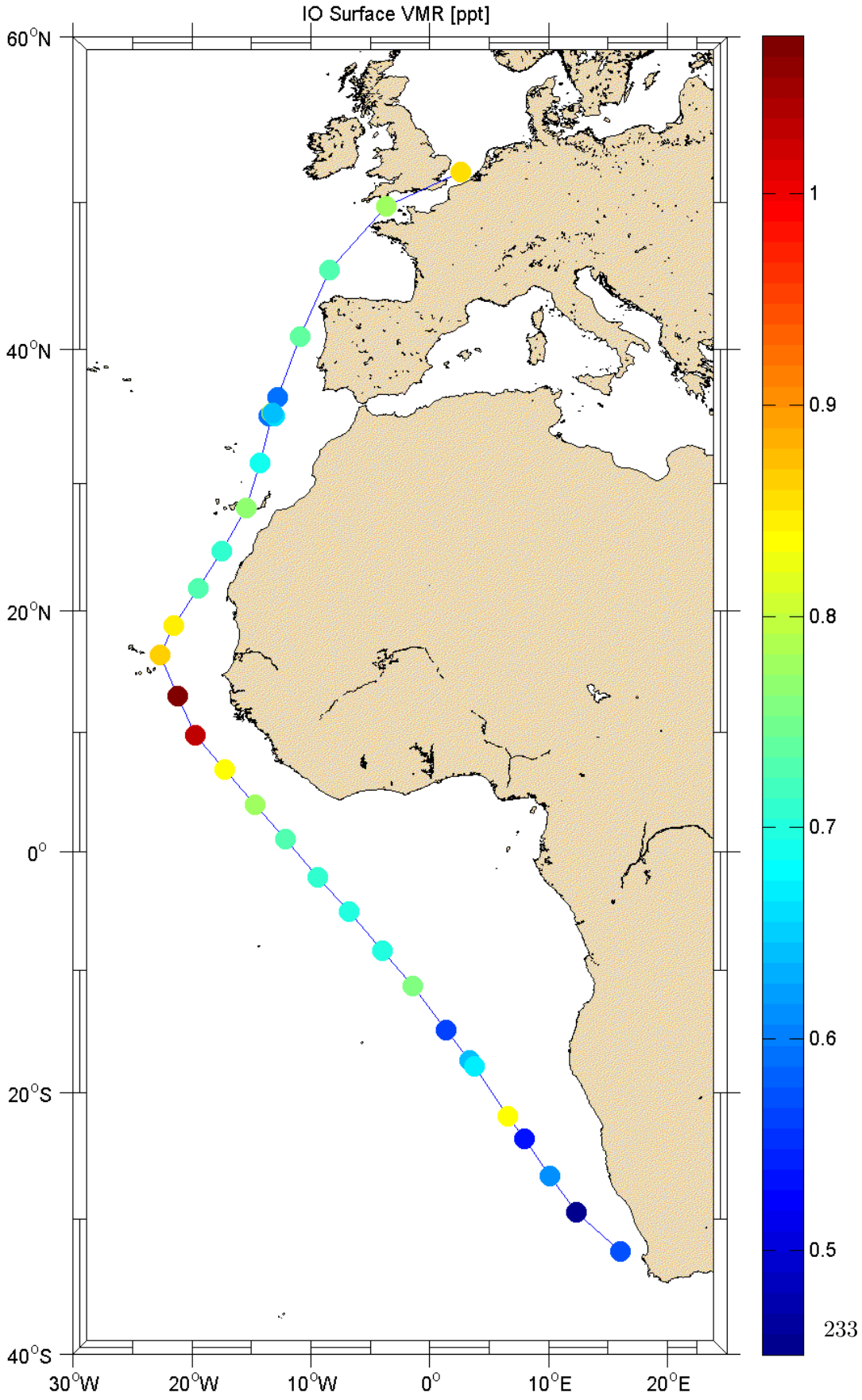

Figure 9.5.: IO surface volume mixing ratios during ANT XVIII in October and November 2011 from Bremerhaven to Cape Town.

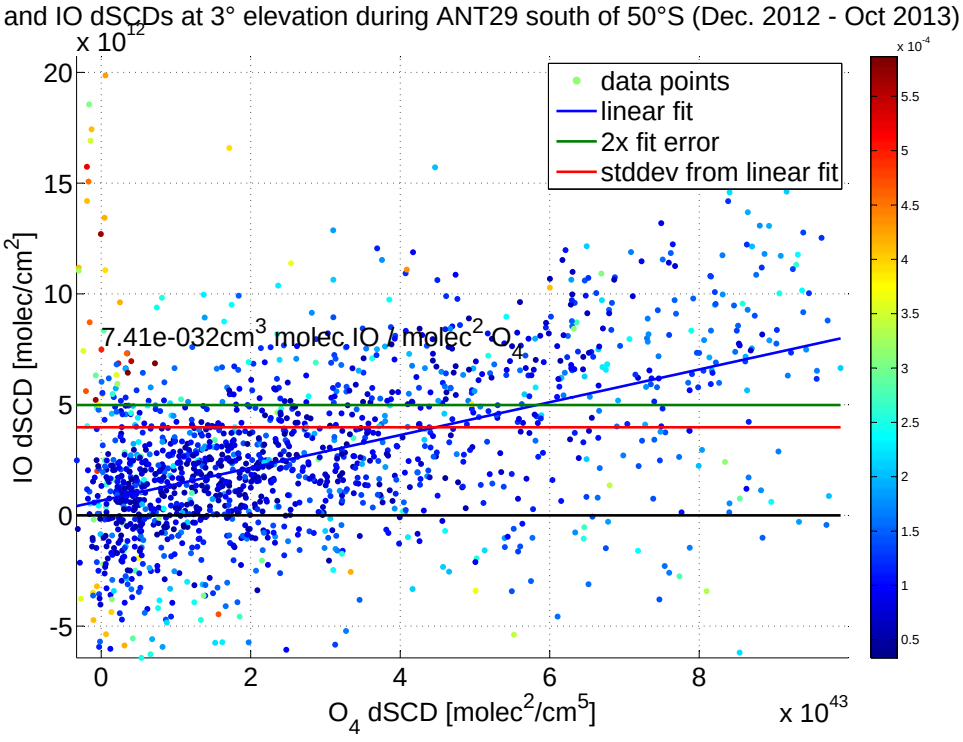

Figure 9.6.: Correlation plot for IO and O_4 (470 nm) dSCD for the complete data set of ANT XXIX south of 50°S. The slope of the fit is $7.4 \cdot 10^{-32}$ cm^3 molec IO molec^{-2} O_4.

9.2.3. BrO

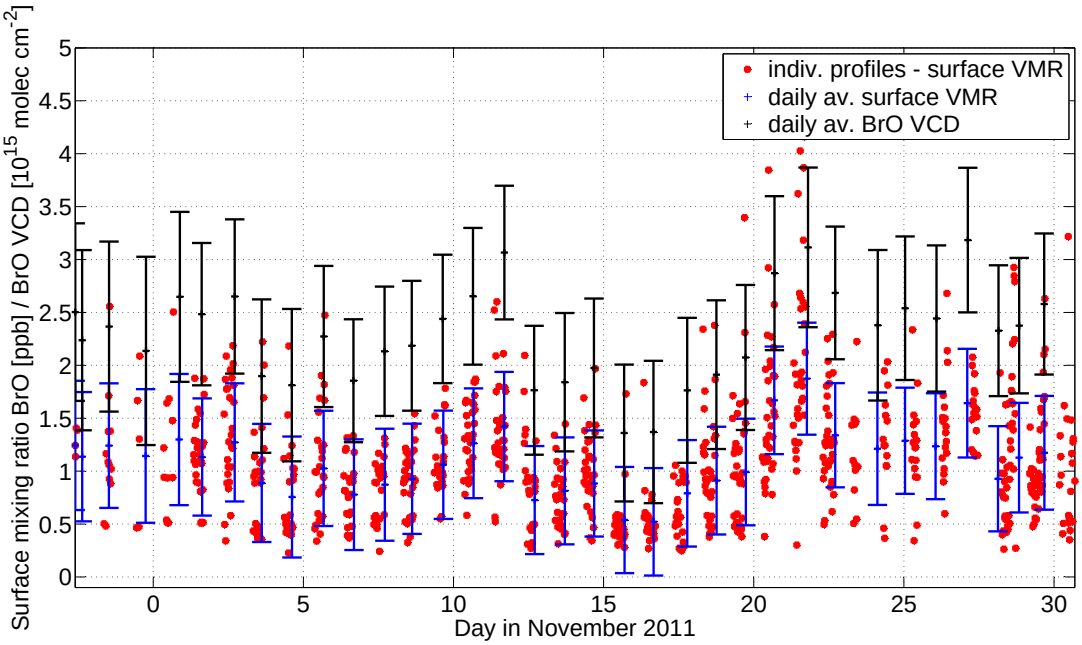

Figure 9.7.: BrO VCD and surface VMR during ANT XXVIII. Error bars indicate the errors obtained from the profile inversion. The minimum on November 15th coincides with polluted air masses from Africa showing enhanced concentrations of HCHO (compare figure 9.13), which were found above the typical height of the MBL, but might still contribute to the sink of reactive bromine. Despite slightly elevated NO_2 values as shown in figure 9.17, BrO concentrations of 1–2 ppt are observed around Cape Verde, on November 10th. Around November 20th, also elevated BrO concentrations were found, while tropospheric NO_2 concentrations were mostly found below detection limit, <50 ppt. The highest BrO dSCDs were observed north of Cape Verde, in clear-sky conditions, while November 20th was partly cloud-covered and yielding lower O_4 dSCDs, indicating a shorted lightpath.

The typical fit error BrO for a 3° elevation spectrum recorded for two minutes is $(8 \pm 3) \cdot 10^{12}$ molec cm^{-2} and a distribution of dSCD at 3° elevation of $(7 \pm 14) \cdot 10^{12}$ molec cm^{-2} was observed. Maximum tropospheric dSCDs were observed around Cape Verde (daily average $2.1 \cdot 10^{13}$ molec cm^{-2}) and the Antarctic shelf ice with dSCDs of the tenfold fit error. The fits show an unexplained residual structure correlated with O_4 absorption for all available O_4 cross-sections, which might indicate an additional tropospheric absorber or problems with the O_4 absorption cross-section. (see subsection 5.1.1.2)
The maximum daily BrO dSCD value of $2.1 \cdot 10^{13}$ molec cm^{-2} shown in figure 9.10 in the Mauritanian upwelling (see also cruise MSM18: subsection 8.1.1) show the highest BrO dSCD for the trajectory which stayed the longest time within the upwelling region.

The maximum values for BrO in the tropics were observed during the morning and afternoon, which cannot be completely explained by O_4 dSCD variations, even though a general correlation of BrO and O_4 dSCDs is observed. This agrees with previous long-path measurements by Read et al. [2008b] and Tschritter [2013], who observed the largest BrO concentrations during sunrise and sunset and a minimum around noon. An example fit is shown in figure 9.8 and the respective profiles for that day in figure 9.11.
The other maximum of BrO dSCD is observed close to Antarctica, with BrO dSCD of up to $5 \cdot 10^{13}$ molec cm^{-2} at large O_4 dSCD. It is not clear if this can be disentangled from the residual structures appearing with increasing O_4 dSCD. A fit is shown in figure 9.9.
Figure 9.11 shows profiles for the 11/10/2011, in the Mauritanian upwelling between Canary islands and Cape Verde. BrO VMR are found between 1–2 ppt, in agreement with daytime measurements in previous studies by Read et al. [2008b] and Tschritter [2013]. Five days later (Figure 9.13), outside the main upwelling, but therefore potentially influenced by outflow of organic compounds from Africa, retrieved BrO concentrations are only half as large.
The other maximum is found at 15°S, with up to 2–4 ppt BrO as shown in figure 9.7.

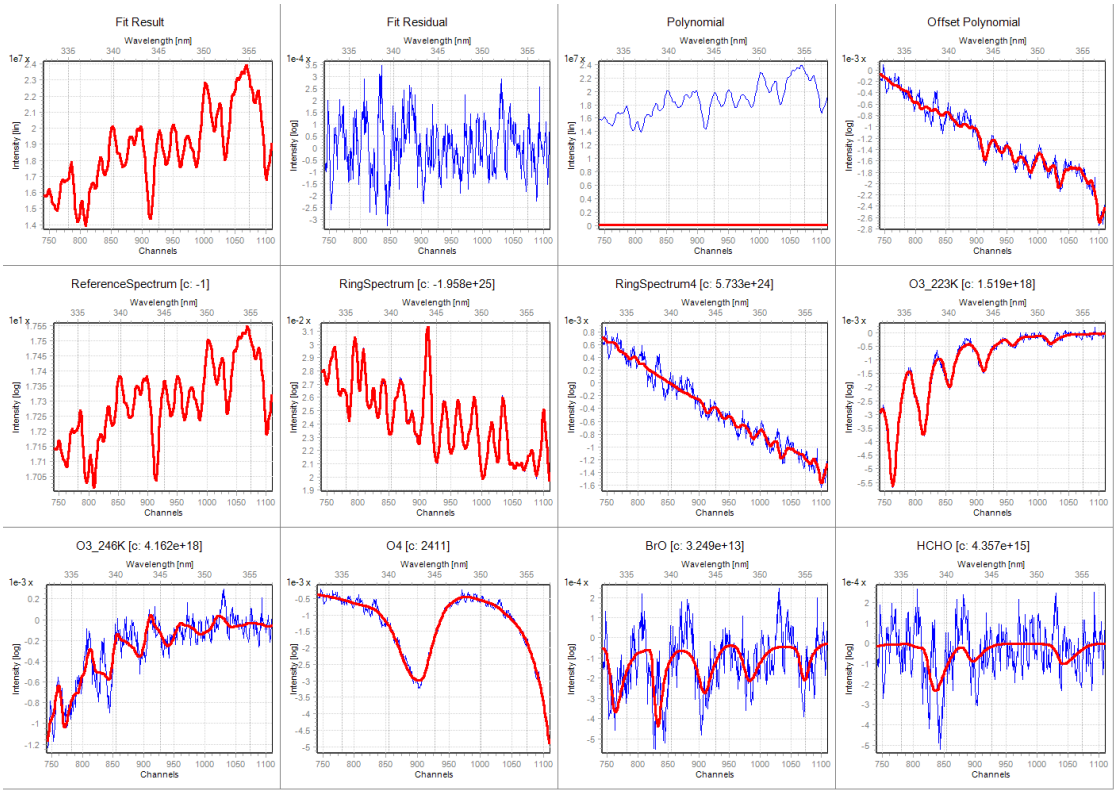

Figure 9.8.: Maximum of tropical BrO dSCDs at 3° elevation during ANT28, the summed spectrum #4375 (four co-added elevation sequences) measured at 21°41', 19°31' north of the Cape Verde islands on Nov. 10th, 2011 at 15:23 UTC.

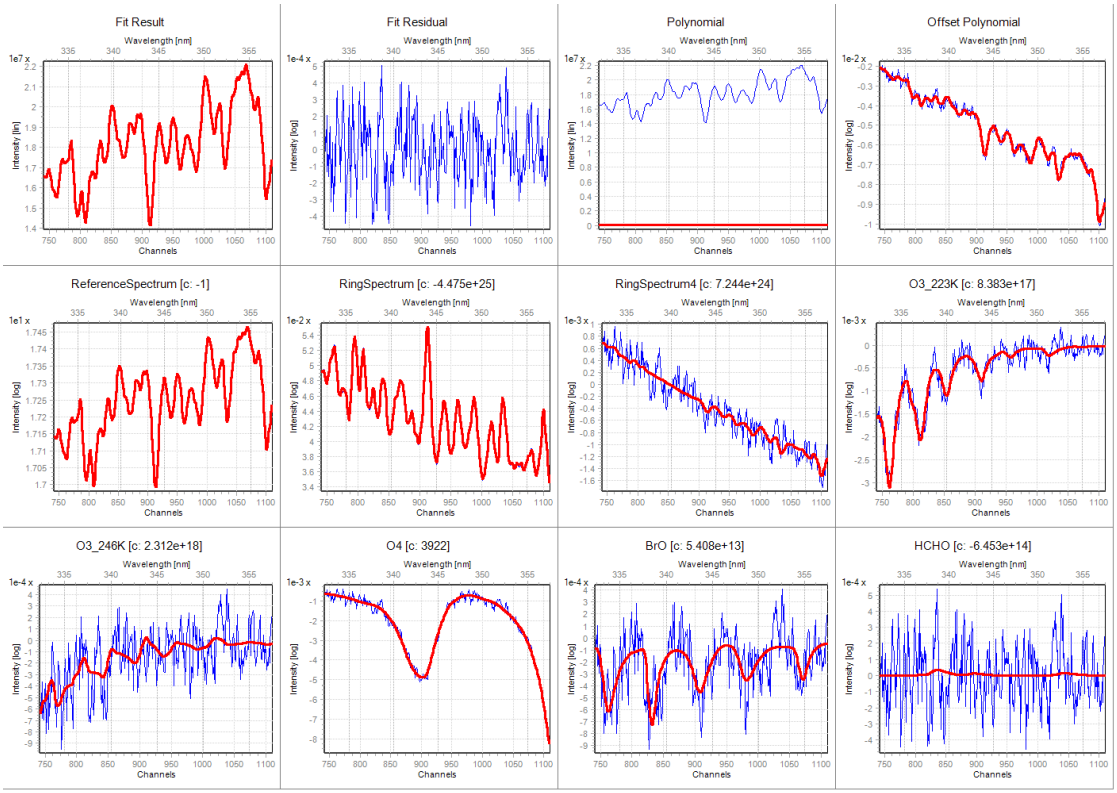

Figure 9.9.: Maximum of BrO dSCDs at 3° elevation during ANT28, the summed spectrum #23072 (four co-added elevation sequences) recorded at 69°S35', 0°52'W close to the coast of Antarctica on December 23rd, 2011 at 12:38 UTC.

When retrieving profile information despite the existing spectral problems of the spectral analysis for small BrO concentrations, BrO daily averaged VCDs vary between $1.4 \cdot 10^{12}$ molec cm^{-2} at 10°N during the day with the maximum HCHO VCD and $2.8 \cdot 10^{12}$ molec cm^{-2} at 10°S, close to Cape Verde Islands, approaching Cape Town and passing Portugal. A vertical BrO column of $2.5 \cdot 10^{12}$ molec cm^{-2} corresponds to 1 ppt of BrO within a boundary layer with a height of 1000 m.

9.2.4. Formaldehyde

Typical fit error HCHO for a 3° elevation spectrum recorded for two minutes is $(1.6 \pm 0.7) \cdot 10^{15}$ molec cm^{-2} and a distribution of dSCD at 3° elevation of $(1.3 \pm 0.5) \cdot 10^{15}$ molec cm^{-2} with maximum tropospheric dSCD close to the equator (daily average $8 \cdot 10^{15}$ molec cm^{-2}) and in the North Sea (10^{16} molec cm^{-2}).
The retrieval of background values is problematic, since the residual structures shown in figure 9.8 can affect the HCHO absorption structures. Nevertheless, tropospheric slant column densities close to Antarctica are low ($< 3 \cdot 10^{15}$ molec cm^{-2}), independent of the O_4 dSCD and thus the size of the residual structures.

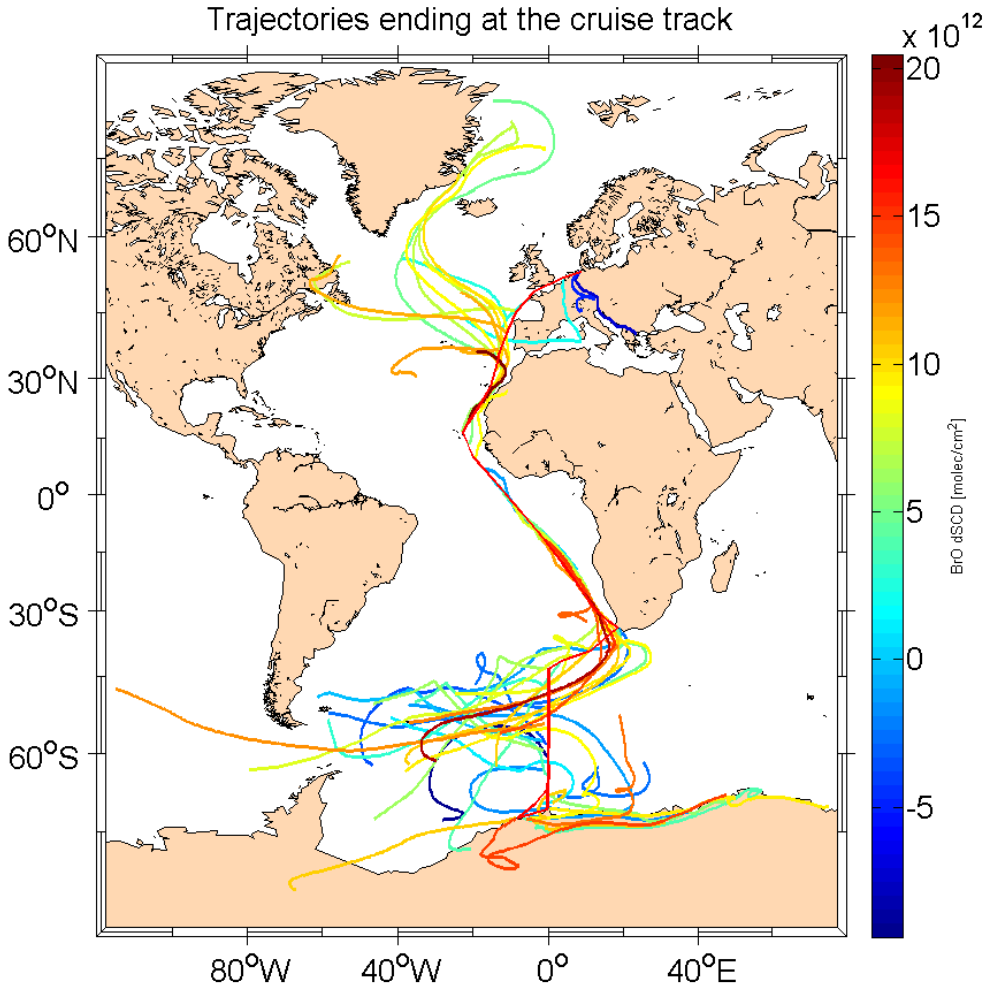

Figure 9.10.: Five day backward trajectories calculated by HYSPLIT from GDAS data for the duration of the cruise. The endpoint of each trajectory was set to a height of 100m. The colour-code corresponds to daily averages of BrO dSCD at an elevation of 3°. Typical open ocean dSCDs were found at $(1--2)\cdot10^{13}$ molec cm^{-2}. Lower values were observed in northern Germany (high NO_2 concentrations) and between Cape Town and Neumayer (short lightpaths due to bad weather). The maximum daily average of BrO dSCDs was found for a trajectory along the Mauritanian upwelling region north of Cape Verde islands.

The HCHO VCDs shown in figure 9.12 agree with satellite observations during the same time, compare figure 1.4 and figure 9.12.

The profile retrieval for HCHO for the tropical maximum indicates a layer of enhanced HCHO concentrations in a height of almost 1000m. This agrees with satellite data

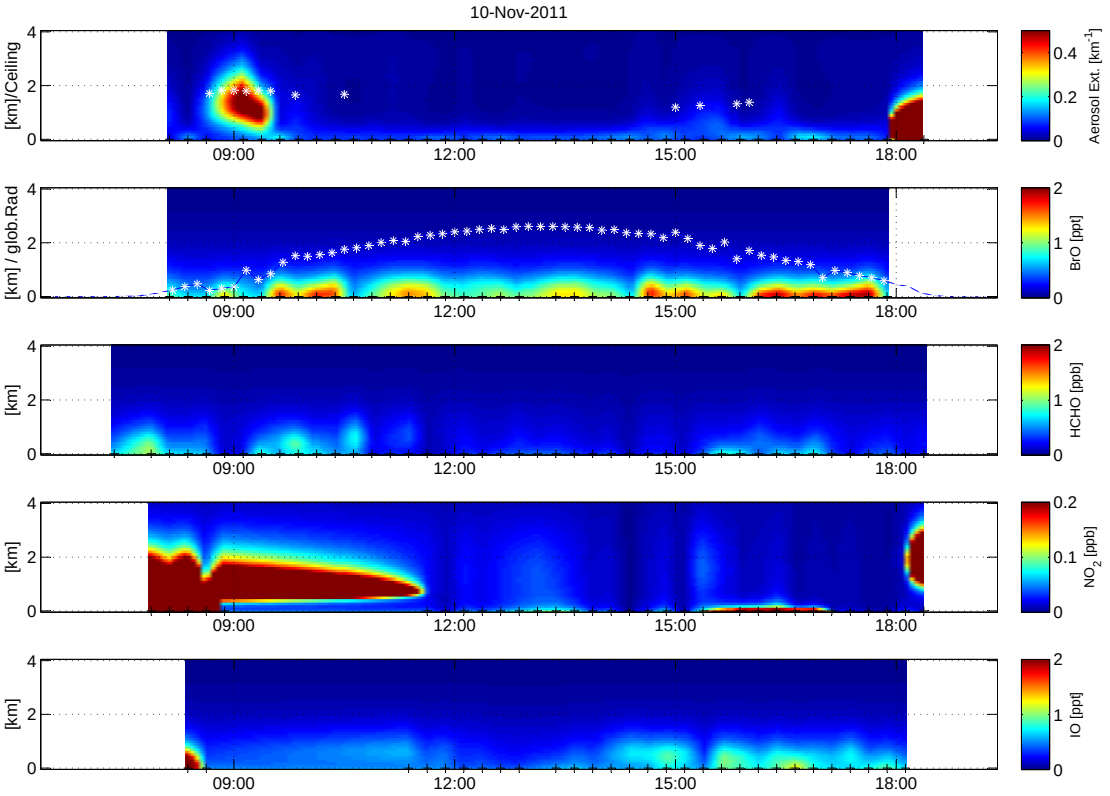

Figure 9.11.: ANT XXVIII on 11/10/2011 at 22°N, 20°W, the day with the maximum BrO dSCD as shown in figure 9.10 with the respective backward-trajectories. From 14:00–19:00 UTC NO_2 surface concentrations were mostly below 50 ppt, before 14:00 UTC above 100 ppt. The profiles are retrieved at a time resolution of 30 and interpolated. The time of individual profiles is marked with a black cross.

observations, which show that a large part of the tropical VCD of formaldehyde is due to continental outflow of organic compounds of biogenic origin or emitted by biomass burning in Africa. This is the main reason for enhanced VCDs of formaldehyde of $5 \cdot 10^{15}$ molec cm^{-2} in the eastern tropical Atlantic. Aerosol profiles for these days also show higher aerosol extinction in these heights. Concentration profiles of IO and BrO for these days show the main part of the IO and BrO close to the sea surface, in agreement with observations on other days. Moreover the surface VMR of HCHO is also similar to other days of measurements in the tropics, at about 500 ppt.

Additionally it agrees with trajectory calculations: The 5-day trajectories shown in figure 9.10 ending at a height of 100m do not show the influence of continental air masses along the cruise track close to the equator, but the trajectories calculated for a height of 750m shown in figure 9.12 do. MODIS observations registered enhanced biomass burning in coastal areas, see figure 9.16. On a previous transatlantic cruise leg

of Polarstern in April 2010 LIDAR measurements showed lofted layers of aerosols in the same region in heights of >1km which were connected to Saharan dust and biomass burning [Kanitz et al., 2013].
Due to the limited information content of the measurements for profile retrievals, especially above heights of 1km, the actual height of the plume cannot be determined. Above heights of 1km, the resulting profile can be interpreted maybe as the best fit between agreement with the a-priori and the information that the absorber is not located in the lowermost layers of the atmosphere. Consequently, the main absorption is placed where the information content begins to decrease, which is roughly where the main amount of HCHO is retrieved here.
A consequence for tropospheric chemistry is, that the enhanced HCHO observed over the tropical Atlantic from satellite is not necessarily resulting in an enhanced sink for BrO in the marine boundary layer, because most of the tropospheric BrO was usually observed close to the ground (MSM18/1: subsection 8.1.1, Martin et al. [2009] and during Poseidon P399 by Tschritter [2013]). Due to its origin, formaldehyde concentrations might be used here as well as a tracer for other organic compounds, such as isoprene, methanol and black carbon.

9.2.5. Glyoxal

For the Polarstern instrument it is not as easily possible to include the strong water vapour absorption at 442 nm as it is for the SMAX-DOAS instrument as e.g. during M91 (chapter 7). The reason might be either caused by the lower spectral resolution compared to the SMAX-DOAS, by not knowing the instrument function as precisely as for the Acton350i of the SMAX-DOAS instrument, together with the instrument function not being constant over the wavelength range of interest or a combination of all factors.
It was therefore necessary to exclude the main water absorption from the fit window, which in turn led to problems to obtain correct O_4 dSCD, because also a part of the underlying O_4 absorption was removed (see figure 5.11 for an overview of absorption cross-section in this spectral range). The slope of the O_4 absorption around 450 nm was observed to result, in the worst case, in false ODs of up to $5 \cdot 10^{-4}$. A compromise was found to have a gap to exclude the water vapour absorption from 441–447 nm. These settings were then also used in Mahajan et al. [2014] for the analysis of the data from Polarstern ANT XXVI, XXVIII and TransBrom on RV Sonne. These settings also exclude the possible influence of changes of the radiative transfer due to strong water vapour absorption lines discussed in section 5.4.
South of Cape Town large negative Glyoxal dSCDs ($-1 \cdot 10^{15}$ molec cm^{-2}) were observed when not accounting for liquid water absorption. It is assumed that more light has passed ocean water on days with overcast conditions. The negative dSCD are removed by including liquid water absorption in the fit. For M91 this was not observed (subsection 7.2.6) due to the weather situation.
The only significant single observations of Glyoxal in the MBL during this cruise are in Cape Town and north of the Canary islands ($\approx (1 \pm 0.2) \cdot 10^{15}$ molec cm^{-2}), both of

which occurred simultaneously with larger absorptions of NO_2, indicating anthropogenic emissions. The case at the Canary islands might have been a passing ship.
Conclusions about background observations of glyoxal are more difficult to draw, since it seems to be difficult if not even impossible to disentangle the water vapour absorption from the absorption of Glyoxal within spectral data, see subsection 5.6.4, especially for the Polarstern MAX-DOAS spectral data at a relative low spectral resolution. Also depending on the actual fit scenario settings, an averaged slope of $1.6 \cdot 10^{-9} \frac{\text{molec Glyoxal cm}^{-2}}{\text{molec H}_2\text{O cm}^{-2}}$ is found. For a water vapour dSCD of typically $5 \cdot 10^{23}$ molec cm^{-2} for an elevation angle of 3° in the tropics this translates to $8 \cdot 10^{14}$ molec cm^{-2} Glyoxal. This agrees with the results for the retrievals done within Mahajan et al. [2014]. This is nevertheless significantly smaller than the values previously reported by Sinreich et al. [2010] for the tropical Pacific.
This is either a real coincidence, or a retrieval problem. The observations of glyoxal absorptions during M91 and MSM18/3 where no glyoxal was found with the better MAX-DOAS instrument indicate indeed spectral retrieval problems for the Polarstern MAX-DOAS instrument, which introduces cross-correlation for H_2O and Glyoxal absorptions. Therefore measurements at low telescope elevation angles were used to correct the glyoxal data based on H_2O dSCD. As shown in figure 9.14 this then leaves the main emission sources: Western Europe (40°N), Canary Islands (30°N), outflow from biomass burning in Africa (10°N) and Cape Town (30°S). The variations at 20°S might be again due to biomass burning or are only unexplained spectral artifacts. All of these measurements are one magnitude smaller than previous measurements reported by Sinreich et al. [2010] for tropical regions.
The apparent correlation with the observations of HCHO in the tropics would make sense regarding the oxidation of organics Vrekoussis et al. [2010], but the measurements are not conclusive enough to prove this point. In this case most of the glyoxal would also be found at the upper boundary of the marine boundary layer, which would make it harder to detect due to lower AMFs.

9.2.6. NO_2

The average NO_2 fit error for low elevation angles was $(2 \pm 1) \cdot 10^{14}$ molec cm^{-2} for a retrieval window from 414–438 nm. Using other fit ranges in the visible wavelength range did not improve the overall result, since strong water vapour absorption lines caused residual structures of more than $5 \cdot 10^{-4}$.
Tropospheric NO_2 was only detected in large amounts on the North Sea after leaving Bremerhaven and in the English channel. Surface concentrations of more than 100 ppb were retrieved, daily averages were 30 ppb on the North Sea and 5 ppb in the English Channel. This corresponds to a tropospheric VCD of $3 \cdot 10^{16}$ molec cm^{-2} in the North Sea on October 28th, 2011 decreasing until the Bay of Biscay to values below 50 ppt on November 1st.
Single profiles between the Canary Islands and Cape Verde exceeding surface mixing ratios of 1 ppb could have been caused by other ships or RV Polarstern itself.

A typical fit error of $2{\cdot}10^{14}$ molec cm^{-2} corresponds roughly to 10 ppt NO_2 at an elevation angle of 3°. Typical averaged dSCDs at an elevation angle of 3° are $3 \cdot 10^{14}$ molec cm^{-2} ($-4 \cdot 10^{14}$ molec cm^{-2} without including a correction for VRS on N_2, see also subsection 5.2.3.1). A determination of NO_2 background values was therefore not possible. Sometimes the profile retrieval could no converge, since the distribution of NO_2 dSCD was below detection limit.

9.3. Comparison of IO dSCD with ANT XXVI

Polarstern cruises ANT XXVI (2009) [Lampel, 2010] and ANT XXVIII (2011) took place during the same time of the year, covering the distance between Bremerhaven/Germany to Cape Verde almost along the same track (see figure 6.1). Using the same retrieval settings for IO, ANT XXVIII shows larger daily averages ($18 \cdot 10^{12}$ molec cm^{-2}) for IO than those observed during ANT XXVI ($11 \cdot 10^{12}$ molec cm^{-2}). During ANT XXVI the maximum IO dSCD at 3° elevation was found at 24°S, during ANT XXVIII close to Cape Verde at at 19°N.
The ship's weather station data shows no significant difference for sea surface and air temperature along the cruise tracks during both years.
The O_4 dSCDs cannot either explain this large difference.
The modification of the spectrometers for stray-light minimization is a major difference between both cruises. The modifications were not as significant for the visible spectrometer, decreasing the instrumental stray-light by a factor of 2–3. But also ANT XXIX in the following year 2012 shows lower IO values south of Cape Verde (typically $11 \cdot 10^{10}$ molec cm^{-2}, daily average at 3° elevation.).
A similar variability was observed for I_2 measurements on Cape Verde by Lawler et al. [2013], where averaged I_2 mixing ratios at night were three times higher in May 2007 compared to May 2009.

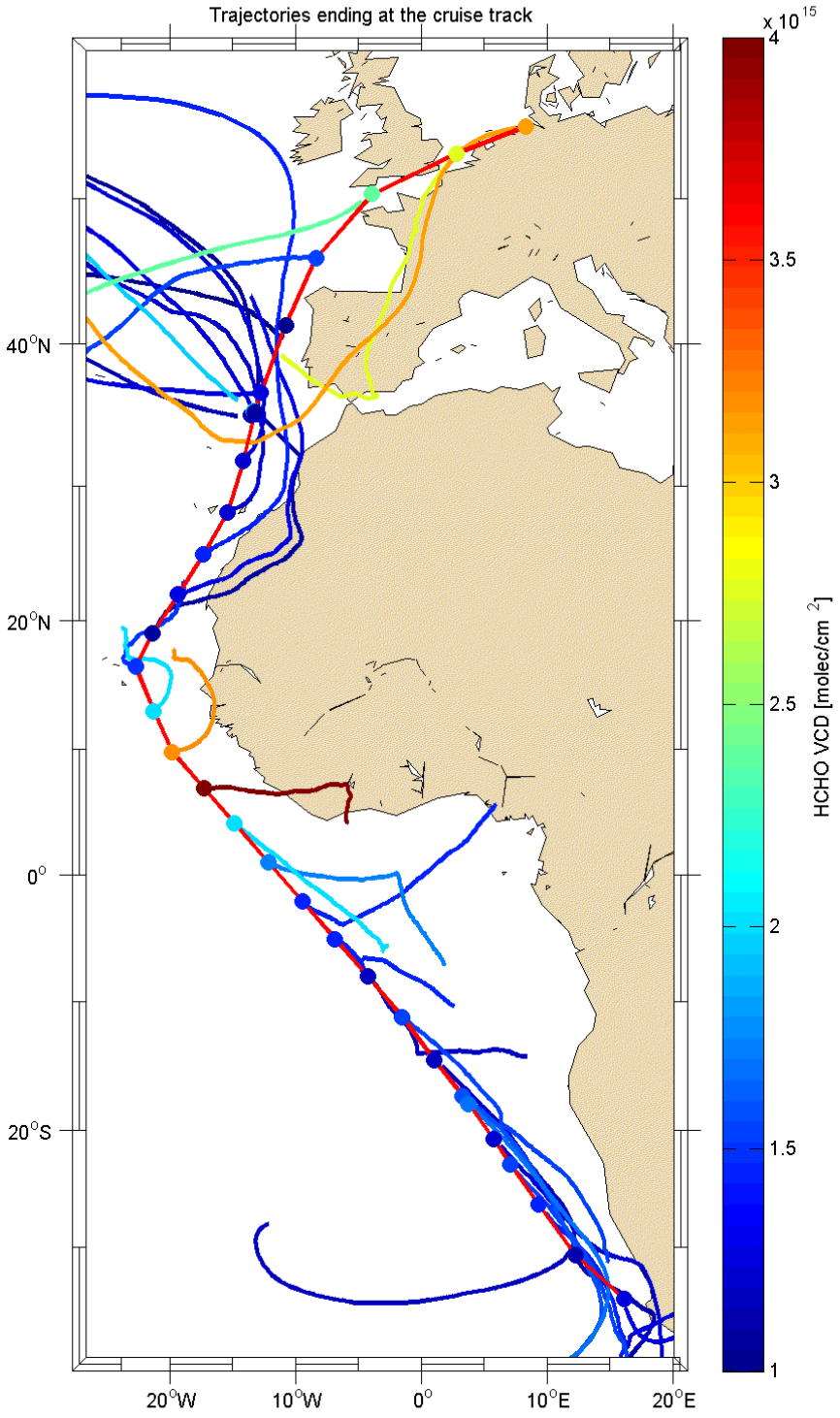

Figure 9.12.: HCHO VCD and 5-day backward trajectories (HYSPLIT, GDAS) for a height of 750m. VCDs agree with satellite observations, e.g. by the OMI instrument (see figure 1.4)

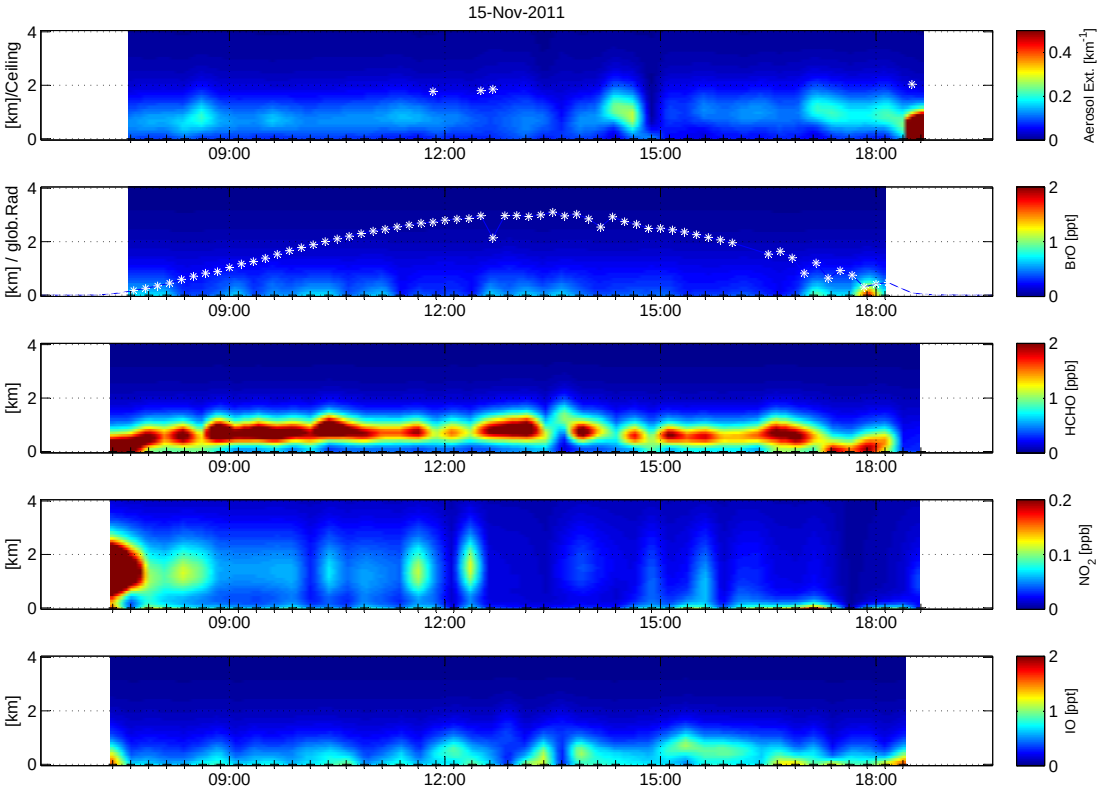

Figure 9.13.: ANT XXVIII on November 15th, 2011 at 8°N, 16°W, the day with the maximum HCHO dSCD as shown in figure 9.12 with the respective backward-trajectory indicating air-masses from Africa above the boundary layer. NO_2 surface VMR varied between 0.2–1.0 ppt.

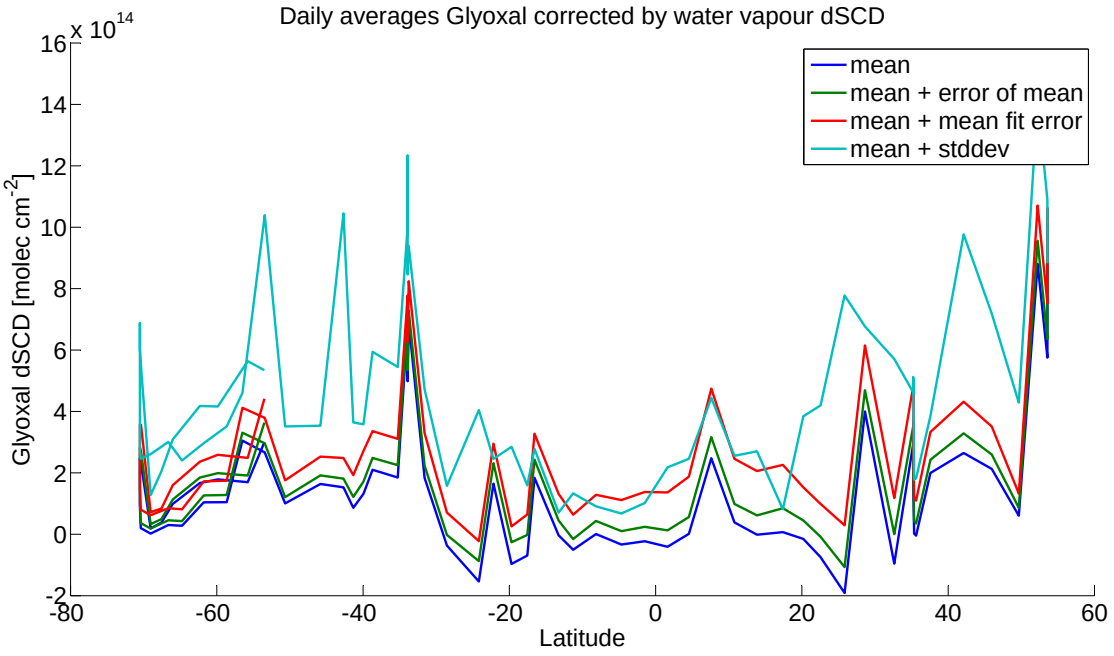

Figure 9.14.: Glyoxal dSCDs during ANT XXVIII when removing the apparent correlation of glyoxal dSCDs with water vapour dSCDs. Glyoxal absorption is still detected in the North Sea, close to the Canary islands, at the maximum of HCHO observations at 10°N and in Cape Town.

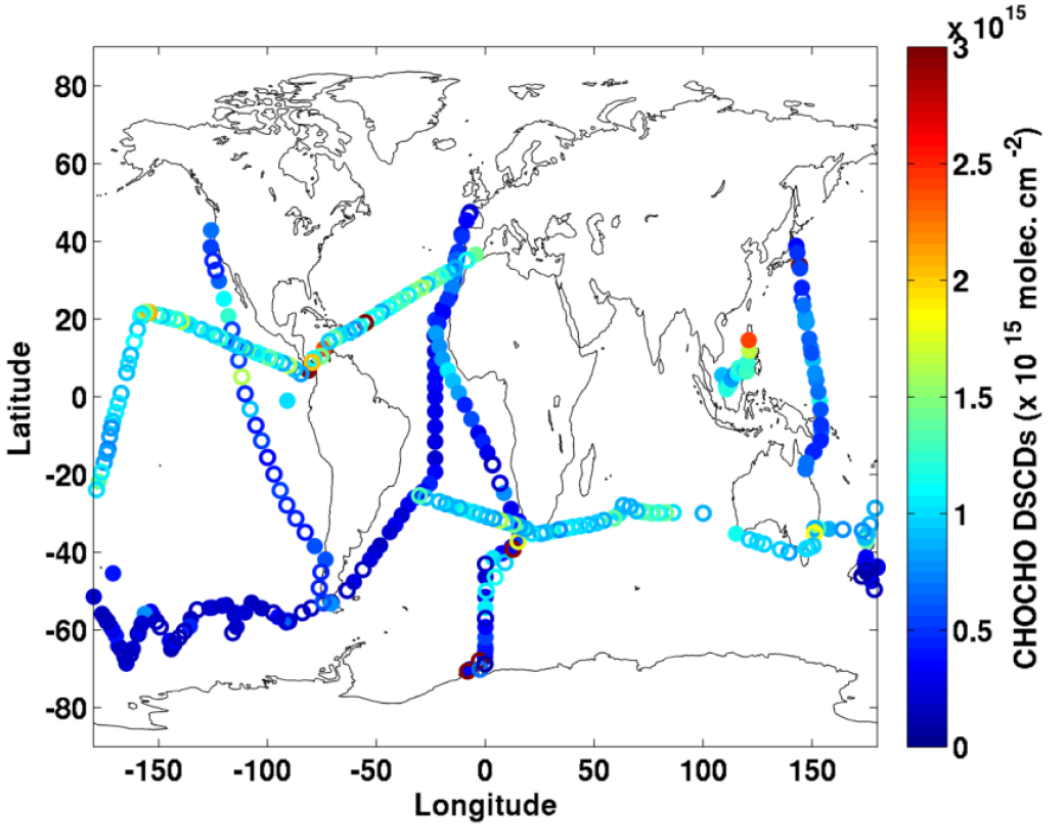

Figure 9.15.: Glyoxal dSCD data for Polarstern ANT XXVI and XXVIII, plotted together with other campaigns in Mahajan et al. [2014]. Filled circles show data points above, open points data points below the respective detection limit.

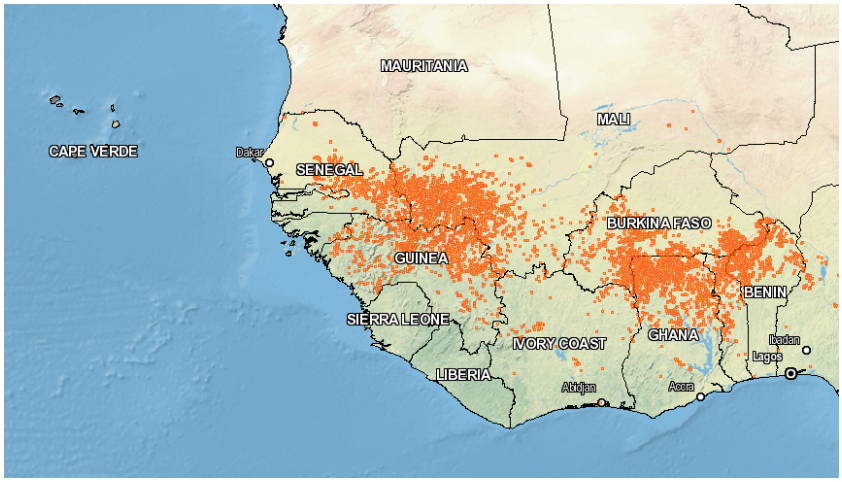

Figure 9.16.: Map of fires detected from MODIS, FIRMS, from 11/11/2011 to 11/18/2011.

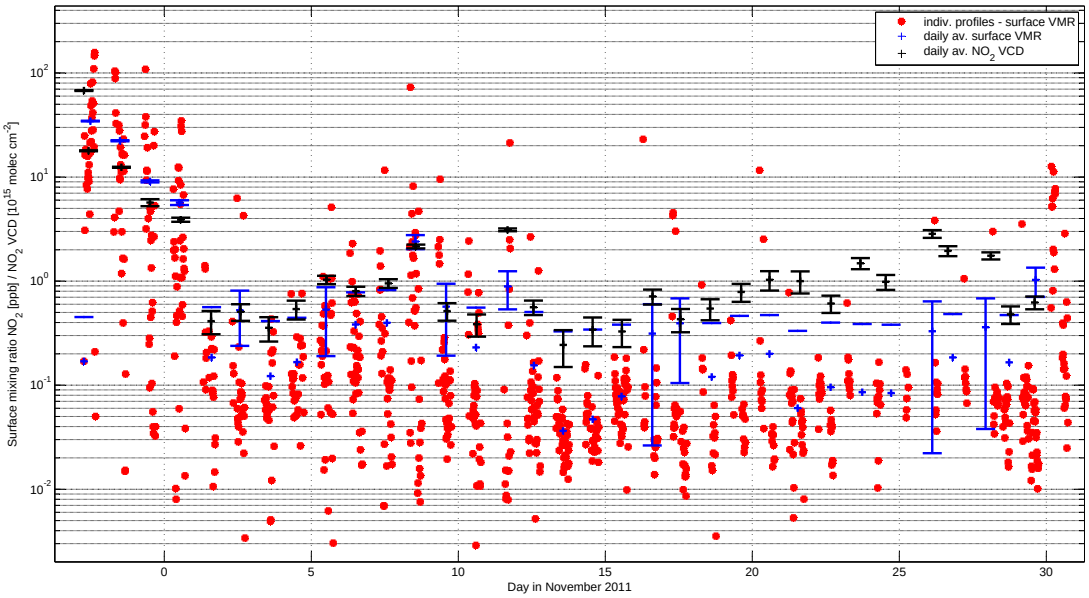

Figure 9.17.: NO_2 VCD and surface VMR during ANT XXVIII. Error bars indicate the errors obtained from the profile inversion. Largest concentrations were observed on the North Sea, some enhanced NO_2 concentrations are observed between the Canary Islands and Cape Verde (November 7th-11th).

10. Polarstern Arctic cruises

The MAX-DOAS was on the Polarstern cruises ARK XXIV(2009), XXV(2010) and XVII(2012) in the Arctic. Only during ARK XXVII the UV spectrometer was already modified to reduce instrumental stray light. Without supervision apart from cleaning the telescope by personal onboard the ship, the instrument recorded during the three cruises in total more than 9 months of MAX-DOAS measurement data.

10.1. Polarstern ARK XXIV

The same setup as during Polarstern ARK XXV measured during ARK XXIV in the Arctic, from 06/19 until 09/29/2009. The observed O_4 dSCD were low on almost all days, indicating low clouds and/or fog. IO was not detected, NO_2 only close to Iceland and Spitsbergen.

10.2. Polarstern ARK XXV

10.2.1. Overview

Throughout the whole cruise the instrument was working and delivered continuous and stable spectra. An overview over typical spectral shifts in shown in figure 4.3.

10.2.2. Results

10.2.2.1. IO

As opposed to Polarstern cruise ARK XXIV with the same setup of spectrometers, during ARK XXV IO dSCDs have been found to be above detection limit during summer, west of Greenland. dSCDs around $2 \cdot 10^{13}$ molec cm^{-2} were observed, exceeding the fit error by a factor of 10–14 when summing four elevation sequences. An example fit is shown in figure 10.2. However, the average dSCD for a fit based on spectra with a total integration time of 8 minutes was $(1 \pm 4) \cdot 10^{12}$ molec cm^{-2} and the fit error of $(1.7 \pm 0.8) \cdot 10^{12}$ molec cm^{-2} for results with an RMS $< 4 \cdot 10^{-4}$. Figure 10.1 shows the dSCDs during the cruise. The size of the dots is proportional to the signal to noise ratio of the O_4 measurements. This pronounces measurements in situations high visibility and sufficient light.
No correlation of IO dSCD and air temperature and/or humidity was observed during the cruise, based on data from the ship's weather-station.
The correlation shown in figure 10.3 agrees with measurements during ANT XXIX in the Antarctic. These column densities correspond, for low aerosol extinction of less than 0.05, to concentrations of 0.2–0.4 ppt within the lowermost kilometre.

Enhanced iodine concentrations during late summer (August–September) of aerosol particles were reported by [Barrie and Barrie, 1990] (see also figure 1.8), which indicates a certain role of iodine in summer-time polar tropospheric chemistry.

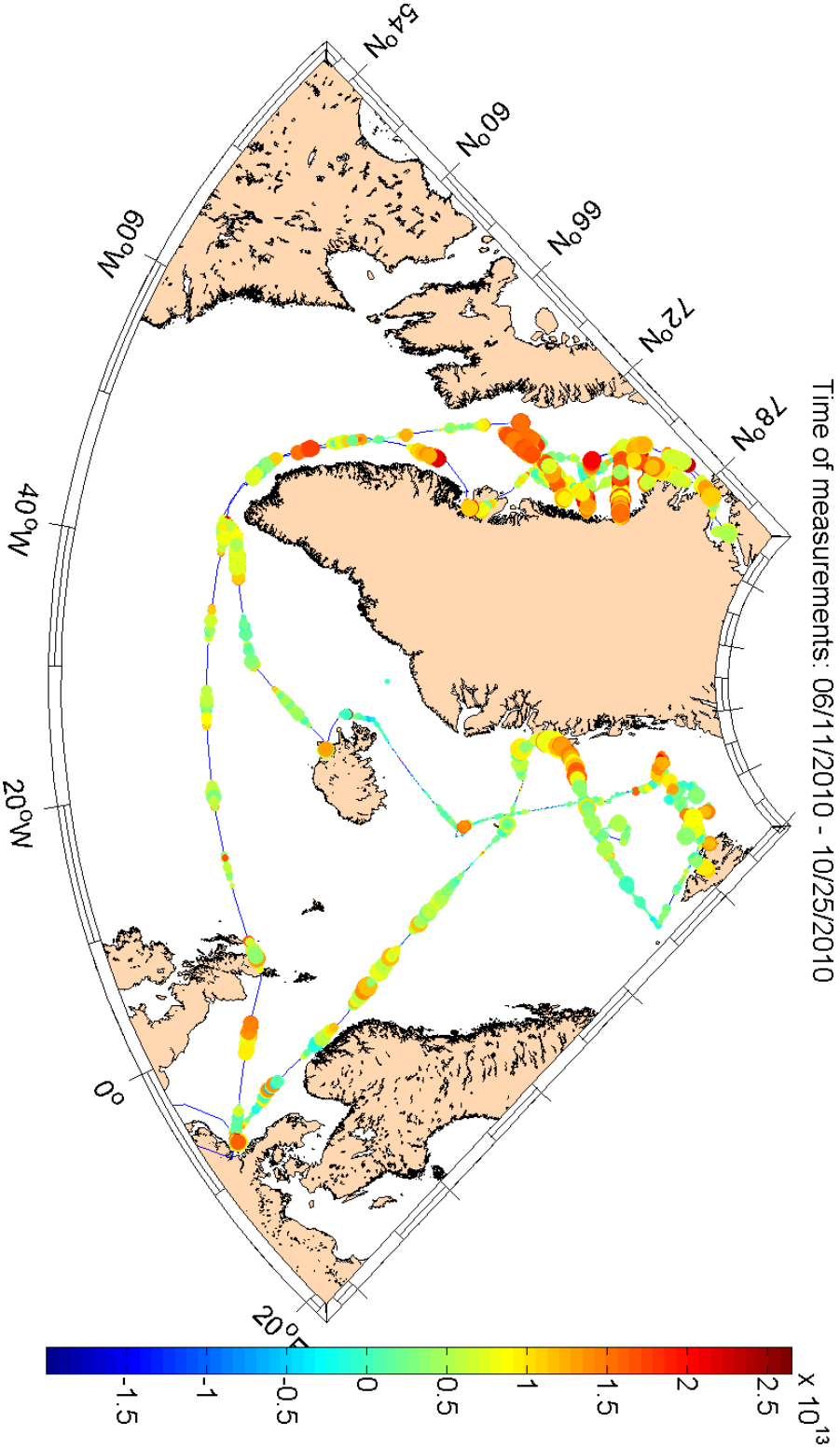

Figure 10.1.: Cruise plot of Polarstern cruise ARK XXV. Additionally measured IO dSCD are plotted. The dSCD of 3° elevation measurements is colour-coded, the size of the data points is proportional to the signal to noise ratio of the O_4 measurements, this means that small dots are drawn for situations with low sunlight intensity and/or low visibility.

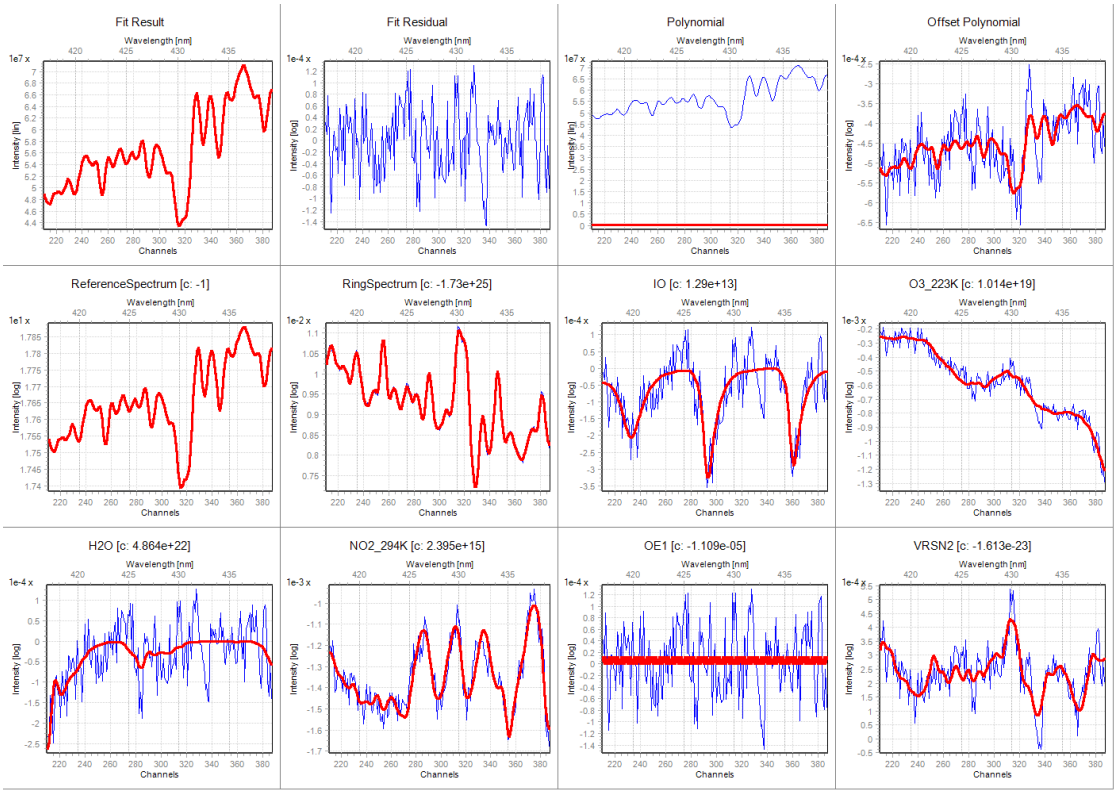

Figure 10.2.: IO fit of a 8-minute spectrum from Polarstern ARK XXV, at 3° elevation on 09/27/2010 at 14:48 at 52°W, 70°N at an air temperature of +5°C in the Davis Strait, a fjord in western Greenland. The IO dSCD is about 14 times higher than the fit error.

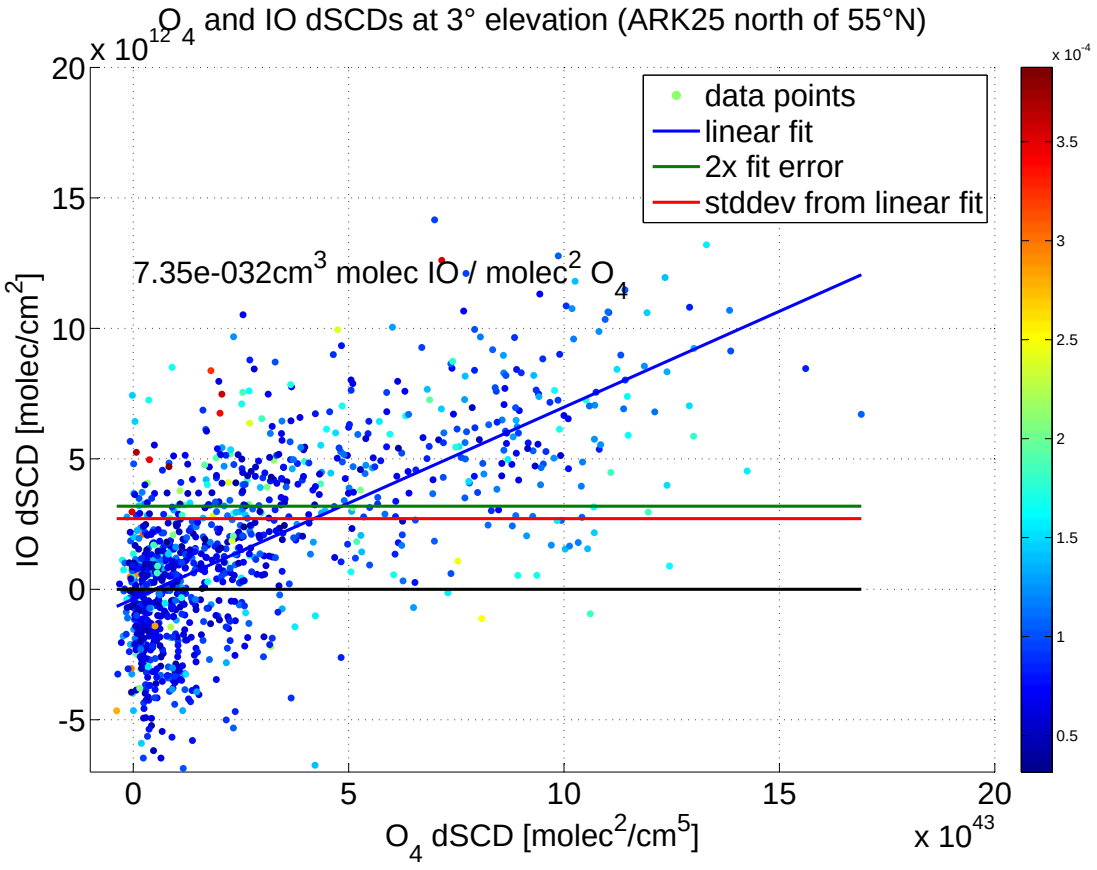

Figure 10.3.: Correlation plot for IO and O_4(470 nm) dSCD for the complete data set of ARK XXV north of 60°N. The slope of the correlation of $7.7 \cdot 10^{-32}$ cm^3 molec IO molec^{-2} O_4, agreeing with observations in Antarctica during ANT XXIX. Colour-code is fit RMS.

10.3. Polarstern ARK XXVII

ARK XXVII was the first Arctic cruise with the stray-light reduced OMT spectrometers on Polarstern during Summer 2012. This led in general to a slightly better RMS when summing the spectra of different elevation sequences.

10.3.1. Results

10.3.1.1. IO

Similar residuals as during previous cruises were observed. Since the O_4 dSCDs at 470 nm are smaller than during ARK XXV, no reliable plot in analogy to figure 10.3 for the correlation of IO and O_4 was possible.

10.3.1.2. BrO

When using the Greenblatt et al. [1990] O_4 cross-section for the evaluation of BrO in the 332–358 nm range, dSCDs of $(3 \pm 8) \cdot 10^{12}$ molec cm^{-2} were obtained at a fit error of $(4.6 \pm 2.9) \cdot 10^{12}$ molec cm^{-2} for a RMS $< 6 \cdot 10^{-4}$ and a telescope elevation of 3°. The maximum ratio of tropospheric dSCD and fit error was 7.3 for a dSCD of $2.6 \cdot 10^{13}$ molec cm^{-2} on 07/28/2012 06:41:18 UTC at 76°N, 10°E south-west of Spitsbergen. Due to residual structures of the same size as the observed BrO absorption, it is not clear if this is a real absorption or only caused by this residual structure which is correlated with the O_4 dSCD. (see also subsection 5.1.1.2).

10.3.1.3. HCHO

The measured HCHO dSCDs showed larger values ($1.7 \cdot 10^{16}$ molec cm^{-2}, up to 12-times the measurement error) close to Europe in the North Sea until 70°N, then dSCDs decreased towards the Arctic to values below $5 \cdot 10^{15}$ molec cm^{-2}. A small maximum was found again close to Spitsbergen with $6 \cdot 10^{15}$ molec cm^{-2}
The same retrieval wavelength range as for BrO was used for HCHO, resulting in fit errors of $(1.0 \pm 0.5) \cdot 10^{15}$ molec cm^{-2} for a RMS $< 6 \cdot 10^{-4}$ and a telescope elevation of 3°.

11. MAD-CAT: Multi Axis DOAS - Comparison campaign for Aerosols and Trace gases

The **M**ulti **A**xis **D**oas - **C**omparison campaign for **A**erosols and **T**race gases (MAD-CAT) campaign took place in summer 2013 in Mainz, Germany on the roof of the Max Planck-Institute for Chemistry (MPIC).

11.1. Overview and other measurements

One NO_2-CE-DOAS instrument and at least 16 MAX-DOAS instruments were operated in parallel during the campaign by different research groups, and additional information was obtained by measurements of webcams, a ceilometer, NO_x concentrations and PM10 and PM2.5 concentration from air quality network Rhineland Palatinate und Hesse.

The Heidelberg '*envimes*' MAX-DOAS instrument measured almost continuously in June and July 2013, measuring into the direction of 50.8° (north-west) at the predefined common elevation angle sequence of 90°, 30°, 15°, 10°, 8°, 6°, 5°, 4°, 3°, 2°, 1°. After the campaign a constant elevation offset of -0.35° was determined.

The measurement procedure measured one-minute spectra at all elevation angles for SZA < 87° and at 90° otherwise. During the night (SZA> 100°), dark current and offset spectra were recorded. During noon (175° < SAA < 185°) also only spectra at 90° were recorded for their potential use as Fraunhofer references, also leaving the possibility to use a spectrum from more than just one minute. For each elevation the previous exposure time for this elevation was used for a 'prescan' to determine the exposure time for the actual measurement at a saturation of 70%. This' prescan' was later added to the actual measurement spectrum to increase the total measurement time.

11.2. Results

The spectra from MAD-CAT were not primarily used to obtain information about concentrations of ozone, NO_2, glyoxal, formaldehyde or water vapour in Mainz, but rather to test the significance of measurements of trace gases in the Marine Boundary Layer (MBL) and exclude possible systematic problems. As the concentrations of all measured compounds in Mainz except IO, H_2O, O_4 and BrO are significantly higher than in the typical MBL, this allows to estimate the effect of e.g. NO_2 and HCHO concentrations on the retrieval of NO_2, as done in subsection 5.1.1.1. Also the effect of Vibrational Raman Scattering (VRS) on N_2/O_2 was observed in subsection 5.2.3.6 for this dataset, excluding interferences with scattering and absorption in seawater.

11.2.1. IO

One of the concerns during previous spectral retrievals of IO was the influence of water vapour absorption on the retrieval of IO. During the hot days in summer a similar water vapour content in the troposphere is to be expected as in tropical regions and no direct iodine source is expected close to Mainz. Due to high concentrations of NO_x, VOCs and aerosols as a sink for iodine, this dataset provides the possibility to test the IO retrieval for its sensitivity towards water vapour absorption. A problem might be the potential influence of glyoxal, which has been clearly detected in Mainz, but not during M91 and MSM18. For details see subsection 5.1.2.1.

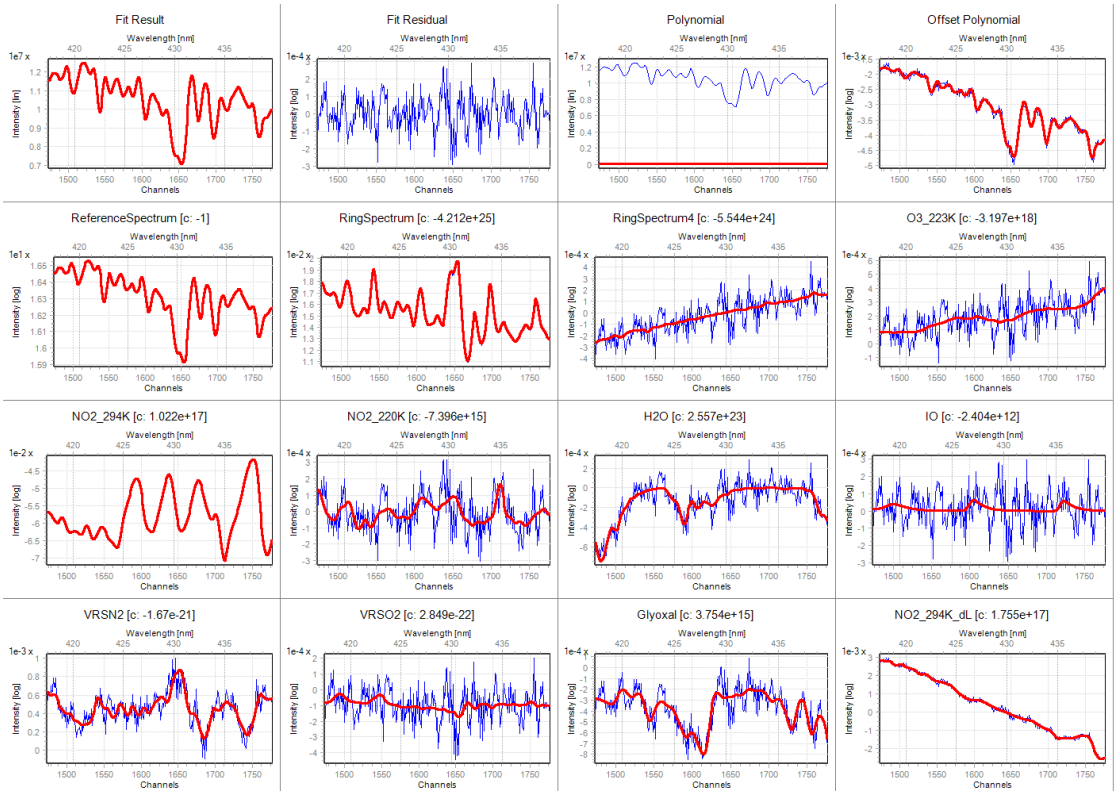

Figure 11.1.: Glyoxal fit (#13388) from MAD-CAT in Mainz, 06/18/2013 11:49 UTC, at 3° elevation for the wavelength interval 417–439 nm. The glyoxal dSCD is slightly smaller than in the fit using the larger fit window including the strong water vapor absorption shown in figure 11.3, but within the measurement error of $6 \cdot 10^{14}$ molec cm^{-2}. (see also subsection 5.1.2.1)

11.2.2. BrO

The MAX-DOAS data of the *envimes* MAX-DOAS was used to determine the effect of O_4 on the spectral retrieval of troposheric BrO in a region where no tropospheric BrO

was expected. The results are summarized in subsection 5.1.1.1.
Furthermore a residual structure observed for various measurements with different instruments described in subsection 5.1.1.2 correlated with the O_4 dSCD was also found in spectral BrO evaluations of MAD-CAT data. Using the residual structure obtained from MAX-DOAS measurements during M91 with another instrument without any modifications for MAD-CAT data reduces the residual drastically as shown in figure 11.2.

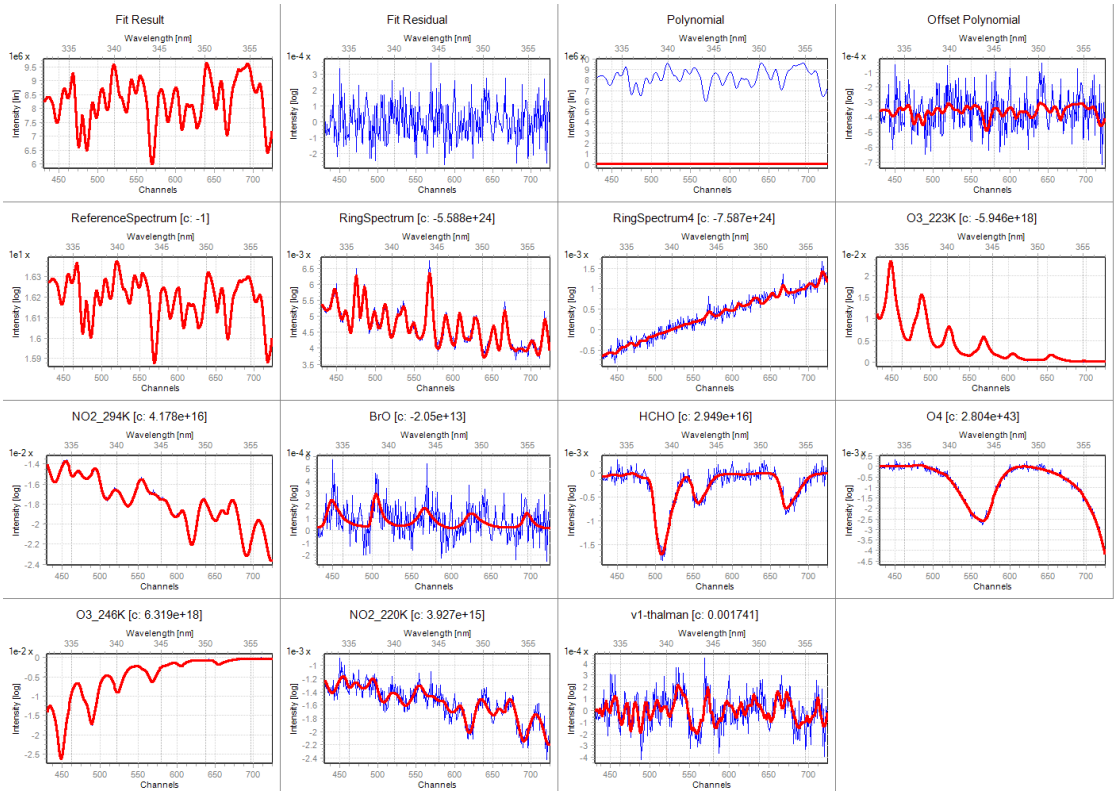

Figure 11.2.: The dominating principal component from a set of residual spectra from MAX-DOAS measurements with an Acton spectrometer in the Peruvian upwelling seems also to be found without any modifications at a similar OD for measurements in Mainz (v1-thalman). However, it results in a negative BrO dSCD. Without this recurring spectrum the residual spectrum is almost perfect.

11.2.3. HCHO

Large HCHO during hot days were observed with a maximum dSCD of 10^{17} molec cm^{-2} corresponding to more than 10ppb of formaldehyde close to the ground. These high columns of HCHO did not significantly influence the retrieval of tropospheric BrO (subsection 5.1.1.1), but their variation allowed to exclude HCHO as the reason for systematic residual structures.

11.2.4. Glyoxal

During the days with large HCHO dSCD also larger glyoxal dSCD were observed, agreeing with preliminary data from other groups. The mixing ratios of about $\approx$ 2ppb ($5 \cdot 10^{15}$ molec cm^{-2}) could have been caused by oxidation of VOCs, leading to enhanced concentrations of HCHO and Glyoxal. The same settings as for the Glyoxal analysis for the data from M91 and MSM18 were applied. This ensures the correctness of the spectral retrievals of the upper limits for glyoxal during those campaigns. An undetected shift of the glyoxal cross-section can be therefore excluded.

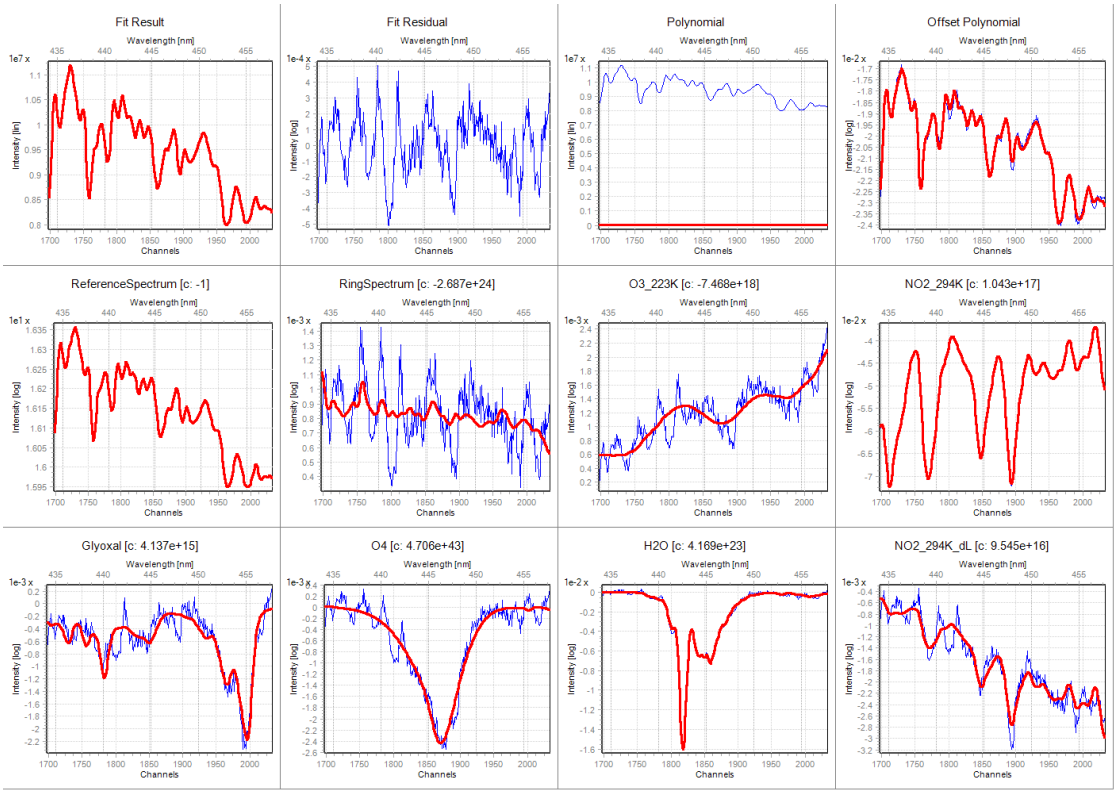

Figure 11.3.: Glyoxal fit (#13388) from MAD-CAT in Mainz, the same spectrum as figure 11.1, but for the wavelength interval 434–458 nm. Possible corrections to the water vapour absorption discussed in section 5.4 and VRS effects also present within this wavelength range have not been included in this fit. *NO2_294K_dL* was included to compensate residual structures caused by AMF-variations of NO_2 within the retrieval interval.

12. Discussion

12.1. Global maps of trace-gas abundances

To obtain a global picture of the trace gases measured throughout different campaigns listed in chapter 6, measured dSCDs of the respective trace gas were plotted on a map for a telescope elevation angle of 3° relative to a Fraunhofer reference spectrum recorded at 40° to avoid direct sunlight entering the telescope during measurements at tropical latitudes. Erroneous fit results were filtered using a maximum value for the fit RMS ($< 6 \cdot 10^{-4}$ for BrO/HCHO, $< 4 \cdot 10^{-4}$ for IO). Fit error weighted daily averages were calculated for the dSCDs and meta-data like time and position. This was necessary to limit the amount of plotted data to a reasonable amount, but also to average fluctuations and/or noise, especially for trace gases close to their respective detection limits. These plots do not include information about light-path length, such as O_4 dSCDs. For ANT XXVIII suface volume mixing ratios were retrieved from MAX-DOAS measurements from Bremerhaven to Cape Town. These are shown in figure 9.5 for IO.
If the data recorded did not allow to select data at the the elevation angles mentioned (TransBrom [Großmann et al., 2013], M77), the data was converted using the elevation angle dependence of dSCDs measured during M91 (similarly as described for M77 in section 7.4).
The retrieved IO dSCD MAX-DOAS data for TransBrom was provided by Katja Großmann (IUP HD) using the retrieval settings from Großmann et al. [2013], and thus not using a VRS correction spectrum for N_2/O_2, which has no effect on the retrieved IO dSCD (see subsection 5.2.3.1). The same applies for the IO MAX-DOAS data for the SHIVA campaign, which was evaluated and provided by Enno Peters (Institute of Environmental Physics, Bremen University). However, both spectral retrievals used the correction spectrum for VRS in liquid water, which can increase the observed IO dSCD by several 10^{12} molec cm^{-2}, while no evidence was found that this effect is significant for positive telescope elevation angles (see subsection 5.2.5).
The BrO/HCHO dSCDs for TransBrom were also provided by Katja Großmann (IUP HD) using the retrieval wavelength interval from 332–358 nm and the Greenblatt et al. [1990] O_4 cross-section.

12.2. IO

Absorptions of iodine monoxide have been observed at all latitudes, ranging from 80°N to 70°S. The distribution of the measured IO dSCDs matched another latitudinal transect published by Mahajan et al. [2012], but effectively yielding 25% lower daily averages, which might have been caused by using an out-dated water vapour cross-section from HITRAN2000 (compare figure 5.30 and table 5.7). Measurements along Antarctica and

in the Arctic showed similar ratios of O_4 and IO dSCDs, which would correspond to a background value of 0.2–0.4 ppt (see subsection 10.2.2.1 for measurements in the Arctic). Coastal measurement in the Bay of Biscay and the English Channel showed for ANT XXVIII IO VMR of 0.75–1.0 ppt, Peters et al. [2005] reported an average of 0.75 ppt IO for LP-DOAS measurements in Brittany.
At tropical latitudes, concentrations of 1 ppt on the Atlantic (see Polarstern ANT XXVIII, close to Cape Verde (subsection 9.2.2), MSM18/3 eastern equatorial upwelling (subsection 8.2.2)) and 1.5 ppt in the Peruvian upwelling (M91, subsection 7.2.4) were obtained from MAX-DOAS measurements. Polarstern had passed Cape Verde islands for three times while the MAX-DOAS instrument was measuring at the same month of the year. This allowed to give an estimate on the variability of IO dSCDs during different years, which is, during October, from 0.4–1.0 ppt or $1.1 \cdot 10^{13}$ molec cm^{-2} – $1.8 \cdot 10^{13}$ molec cm^{-2} for daily averaged dSCDs at 3° telescope elevation. This variability could not be attributed to differences in light path length nor differences in Sea Surface Temperature (SST) or wind speed (see also section 9.3). Tschritter [2013] reported a similar range of IO dSCD averages from $0.8 \cdot 10^{13}$ molec cm^{-2} – $2.0 \cdot 10^{13}$ molec cm^{-2} for long-term measurements on CVAO, but attributed this variation to seasonal differences in the observation time from September 2006 – February 2008.
Previously reported IO mixing ratios at CVAO on Cape Verde by Read et al. [2008b] of 1.5 ppt are based on individual measurements which have measurements errors of 0.5 ppt and also showed negative values of -1 ppt during the night. Therefore the averaged diurnal cycle contains large uncertainties.
This variability might be a part of the explanation of IO observations by LP-DOAS measurements on Cape Verde during HaloCaVe [Tschritter, 2013]: During this campaign in summer 2010 no significant absorption of IO could be detected above a detection limit of 0.5 ppt along a similar light path as the one used by Read et al. [2008b]. Still, this difference is not resolved, but the comparison with CE-DOAS observations during M91 showed that MAX-DOAS measurements of IO are indeed valid and that the observed IO dSCD are not an artefact of water vapour absorption or other, unknown effects.
It has been argued that these high IO concentrations at CVAO in the marine boundary layer cannot be explained by photolysis of halocarbons only based on chemistry models [Mahajan et al., 2010a], which could explain IO concentrations at CVAO up to 0.5 ppt in the afternoon. Additionally, the increase of IO at sunrise would be would be slower than observed in Read et al. [2008b] and M91 (subsection 7.2.4.1), due to the slower photolysis rates of most halocarbons compared to HOI and I_2.
Also the surface water iodide measurements collected over several years by [Chance et al., 2014, in prep.] shown in figure 12.3 shows large variations at similar latitudes. Close to Cape Verde, from 10-20°N, surface water iodide concentrations from 100–200 nM are reported. Also Bluhm [2010] reported this variability for measurements in the Mauretanian upwelling for February 2008 (100 nM I^-) and July 2006 (200 nM I^-). Assuming that release of surface water iodide is the dominating release process relevant for background IO mixing ratios in the MBL, this will lead also to similarly large variation of IO mixing ratios.
During TransBrom [Großmann et al., 2013] chemistry modelling suggested that an ad-

ditional source of iodine is needed to measured iodocarbon concentrations to explain the observed profiles. They estimated the additional flux to 1.0 to $1.8 \cdot 10^8$ molec cm^{-2} s^{-1}. The latitudinal gradient in IO VCD reported in Schönhardt [2009] cannot be confirmed. For both, Arctic and Antarctic measurements the same correlation with O_4 absorption was found, indicating a constant background of 0.2–0.4 ppt for both regions. Also for the free troposphere a constant background with concentrations of the same size was reported by Dix et al. [2013] and Puentedura et al. [2012].

12.2.1. The possible role of iodide

The correlation plots of IO VMR and dSCDs and surface water iodide are shown in figure 12.5 for ANT XXVIII (chapter 9). Surface water iodide concentrations were derived from the data published by [Chance et al., 2014, in prep.] and plotted in figure 12.3 by applying a running mean over 10° latitude from 70°S to 70°N to smooth local variability. Only open ocean data points were selected, coastal measurements show an even higher variability. Coastal measurements can be identified by geolocation, but here also by relative large IO VMR values and relatively low open ocean iodide concentrations at the respective latitudes. These points were omitted for the linear regression and the calculation of the correlation coefficient. Iodide concentrations in surface water itself are relatively well correlated with SST [MacDonald et al., 2013, Chance et al., 2014], therefore also for IO dSCDs a correlation with SST is found for most observations.
The dependence on tropospheric ozone concentrations for the emission fluxes of I_2 and HOI can not be seen from measurement data. Here the northern hemisphere should show larger emissions due to higher background ozone concentrations. The iodide surface concentrations are derived from a series of measurements during different seasons and longitudes, thus the uncertainties of iodide concentrations derived from [Chance et al., 2014, in prep.] for the cruise Polarstern ANT XXVIII are larger than the variations which would have been introduced by variations in ozone concentrations.
For the Peruvian upwelling region, which is another maximum of the latitudinal distribution of IO dSCDs, currently only one data point for surface water iodide concentrations is available (210 nM I^-), but measurements during M77 indicate in general higher concentrations of even more than 300 nM I^- [pers. comm. P. Croot, data from Meteor expedition M77-1 in the Peruvian upwelling, [Croot et al., 2014, in prep.]]. Surface IO concentrations of 1.0–1.5 ppt and daily averaged dSCDs of $2.5 \cdot 10^{13}$ molec cm^{-2} yield an estimation of the surface water iodide content in the Peruvian Upwelling of ≥ 250 nM (figure 12.5), while the correlation of SST and IO VMR would not correctly predict the IO observations during M91 in the Peruvian Upwelling region of 1–1.5 ppt at an SST of typically 18–22 °C. This is a further indication that the IO concentrations are indeed driven by surface iodide concentrations instead of SST.
Combining the IO VMR results from ANT XXVIII/1 and the surface water iodide compilation data from Chance et al. [2014], a linear dependence of iodide in surface ocean water and atmospheric IO is observed, when excluding of coastal influences. The correlation yields for a correlation coefficient of $R = 0.5$ the following relation: A concentration difference of 100 nM I^- in sea surface water results in a difference of 0.6 ppt IO in the

MBL. The small correlation coefficient is partly due to the variability of iodide values in the compilation of measurements. Using this relation agrees furthermore with observations of polar background IO concentrations of (0.3 ± 0.1) ppt and typical IO surface VMR from 0.5–1.0 ppt during MSM18/3, even though the region of the equatorial upwelling and the potential influence of the upwelling system close to Namibia is not explicitly included in Chance et al. [2014].
Due to the possibility of production of iodinated halocarbons from iodide and DOM as described by Martino et al. [2008], the release processes may include emissions of I_2, HOI as suggested by Carpenter et al. [2013] as well as emissions of CH_2I_2 and others.

12.2.2. The role of halocarbons as precursors for RHS

In agreement with previous observations by Tschritter [2013], Großmann et al. [2013] and [Mahajan et al., 2010a], the measurements during M91 presented here showed no direct connection to surface water halocarbon concentrations, but stayed rather constant throughout the whole cruise period of four weeks at values between 1.0-1.4 ppt. No connections to atmospheric abundances of CH_3I, CH_2I_2 or Ch_2ICl were found, despite variations of CH_2I_2 e.g. from 0.3 ppt to 3 ppt in a region with enhanced seawater halocarbon concentrations during M91 [pers. comm. S. Fuhlbrügge]. This is a hint towards a source connected to large reservoir of accessible iodine in the vicinity of the Peruvian coast, which is independent of the local upwelling properties, independent of biological activity as indicated by Chl-a concentrations and independent of seawater halocarbon concentrations. If its emissions can also be easily photolysed within minutes, this can explain the steep increase of IO at sunrise by CE-DOAS measurements.
As pointed out in section 7.3 and shown in figure 12.4, this fast rise of IO concentrations within minutes after sunrise requires iodine containing molecules with a short photolytic lifetime, such as I_2, HOI, IBr and ICl, but possibly also CH_2I_2 and CH_2ICl with tropospheric lifetimes of several minutes. Also $IONO_2$, which can be formed after sunset from IO and NO_2, could take a role here, either as a direct precursor which is photolyzed at sunrise or via deposition of $IONO_2$ on aerosol particles which then eventually can emit I_2, IBr or ICl [Mössinger et al., 2002, and references therein]. This could eventually lead to enhanced emissions of bromine and chlorine from aerosol. However, no increased bromine mixing ratios has been detected. Eventually this mechanisms could have led via aerosol acidification to the enhanced BrO mixing ratios observed during P399 close to the Mauritanian coast reported in Tschritter [2013].
The observation during M91 that even large variations in surface water halocarbon concentrations of compounds with tropospheric lifetimes during daytime of the order of minutes do not lead to any noticeable concentration changes of IO in the troposphere, leads to the assumption that there needs to be another source of iodine in the tropical MBL to maintain a constant volume mixing ratio of 1.0–1.4 ppt IO during the day. This other source of iodine is somehow connected to the upwelling system off Peru. The iodine emissions in this region are, as far as known, one of the largest emissions of iodine world-wide. For an estimate of the total emissions, see subsection 1.2.7.
In the equatorial upwelling region observed during MSM18/3 (chapter 8), relatively low

IO mixing ratios of 0.5 ppt were observed in the western part of the cruise track at 15°W, despite high bio-productivity as indicated by chlorophyll-a measurements. According to the latitude of this area and SST, larger IO VMR were expected. However, mixing ratios increased towards east, up to 1 ppt at 0°E. Here the transport of air masses by trade winds from the upwelling system of the Bengal current along the coasts of Namibia and Angola might play a role due to their in increased emission of halocarbons, but maybe also higher iodide surface water mixing ratios, which were not measured during the cruise. This upwelling region can be easily identified on Chlorophyll-a maps, too (see figure 8.13). A correlation with values from measurements of local surface water content of halocarbons was not observed, neither with concentrations in air (see also section 8.3). Still, relatively long-lived iodinated halocarbon species can provide a certain background concentration of reactive, atmospheric iodine, which could also be deposited on aerosol particles, leading to the typically highly iodine enriched marine aerosol. On the aqueous layer on this aerosol the same reactions as on the sea surface can occur, also leading to the emission of I_2 and HOI and thus also providing short-lived iodine species.

12.2.3. Connection to oxygen minimum zones?

Iodate can be converted quickly to iodide in Oxygen Minimum Zone (OMZ), which are typically found below upwelling regions. Biomass, which is produced close to the surface, eventually sinks down, consuming oxygen and leading to changes in both, chemistry and biology in depths of typically 100-400 m. Under these conditions iodate may be reduced to iodide by bisulphides. Below the Peruvian upwelling region a deep layer of large iodide concentrations has been reported [Croot et al., 2014, in prep.], which could lead, once upwelled, to enhanced iodide concentrations in surface waters and thus enhanced emissions of HOI and I_2. Other mechanisms for the conversion of iodate to iodide include release of iodide from senescent diatoms, sediment chemistry and so forth, described in subsection 2.2.1. These other mechanisms might therefore also be related to higher bio-productivity and proximity to the coast.
As shown in figure 2.3, the most pronounced OMZ in the Pacific is found at the Peruvian coast. These are also found below the upwelling areas in the Atlantic off the Mauritanian coast, the Namibian coast and in the Arabian Sea.
All of these regions show enhanced column densities of IO in satellite measurements by Schönhardt et al. [2008] (Figure 1.7), except the Mauritanian upwelling, where IO has been detected from ground-based measurements, but yielding 25-50% smaller VCDs than in the Peruvian upwelling. A larger variability in IO VCDs from ground-based measurements might explain why the signal of IO from Cape Verde region cannot be detected to be as pronounced as the signal from the Peruvian upwelling in multi-year averages of satellite measurement data. If the IO dSCDs measured during M91 are representative itself for a longer time-series cannot be determined from one campaign. However, since the averaged satellite measurements of IO fit the ship-based observations quite well, this indicates that this ship-based data-set of IO is indeed representative for December/January in the Peruvian upwelling.
The data in figure 2.3 shows slightly higher oxygen levels for the upwelling region off

the Mauritanian coast than for all other large OMZ. Furthermore Bluhm [2010] did not report a correlation of iodide concentrations with the oxygen concentrations in seawater close to Cape Verde.
Agreement with satellite observations (see figure 1.7[1]):

- Peru: The observed MAX-DOAS IO VCDs match the seasonal average retrieved from satellite measurements shown in figure 7.19 in agreement with CE-DOAS measurements for surface concentrations.

- Upwelling Congo/Angola/Namibia: Figure 1.7 shows enhanced IO SCDs in the south-eastern tropical Atlantic during MSM18/3. The observation, that at 15°W less IO can be found than east of 0°W can be confirmed by MAX-DOAS measurements during MSM18/3 (Figure 8.12). This suggests that the rise of IO VCD and VMR during the cruise towards the east was not caused by the equatorial upwelling itself, but by transport processes of IO and its potential precursors from emissions in the coastal upwelling of Angola and Namibia.

- Mauritanian upwelling: The variability of IO dSCDs at comparable circumstances during different Polarstern cruises hints towards a higher variability of IO concentrations in the Mauritanian upwelling. This could have led then to smaller long-term averages shown in the averaged IO SCDs obtained from satellite data. For other upwelling regions no long-term data is available. This variation was also seen in long-term MAX-DOAS measurements by Tschritter [2013].

Enhanced IO VCDs at the coast of Somalia agree with seasonally prevailing north-easterly winds [Resplandy et al., 2012], transporting air masses from the Arabian Sea, from the Somali upwelling, onto the continent. Ship-based measurements in the northern Indian Ocean on top of this large oxygen minimum zone would be interesting.
A conclusion about free-tropospheric IO concentrations cannot be obtained from the comparison of satellite and ground-based VCDs, since the satellite measurements used a reference sector on the Pacific (at 40°S, 160°W and 10° into each direction), therefore an constant background of IO in the free troposphere would cancel out during the retrieval process.

[1] It has to be noted that for the interpretation of figure 1.7 the colour-scale needs to be considered.

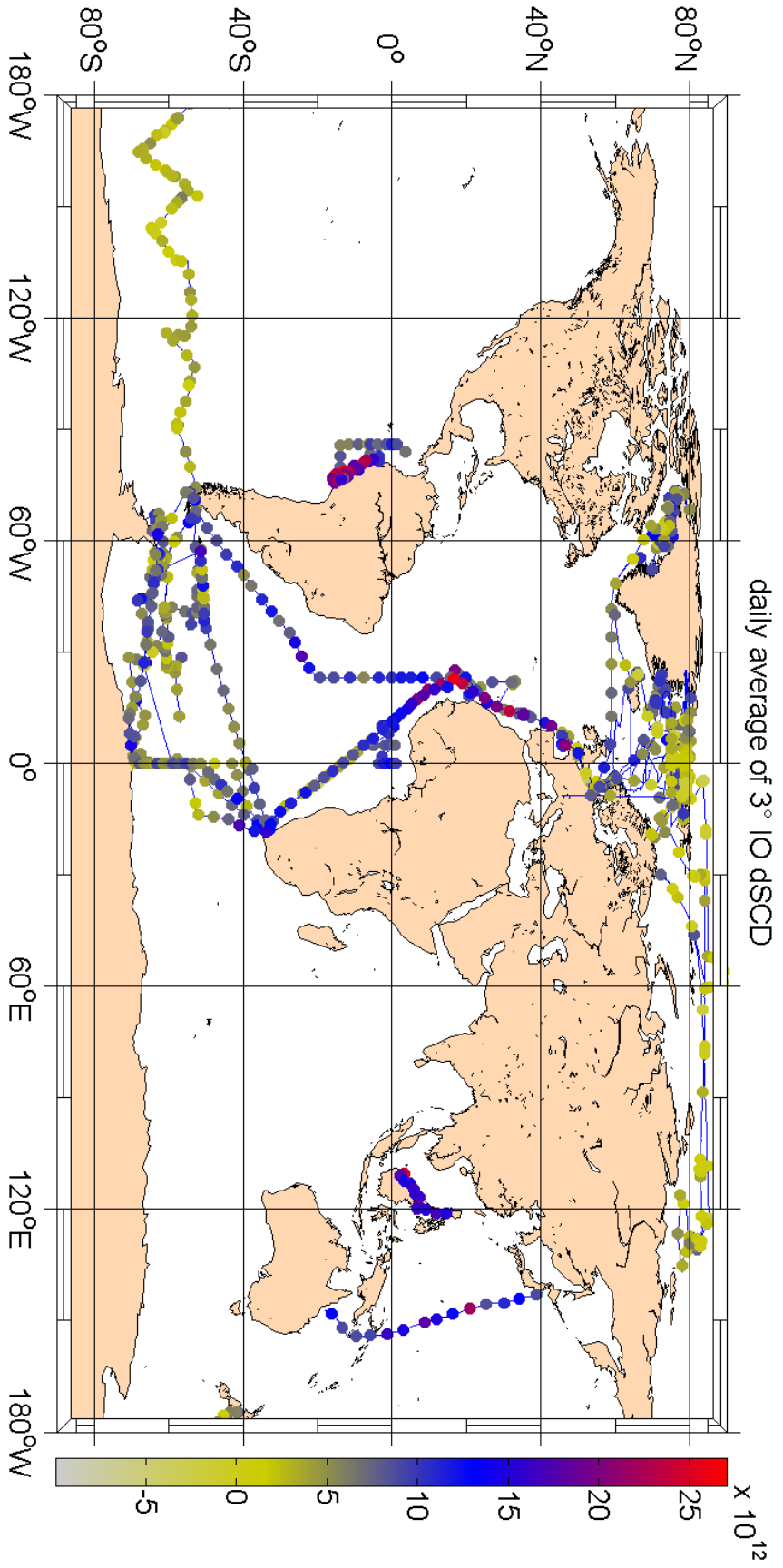

Figure 12.1.: Error weighted daily averages of 3° IO dSCDs. An overview of all campaigns is given in chapter 6.

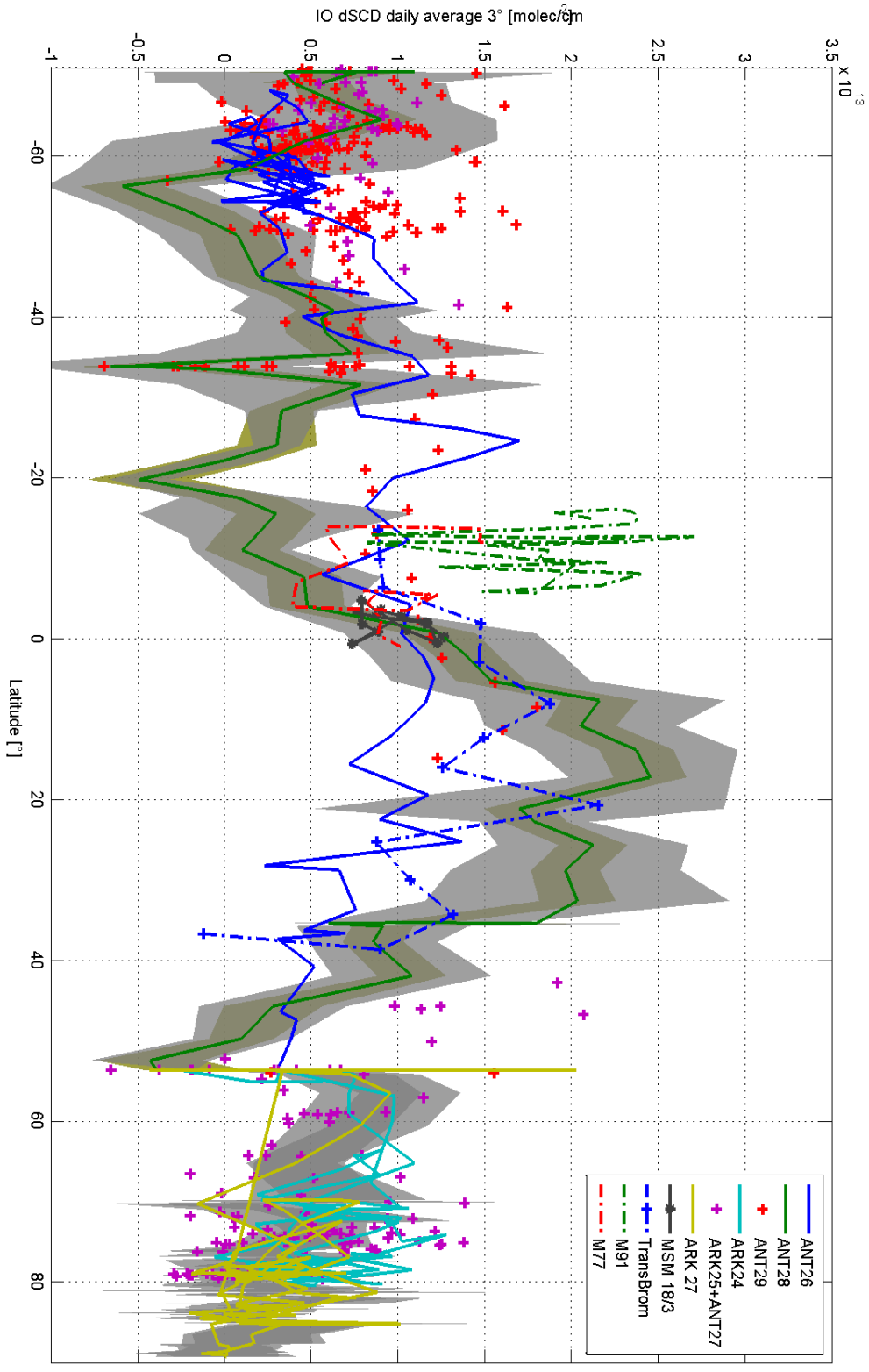

Figure 12.2.: Error weighted daily averages of 3° IO dSCDs and latitude, the same data is shown on a world map in figure 12.1. The standard deviation for ANT XXVIII and ARK XXVII are indicated by a shaded area, the typical fit errors by a greenish shaded area. Negative averages at 50°N and 30°S are caused by large absorptions of NO_2. Note for Arctic/Antarctic measurements larger maximum O_4 dSCDs and thus longer light paths were observed, up to three times longer.

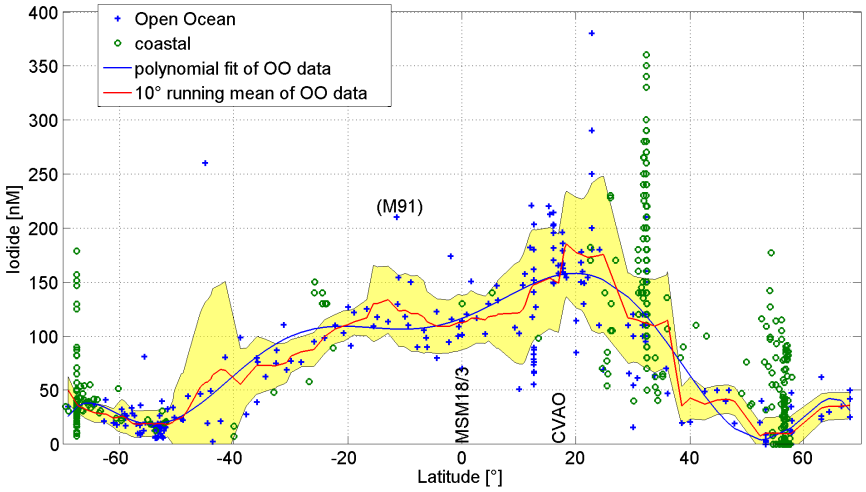

Figure 12.3.: Latitudinal distribution of surface water iodide concentrations according to [Chance et al., 2014, in prep.]. Blue crosses are open ocean measurements, green circles are measurements on a continental shelf or coastal measurements. Most measurements were conducted on the Atlantic, only a few on the Pacific (for a map, see figure 2.5). Data points around 20°N show large variations for the measurement performed during different campaigns. Surface water iodide concentrations during M77 in the Peruvian upwelling region (as M91) indicated surface water iodide concentrations of around 300–500 nM [Croot et al., 2014, in prep.].

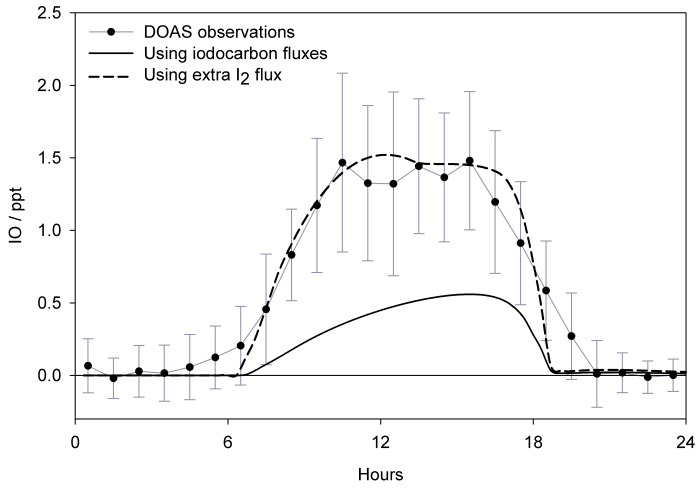

Figure 12.4.: IO mixing ratios modelled by Mahajan et al. [2010a] when using only iodocarbon fluxes and when introducing an additional I_2 source. This modeling study was based on data from Read et al. [2008b].

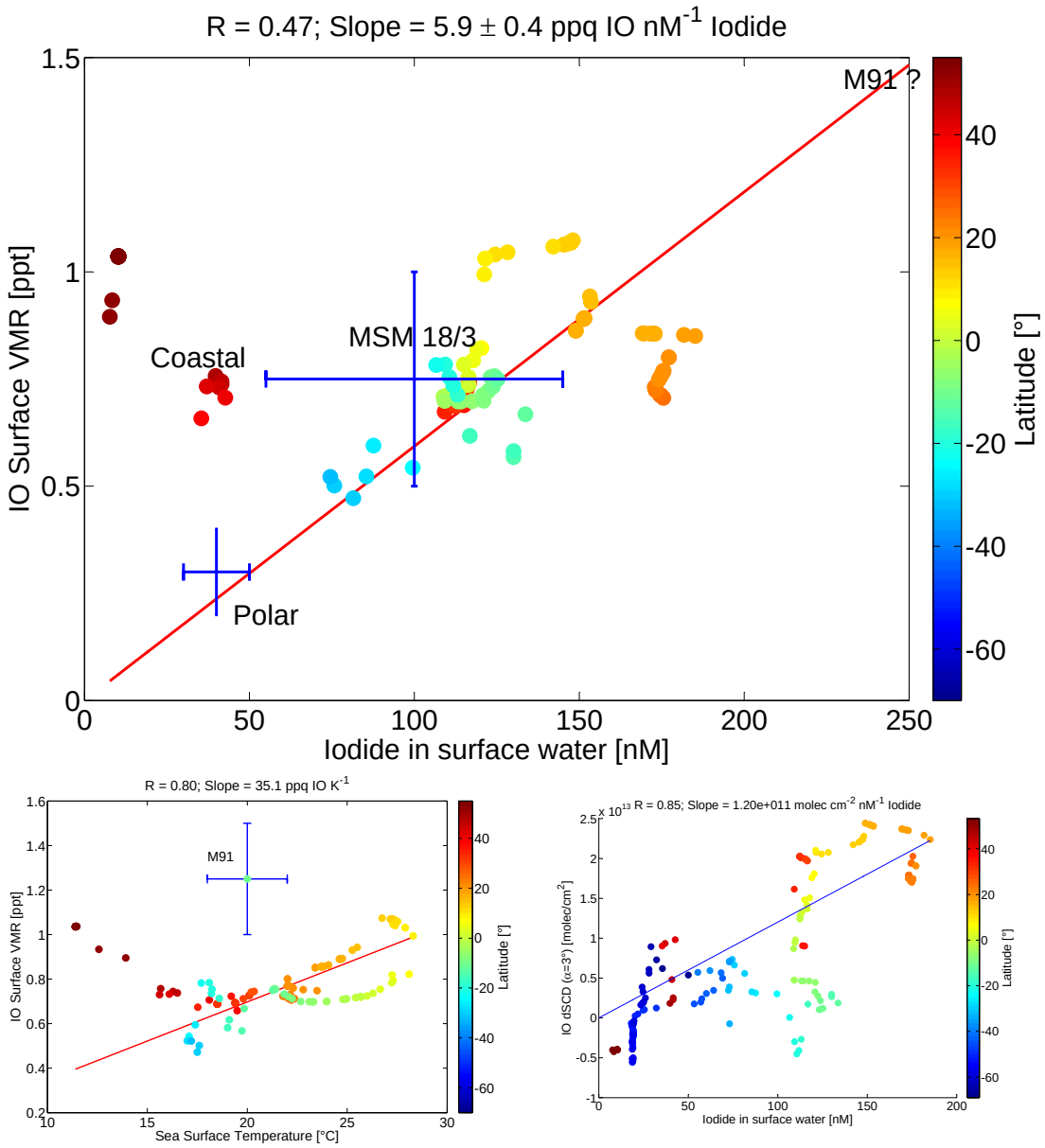

Figure 12.5.: IO Surface VMRs / dSCDs during ANT XXVIII/1 and surface water iodide concentrations from [Chance et al., 2014, in prep.] (see also figure 12.3). During M91 typically 1.5 ppt were observed, but so far no iodide measurements are available. Observations during M77 indicate surface water iodide concentrations above 300 nM. Error bars for other campaigns in the Arctic (ARK XXV), Antarctic (ANT XXIX) and equatorial upwelling(MSM18/3) were included in the plot, but were not included in the regression. Data points measured north of 35°N are measured in coastal areas which are excluded from the latitudinal dependence of iodide in surface water. Figure 12.3 shows large variations for coastal surface water concentrations of iodide.

12.3. BrO

Despite problems with the spectral retrieval, typical concentrations on the tropical open ocean were found around 0.5–2 ppt (ANT28, MSM18/1). To estimate the effect of different spectral settings for the retrievals, measurements in Mainz/Germany were taken as a reference point for selecting the spectral retrieval settings.
For tropical regions the retrieved BrO VMR agreed roughly with Read et al. [2008b], but actual values were slightly lower. This agrees with observations by Tschritter [2013] of 2.5 ppt in the morning and around 1 ppt BrO at noon. (see figure 1.6). The largest BrO VMR were observed on the Atlantic close to the Mauritanian upwelling during Polarstern cruises and at 15°S on the remote Atlantic, dominated by air-masses from the southern Atlantic (compare figure 9.10), in which no significant tropospheric NO_2 concentrations could be detected. This is in agreement with Lee_{2010} who reported the maximum BrO concentrations in their LP-DOAS maesurements on Cape Verde for the days with the lowest NO_x concentrations. The high concentrations which have been seen by LP-DOAS [Tschritter, 2013] measurements and are reproduced by chemistry models during sunrise and sunset [Mahajan et al., 2010a] are actually too late or too early for height-resolved MAX-DOAS measurements, but overall the noon-minimum agrees with MAX-DOAS observations and larger VMR are generally found during the afternoon.
The height of the concentration profile of BrO is typically lower than the one of HCHO and also IO. This indicates larger sinks for BrO than for IO and HCHO. Typical first order loss-rates for BrO in a tropical environment has been estimated for HCHO and various other organic compounds in subsection 1.4.4.1 yielding the need for a strong source of Br in the MBL to maintain constant concentrations around 1–3 ppt. Fluxes of $CHBr_3$ and CH_2Br_2 reported in Hepach et al. [2013] are not sufficient, if no effective recycling mechanism for bromine exists.
During MSM18/1 (April 2011, see subsection 8.1.1) an unexpected bromine input into the MBL of the Atlantic was observed: Cold polar air arrived at a latitude of 33°N within a cold-front system showing enhanced BrO concentrations of 4–6 ppt within the lowermost 500 m. Trajectory calculations indicate the origin of these bromine-rich air-masses in north-east Canada, where satellite observations also indicated elevated BrO concentrations 2-3 days before. The size of the total bromine input during this event was estimated to be comparable to the emissions of $CHBr_3$ and CH_2Br_2 in the Mauritanian upwelling reported in Hepach et al. [2013] during one day. This is up to 50 times more than the emissions of the same compounds on the open ocean. Therefore this mechanism is a significant pathway of bromine into the MBL. Unfortunately neither on the Azores nor on the Canary islands ozone concentrations were monitored within the MBL during that time.
These so called BrO spill-out events have been observed from satellite measurements by Hollwedel [2005] and compared with trajectory calculations, but they have not been observed as far south as 33°N by ground-based measurements.
Due to typically large O_4 dSCD and therefore also large residual structures in the BrO retrieval no background BrO concentrations for polar regions during summer could be obtained, since the measured dSCDs were typically found close to the respective detec-

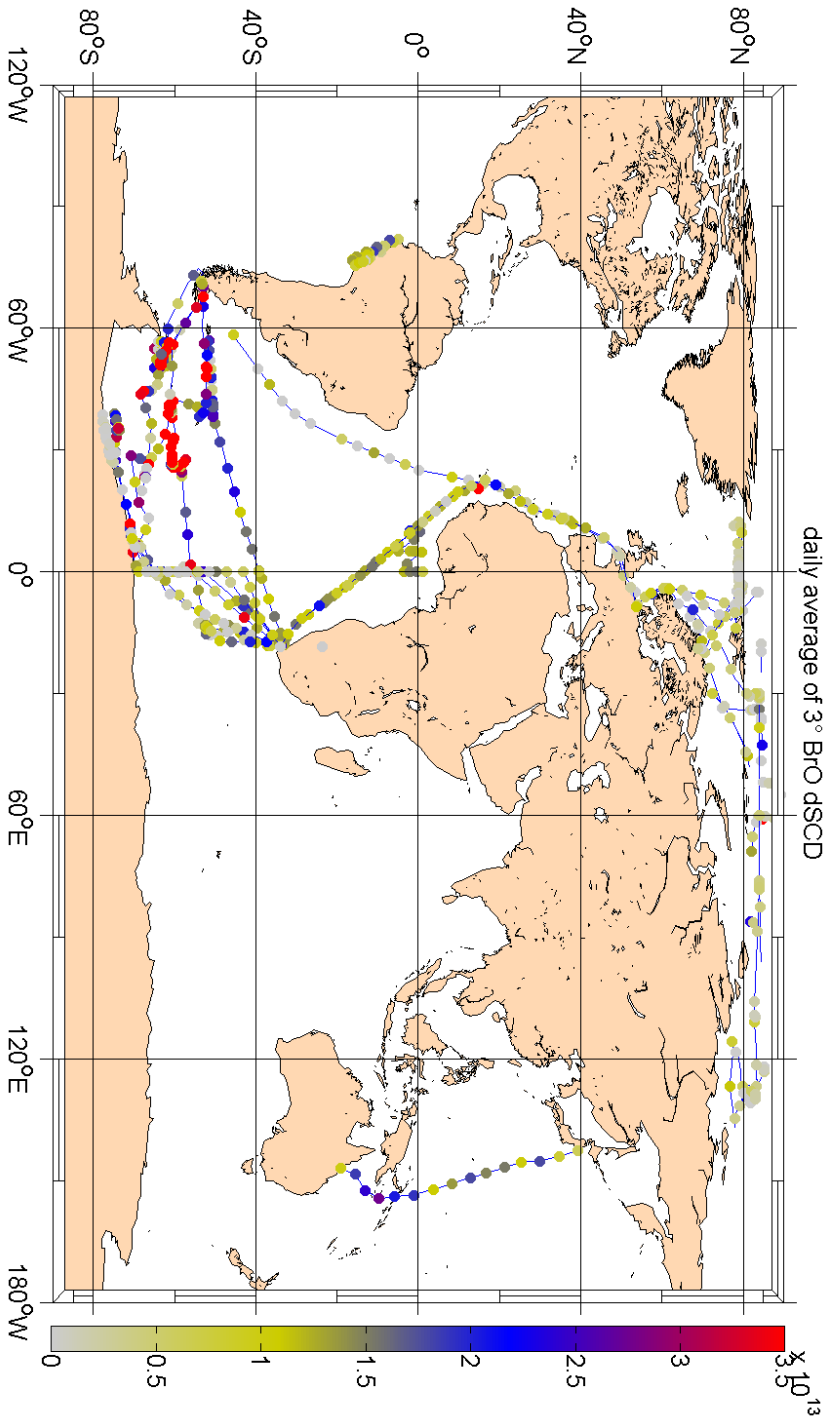

Figure 12.6.: Error weighted daily averages of 3° BrO dSCDs. All data sets were evaluated with the settings listed in section 5.6, only the MSM18/3 cruise (section 8.2) had to be limited to a three-band BrO fit (338 nm–358 nm). The colour-scale is limited to $0 - 3.5 \cdot 10^{13}$ molec cm^{-2}. This cuts off several days in austral spring during ANT XXIX, where BrO dSCDs of more than 10^{15} molec cm^{-2} were observed. Also in February 2014 on ANT XXIX/9 along the coast of Antarctica higher daily averaged BrO values of $3 \cdot 10^{13}$ molec cm^{-2} were observed. Typical fit errors for 3° BrO dSCDs are $(8 \pm 3) \cdot 10^{12}$ molec cm^{-2}.

tion limits.

12.4. Formaldehyde

Tropical background values for formaldehyde (HCHO) were found at 500–1000 ppt, comparable to Peters et al. [2012] on the Western Pacific during TransBrom. Also Weller et al. [2000] observed during a meridional transect on the Atlantic tropical HCHO mixing ratios of around 1 ppb. HCHO VCDs retrieved from MAX-DOAS measurements agreed with monthly averages from satellite observations during ANT XXVIII, compare figure 9.12 and figure 1.4. The profile retrieval indicated that the maximum of HCHO concentrations on the tropical Atlantic is not found within the boundary layer, but in heights around 1000m, which is typically the upper limit of the MBL. Biomass burning observations and trajectory calculations indicate biomass burning in western Africa as the dominant source. Since HCHO is not completely found in the boundary layer, this means that these concentrations of formaldehyde itself and used as a tracer for organic compounds are not necessarily acting as an increased sink for bromine chemistry. Nevertheless, lower BrO concentrations at the surface were observed (practically below the detection limit) of around 0–1 ppt, but these measurements were also not located in an upwelling region.
Compared to measurements on the Atlantic and coastal Pacific during M91, the equatorial mixing ratios of formaldehyde during TransBrom are low, but rise towards the Japanese and Australian coast. Since the dominant source of formaldehyde in the tropics is methane oxidation by OH radicals, this might be connected to the observed minimum in ozone and OH concentrations in the Western Pacific by Rex et al. [2014].

12.5. Glyoxal

Despite the measurements covering a variety of regions around the globe, no glyoxal absorption in the MBL could be detected apart from anthropogenic influences. A previous ground-based MAX-DOAS study [Sinreich et al., 2010] reported dSCDs of $1.5 \cdot 10^{15}$ molec cm^{-2} and more at low elevation angles in the Eastern Pacific. These values can not be confirmed. Satellite observations show vertical columns of up to $(3-5) \cdot 10^{14}$ molec cm^{-2} at measurement errors for retrieval of single spectra $(7-13) \cdot 10^{14}$ molec cm^{-2} for an AMF of 1-2 [Lerot et al., 2010]. The assumption for these measurements is that the values are scattered statistically and can therefore be averaged. Assuming an AMF of 10 for low telescope elevations of MAX-DOAS measurements and that glyoxal is found mainly in the troposphere, this would require dSCD in ground based measurements of $(3-5) \cdot 10^{15}$ molec cm^{-2}. Actual values are found one order of magnitude below, which either means that glyoxal is equally distributed within the free troposphere and the MBL (which would imply further free tropospheric sources), or that these satellite measurements over the open ocean show a bias, due to other absorbers, such as water vapour.
Extensive sensitivity studies on the spectral analysis of MAX-DOAS data for glyoxal revealed that older versions of water vapour cross-sections might result in typical water

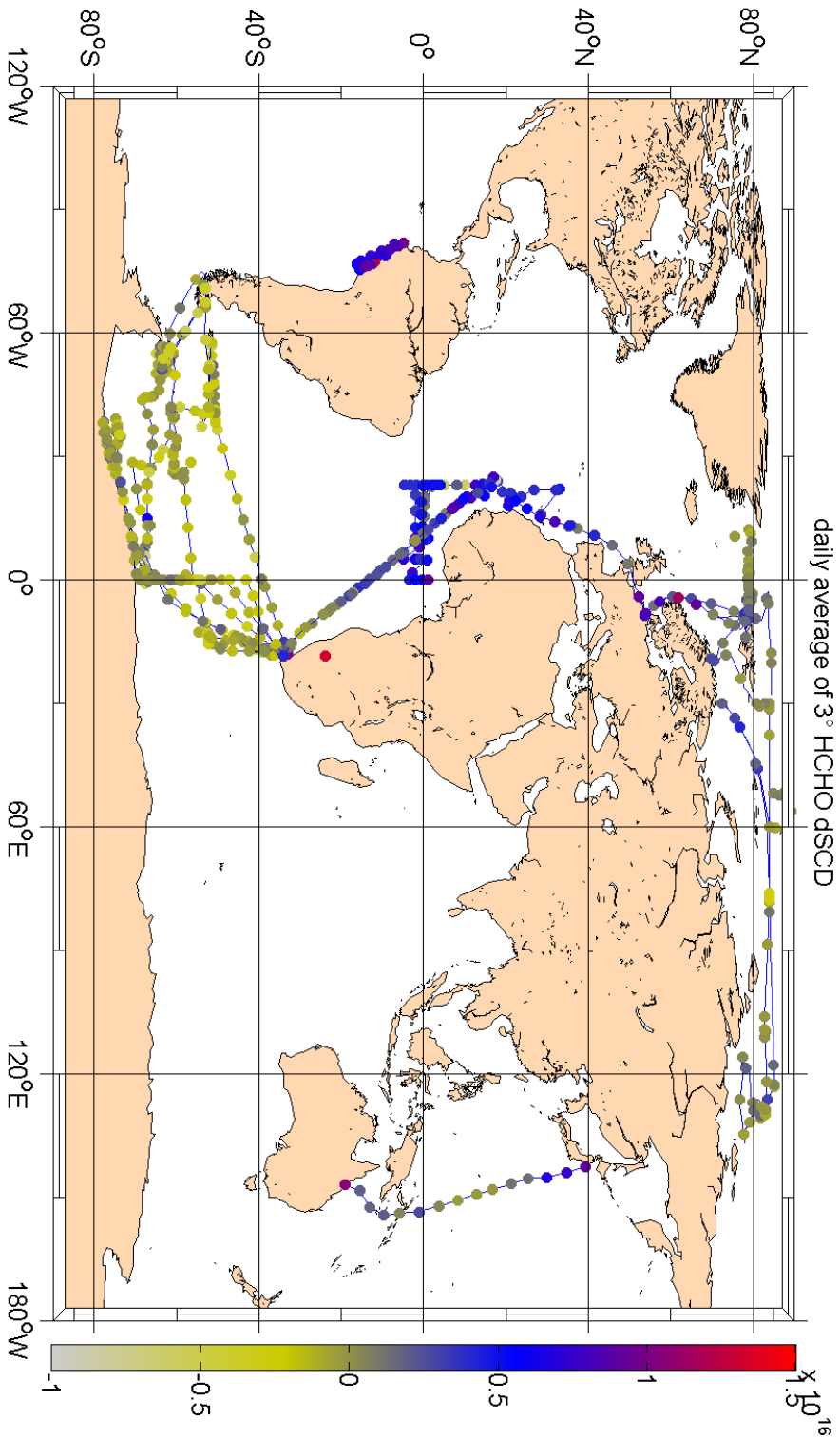

Figure 12.7.: Error weighted daily averages of 3° HCHO dSCDs using the same spectral retrieval settings as for BrO in figure 12.6.

vapour dSCD in a glyoxal dSCDs in the 10^{15} molec cm^{-2}-range (Table 5.7). Furthermore the influence of radiative transfer effects of individual absorption lines of water vapour can be significant at the optical densities which are needed for the detection of glyoxal on the open ocean. The correction for this effect had the largest influence on the spectral retrieval of glyoxal and also modified water vapour dSCDs. Correct modelling of the radiative transfer processes can be important to derive concentration profiles of water vapour, too. (see section 5.4)

Since no significant absorptions of glyoxal in the MBL were found, consequences of glyoxal oxidation as precursors of Secondary Organic Aerosol (SOA) [Connelly et al., 2012] or its abundance in the SML remain hypothetical. Still, CE-DOAS measurements on the Pacific [S. Coburn, pers. comm.] showed concentrations of 30–40 ppt during the Torero campaign. This is close to the current detection limit of the SMAX-DOAS instrument and therefore shows the need for developments leading to MAX-DOAS instruments yielding lower detection limits and better spectral stability for the correct correction of water vapour absorption.

13. Conclusions and Outlook

The aim of this thesis is to quantify the global distribution of reactive Halogen Species (RHS) in the marine Boundary layer (MBL) in order to estimate their effect on the total tropospheric ozone budget. MAX-DOAS measurements were used to gather the necessary information to retrieve mixing ratios of various trace gases in the lower troposphere. The focus was the detection of BrO and IO since these species have the strongest influence on tropospheric ozone chemistry. Within the process of finding reliable settings for their retrieval, uncertainties in the spectral analysis and the respective uncertainties in the literature cross-sections of water vapour, formaldehyde and glyoxal also needed to be addressed. Furthermore CE-DOAS measurements of IO, NO_2, glyoxal and water vapour during two individual campaigns to validate the MAX-DOAS measurements and their conversion to vertical trace-gas profiles.

13.1. Spectral retrieval improvements

The spectral retrieval of almost any reactive trace-gas in the MBL requires precise and stable instruments to achieve the necessary precision to unambiguously identify their absorption structures. Stable spectrometer temperatures and spectrometers with a constant instrument function and low instrumental stray-light are prerequisites for unambiguous detection of trace gas absorptions. The required modifications of various instruments and applications of methods to analyse residual spectra led to possible corrections to known literature cross-sections as well as to the identification of previously neglected radiative transfer effects within the atmosphere.

13.1.1. VRS in air

While explicitly used for measurements for LIDAR measurements, vibrational Raman scattering (VRS) of N_2 and O_2 as the main constituents of the atmosphere was thought to have only a negligible contribution in MAX-DOAS measurement of scattered sunlight. Its contribution to the apparent optical density in MAX-DOAS measurements was unambiguously identified in this work for the first time and its total contribution to the filling-in of Fraunhofer lines was determined from measurement data. The data agrees with previous publications on the cross-section of vibrational Raman scattering for N_2 and O_2. The optical density of the correction for this effect is about 2% of the correction for rotational Raman scattering, which itself is typically 2% of the total intensity of scattered sunlight.

13.1.2. Water vapour

Most of the literature water vapour cross-sections available in the blue wavelength range are based on theoretical calculations. Individual lines are validated by laboratory measurements. The absolute magnitude of the water vapour cross-section in the spectral range from 410–434 nm varied significantly for different versions of HITRAN, HITEMP and BT2. MAX-DOAS measurement data and LP-DOAS measurement data were used to determine the relative strengths of water vapour absorption bands in this spectral range. While the total strength of the main absorption at 442 nm matched meteorological observations on CVAO on Cap Verde, absorptions at 416 nm and 428 nm were overestimated by a factor of two in the most recent version of HITRAN (2012), while previous versions underestimated their contribution to measured optical densities. This explains also unrealistic high water vapour dSCD in previous studies of IO, e.g. Großmann et al. [2013]. In addition the relative absorption band strength was retrieved from LP-DOAS and MAX-DOAS data to obtain correction factors for each of them between 400–480 nm.
These observations allow for a more precise and trustworthy retrieval of IO and glyoxal, since the intervals of the spectral retrieval can cover a broader range of wavelengths to reduce uncertainties. Their total optical densities are especially in tropical regions of the same size as the corrections to the water vapour cross-sections.
Radiative transfer corrections due to the measured absorptions of water vapour at 442 nm in MAX-DOAS data can be significant as well and can largely influence the spectral retrieval of glyoxal.

13.1.3. IO and Glyoxal

IO and glyoxal show absorption structures in the same spectral range from 410–460 nm. Previous publications reported large tropospheric absorptions of glyoxal in the MBL on the Pacific ocean, which could have influenced, at the reported optical densities, the spectral retrieval of IO.
The accuracy of the spectral retrieval of glyoxal and IO was improved significantly by the above-mentioned corrections for VRS and to the water vapour cross-section. For typical measurements the fit error of IO dSCD was reduced by up to 30% by correcting for Vibrational Raman Scattering (VRS)(N_2/O_2) while the total dSCD did not change. Also for glyoxal the fit error was reduced by 20% (subsection 5.2.3.3).
The improvement due to rescaled water vapour absorption bands strongly depends on the spectral retrieval interval. An example is found in figure 5.33.

13.1.4. BrO and HCHO

Already in previous observations BrO and HCHO were known to cause problems with their spectral retrieval, due to cross-sensitivities to ozone absorption and observations of an anti-correlation of BrO and HCHO in evaluations due to their similar spectral absorption structures. Furthermore the absorption of the oxygen dimer O_4 has a significant influence on the results. On top of these problems there is less available light in the

spectral range around 340 nm than for IO in the blue wavelength range, and therefore photon shot noise can be dominating the measurement error.
While the problem of anti-correlations can be addressed by using more information in the spectral retrieval by choosing a wider fit interval, these measures increase the sensitivity to ozone absorptions. Furthermore O_4 might have unknown absorption structures in the new, extended spectral evaluation range, which are not included in the currently available literature cross-sections (see subsection 5.1.1.1). High-precision LP-DOAS measurements could provide more information about the actual shape and size of the O_4 absorption at 328 nm. This information would be useful for spectral DOAS retrievals of BrO, HCHO and SO_2.
Which of the available O_4 absorption cross-section is the most suitable for the retrieval of BrO from 332–358 nm was determined by analysing MAX-DOAS data recorded in Mainz, were no tropospheric BrO absorption is expected. It turned out that the cross-section recorded by Greenblatt et al. [1990] showed the best match of retrieved BrO dSCD. By comparison of MAX-DOAS evaluations with LP-DOAS data on CVAO this conclusion was also drawn before by Tschritter [2013].
Restricting the analysis to a wavelength interval, which was a compromise between width and the influence of ozone, large sets of residual spectra were analysed and similar residual structures were found for different types of spectrometers at different measurement sites around the world. The reason of these unknown residual structure must be located in the lower troposphere, since it is found to correlate with the absorption of O_4. We excluded the possibility, that the reason for these structures was connected to inelastic scattering in the atmosphere. The residual structure is independent of the employed literature O_4 cross-section.
It is needed to address persistent residual structures to have a reliable and precise retrieval of tropospheric BrO from ground-based measurements. These persistent structures show amplitudes of up to $(3 - -4) \cdot 10^{-4}$ while 1 ppt of BrO has an optical density of $3 \cdot 10^{-4}$ along a light-path of 10km at ground-level. A list of possible absorbers is discussed in subsection 5.1.1.2, of which none has been positively identified yet. Often no reliable literature cross-section data is available for the respective molecule.

13.2. Global distributions of reactive trace-gases

13.2.1. IO

The abundance of iodine monoxide in the Peruvian upwelling region was simultaneously measured with CE-DOAS and MAX-DOAS instruments. This first comparison of both measurement techniques for iodine oxide yields agreeing measurements, within their respective measurement errors. Concentrations up to typically 1–1.4 ppt were found during daytime, at night the mixing ratios fell below 0.5 ppt. IO mixing ratios measured by the CE-DOAS rose immediately during sunrise and fell below detection limit with sunset. Due to the required sensitivity the time resolution of the measurements was not better than 10–30 minutes. The MAX-DOAS observations were found to be in agreement with long-time averages of satellite observations of IO in the Peruvian upwelling.

The good agreement of the IO mixing ratios for both instruments and MAX-DOAS observations of IO up to 15 times above the measurement error showed the reliability of the MAX-DOAS data evaluation. This settings were applied to the evaluation of other measurements performed during several years on the research vessel 'Polarstern'. This data set shows a maximum of IO concentrations close to Cape Verde, in the Mauritanian upwelling region and measurements during three years allowed for a first estimate of its variability from ship-based measurements, yielding variations of at least a factor of two from year to year. Furthermore this data-set showed a good correlation with surface water iodide concentrations. The release of iodide from surface waters might be the dominant source of atmospheric iodine.

Measurements during research cruises of 'R/V Polarstern' to the Arctic and Antarctic during the respective summer period yielded significant amounts of IO in the lower troposphere, which was estimated to 0.2–0.4 ppt. No significant difference for both hemispheres was found, despite contradicting satellite observations and ground-based measurements. Large concentrations of more than one ppt of IO during Antarctic summer, as suggested by previous observations, cannot be confirmed, at least not along the cruise tracks.

13.2.2. BrO

Due to problems with the spectral retrievals, theoretical detection limits of 1 ppt cannot be met and no final conclusion about background BrO concentrations in the marine boundary layer can be drawn. Nevertheless the comparison with MAX-DOAS data from **M**ulti **A**xis **D**oas - **C**omparison campaign for **A**erosols and **T**race gases (MAD-CAT) in Mainz allowed for the direct comparison of different retrieval settings yielding a background concentrations of about 1 ppt (MSM18/1) for the tropical/subtropical MBL on the Atlantic (subsection 5.1.1.1).

Only one episode of clearly enhanced BrO concentrations in the MBL was observed: A potential transport event of bromine released in Arctic spring passed the MAX-DOAS on 'R/V Maria S. Merian' at 33°N on April, 22nd, 2011. Calculated backward trajectories led to the conclusion that the origin of the observed bromine rich air mass was found in northern Canada, arriving in the subtropical northern Atlantic within only 2-3 days. The maximum BrO mixing ratios of 4–6 ppt within the lower 500m was found when a front of the deep-pressure system had just passed the position of the ship. This mechanism of bromine transport into the subtropical Atlantic has not been considered before.

The remaining measurements of BrO did not yield any high concentrations of BrO, apart from a possible background value of 0.5–1.5 ppt. No large concentrations as previously reported for the Mauritanian upwelling region could be observed in the Peruvian upwelling region. During M91 slightly increased BrO VMR of 3–4 ppt were observed downwind of the location at which the maximum surface water concentrations of halocarbons were measured (subsection 7.2.3) and the lowest NO_2 concentrations were observed. No concentrations like in the Mauritanian upwelling close to the Mauritanian coast were observed throughout all measurements.

13.2.3. HCHO

Tropospheric formaldehyde concentrations were measured also as a tracer for organic compounds which together can represent one of the major sinks of reactive bromine in the MBL. Typical tropical background values were found at levels of 500–1000 ppt, agreeing with previous measurements on Cape Verde (Figure 1.6). Enhanced concentrations close to Africa at 10°N, which had been previously observed in satellite measurements, were not found at the surface, but in a layer above 750 m, on top of the MBL. These observations agreed with trajectory calculations and biomass burning observations from satellite in south West-Africa. This shows that the outflow of organic compounds with trade winds from Africa onto the Ocean does not necessarily mean that the sink for bromine in the MBL is enhanced, since BrO is mostly found in the MBL.
HCHO VCDs retrieved from MAX-DOAS measurements agreed with monthly averages from satellite observations.

13.2.4. Glyoxal

Glyoxal was not detected in the MBL outside the influence of anthropogenic emissions from western Europe or South-Africa above the detection limit of 35 ppt. It was not detected in the equatorial upwelling region (subsection 8.2.4), on the tropical Atlantic (subsection 9.2.5) and in the Peruvian upwelling region (subsection 7.2.6). Previously reported background values of glyoxal on the open ocean could neither be confirmed for the Pacific nor reported for the Atlantic. Despite a small positive offset of the measured values of 10–20 ppt, no significant observation can be reported. Mean daytime concentrations are thus -4 ± 20 ppt for MSM18/3 (tropical Atlantic) and 10 ± 18 ppt M91 (Peruvian upwelling) at a 2σ detection limit of 35 ppt.
During MAD-CAT in Mainz glyoxal was simultaneously detected by several MAX-DOAS instruments, proving the information that the retrieval settings and the employed literature cross-sections were correct, also for the measurements on the open ocean.
Due to instrumental limitations the measurements of glyoxal with the Polarstern MAX-DOAS instrument based on compact spectrometers with a limited spectral resolution was problematic and showed correlations with water vapour absorptions (subsection 9.2.5).

13.3. Outlook

13.3.1. Spectral Retrieval

Including the correction for vibrational Raman scattering (VRS) in atmospheric DOAS measurements will lead to an improvement of ground-based and satellite retrieval absorptions including the spectral range from 430–440 nm (i.e. IO, water vapour, NO_2, glyoxal and others, such as phytoplankton speciation), since some, if not most, of the systematic residual structures observed above 430 nm can be explained by VRS. For satellite measurements the typical Ring signal, especially in polar regions with a high albedo, are of the order of $5 \cdot 10^{25}$ molec cm^{-2} (see Figure 13.1 at 360 nm, the Ring signal

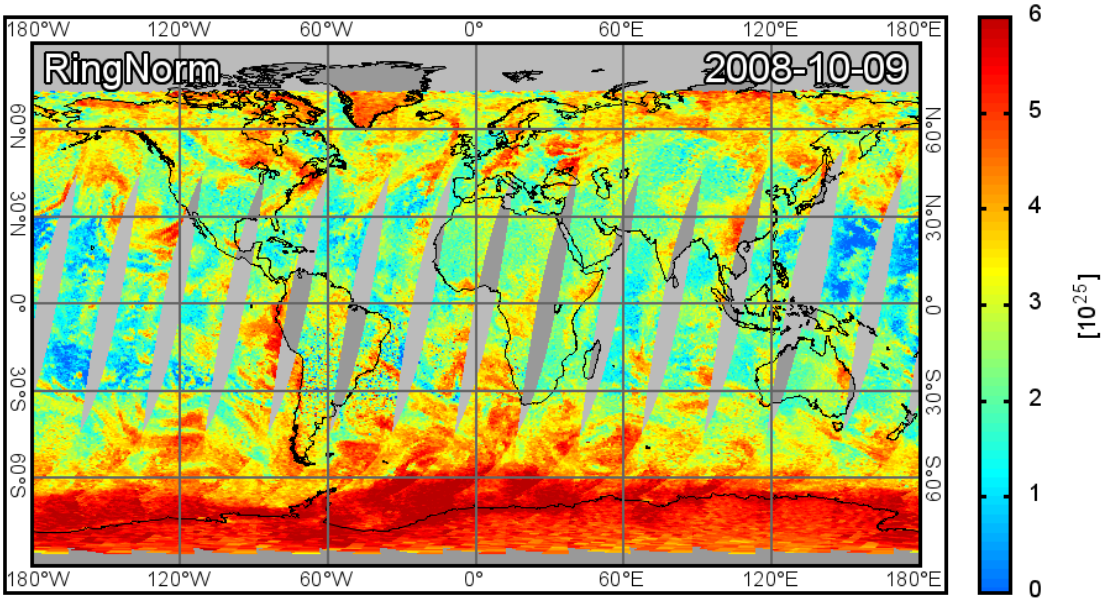

Figure 13.1.: Ring dSCD [$molec/cm^2$] at 360 nm from GOME-2 for 09/10/2008. [Holger Sihler, pers. comm.] A dSCD of $5 \cdot 10^{25}$ molec cm^{-2} will cause residual structures of at typically $4 \cdot 10^{-4}$ in the spectral range between 430 – 440 nm due to vibrational Raman scattering (see subsection 5.2.2).

at longer wavelengths is expected to be larger), therefore a contribution of several 10^{-4} optical density (peak-to-peak) in the residual spectra is expected.

The effect of VRS has been partly compensated in previous MAX-DOAS measurements of IO by applying an additional offset polynomial [e.g. Coburn et al., 2011, Großmann et al., 2013], primarily to compensate for instrumental stray-light. This also corrected for about half of the VRS contribution to the apparent optical density in the IO retrieval interval from 416–438 nm. Thus a part of this effect was compensated already before, without explicitly its reason.

VRS correction for spectral retrievals of IO from satellite data and subsequently the possibility to extend the retrieval interval to three (–438 nm) instead of currently two (–430 nm) IO absorption bands will reduce the typical fit error of IO significantly (30–40%). It will increase the confidence in and the reliability of the spectral retrieval. However, observed column densities will be still close to its detection limit.

Since there are considerable concentrations of IO and BrO in the free troposphere, a separation of ground-based MAX-DOAS measurements into a tropospheric and a free-tropospheric part in the retrieval to gain information about the free troposphere seems to be interesting. For BrO the large stratospheric absorption can be a problem, but for IO the upper limits of its stratospheric abundance are small. Another way might be then to address the concentrations in the free troposphere by cloud-slicing techniques from satellite measurements.

For BrO it is important to identify the reason for the spectral structure in the BrO fit

range and/or investigate possible O_4 absorption structures at 328 nm to extend the BrO fit range further in order to reduce the measurement errors of BrO and HCHO. This might imply the need for explicit corrections for ozone absorption, as suggested in Pukite et al. [2010], even for ground-based measurements using a current Fraunhofer reference. Measurements of concentrations of NO_2 in the remote MBL are as well as the concentrations of RHS close or below current detection limits for MAX-DOAS and CE-DOAS measurements. Improvements of the spectral retrieval by including VRS correction spectra (compare e.g. figure 5.24) removed a negative bias from NO_2 dSCDs, but further improvements are necessary for reliable and absolute measurements of NO_2 concentrations in the range of 10 ppt (corresponding to an OD of 10^{-4} peak-to-peak at around 430 nm). Dedicated corrections for the influence of stratospheric absorption of NO_2 might be necessary.
The example of the M77 expedition (section 7.4) shows that existing data sets, even if only measured with an average instrument, can yield valuable information, when again using the current knowledge about the spectral retrieval and update literature cross-section for the respective molecules.

13.3.2. Chemistry

Chemistry models are needed to combine atmospheric halocarbon measurements and the observations of BrO and IO and to estimate the fluxes necessary to maintain the observed tropospheric RHS concentrations. The sinks can be estimated for each compound and a given concentrations of BrO, but the estimation of the contribution of possible Br-recycling mechanisms on aerosol particles remains uncertain. While numerous publications on release mechanisms for iodine as well as bromine exist, although there is no accepted theory, sink mechanisms for both compounds are typically not discussed in detail.
The diurnal cycle of IO observed by CE-DOAS measurements in agreement with MAX-DOAS measurements during M91 is another point where chemistry models can help to identify the main compounds responsible for the rapid increase of IO concentrations after sunrise and to estimate the role of halocarbons. However, this might require a further reduction of the measurement error of CE-DOAS measurements and/or additional LP-DOAS measurements.

13.3.3. Instrumental

The information from the non-linearity observations during M91 and MAD-CAT were used to optimize the measurement strategy for CE-DOAS measurements during a campaign in the Indian Ocean, Sonne SO235. In the future it might be necessary to implement an optimized readout software to compensate for non-linearity of spectrometers without loosing measurement time due to unnecessary communication between the instrument and the measurement computer. Unfortunately these corrections are normally not done natively on the signal processing board of the spectrometer. Another possibility would be to use spectrometers with detectors which show a less pronounced

non-linearity. For ship measurements, when the instrument does not need to be moved during the campaign, the compact spectrometer could be replaced by a spectrometer with a larger focal length and a better CCD-camera.
It might be furthermore useful to stabilize the temperature of spectrometer electronics board, at least the analogue part converting the actual CCD signal into a digital signal, to avoid instabilities due to temperature dependencies. This might allow for further identification of undiscovered effects at optical depths of less than 10^{-4}. The OMT spectrometer with KHS-electronics board already have the A/D conversion electronics directly at the CCD on the optical bench, therefore it is also temperature stabilized.
Arctic measurements with good spectrometers are needed to finally identify the amount of tropospheric background IO mixing ratios, which might enhance the speed of bromine mediated ozone depletion events during polar spring. This should be done preferably using the SMAX-instrument, which combines high spectral resolution, relatively high light throughput and a constant instrument function. However, the temperature stabilization needs to be improved.
The same applies for measurements of glyoxal in the MBL. Here the correct modelling of water vapour absorption requires even a more stable instrument function as well as the need for corrections of the literature cross-section due to changes in the light path.

Bibliography

A. Adler, R. Youmaran, and S. Loyka. Towards a measure of biometric information. In *Electrical and Computer Engineering, 2006. CCECE '06. Canadian Conference on*, pages 210–213, 2006. doi:10.1109/CCECE.2006.277447.

B. Alicke, K. Hebestreit, J. Stutz, and U. Platt. Detection of iodine oxide in the marine boundary layer. *Nature*, 397:572–573, 1999.

S. R. Aliwell, M. Van Roozendael, P. V. Johnston, A Richter, T. Wagner, D. W. Arlander, J. P. Burrows, D. J. Jones, K. K. Tornkvist, J.-C. Lambert, K. Pfeilsticker, and I. Pundt. Analysis for BrO in zenith-sky spectra: An intercomparision exercise for analysis improvement. *J. Geophys. Res.*, 107(D14):10.1029/2001JD000329, 2002.

B. J. Allan, G. McFiggans, and J. M. C. Plane. Observation of iodine monoxide in the remote marine boundary layer. *J. Geophys. Res.*, 105:14363–14369, 2000.

B. J. Allan, J. M. C. Plane, and G. McFiggans. Observations of OIO in the remote marine boundary layer. *Geophys. Res. Lett.*, 28:1945–1948, 2001.

Larry G Anderson, John A Lanning, Regina Barrell, Joyce Miyagishima, Richard H Jones, and Pamela Wolfe. Sources and sinks of formaldehyde and acetaldehyde: An analysis of denver's ambient concentration data. *Atmospheric Environment*, 30(12):2113–2123, 1996.

Markus Anthofer. Cavity Enhanced-DOAS measurements of iodine oxide. Diploma thesis, Institut für Umweltphysik, Universität Heidelberg, 2013.

Parisa A Ariya, Ashu P Dastoor, Marc Amyot, William H Schroeder, Leonard Barrie, Kurt Anlauf, Farhad Raofie, Andrew Ryzhkov, Didier Davignon, Janick Lalonde, et al. The Arctic: a sink for mercury. *Tellus B*, 56(5):397–403, 2004.

H. M. Atkinson, R.-J. Huang, R. Chance, H. K. Roscoe, C. Hughes, B. Davison, A. Schönhardt, A. S. Mahajan, A. Saiz-Lopez, T. Hoffmann, and P. S. Liss. Iodine emissions from the sea ice of the weddell sea. *Atmospheric Chemistry and Physics*, 12(22):11229–11244, 2012. doi:10.5194/acp-12-11229-2012. URL `http://www.atmos-chem-phys.net/12/11229/2012/`.

S. Baidar, H. Oetjen, S. Coburn, B. Dix, I. Ortega, R. Sinreich, and R. Volkamer. The CU airborne MAX-DOAS instrument: vertical profiling of aerosol extinction and trace gases. *Atmospheric Measurement Techniques*, 6(3):719–739, 2013. doi:10.5194/amt-6-719-2013. URL `http://www.atmos-meas-tech.net/6/719/2013/`.

AR Baker. Inorganic iodine speciation in tropical atlantic aerosol. *Geophysical research letters*, 31(23), 2004.

AR Baker, D Thompson, MLAM Campos, SJ Parry, and TD Jickells. Iodine concentration and availability in atmospheric aerosol. *Atmospheric Environment*, 34(25):4331–4336, 2000.

Andrew Bakun and Craig S Nelson. The seasonal cycle of wind-stress curl in subtropical eastern boundary current regions. *Journal of Physical Oceanography*, 21(12):1815–1834, 1991.

Hermann W Bange, Alina Freing, Annette Kock, and CR Löscher. Marine pathways to nitrous oxide. *Nitrous oxide and climate change. Earthscan, New York*, pages 36–54, 2010.

H.W. Bange. Surface ocean - lower atmosphere study (SOLAS) in the upwelling region off peru - cruise no.M91. *DFG-Senatskommission fuer Ozeanographie, METEOR-Berichte*, 91:69pp, 2013. doi:10.2312/cr_m91. URL `https://portal.geomar.de/metadata/leg/show/316029`.

R. J. Barber, J. Tennyson, G. J. Harris, and R. N. Tolchenov. A high-accuracy computed water line list. *Monthly Notices of the Royal Astronomical Society*, 368(3):1087–1094, 2006. doi:10.1111/j.1365-2966.2006.10184.x. URL `http://mnras.oxfordjournals.org/content/368/3/1087.abstract`.

L.A. Barrie and M.J. Barrie. Chemical components of lower tropospheric aerosols in the high Arctic: Six years of observations. *Journal of Atmospheric Chemistry*, 11(3):211–226, 1990. ISSN 0167-7764. doi:10.1007/BF00118349. URL `http://dx.doi.org/10.1007/BF00118349`.

L.A. Barrie, J.W. Bottenheim, R.C. Schnell, P.J. Crutzen, and R.A. Rasmussen. Ozone destruction and photochemical reactions at polar sunrise in the lower Arctic atmosphere. *Nature*, 334:138–141, 1988.

L. M. Beal and K. A. Donohue. The great whirl: Observations of its seasonal development and interannual variability. *Journal of Geophysical Research: Oceans*, 118(1):1–13, 2013. ISSN 2169-9291. doi:10.1029/2012JC008198. URL `http://dx.doi.org/10.1029/2012JC008198`.

Rachael Beale, Peter S Liss, Joanna L Dixon, and Philip D Nightingale. Quantification of oxygenated volatile organic compounds in seawater by membrane inlet-proton transfer reaction/mass spectrometry. *Analytica chimica acta*, 706(1):128–134, 2011.

Joseph M Beames, Fang Liu, Lu Lu, and Marsha I Lester. Ultraviolet spectrum and photochemistry of the simplest criegee intermediate CH2OO. *Journal of the American Chemical Society*, 134(49):20045–20048, 2012.

S. Beirle, H. Sihler, and T. Wagner. Linearisation of the effects of spectral shift and stretch in DOAS analysis. *Atmospheric Measurement Techniques*, 6(3):661–675, 2013. doi:10.5194/amt-6-661-2013. URL `http://www.atmos-meas-tech.net/6/661/2013/`.

Steffen Beirle, K Folkert Boersma, Ulrich Platt, Mark G Lawrence, and Thomas Wagner. Megacity emissions and lifetimes of nitrogen oxides probed from space. *Science*, 333(6050):1737–1739, 2011.

M Bilde, TJ Wallington, C Ferronato, JJ Orlando, GS Tyndall, E Estupinan, and S Haberkorn. Atmospheric chemistry of CH_2BrCl, $CHBrCl_2$, $CHBr_2Cl$, $CF_3CHBrCl$, and CBr_2Cl_2. *The Journal of Physical Chemistry A*, 102(11):1976–1986, 1998.

S. Bleicher, J. C. Buxmann, R. Sander, T. P. Riedel, J. A. Thornton, U. Platt, and C. Zetzsch. The influence of nitrogen oxides on the activation of bromide and chloride in salt aerosol. *Atmospheric Chemistry and Physics Discussions*, 14(7):10135–10166, 2014. doi:10.5194/acpd-14-10135-2014. URL `http://www.atmos-chem-phys-discuss.net/14/10135/2014/`.

Sergej Bleicher. *Zur Halogenaktivierung im deliqueszenten Aerosol und in Salzpfannen*. Dissertation, Bayreuth University, 2012.

William J Bloss, Thomas J Gravestock, Dwayne E Heard, Trevor Ingham, Gavin P Johnson, and James D Lee. Application of a compact all solid-state laser system to the in situ detection of atmospheric OH, HO_2, NO and IO by laser-induced fluorescence. *Journal of Environmental Monitoring*, 5(1):21–28, 2003.

K. Bluhm, P.L. Croot, O. Huhn, G. Rohardt, and K. Lochte. Distribution of iodide and iodate in the atlantic sector of the southern ocean during austral summer. *Deep Sea Research Part II: Topical Studies in Oceanography*, 58(25-26):2733 – 2748, 2011. ISSN 0967-0645. doi:10.1016/j.dsr2.2011.02.002. URL `http://www.sciencedirect.com/science/article/pii/S0967064511000671`. Physics, Carbon Dioxide, Trace Elements and Isotopes in the Southern Ocean: The Polarstern Expeditions ANT XXIV-3 (2008) and ANT XXIII/3 (2006).

Katrin Bluhm. *The influence of marine phytoplankton on iodine speciation in the Tropical and Southern Atlantic Ocean*. Doctoral thesis/phd, Christian-Albrechts-Universität, 2010. URL `http://oceanrep.geomar.de/10021/`.

Katrin Bluhm, Peter Croot, Kathrin Wuttig, and Karin Lochte. Transformation of iodate to iodide in marine phytoplankton driven by cell senescence. *Aquatic Biology*, 11(1):1–15, 2010. URL `http://eprints.uni-kiel.de/9965/`.

N. Bobrowski and G. Giuffrida. Bromine monoxide / sulphur dioxide ratios in relation to volcanological observations at mt. etna 2006-2009. *Solid Earth*, 3(2):433–445, 2012. doi:10.5194/se-3-433-2012. URL `http://www.solid-earth.net/3/433/2012/`.

K. Bogumil, J. Orphal, T. Homann, S. Voigt, P. Spietz, O.C. Fleischmann, A. Vogel, M. Hartmann, H. Bovensmann, J. Frerik, and J.P. Burrows. Measurements of molecular absorption spectra with the SCIAMACHY pre-flight model: Instrument characterization and reference data for atmospheric remote-sensing in the 230-2380nm region. *J. Photochem. Photobiol. A.*, 157:167–184, 2003.

O. Boucher, C. Moulin, S. Belviso, O. Aumont, L. Bopp, E. Cosme, R. von Kuhlmann, M. G. Lawrence, M. Pham, M. S. Reddy, J. Sciare, and C. Venkataraman. DMS atmospheric concentrations and sulphate aerosol indirect radiative forcing: a sensitivity study to the DMS source representation and oxidation. *Atmospheric Chemistry and Physics*, 3(1):49–65, 2003. doi:10.5194/acp-3-49-2003. URL `http://www.atmos-chem-phys.net/3/49/2003/`.

T. J. Breider, M. P. Chipperfield, N. A. D. Richards, K. S. Carslaw, G. W. Mann, and D. V. Spracklen. Impact of BrO on dimethylsulfide in the remote marine boundary layer. *Geophysical Research Letters*, 37(2), 2010. ISSN 1944-8007. doi:10.1029/2009GL040868. URL `http://dx.doi.org/10.1029/2009GL040868`.

N. J. Bridge and AD Buckingham. The polarization of laser light scattered by gases. *Proceedings of the Royal Society of London. Series A. Mathematical and Physical Sciences*, 295(1442): 334–349, 1966.

J. P. Burrows, A. Dehn, B. Deters, S. Himmelmann, A. Richter, S. Voigt, and J. Orphal. Atmospheric remote-sensing reference data from GOME: 2. temperature-dependent absorption cross sections of O_3 in the 231-794 nm range. *J. Quant. Spec. and Rad. Transf.*, 61:509–517, 1999.

M. Bussemer. Der Ring- Effekt: Ursachen und Einfluß auf die spektroskopische Messung stratosphärischer Spurenstoffe. Diploma thesis, Heidelberg University, Heidelberg, Germany, 1993.

Joelle Buxmann. *'Bromine and Chlorine Explosion' in a Simulated Atmosphere*. Dissertation, Institut für Umweltphysik, Heidelberg University, 2012.

Chris A. Cantrell, James A. Davidson, Anthony H. McDaniel, Richard E. Shetter, and Jack G. Calvert. Temperature-dependent formaldehyde cross sections in the near-ultraviolet spectral region. *The Journal of Physical Chemistry*, 94(10):3902–3908, 1990. doi:10.1021/j100373a008. URL `http://pubs.acs.org/doi/abs/10.1021/j100373a008`.

Kevin Capaldo, James J. Corbett, Prasad Kasibhatla, Paul Fischbeck, and Spyros N. Pandis. Effects of ship emissions on sulphur cycling and radiative climate forcing over the ocean, 1999. URL `http://www.nature.com/nature/journal/v400/n6746/full/400743a0.html`.

SA Carn, AJ Krueger, NA Krotkov, K Yang, and PF Levelt. Sulfur dioxide emissions from Peruvian copper smelters detected by the ozone monitoring instrument. *Geophysical Research Letters*, 34(9), 2007.

LJ Carpenter, ZL Fleming, KA Read, JD Lee, SJ Moller, JR Hopkins, RM Purvis, AC Lewis, K Müller, B Heinold, et al. Seasonal characteristics of tropical marine boundary layer air measured at the Cape Verde Atmospheric Observatory. *Journal of atmospheric chemistry*, 67 (2-3):87–140, 2010.

Lucy J. Carpenter, Samantha M. MacDonald, Marvin D. Shaw, Ravi Kumar, Russell W. Saunders, Rajendran Parthipan, Julie Wilson, and John M. C. Plane. Atmospheric iodine levels influenced by sea surface emissions of inorganic iodine, 2013. URL `http://www.nature.com/ngeo/journal/v6/n2/full/ngeo1687.html`.

K. Chance and R.L. Kurucz. An improved high-resolution solar reference spectrum for earth's atmosphere measurements in the ultraviolet, visible, and near infrared. *Journal of Quantitative Spectroscopy and Radiative Transfer*, 111(9):1289 – 1295, 2010. ISSN 0022-4073. doi:http://dx.doi.org/10.1016/j.jqsrt.2010.01.036. URL `http://www.sciencedirect.com/science/article/pii/S0022407310000610`. Special Issue Dedicated to Laurence S. Rothman on the Occasion of his 70th Birthday.

K. Chance and J. Orphal. Revised ultraviolet absorption cross sections of H_2CO for the HITRAN database. *Journal of Quantitative Spectroscopy and Radiative Transfer*, 112(9):1509 – 1510, 2011. ISSN 0022-4073. doi:10.1016/j.jqsrt.2011.02.002. URL `http://www.sciencedirect.com/science/article/pii/S002240731100080X`.

K. Chance and R. J. D. Spurr. Ring effect studies; Rayleigh scattering, including molecular parameters for rotational Raman scattering and the Fraunhofer spectrum. *Appl. Opt.*, 36: 5224–5230, 1997.

Kelly Chance, Thomas P. Kurosu, and Christopher E. Sioris. Undersampling correction for array detector-based satellite spectrometers. *Appl. Opt.*, 44(7):1296–1304, Mar 2005. doi:10.1364/AO.44.001296. URL `http://ao.osa.org/abstract.cfm?URI=ao-44-7-1296`.

Rosie Chance, Gill Malin, Tim Jickells, and Alex R. Baker. Reduction of iodate to iodide by cold water diatom cultures. *Marine Chemistry*, 105(1-2):169 – 180, 2007. ISSN 0304-4203. doi:http://dx.doi.org/10.1016/j.marchem.2006.06.008. URL `http://www.sciencedirect.com/science/article/pii/S0304420306001150`.

Rosie Chance, Alex R. Baker, Lucy Carpenter, and Tim D. Jickells. The distribution of iodide at the sea surface. *Environ. Sci.: Processes Impacts*, 2014. doi:10.1039/C4EM00139G. URL `http://dx.doi.org/10.1039/C4EM00139G`.

S. Chapman. On ozone and atomic oxygen in the upper atmosphere. *Philos. Mag.*, 10:369–383, 1930.

Samprit Chatterjee and Ali S. Hadi. Influential observations, high leverage points, and outliers in linear regression. *Statistical Science*, 1(3):379–393, Aug 1986. doi:10.1364/AO.35.000074.

K. Clémer, M. Van Roozendael, C. Fayt, F. Hendrick, C. Hermans, G. Pinardi, R. Spurr, P. Wang, and M. De Mazière. Multiple wavelength retrieval of tropospheric aerosol optical properties from maxdoas measurements in beijing. *Atmospheric Measurement Techniques*, 3(4):863–878, 2010. doi:10.5194/amt-3-863-2010. URL `http://www.atmos-meas-tech.net/3/863/2010/`.

S Coburn, B Dix, R Sinreich, and R Volkamer. The CU ground MAX-DOAS instrument: characterization of RMS noise limitations and first measurements near pensacola, FL of BrO, IO, and CHOCHO. *Atmospheric Measurement Techniques*, 4(11):2421–2439, 2011.

Pierre Comon. Independent component analysis, a new concept? *Signal processing*, 36(3): 287–314, 1994.

BM Connelly, DO De Haan, and MA Tolbert. Heterogeneous glyoxal oxidation: a potential source of secondary organic aerosol. *The Journal of Physical Chemistry A*, 116(24):6180–6187, 2012.

Peter Croot, TBD, and TBD. Iodine speciation in the oxygen mininum zone of the peruvian upwelling. *Global Biogeochemical Cycles*, 2014. in preparation.

P. J. Crutzen. The influence of nitrogen oxide on the atmospheric ozone content. *Q.J.R. Meteorol. Soc.*, 96:320–327, 1970.

Colin D O'Dowd and Gerrit De Leeuw. Marine aerosol production: a review of the current knowledge. *Philosophical Transactions of the Royal Society A: Mathematical, Physical and Engineering Sciences*, 365(1856):1753–1774, 2007.

I. De Smedt, M. Van Roozendael, T. Stavrakou, J.-F. Müller, C. Lerot, N. Theys, P. Valks, N. Hao, and R. van der A. Improved retrieval of global tropospheric formaldehyde columns from GOME-2/MetOp-A addressing noise reduction and instrumental degradation issues. *Atmospheric Measurement Techniques*, 5(11):2933–2949, 2012. doi:10.5194/amt-5-2933-2012. URL `http://www.atmos-meas-tech.net/5/2933/2012/`.

Tim Deutschmann. *The radiative transfer simulation model McArtim.* Dissertation, Institut für Umweltphysik, Universität Heidelberg, 2014.

Tim Deutschmann, Steffen Beirle, Udo Friess, Michael Grzegorski, Christoph Kern, Lena Kritten, Ulrich Platt, Cristina Prados-Roman, Janis Pukite, Thomas Wagner, Bodo Werner, and Klaus Pfeilsticker. The monte carlo atmospheric radiative transfer model McArtim: Introduction and validation of jacobians and 3D features. *Journal of Quantitative Spectroscopy and Radiative Transfer*, 112(6):1119 – 1137, 2011. ISSN 0022-4073. doi:http://dx.doi.org/10.1016/j.jqsrt.2010.12.009. URL `http://www.sciencedirect.com/science/article/pii/S0022407310004668`.

TS Dibble, MJ Zelie, and H Mao. Thermodynamics of reactions of ClHg and BrHg radicals with atmospherically abundant free radicals. *Atmospheric Chemistry and Physics*, 12(21): 10271–10279, 2012.

Tommy D Dickey, George W Kattawar, and Kenneth J Voss. Shedding new light on light in the ocean. *Physics Today*, 64:44, 2011.

Andrew G Dickson and Catherine Goyet. *Handbook of methods for the analysis of the various parameters of the carbon dioxide system in sea water*. Carbon Dioxide Information Analysis Center, Oak Ridge National Laboratory, 1994.

Tilman Dinter. Modellierung ozeanischer Rückstreuung unter Einbeziehung von Vibrations-Raman-Streuung und die Auswertung anhand von Satellitendaten. Diploma thesis, Institut für Umweltphysik, Universität Bremen, 2005.

Barbara Dix, Sunil Baidar, James F. Bresch, Samuel R. Hall, K. Sebastian Schmidt, Siyuan Wang, and Rainer Volkamer. Detection of iodine monoxide in the tropical free troposphere. *Proceedings of the National Academy of Sciences*, 2013. doi:10.1073/pnas.1212386110. URL `http://www.pnas.org/content/early/2013/01/22/1212386110.abstract`.

M. Dorf, J. H. Butler, A. Butz, C. Camy-Peyret, M. P. Chipperfield, L. Kritten, S. A. Montzka, B. Simmes, F. Weidner, and K. Pfeilsticker. Long-term observations of stratospheric bromine reveal slow down in growth. *Geophysical Research Letters*, 33(24), 2006. ISSN 1944-8007. doi:10.1029/2006GL027714. URL `http://dx.doi.org/10.1029/2006GL027714`.

R. R. Draxler and G. D. Hess. Description of the HYSPLIT 4 modeling system. NOAA Technical Memorandum ERL ARL-224, NOAA Air Resources Laboratory, Silver Spring, Maryland, U.S.A., 1997.

Juan Du, Li Huang, Qilong Min, and Lei Zhu. The influence of water vapor absorption in the 290-350nm region on solar radiance: Laboratory studies and model simulation. *Geophysical Research Letters*, 40(17):4788–4792, 2013. ISSN 1944-8007. doi:10.1002/grl.50935. URL `http://dx.doi.org/10.1002/grl.50935`.

Patrick Dupré, Titus Gherman, Nikolai F Zobov, Roman N Tolchenov, and Jonathan Tennyson. Continuous-wave cavity ringdown spectroscopy of the 8ν polyad of water in the 25 195 - 25 340 cm range. *The Journal of chemical physics*, 123:154307, 2005.

Vincent Echevin, Olivier Aumont, J Ledesma, and G Flores. The seasonal cycle of surface chlorophyll in the peruvian upwelling system: A modelling study. *Progress in Oceanography*, 79(2):167–176, 2008.

Anna M. Farrenkopf and George W. Luther III. Iodine chemistry reflects productivity and denitrification in the arabian sea: evidence for flux of dissolved species from sediments of western india into the OMZ. *Deep Sea Research Part II: Topical Studies in Oceanography*, 49 (12):2303 – 2318, 2002. ISSN 0967-0645. doi:http://dx.doi.org/10.1016/S0967-0645(02)00038-3. URL `http://www.sciencedirect.com/science/article/pii/S0967064502000383`. The 1994-1996 Arabian Sea Expedition: Oceanic Response to Monsoon al Forcing, Part 5.

F. Ferlemann. *Ballongestützte Messung stratosphärischer Spurengase mit differentieller optischer Absorptionsspektroskopie*. Phd thesis, Heidelberg University, 1998.

Stefan Fickert, Jonathan W. Adams, and John N. Crowley. Activation of Br_2 and BrCl via uptake of hobr onto aqueous salt solutions. *Journal of Geophysical Research: Atmospheres*, 104(D19):23719–23727, 1999. ISSN 2156-2202. doi:10.1029/1999JD900359. URL `http://dx.doi.org/10.1029/1999JD900359`.

Sven E. Fiedler, Achim Hese, and Albert A. Ruth. Incoherent broad-band cavity-enhanced absorption spectroscopy of liquids. *Review of Scientific Instruments*, 76(2):023107–023107–7, 2005. ISSN 0034-6748. doi:10.1063/1.1841872.

Martin A Fischler and Robert C Bolles. Random sample consensus: a paradigm for model fitting with applications to image analysis and automated cartography. *Communications of the ACM*, 24(6):381–395, 1981.

O.C. Fleischmann. New ultraviolet absorption cross-sections of BrO at atmospheric temperatures measured by time-windowing fourier transform spectroscopy. *Journal of Photochemistry and Photobiology A: Chemistry*, 168:117–132, 2004.

U. Frieß. *Spectroscopic Measurements of Atmospheric Trace Gases at Neumayer-Station, Antarctica*. Dissertation, Institut für Umweltphysik, Heidelberg University, 2001.

U. Frieß, T. Wagner, I. Pundt, K. Pfeilsticker, and U. Platt. Spectroscopic measurements of tropospheric iodine oxide at neumeyer station, antarctica. *Geophys. Res. Lett.*, 28:1941–1944, 2001.

U. Frieß P. S. Monks, J. J. Remedios, A. Rozanov, R. Sinreich, T. Wagner, and U. Platt. MAX-DOAS O_4 measurements: A new technique to derive information on atmospheric aerosols: 2. modeling studies. *Journal of Geophys. Res.*, 111, D14203:doi: 10.1029/2005JD006618, 2006.

U. Frieß, T. Deutschmann, B. S. Gilfedder, R. Weller, and U. Platt. Iodine monoxide in the antarctic snowpack. *Atmospheric Chemistry and Physics*, 10(5):2439–2456, 2010. doi:10.5194/acp-10-2439-2010. URL `http://www.atmos-chem-phys.net/10/2439/2010/`.

U. Frieß H. Sihler, R. Sander, D. Pöhler, S. Yilmaz, and U. Platt. The vertical distribution of BrO and aerosols in the Arctic: Measurements by active and passive differential optical absorption spectroscopy. *Journal of Geophysical Research: Atmospheres*, 116(D14), 2011. ISSN 2156-2202. doi:10.1029/2011JD015938. URL `http://dx.doi.org/10.1029/2011JD015938`.

U. Frieß U., T. Wagner, I. Pundt, K. Pfeilsticker, and U. Platt. Spectroscopic measurements of tropospheric iodine oxide at Neumayer Station, Antarctica. *Geophysical Research Letters*, 28(10):1941–1944, 2001. ISSN 1944-8007. doi:10.1029/2000GL012784. URL `http://dx.doi.org/10.1029/2000GL012784`.

Udo Friess, Johannes Zielcke, Denis Pöhler, Tim Hay, Karin Kreher, and Ulrich Platt. Iodine monoxide in the antarctic marine boundary layer: Recent discoveries. In *EGU General Assembly Conference Abstracts*, volume 15, page 8643, 2013.

E. S. Fry, G. W. Kattawar, and R. M. Pope. Integrating cavity absorption meter. *Appl. Opt.*, 31:2055–2065, 1992.

S. Fueglistaler, M. Bonazzola, P. H. Haynes, and T. Peter. Stratospheric water vapor predicted from the lagrangian temperature history of air entering the stratosphere in the tropics. *Journal of Geophysical Research: Atmospheres*, 110(D8), 2005. ISSN 2156-2202. doi:10.1029/2004JD005516. URL `http://dx.doi.org/10.1029/2004JD005516`.

S. Fuhlbrügge, K. Krüger, B. Quack, E. Atlas, H. Hepach, and F. Ziska. Impact of the marine atmospheric boundary layer conditions on VSLS abundances in the eastern tropical and subtropical north atlantic ocean. *Atmospheric Chemistry and Physics*, 13(13):6345–6357, 2013. doi:10.5194/acp-13-6345-2013. URL `http://www.atmos-chem-phys.net/13/6345/2013/`.

Hiroshi Fukazawa and Shinji Mae. The vibrational spectra of ice ih and polar ice. *Physics of Ice Core Records*, pages 25–42, 2000.

L Ganzeveld, D Helmig, CW Fairall, J Hare, and A Pozzer. Atmosphere-ocean ozone exchange: A global modeling study of biogeochemical, atmospheric, and waterside turbulence dependencies. *Global Biogeochemical Cycles*, 23(4), 2009.

H. E. Garcia, R. A. Locarnini, T. P. Boyer, J. I. Antonov an O. K. Baranova, M. M. Zweng, and D. R. Johnson. World ocean atlas 2013, volume 3: Dissolved oxygen, apparent oxygen utilization, and oxygen saturation. *S. Levitus, Ed. NOAA Atlas NESDIS 75*, (27pp), 2014.

J. A. Garland and Hilary Curtis. Emission of iodine from the sea surface in the presence of ozone. *Journal of Geophysical Research: Oceans*, 86(C4):3183–3186, 1981. ISSN 2156-2202. doi:10.1029/JC086iC04p03183. URL `http://dx.doi.org/10.1029/JC086iC04p03183`.

Stefan General. *An Imaging DOAS Instrument for Airborne Studies of 2 and 3-dimensional Trace Gas Distributions in the Troposphere*. Dissertation, Institut für Umweltphysik, Heidelberg University, 2013.

Benjamin S Gilfedder, Michael Petri, and Harald Biester. Iodine speciation in rain and snow: Implications for the atmospheric iodine sink. *Journal of Geophysical Research: Atmospheres (1984–2012)*, 112(D7), 2007.

Jonas Gliß. MAX-DOAS measurements of chlorine and bromine compounds in the volcanic plume of Mt. Etna. Master's thesis, Heidelberg University, 2014.

Juan Carlos Gómez Martín, Stephen H. Ashworth, Anoop S. Mahajan, and John M. C. Plane. Photochemistry of oio: Laboratory study and atmospheric implications. *Geophysical Research Letters*, 36(9), 2009. ISSN 1944-8007. doi:10.1029/2009GL037642. URL `http://dx.doi.org/10.1029/2009GL037642`.

Howard R. Gordon, Marlon R. Lewis, Scott D. McLean, Michael S. Twardowski, Scott A. Freeman, Kenneth J. Voss, and G. Chris Boynton. Spectra of particulate backscattering in natural waters. *Opt. Express*, 17(18):16192–16208, Aug 2009. doi:10.1364/OE.17.016192. URL `http://www.opticsexpress.org/abstract.cfm?URI=oe-17-18-16192`.

J.F. Grainger and J. Ring. Anomalous fraunhofer line profiles. *Nature*, 193:762, 1962.

G. D. Greenblatt, J. J. Orlando, J. B. Burkholder, and A. R. Ravishankara. Absorption measurements of oxygen between 330 and 1140 nm. *J. Geophys. Res.*, 95:18577–18582, 1990.

Daniel Grosjean, Antonio H Miguel, and Tania M Tavares. Urban air pollution in brazil: Acetaldehyde and other carbonyls. *Atmospheric Environment. Part B. Urban Atmosphere*, 24 (1):101–106, 1990.

K. Großmann, U. Frieß, E. Peters, F. Wittrock, J. Lampel, S. Yilmaz, J. Tschritter, R. Sommariva, R. von Glasow, B. Quack, K. Krüger, K. Pfeilsticker, and U. Platt. Iodine monoxide in the western pacific marine boundary layer. *Atmospheric Chemistry and Physics*, 13(6):

3363–3378, 2013. doi:10.5194/acp-13-3363-2013. URL http://www.atmos-chem-phys.net/13/3363/2013/.

Vladimir I. Haltrin and George W. Kattawar. Self-consistent solutions to the equation of transfer with elastic and inelastic scattering in oceanic optics: I. model. *Appl. Opt.*, 32(27):5356–5367, Sep 1993. doi:10.1364/AO.32.005356. URL http://ao.osa.org/abstract.cfm?URI=ao-32-27-5356.

Jaron C Hansen, Yumin Li, Joseph S Francisco, and Zhuangjie Li. On the mechanism of the BrO+CH2O reaction. *The Journal of Physical Chemistry A*, 103(42):8543–8546, 1999.

Trevor Hastie, Robert Tibshirani, and Jerome Friedman. *The elements of statistical learning*, volume 1. Springer New York, 2001. URL http://statweb.stanford.edu/~tibs/ElemStatLearn/.

Heiko Haug. Raman-Streuung von Sonnenlicht in der Erdatmosphäre. Diploma thesis, Institut für Umweltphysik, Ruprecht-Karls-Universität Heidelberg, 1996. D467.

Sayaka Hayase, Akihiro Yabushita, Masahiro Kawasaki, Shinichi Enami, Michael R. Hoffmann, and Agustin J. Colussi. Heterogeneous reaction of gaseous ozone with aqueous iodide in the presence of aqueous organic species. *The Journal of Physical Chemistry A*, 114(19):6016–6021, 2010. doi:10.1021/jp101985f. URL http://pubs.acs.org/doi/abs/10.1021/jp101985f.

K. Hebestreit. *Halogen Oxides in the Mid-Latitudinal Planetary Boundary Layer*. Dissertation, Institute für Umweltphysik, Heidelberg University, 2001.

K. Hebestreit, J. Stutz, D. Rosen, V. Matveiv, M. Peleg, M. Luria, and U. Platt. DOAS measurements of tropospheric bromine oxide in mid-latitudes. *Science*, 283:55–57, 1999.

H. Hepach, B. Quack, F. Ziska, S. Fuhlbrügge, E. L. Atlas, I. Peeken, K. Krüger, and D. W. R. Wallace. Drivers of diel and regional variations of halocarbon emissions from the tropical north east atlantic. *Atmospheric Chemistry and Physics Discussions*, 13(7):19701–19750, 2013. doi:10.5194/acpd-13-19701-2013. URL http://www.atmos-chem-phys-discuss.net/13/19701/2013/.

C. Hermans, A. C. Vandaele, M. Carleer, S. Fally, R. Colin, A. Jenouvrier, B. Coquart, and M.-F. Mérienne. Absorption cross-sections of atmospheric constituents: NO_2, O_2, and H_2O. *Environ. Sci. & Pollut. Res.*, 6(3):151–158, 1999.

A. Hilboll, A. Richter, and J. P. Burrows. Long-term changes of tropospheric NO_2 over megacities derived from multiple satellite instruments. *Atmospheric Chemistry and Physics*, 13(8):4145–4169, 2013. doi:10.5194/acp-13-4145-2013. URL http://www.atmos-chem-phys.net/13/4145/2013/.

Christian Hill, Sergei N. Yurchenko, and Jonathan Tennyson. Temperature-dependent molecular absorption cross sections for exoplanets and other atmospheres. *Icarus*, 226(2):1673 – 1677, 2013. ISSN 0019-1035. doi:http://dx.doi.org/10.1016/j.icarus.2012.07.028. URL http://www.sciencedirect.com/science/article/pii/S0019103512003041.

Robert Holla. Langzeitmessungen von Spurengasen mittels Multi-Axis-DOAS auf den Kapverdischen Inseln. Master's thesis, Institute of Environmental Physics, Heidelberg University, 2009.

Robert Holla. *Reactive Halogen Species above Salt Lakes and Salt Pans*. Dissertation, Institut für Umweltphysik, Heidelberg University, 2013.

Jens Hollwedel. *Observations of Tropospheric and Stratospheric Bromine Monoxide from Satellite*. Dissertation, Institut für Umweltphysik, Universität Heidelberg, 2005.

G. Hönninger, C.v. Friedeburg, and U. Platt. Multi axis differential absorption spectroscopy (MAX-DOAS). *Atmos. Chem. Phys.*, 4:231–245, 2004.

Gerd Hönninger and U Platt. Observations of BrO and its vertical distribution during surface ozone depletion at alert. *Atmospheric Environment*, 36(15):2481–2489, 2002.

Martin Horbanski. A compact resonator based instrument for DOAS measurements of ambient nitrogen dioxide. Diploma thesis, Heidelberg University, 2010.

Martin Horbanski. *Coastal iodine emissions measured with the CE-DOAS technique*. Dissertation, Institut für Umweltphysik, Heidelberg University, 2014.

L Claron Hoskins. Pure rotational raman spectroscopy of diatomic molecules. *Journal of Chemical Education*, 52(9):568, 1975.

A. J. Huisman, J. R. Hottle, M. M. Galloway, J. P. DiGangi, K. L. Coens, W. Choi, I. C. Faloona, J. B. Gilman, W. C. Kuster, J. de Gouw, N. C. Bouvier-Brown, A. H. Goldstein, B. W. LaFranchi, R. C. Cohen, G. M. Wolfe, J. A. Thornton, K. S. Docherty, D. K. Farmer, M. J. Cubison, J. L. Jimenez, J. Mao, W. H. Brune, and F. N. Keutsch. Photochemical modeling of glyoxal at a rural site: observations and analysis from BEARPEX 2007. *Atmospheric Chemistry and Physics*, 11(17):8883–8897, 2011. doi:10.5194/acp-11-8883-2011. URL `http://www.atmos-chem-phys.net/11/8883/2011/`.

Aapo Hyvärinen and Erkki Oja. Independent component analysis: algorithms and applications. *Neural Networks*, 13:411–430, 2000.

Ossama Ibrahim. *Applications on Ground-based Tropospheric Measurements using Multi-Axis Differential Optical Absorption Spectroscopy*. Dissertation, Institut für Umweltphysik, Heidelberg University, 2009.

F. Immler, D. Engelbart, and O. Schrems. Fluorescence from atmospheric aerosol detected by a lidar indicates biogenic particles in the lowermost stratosphere. *Atmospheric Chemistry and Physics*, 5(2):345–355, 2005. doi:10.5194/acp-5-345-2005. URL `http://www.atmos-chem-phys.net/5/345/2005/`.

H. Inaba. Detection of atoms and molecules by raman scattering and resonance fluorescence. In E.David Hinkley, editor, *Laser Monitoring of the Atmosphere*, volume 14 of *Topics in Applied Physics*, pages 153–236. Springer Berlin Heidelberg, 1976. ISBN 978-3-540-07743-5. doi:10.1007/3-540-07743-X_19. URL `http://dx.doi.org/10.1007/3-540-07743-X_19`.

IPCC AR5. *IPCC - Fifth Assessment Report (AR5)*. 2013. URL `http://www.ipcc.ch/report/ar5/index.shtml`.

H. Irie, Y. Kanaya, H. Akimoto, H. Tanimoto, Z. Wang, J. F. Gleason, and E. J. Bucsela. Validation of OMI tropospheric NO_2 column data using MAX-DOAS measurements deep inside the north china plain in june 2006: Mount tai experiment 2006. *Atmospheric Chemistry and Physics*, 8(22):6577–6586, 2008. ISSN 1680-7316. URL `http://www.atmos-chem-phys.net/8/6577/2008/`.

N Jacquinet-Husson, L Crepeau, R Armante, C Boutammine, A Chédin, NA Scott, C Crevoisier, V Capelle, C Boone, N Poulet-Crovisier, et al. The 2009 edition of the GEISA spectroscopic database. *Journal of Quantitative Spectroscopy and Radiative Transfer*, 112(15):2395–2445, 2011.

Zhang Jia-Zhong and Michael Whitfield. Kinetics of inorganic redox reactions in seawater: I. the reduction of iodate by bisulphide. *Marine Chemistry*, 19(2):121–137, 1986.

T.D. Jickells, S.S. Boyd, and A.H. Knap. Iodine cycling in the Sargasso Sea and the Bermuda inshore waters. *Marine Chemistry*, 24(1):61 – 82, 1988. ISSN 0304-4203. doi:http://dx.doi.org/10.1016/0304-4203(88)90006-0. URL `http://www.sciencedirect.com/science/article/pii/0304420388900060`.

Timothy D Jickells and Lucinda J Spokes. Atmospheric iron inputs to the oceans. *IUPAC series on analytical and physical chemistry of environmental systems*, 7:85–122, 2001.

H. S. Johnston. Reduction of stratospheric ozone by nitrogen oxide catalysts from supersonic transport exhaust. *Science*, 173:517–522, 1971.

Charlotte E Jones and Lucy J Carpenter. Solar photolysis of CH_2I_2, CH_2ICl, and CH_2IBr in water, saltwater, and seawater. *Environmental science & technology*, 39(16):6130–6137, 2005.

Moritz Jurgschat. Messung von Spurengasen in der freien Troposphäre mit der MAX-DOAS Methode auf der Umweltforschungsstation Schneefernerhaus. Diploma thesis, Institut für Umweltphysik, Universität Heidelberg, 2012.

Nikolas Kaltsoyannis and John MC Plane. Quantum chemical calculations on a selection of iodine-containing species (IO, OIO, INO_3,$(IO)_2$, I_2O_3, I_2O_4 and I_2O_5) of importance in the atmosphere. *Physical Chemistry Chemical Physics*, 10(13):1723–1733, 2008.

T Kanitz, A Ansmann, R Engelmann, and D Althausen. North-south cross sections of the vertical aerosol distribution over the Atlantic Ocean from multiwavelength raman/polarization lidar during polarstern cruises. *Journal of Geophysical Research: Atmospheres*, 2013.

YJ Kaufman, I Koren, LA Remer, D Tanré, P Ginoux, and S Fan. Dust transport and deposition observed from the terra-moderate resolution imaging spectroradiometer (modis) spacecraft over the Atlantic Ocean. *Journal of Geophysical Research: Atmospheres (1984–2012)*, 110 (D10), 2005.

Astrid Kerweg. *Global Modelling of Atmospheric Halogen Chemistry in the Marine Boundary Layer*. Dissertation, Rheinischen Friedrich-Wilhelms-Universität Bonn, 2005.

MAK Khalil, RA Rasmussen, and SD Hoyt. Atmospheric chloroform ($CHCl_3$): ocean-air exchange and global mass balance. *tellus B*, 35(4):266–274, 1983.

W Knippers, K Van Helvoort, and S Stolte. Vibrational overtones of the homonuclear diatomics (n_2, o_2, d_2) observed by the spontaneous raman effect. *Chemical physics letters*, 121(4):279–286, 1985.

S. Kraus. *DOASIS - A Framework Design for DOAS*. Dissertation, Heidelberg University, 2006.

K. Krüger and B. Quack. Introduction to special issue: the transbrom sonne expedition in the tropical west pacific. *Atmospheric Chemistry and Physics*, 13(18):9439–9446, 2013. doi:10.5194/acp-13-9439-2013. URL `http://www.atmos-chem-phys.net/13/9439/2013/`.

Paul H. Krupenie. The spectrum of molecular oxygen. *Journal of Physical and Chemical Reference Data*, 1(2):423–534, 1972. doi:http://dx.doi.org/10.1063/1.3253101. URL `http://scitation.aip.org/content/aip/journal/jpcrd/1/2/10.1063/1.3253101`.

S Kühl, W Wilms-Grabe, S Beirle, C Frankenberg, M Grzegorski, J Hollwedel, F Khokhar, S Kraus, U Platt, S Sanghavi, et al. Stratospheric chlorine activation in the arctic winters 1995/96–2001/02 derived from gome oclo measurements. *Advances in Space Research*, 34(4): 798–803, 2004.

M. Kuntz. A new implementation of the Humlicek algorithm for the calculation of the voigt profile function. *Journal of Quantitative Spectroscopy and Radiative Transfer*, 57(6):819 – 824, 1997. ISSN 0022-4073. doi:10.1016/S0022-4073(96)00162-8. URL `http://www.sciencedirect.com/science/article/pii/S0022407396001628`.

Steffen Kutterolf, TH Hansteen, K Appel, Armin Freundt, Kirstin Krüger, Wendy Perez, and Heidi Wehrmann. Combined bromine and chlorine release from large explosive volcanic eruptions: A threat to stratospheric ozone? *Geology*, 41(6):707–710, 2013.

J. Lampel, D. Pöhler, J. Tschritter, U. Frieß and U. Platt. On the relative absorption strengths of water vapor in the blue wavelength range. *Atmospheric Measurement Techniques Discussions*, 2013. in prep.

Johannes Lampel. Measurements of reactive halogen species on atlantic transects. Diploma thesis, Institut für Umweltphysik, Universität Heidelberg, 2010.

M. J. Lawler, A. S. Mahajan, A. Saiz-Lopez, and E. S. Saltzman. Observations of I_2 at a remote marine site. *Atmospheric Chemistry and Physics Discussions*, 13(10):25911–25937, 2013. doi:10.5194/acpd-13-25911-2013. URL `http://www.atmos-chem-phys-discuss.net/13/25911/2013/`.

J. D. Lee, G. McFiggans, J. D. Allan, A. R. Baker, S. M. Ball, A. K. Benton, L. J. Carpenter, R. Commane, B. D. Finley, M. Evans, E. Fuentes, K. Furneaux, A. Goddard, N. Good, J. F. Hamilton, D. E. Heard, H. Herrmann, A. Hollingsworth, J. R. Hopkins, T. Ingham, M. Irwin, C. E. Jones, R. L. Jones, W. C. Keene, M. J. Lawler, S. Lehmann, A. C. Lewis, M. S. Long, A. Mahajan, J. Methven, S. J. Moller, K. Müller, T. Müller, N. Niedermeier, S. O'Doherty, H. Oetjen, J. M. C. Plane, A. A. P. Pszenny, K. A. Read, A. Saiz-Lopez, E. S. Saltzman, R. Sander, R. von Glasow, L. Whalley, A. Wiedensohler, and D. Young. Reactive halogens in the marine boundary layer (RHaMBLe): the tropical north atlantic experiments. *Atmospheric Chemistry and Physics*, 10(3):1031–1055, 2010. doi:10.5194/acp-10-1031-2010. URL `http://www.atmos-chem-phys.net/10/1031/2010/`.

Thomas Lehmann. *Inverse Modelling of Spectrometer Instrument Functions*. Dissertation, Institut für Umweltphysik, Heidelberg University, 2014. in prep.

P.A. Leighton. Photochemistry of air pollution. *Academic Press, New York*, 1961.

J Lelieveld, J Van Aardenne, H Fischer, M De Reus, J Williams, and P Winkler. Increasing ozone over the Atlantic Ocean. *Science*, 304(5676):1483–1487, 2004.

C. Lerot, T. Stavrakou, I. De Smedt, J.-F. Müller, and M. Van Roozendael. Glyoxal vertical columns from GOME-2 backscattered light measurements and comparisons with a global model. *Atmospheric Chemistry and Physics*, 10(24):12059–12072, 2010. doi:10.5194/acp-10-12059-2010. URL `http://www.atmos-chem-phys.net/10/12059/2010/`.

H. Leser, G. Hönninger, and U. Platt. MAX-DOAS measurements of BrO and NO_2 in the marine boundary layer. *Geophysical Research Letters*, 30(10), 2003. ISSN 1944-8007. doi:10.1029/2002GL015811. URL http://dx.doi.org/10.1029/2002GL015811.

K. Levenberg. A method for the solution of certain non-linear problems in least squares. *Quart. Appl., Math.*, 2:164–168, 1944.

Sydney Levitus, Ricardo A Locarnini, Timothy P Boyer, Alexey V Mishonov, John I Antonov, Hernan E Garcia, Olga K Baranova, Melissa M Zweng, Daphne R Johnson, and Dan Seidov. *World Ocean Atlas 2009*. 2010.

Can Li, Joanna Joiner, Nickolay A. Krotkov, and Pawan K. Bhartia. A fast and sensitive new satellite SO2 retrieval algorithm based on principal component analysis: Application to the ozone monitoring instrument. *Geophysical Research Letters*, 40(23):6314–6318, 2013a. ISSN 1944-8007. doi:10.1002/2013GL058134. URL http://dx.doi.org/10.1002/2013GL058134.

X. Li, T. Brauers, A. Hofzumahaus, K. Lu, Y. P. Li, M. Shao, T. Wagner, and A. Wahner. Max-doas measurements of NO_2, HCHO and CHOCHO at a rural site in southern china. *Atmospheric Chemistry and Physics*, 13(4):2133–2151, 2013b. doi:10.5194/acp-13-2133-2013. URL http://www.atmos-chem-phys.net/13/2133/2013/.

Fang Liu, Joseph M Beames, Amy M Green, and Marsha I Lester. UV spectroscopic characterization of dimethyl-and ethyl-substituted carbonyl oxides. *The Journal of Physical Chemistry A*, 2014.

Derek A Long and Peter A Curran. Book tools. *Vectors*, 1:381–406, 2002. URL http://www.kinetics.nsc.ru/chichinin/books/spectroscopy/Derek02.pdf.

David G Lowe. Distinctive image features from scale-invariant keypoints. *International journal of computer vision*, 60(2):91–110, 2004.

Peter Lübcke. *Optical remote sensing measurements of bromine and sulphur emissions: Investigating their potential as tracers of volcanic activity*. Dissertation, Institut für Umweltphysik, Heidelberg University, 2014.

S. M. MacDonald, H. Oetjen, A. S. Mahajan, L. K. Whalley, P. M. Edwards, D. E. Heard, C. E. Jones, and J. M. C. Plane. DOAS measurements of formaldehyde and glyoxal above a south-east asian tropical rainforest. *Atmospheric Chemistry and Physics*, 12(13):5949–5962, 2012. doi:10.5194/acp-12-5949-2012. URL http://www.atmos-chem-phys.net/12/5949/2012/.

S. M. MacDonald, J. C. Gómez Martín, R. Chance, S. Warriner, A. Saiz-Lopez, L. J. Carpenter, and J. M. C. Plane. A laboratory characterisation of inorganic iodine emissions from the sea surface: dependence on oceanic variables and parameterisation for global modelling. *Atmospheric Chemistry and Physics Discussions*, 13(12):31445–31477, 2013. doi:10.5194/acpd-13-31445-2013. URL http://www.atmos-chem-phys-discuss.net/13/31445/2013/.

A. S. Mahajan, J. M. C. Plane, H. Oetjen, L. Mendes, R. W. Saunders, A. Saiz-Lopez, C. E. Jones, L. J. Carpenter, and G. B. McFiggans. Measurement and modelling of tropospheric reactive halogen species over the tropical Atlantic Ocean. *Atmospheric Chemistry and Physics*, 10(10):4611–4624, 2010a. doi:10.5194/acp-10-4611-2010. URL http://www.atmos-chem-phys.net/10/4611/2010/.

A. S. Mahajan, J. C. Gómez Martín, T. D. Hay, S.-J. Royer, S. Yvon-Lewis, Y. Liu, L. Hu, C. Prados-Roman, C. Ordóñez, J. M. C. Plane, and A. Saiz-Lopez. Latitudinal distribution of reactive iodine in the eastern pacific and its link to open ocean sources. *Atmospheric Chemistry and Physics*, 12(23):11609–11617, 2012. doi:10.5194/acp-12-11609-2012. URL `http://www.atmos-chem-phys.net/12/11609/2012/`.

Anoop Mahajan, Lisa Whalley, Elena Kozlova, Hilke Oetjen, Luis Mendez, Kate Furneaux, Andrew Goddard, Dwayne Heard, John Plane, and Alfonso Saiz-Lopez. Doas observations of formaldehyde and its impact on the HO_x balance in the tropical atlantic marine boundary layer. *Journal of Atmospheric Chemistry*, 66(3):167 – 178, 2010b. ISSN 01677764.

Anoop S. Mahajan, Marvin Shaw, Hilke Oetjen, Karen E. Hornsby, Lucy J. Carpenter, Lars Kaleschke, Xiangshan Tian-Kunze, James D. Lee, Sarah J. Moller, Peter Edwards, Roisin Commane, Trevor Ingham, Dwayne E. Heard, and John M. C. Plane. Evidence of reactive iodine chemistry in the Arctic boundary layer. *Journal of Geophysical Research: Atmospheres*, 115(D20), 2010c. ISSN 2156-2202. doi:10.1029/2009JD013665. URL `http://dx.doi.org/10.1029/2009JD013665`.

Anoop S. Mahajan, Cristina Prados-Roman, Timothy D. Hay, Johannes Lampel, Denis Pöhler, Katja Großmann, Jens Tschritter, Udo Frieß, Ulrich Platt, Paul Johnston, Karin Kreher, Folkard Wittrock, John P. Burrows, John M.C. Plane, and Alfonso Saiz-Lopez. Glyoxal observations in the global marine boundary layer. *Journal of Geophysical Research: Atmospheres*, 2014. ISSN 2169-8996. doi:10.1002/2013JD021388. URL `http://dx.doi.org/10.1002/2013JD021388`.

Steven L. Manley, Nun-Yii Wang, Maggie L. Walser, and Ralph J. Cicerone. Methyl halide emissions from greenhouse-grown mangroves. *Geophysical Research Letters*, 34(1), 2007. ISSN 1944-8007. doi:10.1029/2006GL027777. URL `http://dx.doi.org/10.1029/2006GL027777`.

T Marbach, S Beirle, U Platt, P Hoor, F Wittrock, A Richter, M Vrekoussis, M Grzegorski, JP Burrows, and T Wagner. Satellite measurements of formaldehyde linked to shipping emissions. *Atmospheric Chemistry and Physics*, 9(21):8223–8234, 2009.

D. W. Marquardt. An algorithm for least-squares estimation of nonlinear parameters. *J. Soc. Indust. Math.*, 11:431–441, 1963.

M. Martin, D. Pöhler, K. Seitz, R. Sinreich, and U. Platt. BrO measurements over the Eastern North-Atlantic. *Atmospheric Chemistry and Physics*, 9(24):9545–9554, 2009. ISSN 1680-7316. URL `http://www.atmos-chem-phys.net/9/9545/2009/`.

M. Martino, G. P. Mills, J. Woeltjen, and P. S. Liss. A new source of volatile organoiodine compounds in surface seawater. *Geophys. Res. Lett*, 39, 2008. doi:10.1029/2008GL036334.

Manuela Martino, Peter S Liss, and John MC Plane. The photolysis of dihalomethanes in surface seawater. *Environmental science & technology*, 39(18):7097–7101, 2005.

G. McFiggans, H. Coe, R. Burgess, J. Allan, M. Cubison, M. R. Alfarra, R. Saunders, A. Saiz-Lopez, J. M. C. Plane, D. Wevill, L. Carpenter, A. R. Rickard, and P. S. Monks. Direct evidence for coastal iodine particles from laminaria macroalgae - linkage to emissions of molecular iodine. *Atmospheric Chemistry and Physics*, 4(3):701–713, 2004. doi:10.5194/acp-4-701-2004. URL `http://www.atmos-chem-phys.net/4/701/2004/`.

Richard Meller and Geert K. Moortgat. Temperature dependence of the absorption cross sections of formaldehyde between 223K and 323K in the wavelength range 225-375 nm. *Journal of Geophysical Research: Atmospheres*, 105(D6):7089–7101, 2000. ISSN 2156-2202. doi:10.1029/1999JD901074. URL `http://dx.doi.org/10.1029/1999JD901074`.

Frederick J. Miller, Daniel B. Menzel, and David L. Coffin. Similarity between man and laboratory animals in regional pulmonary deposition of ozone. *Environmental Research*, 17(1): 84 – 101, 1978. ISSN 0013-9351. doi:http://dx.doi.org/10.1016/0013-9351(78)90064-6. URL `http://www.sciencedirect.com/science/article/pii/0013935178900646`.

Frank J Millero, Rainer Feistel, Daniel G Wright, and Trevor J McDougall. The composition of standard seawater and the definition of the reference-composition salinity scale. *Deep Sea Research Part I: Oceanographic Research Papers*, 55(1):50–72, 2008.

L. T. Molina and F. S. Rowland. Stratospheric sink for chlorofluromethanes: chlorine atom catalyzed destruction of ozone. *Nature*, 249:820–822, 1974.

J. C. Mössinger, D. M. Rowley, and R. A. Cox. The UV-visible absorption cross-sections of $IONO_2$. *Atmospheric Chemistry and Physics*, 2(3):227–234, 2002. doi:10.5194/acp-2-227-2002. URL `http://www.atmos-chem-phys.net/2/227/2002/`.

Juliane C Mössinger, Dudley E Shallcross, and R Anthony Cox. Uv–vis absorption cross-sections and atmospheric lifetimes of CH_2Br_2, CH_2I_2 and CH_2BrI. *Journal of the Chemical Society, Faraday Transactions*, 94(10):1391–1396, 1998.

William F Murphy. The rovibrational raman spectrum of water vapour v1 and v3. *Molecular Physics*, 36(3):727–732, 1978.

Jan-Marcus Nasse. Ship- and helicopter-borne MAX-DOAS measurements of BrO during ANT XXIX/6+7 (tbd). Master's thesis, Heidelberg University, 2014. in prep.

Sabrina Niebling. Langzeit-Messungen von Spurengasen und Aerosolen mittels Multi-Axis-DOAS auf dem Hohenpeißenberg. Diploma thesis, Institut für Umweltphysik, Universität Heidelberg, 2010.

S. Noël, M. Buchwitz, H. Bovensmann, and J. P. Burrows. Validation of SCIAMACHY AMC-DOAS water vapour columns. *Atmospheric Chemistry and Physics*, 5(7):1835–1841, 2005. doi:10.5194/acp-5-1835-2005. URL `http://www.atmos-chem-phys.net/5/1835/2005/`.

C. O'Dowd, J. L. Jimenez, R. Bahreini, R. C. Flagan, J. H. Seinfeld, K. Hämeri, L. Pirjola, M. Kulmala ans S. G. Jennings, and T. Hoffmann. Marine aerosol formation from biogenic iodine emissions. *Nature*, 417:632–636, 2002a.

Colin D O'Dowd and Thorsten Hoffmann. Coastal new particle formation: A review of the current state-of-the-art. *Environmental Chemistry*, 2(4):245–255, 2006.

Colin D O'Dowd, Jose L Jimenez, Roya Bahreini, Richard C Flagan, John H Seinfeld, Kaarle Hämeri, Liisa Pirjola, Markku Kulmala, S Gerard Jennings, and Thorsten Hoffmann. Marine aerosol formation from biogenic iodine emissions. *Nature*, 417(6889):632–636, 2002b.

Anthony O'Keefe and David AG Deacon. Cavity ring-down optical spectrometer for absorption measurements using pulsed laser sources. *Review of Scientific Instruments*, 59(12):2544–2551, 1988.

World Meteorological Organization. *Scientific Assessment of Ozone Depletion 2002: Pursuant to Article 6 of the Montreal Protocol on Substances that Deplete the Ozone Layer*. WMO, 2003.

Robert G Orth and Robert C Dunbar. Photodissociation of nitrous oxide cation. *The Journal of Chemical Physics*, 66(4):1616–1620, 2008.

Yong-le Pan, Stephen Holler, Richard K Chang, Steven C Hill, Ronald G Pinnick, Stanley Niles, Jerold R Bottiger, et al. Single-shot fluorescence spectra of individual micrometer-sized bioaerosols illuminated by a 351-or a 266-nm ultraviolet laser. *Optics letters*, 24(2):116–118, 1999.

K. Pearson. On lines and planes of closest fit to systems of points in space. *Philosophical Magazine*, 2(6):559–572, 1901.

C. M. Penney, R. L. St. Peters, and M. Lapp. Absolute rotational raman cross sections for N_2, O_2, and CO_2. *J. Opt. Soc. Am.*, 64(5):712–716, May 1974. doi:10.1364/JOSA.64.000712. URL `http://www.opticsinfobase.org/abstract.cfm?URI=josa-64-5-712`.

D. Perner and U. Platt. Detection of nitrous acid in the atmosphere by differential opticalabsorption. *Geophys. Res. Lett.*, 6:917–920, 1979.

C. Peters, S. Pechtl, J. Stutz, K. Hebestreit, G. Hönninger, K. G. Heumann, A. Schwarz, J. Winterlik, and U. Platt. Reactive and organic halogen species in three different european coastal environments. *Atmospheric Chemistry and Physics*, 5(12):3357–3375, 2005. doi:10.5194/acp-5-3357-2005. URL `http://www.atmos-chem-phys.net/5/3357/2005/`.

E. Peters. *Improved MAX-DOAS measurements and retrievals focused on the marine boundary layer*. PhD thesis, University of Bremen, Bremen, Germany, 2013.

E. Peters, F. Wittrock, K. Großmann, U. Frieß, A. Richter, and J. P. Burrows. Formaldehyde and nitrogen dioxide over the remote western pacific ocean: SCIAMACHY and GOME-2 validation using ship-based MAX-DOAS observations. *Atmospheric Chemistry and Physics*, 12(22): 11179–11197, 2012. doi:10.5194/acp-12-11179-2012. URL `http://www.atmos-chem-phys.net/12/11179/2012/`.

E. Peters, F. Wittrock, A. Richter, L. M. A. Alvarado, V. V. Rozanov, and J. P. Burrows. Liquid water absorption and scattering effects in doas retrievals over oceans. *Atmospheric Measurement Techniques Discussions*, 7(5):5027–5073, 2014. doi:10.5194/amtd-7-5027-2014. URL `http://www.atmos-meas-tech-discuss.net/7/5027/2014/`.

HM Pickett, RL Poynter, EA Cohen, ML Delitsky, JC Pearson, and HSP Müller. Submillimeter, millimeter, and microwave spectral line catalog. *Journal of Quantitative Spectroscopy and Radiative Transfer*, 60(5):883–890, 1998.

M. Pidwirny. Fundamentals of physical geography. 2nd Edition, 2006. URL `http://www.physicalgeography.net/fundamentals/8q_1.html`. Surface and Subsurface Ocean Currents: Ocean Current Map.

G. Pinardi, M. Van Roozendael, N. Abuhassan, C. Adams, A. Cede, K. Clémer, C. Fayt, U. Frieß, M. Gil, J. Herman, C. Hermans, F. Hendrick, H. Irie, A. Merlaud, M. Navarro Comas, E. Peters, A. J. M. Piters, O. Puentedura, A. Richter, A. Schönhardt, R. Shaiganfar, E. Spinei,

K. Strong, H. Takashima, M. Vrekoussis, T. Wagner, F. Wittrock, and S. Yilmaz. MAX-DOAS formaldehyde slant column measurements during CINDI: intercomparison and analysis improvement. *Atmospheric Measurement Techniques*, 6(1):167, 2013. doi:10.5194/amt-6-167-2013. URL `http://www.atmos-meas-tech.net/6/167/2013/`.

A. J. M. Piters, K. F. Boersma, M. Kroon, J. C. Hains, M. Van Roozendael, F. Wittrock, N. Abuhassan, C. Adams, M. Akrami, M. A. F. Allaart, A. Apituley, S. Beirle, J. B. Bergwerff, A. J. C. Berkhout, D. Brunner, A. Cede, J. Chong, K. Clémer, C. Fayt, U. Frieß, L. F. L. Gast, M. Gil-Ojeda, F. Goutail, R. Graves, A. Griesfeller, K. Großmann, G. Hemerijckx, F. Hendrick, B. Henzing, J. Herman, C. Hermans, M. Hoexum, G. R. van der Hoff, H. Irie, P. V. Johnston, Y. Kanaya, Y. J. Kim, H. Klein Baltink, K. Kreher, G. de Leeuw, R. Leigh, A. Merlaud, M. M. Moerman, P. S. Monks, G. H. Mount, M. Navarro-Comas, H. Oetjen, A. Pazmino, M. Perez-Camacho, E. Peters, A. du Piesanie, G. Pinardi, O. Puentedura, A. Richter, H. K. Roscoe, A. Schönhardt, B. Schwarzenbach, R. Shaiganfar, W. Sluis, E. Spinei, A. P. Stolk, K. Strong, D. P. J. Swart, H. Takashima, T. Vlemmix, M. Vrekoussis, T. Wagner, C. Whyte, K. M. Wilson, M. Yela, S. Yilmaz, P. Zieger, and Y. Zhou. The Cabauw Intercomparison campaign for Nitrogen Dioxide measuring Instruments (CINDI): design, execution, and early results. *Atmospheric Measurement Techniques*, 5(2):457–485, 2012. doi:10.5194/amt-5-457-2012. URL `http://www.atmos-meas-tech.net/5/457/2012/`.

U. Platt and E. Lehrer. *Arctic Tropospheric Ozone Chemistry, ARCTOC, Final Report of the EU-Project No. EV5V-CT93-0318, Heidelberg.* 1997.

U. Platt, L. Marquard, T. Wagner, and D. Perner. Corrections for zenith scattered light DOAS. *Geophys. Res. Letters*, 24(14):1759–1762, 1997.

U. Platt, J. Meinen, D. Pöhler, and T. Leisner. Broadband cavity enhanced differential optical absorption spectroscopy (CE-DOAS) - applicability and corrections. *Atmospheric Measurement Techniques*, 2(2):713–723, 2009. doi:10.5194/amt-2-713-2009. URL `http://www.atmos-meas-tech.net/2/713/2009/`.

Ulrich Platt and Jochen Stutz. *Differential optical absorption spectroscopy.* Springer, Berlin, Heidelberg, 2008. ISBN 978-3-540-75776-4.

Denis Pöhler, Leif Vogel, Udo Frieß and Ulrich Platt. Observation of halogen species in the amundsen gulf, Arctic, by active long-path differential optical absorption spectroscopy. *Proceedings of the National Academy of Sciences*, 107(15):6582–6587, 2010. doi:10.1073/pnas.0912231107. URL `http://www.pnas.org/content/107/15/6582.abstract`.

R. M. Pope and E. S. Fry. Absorption spectrum (380–700 nm) of pure water. II. integrating cavity measurements. *Appl. Opt.*, 36:8710–8723, 1997.

O. Puentedura, M. Gil, A. Saiz-Lopez, T. Hay, M. Navarro-Comas, A. Gómez-Pelaez, E. Cuevas, J. Iglesias, and L. Gomez. Iodine monoxide in the north subtropical free troposphere. *Atmospheric Chemistry and Physics*, 12(11):4909–4921, 2012. doi:10.5194/acp-12-4909-2012. URL `http://www.atmos-chem-phys.net/12/4909/2012/`.

J. Pukite, Janis, S. Kühl, T. Deutschmann, U. Platt, and T. Wagner. Extending differential optical absorption spectroscopy for limb measurements in the UV. *Atmospheric Measurement Techniques*, 3(3):631–653, 2010. doi:10.5194/amt-3-631-2010. URL `http://www.atmos-meas-tech.net/3/631/2010/`.

Birgit Quack and Douglas WR Wallace. Air-sea flux of bromoform: Controls, rates, and implications. *Global Biogeochemical Cycles*, 17(1), 2003.

RA Rasmussen, MAK Khalil, R Gunawardena, and SD Hoyt. Atmospheric methyl iodide (ch3i). *Journal of Geophysical Research: Oceans (1978–2012)*, 87(C4):3086–3090, 1982.

K. A. Read, A. C. Lewis, S. Bauguitte, A. M. Rankin, R. A. Salmon, E. W. Wolff, A. Saiz-Lopez, W. J. Bloss, D. E. Heard, J. D. Lee, and J. M. C. Plane. DMS and MSA measurements in the antarctic boundary layer: impact of BrO on MSA production. *Atmospheric Chemistry and Physics*, 8(11):2985–2997, 2008a. doi:10.5194/acp-8-2985-2008. URL `http://www.atmos-chem-phys.net/8/2985/2008/`.

Katie A Read, Anoop S Mahajan, Lucy J Carpenter, Mathew J Evans, Bruno V E Faria, Dwayne E Heard, James R Hopkins, James D Lee, Sarah J Moller, Alastair C Lewis, Luis Mendes, James B McQuaid, Hilke Oetjen, Alfonso Saiz-Lopez, Michael J Pilling, and John M C Plane. Extensive halogen-mediated ozone destruction over the tropical atlantic ocean. *Nature*, 453(7199):1232–1235, Jun 2008b. doi:10.1038/nature07035. URL `http://dx.doi.org/10.1038/nature07035`.

L. Resplandy, M. Lévy, L. Bopp, V. Echevin, S. Pous, V. V. S. S. Sarma, and D. Kumar. Controlling factors of the oxygen balance in the arabian sea's omz. *Biogeosciences*, 9(12):5095–5109, 2012. doi:10.5194/bg-9-5095-2012. URL `http://www.biogeosciences.net/9/5095/2012/`.

M. Rex, I. Wohltmann, T. Ridder, R. Lehmann, K. Rosenlof, P. Wennberg, D. Weisenstein, J. Notholt, K. Krüger, V. Mohr, and S. Tegtmeier. A tropical west pacific oh minimum and implications for stratospheric composition. *Atmospheric Chemistry and Physics*, 14(9):4827–4841, 2014. doi:10.5194/acp-14-4827-2014. URL `http://www.atmos-chem-phys.net/14/4827/2014/`.

William Hadley Richardson. Bayesian-based iterative method of image restoration. *J. Opt. Soc. Am.*, 62(1):55–59, Jan 1972. doi:10.1364/JOSA.62.000055. URL `http://www.opticsinfobase.org/abstract.cfm?URI=josa-62-1-55`.

A. Richter, M. Begoin, A. Hilboll, and J. P. Burrows. An improved NO_2 retrieval for the GOME-2 satellite instrument. *Atmospheric Measurement Techniques*, 4(6):1147–1159, 2011. doi:10.5194/amt-4-1147-2011. URL `http://www.atmos-meas-tech.net/4/1147/2011/`.

Katja Riedel, Rolf Weller, and Otto Schrems. Variability of formaldehyde in the antarctic troposphere. *Physical Chemistry Chemical Physics*, 1(24):5523–5527, 1999.

Vincenzo Rizi, Marco Iarlori, Giuseppe Rocci, and Guido Visconti. Raman LIDAR observations of cloud liquid water. *Appl. Opt.*, 43(35):6440–6453, Dec 2004. doi:10.1364/AO.43.006440. URL `http://ao.osa.org/abstract.cfm?URI=ao-43-35-6440`.

Clive D Rodgers. Information content and optimisation of high spectral resolution measurements. In *Proc. SPIE*, volume 2830, pages 136–147, 1996.

Clive D. Rodgers. *Inverse Methods for Atmospheric Sounding: Theory and Practice*. World Scientific, 2000.

W. Roedel. *Physik unserer Umwelt: die Atmosphäre*. Springer Verlag, Berlin, 1992.

L.S. Rothman, I.E. Gordon, R.J. Barber, H. Dothe, R.R. Gamache, A. Goldman, V.I. Perevalov, S.A. Tashkun, and J. Tennyson. HITEMP, the high-temperature molecular spectroscopic database. *Journal of Quantitative Spectroscopy and Radiative Transfer*, 111(15):2139 – 2150, 2010. ISSN 0022-4073. doi:10.1016/j.jqsrt.2010.05.001. URL `http://www.sciencedirect.com/science/article/pii/S002240731000169X`. XVIth Symposium on High Resolution Molecular Spectroscopy (HighRus-2009).

L.S. Rothman, I.E. Gordon, Y. Babikov, A. Barbe, D. Chris Benner, P.F. Bernath, M. Birk, L. Bizzocchi, V. Boudon, L.R. Brown, A. Campargue, K. Chance, E.A. Cohen, L.H. Coudert, V.M. Devi, B.J. Drouin, A. Fayt, J.-M. Flaud, R.R. Gamache, J.J. Harrison, J.-M. Hartmann, C. Hill, J.T. Hodges, D. Jacquemart, A. Jolly, J. Lamouroux, R.J. Le Roy, G. Li, D.A. Long, O.M. Lyulin, C.J. Mackie, S.T. Massie, S. Mikhailenko, H.S.P. MÃ$\frac{1}{4}$ller, O.V. Naumenko, A.V. Nikitin, J. Orphal, V. Perevalov, A. Perrin, E.R. Polovtseva, C. Richard, M.A.H. Smith, E. Starikova, K. Sung, S. Tashkun, J. Tennyson, G.C. Toon, Vl.G. Tyuterev, and G. Wagner. The HITRAN2012 molecular spectroscopic database. *Journal of Quantitative Spectroscopy and Radiative Transfer*, 130(0):4 – 50, 2013. ISSN 0022-4073. doi:http://dx.doi.org/10.1016/j.jqsrt.2013.07.002. URL `http://www.sciencedirect.com/science/article/pii/S0022407313002859`. HITRAN2012 special issue.

A. Rozanov, V. Rozanov, M. Buchwitz, A. Kokhanovsky, and J.P. Burrows. Sciatran 2.0 a new radiative transfer model for geophysical applications in the 175-2400nm spectral region. *Advances in Space Research*, 36(5):1015 – 1019, 2005. ISSN 0273-1177. doi:10.1016/j.asr.2005.03.012. URL `http://www.sciencedirect.com/science/article/pii/S0273117705002887`. Atmospheric Remote Sensing: Earth's Surface, Troposphere, Stratosphere and Mesosphere- I.

J Rudolph, A Khedim, R Koppmann, and B Bonsang. Field study of the emissions of methyl chloride and other halocarbons from biomass burning in western africa. *Journal of atmospheric chemistry*, 22(1-2):67–80, 1995.

A. Sadeghi, T. Dinter, M. Vountas, B. B. Taylor, M. Altenburg-Soppa, I. Peeken, and A. Bracher. Improvement to the phytodoas method for identification of coccolithophores using hyperspectral satellite data. *Ocean Science*, 8(6):1055–1070, 2012. doi:10.5194/os-8-1055-2012. URL `http://www.ocean-sci.net/8/1055/2012/`.

A. Saiz-Lopez, J. A. Shillito, H. Coe, and J. M. C. Plane. Measurements and modelling of I_2, IO, OIO, BrO and NO_3 in the mid-latitude marine boundary layer. *Atmospheric Chemistry and Physics*, 6(6):1513–1528, 2006. ISSN 1680-7316. URL `http://www.atmos-chem-phys.net/6/1513/2006/`.

Alfonso Saiz-Lopez, Kelly Chance, Xiong Liu, Thomas P Kurosu, and Stanley P Sander. First observations of iodine oxide from space. *Geophysical Research Letters*, 34(12), 2007a.

Alfonso Saiz-Lopez, Anoop S. Mahajan, Rhian A. Salmon, Stephane J.-B. Bauguitte, Anna E. Jones, Howard K. Roscoe, and John M. C. Plane. Boundary layer halogens in coastal antarctica. *Science*, 317(5836):348–351, 2007b. doi:10.1126/science.1141408. URL `http://www.sciencemag.org/content/317/5836/348.abstract`.

H. Salow and W. Steiner. Die durch Wechselwirkungskräfte bedingten Absorptionsspektra des Sauerstoffes 1. Die Absorptionsbanden des (O_2-O_2)-Moleküls. *Z. Physik*, 99:137–158, 1936.

Craig J Sansonetti and Joseph Reader. Spectrum and energy levels of singly-ionized mercury (Hg II). *Physica Scripta*, 63(3):219, 2001. URL `http://stacks.iop.org/1402-4896/63/i=3/a=007`.

Craig J. Sansonetti, Marc L. Salit, and Joseph Reader. Wavelengths of spectral lines in mercury pencil lamps. *Appl. Opt.*, 35(1):74–77, Jan 1996. doi:10.1364/AO.35.000074. URL `http://ao.osa.org/abstract.cfm?URI=ao-35-1-74`.

Stefan Schmitt. A compact long path DOAS instrument based on fibre-optics and LEDs. Diploma thesis, Institut für Umweltphysik, Universität Heidelberg, 2011.

Schneefernerhaus. www.schneefernerhaus.de, 2013.

A. Schönhardt, A. Richter, F. Wittrock, H. Kirk, H. Oetjen, H. K. Roscoe, , and J. P. Burrows. Observations of iodine monoxide columns from satellite. *Atmospheric Chemistry and Physics*, 8:637–653, 2008. URL `www.atmos-chem-phys.net/8/637/2008/`.

A. Schönhardt, M. Begoin, A. Richter, F. Wittrock, L. Kaleschke, J. C. Gómez Martín, and J. P. Burrows. Simultaneous satellite observations of IO and BrO over Antarctica. *Atmospheric Chemistry and Physics*, 12(14):6565–6580, 2012. doi:10.5194/acp-12-6565-2012. URL `http://www.atmos-chem-phys.net/12/6565/2012/`.

Anja Schönhardt. *DOAS measurements of iodine monoxide from satellite*. Dissertation, Bremen University, 2009.

S. F. Schreier, E. Peters, A. Richter, J. Lampel, F. Wittrock, and J. P. Burrows. Ship-based max-doas measurements of tropospheric no2and so2in the south china and sulu sea. *Atmospheric Environment*, 2014. in prep.

H.W. Schrötter and H.W. Klöckner. Raman scattering cross sections in gases and liquids. In Alfons Weber, editor, *Raman Spectroscopy of Gases and Liquids*, volume 11 of *Topics in Current Physics*, pages 123–166. Springer Berlin Heidelberg, 1979. ISBN 978-3-642-81281-1. doi:10.1007/978-3-642-81279-8_4. URL `http://dx.doi.org/10.1007/978-3-642-81279-8_4`.

C Schulz, JD Koch, DF Davidson, JB Jeffries, and RK Hanson. Ultraviolet absorption spectra of shock-heated carbon dioxide and water between 900 and 3050 k. *Chemical physics letters*, 355(1):82–88, 2002.

K. Seitz. *The Spatial Distribution of Reactive Halogen Species at the Irish West Coast*. PhD thesis, Institute of Environmental Physics, Heidelberg University, Germany, 2009.

K. Seitz, J. Buxmann, D. Pöhler, T. Sommer, J. Tschritter, T. Neary, C. O'Dowd, and U. Platt. The spatial distribution of the reactive iodine species IO from simultaneous active and passive DOAS observations. *Atmospheric Chemistry and Physics*, 10(5):2117–2128, 2010. doi:10.5194/acp-10-2117-2010. URL `http://www.atmos-chem-phys.net/10/2117/2010/`.

A. Serdyuchenko, V. Gorshelev, M. Weber, W. Chehade, and J. P. Burrows. High spectral resolution ozone absorption cross-sections - part 2: Temperature dependence. *Atmospheric Measurement Techniques Discussions*, 6(4):6613–6643, 2013. doi:10.5194/amtd-6-6613-2013. URL `http://www.atmos-meas-tech-discuss.net/6/6613/2013/`.

Chiao-Yao She. Spectral structure of laser light scattering revisited: bandwidths of nonresonant scattering lidars. *Applied optics*, 40(27):4875–4884, 2001.

L Shi, SM Gruenbaum, and JL Skinner. Interpretation of IR and Raman line shapes for H2O and D2O ice Ih. *The Journal of Physical Chemistry B*, 116(47):13821–13830, 2012.

H. Sihler, U. Platt, S. Beirle, T. Marbach, S. Kühl, S. Dörner, J. Verschaeve, U. Frieß, D. Pöhler, L. Vogel, R. Sander, and T. Wagner. Tropospheric BrO column densities in the Arctic derived from satellite: retrieval and comparison to ground-based measurements. *Atmospheric Measurement Techniques*, 5(11):2779–2807, 2012. doi:10.5194/amt-5-2779-2012. URL `http://www.atmos-meas-tech.net/5/2779/2012/`.

Holger Sihler. *Halogen Activation in the Polar Troposphere*. Dissertation, Institut für Umweltphysik, Heidelberg University and MPIC Mainz, 2012.

W. R. Simpson, R. von Glasow, K. Riedel, P. Anderson, P. Ariya, J. Bottenheim, J. Burrows, L. J. Carpenter, U. Frieß, M. E. Goodsite, D. Heard, M. Hutterli, H.-W. Jacobi, L. Kaleschke, B. Neff, J. Plane, U. Platt, A. Richter, H. Roscoe, R. Sander, P. Shepson, J. Sodeau, A. Steffen, T. Wagner, and E. Wolff. Halogens and their role in polar boundary-layer ozone depletion. *Atmospheric Chemistry and Physics*, 7(16):4375–4418, 2007. doi:10.5194/acp-7-4375-2007. URL `http://www.atmos-chem-phys.net/7/4375/2007/`.

R. Sinreich, R. Volkamer, F. Filsinger, U. Frieß, C. Kern, U. Platt, O. Sebastián, and T. Wagner. MAX-DOAS detection of glyoxal during ICARTT 2004. *Atmospheric Chemistry and Physics*, 7(5):1293–1303, 2007. doi:10.5194/acp-7-1293-2007. URL `http://www.atmos-chem-phys.net/7/1293/2007/`.

R. Sinreich, S. Coburn, B. Dix, and R. Volkamer. Ship-based detection of glyoxal over the remote tropical pacific ocean. *Atmospheric Chemistry and Physics*, 10(23):11359–11371, 2010. doi:10.5194/acp-10-11359-2010. URL `http://www.atmos-chem-phys.net/10/11359/2010/`.

A. Smirnov, B. N. Holben, I. Slutsker, D. M. Giles, C. R. McClain, T. F. Eck, S. M. Sakerin, A. Macke, P. Croot, G. Zibordi, P. K. Quinn, J. Sciare, S. Kinne, M. Harvey, T. J. Smyth, S. Piketh, T. Zielinski, A. Proshutinsky, J. I. Goes, N. B. Nelson, P. Larouche, V. F. Radionov, P. Goloub, K. Krishna Moorthy, R. Matarrese, E. J. Robertson, and F. Jourdin. Maritime aerosol network as a component of aerosol robotic network. *Journal of Geophysical Research: Atmospheres*, 114(D6), 2009. ISSN 2156-2202. doi:10.1029/2008JD011257. URL `http://dx.doi.org/10.1029/2008JD011257`.

R Sommariva, WJ Bloss, and R von Glasow. Uncertainties in gas-phase atmospheric iodine chemistry. *Atmospheric Environment*, 57:219–232, 2012.

Roberto Sommariva and Roland von Glasow. Multiphase halogen chemistry in the tropical Atlantic Ocean. *Environmental Science & Technology*, 46(19):10429–10437, 2012. doi:10.1021/es300209f. URL `http://pubs.acs.org/doi/abs/10.1021/es300209f`.

Peter Spietz, Juan Carlos Gómez Martín, and John P. Burrows. Spectroscopic studies of the I_2/O_3 photochemistry: Part 2. improved spectra of iodine oxides and analysis of the IO absorption spectrum. *Journal of Photochemistry and Photobiology A: Chemistry*, 176(1-3):50 – 67, 2005. ISSN 1010-6030. doi:http://dx.doi.org/10.1016/j.jphotochem.2005.08.023. URL `http://www.sciencedirect.com/science/article/pii/S1010603005004156`. In Honour of Professor Richard P. Wayne.

T. Stavrakou, J.-F. Müller, I. De Smedt, M. Van Roozendael, M. Kanakidou, M. Vrekoussis, F. Wittrock, A. Richter, and J. P. Burrows. The continental source of glyoxal estimated by the synergistic use of spaceborne measurements and inverse modelling. *Atmospheric Chemistry and Physics*, 9(21):8431–8446, 2009a. doi:10.5194/acp-9-8431-2009. URL `http://www.atmos-chem-phys.net/9/8431/2009/`.

T. Stavrakou, J.-F. Müller, I. De Smedt, M. Van Roozendael, G. R. van der Werf, L. Giglio, and A. Guenther. Evaluating the performance of pyrogenic and biogenic emission inventories against one decade of space-based formaldehyde columns. *Atmospheric Chemistry and Physics*, 9(3):1037–1060, 2009b. doi:10.5194/acp-9-1037-2009. URL `http://www.atmos-chem-phys.net/9/1037/2009/`.

Lothar Stramma, Eric D Prince, Sunke Schmidtko, Jiangang Luo, John P Hoolihan, Martin Visbeck, Douglas WR Wallace, Peter Brandt, and Arne Körtzinger. Expansion of oxygen minimum zones may reduce available habitat for tropical pelagic fishes. *Nature Climate Change*, 2(1):33–37, 2012.

J. Stutz and U. Platt. Numerical analysis and estimation of the statistical error of differential optical absorption spectroscopy measurements with least-squares methods. *Appl. Opt.*, 35(30): 6041–6053, 1996.

J. Stutz, R. Ackermann, J. D. Fast, and L. Barrie. Atmospheric reactive chlorine and bromine at the Great Salt Lake, Utah. *Geophysical Research Letters*, 29(10):100000–1, May 2002. doi:10.1029/2002GL014812.

J. Stutz, O. Pikelnaya, S. C. Hurlock, S. Trick, S. Pechtl, and R. von Glasow. Daytime OIO in the Gulf of Maine. *grl*, 34:22816, November 2007. doi:10.1029/2007GL031332.

J. Stutz, J. L. Thomas, S. C. Hurlock, M. Schneider, R. von Glasow, M. Piot, K. Gorham, J. F. Burkhart, L. Ziemba, J. E. Dibb, and B. L. Lefer. Longpath DOAS observations of surface BrO at summit, greenland. *Atmospheric Chemistry and Physics*, 11(18):9899–9910, 2011. doi:10.5194/acp-11-9899-2011. URL `http://www.atmos-chem-phys.net/11/9899/2011/`.

Yukio Sugimura and Yoshimi Suzuki. A high-temperature catalytic oxidation method for the determination of non-volatile dissolved organic carbon in seawater by direct injection of a liquid sample. *Marine Chemistry*, 24(2):105–131, 1988.

Craig A Taatjes, Dudley E Shallcross, and Carl J Percival. Research frontiers in the chemistry of criegee intermediates and tropospheric ozonolysis. *Physical Chemistry Chemical Physics*, 16(5):1704–1718, 2014.

MJ Taylor and E Whalley. Raman spectra of ices Ih, Ic, II, III, and V. *The Journal of Chemical Physics*, 40(6):1660–1664, 1964.

Jonathan Tennyson, Peter F. Bernath, Linda R. Brown, Alain Campargue, Attila G. Csaszar, Ludovic Daumont, Robert R. Gamache, Joseph T. Hodges, Olga V. Naumenko, Oleg L. Polyansky, Laurence S. Rothman, Ann Carine Vandaele, Nikolai F. Zobov, Afaf R. Al Derzi, Csaba Fabri, Alexander Z. Fazliev, Tibor Furtenbacher, Iouli E. Gordon, Lorenzo Lodi, and Irina I. Mizus. IUPAC critical evaluation of the rotational-vibrational spectra of water vapor, part III: Energy levels and transition wavenumbers for $H_2^{16}O$. *Journal of Quantitative Spectroscopy and Radiative Transfer*, 117(0):29 – 58, 2013. ISSN 0022-4073. doi:http://dx.doi.org/10.1016/j.jqsrt.2012.10.002. URL `http://www.sciencedirect.com/science/article/pii/S0022407312004311`.

Ryan Miller Thalman and Rainer Volkamer. Temperature dependent absorption cross-sections of O_2-O_2 collision pairs between 340 and 630 nm and at atmospherically relevant pressure. *Phys. Chem. Chem. Phys.*, pages –, 2013. doi:10.1039/C3CP50968K. URL `http://dx.doi.org/10.1039/C3CP50968K`.

N. Theys, M. Van Roozendael, F. Hendrick, X. Yang, I. De Smedt, A. Richter, M. Begoin, Q. Errera, P. V. Johnston, K. Kreher, and M. De Mazière. Global observations of tropospheric BrO columns using gome-2 satellite data. *Atmospheric Chemistry and Physics*, 11(4): 1791–1811, 2011. doi:10.5194/acp-11-1791-2011. URL `http://www.atmos-chem-phys.net/11/1791/2011/`.

VW Truesdale, AJ Bale, and EMS Woodward. The meridional distribution of dissolved iodine in near-surface waters of the Atlantic Ocean. *Progress in Oceanography*, 45(3):387–400, 2000.

Jens Tschritter. *Untersuchung mariner Halogenemissionen im tropischen Atlantik*. Dissertation, Institut für Umweltphysik, Heidelberg University, 2013.

Shizuo Tsunogai and Takashi Henmi. Iodine in the surface water of the ocean. *Journal of the Oceanographical Society of Japan*, 27(2):67–72, 1971. ISSN 0029-8131. doi:10.1007/BF02109332. URL `http://dx.doi.org/10.1007/BF02109332`.

Oliver V. Rattigan, Dudley E. Shallcross, and R. Anthony Cox. Uv absorption cross-sections and atmospheric photolysis rates of CF_3I, CH_3I, C_2H_5I and CH_2ICl. *J. Chem. Soc., Faraday Trans.*, 93:2839–2846, 1997. doi:10.1039/A701529A. URL `http://dx.doi.org/10.1039/A701529A`.

M. van Pinxteren and H. Herrmann. Glyoxal and methylglyoxal in atlantic seawater and marine aerosol particles: method development and first application during the polarstern cruise ANT XXVII/4. *Atmospheric Chemistry and Physics*, 13(23):11791–11802, 2013. doi:10.5194/acp-13-11791-2013. URL `http://www.atmos-chem-phys.net/13/11791/2013/`.

A.C. Vandaele, C. Hermans, P.C. Simon, M. Carleer, R. Colin, S. Fally, M.F. Merienne, A. Jenouvrier, and B. Coquart. Measurements of the NO_2 absorption cross-section from 42 000 cm-1 to 10 000 cm-1 (238-1000 nm) at 220 k and 294 k. *Journal of Quantitative Spectroscopy and Radiative Transfer*, 59(3-5):171 – 184, 1998. ISSN 0022-4073. doi:10.1016/S0022-4073(97)00168-4. URL `http://www.sciencedirect.com/science/article/pii/S0022407397001684`. Atmospheric Spectroscopy Applications 96.

Ruth K Varner, Yong Zhou, Rachel S Russo, Oliver W Wingenter, Elliot Atlas, Craig Stroud, Huiting Mao, Robert Talbot, and Barkley C Sive. Controls on atmospheric chloroiodomethane (CH_2ClI) in marine environments. *Journal of Geophysical Research: Atmospheres (1984–2012)*, 113(D10), 2008.

Patrick R Veres, Peter Faber, Frank Drewnick, Jos Lelieveld, and Jonathan Williams. Anthropogenic sources of VOC in a football stadium: Assessing human emissions in the atmosphere. *Atmospheric Environment*, 77:1052–1059, 2013.

L. Vogel, H. Sihler, J. Lampel, T. Wagner, and U. Platt. Retrieval interval mapping: a tool to visualize the impact of the spectral retrieval range on differential optical absorption spectroscopy evaluations. *Atmospheric Measurement Techniques*, 6(2):275–299, 2013. doi:10.5194/amt-6-275-2013. URL `http://www.atmos-meas-tech.net/6/275/2013/`.

Leif Vogel. *Volcanic plumes: Evaluation of spectroscopic measurements, early detection, and bromine chemistry*. Dissertation, Institut für Umweltphysik, Heidelberg University, 2012.

Rainer Vogt, Rolf Sander, Roland von Glasow, and Paul J Crutzen. Iodine chemistry and its role in halogen activation and ozone loss in the marine boundary layer: A model study. *Journal of Atmospheric Chemistry*, 32(3):375–395, 1999.

S. Voigt, J. Orphal, K. Bogumil, and J. P. Burrows. The temperature dependence (203-293k) of the absorption cross sections of o_3 in the 230-850nm region measured by Fourier-transform spectroscopy. *J. of Photochemistry and Photobiology A*, 143:1–9, 2001.

R. Volkamer, P. Spietz, J. P. Burrows, and U. Platt. High-resolution absorption cross-section of glyoxal in the UV/vis and IR spectral ranges. *J. Photoch. Photobio. A: Chemistry*, 172:35 – 46, 2005a.

Rainer Volkamer, Luisa T Molina, Mario J Molina, Terry Shirley, and William H Brune. DOAS measurement of glyoxal as an indicator for fast VOC chemistry in urban air. *Geophysical Research Letters*, 32(8), 2005b.

R. von Glasow, R. von Kuhlmann, M. G. Lawrence, U. Platt, and P. J. Crutzen. Impact of reactive bromine chemistry in the troposphere. *Atmospheric Chemistry and Physics*, 4(11/12): 2481–2497, 2004. doi:10.5194/acp-4-2481-2004. URL `http://www.atmos-chem-phys.net/4/2481/2004/`.

M. Vountas, A. Richter, F. Wittrock, and J. P. Burrows. Inelastic scattering in ocean water and its impact on trace gas retrievals from satellite data. *Atmospheric Chemistry and Physics*, 3(5):1365–1375, 2003. doi:10.5194/acp-3-1365-2003. URL `http://www.atmos-chem-phys.net/3/1365/2003/`.

M Vountas, Tilman Dinter, Astrid Bracher, JP Burrows, B Sierk, et al. Spectral studies of ocean water with space-borne sensor SCIAMACHY using differential optical absorption spectroscopy (DOAS). *Ocean Science*, 3(3):429–440, 2007.

M. Vrekoussis, F. Wittrock, A. Richter, and J. P. Burrows. Temporal and spatial variability of glyoxal as observed from space. *Atmospheric Chemistry and Physics*, 9(13):4485–4504, 2009. ISSN 1680-7316. URL `http://www.atmos-chem-phys.net/9/4485/2009/`.

M. Vrekoussis, F. Wittrock, A. Richter, and J. P. Burrows. GOME-2 observations of oxygenated VOCs: what can we learn from the ratio glyoxal to formaldehyde on a global scale? *Atmospheric Chemistry and Physics*, 10(21):10145–10160, 2010. doi:10.5194/acp-10-10145-2010. URL `http://www.atmos-chem-phys.net/10/10145/2010/`.

T. Wagner, T. Deutschmann, and U. Platt. Determination of aerosol properties from MAX-DOAS observations of the ring effect. *Atmospheric Measurement Techniques*, 2(2):495–512, 2009. doi:10.5194/amt-2-495-2009. URL `http://www.atmos-meas-tech.net/2/495/2009/`.

T. Wagner, S. Beirle, S. Dörner, U. Friess, J. Remmers, and R. Shaiganfar. Cloud detection and classification based on MAX-DOAS observations. *Atmospheric Measurement Techniques Discussions*, 6(6):10297–10360, 2013a. doi:10.5194/amtd-6-10297-2013. URL `http://www.atmos-meas-tech-discuss.net/6/10297/2013/`.

T. Wagner, S. Beirle, H. Sihler, and K. Mies. A feasibility study for the retrieval of the total column precipitable water vapour from satellite observations in the blue spectral range. *Atmospheric Measurement Techniques*, 6(10):2593–2605, 2013b. doi:10.5194/amt-6-2593-2013. URL `http://www.atmos-meas-tech.net/6/2593/2013/`.

Andreas Wahner, A. R. Ravishankara, S. P. Sander, and R. R. Friedl. Absorption cross section of BrO between 312 and 385 nm at 298 and 223 k. *Chemical Physics Letters*, 152(6):507–512, 1988.

Tim J. Waite and Victor W. Truesdale. Iodate reduction by isochrysis galbana is relatively insensitive to de-activation of nitrate reductase activity - are phytoplankton really responsible for iodate reduction in seawater? *Marine Chemistry*, 81(3-4):137 – 148, 2003. ISSN 0304-4203. doi:http://dx.doi.org/10.1016/S0304-4203(03)00013-6. URL `http://www.sciencedirect.com/science/article/pii/S0304420303000136`.

Hannah Marie Walker. *Field Measurements of reactive tropospheric species using the FAGE technique*. PhD thesis, The University of Leeds, 2013.

Ingo Weinberg, Enno Bahlmann, Walter Michaelis, and Richard Seifert. Determination of fluxes and isotopic composition of halocarbons from seagrass meadows using a dynamic flux chamber. *Atmospheric Environment*, 73:34–40, 2013.

Rolf Weller, O Schrems, A Boddenberg, S Gäb, and M Gautrois. Meridional distribution of hydroperoxides and formaldehyde in the marine boundary layer of the atlantic (48° n-35° s) measured during the albatross campaign. *Journal of Geophysical Research: Atmospheres (1984–2012)*, 105(D11):14401–14412, 2000.

Mark Wenig, Bernd Jähne, and Ulrich Platt. Operator representation as a new differential optical absorption spectroscopy formalism. *Applied optics*, 44(16):3246–3253, 2005.

D. M. Wilmouth, T. F. Hanisco, N. M. Donahue, and J. G. Anderson. Fourier transform ultraviolet spectroscopy of the $A^2\Pi_{3/2} \leftarrow X^2\Pi_{3/2}$ transition of BrO. *J. Phys. Chem.*, 103:8935–8945, 1999.

L. W. Winkler. Der Jodid- und Jodat-Iongehalt des Meerwassers. *Angewandte Chemie*, 29(39): 205–207, 1916. ISSN 1521-3757. doi:10.1002/ange.19160293903. URL `http://dx.doi.org/10.1002/ange.19160293903`.

Peter Winkler. Surface ozone over the Atlantic Ocean. *Journal of atmospheric chemistry*, 7(1): 73–91, 1988.

F. Wittrock, R. Müller, A. Richter, H. Bovensmann, and J. P. Burrows. Measurements of iodine monoxide (IO) above Spitsbergen. *Geophys. Res. Lett.*, 27:1471–1474, 2000.

Folkard Wittrock, Andreas Richter, Hilke Oetjen, John P Burrows, Maria Kanakidou, Stelios Myriokefalitakis, Rainer Volkamer, Steffen Beirle, Ulrich Platt, and Thomas Wagner. Simultaneous global observations of glyoxal and formaldehyde from space. *Geophysical Research Letters*, 33(16), 2006.

Folkard Wittrock, Hannah Walker, Dwayne Heard, Trevor Ingham, Johannes Lampel, Martin Horbanski, Katja Großmann, Astrid Bracher, Justin Sentian, Mihalis Vrekoussis, et al. Measurements of halogen oxides in the western pacific. In *EGU General Assembly Conference Abstracts*, volume 15, page 11808, 2013.

WMO WMO. Scientific assessment of ozone depletion: 2006. *World Meteorological Organisation, Global Ozone Research and Monitoring Project–Report*, 50:572, 2007.

Scientific Assessment of Ozone Depletion: 2010, volume Global Ozone Research and Monitoring Project-Report No. 52, Geneva, Switzerland, 2010. WMO (World Meteorological Organization).

George TF Wong, Ajcharaporn U Piumsomboon, and William M Dunstan. The transformation of iodate to iodide in marine phytoplankton cultures. *Marine Ecology Progress Series*, 237: 27–39, 2002.

Xin Xu and George W Kattawar. Filling in of fraunhofer lines in the ocean by brillouin scattering. *Applied optics*, 33(21):4835–4840, 1994.

M. Yang, R. Beale, P. Liss, M. Johnson, B. Blomquist, and P. Nightingale. Air-sea fluxes of oxygenated volatile organic compounds across the Atlantic Ocean. *Atmospheric Chemistry and Physics Discussions*, 14(6):8015–8061, 2014. doi:10.5194/acpd-14-8015-2014. URL `http://www.atmos-chem-phys-discuss.net/14/8015/2014/`.

Selami Yilmaz. *Retrieval of Atmospheric Aerosol and Trace Gas Vertical Profiles using Multi-Axis Differential Optical Absorption Spectroscopy*. Dissertation, Institut für Umweltphysik, Heidelberg University, 2012.

Y Yokouchi, A Ooki, S Hashimoto, and N Itoh. A study on the production and emission of marine-derived volatile halocarbons. *Western Pacific Air-Sea Interaction Study*, 2014.

Yoko Yokouchi, Masumi Ikeda, Yoko Inuzuka, and Tomohisa Yukawa. Strong emission of methyl chloride from tropical plants. *Nature*, 416(6877):163–165, 2002.

Jonathan P Zehr. New twist on nitrogen cycling in oceanic oxygen minimum zones. *Proceedings of the National Academy of Sciences*, 106(12):4575–4576, 2009.

Xianliang Zhou and Kenneth Mopper. Apparent partition coefficients of 15 carbonyl compounds between air and seawater and between air and freshwater; implications for air-sea exchange. *Environmental science & technology*, 24(12):1864–1869, 1990.

Johannes Zielcke, Johannes Lampel, Udo Frieß, Holger Sihler, Stoyka Netcheva, , and Ulrich Platt. Observations of iodine monoxide in the arctic troposphere. In *EGU General Assembly Conference Abstracts*, 2014.

C. Zindler, A. Bracher, C. A. Marandino, B. Taylor, E. Torrecilla, A. Kock, and H. W. Bange. Sulphur compounds, methane, and phytoplankton: interactions along a north-south transit in the western pacific ocean. *Biogeosciences*, 10(5):3297–3311, 2013. doi:10.5194/bg-10-3297-2013. URL `http://www.biogeosciences.net/10/3297/2013/`.

F. Ziska, B. Quack, K. Abrahamsson, S. D. Archer, E. Atlas, T. Bell, J. H. Butler, L. J. Carpenter, C. E. Jones, N. R. P. Harris, H. Hepach, K. G. Heumann, C. Hughes, J. Kuss, K. Krüger, P. Liss, R. M. Moore, A. Orlikowska, S. Raimund, C. E. Reeves, W. Reifenhäuser, A. D. Robinson, C. Schall, T. Tanhua, S. Tegtmeier, S. Turner, L. Wang, D. Wallace, J. Williams, H. Yamamoto, S. Yvon-Lewis, and Y. Yokouchi. Global sea-to-air flux climatology for bromoform, dibromomethane and methyl iodide. *Atmospheric Chemistry and Physics*, 13(17): 8915–8934, 2013. doi:10.5194/acp-13-8915-2013. URL `http://www.atmos-chem-phys.net/13/8915/2013/`.

A. Appendix

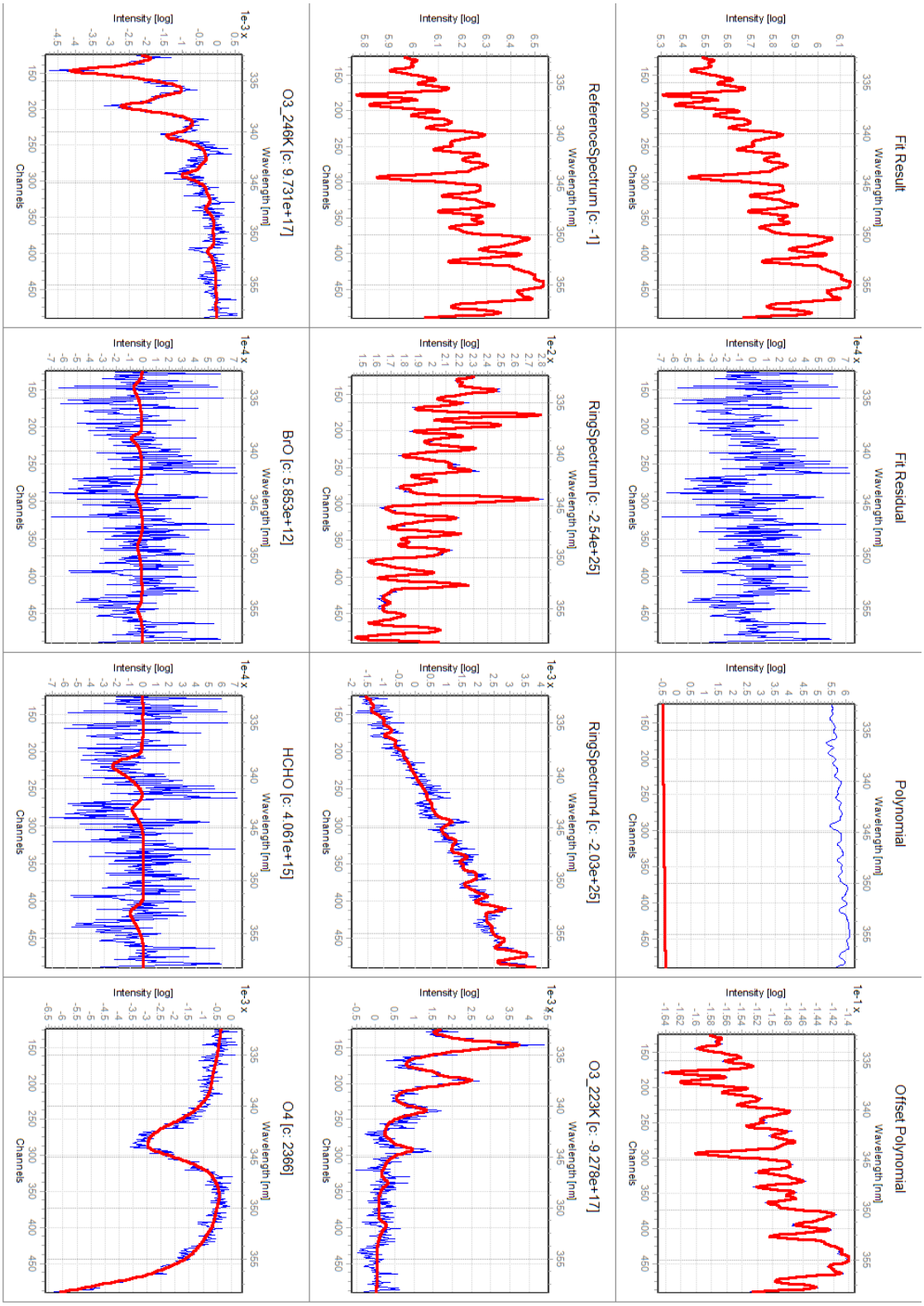

Figure A.1.: BrO fit of spectrum #27268 from SOPRAN M91, 12/18/2012 19:10, at 14.5°S 77.5°W. The residual shows the recurring residual structure observed throughout the cruise shown in figure 5.6. The NO_2 cross-section was below its detection limit and was therefore removed from the plot for clarity.

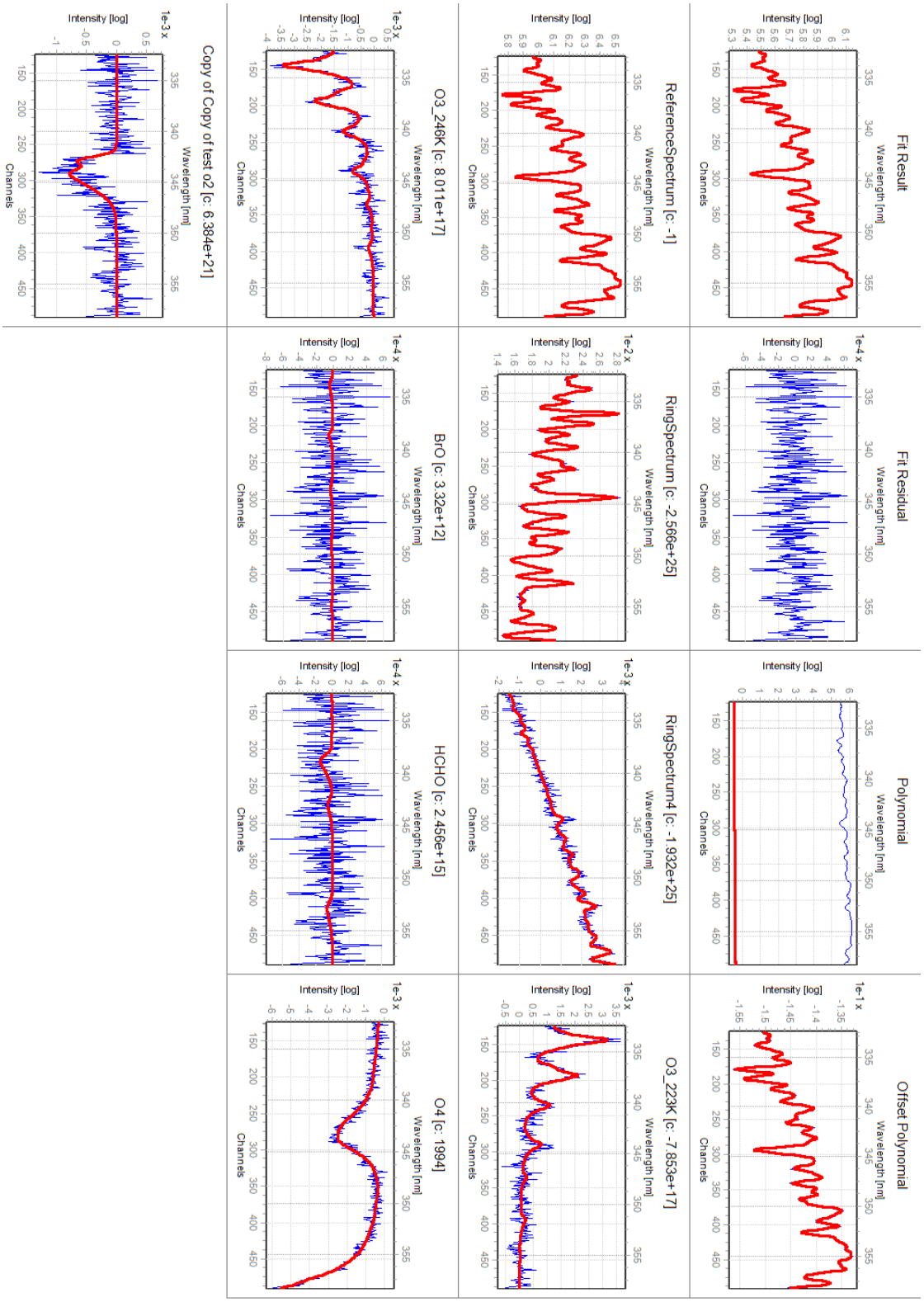

Figure A.2.: Same fit as figure A.1, but including the O_2B absorption convoluted with itself.

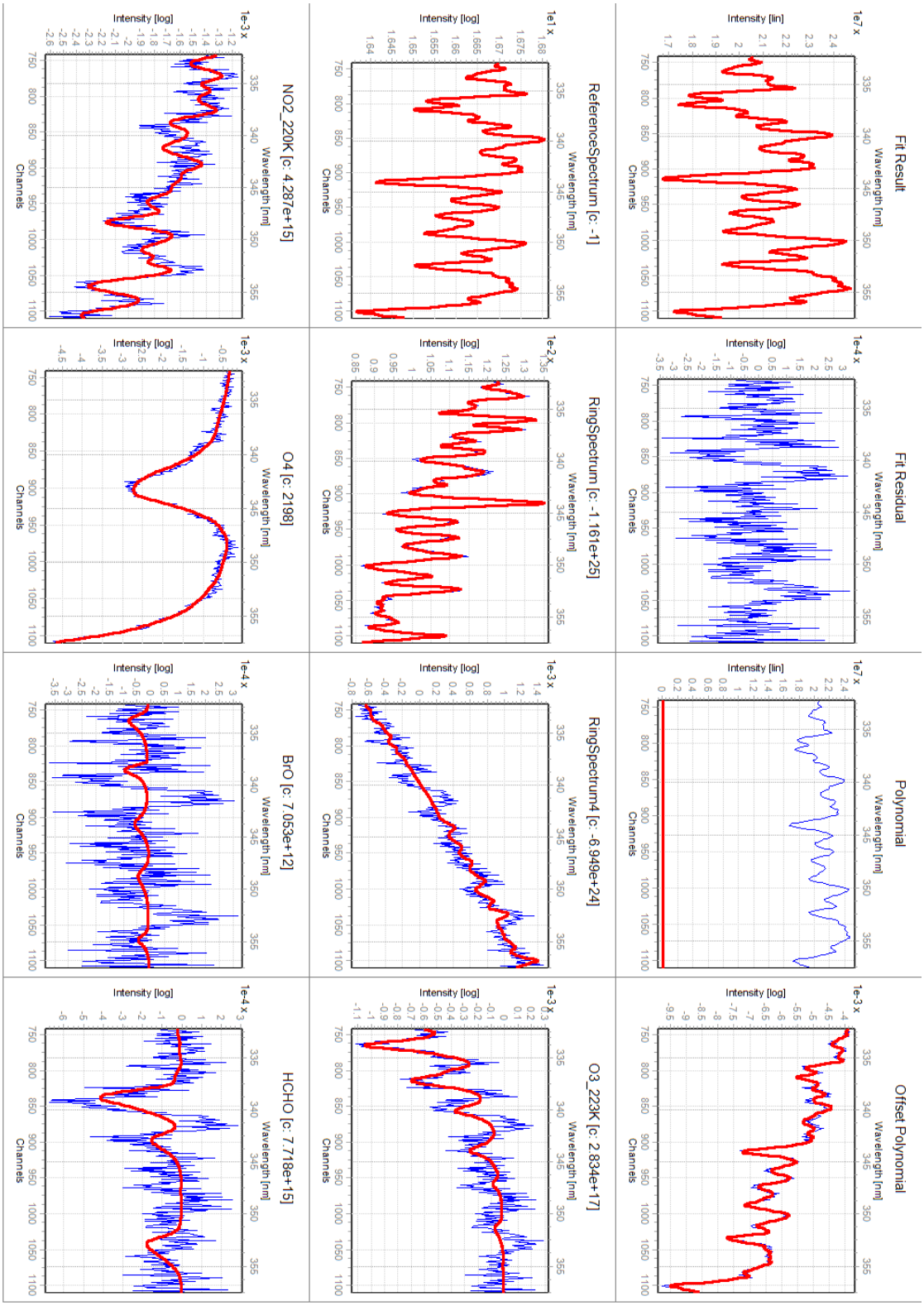

Figure A.3.: BrO fit from ANT28, spectrum #11300, summed for 4 elevation sequences. The residual shows a structure which was also observed for data from M91, see subsection 5.1.1.2

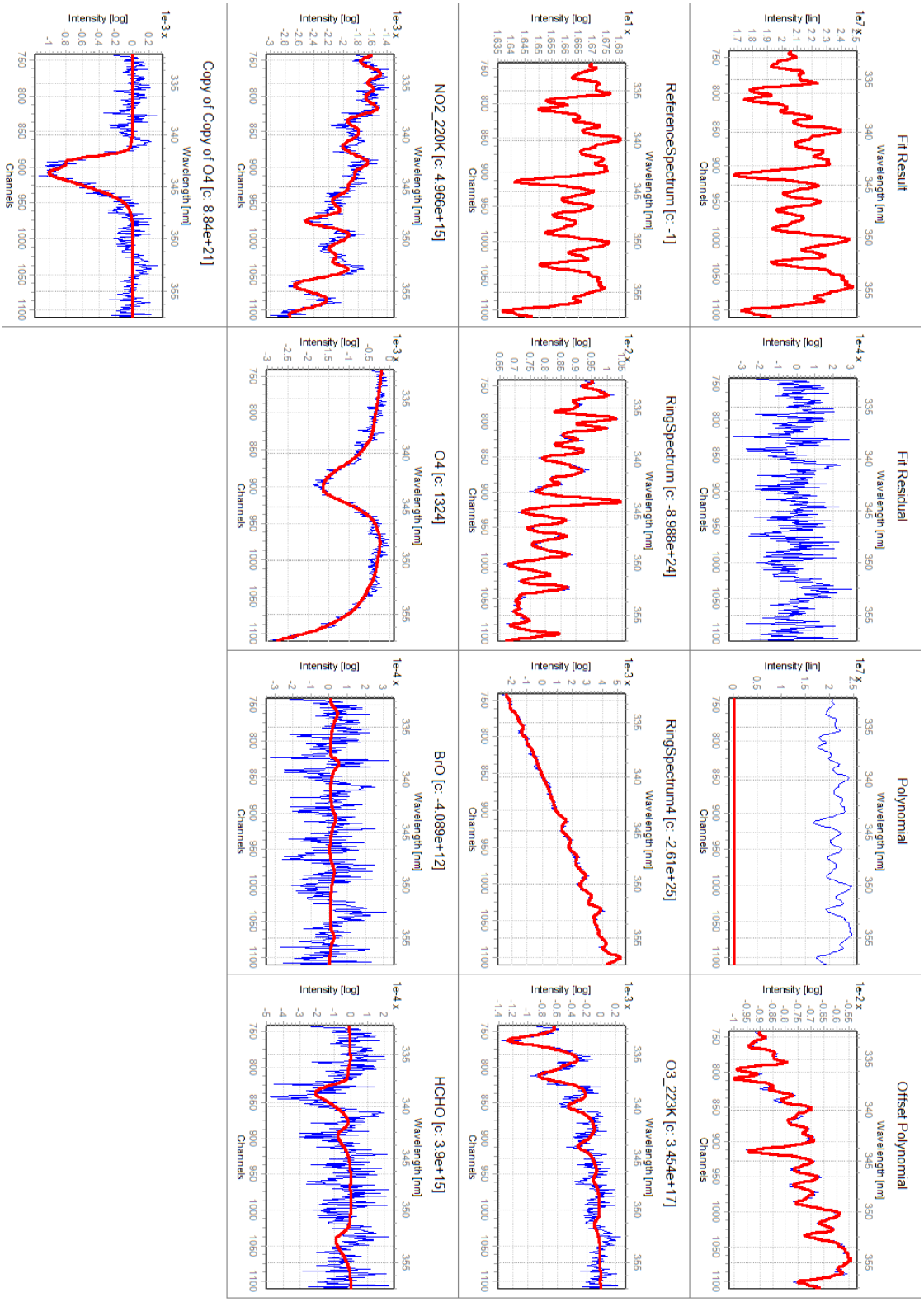

Figure A.4.: Same data as shown in figure A.3, but corrected with a smaller peak than O_4, derived the O_2B absorption band.

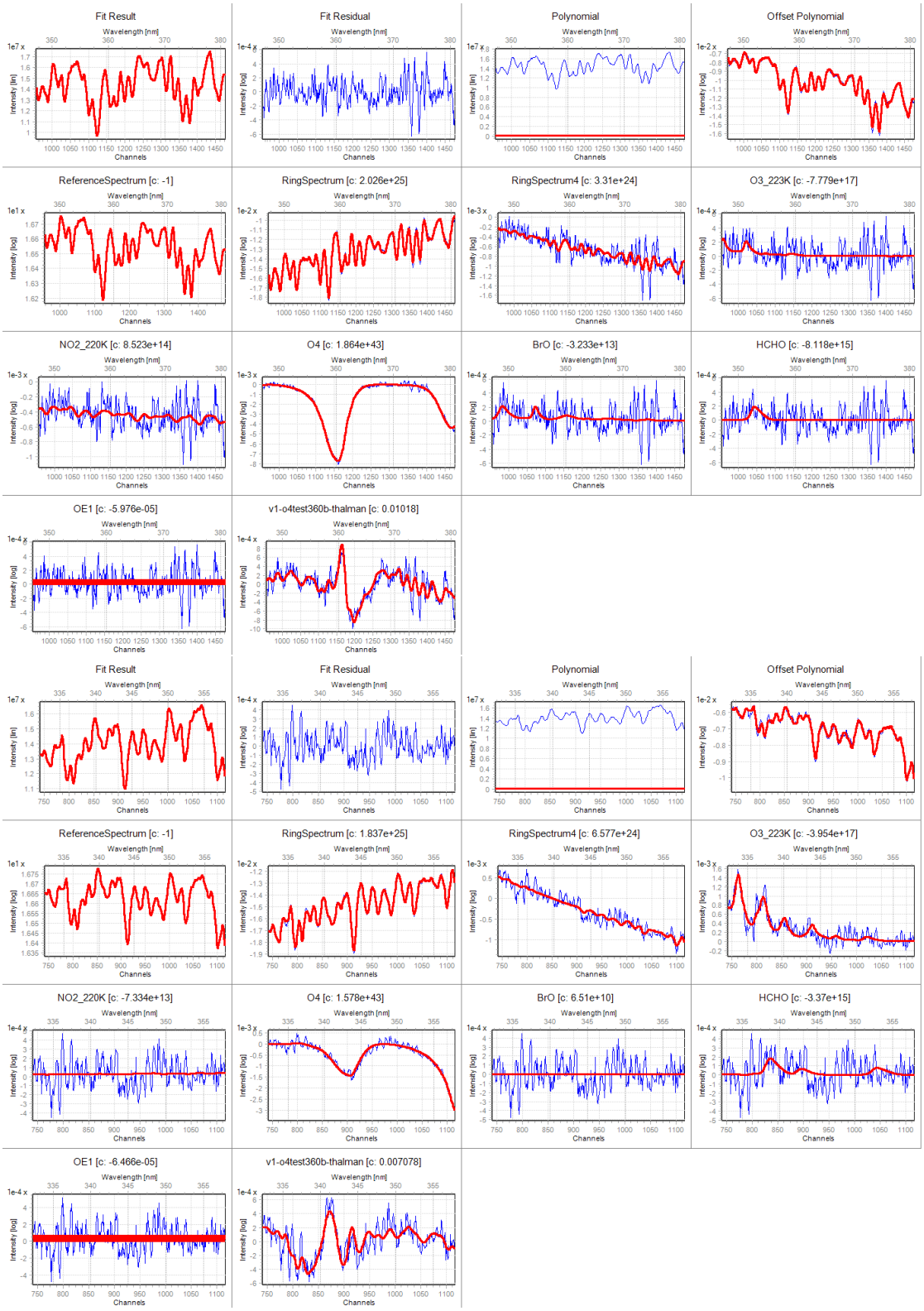

Figure A.5.: The residual spectral structure V1 taken from principal component analysis of MAX-DOAS analysis from SOPRAN M91 was used here for the analysis of MAX-DOAS data from Polarstern ANT28, convoluted with the instrument function to account for the lower spectral resolution.

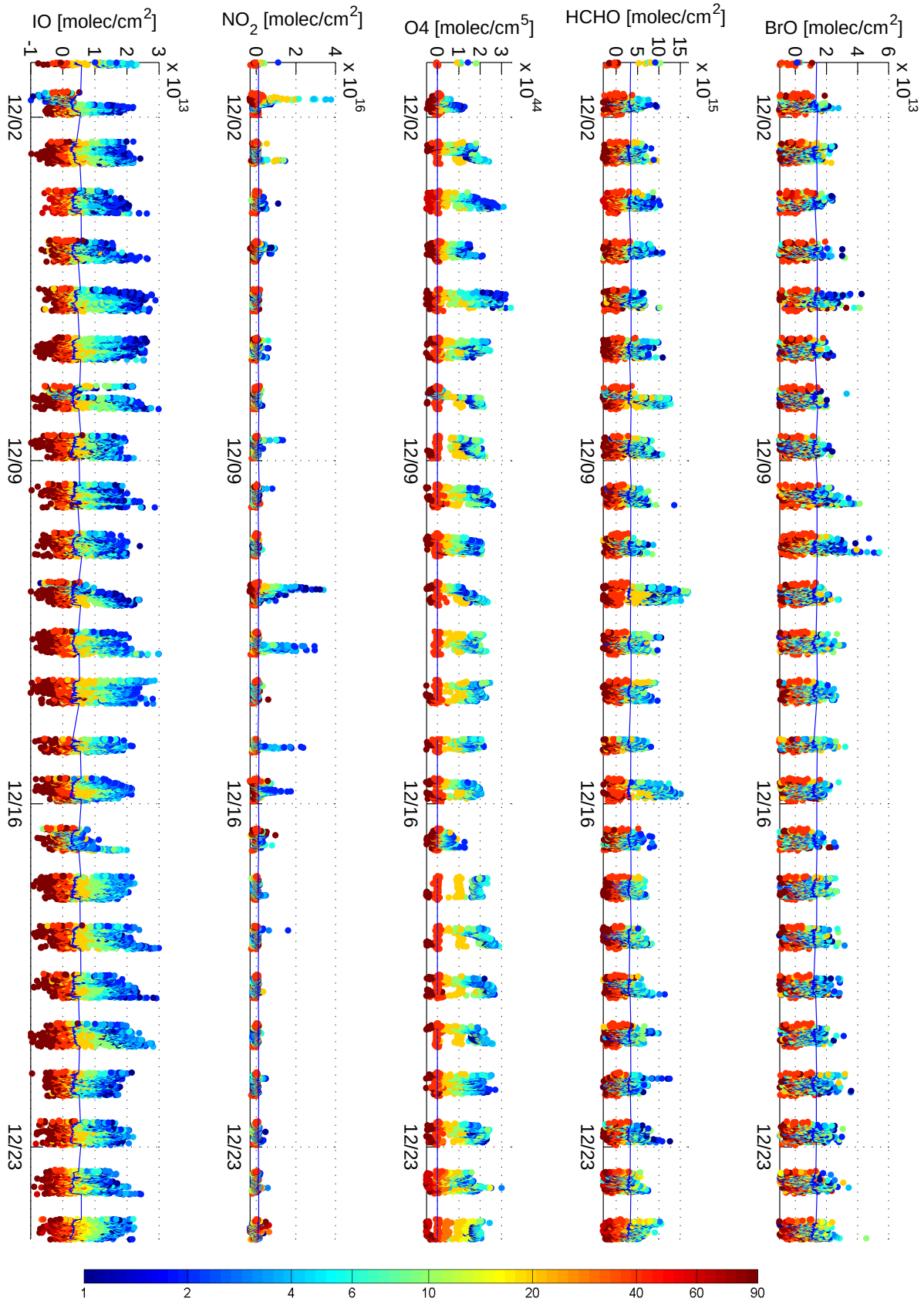

Figure A.6.: MAX-DOAS data from M91 for BrO, HCHO, O_4, NO_2 and IO for the complete duration of the cruise. The blue line indicates the fit error doubled, as estimate for the measurement error.

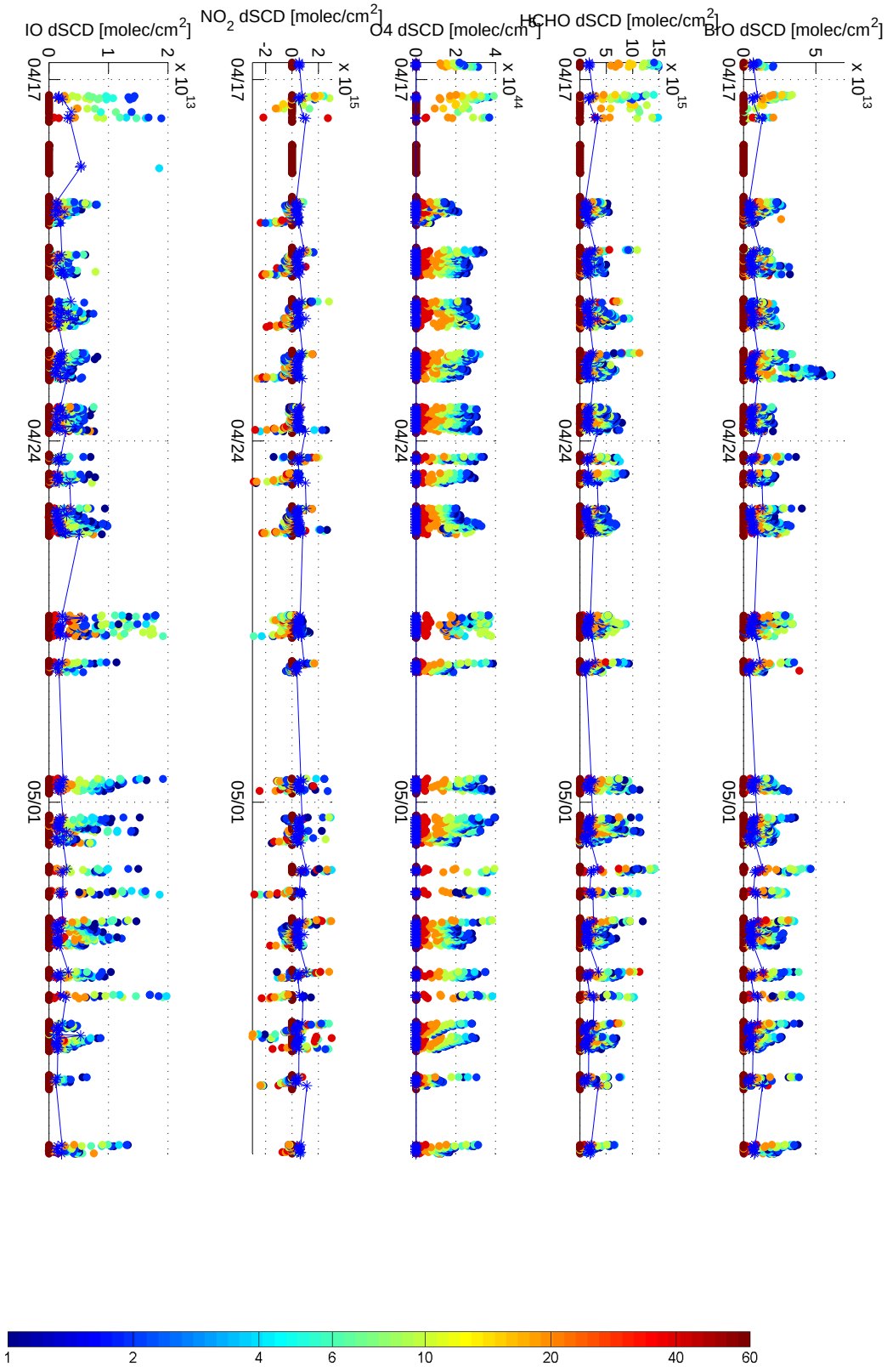

Figure A.7.: Cruise leg MSM 18/1 time series until May 5th, 2011. MSM 18/1 is not shown, due to large spectral shifts.

B. SHIVA campaign Malaysia 2012

Stratospheric Ozone: Halogen Impacts in a Varying Atmosphere (SHIVA) was an international research project supported by the 7th Framework programme of the European Union. By combining measurements from land, ship, aircraft, and space-based platforms and numerical modeling approaches the overall aim of the project was the quantification of the impact of Ozone depleting substances in the stratosphere and to quantify their sources and release mechanisms.

As for DOAS observations, ship-based MAX-DOAS and CE-DOAS measurements were conducted. Also a MAX-DOAS on Borneo measured tropospheric concentrations of various tracegases and a mini-DOAS on the research aircraft Falcon connected these measurements.

MAX-DOAS NO_2 data will be published in [Schreier et al., 2014, in prep.].

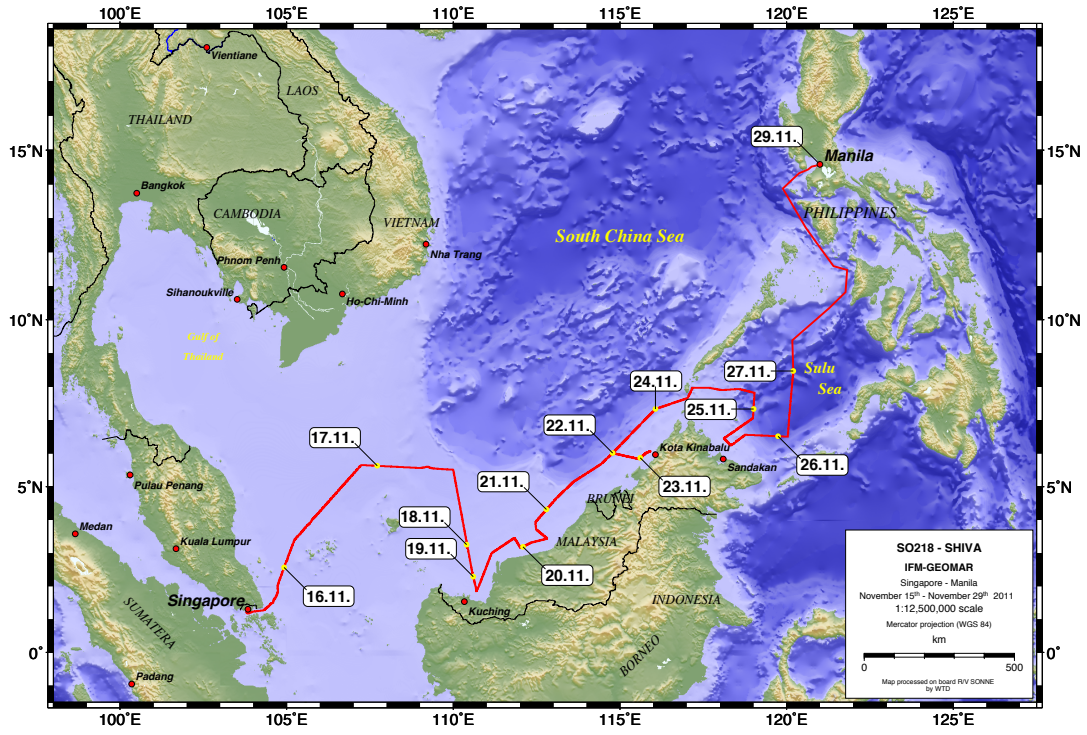

Figure B.1.: SHIVA Sonne SO218 cruise track.

Figure B.2.: The MAX-DOAS telescopes from Bremen and Heidelberg, looking into different directions, Bremen to starboard side, Heidelberg to portside.

B.1. Overview and other measurements

B.2. Results

B.2.1. MAX-DOAS

Due to technical problems with the Heidelberg MAX-DOAS which have been observed during evaluation of the spectra after the cruise, only the MAX-DOAS dataset from the University of Bremen is available. Both MAX-DOAS and the CE-DOAS setup were operated by one person, which left not much time to evaluate the MAX-DOAS spectra of the Heidelberg instrument onboard. Furthermore it was running fine before without any modifications during MSM18 (chapter 8).

B.2.2. CE-DOAS

A comparison to MAX-DOAS and LiF is shown in figure B.3.
CE-DOAS spectra were recorded at a time resolution of 30s, during the measurements of artificial IO the time resolution was lowered to three seconds. This maximum time resolution was used for NO_2 measurements.
For NO_2 a typical fit error was 24 ± 4 ppt for 3000s exposure time, as for 300s, since the dominant residual structure was systematic. The fit error could be decreased to 6ppt for 3000s exposure time (11 ± 6 ppt for 300s) by using night time residual spectra to obtain typical residual structures, but this procedure does not necessarily keep the absolute zero of the NO_2 VMR.
Typical fit errors of IO ranged from 0.16ppt for 26th-27th of November to 0.30ppt for 19th-23th of November. The reason is a longer light path during these periods due to cleaner mirrors and better alignment. On 26th and 27th, all measurements were in agreement with zero, the standard deviation of the data points was a factor of 2-3 higher than the fit error. Data for correction spectra was obtained by PCA from night-time spectra. This implies that this result only tells us that the day-night difference is smaller than 0.45ppt for these days.
The data from 19th to 23rd on the other side shows a diurnal cycle, with IO mixing ratios roughly a ppt higher during daytime than during the night. During this time also more night-time spectra were available to obtain reliable spectra for compensation of residual structures. The mixing ratio of 1ppt agrees with the few data points from MAX-DOAS observations during this time.

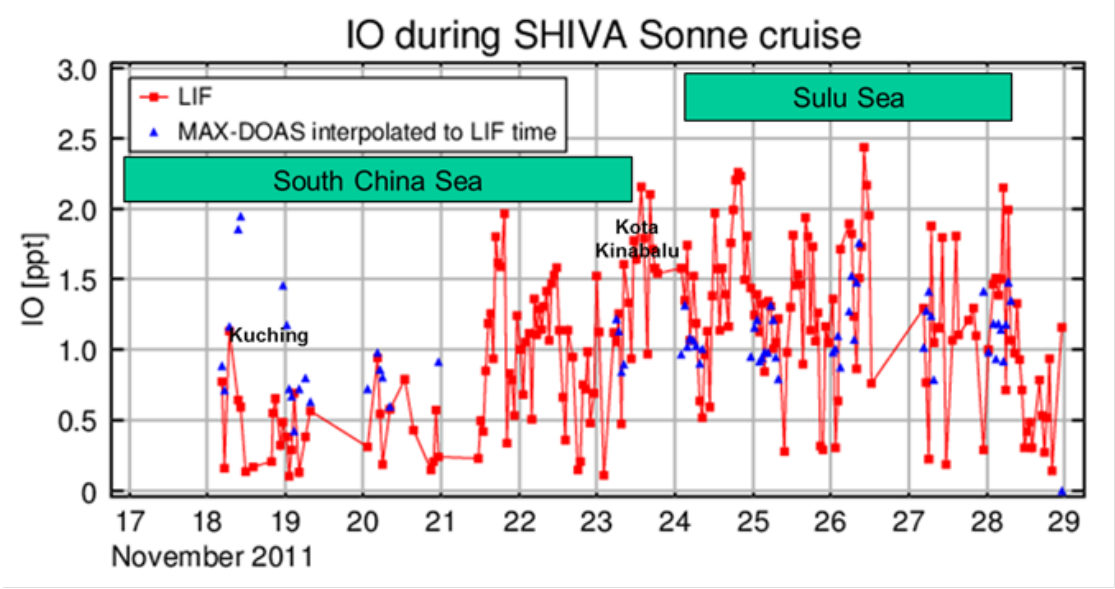

Figure B.3.: MAX-DOAS and LiF [Bloss et al., 2003] derived IO mixing ratios during SHIVA. The CE-DOAS setup did not detect any IO above the detection limit of 1ppt. Based on a plot from Folkard Wittrock, IUP Bremen, Wittrock et al. [2013].

B.2.2.1. Measurements of artificial IO

Together with Hannah Walker and Trevor Ingham (University of Leeds) measurements of artificially produced IO were performed using CH_3I, N_2O and N_2 [Walker, 2013].

$$N_2O + h\nu \longrightarrow O(^1D) + N_2 \quad \text{(B.1)}$$
$$O(^1D) + N_2 \longrightarrow O(^1P) + N_2 \quad \text{(B.2)}$$
$$O(^1P) + CF_3I \longrightarrow IO + CF_3 \quad \text{(B.3)}$$

Due to the open setup of the CE-DOAS instrument, no quantitative measurements were possible. With VMR of up to 10 ppt these were the only measurements of IO during the whole cruise of the CE-DOAS instrument clearly above detection limit. These measurements provide the possibility to test, if there would be actually IO, the wavelength calibration of the absorption spectra relative to each other. These measurements showed that water vapour absorption with $\tau_{H_2O} \approx 7 \cdot 10^{-3}$ and NO_2 absorption with $\tau_{NO_2} \approx 2.5 \cdot 10^{-2}$ were found independently by the fit within 0.03nm, water vapor and IO with an absorption with $\tau_{IO} \approx 1 \cdot 10^{-3}$ within 0.03nm.

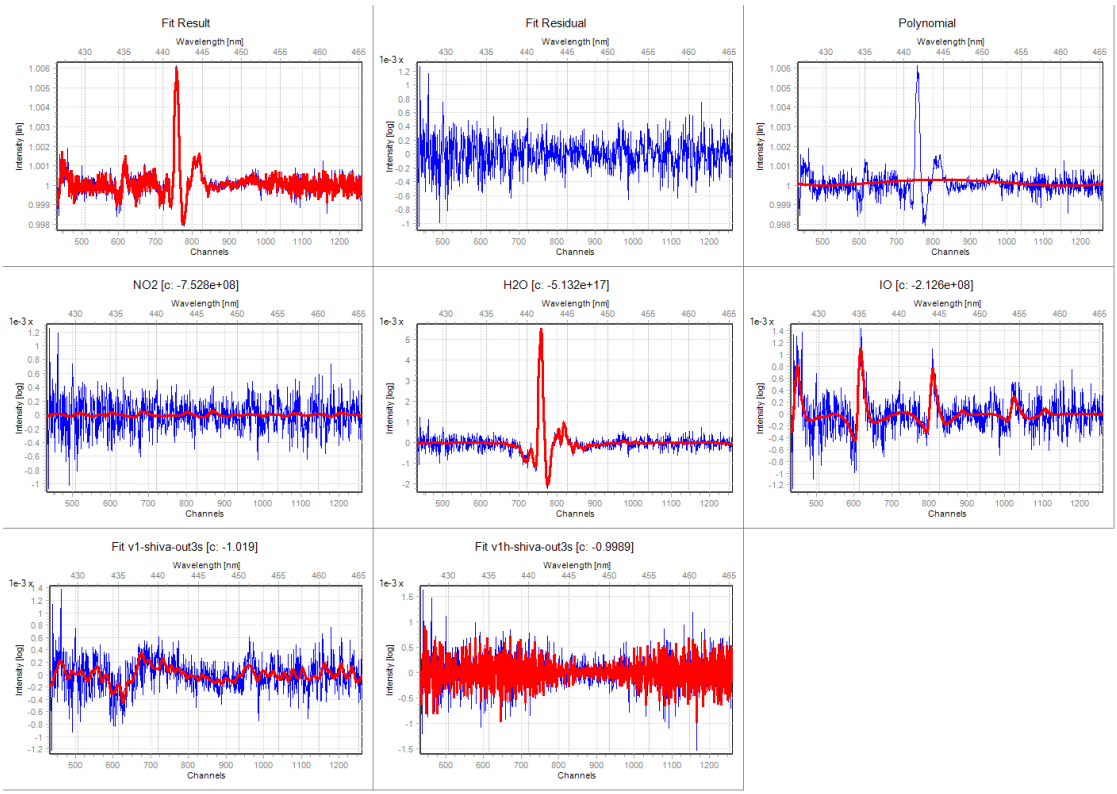

Figure B.4.: Fit of a spectrum from a measurements of artificially produced IO during the SHIVA campaign. The lowermost two spectra were extracted from nighttime measurements for the dominating optical and non optical contributions to the residual (see subsection 3.3.2). The observed IO concentration within the resonator was 10 ± 0.3 ppt, here at a time resolution of 5 minutes.

Name	typ. fit error	VMR IO	Date
tape2	0.155	0.1 ± 0.46 ppt	Nov. 26th
out3s	0.1	-0.07 ± 0.26 ppt	Nov. 27th
out1	0.3	0-1 ppt	Nov 19th – Nov. 23rd

Table B.1.: Overview measurement periods of the CE-DOAS during SHIVA, averaged to a time resolution of 30 min.

C. Acronyms

AMF	Air Mass Factor
Bhv	Bremerhaven
BMBF	Bundesministerium für Bildung und Forschung
CCD	Charge-Coupled Device
CCN	Cloud Condensation Nuclei
Chla	Chlorophyll-a
CE-DOAS	Cavity Enhanced Differential Optical Absorption Spectroscopy
CTD	Conductivity Temperature Density
CVAO	Cape Verde Atmospheric Observatory
CVOO	Cape Verde Ocean Observatory
DIC	Dissolved inorganic carbon
DMS	Dimethyl sulfide
DMSO	Dimethyl sulfoxide
DMSP	Dimethylsulfoniopropionate
DOAS	Differential Optical Absorption Spectroscopy
DOM	Dissolved Organic Matter
dSCD	Differential Slant Column Density
DU	Dobson Unit
FWHM	Full Width Half Maximum
HaloCaVe	HALogens On Cape Verde
ICA	Independent Component Analysis
IVOC	Iodinated Volatile Organic Compound
LiF	Laser-Induced Fluorescence
LIP	Laser-Induced Phosphorescence
LP-DOAS	Longpath Differential Optical Absorption Spectroscopy
MAD-CAT	**M**ulti **A**xis **D**oas - **C**omparison campaign for **A**erosols and **T**race gases
MAX-DOAS	Multi AXis Differential Optical Absorption Spectroscopy
MEMS	Microelectromechanical systems
MBL	Marine Boundary Layer
MPIC	Max Planck-Institute for Chemistry
MSM	Maria S. Merian
NMVOC	Non-Methane Volatile Organic Compound
OD	Optical Density
ODE	Ozone Depletion Event
OMZ	Oxygen Minimum Zone
OVOC	Oxygenated Volatile Organic Compound

PBL	Planetary Boundary Layer
PCA	Principal Component Analysis
PDF	Probability Density Function
ppq	parts per quadrillion (10^{15})
ppt	parts per trillion (10^{12})
ppb	parts per billion (10^{9})
ppm	parts per million (10^{6})
RANSAC	RANdom SAmple Consensus
RHS	Reactive Halogen Specie
RMS	Root Mean Square
RRS	Rotational Raman Scattering
RZA	Relative Solar Azimuth Angle
SOA	Secondary Organic Aerosol
SAA	Solar Azimuth Angle
SCD	Slant Column Density
SCIAMACHY	Scanning Imaging Absorption Spectrometer for Atmospheric CHartographY
SHIVA	Stratospheric Ozone: Halogen Impacts in a Varying Atmosphere
SIFT	Scale-Invariant Feature Transform
SML	Surface MicroLayer
SOLAS	Surface Ocean Lower Atmosphere Studies
SOPRAN	Surface Ocean Processes in the Antropocene
SST	Sea Surface Temperature
SZA	Solar Zenith Angle
TIC	Total inorganic Carbon
TOC	Total organic Carbon
VCD	Vertical Column Density
VOC	Volatile Organic Compound
VRS	Vibrational Raman Scattering
VRRS	Vibrational-rotational Raman Scattering
VSLS	Very Short-Lived Substance
XS	cross-section

D. Acknowledgements

Many people provided me with support, motivation and assistance over the past years, and without them measurement campaigns would not have turned out successful and this thesis would never have been completed (if that's possible to say about a thesis).
Vielen Dank / Thank you

- meinem Doktorvater Herr Prof. Ulrich Platt, für das Vertrauen und die Ruhe die jedem der Arbeitsgruppe entgegengebracht wird und für den Optimismus, dass auch auf dem offenen Ozean aus unseren Messungen noch mehr rauszuholen ist. Und für die vielen kleine Hinweise ('Da gab's vor 20 Jahren mal ne Diplomarbeit ...') zusammen mit vielen Überschlagsrechnungen.
- Herr Prof. Bernd Jähne für die spontane Übernahme des Zweitgutachtens.
- Thomas, Denis und Udo, für viele wichtige Fragen und Antworten.
- Jens, dessen Ruhe am Anfang meiner Zeit in der Umweltphysik bei der Erkenntnis dass das gesamte Spektrometersystem an einem Tag umzubauen ist viel gelehrt hat. Danke für die unterhaltsamen, guten und produktiven Kampagnen.
- Denis, für die gute Vorbereitung auf die CE-DOAS Messungen auf den Schiffen, und für das Hinterfragen vielerlei Messergebnisse
- Die Korrekturleser, auch wenn ich erst (zu) spät das Gefühl hatte irgendwas zumindestens halbfertiges weitergeben zu können: Vielen Dank an Florian, Joëlle, Peter, Udo, Denis, Stefan, Katja, Johannes Z. und Tilman
- Vielen Dank an Johannes Rogenhagen der trotz vielem Stress während der Liegezeit von Polarstern in Bremerhaven immer hilfreich zur Seite stand und während der Expeditionen den Kontakt zu den Bordelektronikern hielt. Vielen Dank auch an diese und nochmal eine Entschuldigung, dass es von unseren Messgeräten keinerlei detaillierten technischen Anleitungen zur Reparatur gibt - es sind halt alles Prototypen.
- Alle, die sich zeitweise um das MAX-DOAS auf Polarstern gekümmert haben, sei es auf See oder im Hafen: Stephan, Joelle, Martin, Sabrina, Jens, Udo, Fiete, Andrea
- Katja für die TransBrom Auswertungen die mit in die Weltkarten von IO und BrO einflossen
- Der ganzen Arbeitsgruppe, der offene Zusammenarbeit erst die guten Messungen erlaubt, immer eine nette Arbeitsatmosphäre bietet und erstaunliches leisten kann, gerade oder trotz der mehr oder minder chaotischen Struktur.
- Tim Deutschmann for providing McArtim, several discussions, his view on things far from the instrumental, measurement-influenced view, which can lead to reconsideration of 'evaluation habits' and his suggestions for the automatic wavelength calibration routine
- Klarerweise an das beste Büro der Welt! ... und Martin, Stefan und Lara für das volle Spektrum von dummen Witzen bis zu sinnvollen Diskussionen
- Karl-Heinz Schmidt für die Bereitschaft mit nach Bremerhaven zu kommen und für die unkomplizierte Zusammenarbeit
- an Johannes Z. der mir hoffentlich die schlimmsten Sensitivitätsstudien zum MAX-DOAS Profilretrieval in the letzten Wochen vorenthalten hat
- All scientists onboard different ships during different cruises for helping, valuable discussions and a good time onboard. Especially, thanks to Trevor and Hannah during SHIVA for keeping an optimistic and humorous view on the life onboard.
- Das IUP in Bremen und inbesondere dort Folkard Wittrock, Enno Peters und Anja Schönhardt für die nette Zusammenarbeit bei SHIVA, MAD-CAT und Satelliten IO

- 'Hermann Bungee, Steven Foolbridge and the Gang' for having a great campaign in the Peruvian upwelling
- Luis Mendes and Alder for support of the measurements on CVAO - It was always nice to work on the station with you!
- Rosie Chance for providing her compilation of iodide data.
- Annette Kock and Evgenia Ryabenko for taking care of the MAX-DOAS measurement during M77
- All crews on the ships for supporting the scientific work and welcoming the scientists in 'their home'
- Chief scientists and their 'assistants' onboard of the respective ships due to their role of keeping up the good mood on a ship when everybody is sleep-deprived and 'running on autopilot'
- meine Eltern und Großeltern für die Unterstützung während des Studiums und der Promotion. Und ja, Oma, irgendwann arbeite ich vielleicht auch Vollzeit ;-)
- Andrea, die mich unterstützt hat, die vielen Messkampgnen akzeptiert und auch selbst viel auf sich genommen hat damit ich meine Arbeit hier abschließen konnte.